Journal of Experimental and Theoretical Physics, Vol. 94, No. 3, 2002, pp. 453–458.
Translated from Zhurnal Éksperimental'noĭ i Teoreticheskoĭ Fiziki, Vol. 121, No. 3, 2002, pp. 531–537.

GRAVITATION, ASTROPHYSICS

Nonthermal Radiation of Rotating Black Holes

R. V. Korkin* and I. B. Khriplovich**

Budker Institute of Nuclear Physics, Siberian Division, Russian Academy of Sciences, pr. Akademika Lavrent'eva 11, Novosibirsk, 630090 Russia
Novosibirsk State University, Novosibirsk, 630000 Russia
** e-mail: korkin@vxinpz.nsk.su*
*** e-mail: khriplovich@inp.nsk.su*
Received August 15, 2001

Abstract—The nonthermal radiation of a Kerr black hole is considered as the tunneling of particles being produced through an effective Dirac gap. In the leading semiclassical approximation, this approach is also applicable to bosons. Our semiclassical results for photons and gravitons are consistent with those obtained previously. For neutrinos, the result of our complete quantum-mechanical calculation is about twice as large as the previous one. © *2002 MAIK "Nauka/Interperiodica"*.

1. INTRODUCTION

The amplification of an electromagnetic wave as it reflects from a rotating black hole, so-called superradiation, was predicted by Zel'dovich [1] and Misner [2]. Subsequently, this effect was studied in detail by Starobinsky and Churilov [3] for electromagnetic and gravitational waves (see also [4]). It seems obvious enough that, if the amplification of a wave is possible during its reflection, then its generation by a rotating black hole is also possible. Indeed, a direct calculation by Page [5] has shown that the nonthermal radiation being discussed does exist not only for bosons, photons, and gravitons but also for neutrinos. The latter result appears somewhat puzzling, because there is no superradiation for fermions.

Here, we consider these processes from a different perspective, more specifically, as the tunneling of quanta being produced through an effective Dirac gap. Of course, this approach by itself is applicable to fermions alone. It is clear, however, that the production of fermions and bosons in the leading semiclassical approximation is described by the same (to within the spin statistical weight) relations.

Note that, in their recent paper [6] (it became known to us after this paper had been written), Calogeracos and Volovik considered a similar mechanism for describing the friction experienced by a rotating body in a superfluid at $T = 0$: the quantum tunneling of quasiparticles into the region where their energy in a rotating frame is negative.

Our semiclassical results for photons and gravitons are in reasonable qualitative agreement with the calculation [5]. It would be unreasonable to expect close quantitative agreement here, because the action inside the barrier for the most significant partial waves exceeds unity only slightly, if at all. As for neutrinos, the imaginary part of the action for them at the total angular momenta of major importance is appreciably smaller than unity. Therefore, we performed a complete numerical quantum-mechanical calculation of the effect for the spin $s = 1/2$. Here, our result is about twice that presented in [5]. Unfortunately, because of the lack of details in [5], we cannot establish the cause of this discrepancy.

2. SCALAR FIELD

We begin with a problem that is basically of methodological interest rather than of direct physical interest, with the radiation of scalar massless particles by a rotating black hole.

We start the semiclassical solution of the problem with the standard Hamilton–Jacobi equations for the motion of a massless particle in a Kerr field (see, e.g., [7]):

$$\left(\frac{\partial S_r(r)}{\partial r}\right)^2 = -\frac{\kappa^2}{\Delta} + \frac{[(r^2+a^2)\varepsilon - a l_z]^2}{\Delta^2}, \qquad (1)$$

$$\left(\frac{\partial S_\theta(\theta)}{\partial \theta}\right)^2 = \kappa^2 - \left(a\varepsilon\sin\theta - \frac{l_z}{\sin\theta}\right)^2. \qquad (2)$$

Here, $S_r(r)$ and $S_\theta(\theta)$ are the radial and angular actions, respectively;

$$\Delta = r^2 - r_g r + a^2, \quad r_g = 2kM;$$

$\mathbf{a} = \mathbf{J}/M$ is the angular momentum of the black hole, in units of its mass M; ε is the particle energy; and l_z is the projection of the particle angular momentum onto $\mathbf{a}$ (the speed of light c is assumed to be unity everywhere).

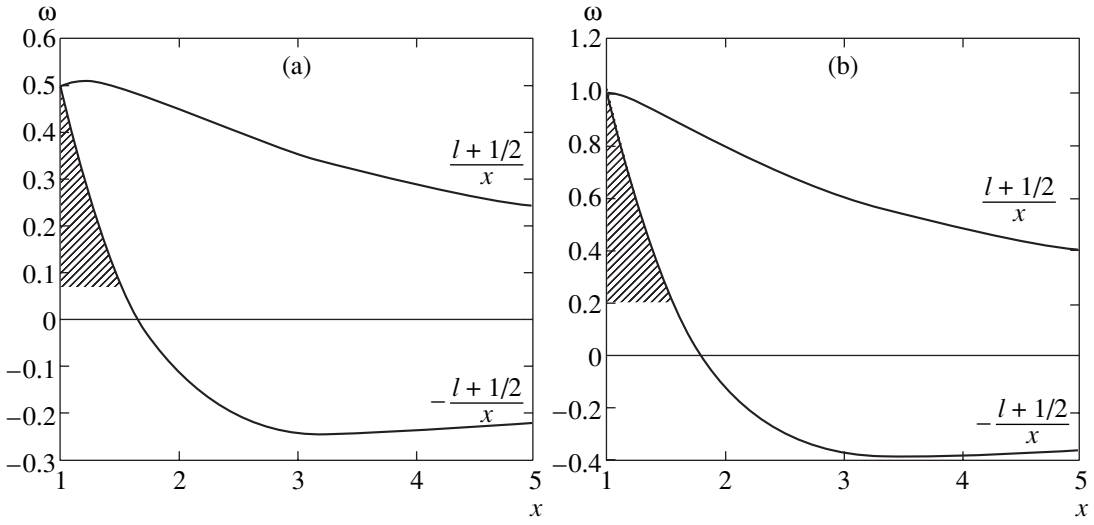

Fig. 1. The energy gap for (a) $l = 1$and (b) $l = 2$.

As for the constant κ^2 of the separation of variables, it is equal to the particle angular momentum squared $\mathbf{l}^2$ in the spherically symmetric limit $a \longrightarrow \infty$, or to $l(l+1)$ in quantum mechanics (the Planck constant $\hbar$ is also assumed to be unity everywhere). The influence of the black-hole rotation, i.e., finite a, on κ^2 is taken into account by using perturbation theory applied to Eq. (2). The result is [3]

$$\kappa^2 = l(l+1) - 2\omega\alpha l_z + \frac{2}{3}\omega^2\alpha^2\left[1 + \frac{3l_z^2 - l(l+1)}{(2l-1)(2l+3)}\right]. \quad (3)$$

Here and below, we use the dimensionless variables

$$\omega = \varepsilon kM, \quad x = r/kM, \quad \alpha = a/kM.$$

Recall that the following substitution should be made in the semiclassical approximation:

$$l(l+1) \longrightarrow (l+1/2)^2.$$

Furthermore, in the exact quantum-mechanical problem, when reducing the radial wave equation to canonical form,

$$R'' + p^2(r)R = 0,$$

additional [compared to the right-hand side of Eq. (1)] nonclassical terms emerge in the expression for $p^2(r)$, which, strictly speaking, should have been included at $l \approx 1$. However, in what follows, we discard these nonclassical corrections to $p^2(r)$, which does not qualitatively affect our results.

Figure 1 shows the dependence of the boundaries of the classically inaccessible region, where the radial momentum squared p^2 is negative, on distance x for various orbital angular momenta. The gap vanishes on the horizon [8]. When $r \longrightarrow \infty$, the boundaries of the classically inaccessible region behave as $\pm(l+1/2)/r$. In other words, in a sense, the centrifugal term for massless particles acts as the mass squared. Note that, for $l > 1$, both branches of the equation $p^2(r) = 0$ fall, while, at $l = 1$, one branch near the horizon rises and the other falls. Thus, the radiation mechanism is tunneling, the escape of particles from the hatched region to infinity.

Note the analogy between the radiation of charged particles by a charged black hole and the effect under discussion. In the former case, the radiation is attributable to Coulomb repulsion, while, in the case considered here, it is attributable to the repulsive interaction between the particle and black-hole angular momenta [9].

The action inside the barrier for the radial equation (1) is

$$|S_r| = \int dx \sqrt{\frac{k^2}{(x-1)^2} - \frac{[\omega(x^2+1) - l_z]^2}{(x-1)^4}}, \quad (4)$$

the integral being taken between two turning points. For the time being, we restrict ourselves to the case of an extreme black hole, $a = kM$. Note that because of the singular dependence of p on x, the action inside the barrier does not vanish at $l > 1$ even for the maximum energy $\omega = l_z/2$. It remains all the more finite at $l = 1$ [cf. Figs. 1a and 1b].

The repulsive interaction is proportional to the projection l_z of the particle angular momentum and enters into the tunneling probability in the exponent, while the barrier depends on the orbital angular momentum l itself. Therefore, it is clear that particles with l_z close to l will mainly contribute to the effect. Our numerical calculation shows that the contribution of states with $l_z \neq l$ may be disregarded altogether. In addition, since the action inside the barrier decreases with increasing

energy, particles with energy close to the maximum one mainly contribute to the effect.

Unfortunately, an analytic calculation of the action inside the barrier cannot be performed to completion even for an extreme black hole. Therefore, to get a qualitative idea of how the effect behaves, we make use of a simplified expression for κ^2:

$$\kappa^2 = l^2 + l - 2\omega l + \omega^2. \quad (5)$$

[The results of a more accurate numerical calculation using expression (3) are presented below.] In this approximation, a simple analytic formula for the action inside the barrier can be derived for all angular momenta except $l = 1$. Let

$$\omega = \frac{l}{2}(1 - \delta),$$

where $\delta \ll 1$; precisely this energy range gives the largest contribution to the radiation. The turning points of interest, which lie to the right of the horizon, are then

$$x_{1,2} = 1 + \frac{2\delta}{2 \pm \sqrt{1 + 4/l}}. \quad (6)$$

We now easily find that

$$|S_{an}| = \frac{\pi l}{2}\left(2 - \sqrt{3 - \frac{4}{l}}\right). \quad (7)$$

It is easy to see from this expression for the action that the term l (following l^2) in formula (5) is significant even for large angular momenta: it generates the terms $4/l$ in formulas (6) and (7), increasing $|S|$ for $l \gg 1$ by $\pi/\sqrt{3}$. Accordingly, the transmission coefficient

$$D = \exp(-2|S|)$$

decreases approximately by a factor of 40. Note that even the transition in κ^2 from $l(l + 1)$ to $(l + 1/2)^2$ appreciably reduces the effect for l comparable to unity; however, this suppression disappears at large angular momenta.

It follows from formula (7) that the action inside the barrier is large; it monotonically increases with l starting from $|S| = \pi$ at $l = 2$. As for $l = 1$, a comparison of Figs. 1a and 1b shows that the barrier here is wider than at $l = 2$ and, accordingly, the action must be larger. Indeed, our numerical calculation of the action inside the barrier $|S|$ with κ^2 given by formula (3) confirms these estimates. Its results are presented in Table 1, where the analytic estimates $|S_{an}|$ with formula (5) are also given for comparison. Incidentally, this comparison shows that the approximate analytic formula (5) is good. The numbers in Table 1 refer to an extreme black hole and to the maximum energy of the emitted particles. It is clear, however, that the passage to nonextreme black holes, lower energies, and larger l only causes the action inside the barrier to increase. Since the action here proves to be always larger than unity, it is quite reasonable to use the semiclassical approximation inside the barrier.

Table 1. The action inside the barrier for scalar particles

l	1	2	3
$\|S\|$	3.45	3.15	3.33
$\|S_{an}\|$		3.14	3.34

Let us now check whether it is applicable to the left of the barrier. The corresponding condition takes the usual form

$$\frac{d}{dx}\frac{1}{p(x)} \ll 1. \quad (8)$$

In other words, the minimum size of the initial wave packet to the left of the barrier should not exceed the distance from the horizon to the turning point. Near the horizon, we may disregard the term related to the centrifugal barrier in the expression for momentum $p(x)$, so that

$$\frac{d}{dx}\frac{1}{p(x)} \approx \frac{d}{dx}\frac{(x-1)^2}{\omega(x^2 + \alpha^2) - \alpha l}.$$

It is easy to verify that, for moderately large l, which are of importance in our case, this expression is comparable to unity and condition (8) is not satisfied. Nevertheless, despite this circumstance and the neglect of the nonclassical corrections to $p^2(r)$ mentioned above, the results of our semiclassical calculation presented below are qualitatively correct.

Let us turn back to the calculation of the radiation intensity. The radial current density of free particles in the energy range $d\varepsilon$ for $r \longrightarrow \infty$ is

$$j_r(\varepsilon, l)d\varepsilon = \sum \frac{d^3p}{(2\pi)^3}\frac{\partial\varepsilon}{\partial p_r} = \sum_{l, l_z}\frac{2\pi dp_r}{(2\pi)^3 r^2}\frac{\partial\varepsilon}{\partial p_r}. \quad (9)$$

Indeed, the initial summation here reduces to integration over the azimuthal angle of vector $\mathbf{l}$, which gives 2π, and to allowance for the contributions of all projections l_z of the orbital angular momentum. In our cases, as was already pointed out, it will suffice to take into account only one of them, $l_z = l$. Using the identity

$$\frac{\partial\varepsilon}{\partial p_r}dp_r = d\varepsilon,$$

we find that the total flux of free particles for $r \longrightarrow \infty$ is

$$4\pi r^2 j_r(\varepsilon, l) = 4\pi r^2 \sum_{l_z}\frac{2\pi}{(2\pi)^3 r^2} \longrightarrow \frac{1}{\pi}. \quad (10)$$

It can be easily seen that the total flux of the emitted particles in our problem differs from the latter expression only by the barrier penetration factor. Thus, in our

Table 2. The losses of mass (in units of $10^{-3}/\pi M^2$) and angular momentum (in units of $10^{-3}/\pi M$) through the radiation of scalar particles

α	$\lvert dM/dt\rvert$	$\lvert dJ/dt\rvert$
0.999	2.6	6.4
0.9	0.19	0.77

Table 3. The action inside the barrier for photons and gravitons

	$s = 1$		$s = 2$	
j	1	2	2	3
$\lvert S\rvert$	1.84	2.17	1.0	1.7

semiclassical approximation, we derive the following expression for the mass loss by a black hole per unit time:

$$\frac{dM}{dt} = \frac{1}{\pi}\sum_{l=0}^{\infty}\int_0^{\varepsilon_{\max}} \varepsilon \exp(-2|S(\varepsilon, l)|)d\varepsilon. \qquad (11)$$

Here, the maximum energy of the emitted quanta is

$$\varepsilon_{\max} = \frac{al}{r_h^2 + a^2}, \qquad (12)$$

where

$$r_h = kM + \sqrt{k^2M^2 - a^2}$$

is the radius of the horizon of a Kerr black hole.

The analogous expression for the loss of angular momentum is

$$\frac{dJ}{dt} = \frac{1}{\pi}\sum_{l=1}^{\infty}\int_0^{\varepsilon_{\max}} l \exp(-2|S(\varepsilon, l)|)d\varepsilon. \qquad (13)$$

The losses of mass and angular momentum by a black hole numerically calculated for different rotation parameters α from formulas (11) and (13) are given in Table 2. Here and below, we present, for spinning particles, only the results for sufficiently rapid rotation, $\alpha \approx 1$. The point is that as α decreases further, the thermal radiation not only rapidly increases in intensity but the effect being discussed also decreases even more rapidly. Since this effect becomes much smaller than the thermal one for smaller α, there is little sense in considering it there.

As we see from Table 2, the rate of angular-momentum loss by a black hole is higher, in comparable units, than its mass loss rate. In fact, this immediately follows from expression (12). Even from this expression, we can see that the ratio of the corresponding numbers is 2 : 1 even for the maximum possible energy. The actual ratios are even larger. Hence, the following important conclusion can be drawn: extreme black holes do not exist. Even if an extreme black hole were formed somehow, it would immediately become nonextreme during the radiation.

3. THE RADIATION OF PHOTONS AND GRAVITONS

We begin our investigation of the radiation of real particles with an electromagnetic field. A photon has two modes of different parity: the so-called electric mode with $l = j \pm 1$ and the magnetic mode with $l = j$ [10]. It follows from duality invariance that the radiation intensities for these two modes are equal. Therefore, it will suffice to restrict our analysis to solving the problem for the magnetic mode and then double the result.

It can be shown that the situation with gravitational waves is similar. Again, there are two modes, which, in view of specific duality, contribute equally to the radiation, with $l = j$ for one of these modes.

Clearly, the radial equation for the mode with $l = j$ in the semiclassical approximation is the same as that for the scalar field, but with a different κ^2. This can also be shown based on the so-caller Teukolsky equation [11] [again, disregarding the nonclassical corrections to $p^2(r)$]. The eigenvalues of the angular equation for particles with spin s, which were also obtained here using perturbation theory, are [3]

$$\begin{aligned}\kappa^2 = {} & j(j+1) + \frac{1}{4} - 2\alpha\omega j_z - \frac{2\alpha\omega j_z s}{j(j+1)} \\ & + \alpha^2\omega^2\left\{\frac{2}{3}\left[1 + \frac{3j_z^2 - j(j+1)}{(2j-1)(2j+3)}\right]\right. \\ & - \frac{2s^2}{j(j+1)}\frac{3j_z^2 - j(j+1)}{(2j-1)(2j+3)} \\ & + 2s^2\left[\frac{(j^2-s^2)(j^2-j_z^2)}{j^2(2j-1)(2j+1)}\right. \\ & \left.\left. - \frac{((j+1)^2 - j_z^2)((j+1)^2 - s^2)}{(j+1)^3(2j+1)(2j+3))}\right]\right\}. \end{aligned} \qquad (14)$$

This expression includes the term 1/4, which is needed for the correct semiclassical description. Note that the constraint $j \geq s$ follows from an analysis of the helicity of a massless particle. Accordingly, $j \geq 1$ for a photon and $j \geq 2$ for a graviton. Just as in the scalar case, the states with the maximum projection of the angular momentum, $j_z = j$, mainly contribute to the radiation.

Let us first discuss whether the semiclassical approximation is applicable here. As for the situation to the left of the barrier, it does not differ qualitatively from the scalar case. The situation inside the barrier is

different. As we see from Eq. (14), the presence of spin causes κ^2 and, accordingly, the centrifugal repulsion to decrease. As a result, the barrier, along with the action inside it, also decreases. This qualitative result is confirmed by our numerical calculation of $|S|$ for photons and gravitons with the maximum projection of the angular momentum $j_z = j$ and the maximum energy for an extreme black hole (see Table 3). Thus, one might expect the accuracy of the semiclassical results to be lower here than that in the scalar case.

The semiclassical formulas for electromagnetic and gravitational radiation formally differ from the corresponding scalar formulas (11) and (13) only by the extra factor 2, which reflects the existence of two modes. The results of this calculation are presented in Table 4. For comparison, this table gives (in parentheses) the results of a complete quantum-mechanical calculation [5], which also takes into account the thermal radiation.

We see from Table 4 that our semiclassical calculation agrees with the complete one only qualitatively even for $\alpha = 0.999$, when the thermal radiation is negligible. This is no surprise, considering that the semiclassical action in the problem under consideration exceeds unity only slightly, if at all. This explanation is supported by the fact that, for a photon, where $|S|$ is appreciably larger (see Table 3), the agreement between the semiclassical and complete calculations is considerably better.

4. THE RADIATION OF NEUTRINOS

Finally, let us consider the radiation of neutrinos, massless particles with spin 1/2, by a rotating black hole. The wave function of a two-component neutrino can be written as (see, e.g., [5])

$$\psi = \exp(-i\varepsilon t + i j_z \phi)\begin{pmatrix} R_1 & S_1 \\ R_2 & S_2 \end{pmatrix}. \qquad (15)$$

It is important that, in the Kerr metric, the wave equations for neutrinos also allow for the separation of variables [11]. The radial equations in dimensionless variables are

$$\begin{aligned} \frac{dR_1}{dx} - i\frac{\omega(x^2+\alpha^2) - j_z\alpha}{\Delta}R_1 &= \frac{\kappa}{\sqrt{\Delta}}R_2, \\ \frac{dR_2}{dx} + i\frac{\omega(x^2+\alpha^2) - j_z\alpha}{\Delta}R_2 &= \frac{\kappa}{\sqrt{\Delta}}R_1. \end{aligned} \qquad (16)$$

The corresponding angular equations are

$$\begin{aligned} \frac{dS_1}{d\theta} + \left(\omega\alpha\sin\theta - \frac{j_z}{\sin\theta}\right)S_1 &= \kappa S_2, \\ \frac{dS_2}{d\theta} - \left(\omega\alpha\sin\theta - \frac{j_z}{\sin\theta}\right)S_2 &= -\kappa S_1. \end{aligned} \qquad (17)$$

Table 4. The losses of mass (in units of $10^{-3}/\pi M^2$) and angular momentum (in units of $10^{-3}/\pi M$) through the radiation of photons and gravitons

	$s = 1$		$s = 2$	
α	$\lvert dM/dt\rvert$	$\lvert dJ/dt\rvert$	$\lvert dM/dt\rvert$	$\lvert dJ/dt\rvert$
0.999	16.5 (9.6)	39 (24)	66 (228)	148 (549)
0.9	0.72 (2.26)	2.8 (8.2)	0.58 (12.9)	2 (48)

Table 5. The losses of mass (in units of $10^{-3}/\pi M^2$) and angular momentum (in units of $10^{-3}/\pi M$) through neutrino radiation

α	$\lvert dM/dt\rvert$	$\lvert dJ/dt\rvert$
0.99	4.4 (2.1)	11 (5.65)
0.9	0.7 (1)	2.7 (3.25)

The same formula (14) holds for κ^2 but now, of course, with $s = 1/2$. Just as for bosons, in practice, it will suffice to take into account the states with $j_z = j$.

It is essential that, at infinity (for $x \longrightarrow \infty$) and on the horizon (for $x \longrightarrow 1$), R_1 corresponds to a wave running to the right, while R_2 for $x \longrightarrow \infty$ and $x \longrightarrow 1$ corresponds to a wave running to the left. [For this classification of solutions, it is convenient to use the so-called "tortoise" coordinate $\xi(x)$; $\xi \approx x \longrightarrow +\infty$ for $x \longrightarrow \infty$ and $\xi \approx \ln(x-1) \longrightarrow -\infty$ for $x \longrightarrow 1$.] It is quite natural that the radial current density here is

$$j_r = |R_1|^2 - |R_2|^2.$$

We are interested in the probability of penetrating the barrier for the state that appears as an outgoing wave at infinity. For neutrinos or antineutrinos, this state has a fixed helicity but has no definite parity. Meanwhile, the potential barrier in our problem depends, roughly speaking, on the orbital angular momentum and, therefore, is much lower for the states with $l = j - 1/2$ than it is for the states with $l = j + 1/2$. (These states with a given l have a definite parity and are a superposition of neutrinos and antineutrinos.) Moreover, at $l = j - 1/2$ for the small j that mainly contribute to the radiation, the action either has no imaginary part at all or its imaginary part is small, so that our above approach is inapplicable. Therefore, we will numerically solve the exact problem of neutrino radiation.

Technically, it is convenient to determine the reflection coefficient R in the problem of neutrino scattering off a black hole and then use the obvious relation for the sought-for transmission coefficient D,

$$D = 1 - R.$$

In this case, the expressions for the losses of mass and angular momentum by a black hole are

$$\frac{dM}{dt} = \frac{1}{\pi}\sum_{j=1/2}^{\infty}\int_0^{\varepsilon_{\max}} \varepsilon D(\varepsilon, j)d\varepsilon, \quad (18)$$

$$\frac{dJ}{dt} = \frac{1}{\pi}\sum_{j=1/2}^{\infty}\int_0^{\varepsilon_{\max}} jD(\varepsilon, j)d\varepsilon, \quad (19)$$

$$\varepsilon_{\max} = \frac{aj}{r_h^2 + a^2}. \quad (20)$$

The results obtained by numerically solving the system of radial equations (16) are presented in Table 5. The results from [5], which include the contribution of Hawking radiation, are given in parentheses. For a nearly extreme black hole at $\alpha = 0.99$, where there is virtually no thermal radiation, our results are approximately twice as large as the previous ones.

ACKNOWLEDGMENTS

We are grateful to G.E. Volovik, who drew our attention to the paper [6]. This study was supported in part by the Russian Foundation for Basic Research (project no. 01-02-16898), the Leading Scientific Schools (project no. 40-15-96811), the Ministry of Education (project no. E00-3.3-148), and the Federal Program Integration-2001.

REFERENCES

1. Ya. B. Zel'dovich, Pis'ma Zh. Éksp. Teor. Fiz. **14**, 270 (1971) [JETP Lett. **14**, 180 (1971)]; Zh. Éksp. Teor. Fiz. **62**, 2076 (1972) [Sov. Phys. JETP **35**, 1085 (1972)].
2. C. W. Misner, Bull. Am. Phys. Soc. **17**, 472 (1972).
3. A. A. Starobinskiĭ, Zh. Éksp. Teor. Fiz. **64**, 48 (1973) [Sov. Phys. JETP **37**, 28 (1973)]; A. A. Starobinskiĭ and S. M. Churilov, Zh. Éksp. Teor. Fiz. **65**, 3 (1973) [Sov. Phys. JETP **38**, 1 (1974)].
4. J. D. Bekenstein and M. Schiffer, Phys. Rev. D **58**, 064014 (1998).
5. D. N. Page, Phys. Rev. D **14**, 3260 (1976).
6. A. Calogeracos and G. E. Volovik, Pis'ma Zh. Éksp. Teor. Fiz. **69**, 257 (1999) [JETP Lett. **69**, 281 (1999)]; cond-mat/9901163.
7. L. D. Landau and E. M. Lifshitz, *The Classical Theory of Fields* (Nauka, Moscow, 1988; Pergamon, Oxford, 1975).
8. N. Deruelle and R. Ruffini, Phys. Lett. B **52B**, 437 (1974).
9. W. G. Unruh, Phys. Rev. D **10**, 3194 (1974).
10. V. B. Berestetskii, E. M. Lifshitz, and L. P. Pitaevskii, *Quantum Electrodynamics* (Nauka, Moscow, 1989; Pergamon, Oxford, 1982).
11. S. A. Teukolsky, Phys. Rev. Lett. **29**, 1114 (1972).

Translated by V. Astakhov

Journal of Experimental and Theoretical Physics, Vol. 94, No. 3, 2002, pp. 459–469.
Translated from Zhurnal Éksperimental'noĭ i Teoreticheskoĭ Fiziki, Vol. 121, No. 3, 2002, pp. 538–550.

GRAVITATION, ASTROPHYSICS

Symmetric Heat and Mass Transfer in a Rotating Spherical Layer

S. V. Starchenko[a, *] and M. S. Kotel'nikova[b]

[a]*Borok Geophysical Observatory, Joint Institute of Physics, Russian Academy of Sciences, Yaroslavskaya oblast, 152742 Russia*

**e-mail: starche@izmiran.rssi.ru*

[b]*Institute of Earth Magnetism, Ionosphere, and Propagation of Radio Waves, Russian Academy of Sciences, Troitsk, Moscow oblast, 142017 Russia*

Received September 28, 2001

Abstract—The general theory of heat and mass transfer maintaining rotation with slightly different velocities under conditions typical for cores of planets in the solar system is developed for the first time. The analytic solution is obtained for thermal and diffusion equations without nonlinear terms responsible for the convective transfer. This spherically symmetric basic solution is applicable when the thermal flux from a planet core is weaker than or comparable to the adiabatic (radiative) flux. In the general case, by subtracting the basic solution, we simplified the inhomogeneous system of convective equations to obtain a completely homogeneous and dimensionless system. The latter system is controlled by two asymptotically small parameters: the Rossby number $\epsilon \le 10^{-5}$, which characterizes the relative value of differential rotation, and the generalized Eckman number $E \le 10^{-12}$, which characterizes the relative role of viscosity-diffusion effects during rapid rotation. The principal order of the solution for $\epsilon \longrightarrow 0$ and then for $\sqrt{E} \longrightarrow 0$, for the transfer coefficients close to molecular coefficients, results in the basic flow, which is symmetric with respect to the rotation axis and directed predominantly along the azimuth. The basic-flow liquid ascends from a solid core along spirals inside an axial cylinder in contact with the equator of the solid core and descends in a narrow layer along the cylinder walls. The moment of viscous forces in the inner boundary Eckman layer provides a faster rotation of the inner solid core of terrestrial planets compared to a massive outer mantle due to the growth of the solid core at the expense of a low-density liquid core. © *2002 MAIK "Nauka/Interperiodica".*

1. INTRODUCTION

Phenomena related to planetary magnetism have been directly observed and used by mankind over several tens of centuries. But only paleomagnetism originated in the middle of the last century allowed us to calculate the history of the geomagnetic field in billions of years, while cosmic studies performed ten–twenty years ago provided at last sufficiently detailed information on the magnetic fields of most planets of the solar system and their satellites. The comprehensive observation data accumulated at present allow one to perform both direct and comparative analysis of the geomagnetic field for solving the geodynamo problem.

The first successful three-dimensional numerical model of the MHD dynamo of the planetary type developed in 1995 was based on such a simple Boussinesq approximation that the application of this model to planets was doubted [1]. For this reason, the same authors published two years later several particular solutions of the complete system of geodynamo equations [2], which was derived earlier in the inelastic approximation, which is realistic for planet cores [3]. The solution of these extremely involved equations gave a magnetic field on the planet surface which was comparable with that obtained by solving the simplified system.

Since then, various authors who had access to powerful computers in Europe, Japan, and the United States have proposed many numerical models of the MHD dynamo, which reconstructed rather conclusively the morphology, magnitude, and evolution of the magnetic field observed on Earth's surface (see [4, 5] and references therein). However, all these models used the Boussinesq approximation, which cannot be used for the description of the interior of planets [13], and treated viscosity-diffusion effects assuming the stability of numerical schemes. This inevitably leads, and will lead in the forseeable future, not only to a huge overstatement (by seven or more orders of magnitude!) of the transfer coefficients compared to their true planetary values [7] but also to such nonphysical effects as hyperviscosity.

Therefore, at present the most relevant geodynamo problems are as follows:

(i) The justified simplification of a complete geodynamo system of equations;

(ii) the construction of an adequate model of viscosity-diffusion effects;

(iii) the determination of kinematic mechanisms generating a magnetic field observed on Earth's surface in order to narrow the number of acceptable MHD dynamo models as much as possible.

It is natural to start the study of heat-and-mass transfer in the cores of terrestrial planets by neglecting a magnetic field. Having solved this problem, we can analyze whether or not the obtained flow of a conducting liquid can excite a magnetic field, which gives simultaneously the answer to the question why Venus or Mars is not capable of maintaining its own magnetic field.

The flows themselves are produced by the Archimedean buoyancy force, which appears predominantly due to the floating of the excess light impurity from the boundary with the inner solid core of terrestrial planets during the growth of the latter. The corresponding convection induced by thermal and composition effects in a rapidly rotating spherical layer was never examined. The initial equations for this convection (see Section 2) were analyzed thirty years ago in paper [3]. These equations seemed so complicated that nobody has even tried to study them analytically. Moreover, the only numerical investigation of these equations known to us [2, 8] deals with the magnetohydrodynamic variant, whereas the basic nonmagentic study was not performed.

We show in Section 3 that initial equations from Section 2 admit the basic spherically symmetric analytic solution if we neglect nonlinear terms responsible for the convective process. By subtracting the basic solution, we simplify in Section 4 the initial inhomogeneous system of convection equations to obtain a completely homogeneous and dimensionless system. Then, we show in Section 5 that the nonmagnetic liquid flow in the principal order is directed along the azimuth and is concentrated inside the axial cylinder in contact with the equator of a solid core. The corresponding magnetic moment of viscous forces in the inner boundary Eckman layer provides a faster rotation of the inner solid core of terrestrial planets compared to the massive upper mantle because of the solid core growth at the expense of a low-density liquid core. In Section 6, we estimate the growth rate of the solid core and the range of applicability of the spherically symmetric basic solution found by us, which is a purely diffusion solution. Finally, Section 7 is devoted to discussion and conclusions.

2. INITIAL EQUATIONS

A spherical liquid layer under study is always in the state that is close to a hydrostatic equilibrium state that would be realized in the complete absence of convection. We assume that this initial state is completely specified and call it the Reference State (RS). We will denote all the corresponding initial quantities by a bar. Convection occurs due to cooling of a planet and floating of a light impurity in a liquid outer core during the growth of an inner solid core. The mass fraction of the light impurity, which we call here the concentration, is denoted by ξ, and the specific entropy is denoted by S.

The initial RS is an adiabatic, well-mixed state. Therefore, the RS entropy and concentration depend only on time, i.e.,

$$\nabla\bar{S} = 0, \quad \nabla\bar{\xi} = 0.$$

The rest of the RS quantities (the density $\bar{\rho}$, generalized pressure $\bar{p}$, temperature $\bar{T}$, and chemical potential $\bar{\mu}$) depend on the time t and the spherical radius r ($r = 0$ at the planet center). Hereafter, the prime denotes a radial derivative. For example, the radial derivative

$$\bar{\mu}' = d\bar{\mu}/dr$$

is proportional to the gravitational acceleration $\bar{g}$; according to [3], $\bar{\mu}' \approx 0.6\bar{g}$ for the Earth. The gravitational acceleration $\bar{g}$ in the RS is also related to the adiabatic temperature gradient by the expression

$$\bar{T}' = \alpha\bar{T}\bar{g}/c_p,$$

where α is the isothermal coefficient of volume expansion and c_p is the specific heat at constant pressure. Inside Earth's outer core, $c_p \approx 8 \times 10^2$ J/(kg K) and $\alpha \approx 10^{-5}$ K^{-1} [3, 9].

Convection is described by variables without the bar, which represent the field of perturbations of the RS; i.e., V, $\bar{p} + p$, $\bar{\xi} + \xi$, and $\bar{S} + S$ are real physical quantities. Convection in the cores of planets is described by equations of velocity (1), diffusion (2a), and heat transfer (2b). These equations were initially derived for Earth's core [3] using the above properties of the RS and the inelastic approximation $\nabla(\bar{\rho}\mathbf{V}) = 0$. The latter approximation represents a simplification of the continuity equation that is quite admissible for liquid cores of planets:

$$\nabla(\bar{\rho}\mathbf{V}) = 0, \tag{1a}$$

$$\kappa_V\nabla^2\mathbf{V} = D\mathbf{V}/Dt + 2\Omega\times\mathbf{V} + \nabla(p/\bar{\rho}) + (\bar{T}'S + \bar{\mu}'\xi)\mathbf{1}_r; \tag{1b}$$

$$\nabla(\bar{\rho}\kappa_\xi\nabla\xi) = \bar{\rho}(D\xi/Dt + \dot{\bar{\xi}}), \tag{2a}$$

$$\nabla(\bar{\rho}\bar{T}\kappa_S\nabla S) = \bar{\rho}\bar{T}\left(\frac{DS}{Dt} + \dot{\bar{S}}\right) + \frac{(r^2\bar{q})'}{r^2} - \bar{\rho}\bar{\mu}'\kappa_\xi\frac{\partial\xi}{\partial r}. \tag{2b}$$

Here,

$$\frac{D}{Dt} = \frac{\partial}{\partial t} + (\mathbf{V}\nabla)$$

is the substantional derivative, the mean values of ξ and S are zero, and

$$A \equiv -\bar{T}'S - \bar{\mu}'\xi$$

is the radial acceleration produced by the Archimedean force, which determines the convection rate. The outflow or a negative heat flow $(r^2\bar{q})'/r^2$ in Eq. (2b) appears due to the deviation from the adiabatic value of the specific radiation heat or conductivity, which is defined as

$$\bar{q}(r) = -c_p\kappa_T\bar{\rho}\bar{T}' > 0.$$

This outflow is compensated by the cooling term $\bar{\rho}\bar{T}\dot{\bar{S}} < 0$, which maintains the RS to a highest extent. Small thermal terms caused by viscosity in Eq. (2b) are neglected.

The molecular values of poorly known transfer coefficients $\kappa_{V,\xi,S}$ (i.e., the viscosity and diffusion coefficients) are of the order of magnitude of the thermal diffusion coefficient κ_T. The value of the latter for the Earth is estimated between 2×10^{-6} and 6×10^{-6} m^2/s [3, 9]. In the case of convection, the transfer coefficients represent complicated turbulent tensors. All their characteristic values are assumed to be close to $\kappa \approx 2$ m^2/s inside Earth's core [3].

The long-term behavior of processes of cooling and mixing in Eqs. (2) are described by the derivatives

$$\dot{\bar{S}} = \frac{d\bar{S}}{dt} \le 0, \quad \dot{\bar{\xi}} = \frac{d\bar{\xi}}{dt} \ge 0.$$

The positive value $-\dot{\bar{S}} \sim 10^{-15}$ W/(kg K) for the Earth is of the order of magnitude of the specific entropy caused by the thermal conductivity $(r^2\bar{q})'/r^2\bar{\rho}\bar{T}$.

On the velocity in Eq. (1) near the boundary of a solid inner core (where $r = r_i$), the condition of attachment $\mathbf{V} = \mathbf{V}_i$ is imposed. In this case, the velocity $\mathbf{V}_i \approx \omega_i r_i \sin\theta \mathbf{1}_\varphi$ of the core as a solid is mainly caused by the angular rotation ω_i. The condition of attachment is also imposed on the outer ($r = r_o$) sphere (mantle). The velocity of the massive mantle is $\mathbf{V}_o \approx 0$ in our reference system rotating with a constant angular velocity $\mathbf{\Omega} = \Omega\mathbf{1}_z$, so that the total inertia moment of the planet is zero.[1]

The freezing of the outer core to the inner one results in the following boundary conditions for Eqs. (2) for $r = r_i(t, \theta, \varphi)$:

$$\rho_i \Delta S \frac{\partial r_i}{\partial t} = -\bar{\rho}\kappa_S \frac{\partial S}{\partial r}, \tag{3a}$$

$$\rho_i \Delta\xi \frac{\partial r_i}{\partial t} = -\bar{\rho}\kappa_\xi \frac{\partial \xi}{\partial r}. \tag{3b}$$

[1] Hereafter, the indices i and o refer to variables used in inner and outer layers, respectively.

The slow growth rate of the inner core

$$\frac{\partial r_i}{\partial t} = -r_i\left(\frac{f_S}{c_p}\frac{\partial S}{\partial t} + f_\xi \frac{\partial \xi}{\partial t}\right)$$

depends on the corresponding freezing numbers $f_{S,\xi}$], which are approximately equal to $f_S \approx 33$ and $f_\xi \approx 70$ for the Earth, according to estimates performed in paper [3]. The jumps of the entropy and concentration on passing the boundary are approximately equal to $\Delta S \approx 190$ J/(kg K) and $\Delta\xi \approx 0.065$. Note that the values of these quantities reported in paper [9] are approximately two times lower than the above values.

The concentration flow from the outer core through the impenetrable boundary with the mantle should be absent, and the boundary condition for entropy is determined by the specific thermal flux q_S. From here, we obtain the outer boundary condition for Eqs. (2) for $r = r_o$:

$$\frac{\partial \xi}{\partial r} = 0, \tag{4a}$$

$$-\bar{T}\bar{\rho}\kappa_S \frac{\partial S}{\partial r} = q_o - \bar{q}_o. \tag{4b}$$

The nonadiabatic specific thermal flow $q_o - \bar{q}_o$ is defined as the difference between the total specific thermal flow $q_o(t, \theta, \varphi)$ and the flow caused by the thermal conductivity $\bar{q} = -c_p\kappa_T\bar{\rho}\bar{T}'$ for $r = r_o$, i.e., $\bar{q}_o = \bar{q}(r_o)$. The total thermal flow q_o coming from Earth's core is not adequately known, and it can be even weaker than the adiabatic flow caused by the conductivity. Therefore, even the sign of the mean value $q_o - \bar{q}_o$ over the sphere's surface q_S is unknown. For the Earth, the value of $q_S \approx \pm 10^{-2}$ W/m^2 [2].

By neglecting nonlinear terms in (2), we can obtain the general solution of (2), which satisfies the boundary conditions (3) and (4) for specified parameters. This solution allows us to rewrite master equations (1) and (2) in a simple homogeneous form (without terms caused by sources), by determining the characteristic values of the inhomogeneous entropy S and concentration ξ. We will also justify below the neglect of nonlinear terms in (2) in the asymptotic system.

3. SPHERICALLY SYMMETRIC SOLUTION

Sources (1) and (2) can depend only on the spherical radius r and time t. Therefore, to take their influence into account, we will find the radially symmetric solution ξ_r, S_r for linearized equations (2a) and (2b) from the equations

$$\frac{(r^2\bar{\rho}\kappa_\xi\xi_r')'}{r^2\bar{\rho}} = \dot{\xi}_r + \dot{\bar{\xi}}, \tag{5a}$$

$$\frac{(r^2\bar{\rho}\bar{T}\kappa_S S_r')'}{r^2\bar{\rho}\bar{T}} = \dot{S}_r + \dot{\bar{S}} + \frac{(r^2\bar{q})'}{r^2\bar{\rho}\bar{T}} - \frac{\bar{\mu}'\kappa_\xi\xi_r'}{\bar{T}}. \quad (5b)$$

Four boundary conditions are imposed on Eqs. (5a) and (5b) in accordance with conditions (3) and (4):

$$\frac{\bar{\rho}\kappa_S}{\rho_i\Delta S}\frac{S_r'}{r_i} = \frac{f_S}{c_p}\dot{S}_r + f_\xi\dot{\xi}_r = \frac{\bar{\rho}\kappa_\xi}{\rho_i\Delta\xi}\frac{\xi_r'}{r_i} \quad \text{at } r = r_i, \quad (6a)$$

$$\xi_r' = 0, \quad \bar{T}\bar{\rho}\kappa_S S_r' = -q_S \ (= \text{const}) \quad \text{at } r = r_o. \quad (6b)$$

Parameters (1)–(6) are assumed constant, i.e.,

$$\bar{\rho}\kappa_\xi = \rho\kappa, \quad \bar{\rho}\bar{T}\kappa_S = \rho T\kappa$$

with constant values $\bar{\rho} = \rho$, $\bar{T} = T$, and κ. The exceptions are the radial derivatives of the RS quantities, which can be adequately estimated using radial linear dependence:

$$\bar{T}' = -T''r, \quad \bar{\mu}' = -\mu''r,$$
$$\bar{\rho}' = -\rho''r, \quad \bar{q} = -c_p\kappa_T\bar{\rho}\bar{T}' = (\bar{q}_o/r_0)r.$$

By using the above simplifications, we can obtain the solution of (5) in the form

$$\xi_r' = \frac{1}{r^2\kappa}\int_{r_o}^{r}(\dot{\xi}_r + \dot{\bar{\xi}})r^2dr,$$

$$S_r' + \frac{q_S}{T\rho\kappa} = \frac{1}{r^2\kappa}\int_{r_o}^{r}\left(\dot{S}_r + \dot{\bar{S}} + \frac{3q_o}{r_o\rho T} + \frac{\mu''r\kappa\xi_r'}{T}\right)r^2dr,$$

which satisfies the outer boundary conditions (6b).

By assuming that the required solution of (5) can be represented in the form

$$(\xi_r, S_r) = f(t) + F(r),$$

we obtain

$$\xi_r' = \frac{\dot{\xi}_r + \dot{\bar{\xi}}}{3\kappa}\left(r - \frac{r_o^3}{r^2}\right),$$

$$S_r' = \frac{\dot{S}_r + \dot{\bar{S}} + 3q_o/r_o\rho T}{3\kappa}\left(r - \frac{r_o^3}{r^2}\right) + \mu''\frac{\dot{\xi}_r + \dot{\bar{\xi}}}{15\kappa T}\left(r^3 - \frac{5}{2}r_o^3 + \frac{3r_o^5}{2r^2}\right) - \frac{q_S}{T\rho\kappa}.$$

These equations substituted into the inner boundary condition (6a) give the general solution of (5) and (6) in the form

$$\xi_r = \xi_o + \frac{(\dot{\xi}_r + \dot{\bar{\xi}})}{3\kappa}\left(\frac{r^2}{2} + \frac{r_o^3}{r} - \frac{3r_o^2}{2}\right), \quad (7a)$$

$$S_r = S_o + \frac{q_S}{T\rho\kappa}(r_o - r) + \frac{(\dot{S}_r + \dot{\bar{S}} + 3q_o/r_o\rho T)}{3\kappa}\left(\frac{r^2}{2} + \frac{r_o^3}{r}\frac{3r_o^2}{2}\right) + \frac{\mu''(\dot{\xi}_r + \dot{\bar{\xi}})}{6\kappa T}\left(\frac{r^4}{10} - r_o^3r - \frac{3r_o^5}{5r} + \frac{3r_o^4}{2}\right), \quad (7b)$$

where ξ_o and S_o are constants, which are determined from the condition that the mean values of ξ_r and S_r are zero and from equations

$$\dot{\xi}_r + \dot{\bar{\xi}} = \left\{\frac{q_S}{T\rho} - \frac{\bar{q}_o}{r_oT\rho}\left(r_i - \frac{r_o^3}{r_i^2}\right) - \frac{c_p}{3f_s}\left(f_\xi\dot{\bar{\xi}} + \frac{f_S}{c_p}\dot{\bar{S}}\right)\left(r_i - \frac{r_o^3}{r_i^2}\right)\right\} \times \left\{\frac{\mu''}{30T}\left(2r_i^3 - 5r_o^3 + \frac{3r_o^5}{r_i^2}\right) + \left[\frac{c_p}{3f_S}\left(\frac{\rho}{3\rho_i\Delta\xi r_i}\left(r_i - \frac{r_o^3}{r_i^2}\right) - f_\xi\right) - \frac{\Delta S}{3\Delta\xi}\right]\left(r_i - \frac{r_o^3}{r_i^2}\right)\right\}^{-1}, \quad (7c)$$

$$\dot{S}_r + \dot{\bar{S}} = \frac{c_p}{f_S}(\dot{\xi}_r + \dot{\bar{\xi}}) \times \left[\frac{\rho}{3\rho_i\Delta\xi r_i}\left(r_i - \frac{r_o^3}{r_i^2}\right) - f_\xi\right] + \frac{c_p}{f_S}\left(f_\xi\dot{\bar{\xi}} + \frac{f_S}{c_p}\dot{\bar{S}}\right). \quad (7d)$$

To calculate ξ_0 and S_0, we will use fluid outer core (FOC) integrals [8]:

$$\int_{FOC}\bar{\rho}S_rdV = 4\pi\rho\int_{r_i}^{r_o}S_rr^2dr = 0, \quad (8a)$$

$$\int_{FOC}\bar{\rho}\xi_rdV = 4\pi\rho\int_{r_i}^{r_o}\xi_rr^2dr = 0. \quad (8b)$$

Figure 1 shows the radial distributions of the concentration and entropy for the values of parameters used in numerical calculations in paper [8]. The parameters $r_o = 3.480 \times 10^6$ m, $r_i = 1.222 \times 10^6$ m, $\rho = 11 \times 10^3$ kg/m^3, and $\rho_i = 12.1666 \times 10^3$ kg/m^3 were taken

from the PREM seismic model [10]; $c_p = 840$ J/(kg K), $T = 4800$ K, $\mu'' = 2 \times 10^{-6}$ s^{-2}, $T'' = 2.5 \times 10^{-10}$ K/m^2, $\kappa_T = 5 \times 10^{-6}$ m^2/s, $\bar{q}_o = 4 \times 10^{-2}$ W/m^2, $f_\xi = 70$, $f_S = 33$, $\Delta\xi = 0.065$, $\Delta S = 190$ J/(kg K), $q_S = 1.4 \times 10^{-2}$ W/m^2, $\kappa = 2$ m^2/s, and $\dot{\bar{\xi}} = 5 \times 10^{-20}$ s^{-1}, $\dot{\bar{S}} = -1 \times 10^{-16}$ W/(kg K) [8]. In this case, we obtain $S_o = -4.999 \times 10^{-4}$ J/(kg K) and $\xi_o = -2.976 \times 10^{-8}$. The obtained values of the spherically symmetric entropy and concentration differ from the results of the numerical magnetohydrodynamic simulations [8] by only several times.

The typical values of the gradients of these quantities in fact coincide with the results obtained in papers [2, 8] despite the fact that the energy of the magnetic field in these papers, which we neglected, was several orders of magnitude greater than the energy of the velocity field. Therefore, the purely diffusion solution (7) found by us should determine the sources of not only nonmagnetic but also MHD convection.

The values of all parameters used in (7) are known quite accurately, except the diffusion coefficient k, the mean thermal flow q_S, and the time derivatives $\dot{\bar{\xi}}$ and $\dot{\bar{S}}$. The latter are directly related to the comparatively well known thermal and composition flows in planets. One of the derivatives can be excluded from the solution by using the equation of the general energy balance inside Earth's outer core in the form presented in Eq. (11) in paper [5]

$$M_o(\bar{T}_* \dot{\bar{S}} + \bar{\mu}_* \dot{\bar{\xi}}) = -Q_o + L\dot{M}_i + Q_i, \qquad (9)$$

where M_o is the outer core mass, L is the internal heat released upon freezing, and M_i is the inner core mass. Following [2, 3, 9] and the PREM model [10], we find that $M_o = 1.9 \times 10^{24}$ kg and $\bar{T}_*$ and $\bar{\mu}_*$ are close to the values of $\bar{T}$ and $\bar{\mu}$ reported above. The positive quantities Q_o and Q_i are the total radial thermal flows from and to the outer core, respectively. The heat inflow Q_i from the inner core and any energy contributions related to the precession and ebb and flow processes in the outer core can be neglected in the energy balance equations because they are considerably smaller than Q_o. In addition, we neglect any energy contributions produced by the core radioactivity, which are not accurately known at present. The value of $\dot{\bar{\xi}}$ can also be estimated from the growth rate of the inner core as

$$\dot{\bar{\xi}} = \bar{\xi}\frac{\dot{M}_i}{M_o} = \bar{\xi}\frac{4\pi r_i^2 \rho_i \dot{r}_i}{M_o}. \qquad (10a)$$

After the substitution of this expression to the energy balance equation and the replacement of total thermal flows by specific flows, we obtain the relation between $\dot{\bar{S}}$ and the growth rate of the inner core

$$\dot{\bar{S}} = \frac{4\pi}{TM_o}[-r_o^2(q_S + \bar{q}_o) + r_i^2 \rho_i \dot{r}_i (L - \mu\bar{\xi})]. \qquad (10b)$$

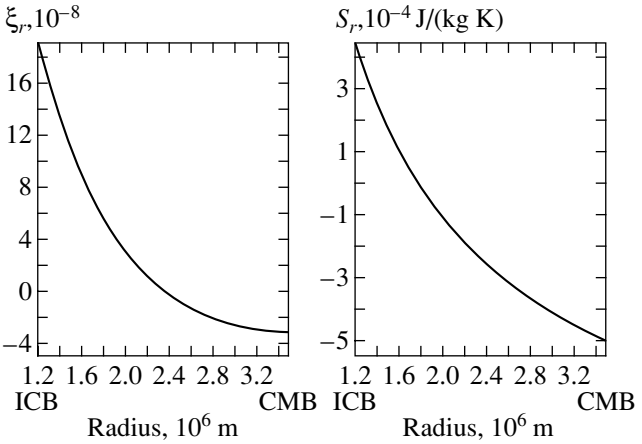

Fig. 1. Radial distribution of the spherically symmetric mass fraction (concentration) ξ_r of the light component and the specific entropy S_r for the values of parameters from [5].

Thus, by specifying the growth rate $\dot{r}_i$ of the inner core, the transfer coefficient κ, and the thermal flow q_S, we can always obtain from (7)–(10) the purely diffusion and spherically symmetric solutions (ξ_r, S_r) of linearized equations of heat-and-mass transfer (2), which satisfy conditions (3) and (4) at the boundaries of liquid cores of planets.

4. HOMOGENEOUS AND ASYMPTOTIC SYSTEMS

By replacing S by $S + S_r$ and ξ by $\xi + \xi_r$ in (1) and (2), where $S_r(t, r)$, and $\xi_r(t, r)$ are spherically symmetric solutions (7) of Eqs. (5) and (6), and using the parameters from Section 3, we obtain the homogeneous system

$$\nabla(\bar{\rho}\mathbf{V}) = 0, \qquad (11a)$$

$$\kappa_V \nabla^2 \mathbf{V} = \frac{D\mathbf{V}}{Dt} + 2\boldsymbol{\Omega} \times \mathbf{V} + \nabla P - (T''S + \mu''\xi)\mathbf{r}, \qquad (11b)$$

$$\kappa\nabla^2\xi = \frac{D\xi}{Dt} + \xi_r' V_r, \qquad (12a)$$

$$\kappa\nabla^2 S = \frac{DS}{Dt} + S_r' V_r + \frac{\mu''\kappa}{\bar{T}} r\frac{\partial\xi}{\partial r}. \qquad (12b)$$

Here, P is the generalized pressure satisfying the expression

$$\nabla P = \nabla\frac{p}{\bar{\rho}} - (T''S_r + \mu''\xi_r)\mathbf{r}.$$

The solutions of the system (11), (12) should satisfy the boundary conditions

$$\mathbf{V} = \mathbf{V}_i \text{ at } r = r_i(t, \theta, \varphi), \tag{13a}$$

$$\mathbf{V} = \mathbf{V}_o \text{ at } r = r_o, \tag{13b}$$

$$\rho_i \Delta S \frac{\partial r_i}{\partial t} = -\bar{\rho}\kappa \frac{\partial S}{\partial r}, \tag{14a}$$

$$\rho_i \Delta\xi \frac{\partial r_i}{\partial t} = -\bar{\rho}\kappa \frac{\partial \xi}{\partial r} \text{ at } r = r_i(t, \theta, \varphi), \tag{14b}$$

$$\frac{\partial \xi}{\partial r} = 0, \tag{15a}$$

$$-\bar{T}\bar{\rho}\kappa_S \frac{\partial S}{\partial r} = q \text{ at } r = r_o. \tag{15b}$$

The specified thermal flow q has a nonzero mean value calculated over the surface of the outer sphere for $r = r_o$.

The characteristic values S_* and ξ_* of the radially symmetric solution (7) can reasonably be used as optimal units for measuring the entropy and concentration of the light impurity. By measuring then the distances in terms of the inner-core radius r_i, the velocity in terms of the typical differential rotation $r_i\Delta\Omega$, and the time in terms of $1/\Delta\Omega$ (i.e., $r := r_i r$, $t := t/\epsilon\Omega$, $\mathbf{V} := r_i\epsilon\Omega\mathbf{V}$, $\xi := \xi_*\xi$, $S := S_*S$), we obtain from the homogeneous system (11), (12) the dimensionless asymptotic system

$$\nabla\mathbf{V} = arV_r, \tag{16a}$$

$$\epsilon\frac{D\mathbf{V}}{Dt} - (hS + \xi)\mathbf{r} + 2\mathbf{1}_z \times \mathbf{V} + \nabla P = E_V\nabla^2\mathbf{V}, \tag{16b}$$

$$\epsilon\left(\frac{D\xi}{Dt} + \xi'_r V_r\right) = E_\xi\nabla^2\xi, \tag{17a}$$

$$\epsilon\left(\frac{DS}{Dt} + S'_r V_r\right) + \frac{\epsilon}{R} r\frac{\partial \xi}{\partial r} = E_S\nabla^2 S, \tag{17b}$$

$$\epsilon = \frac{\mu'' r_i \xi'_*}{\Omega^2} \ll 1, \tag{18a}$$

$$E_{V,\xi,S} = \frac{\kappa_{V,\xi,S}}{r_i^2\Omega} \ll 1. \tag{18b}$$

Here, $\epsilon = \Delta\Omega/\Omega$ is the main asymptotic parameter (the Rossby number) characterizing a very small deviation from an almost "solid-state" rotation in the spherical layer under study. Small numbers $E_{V,\xi,S}$ can be called the generalized Eckman numbers because it is reasonable to use for the viscosity coefficient κ_V the same value as for the diffusion coefficient $\kappa_{\xi,S}$ upon both molecular and "turbulent" heat-and-mass transfer. The rest of the parameters are chosen based on geophysical considerations:

$$a = \frac{r_i^2\rho''}{\rho} < 1, \quad h = \frac{T''S'_*}{\mu''\xi'_*} < 1, \quad R = \frac{TS'_* r_i}{\Omega\kappa_\xi} \gg 1, \tag{19}$$

where a is the stratification, h is the thermal floatability, and R is the Rayleigh number. The asymptotic system (16), (17) should satisfy the following ten dimensionless boundary conditions:

$$\mathbf{V} = \mathbf{V}_o, \quad \xi' = 0, \quad S' = -q(t, \theta, \varphi) \tag{20}$$

for $r = r_o/r_i$, $\int q d^2 r = 0$, and

$$\mathbf{V} = \mathbf{V}_i, \quad E_S I_S S' = \epsilon(I_t\dot{S} + \dot{\xi}) = E_\xi I_\xi \xi' \text{ at } r = 1 \tag{21}$$

for $r = 1$.

Here, the specified thermal flow q has the nonzero mean value calculated over the surface of the outer sphere for $r = 1$. The modulus of the inner angular rotational velocity ω_i is smaller than or of the order of unity, while its characteristic scale $\Delta\Omega$ is determined by Eq. (18a). The values of quantities specified by the inner boundary conditions and the corresponding characteristic geophysical values are

$$I_S = \frac{\rho S'_*}{\rho_i \Delta S f_\xi \xi'_*} \approx I_\xi = \frac{\rho}{\rho_i \Delta\xi f_\xi} \approx \frac{1}{5}, \quad I_t = \frac{f_S S'_*}{c_p f_\xi \xi'_*} \approx 2. \tag{22}$$

The asymptotic parameter ϵ controls convection in accordance with its definition (18a). Therefore, the value of ϵ should increase from zero at the beginning of convection. This allows us to neglect nonlinear terms in (2), as we did in the previous section and below. Such neglect can no longer always be justified during convection because other small parameters $E_V \sim E_S \sim E_\xi \ll 1$ are also present in (16)–(21). The effects related to these parameters can be not so substantial as effects caused by an increase in ϵ. This will require the consideration of the asymptotic limit over the fixed Eckman number and then over the Rossby number, which will probably lead to the known convective solutions (see, for example, [11]). By studying below the beginning of convection in planet cores, we will calculate first the asymptotic limit over a small parameter ϵ and then over E.

5. ASYMPTOTIC SOLUTION

We will seek the solution of (16), (17) as the expansion in powers of a small parameter ϵ

$$(\mathbf{V}, P, \xi, S) = (\mathbf{V}_0, P_0, \xi_0, S_0) + (\mathbf{V}_1, P_1, \xi_1, S_1)\epsilon + O(\epsilon^2). \tag{23}$$

The entropy S and concentration ξ in the zero order are identically zero according to the corollary of the Neumann theorem:

$$\left.\begin{aligned}&\nabla^2\xi_0 = 0,\\ &\xi_0'(r=1, r=r_o/r_i) = 0,\\ &\int\xi_0 d^3r = 0\end{aligned}\right\} \longrightarrow \xi_0 = 0, \tag{24}$$

$$\left.\begin{aligned}&\nabla^2 S_0 = 0,\\ &S_0'(r=1, r=r_o/r_i) = 0 = -q = 0,\\ &\int S_0 d^3r = 0\end{aligned}\right\} \longrightarrow S_0 = 0. \tag{25}$$

The equations for the velocity in the zero order

$$\nabla\mathbf{V}_0 = arV_{0r}, \quad 2\mathbf{1}_z\times\mathbf{V}_0 + \nabla P_0 = E_V\nabla^2\mathbf{V}_0, \tag{26}$$

should satisfy the corresponding boundary conditions (20), (21), which take the form

$$\mathbf{V}_o = \mathbf{0}, \tag{27a}$$

$$\begin{aligned}\mathbf{V}_i = {}& \mathbf{1}_\varphi[d\sin\theta - p\cos\theta\cos(\varphi-\varphi_p)]\\ &- \mathbf{1}_\theta p\sin(\varphi-\varphi_p)\end{aligned} \tag{27b}$$

in terms of the differential rotation $d(t)$ and precession $p(t)$ of the inner solid core in the case of an infinitely heavy solid mantle. These conditions determine $\mathbf{V}_0 = \mathbf{V}_0(E_V, d, p, \mathbf{r})$, as we will show below.

By using the fast rotation (almost nonviscous) approximation, we obtain

$$\begin{aligned}&\delta \equiv \sqrt{E_V} \ll 1 \longrightarrow (\mathbf{V}_0, P_0)\\ &= (\mathbf{V}_{00}, P_{00}) + (\mathbf{V}_{01}, P_{01})\delta + O(\delta^2) + \ldots.\end{aligned} \tag{28}$$

Outside thin shear (for $s \equiv r\sin\theta = 1$) and boundary ($r = 1$, $r = r_o/r_i$) layers, we have

$$\nabla\mathbf{V}_{00} = arV_{00r}, \quad 2\mathbf{1}_z\times\mathbf{V}_{00} = -\nabla P_{00}. \tag{29}$$

The conditions of impenetrability

$$V_{00r} = 0 \text{ at } r = 1, \quad r = r_o/r_i$$

in Eqs. (29) give the conditions

$$V_{00\theta} = 0, \tag{30a}$$

$$V_{00r} = 0, \tag{30b}$$

$$V_{00\varphi} = V_{00\varphi}(t, s), \tag{30c}$$

$$P_{00} = P_{00}(t, s). \tag{30d}$$

Inside boundary Eckman layers, conditions (30b) and (30c) remain valid, whereas $V_{00\theta} \neq 0$ and $P_{00} = 0$. In this case, equations for the velocity (26) take the form (except its geophysical part)

$$-2V_{00\varphi}\cos\theta = \delta^2 V_{00\theta}'', \tag{31a}$$

$$2V_{00\theta}\cos\theta = \delta^2 V_{00\varphi}''. \tag{31b}$$

Equations (31) should satisfy the boundary conditions (27), while outside the boundary layers we have $V_{00\theta} \longrightarrow 0$ and $V_{00\varphi} \longrightarrow$ (30c).

Thus, the parameter $p \sim \max(\delta, \epsilon)$ in (27b) is a small parameter, and the flow maintained at $d \sim 1$ (see below) (27) is symmetric with respect to the rotation axis in the principal order. The solution of Eqs. (31) taking into account (30) gives the initial zero-order profile of the differential rotation outside (for $|\eta| \gg 1$) and inside (for $\eta \sim 1$) boundary Eckman layers [12] in the form

$$\begin{aligned}\omega \equiv \frac{V_{00\varphi}}{s} = {}& d(1 - e^{\eta_o}\cos\eta_o)\\ &\times\left[1 - \frac{(1-e^{-\eta_i}\cos\eta_i)\sqrt[4]{1-s^2}}{\sqrt[4]{1-s^2} + \sqrt[4]{1-s^2}\,r_i^2/r_o^2}\right], \quad s \le 1,\\ \omega = {}& 0, \quad s > 1.\end{aligned} \tag{32}$$

Here,

$$\eta_{i,o} \equiv (r_{i,o} - 1)\cos\theta/\delta$$

are the "stretched" variables in the inner and outer boundary Eckman layers for $1 \ge r \ge r_o/r_i$.

Equation (32) determines the inner viscous rotational moment M [13] in dimensional units

$$\begin{aligned}M = {}& -(r_i^3\kappa_V\rho\epsilon\Omega)4\pi\int_0^{\pi/2}\left[\frac{\partial\omega}{\partial r}\right]_{r=1}\sin^2\theta\, d\theta\\ &\approx r_i^4\rho(\epsilon d\Omega)\sqrt{\kappa_V\Omega}.\end{aligned} \tag{33}$$

By equating the expression for the increasing angular momentum to expression (33) at a constant angular rotational velocity $\epsilon d\Omega$ and density ρ_i of the inner sphere, we can write the equation for the inertia moment I

$$\dot{I}(\Omega + \epsilon d\Omega) = M, \tag{34a}$$

where

$$I = (8\pi/15)r_i^5\rho_i. \tag{34b}$$

Taking into account that ϵ is small, we obtain from (33) and (34) the estimate

$$\epsilon d\Omega \approx 10\dot{r}_i\sqrt{\Omega/\kappa_V} \tag{35}$$

for a higher angular rotational velocity of the inner sphere relative to the outer sphere. This gives

$$d \approx \frac{10}{\tau_i\Omega\epsilon E_V^{1/2}} = 1$$

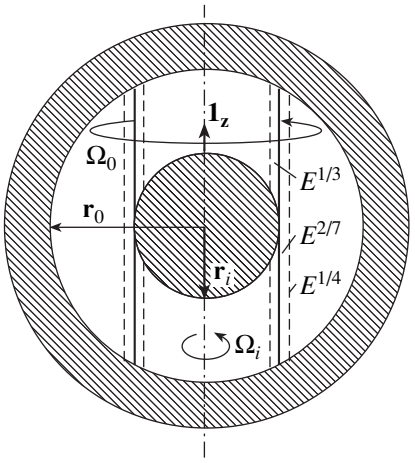

Fig. 2. Structure of the axially symmetric rotation of the flow in a spherical layer with the inner radius r_i, the outer radius r_o, and the small Eckman number E. The outer angular rotational velocity Ω_o is slightly lower than the inner velocity Ω_i.

for the parameters of terrestrial planets $\tau_i \equiv r_i/\dot{r}_i = 10^{17}$ s (approximately 3 billion years [2, 9]), $\Omega = 10^{-4}$ s^{-1}, typical $\epsilon = 10^{-5}$ from the previous section, and $E_V = 10^{-14}$ with the molecular viscosity $\kappa_V \approx 10^{-6}$ m^2/s.

Figure 2 shows the structure of the axially symmetric flow (32) generated due to a faster rotation of the inner sphere (solid core) relative to the outer mantle. This faster rotation forms in the liquid outer core the so-called Taylor column—the liquid volume entrained by a solid moving in the liquid, when the Coriolis force and the pressure gradient dominate in the system, whereas the viscosity effect is small. The surface of the Taylor column is called a tangential cylinder. The generatrices of this cylinder are parallel to the rotation axis and are in contact with the inner core at the equatorial points. The dynamics of flows inside and outside of the tangential cylinder strongly differ.

The liquid outside the tangential cylinder is involved in the solid-state rotation at the velocity of the mantle, whereas the liquid inside the cylinder moves at a velocity that is intermediate between the velocities of the inner core and mantle. The small-scale flows are concentrated in the boundary Eckman layer and in a free shear layer, which provides the return meridional flow and smooths strong gradients near the tangential cylinder. The structure of this layer was determined by Stewarson [14, 15]. The velocity jump is eliminated outside the tangential cylinder in the Stewarson layer of thickness $E^{1/4}$. The remaining shear discontinuity is removed inside the tangential cylinder in the Stewarson layer of thickness $E^{2/7}$, while the discontinuity of the meridional liquid flow is eliminated in the layer of thickness $E^{1/3}$.

6. ADMISSIBLE DIFFUSION SOLUTIONS

Let us determine the range of the thermal flow q_S and of the growth rates $\dot{r}_i$ of the solid core where the spherically symmetric solution obtained in Section 3 is applicable. To use the smallest number of not well-known parameters, we exclude the time derivatives $\dot{\bar{\xi}}$ and $\dot{\bar{S}}$ from Eqs. (7c) and (7d). By using Eqs. (8a) and (8b) and the boundary condition

$$\dot{r}_i = -\frac{\rho}{\rho_i \Delta\xi}(\dot{\xi}_r + \dot{\bar{\xi}})\left(r_i - \frac{r_o^3}{r_i^2}\right), \tag{36}$$

we express the sum

$$f_\xi \dot{\bar{\xi}} + \frac{f_S}{c_p}\dot{\bar{S}} = \dot{r}_i \frac{4\pi r_i^2 \rho_i}{M_o} \times \left[f_\xi \bar{\xi} + \frac{f_S}{c_p T}(L - \mu\bar{\xi})\right]\frac{f_S}{c_p}\frac{4\pi r_o^2}{T M_o}(q_S + \bar{q}_o) \tag{37}$$

in terms of the growth rate $\dot{r}_i$ of the inner nucleus. By substituting (37) into (7c) and (7d) and the result obtained into (36), we derive the equation for determining $\dot{r}_i$ in terms of the known parameters and the thermal flow q_S:

$$\dot{r}_i = -\left\{\frac{\rho}{3\rho_i \Delta\xi T}\frac{1}{D}\left(r_i - \frac{r_o^3}{r_i^2}\right)\left[q_S\left(\frac{1}{\rho} + \frac{4\pi r_o^2}{3M_o}\left(r_i - \frac{r_o^3}{r_i^2}\right)\right) - \bar{q}_o\left(\frac{1}{\rho r_o} - \frac{4\pi r_o^2}{3M_o}\right)\left(r_i - \frac{r_o^3}{r_i^2}\right)\right]\right\}\left\{1 - \frac{4\pi\rho r_i^2}{9\Delta\xi M_o}\frac{c_p}{f_S} \times \frac{1}{D}\left(r_i - \frac{r_o^3}{r_i^2}\right)\left[f_\xi\bar{\xi} + \frac{f_S}{c_p T}(L - \mu\bar{\xi})\right]\right\}^{-1}, \tag{38}$$

where D is the denominator from (7d):

$$D = \frac{\mu''}{30T}\left(2r_i^3 - 5r_o^3 + \frac{3r_o^5}{r_i^2}\right) + \left[\frac{c_p}{3f_S}\left[\frac{\rho}{3\rho_i\Delta\xi r_i}\left(r_i - \frac{r_o^3}{r_i^2}\right) - f_\xi\right] - \frac{\Delta S}{3\Delta\xi}\right]\left(r_i - \frac{r_o^3}{r_i^2}\right).$$

The dependence of the growth rate $\dot{r}_i$ of the inner core on the thermal flow q_S is shown in Fig. 3. The growth condition $\dot{r}_i > 0$ is not satisfied if the total thermal flow q_o coming from Earth's core is greater than the adiabatic flow $\bar{q}_o$ caused by the thermal conductivity (i.e., for $q_S > 0$). In this case, the spherically symmetric diffusion solution alone is not sufficient, and to provide

the positive growth rate of the core, an additional convection is necessary (which can even be weak).

On the contrary, when the thermal flow is weaker than the adiabatic flow (i.e., $q_S < 0$), the diffusion solution can itself (without convection) maintain the differential rotation (32). In this case, the growth rate of the inner core increases with increasing modulus $|q_S|$ of the thermal flow. Thus, for the value of $q_S = -0.01$ W/m^2 used in paper [2], the growth rate is approximately 0.27×10^{-11} m/s. For comparison, the authors of paper [9] obtained $\dot{r}_i \approx 10^{-11}$ m/s. In paper [3], a lower value $\dot{r}_i \approx 0.6 \times 10^{-11}$ m/s was used, while the numerical model [2] based on the age of the inner core of approximately 1.3 billion years gives $\dot{r}_i \approx 1.3 \times 10^{-11}$ m/s.

After the substitution of $\dot{r}_i$ into (37), the sum $f_\xi\dot{\bar{\xi}} + (f_S/c_p)\dot{\bar{S}}$ in Eqs. (7) is already expressed only in terms of q_S and the known quantities. As a result, we can rewrite (7c) and (7d), by excluding the time derivatives $\dot{\bar{\xi}}$ and $\dot{\bar{S}}$, in the form

$$\dot{\xi}_r + \dot{\bar{\xi}} = \frac{1}{DT}\left[q_S\left(\frac{1}{\rho} + \frac{4\pi r_o^2}{3M_o}\left(r_i - \frac{r_o^3}{r_i^2}\right)\right) - \bar{q}_o\left(\frac{1}{\rho r_o} - \frac{4\pi r_o^2}{3M_o}\right)\left(r_i - \frac{r_o^3}{r_i^2}\right)\right] \quad (39a)$$

$$\times\left\{1 - \frac{4\pi\rho r_i^2}{9\Delta\xi M_o}\frac{c_p}{f_S}\frac{1}{D}\left(r_i - \frac{r_o^3}{r_i^2}\right)^2\left[f_\xi\bar{\xi} + \frac{f_S}{c_pT}(L - \mu\bar{\xi})\right]\right\}^{-1},$$

$$\dot{S}_r + \dot{\bar{S}} = \frac{c_p}{f_S}\left[\frac{\rho}{3\Delta\xi}\left(r_i - \frac{r_o^3}{r_i^2}\right)\right.$$

$$\left.\times\left(\frac{1}{\rho_i r_i} - \frac{4\pi r_i^2}{M_o}\left(f_\xi\bar{\xi} + \frac{f_S}{c_pT}(L - \mu\bar{\xi})\right)\right) - f_\xi\right] \quad (39b)$$

$$\times(\dot{\xi}_r + \dot{\bar{\xi}}) - \frac{4\pi r_o^2}{TM_o}(q_S + \bar{q}_o).$$

After the substitution of (39a) and (39b) into (7a) and (7b), two uncertain parameters remain, namely, the mean thermal flow q_S and the diffusion coefficient κ. The diffusion coefficient is determined with an accuracy within several orders of magnitude. Therefore, to determine the characteristic gradients of entropy and concentration and their dependences on the thermal flow, it is convenient to introduce the dimensionless analogs of gradients of a radially symmetric solution, from which κ can be excluded by multiplying ξ_r' and S_r' by the combinations $\kappa\rho\mu'' r_i^2/\bar{q}_o$ and $\kappa\rho\mu'' r_i^2/c_p\bar{q}_o$, respectively, i.e.,

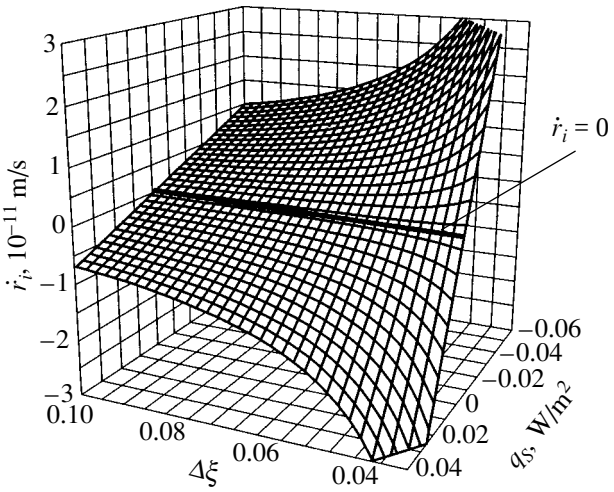

Fig. 3. Dependence of the growth rate $\dot{r}_i$ of the inner sphere (core) on the specific nonadiabatic thermal flow q_S and the concentration jump $\Delta\xi$.

$$\xi_{dl}' = \frac{\kappa\rho\mu'' r_i^2}{\bar{q}_o}\xi_r' = \frac{\rho\mu'' r_i^2}{\bar{q}_o}\frac{\dot{\xi}_r + \dot{\bar{\xi}}}{3}\left(r - \frac{r_o^3}{r^2}\right), \quad (40a)$$

$$S_{dl}' = \frac{\kappa\rho\mu'' r_i^2}{c_p\bar{q}_o}S_r' = \frac{\rho\mu'' r_i^2}{c_p\bar{q}_o}$$

$$\times\left[\frac{\dot{S}_r + \dot{\bar{S}} + 3q_o/r_o\rho T}{3}\left(r - \frac{r_o^3}{r^2}\right)\right. \quad (40b)$$

$$\left.+ \mu''\frac{\dot{\xi}_r + \dot{\bar{\xi}}}{15T}\left(r^3 - \frac{5}{2}r_o^3 + \frac{3r_o^5}{2r^2}\right) - \frac{q_S}{T\rho}\right].$$

Figures 4a and 4b show the dependences of dimensionless gradients on the thermal flow q_S normalized to the adiabatic flow $\bar{q}_o$. The values of the thermal gradient q_S are considered in the range -0.05 W/m^2 $< q_S <$ 0.08 W/m^2, so that the dimensionless gradient lies in the range $q_S/\bar{q}_o \in (-1.25; 2)$. The range of values of the thermal flow q_S at which the gradient minima are reached at the boundary of the inner core includes the range of values of q_S for which the obtained spherically symmetric diffusion solution is valid. We will calculate below the exact boundaries of this region. The growth rate of the inner core should be positive. This gives the conditions for determining the range of the thermal flow q_S in which the obtained diffusion solution will satisfy this requirement. We obtain from the boundary condition (6a)

$$\xi_r' = \frac{\dot{\xi}_r + \dot{\bar{\xi}}}{3\kappa}\left(r_i - \frac{r_o^3}{r_i^2}\right) < 0, \quad (41a)$$

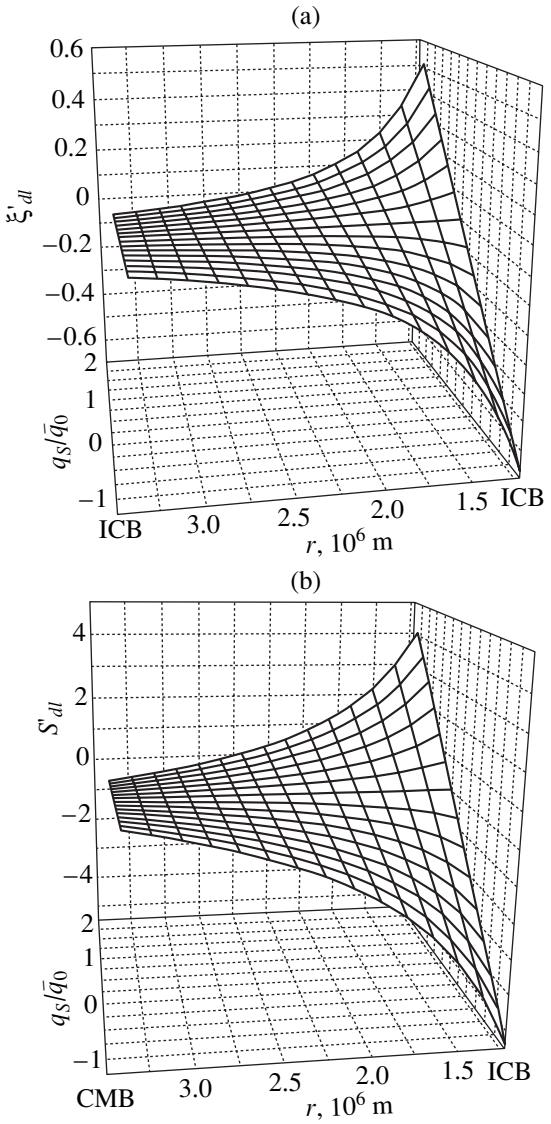

Fig. 4. Dependence of the spherically symmetric dimensionless gradient of the mass fraction (concentration) ξ'_{dl} of the light component (a) and of the specific entropy S'_{dl} (b) on the nonadiabatic thermal flow q_S normalized to the adiabatic thermal flow $\bar{q}_o$.

$$S'_r = \frac{\dot{S}_r + \dot{\bar{S}} + 3q_o/r_o\rho T}{3\kappa}\left(r_i - \frac{r_o^3}{r_i^2}\right) + \mu''\frac{\dot{\xi}_r + \dot{\bar{\xi}}}{15T\kappa}\left(r_i^3 - \frac{5}{2}r_o^3 + \frac{3r_o^5}{2r_i^2}\right) - \frac{q_S}{T\rho\kappa} < 0. \quad (41b)$$

The factor

$$\frac{\rho\mu''r_i^2}{3\bar{q}_0}\left(r_i - \frac{r_o^3}{r_i^2}\right)$$

in (41a) is negative, so that the sum $\dot{\xi}_r + \dot{\bar{\xi}}$ should be positive. The sign of this sum is determined by the sign of the factor

$$\left[q_S\left(\frac{1}{\rho} + \frac{4\pi r_o^2}{3M_o}\left(r_i - \frac{r_o^3}{r_i^2}\right)\right) - \bar{q}_o\left(\frac{1}{\rho r_o} - \frac{4\pi r_o^2}{3M_o}\right)\left(r_i - \frac{r_o^3}{r_i^2}\right)\right],$$

because the other factors are positive. Therefore, we obtain the condition that limits q_S from above:

$$q_S < \bar{q}_o\left(\frac{1}{\rho r_o} - \frac{4\pi r_o^2}{3M_o}\right)\left(r_i - \frac{r_o^3}{r_i^2}\right) \times \left[\frac{1}{\rho} + \frac{4\pi r_o^2}{3M_o}\left(r_i - \frac{r_o^3}{r_i^2}\right)\right]^{-1}. \quad (42a)$$

Then, we obtain the condition

$$\frac{\dot{S}_r + \dot{\bar{S}} + 3q_o/r_o\rho T}{3}\left(r_i - \frac{r_o^3}{r_i^2}\right) - \frac{q_S}{T\rho} < \mu''\frac{\dot{\xi}_r + \dot{\bar{\xi}}}{15T}\left(-r_i^3 + \frac{5}{2}r_o^3\frac{3r_o^5}{2r_i^2}\right)$$

from (41b). The quantity $\dot{\xi}_r + \dot{\bar{\xi}}$ on the right-hand side is positive. By using this condition, the requirement that entropy should decrease with time (cooling of the inner core), and expression (39b), we obtain the condition that limits the thermal flow q_S from below:

$$q_S > -\bar{q}_o\alpha, \quad (42b)$$

where the coefficient

$$\alpha = \left|\left[\left(\frac{1}{\rho r_o} - \frac{4\pi r_o^2}{3M_o}\right)\left(r_i - \frac{r_o^3}{r_i^2}\right)C_\alpha - 4\pi\frac{f_S r_o^2 D}{c_p M_o}\right] \times \left[\left(\frac{1}{\rho} + \frac{4\pi r_o^2}{3M_o}\left(r_i - \frac{r_o^3}{r_i^2}\right)\right)C_\alpha - 4\pi\frac{f_S r_o^2 D}{c_p M_o}\right]^{-1}\right|,$$

$$C_\alpha = \left[\left(\frac{\rho}{3\Delta\xi}\left(r_i - \frac{r_o^3}{r_i^2}\right)\right) \times \left(\frac{1}{\rho_i r_i} - \frac{4\pi r_i^2}{M_o}\left[f_\xi\bar{\xi} + \frac{f_S}{c_p T}(L - \mu\bar{\xi})\right]\right) - f_\xi\right] \times \left[1 - \frac{4\pi\rho r_i^2}{9\Delta\xi M_o}\frac{c_p}{f_S}\frac{1}{D}\left(r_i - \frac{r_o^3}{r_i^2}\right)^2\right] \times \left[f_\xi\bar{\xi} + \frac{f_S}{c_p T}(L - \mu\bar{\xi})\right]^{-1}.$$

For the values of parameters in the PREM model [10] and $\bar{\bar{\xi}} = 0.07$, and $L = 1 \times 10^6$ J/kg [5], the upper limit of the thermal flow, at which the flow can be described by the diffusion solution alone by neglecting convection, is $q_S \approx -0.0095$ W/m^2 and the lower limit is $q_S \approx -0.043$ W/m^2.

7. DISCUSSION AND CONCLUSIONS

The flow of a viscous incompressible liquid between two concentric spheres rapidly rotating around an axis at slightly different velocities (see Fig. 2) has been studied beginning from the middle of the past century [12, 15]. Later, this flow was used to describe both nonmagnetic [13] and MHD flows [2, 16] in cores of the Earth and other planets.

However, no mechanism has been proposed so far for the description of a faster rotation of the inner sphere (solid core) relative to the outer mantle. Our estimate (35) gives for the first time a quite realistic value of the angular rotational velocity $\epsilon d\Omega \approx 10^{-9}$ s^{-1} of the solid core relative to the mantle for the terrestrial parameters of the growth rate of the core $\dot{r}_i \approx 10^{-11}$ m/s (see [3, 9] and Section 6) and molecular viscosity $\kappa_V \approx 10^{-6}$ m^2/s [17].

The corresponding axially symmetric differential rotation and a weak meridional circulation (see Section 5) can be insufficient for excitation of the magnetic field of a planet, by describing the situation that is similar to that existing in the liquid cores of Mars and Venus. A sufficiently powerful flow should excite first of all a magnetic field that is strongly asymmetric with respect to the rotation axis of the planet. If this asymmetric magnetic field cannot produce a strong asymmetric flow, the planetary dynamo will remain in the kinematic regime, as is probably observed for Uranus and Neptune [18]. In the dynamic regime, which is more realistic for Earth, Saturn, and Jupiter [5], the asymmetric MHD flow will produce a magnetic field that will be predominantly symmetric relative to the rotation axis. Therefore, a further development of the approaches proposed in our paper will allow us to solve the basic problems of the planetary MHD dynamo.

In this paper, we have obtained the following basic results.

(i) We have described the convection controlling the composition–thermal effects during the almost solid-state rotation of a spherical layer in the inelastic approximation, which is appropriate for liquid cores of terrestrial planets.

(ii) We have found the analytic spherically symmetric solution of the heat transfer and diffusion equations, which allows the simplification of these initially inhomogeneous equations to make them completely homogeneous equations.

(iii) By scaling the floatability equations, the velocity, and boundary conditions, we have obtained the dimensionless system in which the small Rossby and Eckman numbers characterizing the nonuniformity and velocity of rotation were used as asymptotic parameters.

(iv) The principal asymptotic order in the Rossby number and then in the Eckman number gives the solution determining the flow that is maintained by the differential rotation of solid boundaries of a spherical layer.

(v) The angular momentum in the liquid shell is redistributed due to the growth of the inner sphere, resulting in a faster rotation of the inner sphere with respect to the outer mantle.

ACKNOWLEDGMENTS

The authors thank A. Soward, C. Jones, A. Anufriev, and M. Reshetnyak for fruitful discussions. This work was supported by the INTAS, grant no. 99-00348.

REFERENCES

1. G. A. Glatzmaier and P. H. Roberts, Phys. Earth Planet. Inter. **91**, 63 (1995).
2. G. A. Glatzmaier and P. H. Roberts, Contemp. Phys. **38**, 269 (1997).
3. S. I. Braginsky and P. H. Roberts, Geophys. Astrophys. Fluid Dyn. **79**, 1 (1995).
4. P. H. Roberts, C. A. Jones, and A. R. Calderwood, in *Earth's Core and Lower Mantle*, Ed. by C. A. Jones, A. M. Soward, and K. Zhang (Gordon and Breach, London, 2001).
5. S. V. Starchenko and C. A. Jones, submitted to Icarus (2002).
6. S. V. Starchenko, Zh. Éksp. Teor. Fiz. **115**, 1708 (1999) [JETP **88**, 936 (1999)]; S. V. Starchenko, NATO Sci. Ser., Ser. II: Math., Phys. Chem. **26**, 217 (2001).
7. S. V. Starchenko, Phys. Earth Planet. Inter. **117**, 225 (2000).
8. G. A. Glatzmaier and P. H. Roberts, Physica D (Amsterdam) **97**, 81 (1996).
9. J. R. Lister and B. A. Buffett, Phys. Earth Planet. Inter. **91**, 17 (1995).
10. A. M. Dziewonski and D. L. Anderson, Phys. Earth Planet. Inter. **25**, 297 (1981).
11. F. H. Busse, J. Fluid Mech. **44**, 441 (1970).
12. I. Proudman, J. Fluid Mech. **1**, 505 (1956).
13. L. V. Nikitina and A. A. Ruzmaĭkin, Geomagn. Aéron. **30**, 127 (1990).
14. K. Stewartson, J. Fluid Mech. **3**, 299 (1957).
15. K. Stewartson, J. Fluid Mech. **26**, 131 (1966).
16. S. V. Starchenko, Zh. Éksp. Teor. Fiz. **112**, 2056 (1997) [JETP **85**, 1125 (1997)].
17. G. A. Wijs *et al.*, Nature **392**, 805 (1998).
18. A. A. Ruzmaikin and S. V. Starchenko, Icarus **93**, 82 (1991).

Translated by M. Sapozhnikov

Journal of Experimental and Theoretical Physics, Vol. 94, No. 3, 2002, pp. 470–481.
Translated from Zhurnal Éksperimental'noĭ i Teoreticheskoĭ Fiziki, Vol. 121, No. 3, 2002, pp. 551–564.

NUCLEI, PARTICLES, AND THEIR INTERACTION

Critical Enhancement of Nonlinear Response in Fast Photorefractive Crystals

M. V. Gorkunov[a], E. V. Podivilov[b], and B. I. Sturman[b, *]

[a]*Shubnikov Institute of Crystallography, Russian Academy of Sciences, Leninskii pr. 59, Moscow, 117333 Russia*
[b]*International Institute for Nonlinear Studies, Russian Academy of Sciences, Novosibirsk, 630090 Russia*
**e-mail: sturman@iae.nsk.su*

Received August 14, 2001

Abstract—It is shown that when approaching the spatial subharmonics generation threshold in fast photorefractive crystals (the sillenites, CdTe), a practically unlimited (singular) amplification of the nonlinear photorefractive response is possible, which results in a drastic increase in the spatial amplification of weak signals. A theory of critical spatial amplification is developed. This theory takes into account real attributes of fast photorefractive crystals such as the vectorial nature of wave coupling and nonuniform broadening of resonances owing to light absorption. The theory is applied to the analysis of the observable characteristics of critical enhancement and to optimization of the conditions of experiments aimed at the detection and investigation of this phenomenon. © *2002 MAIK "Nauka/Interperiodica".*

1. INTRODUCTION

Photorefractive nonlinearity, which is inherent in the majority of photosensitive non-centrosymmetrical materials, manifests itself in the degenerate (in frequency) interaction of light waves even in the range of small intensities. The main elements of this nonlinearity are the charge separation under light, the change of the optical susceptibility owing to the linear electro-optic effect, and diffraction on the induced variations of the optical density [1–3]. The rate of spatial amplification is determined by the product of the corresponding electro-optic coefficient and the space-charge field induced inside the crystal. Often, this rate attains its maximum already at milliwatt light power. The nonlinear response time is determined by the rate of charge separation and is usually inversely proportional to the light intensity.

Unfortunately, photorefractive materials exhibiting strong spatial amplification ($\Gamma = 10^1$–10^2 cm^{-1}), such as $LiNbO_3$ or $BaTiO_3$, are very slow. The response time, t_r, of these materials is of the order of 10^2 s, which is not acceptable for many applications and is inconvenient for experiments. On the other hand, fast photorefractive materials, such as cubic crystals of the sillenite family (BSO, BTO, and BGO) and cubic semiconductors (CdTe, GaAs, and others), possess an insufficiently strong nonlinearity ($\Gamma < 1$ cm^{-1}).

Since a fast response is imperative, considerable effort has been spent to investigate the photorefractive properties of cubic crystals and also to enhance their nonlinearity [2–5]. These efforts resulted in the discovery of a number of fundamental effects related to the resonance (linear and nonlinear) excitation of low-frequency weakly damped space-charge waves inherent in fast electrically biased materials [6–8]. If $\mathbf{K} = \mathbf{k}_1 - \mathbf{k}_2$ is the wave vectors of the light waves 1 and 2 and $\Omega = \omega_1 - \omega_2$ is a small frequency detuning between them, then the condition of the linear resonance between the driving interference light pattern and the space-charge field characterized by the wave vector $\mathbf{K}$ is $\Omega = \omega_K$, where ω_K is the eigenfrequency of the space-charge wave. If $\mathbf{K}$ is parallel to the applied electric field $\mathbf{E}_0$, then the simplest model capable of describing the space-charge waves and applicable (at least) to the sillenites yields the dispersion law [8]

$$\omega_K = \frac{4\pi}{\varepsilon_0}\frac{\alpha I_0}{\hbar\omega}\frac{1}{KE_0}, \quad (1)$$

where ε_0 is the static dielectric constant, α is the absorption coefficient, I_0 is the total intensity, and $\hbar\omega$ is the energy of a light quantum. This law is valid within the region of K and E_0 where the frequency ω_K is considerably larger than the decay constant γ_K. Under linear resonance conditions, the amplitude of the space-charge field E_K increases by a factor of $Q_K \equiv |\omega_K|/\gamma_K$ compared to the case $\Omega = 0$. This effect is known as the DC enhancement of the photorefractive response [2, 4]. A similar enhancement effect occurs in the case of application of an alternating AC field [3, 9]. In the sillenites, the quality factor Q_K does not usually exceed 6–8.

Another fundamental effect caused by the presence of weakly damped space-charge waves is their parametric excitation, which is often called the generation of spatial subharmonics [2, 8, 10, 11]. This subharmonic generation also occurs during two-wave mixing in the presence of a frequency detuning Ω. The subharmonic

$K/2$ possesses the minimum excitation threshold, and the corresponding parametric resonance condition is

$$\Omega = 2\omega_{K/2} \equiv 4\omega_K.$$

The threshold condition at the resonance point is

$$m > m_{\text{th}} = 3/Q_{K/2},$$

where m is the contrast of the light interference pattern; it varies from 0 to 1 depending on the ratio of the pump intensities. The excitation of the $K/2$ subharmonic at $m > m_{th}$ is soft; i.e., it is not accompanied by the jump in the amplitude $E_{K/2}(m)$ [12–14].

Recently, it has been shown [15] that the rate Γ of the exponential spatial amplification of a weak central light beam (see Fig. 1) has to experience a critical enhancement

$$\Gamma \propto (m_{th} - m)^{-1}$$

when approaching (from below) the parametric instability threshold. The physical reason for this singularity is the fact that the decay constant for the space-charge wave with the wave vector $K/2$ goes to zero at the instability threshold. The mechanism of the critical spatial amplification of the central beam includes the interference (hybridization) of the parametric processes caused by the optical and material nonlinearities. To our best knowledge, there are no analogues of this mechanism among the known nonlinear phenomena. Implementation of the critical enhancement opens new possibilities for applications.

Unfortunately, the model considered in [15] is illustrative. More precisely, it cannot be used to describe the effect in question and formulate the conditions for its experimental detection and investigation. This is due to several reasons. First, the optical nonlinearity of cubic crystals is vectorial in nature; i.e., the spatial changes of the light intensity and polarization cannot be separated [16, 17]. Second, the space-charge wave eigenfrequencies decrease across the crystal owing to the linear light absorption (Fig. 1), which leads to the nonuniform broadening of resonances [18, 19]. Third, optical effects in cubic crystals are sensitive to orientation of the vector $\mathbf{K}$ (and $\mathbf{E}_0$) about the crystallographic axes [3, 16]. All these important features of the effect under study were not taken into account in [15].

In this paper, we propose a full-scale theory of the critical photorefractive enhancement in fast cubic crystals. It incorporates all the above-mentioned attributes of the optical and material nonlinearities. Our theory provides the reader with recommendations for the optimization of the effect and describes its main output characteristics as functions of the experimentally controlled parameters. The theory is based on the results of the preceding theoretical and experimental studies on the parametric excitation of the space-charge waves [8, 10, 12–14] and the vectorial wave coupling [17, 19].

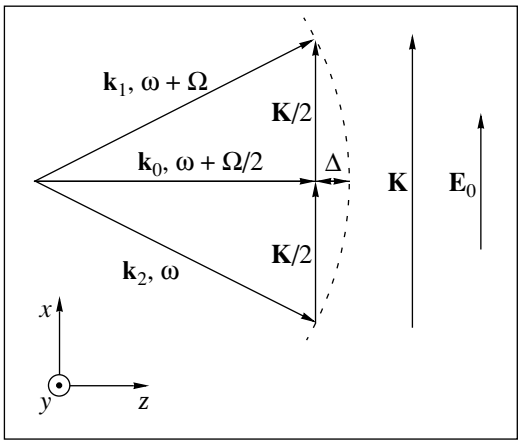

Fig. 1. Basic interaction scheme. The wave vectors $\mathbf{k}_1$, $\mathbf{k}_2$, and $\mathbf{k}_0$ refer to the pump beams and to the weak central beam being amplified; Ω is the frequency detuning; and Δ is the Bragg mismatch.

The paper is organized as follows. In Section 2, we introduce the necessary relations of the theory of parametric excitation of space-charge waves and the basic equations of the vectorial coupling of light waves in cubic crystals. Then, the main approximations are considered, and equations of the theory of critical enhancement are formulated. In Section 3, we perform a unitary transformation to new variables which simplifies the vectorial equation for the amplitude of the central beam. In Section 4, we discuss the values of the optical and material parameters of BSO and BTO crystals that are most promising for experimental studies of the critical effects and make the necessary estimates of the parameters entering the theory. In Section 5, the limiting case of thin crystals, which admits a complete analytical analysis, is considered. This case provides a basis for understanding many properties of the effect in question. In Section 6, the results of numerical simulation of the critical enhancement in BSO and BTO crystals are presented. These results are compared with the predictions of the simplified model. Section 7 comprises discussion of the results obtained, recommendations for experiments, and conclusions.

2. BASIC RELATIONS

A geometric diagram of the critical enhancement is presented in Fig. 1. The applied field $\mathbf{E}_0$ and the fundamental grating vector $\mathbf{K}$ are parallel to the x axis and perpendicular to the propagation direction z. The frequency detuning between the pump beams 1 and 2 is Ω, and the detuning for the weak central beam 0 is $\Omega/2$. Below we assume that $\Omega \approx 4\omega_K(z)$ in the whole crystal, which means that its thickness d is small compared to the absorption length α^{-1}. This assumption does not mean that the effect of the linear absorption on the critical enhancement is small since the frequency width of

the parametric resonance is determined by the damping constant $\gamma_{K/2}$, which is small compared to $\omega_{K/2} = 2\omega_K$. However, this restriction allows us to assume that Ω is substantially greater than ω_K; i.e., the direct excitation of the fundamental grating by the pump beams 1 and 2 is not resonant. For convenience, we set $k_0 = (k_{1,2})_z$, as was done in [15]. A small deficit of the wave vector Δ (the Bragg mismatch) can be easily taken into account within the approximation of slowly varying amplitudes.

As follows from the geometric diagram, the intensity grating formed by the pump beams 1 and 2 propagates with the same velocity Ω/K as the gratings induced by the wave pairs (1, 0) and (0, 2). Furthermore, the condition for parametric excitation of the subharmonic $K/2$ by the pump beams coincides with the condition of its linear excitation by the above-mentioned wave pairs.

The basic relations consist of coupled equations for the scalar amplitudes of the space-charge field gratings and for the vectorial amplitudes of light waves. The structure of these equations is determined by the properties of the material and optical nonlinearities. In the framework of the conventional single-center model of charge transfer [1, 2], the amplitude of the electric field on the spatial frequency $K/2$ and the time frequency $\Omega/2$ normalized by the magnitude of the applied field E_0 and denoted by $e_{K/2}$ obeys the equation (see [8, 14])

$$[\partial_t + \gamma_{K/2} + i\omega_{K/2} - i\Omega/2]e_{K/2} = i|\omega_{K/2}|(2e_K e^*_{K/2} - \mathbf{a}_0 \cdot \mathbf{a}^*_2 - \mathbf{a}_1 \cdot \mathbf{a}^*_0). \quad (2)$$

Here, e_K is the amplitude of the fundamental grating normalized by E_0, and $\mathbf{a}_{0,1,2}$ are the vectorial amplitudes of the light waves 0, 1, and 2 normalized by the square root of their total intensity I_0. Within the undepleted pump approximation, we have

$$|\mathbf{a}_1|^2 + |\mathbf{a}_2|^2 = 1.$$

The structure of the left-hand side of Eq. (2) is typical of resonance wave phenomena. The first term on the right-hand side describes the coupling of the grating $K/2$ with the fundamental grating; it is responsible for the parametric excitation of the subharmonic. The second and third terms in the parentheses describe the linear excitation of the subharmonic $K/2$ by the wave pairs (0, 2) and (1, 0); the quantities $2|\mathbf{a}_0 \cdot \mathbf{a}^*_2|$ and $2|\mathbf{a}_1 \cdot \mathbf{a}^*_0|$ are simply the values of the contrast of the interference patterns formed by those pairs. Each of the above contributions to the right-hand side is well known in theory and is confirmed experimentally.

Since the excitation of the fundamental grating is not resonant,

$$\Omega - \omega_K \approx 3\omega_K \gg \gamma_K,$$

its amplitude obeys the simple equation (see [8])

$$e_K = \mathbf{a}_1 \cdot \mathbf{a}^*_2/3.$$

It is valid up to the contrast

$$m \equiv 2|\mathbf{a}_1 \cdot \mathbf{a}^*_2| = 1.$$

In steady state, Eq. (2) can be easily solved with respect to $e_{K/2}$. Taking into account the fact that $\gamma_{K/2}$ and $\omega_{K/2}$ are proportional to $I_0 \propto \exp(-\alpha z)$, we write the corresponding equation in the form

$$e_{K/2} = \frac{-i\tilde{Q}}{1-\xi^2} \times \left[\mathbf{a}_0 \cdot \mathbf{a}^*_2 + \mathbf{a}^*_0 \cdot \mathbf{a}_1 - \frac{2i}{3}\tilde{Q}^*(\mathbf{a}_1 \cdot \mathbf{a}^*_2)(\mathbf{a}_0 \cdot \mathbf{a}^*_1 + \mathbf{a}^*_0 \cdot \mathbf{a}_2)\right], \quad (3)$$

where

$$\tilde{Q} = [Q^{-1}_{K/2} + i\delta(z)]^{-1}$$

is the complex resonance factor,

$$\delta = 1 - \Omega\exp(\alpha z)/4\omega_K(0)$$

is the dimensionless detuning from the parametric resonance, and

$$\xi = m|\tilde{Q}|/3 < 1$$

is a parameter that describes the proximity to the subharmonic generation threshold. At $\xi \longrightarrow 1$, the subharmonic amplitude $e_{K/2} \longrightarrow \infty$. The quantity $|\tilde{Q}|$ can be considered as an effective quality factor that takes into account the spatially dependent detuning from the resonance. At $\delta = 0$, we have $\tilde{Q} = Q_{K/2}$. The larger $|\delta|$, the bigger the threshold value of the contrast. Clearly, the minimum threshold value of m corresponding to $\delta = 0$ is

$$m_{th} = 3/Q_{K/2}.$$

Among the equations for the light wave amplitudes, the equation for $\mathbf{a}_0 = (a_0)_{x,y}$ is the most important. This amplitude changes owing to linear and nonlinear effects. The relevant linear effects are the optical activity, the optical anisotropy induced by the applied field, and the Bragg mismatch. The nonlinear processes are diffraction of the pump waves 1 and 2 from the grating $\mathbf{K}/2$ (see Fig. 1). All these processes are inertia-free at the scale of the characteristic nonlinear response time. As a result, the equation for $\mathbf{a}_0$ does not include any time derivatives and can be written in the form

$$(\partial_z - i\Delta + i\boldsymbol{\kappa} \cdot \hat{\boldsymbol{\sigma}})\mathbf{a}_0 = iE_0(\nu_0 + \boldsymbol{\nu} \cdot \hat{\boldsymbol{\sigma}})(e^*_{K/2}\mathbf{a}_1 + e_{K/2}\mathbf{a}_2). \quad (4)$$

Here $\hat{\boldsymbol{\sigma}} = (\hat{\sigma}_1, \hat{\sigma}_2, \hat{\sigma}_3)$ is the standard set of σ matrices (Pauli matrices) [20]; $\boldsymbol{\kappa} = (\kappa_1, \rho, \kappa_3)$, $\boldsymbol{\nu} = (\nu_1, 0, \nu_3)$, and ν_0 are certain known quantities [17]; and ρ is the rota-

tory power. The absorption coefficient α does not enter (4) because the light amplitudes are normalized by $I_0(z) \propto \exp(-\alpha z)$. The zero value of the component ν_2 is explained by the fact that the light induced space-charge grating does not affect the optical activity. The parameter ν_0 describes the isotropic part of the interaction matrix, and the components $\nu_{1,3}$ describe its anisotropic part that changes the polarization state under diffraction. The use of the σ representation significantly simplifies the analysis of the vectorial wave coupling [17, 19].

It is essential that the parameters $\kappa_{1,3}$, $\nu_{1,3}$, and ν_0 can be calculated for any particular optical configuration, i.e., for any orientation of $\mathbf{K}$ and $\mathbf{E}_0$ with respect to the crystallographic axes of cubic crystals [17, 21]. In practical terms, the case $\mathbf{K}, \mathbf{E}_0 \perp [110]$, $z \parallel [110]$ is of prime importance; it is relevant to all known experiments on the subharmonic generation and to most experiments on two-wave mixing. Restricting ourselves to this case, we have

$$\kappa_1 = qE_0 \sin\zeta, \quad \kappa_3 = -0.5qE_0 \cos\zeta,$$

where

$$q = \pi n^3 r_{41}/\lambda,$$

ζ is the angle between $\mathbf{K}$ and [001], n is the refractive index, r_{41} is the only nonzero electro-optic coefficient for the crystals of group 23 (the sillenites) and $\bar{4}2m$ (semiconductors), and λ is the light wavelength. The parameters $\nu_{0,1,3}$ generally include not only the electro-optic but also elasto-optic contributions caused by piezoelectric deformations [22, 23]. In many important cases (see also below) the elasto-optic contributions are either zero or negligibly small. With these contributions neglected, we have

$$\nu_0 = 0.5q\cos\zeta, \quad \nu_1 = q\sin\zeta, \quad \nu_3 = -0.5q\cos\zeta.$$

For experiments, the so-called longitudinal ($\mathbf{K} \parallel \mathbf{E}_0 \parallel [001]$) and transverse ($\mathbf{K} \parallel \mathbf{E}_0 \parallel [001]$) optical configurations are most important. In both cases, neglect of the elasto-optic contributions to $\nu_{0,1,3}$ is fully justified. In the longitudinal case, we have

$$\kappa_1 = 0, \quad \kappa_3 = -qE_0/2, \quad \nu_0 = q/2,$$

$$\nu_1 = 0, \quad \nu_3 = -q/2,$$

whereas in the transverse geometry

$$\kappa_1 = qE_0, \quad \kappa_3 = 0,$$

$$\nu_0 = \nu_3 = 0, \quad \nu_1 = q.$$

Note that in the transverse configuration, the isotropic part of the interaction matrix is absent ($\nu_0 = 0$), and in the longitudinal case this part is equal in magnitude to the anisotropic part. The cases where the isotropic part of interaction is dominating do not occur in cubic photorefractive crystals. We also note that the opposite directions of crystallographic axes (e.g., [001] and $[00\bar{1}]$) are usually indistinguishable in experiment. The necessary sign of r_{41} can be chosen by rotating the sample by 180° about the propagation axis [110].

The amplitudes of the pump waves $\mathbf{a}_{1,2}$ that enter Eq. (4) cannot be treated as constants. They vary as the waves propagate in the crystal at least owing to the linear effects (optical activity and the birefringence induced by the applied field). The influence of the nonlinear effects on $\mathbf{a}_{1,2}$ can be neglected within a wide range of the input parameters. The influence of the central beam on pump beams is small for a sufficiently small amplitude $\mathbf{a}_0(0)$ and the crystal thickness d; the mutual influence of the pump beams 1 and 2 via diffraction from the K grating is small because of the nonresonant nature of its excitation. Actually, the latter effect is small for $d \lesssim 3$–4 mm, while the critical enhancement of the central beam remains very large even for smaller values of the thickness (see also below). Thus, the amplitudes $\mathbf{a}_{1,2}$ obey the linear equation

$$(\partial_z - i\boldsymbol{\kappa} \cdot \hat{\boldsymbol{\sigma}})\mathbf{a}_{1,2} = 0. \tag{5}$$

The validity of the paraxial approximation, i.e., the possibility to neglect the components $(a_{1,2})_z$, is beyond any question in our case because the angles between the propagation directions and the z axis do not exceed several degrees inside the crystal. The system of equations (3)–(5) is sufficient for the description of the critical enhancement.

3. INTERACTION REPRESENTATION

In order to get rid of the dependence $\mathbf{a}_{1,2}(z)$ and the linear term $\boldsymbol{\kappa} \cdot \hat{\boldsymbol{\sigma}}$ in Eq. (4), it is useful to perform the unitary transformation

$$\mathbf{a}_{0,1,2} = \exp(iz\boldsymbol{\kappa} \cdot \hat{\boldsymbol{\sigma}})\mathbf{b}_{0,1,2}. \tag{6}$$

The transformation to the new variables $\mathbf{b}_{0,1,2}$ is similar to the usage of the interaction representation in quantum mechanics [20]. The new amplitudes of the pump waves do not depend on z, and they are equal to the corresponding input values of the initial amplitudes:

$$\mathbf{b}_{1,2}(z) = \mathbf{b}_{1,2}(0) = \mathbf{a}_{1,2}(0).$$

When transforming Eq. (4), one has to use Eq. (3) for $e_{K/2}$. For simplicity, we assume that the input polarizations of the pump beams are identical, and the phase of the central beam is measured from the half-sum of the

Table

	n	$\lvert r_{41}\rvert$	$\lvert\rho\rvert$	ε_0	$q = \pi n^3 r_{41}/\lambda$	$\lvert\rho/q\rvert$
BSO	2.6	4.5×10^{-10} cm/V	38.8 deg/mm	56	0.48 $(\text{kV})^{-1}$	13.8 kV/cm
BTO	2.58	4.75×10^{-10} cm/V	6.5 deg/mm	47	0.4 $(\text{kV})^{-1}$	2.8 kV/cm

phases of the input pump beams. As a result, the equation for $\mathbf{b}_0$ can be written in the form

$$\begin{aligned}(\partial_z - i\Delta)\mathbf{b}_0 &= -\frac{E_0}{1-\xi^2}\\ &\times [(\mathbf{b}_0 \cdot \mathbf{e}_0^*)(\tilde{Q}'W_0 - i\tilde{Q}'' + im_0|\tilde{Q}|\xi)\\ &+ i(\mathbf{b}_0^* \cdot \mathbf{e}_0)(|\tilde{Q}|\xi - m_0\tilde{Q}'')](\nu_0 + \mathbf{h}\cdot\hat{\boldsymbol{\sigma}})\mathbf{e}_0,\end{aligned} \tag{7}$$

where

$$W_0 = |\mathbf{a}_1(0)|^2 - |\mathbf{a}_2(0)|^2$$

is the normalized pump intensity difference at the input,

$$m_0 = \sqrt{1 - W_0^2}$$

is the input value of the contrast, $\mathbf{e}_0$ is the unit polarization vector for the pump,

$$\xi = m_0|\tilde{Q}|/3$$

is the parameter describing the proximity to the generation threshold (now, this parameter depends on the input value of the contrast), and $\tilde{Q}'$ and $\tilde{Q}''$ are the real and imaginary parts of $\tilde{Q}$. The vector $\mathbf{h}$ on the right-hand side of Eq. (7) depends on z:

$$\begin{aligned}\mathbf{h} &= \boldsymbol{\nu} - 2\sin^2(\kappa z)[\boldsymbol{\nu} - \mathbf{n}(\mathbf{n}\cdot\boldsymbol{\nu})]\\ &+ \mathbf{n}\times\boldsymbol{\nu}\sin(2\kappa z),\end{aligned} \tag{8}$$

where $\mathbf{n} = \boldsymbol{\kappa}/\kappa$. The appearance of this dependence comes from the noncommutativity of the operators $\boldsymbol{\nu}\cdot\hat{\boldsymbol{\sigma}}$ and $\boldsymbol{\kappa}\cdot\hat{\boldsymbol{\sigma}}$. Thus, Eq. (7) includes two sources of the spatial inhomogeneity—the dependence $\tilde{Q}(z)$, which occurs owing to the light absorption and corresponds to the nonuniform broadening of the resonance, and the dependence $\mathbf{h}(z)$, which describes the vectorial character of the optical nonlinearity in cubic crystals. To return to the scalar case considered in [15], it is necessary to set

$$\alpha = 0, \quad \Omega = 4\omega_K, \quad \rho = 0$$

in Eq. (7) and, in addition, to equate the polarization vector $\mathbf{e}_0$ to an eigenvector of the operator $\boldsymbol{\nu}\cdot\hat{\boldsymbol{\sigma}}$.

The main feature of Eq. (7) responsible for the critical enhancement is the factor $(1 - \xi^2)^{-1}$, which grows infinitely when approaching the subharmonic generation threshold. Another interesting feature is a coupling between the amplitudes $\mathbf{b}_0$ and $\mathbf{b}_0^*$. Such a coupling is typical of parametric wave processes. In our particular case, this coupling is expected from the geometric diagram in Fig. 1; it exists even when the parametric coupling between $\mathbf{e}_{K/2}$ and $\mathbf{e}_{K/2}^*$ in Eq. (2) is absent. The neglect of the material nonlinearity in Eq. (7) is equivalent to setting ξ equal to zero.

Note that the use of the amplitudes $\mathbf{b}$ instead of $\mathbf{a}$ does not result in any substantial complication of the calculation of the observable characteristics; indeed, the unitary transformation does not change the scalar product of vectors. In particular, we have

$$|\mathbf{a}_0(z)|^2 = |\mathbf{b}_0(z)|^2, \quad \mathbf{a}_1(z)\cdot\mathbf{a}_2^*(z) = \mathbf{b}_1(z)\cdot\mathbf{b}_2^*(z),$$

and so on.

4. OPTICAL AND MATERIAL PARAMETERS FOR BSO AND BTO CRYSTALS

In order to understand the importance of various contributions and the possible range of variation of the basic parameters of the theory, we present some data and numerical estimates for the sillenites BTO and BSO known from the literature. The simple model of the charge separation used above is experimentally verified for these materials. Most experiments on the subharmonic generation have been performed with BSO crystals at $\lambda = 514$ nm. For BTO crystals, the greater part of experiments dealt with measurements of the beam coupling characteristics at $\lambda = 633$ nm.

The table lists the values of the main parameters for BSO and BTO crystals, which are free of model assumptions. They are not much different from each other except for the rotatory power, which is much greater for BSO. The ratio ρ/q presented in the table is interpreted as the field at which the electro-optic contribution to the optical susceptibility becomes comparable with that of the optical activity. At $\rho \gg |qE_0|$ and $\rho \ll |qE_0|$, the optical eigenmodes are polarized almost circularly and almost linearly, respectively. Since the fields typically used in experiments on the subharmonic generation are in the range 6–8 kV/cm, we conclude that in BSO crystals we deal with the first case and in BTO crystals, with the second case. This circumstance is important for characterization of the critical enhancement.

The dependence of the quality factor $Q_{K/2}(E_0)$ is controlled by two material parameters—the trap concentration N_t and the mobility–lifetime product for pho-

toelectrons $\mu\tau$ [8]. According to the literature [2, 3], the concentration N_t for BSO and BTO crystals can be estimated as 10^{16} cm^{-3} and 3×10^{16} cm^{-3}, respectively. The values of $\mu\tau$ in BSO vary in the range 10^{-7}–10^{-6} cm^2/V, and in BTO crystals in the range $3 \times (10^{-8}$–$10^{-7})$ cm^2/V. We choose 3×10^{-7} and 10^{-7} cm^2/V as representative values of $\mu\tau$ for BSO and BTO, respectively. These values are far from being extreme.

Figure 2 depicts the contour lines of the quality factor $Q_{K/2}$ on the K, E_0 plane. It also shows the corresponding values of the pump half-angle θ_p in air. One sees that the values of the quality factor $Q_{K/2} > 3$, which are necessary for the generation of the subharmonic $K/2$, are attainable in a wide range of fields and angles. For BSO, the saturation of $Q_{K/2}$ with an increase in the applied field occurs somewhat sooner than for BTO; the optimum angles are also smaller for BSO crystals. At a fixed E_0, the same value of the quality factor occurs for two different values of K (of the angle θ_p).

The Bragg mismatch Δ, which is also an important parameter of our theory, is expressed in terms of θ_p and λ as $\Delta = \pi\theta_p^2/n\lambda$. Large values of Δ that impede diffraction into the central beam must have a negative effect on the critical enhancement. For this reason, it is practical to choose the minimum of the values θ_p mentioned above. In turn, this value is relatively small in BSO crystals.

The characteristic length at which the pump waves substantially change their amplitudes owing to diffraction from the K grating can be estimated as $2/|qE_0|$. At $E_0 = 7$ kV/cm, it is about 6–8 mm for both BTO and BSO crystals.

For BSO crystals, the absorption coefficient α at the wavelength 514 nm ranges from 1 to 2.5 cm^{-1}; for BTO, $\alpha \approx 0.5$ cm^{-1} at $\lambda = 633$ nm [3, 24].

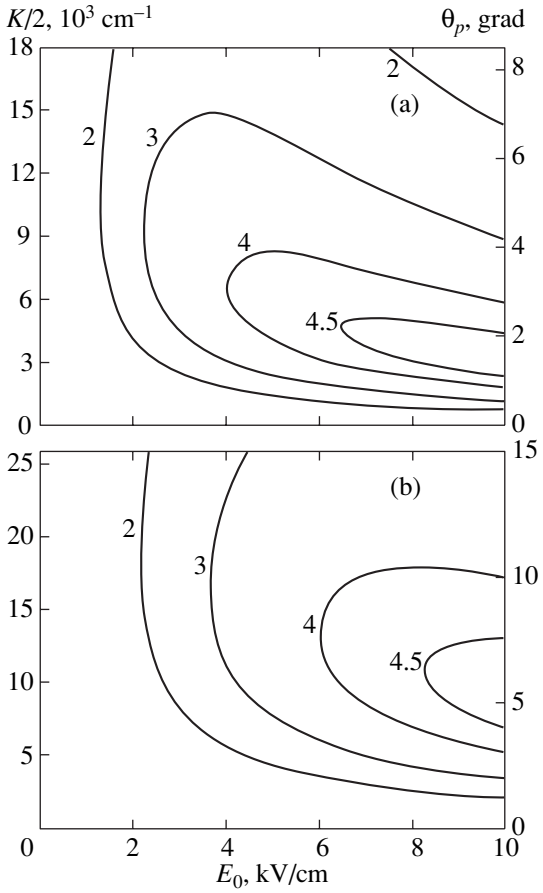

Fig. 2. Contour lines of the quality factor, $Q_{K/2}(E_0)$ = const, for BSO (a) and BTO (b) crystals. In the case (a), $\mu\tau = 3 \times 10^{-7}$ cm^2/V and $N_t = 10^{16}$ cm^{-3}; in the case (b), $\mu\tau = 10^{-7}$ cm^2/V and $N_t = 3 \times 10^{16}$ cm^{-3}. The other material parameters are listed in the table. The recalculation of the spatial frequency $K/2$ to the pump half-angle θ_p is carried out for $\lambda = 514$ (a) and 633 nm (b).

5. SPATIALLY UNIFORM MODEL

It has already been mentioned that the necessary condition for the applicability of Eq. (7) is

$$|qE_0|d \ll 1.$$

It is equivalent to the condition of a small energy exchange between the pump beams 1 and 2 owing to diffraction from the fundamental grating. In experiments on the subharmonic generation, this condition is usually fulfilled for $d \lesssim 3$–4 mm. Furthermore, we know that Eq. (7) includes two sources of the spatial inhomogeneity—$\mathbf{h}(z)$ and $\tilde{Q}(z)$. The characteristic scales at which the variation of these parameters becomes substantial can be estimated as ρ^{-1} and $2/\alpha Q_{K/2}$. They are about 1–2 mm for BSO and somewhat greater for BTO. If the thickness d is much smaller than this quantity, we can neglect the effect of inhomogeneity in Eq. (7) and use the simplified spatially uniform vectorial model in which

$$\mathbf{h} = \mathbf{v}, \quad \omega_K = \omega_K(0),$$

$$\delta = \frac{\Omega - 4\omega_K}{4\omega_K}, \quad \tilde{Q} = (Q_{K/2}^{-1} + i\delta)^{-1}, \quad \xi = m_0|\tilde{Q}|/3$$

are constants. Because of the critical dependence of the right-hand side of Eq. (7) on ξ, the effect of spatial amplification remains strong within the simplified model. Finally, we note that the difference between the amplitudes $\mathbf{a}(z)$ and $\mathbf{b}(z)$ is negligibly small in the limit under consideration.

Assuming the coefficients in the vectorial equation (7) to be constants, taking the scalar product of this equation with $\mathbf{e}_0^*$, and setting $(\mathbf{e}_0^* \cdot \mathbf{a}_0)$, $(\mathbf{e}_0 \cdot \mathbf{a}_0^*) \propto \exp(\Gamma z)$, we obtain an eigenvalue problem for the increment Γ.

This problem has two solutions

$$\Gamma_{\pm} = f_1 \pm \sqrt{g^2 - f_2^2}, \tag{9}$$

where

$$f_1 = -\frac{\bar{\nu}E_0\tilde{Q}'W_0}{1-\xi^2},$$

$$f_2 = \Delta - \frac{\bar{\nu}E_0}{1-\xi^2}(m_0\xi|\tilde{Q}| - \tilde{Q}''), \tag{10}$$

$$g = \frac{\bar{\nu}E_0}{1-\xi^2}(m_0\tilde{Q}'' - \xi|\tilde{Q}|),$$

and $\bar{\nu} = \nu_0 + \boldsymbol{\nu}\cdot\mathbf{s}_0$ is the effective coupling constant, which depends on the polarization of the pump beams through the Stokes vector $\mathbf{s}_0$ [25]. For the linear input polarization, the components of the Stokes vector are expressed in terms of the angle φ_0 between the polarization plane and the direction of the crystallographic [001] axis as

$$\mathbf{s}_0 = (\sin 2\varphi_0, 0, \cos 2\varphi_0).$$

For the circular polarization, we have

$$\mathbf{s}_0 = (0, \pm 1, 0).$$

The spatial dependence of the amplitude projection $a_0 = \mathbf{e}_0^* \cdot \mathbf{a}_0(z)$ generally includes two exponential factors

$$a_0 = \frac{1}{2\sqrt{g^2 - f_2^2}}\{[a_0(0)(f-\Gamma_+) - iga_0^*(0)]e^{\Gamma_+ z} - [a_0(0)(f-\Gamma_-) - iga_0^*(0)]e^{\Gamma_- z}\}, \tag{11}$$

where $f = f_1 - if_2$. The preexponential factors (11) depend on the input phase $\Phi_0 = \arg[a_0(0)]$, which is typical of parametric processes. If one of these factors goes to zero, then the two-component vector $[a_0(0), a_0^*(0)]$ is an eigenvector of the actual value of the increment. If $\exp[(\Gamma_+ - \Gamma_-)d] \gg 1$, then the effect of the spatial amplification is related mainly to the first term in (11) (see also below).

The amplitude $\mathbf{a}_0(z)$ can be found from Eqs. (7) and (11) by straightforward integration. It has two components, one of which is parallel and the other is perpendicular to the vector $(\nu_0 + \boldsymbol{\nu}\cdot\hat{\boldsymbol{\sigma}})\mathbf{e}_0$; only the first component experiences spatial amplification. In the general case, the vectorial amplitude $\mathbf{a}_0(z)$ changes its direction during propagation. However, in the important case when $\mathbf{a}_0(0) \parallel \mathbf{e}_0$ and the pump polarization vector $\mathbf{e}_0$ is an eigenvector of the operator $\boldsymbol{\nu}\cdot\hat{\boldsymbol{\sigma}}$, the direction $\mathbf{a}_0(z)$ remains unchanged, and the spatial amplification problem is reduced to the scalar problem. For the longitudinal geometry ($\mathbf{K} \parallel [001]$), this corresponds to the polarization angle $\varphi_0 = 0$ or $\pi/2$; for the transverse configuration ($\mathbf{K} \perp [001]$), we have $\varphi_0 = \pm 45°$ instead.

Consider the properties of the increment Γ, which is the main characteristic of the spatial amplification, in more detail. As seen from (9), the values $\Gamma_{\pm}$ are real for $g^2 \geq f_2^2$. This case corresponds to Bragg diffraction into the central beam; it occurs for a sufficiently small mismatch Δ and a sufficiently strong parametric coupling. The latter means that ξ is close to the critical unit value. At $g^2 \leq f_2^2$, we are in the region of off-Bragg diffraction; here $\Gamma_+ = \Gamma_-^*$; i.e., the real parts $\Gamma_{\pm}'$ coincide.

In the vicinity of the instability threshold, when $\xi \longrightarrow 1$, Eqs. (10) and (11) become much simpler; one of the values $\Gamma_{\pm}$ tends to infinity, and the other one remains finite. The singular value of the increment (Γ_+) is positive if $\bar{\nu}W_0E_0 < 0$. In this case, which is of major importance, we have

$$\Gamma_+ \approx -\frac{3E_0W_0(\nu_0 + \boldsymbol{\nu}\cdot\mathbf{s}_0)}{m_0[(1+\delta^2 Q_{K/2}^2)^{1/2} - Q_{K/2}m_0/3]}. \tag{12}$$

The negative sign of the product $\bar{\nu}W_0E_0$ can be achieved either by the interchange of the pump intensities (the change of sign of W_0) or by a 180° rotation of the crystal about the z axis (the change of the signs of ν_0 and $\boldsymbol{\nu}$). The change of the sign of E_0 is not desirable because it leads to the change of the sign of ω_K. It is worth noting that in the vicinity of the singularity the cases

$$\bar{\nu}E_0 < 0, \quad W_0 > 0$$

and

$$\bar{\nu}E_0 > 0, \quad W_0 < 0$$

are equivalent. Generally, the second combination is preferable. In this case, the negative nonlinear correction of the wave vector length k_0 compensates for the Bragg mismatch Δ (see Fig. 1). The expression in square brackets in the denominator of Eq. (12) is simply the distance to the instability threshold with account for the detuning δ. At

$$m_0 < m_{th} = 3/Q_{K/2},$$

our theory is valid in the entire resonance region, whereas at $m_0 > m_{th}$ the field of applicability is restricted to the resonance wings

$$|\delta| > Q_{K/2}^{-1}\sqrt{(m/m_{th})^2 - 1}.$$

The absolute value of the coupling parameter in (12) depends on the pump polarization and the optical configuration in question. Since $\nu_2 = 0$, the scalar product $\boldsymbol{\nu}\cdot\mathbf{s}_0$ attains its minimum and maximum when the pump polarization is linear, i.e., $s_2 = 0$. Accordingly, the

maximum and minimum (in terms of polarization) values of $|\bar{\nu}|$ are $|\nu_0| \pm |\mathbf{\nu}|$. For the longitudinal configuration *L*, we have

$$|\nu_0| + |\mathbf{\nu}| = |q| = \pi n^3 |r_{41}|/\lambda, \quad |\nu_0| - |\mathbf{\nu}| = 0,$$

and these values correspond to the polarization angles $\varphi_0 = \pi/2, 0$. For the transverse configuration *T*, we have

$$\nu_0 = 0, \quad |\mathbf{\nu}| = |q|;$$

i.e., the maximum value $|\bar{\nu}|_{\max} = |q|$ is the same as for the longitudinal configuration. This value corresponds to $\varphi_0 = \pm 45°$. As for the sign of $\bar{\nu}$, it can be optimized by a 180° rotation of the sample about the propagation axis *z*. Finally, we note that under the circular pump polarization we have $\mathbf{\nu} \cdot \mathbf{s}_0 = 0$; this means that Γ_+ is smaller by a factor of two compared to the above maximum value for the *L* geometry and goes to zero in the *T* configuration.

In experiment, the main parameters controlling the critical behavior of Γ are the frequency detuning Ω and the normalized pump intensity difference W_0. Figures 3*a* and 3*b* show the dependences of the real part of the increment $\Gamma'_\pm(\Omega, W_0)$ plotted on the basis of Eqs. (9) and (10) for the values of the parameters of BSO and BTO crystals presented in the table. The values of $\mu\tau$ and N_t are the same as in Fig. 2:

$$E_0 = 7 \text{ kV/cm}, \quad Q_{K/2} = 4,$$

$$\Delta = 20.7 \text{ and } 280 \text{ cm}^{-1};$$

and the values of Δ correspond to the dependence $Q_{K/2}(E_0, K)$ in Figs. 2a and 2b. The dotted curves show the dependence of the branch $\Gamma'_-(\Omega)$ in the two-valuedness region.

As seen from Fig. 3, $\Gamma'(\Omega)$ has two bifurcation points where the square root in (9) goes to zero. These points divide the regions of Bragg (the central region) and off-Bragg diffraction. The values of W_0 in Fig. 3a, which are equal to –0.8, –0.75, and –0.7, correspond to $m_0 \approx 0.6$, 0.66, and 0.71, respectively; these values of m_0 are smaller than the minimum threshold contrast $m_{th} = 0.75$. Equation (9) holds true in the whole region of the parametric resonance; the function $\Gamma_+(\Omega)$ is characterized here by a clearly pronounced peak whose amplitude increases with decreasing $|W_0|$. The values $W_0 = -0.65$ and –0.6 correspond to $m_0 = 0.76$ and 0.8, which are above the threshold value $m_{th} = 0.75$. In this case, our theory is applicable only for the resonance wings

$$3\delta > (m_0^2 - m_{th}^2)^{1/2}.$$

The boundaries of the permitted region are marked by dots on the corresponding branch of $\Gamma_-(\Omega)$. As we approach these boundaries, $\Gamma_+ \longrightarrow \infty$.

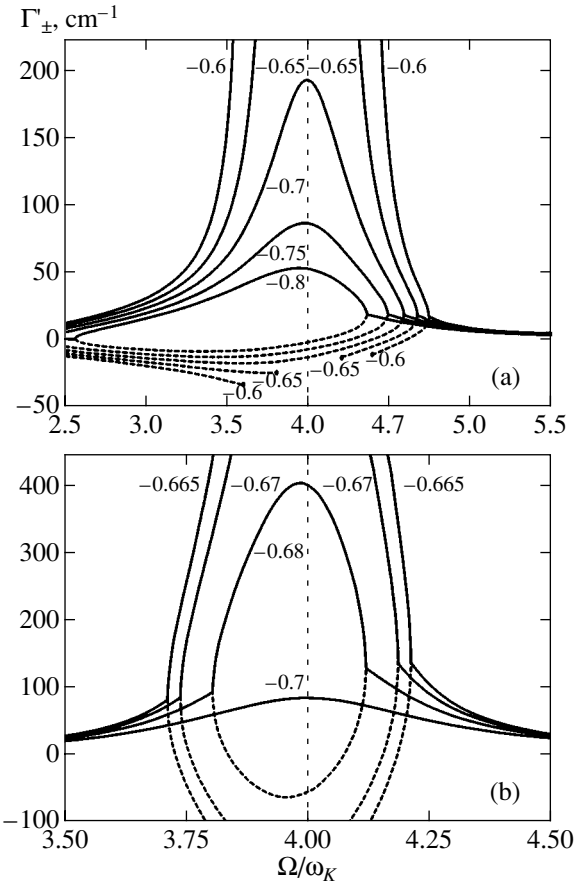

Fig. 3. Dependence $\Gamma'_\pm(\Omega, W_0) = \mathrm{Re}\Gamma_\pm$ for BSO (a) and BTO (b) crystals. In the case (a), $\mu\tau = 3 \times 10^{-7}$ cm^2/V, $N_t = 10^{16}$ cm^{-3}, and $\Delta \approx 20.7$ cm^{-1}. In the case (b), $\mu\tau = 10^{-7}$ cm^2/V, $N_t = 3 \times 10^{16}$ cm^{-3}, and $\Delta \approx 280$ cm^{-1}. The values $W_0 = -0.8$, –0.75, –0.7, –0.65, and –0.6 in (a) correspond to the ratios $m_0/m_{th} \approx 0.8$, 0.88, 0.95, 1.01, and 1.07, respectively. In figure (b), the values $W_0 = -0.7$, –0.68, –0.67, and –0.665 correspond to the ratios $m_0/m_{th} \approx 0.95$, 0.98, 0.99, and 0.996, respectively.

All curves in Fig. 3b (BTO crystals) are plotted for $m_0 < m_{th}$. In order to realize the Bragg regime, it is necessary to approach the instability threshold very closely. The nearer this threshold, the more pronounced the peak $\Gamma_+(\Omega)$ in the Bragg region. This feature is explained by a greater value of Δ; ultimately, it is caused by the values of the material parameters $\mu\tau$ and N_t (see also Fig. 2). All other factors being equal, the values of Γ_+ for BTO crystals are smaller than those for BSO.

Finally, we note that all curves in Fig. 3 correspond to the most preferable combination of signs

$$W_0 < 0, \quad \bar{\nu} E_0 > 0.$$

A simultaneous change of the signs of W_0 and $\bar{\nu}$ results in a decrease in the increment and shifts the bifurcation

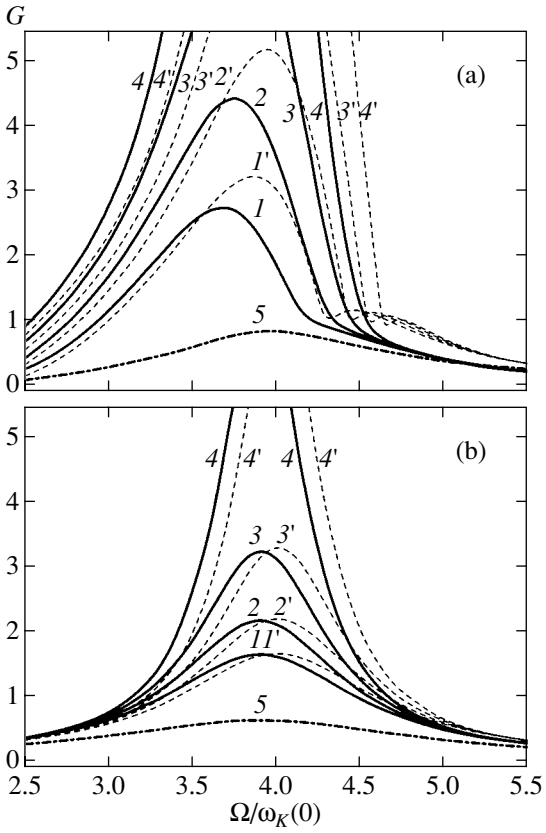

Fig. 4. Dependence of the amplification factor G on Ω and W_0 in the L geometry for BSO (a) and BTO (b) crystals. Curves *1*, *1*'; *2*, *2*'; *3*, *3*'; and *4*, *4*' correspond to $W_0 = -0.85$, –0.8, –0.75, and –0.7; curves 5 are plotted with the material nonlinearity neglected for $W_0 = -0.7$. In the case (a), $\mu\tau = 3 \times 10^{-7}$ cm^2/V, $N_t = 10^{16}$ cm^{-3}, $\theta_p \approx 1.2°$, and $\alpha = 1$ cm^{-1}. In the case (b), $\mu\tau = 10^{-7}$ cm^2/V, $N_t = 3 \times 10^{16}$ cm^{-3}, $\theta_p \approx 10°$, and $\alpha = 0.5$ cm^{-1}

points towards larger values of the increment. In the vicinity of the singularity, where $\Gamma_+ \gg |\bar{\nu}E_0|$, the influence of the sign choice becomes less important in accordance with (12).

We now briefly consider the properties of the spatial amplification described by Eq. (11). It is clear that within the Bragg region, where $\Gamma_+ \gg \Gamma_-$, the spatial growth of $\mathbf{a}_0$ is described mainly by the exponent $\exp(\Gamma_+ z)$. Here, the parameters maximizing Γ_+, in particular, the linear pump polarization specified above, are preferable. The optimum input polarization of the central beam is clearly the same as for the pump beams. In this case, $\mathbf{a}_0(z)$ does not change its direction, and the vectorial problem for the critical spatial enhancement reduces to a scalar one. The only variable parameter remaining at our disposal is the central beam phase Φ_0. The phase dependence (with a period of π) of the factor multiplying $\exp(\Gamma_+ z)$ is of minor importance except for a narrow neighborhood of the point Φ_0^+, where this factor goes to zero. The value of the phase that is undesirable for the spatial amplification is given by the expression

$$2\Phi_0^+ = \pi + \Phi_1 + \Phi_2 + \arctan(\sqrt{g^2 - f_2^2}/f_2),$$

where $\Phi_{1,2}$ are the input phases of the pump beams. In an experiment, Φ_0 and Φ_0^+ can coincide only incidentally. Note that fluctuations of the input phases can "smear" the sharp dependence $|\mathbf{a}_0(\Phi_0)|$ at $\Phi_0 \approx \Phi_0^+$.

Within the off-Bragg region, both exponents in (11) are important for the amplification. The dependence on the phase Φ_0 is very weak here. In the vicinity of the increment bifurcation points, the function $|\mathbf{a}_0(\Omega)|^2$ can show sharp oscillations, and the dependence $|\mathbf{a}_0(z)|^2$ can become nonmonotonic.

6. NUMERICAL SIMULATION

Beyond the simplified spatially uniform model, Eq. (7) defies analytical solution, and the main tool for the analysis is numerical simulation. The effect of the two factors of spatial inhomogeneity is qualitatively clear. The spatial dependence $\delta(z)$ caused by the light absorption results in a shift and broadening of the frequency peaks but does not affect the direction of the vector $\mathbf{b}_0(z)$. The spatial dependence $\mathbf{h}(z)$ caused mainly by optical activity forces $\mathbf{b}_0(z)$ to change both in magnitude and in direction. Both these factors are certainly negative, and our purpose is to analyze their influence under the conditions that are typical of experiments with BSO and BTO crystals. The simplified model provides here a good reference point for comparison.

We choose the factor

$$G = \log\frac{|\mathbf{b}_0(d)|^2}{|\mathbf{b}_0(0)|^2} \equiv \log\frac{|\mathbf{a}_0(d)|^2}{|\mathbf{a}_0(0)|^2}$$

as the basic experimental parameter to be considered. It is merely the amplification factor on a logarithmic scale. The main variable parameters are Ω and W_0. The material parameters correspond to the table and Fig. 3.

Solid curves in Figs. 4a and 4b show the dependences $G(\Omega, W_0)$ in the longitudinal geometry for BSO and BTO crystals at $d = 1$ mm, $E_0 = 7$ kV/cm, and $Q_{K/2} = 4$. The dashed curves correspond to the simplified model, and two dot-and-dash curves are plotted with the material nonlinearity neglected (the standard theory) for $W_0 = -0.7$. All the values of W_0 refer to the case $m_0 < m_{th} = 0.75$.

It is seen that the effects of spatial inhomogeneity substantially, though not drastically, affect the spatial amplification at the chosen thickness d. They result mainly in a shift of the resonance peak to the left.

A greater decrease in the peak values of $G(\Omega)$ for BSO crystals is caused by the larger value of the rotatory power ρ. Smaller absolute values of the amplification factor for BTO crystals come from the larger value of the Bragg mismatch Δ. Specific features in the behavior of the right wings of the dashed curves in Fig. 4a are caused by the bifurcation of the function $\Gamma'(\Omega)$, i.e., by the transition from the Bragg to off-Bragg diffraction regime. A considerable gain in the amplification factor owing to the critical effects draws attention. At $W_0 = -0.8$ ($m_0/m_{th} \approx 0.8$), this gain is more than three orders of magnitude for BSO and about two orders of magnitude for BTO crystals. As we approach the threshold, this gain increases.

At $d = 1$ mm, the behavior of $G(\Omega, W_0)$ changes only insignificantly when switching to the transverse geometry if the input polarization angle is optimized ($\varphi_0 = \pm 45°$). A simultaneous change of signs of W_0 and $\bar{\nu}$ does not lead to new effects.

Figures 5a and 5b illustrate the modification of the spectrum $G(\Omega)$ for BSO and BTO crystals with an increase in the thickness d for the transverse geometry. For BSO crystals, the increase in d actually does not lead to the growth of G starting from $d = 1$ mm. This feature is fully determined by the effect of optical activity. For BTO crystals, which are characterized by a much smaller value of ρ, the situation is quite different. Here, the increase in d results in a noticeable shift of the resonance towards lower frequencies (because of light absorption), but it does not lead to any substantial saturation of the peak value of $G(\Omega)$. This is explained by the suppression of the optical rotation by the applied electric field [17]. Finally, we note that, in the longitudinal geometry, the negative influence of optical activity is pronounced somewhat more weakly than in the transverse geometry. This is due to the presence of the isotropic part in the interaction matrix ($\nu_0 \neq 0$).

Figure 6 illustrates the influence of optical activity on the spectrum $G(\Omega)$ in BSO crystals for $d = 1$ mm. The dashed curve corresponds to the simplified model ($\alpha = \rho = 0$), and the solid curves *1–4* are plotted for $\alpha = 0$, 1, 1.7, and 2.5 cm^{-1}, respectively. The comparison of the dashed curve with curve 1 shows that optical activity does not change the shape of the peak; it only slightly reduces its magnitude. It is seen from curves *1–4* that an increase in α results in a noticeable broadening of the resonance peak, its shift, and smearing of the frequency peculiarities on the right wing. However, this increase does not drastically influence the properties of the critical enhancement.

In addition to the factor G, which describes the intensity amplification, the variation of the polarization of the central beam deserves attention. This variation can be described by the parameter

$$C_{01} = \frac{|\mathbf{b}_0(d) \cdot \mathbf{b}_1^*(d)|}{|\mathbf{b}_0(d)||\mathbf{b}_1(d)|} = \frac{|\mathbf{a}_0(d) \cdot \mathbf{a}_1^*(d)|}{|\mathbf{a}_0(d)||\mathbf{a}_1(d)|},$$

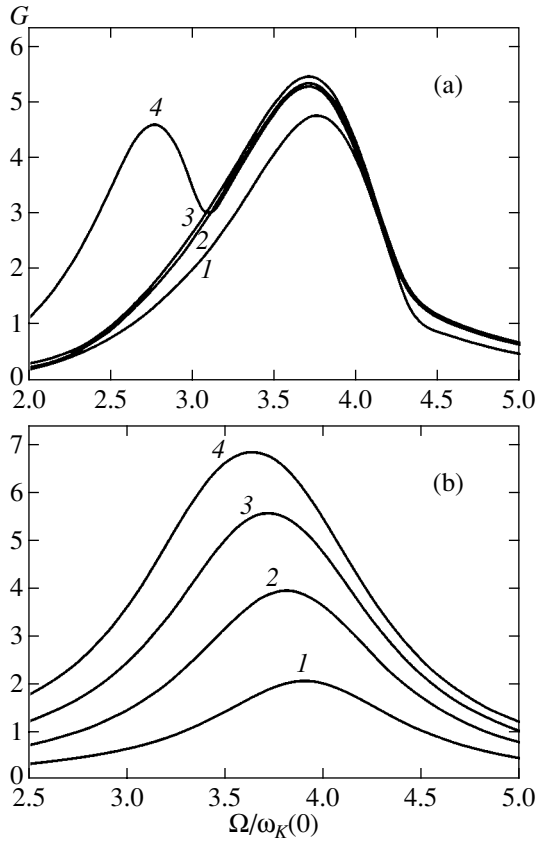

Fig. 5. Dependence of the amplification spectrum $G(\Omega)$ on the crystal thickness in the T geometry for BSO (a) and BTO (b) crystals. Curves *1–4* correspond to $d = 1$, 2, 3, and 4 mm, respectively; $W_0 = -0.8$ ($m_0/m_{th} \approx 0.8$); the other parameters are the same as in Fig. 4.

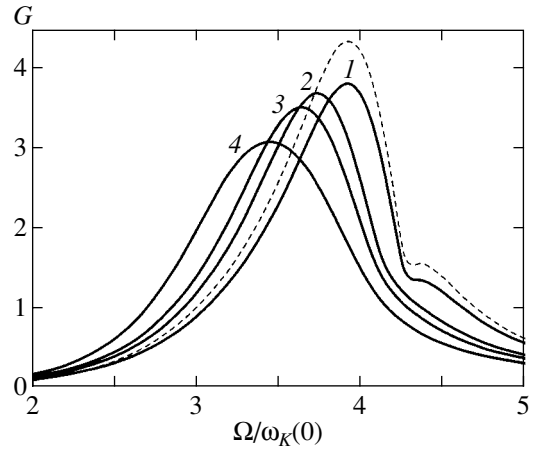

Fig. 6. Dependence of the amplification spectrum $G(\Omega)$ on the absorption coefficient α in the L geometry for BSO crystals (see the text). The chosen parameters are $\mu\tau = 6 \times 10^{-7}$ cm^2/V, $N_t = 10^{16}$ cm^{-3}, $Q_{K/2} = 6$, and $W_0 = 0.95$ ($m_0/m_{th} \approx 0.62$).

which can be considered as the cosine of the angle between the complex-valued vectors $\mathbf{a}_0(d)$ and $\mathbf{a}_1(d)$. Computations show that C_{01} is close to unity for $d = 1$ mm and $G \lesssim 4$–5. However, the dependence $C_{01}(\Omega)$ under-

goes a sharp change when passing from the Bragg to off-Bragg region of the frequency detuning. Discovery of this feature would directly indicate the increment bifurcation.

7. DISCUSSION AND CONCLUSIONS

The theory of the critical enhancement of the photorefractive response presented in this paper accounts for the main attributes of possible experiments in cubic crystals, namely, the vectorial nature of beam coupling, nonuniform broadening of the resonance, the expected dependences on the frequency detuning, polarization and orientation degrees of freedom, and the possibility of varying the material parameters. This theory enables us to predict various regularities to be expected and to form a general pattern of new phenomena. We suppose that our theory forms a basis for the performance of specially designed experiments aimed at the discovery and study of the critical spatial amplification.

It follows from the results obtained that the use of BSO and BTO crystals thicker than $d \approx 1$ cm, which is typical for photorefractive experiments, is impractical for the critical enhancement. So thick crystals are not necessary to obtain the desired large amplification. Furthermore, they are dangerous from the point of view of generating parasitic and poorly controlled secondary effects associated, for example, with the energy exchange between the pump beams. We expect that the use of crystals with $d \approx 1$ mm is necessary for effective experiments. Such thin samples allow one to reach the amplification factor of about 10^3–10^4, which is sufficient for all practical purposes; to eliminate possible noncritical side effects; and to make the characteristics of the major effect controllable and close to optimal. The use of such samples is still consistent with the application of the desired electric fields $E_0 \approx 7$–10 kV/cm. Finally, the use of thin samples makes it possible to decrease the transverse size of the crystals, which allows us to increase the pump intensity and reduce in this way the nonlinear response time.

It has to be noted that the critical increase in the increment Γ within the spatially uniform model is limited by the inequality

$$\Gamma \ll 2\pi/K.$$

This limitation comes from the electrostatic boundary effects; more precisely, the space-charge field is reduced when the effective grating thickness Γ^{-1} becomes comparable with its spacing. Since, in experiments on the subharmonic generation, the grating spacing $2\pi/K$ is about 10–30 μm, the limiting values of the increment are expected to be in the range 10^2–10^3 cm^{-1}. With such large amplification rates (and $d \approx 1$ mm), the effect of pump depletion can be substantial. For practical purposes, it would be sufficient to reach the increment magnitude of several dozen inverse centimeters.

The theory offers simple recommendations with respect to how to perform experiments and to identify the critical enhancement. The initially selected (possibly thick) samples must exhibit the subharmonic generation. The choice between the longitudinal and transverse geometries is not crucial; however, the optimum polarizations for these configurations are different. It is advisable to investigate the spectral dependence of the amplification factor below the minimum threshold of the parametric instability, $m_0 < m_{th}$, when the whole range of the frequency detuning is available for experiment and no spatial subharmonics can arise spontaneously. The interchange of the pump beam intensities has to suppress the effect of critical enhancement. A sharp attenuation of the central beam intensity when any of the two pump beams is blocked is direct proof of the criticality.

The theory developed in this paper corresponds to the excitation of spatial subharmonics by a DC field. At the same time, it is known (see [2]) that subharmonics can be generated under an alternating voltage in the absence of frequency detuning between the pump beams (the AC technique). We believe that the AC method can also be used for the critical enhancement. Its analysis requires, however, the higher spatial harmonics ($2K$, $3K$, and so on) to be taken into account [26].

BGO crystals, which belong to the sillenite family, and the semiconductor CdTe are also candidates for the investigation of the critical enhancement, since they exhibit the subharmonic generation [27, 28]. The advantage of CdTe crystals is their fast response and the absence of optical activity. The analysis of the critical enhancement in these materials presents difficulties because of the shortage of information on the charge transfer processes under light. We hope that this information will be obtained in the coming years.

ACKNOWLEDGMENTS

The work was supported by the Russian Foundation for Basic Research, project no. 99-02-17121.

REFERENCES

1. *Topics in Applied Physics*, Vols. 61 and 62: *Photorefractive Materials and Their Applications*, Ed. by P. Günter and J. P. Huignard (Springer-Verlag, Berlin, 1988, 1989), Parts I and II.
2. L. Solymar, D. J. Webb, and A. Grunnet-Jepsen, *The Physics and Applications of Photorefractive Materials* (Clarendon, Oxford, 1996).
3. M. P. Petrov, S. I. Stepanov, and A. V. Khomenko, *Photorefractive Crystals in Coherent Optics* (Nauka, St. Petersburg, 1991).
4. P. Refregier, L. Solymar, H. Rajbenbach, and J. P. Huignard, J. Appl. Phys. **58**, 45 (1985).
5. C. S. K. Walsh, A. K. Powell, and T. J. Hall, J. Opt. Soc. Am. B **7**, 288 (1990).

6. R. F. Kazarinov, R. A. Suris, and B. I. Fuks, Fiz. Tekh. Poluprovodn. (Leningrad) **6**, 572 (1972) [Sov. Phys. Semicond. **6**, 500 (1972)].
7. N. G. Zhdanova, M. S. Kagan, R. A. Suris, and B. I. Fuks, Zh. Éksp. Teor. Fiz. **74**, 364 (1978) [Sov. Phys. JETP **47**, 189 (1978)].
8. B. I. Sturman, M. Mann, J. Otten, and K. H. Ringhofer, J. Opt. Soc. Am. B **10**, 1919 (1993).
9. S. I. Stepanov and M. P. Petrov, Opt. Commun. **53**, 292 (1985).
10. A. Blendovskiĭ, J. Otten, K. H. Ringhofer, and B. I. Sturman, Zh. Éksp. Teor. Fiz. **102**, 406 (1992) [Sov. Phys. JETP **75**, 215 (1992)].
11. B. I. Sturman, A. I. Chernykh, and E. A. Shamonina, Zh. Éksp. Teor. Fiz. **114**, 1034 (1998) [JETP 87, 563 (1998)].
12. T. E. McClelland, D. J. Webb, B. I. Sturman, and K. H. Ringhofer, Phys. Rev. Lett. **73**, 3082 (1994).
13. B. I. Sturman, T. E. McClelland, D. J. Webb, *et al.*, J. Opt. Soc. Am. B **12**, 1621 (1995).
14. B. I. Sturman, M. Aguilar, F. Agullo-Lopez, and K. H. Ringhofer, Phys. Rev. E **55**, 6072 (1997).
15. E. V. Podivilov, B. I. Sturman, H. C. Pedersen, and P. M. Johansen, Phys. Rev. Lett. **85**, 1867 (2000).
16. A. Marrakchi, R. V. Johnson, and A. R. Tanguey, J. Opt. Soc. Am. B **3**, 321 (1986).
17. B. I. Sturman, E. V. Podivilov, V. P. Kamenov, *et al.*, Zh. Éksp. Teor. Fiz. **119**, 125 (2001) [JETP **92**, 108 (2001)].
18. D. J. Webb and L. Solymar, Opt. Commun. **83**, 287 (1991).
19. B. I. Sturman, A. I. Chernykh, V. P. Kamenov, *et al.*, J. Opt. Soc. Am. B **17**, 985 (2000).
20. L. D. Landau and E. M. Lifshitz, *Course of Theoretical Physics*, Vol. 3: *Quantum Mechanics: Non-Relativistic Theory* (Nauka, Moscow, 1996; Pergamon, New York, 1977).
21. V. P. Kamenov, Y. Hu, E. Shamonina, *et al.*, Phys. Rev. E **62**, 2863 (2000).
22. S. I. Stepanov, S. M. Shandarov, and N. D. Khat'kov, Fiz. Tverd. Tela (Leningrad) **29**, 1454 (1987) [Sov. Phys. Solid State **29**, 1754 (1987)].
23. V. V. Shepelevich, S. M. Shandarov, and A. E. Mendel, Ferroelectrics **110**, 235 (1990).
24. H. Tuovinen, A. A. Kamshilin, and T. Jaaskelainen, J. Opt. Soc. Am. B **14**, 3383 (1997).
25. L. D. Landau and E. M. Lifshitz, *The Classical Theory of Fields* (Nauka, Moscow, 1973; Pergamon, Oxford, 1975).
26. P. M. Johansen, H. C. Pedersen, E. V. Podivilov, and B. I. Sturman, Phys. Rev. A **58**, 1601 (1998).
27. I. Richter, A. Grunnet-Jepsen, J. Takacs, and L. Solymar, IEEE J. Quantum Electron. **30**, 1645 (1994).
28. K. Shcherbin, Appl. Phys. B **71**, 123 (2000).

Translated by A. Klimontovich

Journal of Experimental and Theoretical Physics, Vol. 94, No. 3, 2002, pp. 482–488.
Translated from Zhurnal Éksperimental'noĭ i Teoreticheskoĭ Fiziki, Vol. 121, No. 3, 2002, pp. 565–572.

NUCLEI, PARTICLES, AND THEIR INTERACTION

On the Problem of Homogenizing One-Dimensional Systems

A. P. Vinogradov* and A. V. Merzlikin

Institute of Theoretical and Applied Electrodynamics, Joint Institute of High Temperatures, Russian Academy of Sciences, Moscow, 127412 Russia

**e-mail: vinogr@vinogr.msk.ru*

Received August 31, 2001

Abstract—The possibility of introducing effective one-dimensional medium parameters in the long-wave approximation is considered. A layered system was used as a model of one-dimensional medium. The effective parameters were shown to be functions of sample thickness. Both periodic and random media were studied; the thicknesses of random samples were assumed to be much smaller than the localization length, which allowed us to ignore the localization effect. The results are compared with the Rytov solution. The wave vector was found to tend to the Rytov value as the thickness of the sample increased, whereas the characteristic impedance had no limit in the long-wave approximation. What is more, the characteristic impedance could differ from the Rytov value by 100%. The results were obtained by computer simulation of the propagation of electromagnetic waves in a layered system. © *2002 MAIK "Nauka/Interperiodica".*

1. INTRODUCTION

The problem of the propagation of waves in a one-dimensional nonuniform medium traditionally attracts attention of researchers [1–3]. This is caused by both comparative simplicity of the problem and its importance for understanding the physics of processes that occur during wave propagation in nonuniform media. In this work, we restrict our consideration to the long-wave approximation, when the scale of inhomogeneities d (period or correlation length) is much smaller than wavelength λ. For disordered media, we also use the condition of smallness of system size L compared with localization length L_{loc}; this condition excludes localization effects. For one-dimensional systems in the long-wave limit, $L_{loc} \sim \lambda(\lambda/d)$ (see [3]), which is much larger than the wavelength. For this reason, a fairly large range of L values such that the inequality $\lambda \ll L \ll L_{loc}$ is satisfied exists in the problem under consideration. The last condition means that we can consider optically thick system and ignore localization effects.

Although exactly solving the problem poses no computational difficulties, the thing that interests us under the conditions specified above is often the distribution of fields averaged over a physically infinitesimal volume rather than the true distribution of fields [4]. Finding these fields is related to the so-called homogenizing problem. This is the determination of the equations that describe the behavior of averaged fields in media with given properties (given distributions of permittivity and magnetic permeability) at the microscopic level and the equations satisfied by true microscopic fields. Used as microscopic equations are Laplace equations under static conditions and systems of material Maxwell equations for fields varying in time. It is assumed that averaged fields satisfy the same equations but with effective material parameters, permittivity ε_{eff} and permeability μ_{eff}. A strict proof of the validity of this assumption and an algorithm for calculating ε_{eff} and μ_{eff} only exist for infinite periodic systems in a constant field [5]. They are based on the so-called theory of G convergence. Central to G-convergence theory is the fact that the constant field potential obeys the dimensionless Laplace equation. All linear dimensions can then be measured in d units. As a result, the dependence of any value on system size L can only manifest itself as a function of the L/d ratio. The tendency of L/d to infinity can be achieved either when L tends to infinity or when d tends to zero. This gives physical meaning to considering infinitely large systems, that is, systems in which the strict inequality $L \gg d$ is fulfilled.

The homogenizing problem, which usually reduces to finding ε_{eff} and μ_{eff}, becomes multiscale for Maxwell equations. Scales related to the equations themselves, namely, a set of local wavelengths $\lambda = \lambda_0/\sqrt{\varepsilon\mu}$, where $\lambda_0 = 2\pi/k_0$ is the wavelength in vacuum and k_0 is the wave number, appear. The transition from a finite to an infinite system involves certain difficulties in the presence of many scales [6], which makes the results of G-convergence theory generally inapplicable. Nevertheless, it is usually assumed [7–9] that, if linear size l_{avr} of an infinitesimal volume satisfies the inequality

$$d \ll l_{avr} \ll \lambda_0, \tag{1}$$

then averaged fields obey macroscopic Maxwell equations containing effective material constants. Clearly, if the strict inequality

$$d\sqrt{\varepsilon_{max}\mu_{max}} \ll \lambda_0 \tag{2}$$

is satisfied, as is assumed in this work ("max" labels maximum local permittivity and permeability values), we can always select l_{avr} that satisfies (1). This must be sufficient for introducing effective parameters [7–9]. We show below that the fulfillment of inequality (2) in a one-dimensional system does not guarantee the existence of effective material parameters.

The problem of finding the effective parameters of a one-dimensional periodic medium in a constant field was solved long ago [10, 11]. For instance, if the field is directed along layers, $\varepsilon_{eff} = \langle\varepsilon\rangle$ by virtue of continuity of the tangential field component. For variable fields, a solution for an infinite periodic medium comprising layers with ε_1, μ_1 and ε_2, μ_2 effective parameters was found by Rytov [12–14]. Works by Rytov became classic and originated investigations concerned with homogenizing one-dimensional media of various natures [14–19].

Let us briefly consider the results obtained by Rytov. He derived a dispersion equation for the effective wave number (effective refractive index). For nonmagnetic ingredients considered in this work, this equation takes the form

$$\cos(k_0 n_{eff}^{Ryt} 2d) = \cos(k_0\sqrt{\varepsilon_1}d)\cos(k_0\sqrt{\varepsilon_2}d) - \frac{1}{2}\left(\sqrt{\frac{\varepsilon_1}{\varepsilon_2}} + \sqrt{\frac{\varepsilon_2}{\varepsilon_1}}\right)\sin(k_0\sqrt{\varepsilon_1}d)\sin(k_0\sqrt{\varepsilon_2}d). \quad (3)$$

In addition, Rytov introduced the effective characteristic impedance defined as the ratio $Z_{eff} = \langle E\rangle/\langle H\rangle$ (averaging is performed over the period), which allowed the effective permittivity and permeability to be found. Note that an effective permeability different from one appears even with nonmagnetic ingredients. If (2) is satisfied, it is easy to obtain the following equations for the effective parameters [14]:

$$\varepsilon_{eff} = \langle\varepsilon\rangle\left[1 + ik_0\frac{d_1 d_2}{4(d_1 + d_2)}\frac{\varepsilon_2 - \varepsilon_1}{\sqrt{\langle\varepsilon\rangle}}\right],$$
$$\mu_{eff} = 1 - ik_0\frac{d_1 d_2}{4(d_1 + d_2)}\frac{\varepsilon_2 - \varepsilon_1}{\sqrt{\langle\varepsilon\rangle}}. \quad (4)$$

Note that ε_{eff} and μ_{eff} are complex values, although ε_1 and ε_2 are real.[1] What is more, one of the ε_{eff} and μ_{eff} values has a negative imaginary part depending on the selection of the first and second layers. This makes it difficult to assign physical meaning to them.

Negative imaginary susceptibility parts are usually related to energy generation [6]. The equation for energy dissipation (generation), however, contains both susceptibilities, and the negative imaginary part of one of them can be compensated by the positive imaginary part of the other (see [20]). To analyze the physical meaning of each separate susceptibility and identify the negative imaginary part (for definiteness, of μ_{eff}) with radiation amplification, it is necessary to place the sample into a magnetic field antinode, where the electric field can be ignored. Such an experiment can only be performed with a finite system rather than an infinite system analyzed by Rytov. For this reason, we considered the problem of a finite system.

The approach suggested by Rytov, which was based on the use of the Floquet–Bloch theorem, is inapplicable to finite samples, in which translational invariance is violated. In addition, the characteristic impedance definition cannot be used, because two waves propagating in opposite directions and having $\langle E\rangle/\langle H\rangle$ ratios of different signs are excited within a sample under the action of a plane incident wave. It follows that the ratio between the mean values of complete fields depends not only on the local properties of the material but also on the ratio between the amplitudes of these waves.

In this work, we consider several alternative definitions of effective parameters. Our definitions are first and foremost based on the experimental procedures used for measuring effective parameter values. Following the MW terminology, these procedures will be called waveguide and resonator. In conclusion, we consider the approach based on the self-consistent effective medium method.

2. WAVEGUIDE METHOD FOR DETERMINING ε_{eff} AND μ_{eff}

In this approach, measurements are taken in a waveguide [21] or in free space [22]. The ε and μ values are determined from transmission T and reflection R incident wave coefficients[2] [23]. It is assumed that the sample consists of a uniform material with the refractive index

$$n = \frac{k}{k_0} = \sqrt{\varepsilon\mu} \quad (5a)$$

and characteristic admittance

$$Y = \sqrt{\frac{\varepsilon}{\mu}} = \frac{1}{Z}, \quad (5b)$$

where Z is the characteristic impedance. At normal plane wave incidence on the sample,

$$Y_{eff} = \sqrt{\frac{(1-R)^2 - T^2}{(1+R)^2 - T^2}}, \quad (6)$$

$$e^{ik_{eff}Nd} = \frac{T(1 + 1/Z_{eff})}{1/Z_{eff} + R/Z_{eff} + 1 - R}. \quad (7)$$

[1] Rytov had to restrict consideration to nondissipative systems because he considered infinite media.

[2] We consider optically thick samples and therefore do not discuss the classic short circuit–free running procedure [20], which only gives reliable results at optical thicknesses of the order of one-fifth of the wavelength.

In this work, the T and R values were found from the exact solution to the system of Maxwell equations. If the x axis is perpendicular to layers, the other axes can be selected in such a way that the electric and magnetic field will have one nonzero component each. A complete solution is obtained by sewing together solutions at layer boundaries. In each layer, the solution is the sum of two waves, one of which propagates in the positive axis x direction and the other propagates in the opposite direction. Let their amplitudes in the jth layer be denoted by A_j and B_j We easily find that

$$\begin{pmatrix} A_{j+1} \\ B_{j+1} \end{pmatrix} = M_j \begin{pmatrix} A_j \\ B_j \end{pmatrix}, \tag{8}$$

where

$$M_j = \frac{1}{2\sqrt{\varepsilon_{j+1}}} \begin{vmatrix} (\sqrt{\varepsilon_j} + \sqrt{\varepsilon_{j+1}})\exp[i(\sqrt{\varepsilon_j} - \sqrt{\varepsilon_{j+1}})k_0 jd] & (\sqrt{\varepsilon_j} - \sqrt{\varepsilon_{j+1}})\exp[-i(\sqrt{\varepsilon_j} + \sqrt{\varepsilon_{j+1}})k_0 jd] \\ (\sqrt{\varepsilon_j} - \sqrt{\varepsilon_{j+1}})\exp[i(\sqrt{\varepsilon_j} + \sqrt{\varepsilon_{j+1}})k_0 jd] & (\sqrt{\varepsilon_j} + \sqrt{\varepsilon_{j+1}})\exp[i(\sqrt{\varepsilon_{j+1}} - \sqrt{\varepsilon_j})k_0 jd] \end{vmatrix}.$$

Assuming the incident wave amplitude to be equal to unity, we obtain equations for determining R and T values,

$$\begin{pmatrix} T \\ 0 \end{pmatrix} = M \begin{pmatrix} 1 \\ R \end{pmatrix}, \tag{9}$$

where $M = (M_N, M_{N-1}, \ldots, M_1, M_0)$. Using Eqs. (6) and (7), we determine k_{eff} and Y_{eff}, and the calculate

$$\mu_{\text{eff}} = \frac{k_{\text{eff}}}{Y_{\text{eff}} k_0}, \quad \varepsilon_{\text{eff}} = \frac{k_{\text{eff}} Y_{\text{eff}}}{k_0}.$$

First, consider a periodic system of layers. As concerns the change in the direction of wave incidence to the opposite, there exist two fundamentally different cases for an even number of layers (integer number of periods, the system is asymmetric) and an odd number of layers (half-integer number of periods, the system is symmetrical).

2.1. Even Number of Layers

If the number of layers is even, the effective refractive index $n_{\text{eff}} = k_{\text{eff}}/k_0$ (Fig. 1a) tends to the Rytov value as the size of the system increases. Note that, in contrast to the Rytov solution, the n_{eff} value at an arbitrary finite sample thickness has a nonzero imaginary part. This cannot be ascribed to numerical experiment errors, because, first, the n_{eff} value in first-order perturbation theory with respect to $k_0 d$ is complex for a sample consisting of one period (two layers),

$$n_{\text{eff}} = \sqrt{\varepsilon_{\text{eff}}\mu_{\text{eff}}} = \sqrt{\frac{\varepsilon_1 + \varepsilon_2}{2}} + i\frac{(\varepsilon_1 - \varepsilon_2)(\varepsilon_1 + \varepsilon_2 - 2)}{16\sqrt{(\varepsilon_1 + \varepsilon_2)/2}} k_0 d.$$

Secondly, the fulfillment of the law of conservation of energy, $|R|^2 + |T|^2 = 1$, was controlled during calculations. The deviation from one did not exceed 10^{-14}. It follows that, in reality, there is no absorption or electromagnetic wave amplification. Only wave amplitude beats are observed as a function of sample thickness. The presence of an imaginary part of n_{eff} is compensated by the presence of an imaginary part of Y_{eff}. The change in the wave propagation direction changes the sign of the imaginary parts.

The refractive index tends to the Rytov (purely real) value as sample thickness increases; namely,

$$n_{\text{eff}} - n_{\text{eff}}^{\text{Ryt}} = \frac{d}{L} F(k_{\text{eff}}^{\text{Ryt}} L),$$

where $F(x)$ is a periodic function.[3]

Admittance Y_{eff} of the system oscillates with a period of $0.5\lambda_{\text{eff}} = \pi/k_{\text{eff}}$ (Fig. 1b). The effective susceptibilities are functions of both n_{eff} and Y_{eff} and therefore show combined behavior. Their behavior tends to periodic with the same period as that characteristic of Y_{eff} and $F(x)$ as sample thickness tends to infinity. The real parts of ε_{eff} and μ_{eff} differ from the solution obtained by Rytov [14] only in the second order in $k_0 d$, whereas the difference between the imaginary parts of ε_{eff} and μ_{eff} and the Rytov values is of the order of $k_0 d$.

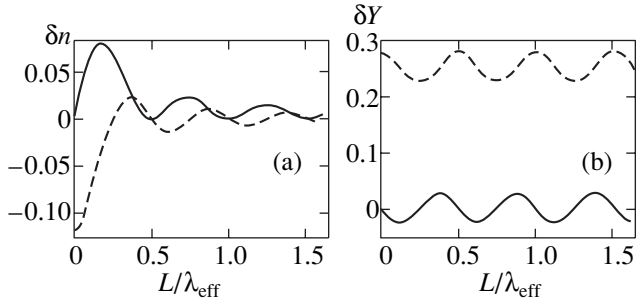

Fig. 1. Sample thickness dependences of (a) $\delta n = n_{\text{eff}} - n_{\text{eff}}^{\text{Ryt}}$ and (b) $\delta Y = (\sqrt{\varepsilon_{\text{eff}}/\mu_{\text{eff}}} - Y_{\text{eff}}^{\text{Ryt}}) \times 100$ for a periodic system with an even number of layers. Sample thickness is in effective wavelength $\lambda_{\text{eff}} = \lim_{L\to\infty}(2\pi/k_{\text{eff}})$ units. Parameter values: $\varepsilon_1 = 2$, $\varepsilon_2 = 3$, and $k_0 d = 0.01$. Real and imaginary parts are shown by solid and dashed curves, respectively.

[3] The F function at small $\varepsilon_1 - \varepsilon_2$ values can be approximated by the equations $\mathrm{Re}\,F = \sin^2(k_{\text{eff}}^{\text{Ryt}} L)$ and $\mathrm{Im}\,F = \sin(k_{\text{eff}}^{\text{Ryt}} L)$.

2.2. Odd Number of Layers

When the number of layers is odd, the behavior of n_{eff} almost fully coincides with that predicted by the Rytov theory. The effective refractive index is a purely real value and tends to the Rytov value

$$n_{\text{eff}} - n_{\text{eff}}^{\text{Ryt}} \sim \frac{d}{L}$$

(Fig. 2a). The square of the effective admittance is also purely real (although it can take on negative values),[4] but, unlike n_{eff}, gives periodic spikes of various amplitudes (Fig. 2b). Note that the amplitude of spikes does not damp as L increases. Spikes are observed when one more layer is imposed on an almost transparent plate of thickness $\lambda_{\text{eff}}/2$ comprising an even number of layers. To qualitatively explain the phenomenon, suppose that a sample containing an odd number of layers is a two-layer sample. Let the first layer have permittivity ε_1 and thickness d, and the second layer, permittivity $(\varepsilon_1 + \varepsilon_2)/2$ (this is close to the Rytov solution) and thickness $L_{\text{odd}} = (N-1)d$. Calculate Y_{eff}^2 for such a two-layer sample under the conditions

$$\sqrt{\varepsilon_1}k_0 d \ll 1, \quad \frac{\sqrt{\varepsilon_1 + \varepsilon_2}}{2}k_0 L_{\text{odd}} - \pi l \ll 1,$$

where l is an integer number. This yields

$$\frac{\varepsilon_{\text{eff}}}{\mu_{\text{eff}}} = \frac{\varepsilon_1 + \varepsilon_2}{2} + \frac{\varepsilon_1 - \varepsilon_2}{2}\frac{k_0 d\sqrt{(\varepsilon_1 + \varepsilon_2)/2}}{k_0 L\sqrt{(\varepsilon_1 + \varepsilon_2)/2} - \pi l}. \quad (10)$$

Close to the transparency region, $\varepsilon_{\text{eff}}/\mu_{\text{eff}}$ behaves as the ratio

$$\frac{(\varepsilon_1 - \varepsilon_2)k_0 d}{L - 0.5l\lambda_{\text{eff}}}.$$

That is, admittance Y_{eff} tends to infinity as L tends to $0.5\lambda_{\text{eff}}l$. The random finite-amplitude spikes observed in numerical experiments are related to the incommensurability of d and λ_{eff}.

As a consequence of such a behavior of Y_{eff}, ε_{eff} and μ_{eff} may arbitrarily differ from the solution found by Rytov (Fig. 3).

2.3. Medium with Absorption

If local energy absorption is possible, the amplitude of effective admittance spikes observed for samples with odd numbers of layers decreases as sample thickness increases, and Y_{eff} tends to some value different from the Rytov solution (Fig. 4).

[4] Note that, according to (6), a change in the direction of wave incidence changes Y_{eff}^2 to its complex conjugate. On the other hand, for a system with an odd number of layers, Y_{eff}^2 should not change; it follows that Y_{eff}^2 is a purely real value.

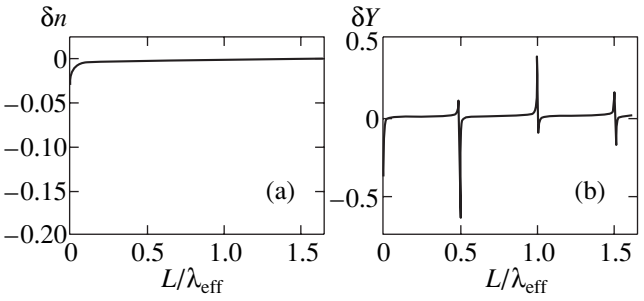

Fig. 2. Sample thickness dependences of (a) $\delta n = n_{\text{eff}} - n_{\text{eff}}^{\text{Ryt}}$ and (b) $\delta Y = \sqrt{\varepsilon_{\text{eff}}/\mu_{\text{eff}}} - Y_{\text{eff}}^{\text{Ryt}}$ for a periodic system with an odd number of layers. Parameter values are the same as in Fig. 1.

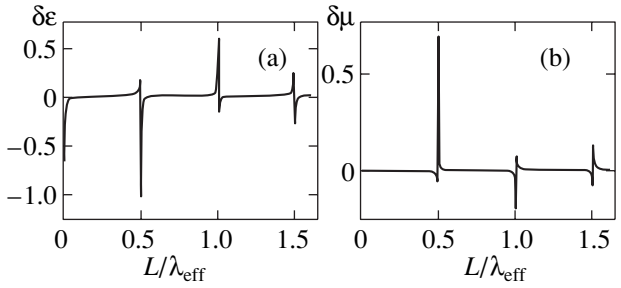

Fig. 3. Sample thickness dependences of (a) $\varepsilon_{\text{eff}} - \varepsilon_{\text{eff}}^{\text{Ryt}}$ and (b) $\mu_{\text{eff}} - \mu_{\text{eff}}^{\text{Ryt}}$ for a periodic system with an odd number of layers. Parameter values are the same as in Fig. 1.

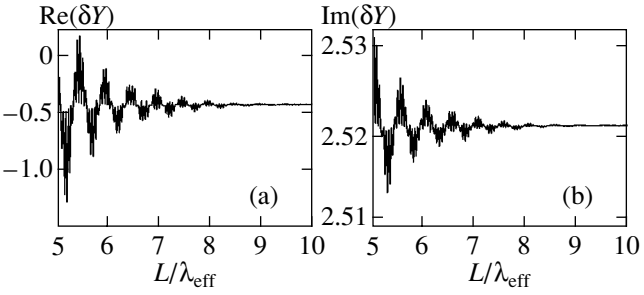

Fig. 4. Sample thickness dependences of (a) $\text{Re}(\delta Y) = \text{Re}(\sqrt{\varepsilon_{\text{eff}}/\mu_{\text{eff}}} - \sqrt{\varepsilon_{\text{eff}}^{\text{Ryt}}/\mu_{\text{eff}}^{\text{Ryt}}}) \times 10^4$ and (b) $\text{Im}(\delta Y) = \text{Im}(\sqrt{\varepsilon_{\text{eff}}/\mu_{\text{eff}}} - \sqrt{\varepsilon_{\text{eff}}^{\text{Ryt}}/\mu_{\text{eff}}^{\text{Ryt}}}) \times 100$ for a periodic system with absorption. Parameter values: $\varepsilon_1 = 2 + 0.5i$, $\varepsilon_2 = 3 + 0.5i$, and $k_0 d = 0.1$.

Note that the limiting Y_{eff} value is attained for the sample thickness at which the sample becomes nontransparent. According to (6), this value equals the input admittance. The difference of the latter from the value obtained by analytic continuation of the Rytov solution to the region of complex local susceptibilities

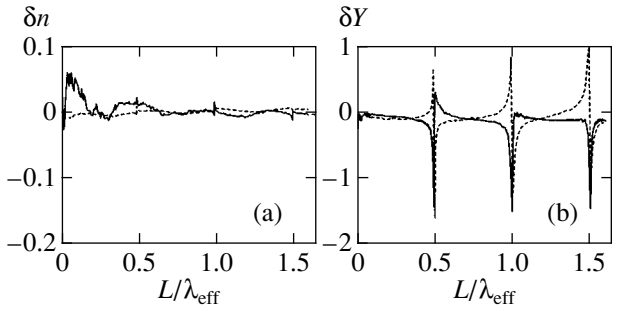

Fig. 5. Sample thickness dependences of (a) $\delta n = n_{\text{eff}}(L) - n_{\text{eff}}^{\text{Ryt}}$ and (b) $\delta Y = Y_{\text{eff}}(L) - Y_{\text{eff}}^{\text{Ryt}}$ for a random system. Parameter values are the same as in Fig. 1. Real and imaginary parts are plotted as solid and dashed curves, respectively.

is evidence of the existence of a transition layer. In this layer, the solution differs from the Rytov solution, and the input admittance is formed.

3. RESONATOR METHOD FOR DETERMINING ε_{eff} AND μ_{eff} (EVEN NUMBER OF LAYERS)

In the resonator method for determining ε and μ, an optically thin sample is placed into a resonator cavity with a known resonance frequency. Resonance frequency and Q factor measurements are related to the real and imaginary susceptibility parts, respectively [22, 4]. The sample is usually placed first into an electric field antinode and then into a magnetic field antinode, which allows ε and μ to be independently determined.

Following this scheme, a sample consisting of two layers was placed into an electric field antinode (into the center of a one-dimensional resonator) and then on one of cavity walls (magnetic field antinode). Two resonance frequencies were numerically determined. They were set equal to the resonance frequencies of the cavity with a uniform sample, whence the ε_{eff} and μ_{eff} parameters were calculated. The law of the conservation of energy is satisfied no matter what the position of the sample in the cavity, and the Q factor therefore remains infinitely large. For this reason, the imaginary ε_{eff} and μ_{eff} parts equal zero. The real parts insignificantly differ from the static values $\varepsilon_{\text{eff}} = 2.5$ and $\mu_{\text{eff}} = 1$ [these are also the real parts of (4)]. For instance, for $\varepsilon_1 = 3$ and $\varepsilon_2 = 2$, we have $\varepsilon_{\text{eff}} = 2.5092$ and $\mu_{\text{eff}} = 0.9099$ when the sample is placed in the center and at the left wall and $\varepsilon_{\text{eff}} = 2.5076$ and $\mu_{\text{eff}} = 1.1146$ when the sample is placed in the center and at the right wall.

The problem has an exact solution, and we may therefore use almost any two sample positions in this approach. Each pair of positions generates ε_{eff} and μ_{eff} values of its own. Exceptions are positions symmetrical with respect to the cavity center, in which resonance frequencies for a uniform sample coincide. It is noteworthy that the frequencies for the sample under study are then different, which shows that the sample cannot at all be assigned any effective parameters.

4. EFFECTIVE MEDIUM THEORY METHOD FOR DETERMINING EFFECTIVE PARAMETERS

Consider a different method for determining ε and μ. Let us immerse the sample into a medium with ε_{eff} and μ_{eff}. The sample should then be transparent; that is, the reflection coefficient should equal zero, and the phase incursion should correspond to the phase incursion for a uniform substance.

The ε_{eff} and μ_{eff} parameters determined in this way do not depend on the direction of wave incidence because of the universality of the condition of transparency, although, generally, reflection coefficients depend on the direction of wave incidence. This can conveniently be proved using the M-matrix properties. It follows from (8) that the determinant of the M matrix of one uniform layer equals one. As the determinant of the product of matrices equals the product of the determinants [24], the determinant of the M matrix of an arbitrary number of layers also equals one. On the other hand, the M matrix can be expressed via four values, namely, the reflection R_L and transmission T_L coefficients when the wave is incident on the layer from the left and the reflection R_R and transmission T_R coefficients when the wave is incident on the layer from the right,

$$M = \begin{vmatrix} T_L - \dfrac{R_R R_L}{T_R} & \dfrac{R_R}{T_R} \\ -\dfrac{R_L}{T_R} & \dfrac{1}{T_R} \end{vmatrix}.$$

It is easy to see that the determinant of this matrix equals T_L/T_R. As $\det M = 1$, we have $T_L = T_R$. It follows that the transparency condition ($|T| = 1$) is independent of the direction of wave incidence. Note, however, that the reflection and transmission coefficients, although they are equal in magnitude (for nonabsorbing media), generally have different phases even at the transparency point. This is the reason why the waveguide method gives different "right" and "left" effective parameters for asymmetric samples. The reflection coefficients calculated by the effective medium method are zero. Their phases therefore do not play any role. This condition guarantees symmetry of an arbitrary system.

Although the Y_{eff} value is independent of the thickness of a plate containing an even number of layers, it coincides neither with the Rytov solution nor with the values obtained by the waveguide or resonator method. The independence of ε_{eff} and μ_{eff} on sample thickness is apparent. It is only observed when the sample is immersed into a medium with effective parameters.

If the number of layers is odd, Y_{eff} coincides with the effective admittance calculated from reflection and transmission coefficients, because $R_L = R_R$ for a symmetrical layer independent of the environment.

5. RANDOM MEDIUM

It has been shown above that a one-dimensional periodic medium cannot be correctly described in terms of ε_{eff} and μ_{eff}. We must consider a random sample to determine whether or not the periodic dependence of ε_{eff} and μ_{eff} is a consequence of medium periodicity.

Let layers with ε_1 and ε_2 be arranged randomly. The calculated $n_{\text{eff}}(L)$ and $Y_{\text{eff}}(L)$ values are shown in Fig. 5 as functions of sample thickness. One can see that $n_{\text{eff}}(L)$ is a self-averaging function, whereas $Y_{\text{eff}}(L)$ is not. Averaging $Y_{\text{eff}}(L)$ and $n_{\text{eff}}(L)$ over an ensemble gives the dependences shown in Fig. 6. The dependence of $\langle Y_{\text{eff}}\rangle$ on sample thickness bears no resemblance to the thickness dependence of the admittance of a separate realization.

If there is absorption and the thickness of the sample increases (layers are added) on the side of the passed wave, $Y_{\text{eff}}(L)$ experiences self-averaging. T tends to zero as the thickness increases, and all information about the composite is contained only in R. The $Y_{\text{eff}}(L)$ value therefore tends to the input admittance, which does not coincide with $\langle Y_{\text{eff}}\rangle$. This is obvious in the limiting case of strong absorption, because $Y_{\text{eff}}(L)$ then equals the admittance of the first layer. Any averaging over an ensemble causes loss of information about which layer is the first and which the second. For this reason, ensemble averages never equal observed values.

6. CONCLUSION

It follows from the results obtained in this work that the effective permittivity and permeability can only be introduced in the description of one-dimensional media in the quasi-static limit $d \ll L \ll \lambda$, when the static mixing formulas work, for instance, for normal incidence $\varepsilon_{\text{eff}} = \langle\varepsilon\rangle$ and $\mu_{\text{eff}} = \langle\mu\rangle$. An attempt at taking into account corrections related to radiation lag on the scale of inhomogeneities leads to the impossibility of determining the material parameters proper, because ε_{eff} and μ_{eff} depend on sample thickness L and therefore describe the sample rather than the material. The deviations of sample ε_{eff} and μ_{eff} values from those obtained by Rytov [3, 4] may amount to hundreds of percent at $L = \infty$ even at small $k_0 d$ values. This is caused by the multiscale character of Maxwell equations.

The $d \ll \lambda$ condition is insufficient for obtaining a limit that does not depend on surrounding space properties. Such a limit requires the fulfillment of the inequality

$$L \ll \lambda. \tag{11}$$

In other words, the transition to an infinite system in the dynamic case is meaningless. This situation is similar to that arising in quantum mechanics in solving the problem of above-the-barrier particle scattering. The solution to the problem with a rectangular potential then does not tend to the solution to the problem with a step potential. As is known, in statics, the solution to the infinite problem accurate to d/L is also the solution to the finite problem. Obtaining the solution to the infinite problem in statics requires that passage to the limit be generally performed as follows: first, we let λ tend to infinity, and, next, sample thickness is increased.

The difference in the behavior of a one-dimensional system at zero and finite frequencies is likely to be related to a much larger transverse size of the sample compared with the wavelength, which violates condition (11) (see the problem of diffraction on an infinite wire [25]).

Note also the importance of the difference of the wave number from that predicted by the Rytov theory. It tends to the Rytov value, but the difference from this limit is substantial at arbitrary L because

$$\lim_{L\to\infty}(k_{\text{eff}}(L)L - k_{\text{eff}}^{\text{Ryt}}L) \neq 0.$$

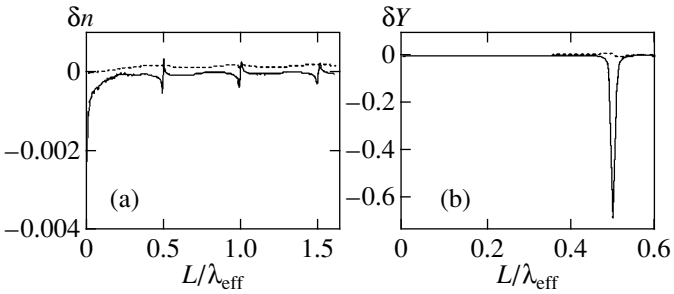

Fig. 6. Sample thickness dependences of (a) $\langle n_{\text{eff}}(L)\rangle - n_{\text{eff}}^{\text{Ryt}}$ and (b) $\langle Y_{\text{eff}}(L)\rangle - Y_{\text{eff}}^{\text{Ryt}}$; averaging was performed over 10^4 realizations. Parameter values are the same as in Fig. 1. Real and imaginary parts are plotted as solid and dashed curves, respectively.

ACKNOWLEDGMENTS

The authors thank A.M. Dykhnya and S.A. Rybak for discussions. This work was financially supported by the Russian Foundation for Basic Research (projects nos. 00-15-96570 and 01-02-17962).

REFERENCES

1. S. A. Gradeskul and V. D. Frelikher, Usp. Fiz. Nauk **160**, 239 (1990) [Sov. Phys. Usp. **33**, 134 (1990)].

2. G. Ya. Slepyan, A. V. Gurevich, and S. A. Maximenko, Phys. Rev. E **51**, 2543 (1995).
3. P. Sheng, *Introduction to Wave Scattering, Localization, and Mesoscopic Phenomena* (Academic, London, 1995)
4. L. D. Landau and E. M. Lifshitz, *Course of Theoretical Physics*, Vol. 8: *Electrodynamics of Continuous Media* (Nauka, Moscow, 1992; Pergamon, New York, 1984).
5. E. Sanchez-Palencia, *Non-Homogeneous Media and Vibration Theory* (Springer-Verlag, Berlin, 1980; Mir, Moscow, 1984).
6. A. N. Lagarkov and A. P. Vinogradov, in *Advances in Complex Electromagnetic Materials*, Ed. by A. Priou, A. Sihvola, S. Tretyakov, and A. Vinogradov (Kluwer, Dordrecht, 1997), NATO ASI Ser., Ser. 3: High Technol. **28**, 117 (1997).
7. J. E. Sipe and J. van Kranendonk, Phys. Rev. A **9**, 1806 (1974).
8. R. Landauer, AIP Conf. Proc. **40**, 2 (1978).
9. A. P. Vinogradov and A. V. Aivazian, Phys. Rev. E **60**, 987 (1999).
10. W. Voigt, *Lehrbuch der Kristallphysik* (Teubner, Berlin, 1928).
11. A. Reuss, Z. Angew. Math. Mech. **9**, 49 (1929).
12. S. M. Rytov, Zh. Éksp. Teor. Fiz. **29**, 605 (1955) [Sov. Phys. JETP **2**, 466 (1955)].
13. S. M. Rytov, Akust. Zh. **2**, 71 (1956) [Sov. Phys. Acoust. **2**, 68 (1956)].
14. L. M. Brekhovskikh, *Waves in Layered Media* (Akad. Nauk SSSR, Moscow, 1957; Academic, New York, 1960).
15. P. Yeh, A. Yariv, and Chi-Shain Hong, J. Opt. Soc. Am. **67**, 423 (1977).
16. B. Djafari Rouhani and J. Sapriel, Phys. Rev. B **34**, 7114 (1986).
17. E. Akcakaya and G. W. Farnell, J. Appl. Phys. **64**, 4469 (1988).
18. E. M. Kikarin and D. V. Petrov, Kristallografiya **34**, 1072 (1989) [Sov. Phys. Crystallogr. **34**, 648 (1989)].
19. I. V. Semchenko, Kristallografiya **35**, 1047 (1990) [Sov. Phys. Crystallogr. **35**, 617 (1990)].
20. V. P. Silin and A. A. Rukhadze, *Electromagnetic Properties of Plasma and Plasmalike Media* (Gosatomizdat, Moscow, 1961).
21. A. A. Brandt, *Research of Dielectrics on Ultrahigh Frequencies* (Fizmatgiz, Moscow, 1963), p. 403.
22. A. N. Lagarkov, S. M. Matytsin, K. N. Rozanov, and A. K. Sarychev, J. Appl. Phys. **84**, 3806 (1998).
23. G. Francsechetti, Alta Freq. **36**, 757 (1967).
24. A. I. Mal'tsev, *Foundations of Linear Algebra* (Nauka, Moscow, 1970).
25. R. B. Vaganov and B. Z. Katsenelenbaum, *Foundations of Diffraction Theory* (Nauka, Moscow, 1982).

Translated by V. Sipachev

Journal of Experimental and Theoretical Physics, Vol. 94, No. 3, 2002, pp. 489–497.
Translated from Zhurnal Éksperimental'noĭ i Teoreticheskoĭ Fiziki, Vol. 121, No. 3, 2002, pp. 573–582.

NUCLEI, PARTICLES, AND THEIR INTERACTION

Dissociative Recombination of Electrons and O_2^+ Molecular Ions in the Field of Intense Visible Laser Radiation

G. V. Golubkov*, M. G. Golubkov, and A. N. Romanov

Semenov Institute of Chemical Physics, Russian Academy of Sciences, ul. Kosygina 4, Moscow, 117977 Russia
**e-mail: golubkov@center.chph.ras.ru*

Received September 18, 2001

Abstract—We analyze the low-temperature dissociative recombination reaction $e^- + O_2^+ \longrightarrow O(^1D) + O(^3P)$ in the field of visible monochromatic laser radiation. The analysis is performed in terms of the multichannel quantum defect theory using the stationary formalism of the radiative collision matrix. We calculate the dependences of the reaction cross section on the incident electron energy, the external electromagnetic field strength and frequency, and also the angle between the directions of the electron beam and the electric vector for linearly polarized radiation. The cross section is shown to increase by several orders of magnitude for a certain choice of these parameters, suggesting the possible laser stimulation of this reaction. © *2002 MAIK "Nauka/Interperiodica".*

1. INTRODUCTION

The dissociative recombination reaction between slow electrons e^- and molecular ions XY^+,

$$e^- + XY^+ \longrightarrow X + Y^*, \quad (1)$$

plays an important role in the processes that take place in the Earth's ionosphere and upper atmosphere and is the subject of intensive experimental and theoretical studies [1]. Investigation of this reaction in an external electromagnetic field is also of great importance both in the theory of radiative collisions and in developing laser stimulation methods for elementary processes involving atoms and molecules [2].

Under the condition ($\hbar = m_e = e = 1$)

$$pf\omega_f^{-2} \ll 1, \quad p = \sqrt{2E_e} \quad (2)$$

(p is the incident electron momentum; f and ω_f are the electromagnetic field amplitude and frequency, respectively), the vibration amplitude of the electron is much smaller than its wavelength and the external field does not affect the electron motion; i.e., it has a certain energy E_e. If the field does not produce any dipole-allowed transitions in an isolated XY^+ ion, then it acts most effectively on the states formed at an intermediate stage of the process, because the field action on the (electron + target) system here is possible only if the latter has internal structure [3]. For positive molecular ions, this structure is related to the formation of an intermediate XY** complex. Under condition (2), the electromagnetic field effect must show up during the formation of this complex, when the electron motion is a multichannel one. Note that the problem of a strong electromagnetic field effect on the intermediate complex differs from conventional nonstationary problems of the theory of laser interaction with atoms and molecules [4–6]. The difference lies in the fact that the time when the intermediate complex emerges cannot be determined (under quantum conditions) and that the study needs to be carried out in the coupling of closed channels with continua.

It should be explained what the strong laser radiation is. We have in mind an external field that is weak compared to the intra-atomic field (e.g., the field strength for the ground atomic state of hydrogen is $f_a \approx 5 \times 10^9$ V/cm, which corresponds to a radiation intensity of the order of 10^{17} W/cm^2) but strongly couples intermediate Rydberg states, which are steady (or quasi-steady) in its absence. In that case, the coupling coefficients prove to be large and perturbation theory is inapplicable.

An additional constraint on the external field strength,

$$fD \ll 1, \quad (3)$$

where D is the transition dipole moment, allows us to restrict our analysis to the following two types of transitions when describing reaction (1): a nonradiative ($k = 0$) transition and an induced ($k = 1$) transition with the radiation of a single photon. The index k denotes the change in the number of photons in the system.

In this study, we investigate the dissociative recombination reaction between slow electrons and O_2^+ molecular ions via direct and resonance nonradiative

($k = 0$) transitions to the Schumann–Runge ($B^3\Sigma_u^-$) continuum, as well as via free–bound radiative ($k = 1$) transitions to the $n_1 p\pi_u$ (Σ_u^-) predissociation Rydberg states under intense visible ($23\,000 < \omega_f < 25\,000$ cm^{-1}) monochromatic laser radiation:

$$e^-(l\Lambda) + O_2^+(^2\Pi_g, v = 0)$$
$$\xrightarrow{k\omega_f} [O_2^{**}(n_k p\pi_u(\Sigma_u^-)) \longleftrightarrow O_2^*(B^3\Sigma_u^-)] \longrightarrow O(^3P) + O(^1D). \quad (4)$$

Here, n_k is the principal quantum number for a given k; v is the vibrational quantum number; and l and Λ are the electron orbital angular momentum and its projection onto the molecular axis, respectively. The electron energy is assumed to be low and lie within the range $0 < E_e < \omega$, where ω is the ion vibration frequency. Therefore, we disregard bound–bound dipole-allowed transitions from the intermediate $n_0 l\Lambda_g$ resonance Rydberg states to the $n_1 p\pi_u$ ($^3\Sigma_u^-$) predissociation states, since their contribution relative to the leading $n_0 p\pi_u$ series turns out to be small [7]. We also exclude direct radiative transitions from the $n_0 l\Lambda_g$ states to the Schumann–Runge continuum and to the low-lying $3p\pi_u$ ($^3\Sigma_u^-$) Rydberg state interacting with it, because these are of no interest in the spectral range under consideration. In addition, we ignore nonradiative transitions to the dissociative $2^3\Pi_g$ state, which correlates with the products of reaction (4) at infinity, because, according to [8], its term crosses the ion term near the right turning point of the vibronic ($v = 3$) state and the configuration coupling here is weak.

We perform our analysis in terms of the multichannel quantum defect theory using the stationary formalism of the radiative collision matrix [3]. The stationary approach is valid if the laser-pulse duration is much longer than the time scales of intramolecular transitions in the intermediate complex. For example, the predissociation time scales for a highly excited XY** molecule are of the order of 10^{-11} s. The intensity of typical tunable lasers widely used in various photoprocesses ranges from 10^{12} to 10^{14} W/cm^2, the pulse duration is $\tau \sim 10^{-8}$ s, and the pulse repetition period is $\Delta\tau \sim 10^{-3}$ s. The broadening through saturation and the rotational broadening here do not exceed 10^{-1} cm^{-1}, while the Doppler broadening is eliminated in a standard way by means of light-beam splitting [9]. Since the accuracy of measuring the energy dependence of the cross sections for reaction (1) does not exceed $\Delta E \sim 10^{-3}$ eV, the spread in external-radiation frequency f in the pulse may be disregarded, assuming the radiation to be monochromatic.

Taking into account the above constraints, we analyzed the dependences of the cross section for reaction (4) on the external field frequency and strength, as well as on the angle between the directions of the electron beam and the electric field of linearly polarized laser radiation.

2. AN INTEGRAL VERSION OF THE MULTICHANNEL QUANTUM DEFECT THEORY

Assuming the external electromagnetic field to be classical (taking the average number of photons to be large, $N_0 \gg 1$), we will describe the interaction of the $XY^+ + e^-$ system with this field by a time-periodic dependence,

$$\mathbf{u}_f = 2\mathbf{V}^f \cos\omega_f t, \quad \mathbf{V}^f = \frac{\mathbf{D}f}{2}. \quad (5)$$

Under condition (2), our analysis can then be performed in terms of the stationary multichannel quantum defect theory, in which the field is taken into account by introducing quasi-energetic states and related new channels of motion [3]. The subsequent analysis is based on information about adiabatic terms of the intermediate Rydberg complex XY**. We will also deal with the rotationally adiabatic spectral range, $Bn^3 \ll 1$ (B is the rotational ion constant and n is the principal quantum number of the Rydberg level), where the molecular axis during the collision is assumed to be fixed and the analysis is carried out in the coordinate system associated with the molecule. We define the zero Hamiltonian $\mathbf{H}_0$ on a Coulomb basis in such a way that all interactions in the isolated (diabatic) X + Y* configuration are accurately taken into account. In that case, in the total Hamiltonian of the system

$$\mathbf{H} = \mathbf{H}_0 + \mathbf{V},$$

the operator $\mathbf{V}$ is the sum

$$\mathbf{V} = \mathbf{V}^e + \mathbf{V}^f, \quad (6)$$

where the electrostatic interaction operator

$$\mathbf{V}^e = \mathbf{V}_{nc} + \mathbf{V}^{CI} \quad (7)$$

includes the non-Coulomb part of the interaction with the ion core $\mathbf{V}_{nc}$ and the configuration interaction $\mathbf{V}^{CI}$ (it relates the $e^- + XY^+$ and X + Y* configurations, which we denote by q and β, respectively). We also require that the Coulomb ($|q_k\rangle$) and dissociative ($|\beta_k\rangle$) basis wave functions be normalized on the energy scale as

$$\langle q_k(E)|q_{k'}(E')\rangle = \langle \beta_k(E)|\beta_{k'}(E')\rangle = \pi\delta(E - E')\delta_{kk'}.$$

Here, the total energy E of the system is measured from the ion ground state. These wave functions are peculiar in that at distances r of the order of atomic distances ($r \sim 1$) from the ion core, they describe a fast electron and a slow nuclear subsystem; i.e., they are adiabatic. The functions $|\beta_k\rangle$ can be independently calculated in the Born–Oppenheimer approximation by conventional

methods of quantum chemistry. In this case, the matrix elements $\langle q_k|\mathbf{V}^e|q_k'\rangle$ are responsible for vibronic transitions in the $e^- + XY^+$ system and are diagonal in k, $\langle q_k|\mathbf{V}^e|\beta_k\rangle$ describe the configuration interaction of the $e^- + XY^+$ and X + Y* states, and the elements of operator $\mathbf{V}^f$ couples the states with $k, k' = \pm 1$.

2.1. Basic Equations of the Theory

The multichannel quantum defect theory gives the following fundamental equation for the radiative multichannel scattering **T** matrix [7]:

$$\mathbf{T} = \mathbf{t} + \mathbf{t}\sum_{v,k}|q_k\rangle\langle q_k|\cot(\pi\nu_{vk})\mathbf{T} - i\mathbf{t}\sum_{\beta,k}|\beta_k\rangle\langle\beta_k|\mathbf{T}, \quad (8)$$

where $\nu_{v,k} = (-2\varepsilon_{vk})^{-1/2}$ is the effective principal quantum number that corresponds to the electron energy

$$\varepsilon_{vk} = E_e - v\omega_v - k\omega_f.$$

The operator **t** describes the electron interaction with the ion core in an electromagnetic field and satisfies the integral equation

$$\mathbf{t} = \mathbf{V} + \mathbf{VGt}, \quad (9)$$

where the Green operator **G** is a smooth function of the energy E and is represented by contributions of the Rydberg $e^- + XY^+$ states (minus the polar singularities attributable to the manifestation of discrete level structure of the Coulomb center) and the dissociative X + Y* states, i.e.,

$$\mathbf{G} = \frac{1}{\pi}\sum_{v,k}P\int\frac{|q_k\rangle\langle q_k|}{\varepsilon_{vk}-\varepsilon}d\varepsilon + \frac{1}{\pi}\sum_{\beta,k}P\int\frac{|\beta_k\rangle\langle\beta_k|}{E-k\omega_f-\varepsilon_\beta}d\varepsilon_\beta. \quad (10)$$

Here, P denotes the principal value of the integral. Note that the operator **G** is defined without the interaction **V**.

Equation (8) admits an algebraic construction of the unitary scattering **S** matrix (related to the **T** operator by $\mathbf{S} = \mathbf{I} - 2i\mathbf{T}$), irrespective of how many channels of motion are taken into account. The elements $T_{q_mq_{m'}}$ and $T_{q_m\beta_{m'}}$ with the indices of open channels [where $E > v\omega_v + k\omega_f$ and the functions $\cot(\pi\nu_{vk}) = -i$] describe the amplitudes of inelastic scattering and the dissociative recombination reaction (1), respectively. In this case, the smallness of the configuration coupling in combination with the parameter $a_0/R_e^+ \ll 1$ (a_0 is the zero vibration amplitude and R_e^+ is equilibrium distance) allows us to restrict our analysis to a finite number of vibronic states.

2.2. Elements of the Reaction **t** Matrix

The reaction matrix in Eq. (8) is the sum of two operators that characterize the electrostatic and field interactions,

$$\mathbf{t} = \mathbf{t}^e + \mathbf{t}^f. \quad (11)$$

The electrostatic interaction elements are defined as [7]

$$t^e_{v_kv_k'} = t^{(0)}_{v_kv_k'} + \frac{1}{\pi}\sum_\beta P\int\frac{V^e_{v_k\beta_k}V^e_{\beta_kv_k'}}{E-k\omega_f-\varepsilon_\beta}d\varepsilon_\beta,$$
$$t^e_{v_k\beta_k} = V^e_{v_k\beta_k} + \frac{1}{\pi}\sum_{v'}P\int\frac{t^{(0)}_{v_kv_k'}V^e_{v_k'\beta_k}}{\varepsilon_{v'k}-\varepsilon}d\varepsilon, \quad (12)$$
$$t^{(0)}_{v_kv_{k'}'} = -\langle\chi_v|\tan(\pi\mu_{l\Lambda})|\chi_{v'}\rangle\delta_{kk'},$$

where $\mu_{l\Lambda}$ is the level diabatic quantum defect (without the configuration interaction $\mathbf{V}^{CI}$).

To within terms quadratic in $\mathbf{V}^f$, the second term in Eq. (11) responsible for the effective interaction with the external field is

$$\mathbf{t}^f = [1 + \mathbf{V}^e\mathbf{G}(E)][\mathbf{V}^f + \mathbf{V}^f\mathbf{G}(E)\mathbf{V}^f] \times [1 + \mathbf{G}(E)\mathbf{V}^e]. \quad (13)$$

In the linear (in $\mathbf{V}^f$) approximation, the matrix elements of operator $\mathbf{t}^f$ are

$$t^f_{vv'}(l\Lambda \longrightarrow l_\beta\Lambda_\beta) = \frac{1}{2}fr(l\Lambda \longrightarrow l_\beta\Lambda_\beta)S^{l\Lambda,\,l_\beta\Lambda_\beta}\delta_{vv'}, \quad (14)$$

where $l\Lambda$ are the Rydberg states allowed by selection rules for a radiative transition to the final $l_\beta\Lambda_\beta$ state of the system. For the radial parts of the free–bound dipole transitions specified on the Coulomb basis distorted by the interaction with the core, we have [10]

$$r(l\Lambda \longrightarrow l_\beta\Lambda_\beta) = \frac{1}{\pi}\Gamma\left(\frac{2}{3}\right)\left(\frac{4}{3}\right)^{1/3}\omega_f^{-5/3} \times \cos\left[\pi\left(\Delta\mu_{l_\beta\Lambda_\beta,\,l\Lambda} + \frac{1}{6}\right)\right], \quad (15)$$
$$\Delta\mu_{l_\beta\Lambda_\beta,\,l\Lambda} = \mu_{l_\beta\Lambda_\beta}(R_e^+) - \mu_{l\Lambda}(R_e^+).$$

The angular parts of the matrix element (14) in the coordinate system associated with the molecular axis are given by

$$S^{l\Lambda,\,l'\Lambda'} = \sqrt{\frac{4\pi(2l'+1)}{3(2l+1)}} \times (l'100|l0)(l'1\Lambda'\Lambda-\Lambda'|l\Lambda)Y^*_{1,\,\Lambda-\Lambda'}\left(\frac{\mathbf{f}}{f}\right), \quad (16)$$

where $Y_{l\Lambda-\Lambda'}(\mathbf{f}/f)$ is the spherical function [11].

2.3. Partial and Total Cross Sections for the Dissociative Recombination Reaction

Below, we assume that the XY^+ molecular ion is in its ground vibrational $v = 0$ state. Nonradiative transitions with the formation of Rydberg complexes XY** in the $v_0 = 1$ and $k = 0$ states and transitions to the $v_1 = 0$ and $k = 1$ states, which are accompanied by the radiation of a field quantum, make the largest contribution to the reaction. Given that elements (12) and (14) are small (in the two-channel approximation in vibronic coupling), the partial amplitudes of these transitions in the coordinate system associated with the molecular axis are

$$T_{0_0\beta_0} = \frac{t^e_{0_0\beta_0}(z_{10} + i\gamma^f_{1_0}) + t^e_{1_0\beta_0}t^e_{1_00_0}}{z_{10} + i\gamma_{1_0}},$$
$$T_{0_0\beta_1} = \frac{t^f_{0_00_1}(l\Lambda \longrightarrow l_\beta\Lambda_\beta)t^e_{0_1\beta_1}(l_\beta\Lambda_\beta)}{z_{01} + i\gamma_{0_1}}, \quad (17)$$

where

$$z_{vk}(E_e l\Lambda) = \tan((\pi\nu_{vk}(E_e)) - t^e_{v_kv_k}(l\Lambda)).$$

The decay rates from the $l_\beta\Lambda_\beta$ states in (17) appear as follows:

$$\gamma_{1_0} = \gamma^i_{1_0} + \gamma^\beta_{1_0} + \gamma^f_{1_0}, \quad \gamma_{0_1} = \gamma^\beta_{0_1} + \gamma^f_{0_1}. \quad (18)$$

These include the partial rates of self-ionization (γ^i), predissociation (γ^β), and field decay (γ^f), which can be expressed in terms of the matrix elements as

$$\gamma^i_{v_k} = \left|t^e_{v_k(v-1)_k}\right|^2, \quad \gamma^\beta_{v_k} = \left|t^e_{v_k\beta_k}\right|^2,$$
$$\gamma^f_{v_k} = \sum_{l\Lambda}\left|t^f_{v_kv_{k-1}}(l\Lambda \longrightarrow l_\beta\Lambda_\beta)\right|^2.$$

The total cross section for the dissociative recombination reaction for a transition to the dissociative β channel is

$$\sigma_{0\beta}(\theta_e) = \frac{8\pi^2}{E_e}$$
$$\times g\sum_{k=0,1}\left\langle\left|\sum_{l\Lambda} i^l e^{i\delta_l}Y^*_{l\Lambda}(\mathbf{n})T_{0_0\beta_k}(l\Lambda \longrightarrow l_\beta\Lambda_\beta)\right|^2\right\rangle, \quad (19)$$
$$\delta_l = \arg\left(\Gamma\left(l + 1 - \frac{i}{p}\right)\right].$$

Here, the vector **n** specifies the direction of the incident electron beam relative to the molecular XY axis, θ_e is the angle between the vectors **n** and **f**, g is the spin factor, $\Gamma(x)$ is the gamma function, and $\langle\ldots\rangle$ denotes averaging over all possible orientations of the molecule.

Substituting (17) into (19), we rewrite it as the sum

$$\sigma_{0\beta} = \sigma_{0_0\beta_0} + \sigma_{0_0\beta_1}, \quad (20)$$

where the first term,

$$\sigma_{0_0\beta_0} = \frac{8\pi^2}{E_e}g$$
$$\times\left\langle\sum_m\left|D^{*l}_{\Lambda m}(0, \theta, \pi - \varphi)Y^*_{lm}(\theta_e\varphi_e)T_{0_0\beta_0}(l\Lambda \longrightarrow l_\beta\Lambda_\beta)\right|^2\right\rangle, \quad (21)$$

describes the nonradiative ($k = 0$) transition and the second term,

$$\sigma_{0_0\beta_1} = \frac{2\pi^2 f^2}{E_e}g\left\langle\frac{\tilde\gamma^f_{0_1}(\mathbf{n}, \mathbf{f})\gamma^\beta_{0_1}}{z^2_{01}(l_\beta\Lambda_\beta) + \gamma^2_{0_1}}\right\rangle, \quad (22)$$

is responsible for the transition accompanied by the radiation of a field quantum ($k = 1$). Expression (22) clearly demonstrates the formation of additional interference structure in the cross section (20) through the contribution of the $l\Lambda$ channels to the field-induced population of the predissociation $n_1l_\beta\Lambda_\beta$ states.

When we calculate the quantity $\tilde\gamma^f_{0_1}(\mathbf{n}, \mathbf{f})$, it is convenient to pass, as in (21), to a coordinate system where the direction of vector **f** is preferential. This quantity is then defined as

$$\tilde\gamma^f_{0_1}(\mathbf{n}, \mathbf{f}) = \left|\sum_{l\Lambda, m} r(l\Lambda \longrightarrow l_\beta\Lambda_\beta)\sqrt{\frac{4\pi(2l_\beta + 1)}{3(2l + 1)}}\right.$$
$$\times(l_\beta 100|l0)(l_\beta 1\Lambda_\beta\Lambda - \Lambda_\beta|l\Lambda)D^{*l}_{\Lambda m}(0, \theta, \pi - \varphi)$$
$$\left.\times Y_{1,\Lambda_\beta-\Lambda}(\theta, 0)Y^*_{lm}(\theta_e, \varphi_e)e^{i\delta_l}\right|^2, \quad (23)$$
$$m = \pm l, \pm(l-1), \ldots, \pm 1, 0.$$

Here, $D^l_{\Lambda m}(\alpha, \beta, \gamma)$ is the Wigner generalized spherical function [11]; θ and φ, and θ_e and φ_e are the spherical angles that specify the directions of the molecular axis and the incident electron beam relative to the direction of vector **f**, respectively. In this case, the angle-unaveraged expressions for the partial cross sections (21) and (22) depend on θ and on the difference $\varphi - \varphi_e$. The corresponding averaging is subsequently performed over them.

The general properties of the cross section (20) can be established from the form of amplitudes (17). The energy dependence $\sigma_{0\beta}(E_e)$ must have a distinct resonance structure formed by the superposition of two types of Rydberg series. The first type corresponds to the $l_\beta\Lambda_\beta$ series of vibronic resonances of the closed ($v = 1$) channel converging to the threshold $E_e = \omega$. The second type must include a sequence of field-induced Breit–Wigner resonances from the group of optically resolved $l\Lambda$ series converging to the threshold $E_e = \omega_f$. Since $\omega \ll \omega_f$, these resonances are rare and

may be absent altogether in the energy range $0 < E_e < \omega$ under consideration.

The behavior of the partial and total cross sections as a function of the external field strength can be described as follows. At small f, a major factor affecting the partial cross section (21) for the nonradiative transition must be the broadening of the resonance lines in the $l_\beta\Lambda_\beta$ series, which is significant for $\Gamma^f > \Gamma^e$, where the natural and field-induced FWHMs are given by

$$\Gamma^e = \frac{\gamma^i + \gamma^\beta}{\pi n_1^3}, \quad \Gamma^f = \frac{\gamma^f}{\pi n_0^3}$$

(corresponding to $f \geq 10^{-4}$ at. unit). At large field strengths, $f > 10^{-2}$ at. unit, the cross section $\sigma_{0_0\beta_0}$ ceases to depend on f and reduces to the expression

$$\sigma_{0_0\beta_0} = \frac{2\pi}{E_e} g\gamma^\beta_{0_0},$$

which describes the direct transition to the dissociative continuum (with no involvement of intermediate Rydberg states) in the absence of a field.

Obviously, the dependence of the total cross section (20) on f is more complex. Thus, at a small field strength (of the order of 10^{-4} at. unit or larger), the height of the field-induced resonance peaks must increase as f^2. For f ~ 10^{-3}–10^{-2} at. unit, the cross section increases, producing a distinct resonance structure. The subsequent increase in strength (up to $f \sim 10^{-1}$ at. unit) causes a smoothing of the overall pattern and a broadening of the field-induced resonances against the background of a slowly changing dependence on f.

It is also easy to find the dependence of the cross section on the external radiation frequency ω_f. Clearly, it must reach a maximum at a frequency at which the laser-induced $n_1 l_\beta \Lambda_\beta$ ($v = 0$) Rydberg states of the closed channel with the excitation threshold $E_e = \omega_f$ for small principal quantum numbers n_1 fall within the electron energy range $0 < E_e < \omega$ of interest.

3. THE WAVE FUNCTIONS AND TERMS OF THE O_2 MOLECULE

The wave functions of intermediate Rydberg states for the Hamiltonian $\mathbf{H}_0$ chosen can be written as

$$|q_k\rangle = \pi^{1/2}\phi_{v_k l}(r)\varphi_+(\mathbf{x})\chi_v(R)Y_{l\Lambda}\left(\frac{\mathbf{r}}{r}\right)|k\rangle, \qquad (24)$$

where $\varphi_+(\mathbf{x})$ is the electron wave function of the XY^+ ion, $\{\mathbf{x}\}$ is the set of core electron coordinates, R is the internuclear distance, and $|k\rangle$ is the photon part of the total wave function (24). The regular (at zero) radial Coulomb wave function $\phi_{v_k l}$ at distances

$$\left(l + \frac{1}{2}\right)^2 \ll r \ll |E_e|^{-1}$$

is [10]

$$\phi_{v_k l} = \left(\frac{2}{\pi^2 r^3}\right)^{1/4} \sin\left[\sigma_l(r) - \pi\left(l + \frac{1}{4}\right)\right]. \qquad (25)$$

At small $l \ll |\varepsilon_{vk}|^{-1/3}$ to a first order in the small parameter $r|\varepsilon_{vk}|$, the quasiclassical phase is

$$\sigma_l(r) = (8r)^{1/2} + \frac{1}{3}(2r^3)^{1/2}|\varepsilon_{vk}|.$$

For the nuclear wave functions $\chi_{\beta_k}(R)$, we may use the quasiclassical approximation and the fact that, for a sufficiently steep dissociative term $U_\beta(R)$ near the classical turning point R_k^*, where

$$\varepsilon_k = E - k\omega_f = U_\beta(R_k^*),$$

the Winans–Stueckelberg approximation [12] holds if $U'_\beta a_0 \gg \omega$:

$$\chi\beta_k(R) = \left|U'_\beta(R)\right|^{-1/2}\delta(R - R_k^*(\varepsilon_k)). \qquad (26)$$

Assuming that only one dissociative β channel exists in the quantum system under consideration, we have for the elements $t^e_{v_k v'_k}$ in Eq. (12)

$$t^e_{v_k v'_k} = t^{(0)}_{v_k v'_k} + \frac{1}{\pi} P\int \frac{V_\beta^2(R)\chi_v(R)\chi_{v'}(R)}{\varepsilon_k - U_\beta(R)} dR. \qquad (27)$$

Here, $V_\beta(R)$ is the electron part of the configuration interaction related to the splitting of the Rydberg $l_\beta\Lambda_\beta$ and dissociative β terms by

$$\Delta_{n_k\beta} = \frac{2V_\beta}{(\pi n_k^3)^{1/2}}.$$

To estimate the locations of the vibronic $n_0 l_\beta \Lambda_\beta$ ($v = 1$) and field-induced $n_1 l_\beta \Lambda_\beta$ ($v = 0$) resonance levels, it is convenient to use the adiabatic quantum defect [7]

$$\tilde{\mu}_{n_k l\Lambda}(R) = \mu_{n_k l\Lambda}(R) + \Delta\mu_{n_k l\Lambda}(R). \qquad (28)$$

The shift $\Delta\mu_{n_k l\Lambda}$ is attributable to the second term in Eq. (27) and is given by the expression

$$\Delta\mu_{n_k l\Lambda}(R) = \frac{1}{\pi}\arctan\left[\frac{\pi V_\beta^2(R)}{U_\beta(R) + k\omega_f - U^{**}_{n_k l\Lambda}(R)}\right], \qquad (29)$$

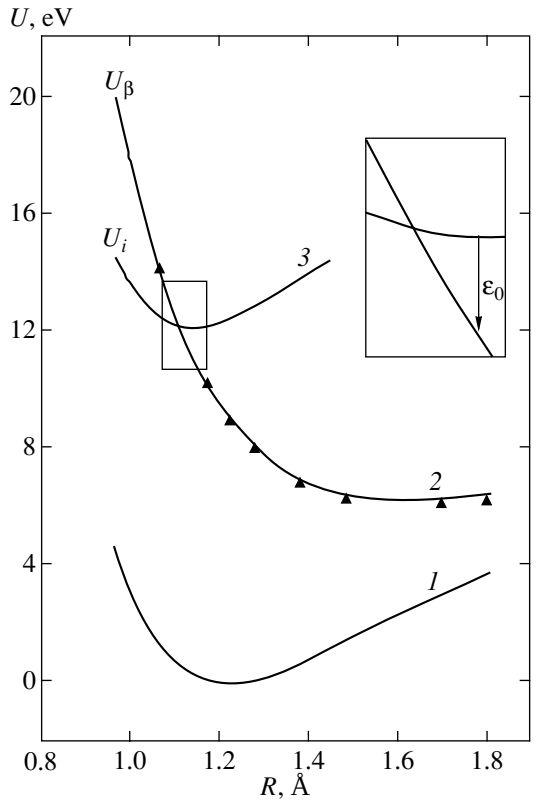

Fig. 1. Potential curves for the ground $X^3\Sigma_g^-$ (*1*), electron-excited $B^3\Sigma_g^-$ (*2*), and ion $X^2\Pi_g$ (*3*) states of the O_2 molecule whose energy is counted off from the $X^3\Sigma_g^-$ state. The solid lines and triangles represent the results of our calculations and the data from [18], respectively.

in which the Rydberg term is defined as

$$U^{**}_{n_k l\Lambda}(R) = U_i(R) - \frac{1}{2(n_k - \tilde{\mu}_{n_k l\Lambda}(R))^2}.$$

Near the equilibrium position, $R = R_e^+$, this shift takes the form

$$\Delta\mu_{n_k l\Lambda}(R_e^+) = \frac{1}{\pi}\arctan\left[\frac{\pi V_\beta^2(R_e^+)}{\varepsilon_0 + k\omega_f}\right], \qquad (30)$$

$$\varepsilon_0 = U_\beta(R_e^+) - U_i(R_e^+).$$

If $\varepsilon_0 + k\omega_f < 0$, then the configuration shift is negative and the corresponding level rises. Otherwise, this level lowers. The latter takes place for the O_2 molecule.

3.1. Potential Curves

We computed the diabatic $^3\Sigma_u^-$ valence term and the ion term using the GAMESS code [13] by the multireference double configuration interaction (MRD-CI) method [14] with the reference configurations obtained by the CASSCF (complete active space self-consisted field) method [15] over the complete valence space ($2\sigma_g$, $2\sigma_u$, $3\sigma_g$, $1\pi_u$, $1\pi_g$, $3\sigma_u$) in the single-electron basis [6*s*, 3*p*, 2*d*, 1*f*] taken from [16]. The absence of diffuse Gaussian functions made it possible to obtain the diabatic valence terms with no admixture of Rydberg states. The $^3\Sigma_u^-$ term was computed in the D_{2h} symmetry with the wave function averaged over two lower states. Here, we used 48 reference configurations and performed the subsequent MRD-CI computation with 1 189 512 CSF (configuration state function) configurations. The corresponding CASSCF wave function of the ion was computed with averaging over two degenerate components of the $^2\Pi_g$ state. The MRD-CI extension included 1 564 542 CSF configurations. Our computed ion term was slightly underestimated in energy because of the characteristic features of the MRD-CI method itself. It had to be displaced upward along the energy scale, as is usually done (see, e.g., [16]), to reproduce the experimental ionization potential [17]. Our final results are shown in Fig. 1. The computed terms agree well with the data from [18], and the direct-transition energy is $\varepsilon_0 = 0.713$ eV. Therefore, we used the results from [18] for the electron part of the configuration interaction $V_\beta(R)$.

4. THE CROSS SECTION FOR THE $e^- + O_2^+$ REACTION IN AN EXTERNAL ELECTROMAGNETIC FIELD

We computed the cross section for reaction (4) in the seven-channel approximation [five open ($v = 0$) channels, one closed ($v = 1$) channel, and one open dissociative β channel] using formulas (20)–(23). In the energy range $E_e \le 0.6$ eV of interest, there are no vibronic states with $v \ge 2$ and using this approximation is quite justifiable [19]. We took $\mu_{p\pi_u}(R_e^+) = 0.74$ [20] for the diabatic quantum defect of the intermediate $p\pi_u(^3\Sigma_u^-)$ series; the derivatives calculated from the data in [21] are

$$\mu'_{p\pi_u}(R_e^+) = 0.07, \quad \mu''_{p\pi_u}(R_e^+) = 0.02.$$

The corresponding parameters for the entrance channels s_σ, d_σ, d_π, and d_δ were determined in a similar way. The Frank–Condon factors appearing in the definition of the partial predissociation rates $\gamma^\beta_{v_k}$ were computed with the Morse vibrational wave functions [22] for the ion term $U_i(R)$ and with the wave functions (26) for the dissociative term $U_\beta(R)$. These terms are shown in Fig. 1.

4.1. Energy Dependence of the Cross Section

The dependence of the cross section on the incident electron energy E_e for various field strengths f calculated with $\omega_f = 24040$ cm^{-1} and $\theta_e = \pi/2$ is shown in Fig. 2. In the absence of any field ($f = 0$), we observed the characteristic Fano–Feishbach resonance structure produced by a nonradiative transition with the population of the intermediate $n_0 p\pi_u(^3\Sigma_u^-,\ v_0 = 1)$ Rydberg series, which decays into the dissociative Schumann–Runge continuum ($^1D + {}^3P$). The parentheses (n_0, v_0) and arrows denote the corresponding resonance lines. The first resonance (with a dip near $E_e = 0.03$ eV) corresponds to the principal quantum number $n_0 = 9$. Here, the frequency ω_f is chosen in such a way that the field-induced resonances $n_1 p\pi_u(^3\Sigma_u^-,\ v_1 = 0)$ from the entrance channels of electron motion s_σ, d_σ, d_π, and d_δ are located near this dip. This value significantly exceeds the vertical transition energy (see Fig. 1).

As would be expected, the field-induced resonances clearly show up starting from $f \geq 10^{-3}$ at. unit. They correspond to $n_1 = 3$ and are split through the intense field interaction. The largest field effect is reached for $f \geq 10^{-2}$ at. unit. A noticeable field effect is also observed in the wings of the energy dependence at $f \approx 10^{-1}$ at. unit.

4.2. Dependence of the Cross Section on Frequency ω_f

The frequency dependence of the cross section is shown in Fig. 3 for three electron energies E_e. It is bell-shaped with the energy-dependent maximum at $\omega_f^{\max}(E_e)$, at which the cross section increases approximately by two orders of magnitude relative to the characteristic frequencies in the wings of this curve. The field effect is largest for the electron energy $E_e = 0.03$ eV at $\omega_f^{\max} = 24040$ cm^{-1}. In the energy range $0 < E_e \leq 0.6$ eV under consideration, the $\omega_f^{\max}$ range lies outside the interval $\Delta\omega_f = 23000$–25000 cm^{-1} and belongs to the visible spectral range. The latter is of particular importance in using tunable lasers to measure the cross section for reaction (4). The interval $\Delta\omega_f$ does not depend on the field strength or on the angle θ_e between the vectors **n** and **f**.

Here, the energy dependence of $\omega_f^{\max}$ turns out to be linear and is determined by the second term in expression (20), which describes the transition with the radiation of a field quantum ($k = 1$), from the condition $z_{01}(E_e, l_\beta, \Lambda_\beta) = 0$. At low energies, $E_e \ll 1$, this dependence can be represented as

$$\omega_f^{\max}(E_e) = \omega_f^{\max}(0) + E_e, \qquad (31)$$

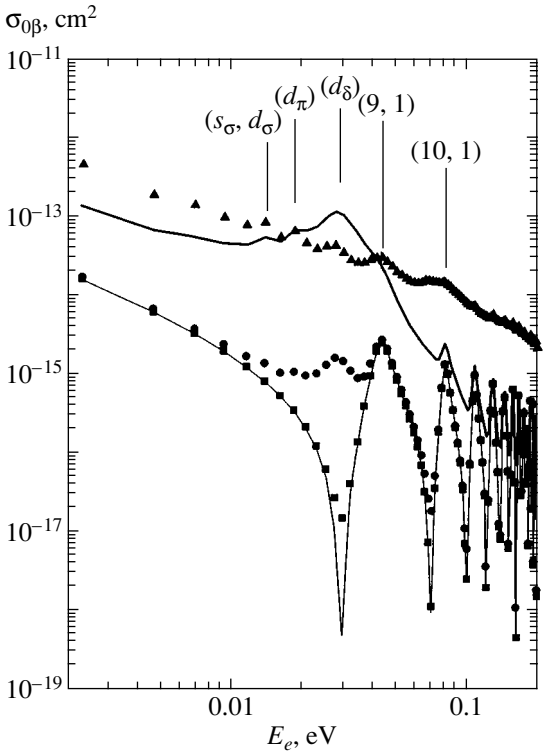

Fig. 2. Cross section for the reaction $O_2^+ + e^- \xrightarrow{k\omega_f} O(^1D) + O(^3P)$ versus electron energy E_e for the following external-field strengths: $f = 0$ (thin line), 5×10^5 (squares), 5×10^6 (circles), 5×10^7 (heavy line), and 5×10^8 (triangles) V/cm.

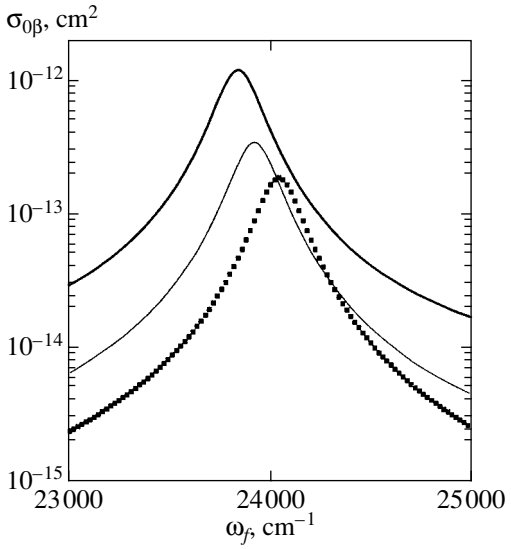

Fig. 3. Cross section for the reaction $O_2^+ + e^- \xrightarrow{k\omega_f} O(^1D) + O(^3P)$ versus frequency ω_f calculated at $f = 1.15 \times 10^8$ V/cm and $\theta_e = \pi/2$ for three electron energies: $E_e = 0.005$ (heavy line), 0.015 (thin line), and 0.03 eV (squares).

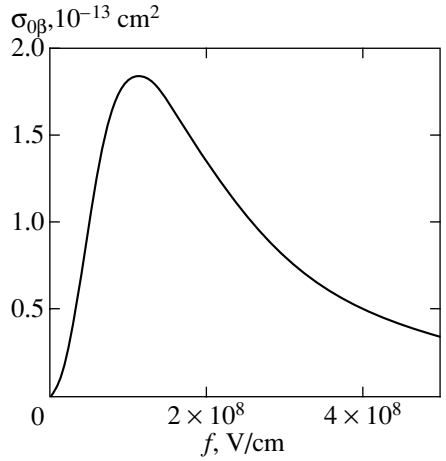

Fig. 4. Cross section for the reaction $O_2^+ + e^- \xrightarrow{k\omega_f} O(^1D) + O(^3P)$ versus external-field strength f.

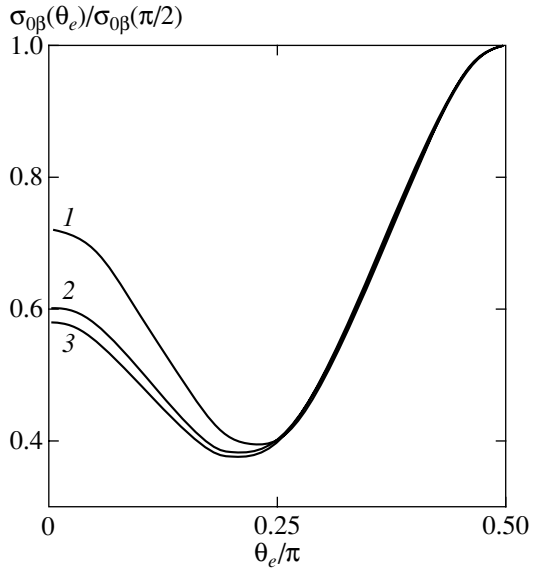

Fig. 5. Cross-section ratio $\sigma_{0\beta}(\theta_e)/\sigma_{0\beta}(\theta_e = \pi/2)$ versus θ_e calculated at $E_e = 0.03$ eV and $\omega_f = 24040$ cm^{-1} for three external-field strengths: $f = 5 \times 10^8$ (*1*), 5×10^7 (*2*), and 5×10^6 (*3*) V/cm.

where, according to (30), $\omega_f^{\max}(0)$ is the solution to the transcendental equation

$$\omega_f^{\max}(0) = \frac{\pi^2}{2} \times \left\{ \mu_{n_1 l_\beta \Lambda_\beta}(R_e^+) + \frac{1}{\pi} \arctan\left[\frac{\pi V_\beta^2(R_e^+)}{\varepsilon_0 + \omega_f^{\max}(0)} \right] \right\}^{-2} \quad (32)$$

and is approximately equal to 0.108.

4.3. Dependence of the Cross Section on External-Field Strength

The dependence of the cross section on f is shown in Fig. 4 for the following parameters:

$$E_e = 0.03 \text{ eV}, \quad \omega_f^{\max} = 24040 \text{ cm}^{-1}, \quad \theta_e = \pi/2,$$

for which the effect is at a maximum and the cross section for reaction (4) increases by five orders of magnitude (see Fig. 2). The computed curve faithfully reproduces the salient features of the field effect on the dissociative recombination reaction: the quadratic increase in cross section for small f, its peaking at $f^{\max} = 1.15 \times 10^8$ V/cm, and the falloff proportional to $1/f^2$ at large f. Such a situation is typical of the radiative and collisional processes involving intermediate Rydberg states [23, 24].

5. ANGULAR DEPENDENCE

The angular dependence of the cross section ratio $\sigma_{0\beta}(\theta_e)/\sigma_{0\beta}(\pi/2)$ computed for three field strengths f at a fixed incident electron energy, $E_e = 0.03$ eV, is shown in Fig. 5. We see that, at small angles θ_e, the cross section slightly rises with external field strength. The maximum value does not depend on f and is reached at $\theta_e = \pi/2$ when the electron and light beams are directed at a small angle to each other. Under these conditions, the interaction region is extended enough and the field effect is largest.

The dependence of the relative cross section on the electron energy E_e shows a similar pattern. The distinction lies in the behavior of the cross section at small angles θ_e, where this dependence is irregular.

6. CONCLUSION

Let us now discuss the most important results of our study. First, note that the efficiency of the field effect on the dissociative recombination reaction $e^- + O_2^+ \longrightarrow O(^1D) + O(^3P)$ is achieved by purposefully creating the resonance conditions that allow one to populate the field-induced intermediate $n_1 p\pi_u(v_1 = 0)$ Rydberg states with small principal quantum numbers n_1 whose predissociation rate is high enough. In this case, the range of incident radiation frequencies ω_f in which these conditions are realized lies in the visible spectral range, for which the characteristic induced-transition energies are much higher than the energy ε_0 (see Fig. 1).

An important merit of our theory is its simplicity. This is achieved by limiting the range of incident electron energies E_e in which there are no resonances from far Rydberg series with large vibrational quantum numbers ($v \geq 2$). Note also that, for an optimum choice of the system parameters (ω_f, f, and θ_e), the field effect enhances reaction (4) by several orders of magnitude, which may serve as a reliable criterion when carrying

out the corresponding experiments. It may also well be that using circular rather than linear light polarization is most convenient for measurements. This requires a certain modification of the theory when calculating the field matrix elements but will not lead to fundamentally new results.

The problem becomes more difficult when the incident electron energy E_e increases, which requires incorporating a larger number of vibronic states and new decay channels of the intermediate complex XY** into the overall scheme. These include, for example, the dissociative $2^2\Pi_g$ configuration; the interaction with the latter necessitates allowance for the coupling between the s_σ and d_σ channels of motion [19]. The question arises as to what the influence of the rotational excitation of the initial O_2^+ ion on the rate of reaction (4) is. Its solution requires developing a special procedure for deciphering the resonance structure of the cross section. All these questions need to be theoretically studied, because increasing the reaction temperature significantly enhances the experimental capabilities.

ACKNOWLEDGMENTS

This study was supported by the INTAS (grant no. 99-00039).

REFERENCES

1. *Dissociative Recombination: Theory, Experiment, and Applications*, Ed. by M. Larsson, J. B. A. Mitchell, and I. F. Schneider (World Sci., Singapore, 2000).
2. G. V. Golubkov and G. K. Ivanov, Izv. Ross. Akad. Nauk, Ser. Khim. **3**, 367 (1994).
3. G. K. Ivanov and G. V. Golubkov, Zh. Éksp. Teor. Fiz. **99**, 1404 (1991) [Sov. Phys. JETP **72**, 783 (1991)].
4. N. B. Delone and V. P. Kraĭnov, *Atom in a Strong Light Field* (Atomizdat, Moscow, 1978).
5. Yu. I. Geller and A. K. Popov, *Laser Inducing of Resonances in Continuous Spectra* (Nauka, Novosibirsk, 1981).
6. V. M. Akulin and N. V. Karlov, *Intense Resonant Interactions in Quantum Electronics* (Nauka, Moscow, 1987).
7. G. V. Golubkov and G. K. Ivanov, Zh. Éksp. Teor. Fiz. **104**, 3334 (1993) [JETP **77**, 574 (1993)].
8. S. L. Guberman, in *Physics of Ion-Ion and Electron-Ion Collisions*, Ed. by F. Brouillard and J. W. McGowan (Plenum, New York, 1983; Mir, Moscow, 1986).
9. V. S. Letokhov, *Laser Photoionization Spectroscopy* (Nauka, Moscow, 1987).
10. E. M. Balashov, G. V. Golubkov, and G. K. Ivanov, Zh. Éksp. Teor. Fiz. **86**, 2044 (1984) [Sov. Phys. JETP **59**, 1188 (1984)].
11. A. S. Davydov, *Theory of Atomic Nucleus* (Fizmatgiz, Moscow, 1958).
12. J. S. Winans and E. C. G. Stueckelberg, Proc. Natl. Acad. USA **14**, 867 (1928).
13. M. W. Schmidt, K. K. Baldridge, J. A. Boatz, *et al.*, J. Comput. Chem. **14**, 1347 (1993).
14. R. J. Buenker and S. D. Peyerimhoff, Theor. Chim. Acta **35**, 33 (1974).
15. T. H. Dunning, J. Chem. Phys. **90**, 1007 (1989).
16. S. L. Guberman and A. Giusti-Suzor, J. Chem. Phys. **95**, 2602 (1991).
17. R. G. Tonkyn, J. W. Winniczek, and M. G. White, Chem. Phys. Lett. **164**, 137 (1989).
18. R. P. Saxon and B. Liu, J. Chem. Phys. **73**, 870 (1980).
19. M. G. Golubkov, G. V. Golubkov, and G. K. Ivanov, J. Phys. B **30**, 5511 (1997).
20. A. Sur, C. V. Ramana, W. A. Chupka, *et al.*, J. Chem. Phys. **84**, 69 (1986).
21. D. C. Cartwright, W. J. Hunt, W. Williams, *et al.*, Phys. Rev. A **8**, 2436 (1973).
22. L. D. Landau and E. M. Lifshitz, *Course of Theoretical Physics*, Vol. 3: *Quantum Mechanics: Non-Relativistic Theory* (Fizmatgiz, Moscow, 1963; Pergamon, New York, 1977).
23. G. K. Ivanov, G. V. Golubkov, and S. V. Drygin, Zh. Éksp. Teor. Fiz. **107**, 1503 (1995) [JETP **80**, 840 (1995)].
24. G. K. Ivanov and G. V. Golubkov, Zh. Éksp. Teor. Fiz. **115**, 1987 (1999) [JETP **88**, 1087 (1999)].

Translated by V. Astakhov

Journal of Experimental and Theoretical Physics, Vol. 94, No. 3, 2002, pp. 498–508.
Translated from Zhurnal Éksperimental'noĭ i Teoreticheskoĭ Fiziki, Vol. 121, No. 3, 2002, pp. 583–595.

NUCLEI, PARTICLES, AND THEIR INTERACTION

Description of the Inner State and Kinetics of Rydberg Atoms Based on the Kinetic Boltzmann Equation for Rydberg Electrons

T. I. Privalov and A. M. Shalagin*

Institute of Automatics and Electrometry, Siberian Division, Russian Academy of Sciences, Novosibirsk, 630090 Russia

**e-mail: shalagin@iae.nsk.su*

Received October 8, 2001

Abstract—The inner characteristics and kinetics of Rydberg atoms (RAs) excited selectively over energy in a buffer gas are considered using the kinetic equation for a classical distribution function of Rydberg electrons (REs). The distribution of REs over coordinates and velocities in a moving RA is found in the general case. In a moving RA, the effect of "blowing off" an electron cloud by a buffer gas is substantial. In this case, however, the average values of the kinetic and potential energies of REs weakly deviate from those predicted by the virial theorem. The latent and macroscopic polarizations of the medium caused by the blowing-off effect are predicted. The macroscopic polarization appears upon velocity-selective excitation of RAs and produces the bias current, which transforms to a usual electric current when the integrity of the RA is lost due to the blowing-off effect. The calculated "electron" contribution to the transport frequency of collisions of the RA with buffer gas atoms proved to be small compared to that from the ion core. *© 2002 MAIK "Nauka/Interperiodica".*

1. INTRODUCTION

The Rydberg states of atoms are currently extensively studied both theoretically and experimentally [1–7]. It is possible now to excite the Rydberg states of alkali metal atoms selectively both over energies and velocities using a variety of experimental methods. There are conventionally three most important groups of problems in the study of the Rydberg states of atoms and molecules that are widely investigated at present. Great attention has been paid to the study of the change in the energy and angular momentum of Rydberg atoms (RAs) in collisions with buffer particles (atoms, ions, molecules, etc.) [3, 5, 6] upon energy-selective excitation of RAs. The detailed studies of the interaction of RAs with electromagnetic waves (laser radiation, microwave radiation in a high-Q resonator) yielded a number of fundamental results [7, 8]. Finally, recent investigations of the dynamics of wave packets of highly excited Rydberg states produced upon excitation of RAs by ultrashort laser pulses [9, 10] opened up the possibility for studies in the intermediate field between quantum and classical mechanics.

In this paper, we study the inner characteristics and kinetics of a RA selectively excited over energy or velocity and analyze its collisions buffer particles. It is known that the movement of Rydberg electrons (REs) in the hydrogen-like potential of an atomic core can be described classically with good accuracy. It is important in this case that electrically neutral buffer atoms do not interact with the RA as a whole, REs and the ion core behaving as independent scattering centers.

Collisions of a RA with thermal buffer gas atoms have been analyzed for the first time by Fermi [11]. Fermi showed that for some processes characterizing the RA as a whole the dominant factor is collisions of REs with buffer atoms, while the interaction of REs with the ion core can be neglected during collisions. During a collision with a much heavier buffer atom, the RE rapidly loses its momentum, whereas its kinetic energy changes during many collisions (energy diffusion).

In this paper, we will follow the approach that was first proposed by Pitaevsky [12], who described the bound and free states of electrons by a single classical distribution function. This approach proved to be very efficient for studying characteristics of weakly ionized plasma. We will use the concept of the RE "gas" from this approach and introduce a classical distribution function for this gas, which satisfies the Boltzmann equation. Unlike the formulation of the problem in [12], in our case, REs are created not from free electrons but from low-lying energy states upon selective laser excitation.

Thus, our approach is based on the introduction of the distribution function of REs over velocities and coordinates (relative to the atomic core) and of the collision integral for REs and buffer atoms. Using these functions, we solve the corresponding kinetic equations for the RE "gas."

By using the kinetic Boltzmann equation, we found the distribution function of REs both in the absence of the directional RA flux and in its presence. The directional RA flux distorts the spatial distribution of REs relative to the ion core and the velocity distribution of

REs. We found out that in this case a permanent dipole moment of the RA appears, which is manifested either as polarization of the gas or in the latent form (for RA subensembles with the specified velocity of the directional movement), or in the explicit macroscopic form (upon velocity-selective excitation of Rydberg states). We obtained the relation between the average potential energy and the average kinetic energy of REs as an analog of the known virial theorem. We also calculated the contribution of REs to the transport frequency of collisions of RAs with buffer atoms.

2. CLASSICAL REGION FOR RYDBERG ELECTRONS AND THE *l* MIXING

It is well known that the movement of a particle can be described quasi-classically if its de Broglie wavelength is much shorter than the characteristic spatial scale of the problem. For the $|n, l\rangle$ state with the principal quantum number n and the orbital quantum number l, the corresponding condition of the classical behavior in a Coulomb field is well known:

$$n \gg l, \quad l \gg 1. \tag{1}$$

"An accidental" degeneracy in the Coulomb field results in the independence of the $|n, l\rangle$ state energy of the quantum number l, and the degeneracy order of the $|n, l\rangle$ state equals n^2.

A sufficiently high excited state of the RE ($n \gtrsim 10$) tends naturally to the classical limit (1). In the simplest model, we can neglect the difference between the ion-core potential in which the RE moves and the Coulomb potential. In this case, the RE state proves to be degenerate in l. Collisions with buffer particles efficiently mix degenerate states with different l (the so-called l mixing [5, 6]). For this reason, the velocity distribution of REs tends to the isotropic distribution even at not very large quantum numbers n.

To take into account the difference between the ion-core and Coulomb potentials, the l-mixing process should be analyzed in more detail. The non-Coulomb interaction of the RE with the ion core results in the shift of the energy level E_{nl} of the $|n, l\rangle$ state and removes the "accidental" degeneracy according to the Rydberg formula

$$E_{nl} = -\frac{R_\infty}{2(n-\delta_l)^2}, \tag{2}$$

where R_∞ is the Rydberg constant and δ_l is the quantum defect depending on l. The quantum defect δ_l rapidly decreases with increasing l in the interval $l = 0, 1, \ldots, n-1$. For fixed l, the quantum defect increases with increasing atomic number of the RA (table). In the state with $l = 0$ (the s state), the RE has the maximum impact parameter relative to the nucleus (the so-called penetrating orbits), so that the wave functions of the RE and ion core strongly overlap. For this reason, the s state has a small quantum defect.

Limiting (for $n \gg 1$) values of the quantum defect δ_l [14] for the states of alkali-metal atoms

	$\|n, 0\rangle$	$\|n, 1\rangle$	$\|n, 2\rangle$	$\|n, 3\rangle$
Li	0.4	0.05	0.002	−0.00008
Na	1.35	0.85	0.015	0.0014
K	2.18	1.71	0.28	0.01
Rb	3.13	2.65	1.347	0.0163
Cs	4.05	3.6	2.47	0.0334

The energy interval in which the levels with specified values of n and different $l = 0, 1, \ldots, n-1$ for $n \gg 1$ are located is, according to expression (2),

$$\Delta E \approx \frac{R_\infty \delta_0}{n^3}. \tag{3}$$

This interval becomes small relative to the thermal energy of a buffer particle when $n^3 > R_\infty \delta_0 / k_B T \approx 10^3 \delta_0$, where k_B is the Boltzmann constant and T is the temperature (we used room temperature for the estimate). Based on this estimate and taking into account the data in the table, we can expect that efficient l mixing can occur even at $n > 10$–15. The estimate of the efficiency of l mixing using the Massey parameter yields approximately the same result.

Therefore, the motion of the RE can be treated as classical, with a rapid establishment of the isotropic velocity distribution compared to a slow (diffusion) process of the energy change.

3. KINETIC EQUATIONS FOR "GAS" OF RYDBERG ELECTRONS

The distribution function $f(\mathbf{r}, \mathbf{v})$ of REs in the potential $U_0(\mathbf{r})$ obeys the kinetic equation

$$\frac{\partial}{\partial t} f(\mathbf{r}, \mathbf{v}) + (\mathbf{v} \cdot \nabla) f(\mathbf{r}, \mathbf{v}) - \frac{1}{m_e}\left(\nabla U_0(\mathbf{r}) \cdot \frac{\partial}{\partial \mathbf{v}}\right) f(\mathbf{r}, \mathbf{v}) = S(\mathbf{r}, \mathbf{v}), \tag{4}$$

where m_e is the electron mass and $S(\mathbf{r}, \mathbf{v})$ is the integral of collisions between the RE and buffer-gas atoms. The function $f(\mathbf{r}, \mathbf{v})$ is naturally normalized as

$$\iint f(\mathbf{r}, \mathbf{v}) d\mathbf{r} d\mathbf{v} = 1$$

(one electron per Rydberg atom). In particular calculations of the distribution function for the RE, we will use the Coulomb potential

$$U_0(\mathbf{r}) \equiv -\frac{e^2}{r}$$

of the ion core, where e is the electron charge.

The collision integral $S(\mathbf{r}, \mathbf{v})$ has the following form:

$$S(\mathbf{r}, \mathbf{v}) = -\nu_e(\mathbf{v}) f(\mathbf{r}, \mathbf{v}) + \int A(\mathbf{v}|\mathbf{v}') f(\mathbf{r}, \mathbf{v}') d\mathbf{v}', \quad (5)$$

where the collision frequency $\nu_e(\mathbf{v})$ is related to the kernel $A(\mathbf{v}|\mathbf{v}')$ of the collision integral by the known expression

$$\nu_e(\mathbf{v}) = \int A(\mathbf{v}'|\mathbf{v}) d\mathbf{v}', \quad (6)$$

which follows from the condition of conservation of the number of particles in elastic collisions ($\int S(\mathbf{r}, \mathbf{v})\, d\mathbf{v} = 0$).

Equation (4) has the same form in any reference system. We will use two reference systems: the reference system coupled with the ion core of the RA (to describe the RE state in the RA) and the laboratory system in which buffer gas is immobile as a whole and has an equilibrium velocity distribution and in which the characteristics of the collision integrals are usually simulated and determined. In the first system, we will use the notation of Eq. (4) for coordinates and velocities of REs. We denote the RE velocity in the laboratory system as $\mathbf{w}$. The distribution function for REs in the laboratory system is $\tilde{f}(\tilde{\mathbf{r}}, \mathbf{w})$, where $\tilde{\mathbf{r}} = \mathbf{r_R} + \mathbf{r}$ and $\mathbf{r_R}$ is the radius vector of the ion core of the RA in the laboratory system. For the specified velocity $\mathbf{u}$ of RAs in the laboratory system and the spatially uniform distribution of their concentration, the functions $\tilde{f}$ and f are related by the expression

$$\tilde{f}(\mathbf{r_R} + \mathbf{r}, \mathbf{u} + \mathbf{v}) = f(\mathbf{r}, \mathbf{v}).$$

The function $f(\mathbf{r}, \mathbf{v})$ depends parametrically on $\mathbf{u}$.

We can obtain hydrodynamic equations from kinetic equation (4) taking into account expression (5). To do this, we introduce the corresponding hydrodynamic characteristics of the RE gas: the density $f(\mathbf{r})$ and flux $\mathbf{j}$, the pressure tensor $P_{\alpha\beta}(\alpha, \beta = x, y, z)$], and the internal frictional force $\mathbf{F}(\mathbf{r})$ for electrons

$$f(\mathbf{r}) = \int f(\mathbf{r}, \mathbf{v}) d\mathbf{v}, \quad \mathbf{j} = \int \mathbf{v} f(\mathbf{r}, \mathbf{v}) d\mathbf{v},$$
$$P_{\alpha\beta} = m_e \int v_\alpha v_\beta f(\mathbf{r}, \mathbf{v}) d\mathbf{v}, \quad \alpha, \beta = x, y, z, \quad (7)$$
$$\mathbf{F}(\mathbf{r}) = m_e \int \mathbf{v} S(\mathbf{r}, \mathbf{v}) d\mathbf{v}.$$

The continuity equation

$$\frac{\partial}{\partial t} f(\mathbf{r}) + \operatorname{div} \mathbf{j} = 0 \quad (8)$$

is obtained after integration of the kinetic equation (4) over velocities taking into account the conservation of the number of particles. By multiplying Eq. (4) by $\mathbf{v}$ and integrating the result, we obtain the equation of the hydrodynamic Euler equation type

$$m_e \frac{\partial}{\partial t} j_\alpha + \sum_\beta \frac{\partial}{\partial \beta} P_{\alpha\beta} = -f(\mathbf{r}) \frac{\partial}{\partial \alpha} U_0(\mathbf{r}) + F_\alpha(\mathbf{r}). \quad (9)$$

Consider the general case of the directional movement of the RA at the velocity $\mathbf{u}$. We will use the known expression (see, for example, [13]) for the frictional force in the rest system of buffer gas

$$\mathbf{F}(\mathbf{r}) = -m_e \int \mathbf{w} \nu_e^{\mathrm{tr}}(w) \tilde{f}(\mathbf{r}, \mathbf{w}) d\mathbf{w},$$
$$\nu_e^{\mathrm{tr}}(w) = \int \left(1 - \frac{\mathbf{w}\mathbf{w}'}{w^2}\right) \tilde{A}(\mathbf{w}', \mathbf{w}) d\mathbf{w}', \quad (10)$$

where $\nu_e^{\mathrm{tr}}(w)$ is the transport collision frequency for electrons and $\tilde{A}(\mathbf{w}', \mathbf{w})$ is the kernel of the collision integral for REs in the laboratory system. Taking into account the invariance of the force relative to inertial reference systems, we can readily express $\mathbf{F}(\mathbf{r})$ in terms of the distribution function of REs in the reference system coupled with the RA:

$$\mathbf{F}(\mathbf{r}) = -m_e \int (\mathbf{u} + \mathbf{v}) \nu_e^{\mathrm{tr}}(|\mathbf{u} + \mathbf{v}|) f(\mathbf{r}, \mathbf{v}) d\mathbf{v}. \quad (11)$$

Note that $u \sim \nabla_R \ll \nabla_e$, where ∇_R and ∇_e are the average (most probable) velocities of the RA in the gas mixture and of the RE, respectively. Therefore, we can set $\nu_e^{\mathrm{tr}}(|\mathbf{u} + \mathbf{v}|) \approx \nu_e^{\mathrm{tr}}(v)$ in integral (11) with good accuracy. Thus, we have

$$\mathbf{F}(\mathbf{r}) \approx -m_e \int (\mathbf{u} + \mathbf{v}) \nu_e^{\mathrm{tr}}(v) f(\mathbf{r}, \mathbf{v}) d\mathbf{v}. \quad (12)$$

The quantity $\nu_e^{\mathrm{tr}}(v)$ is a sufficiently smooth function of the velocity modulus. Therefore, upon excitation of the RE to the state with the energy E_n at the stage of the process when the diffusion of energy was not yet manifested, we can take out $\nu_e^{\mathrm{tr}}(v)$ from the integral sign in (12) with the value of v equal to $v_n(\mathbf{r})$, which is specified by the value E_n of the total energy of the RE and is determined by the law of conservation of energy for the specified point $\mathbf{r}$. As a result, we obtain

$$\mathbf{F}(\mathbf{r}) = -m_e \nu_e^{\mathrm{tr}}(v_n(\mathbf{r}))[\mathbf{j} + f(\mathbf{r})\mathbf{u}]. \quad (13)$$

We will solve hydrodynamic equations (8) and (9), taking into account (13), beginning from the simplest case of an immobile RA in the reference system coupled with the buffer gas ($\mathbf{u} = 0$). We assume that the directions of velocities of REs were efficiently mixed in collisions. From the point of view of Eqs. (8) and (9), this means the stationary conditions under which the

pressure tensor can be calculated using the approximation

$$f(\mathbf{r}, \mathbf{v}) = f(\mathbf{r})\frac{\delta(v^2 - v_n^2(r))}{2\pi v_n(r)} \quad (14)$$

for the distribution function.

In this case, the problem has an obvious spherical symmetry. The RE velocity $v_n(r)$ is related to the total energy E_n and the potential energy $U_0(r)$ by the expression

$$v_n^2(r) = \frac{2}{m_e}[E_n - U_0(r)]. \quad (15)$$

The frictional force for the RE gas in Eq. (9) vanishes due to symmetry. The distribution function (14) gives the following expression for the pressure tensor:

$$P_{\alpha\beta} = \frac{m_e}{3}v_n^2(r) f(\mathbf{r})\delta_{\alpha\beta}. \quad (16)$$

Under stationary conditions, Eq. (9) takes the form

$$\frac{m_e}{3}\nabla(f(\mathbf{r})v_n^2(r)) + f(\mathbf{r})\nabla U_0(\mathbf{r}) = 0. \quad (17)$$

It follows from relation (15) that $\nabla U_0(\mathbf{r}) = -m_e\nabla(v_n^2(r)/2)$. After substituting into (17), this leads to the equation

$$\nabla\left\{\frac{f(\mathbf{r})}{v_n(r)}\right\} = 0 \quad (18)$$

with the obvious spherically symmetric solution

$$f(\mathbf{r}) = Cv_n(r), \quad C = \left\{\int v_n(r)d\mathbf{r}\right\}^{-1}. \quad (19)$$

We determined the integration constant C from the normalization condition for the distribution function

$$\int f(\mathbf{r})d\mathbf{r} = 1,$$

the integration region being limited by the classical condition $|E_n| + U_0(r) < 0$.

Below, we will use the convenient atomic characteristics [14]: the Rydberg constant $R_\infty = m_e e^4/\hbar^2 = 27.21$ eV; the Bohr radius $a_0 = \hbar^2/m_e e^2 = 5.3 \times 10^{-9}$ cm; the atomic frequency unit $\nu_0 = m_e e^4/\hbar^3 = 4.13 \times 10^{16}$ s^{-1}; and the atomic velocity unit $v_0 = e^2/\hbar = 2.18 \times 10^8$ cm/s.

With the use of these characteristics, the density distribution of REs in the RA is described by the expression

$$f(\mathbf{r}) = \frac{4}{\pi^2 r_n^3}\sqrt{\frac{r_n}{r} - 1}, \quad 0 \le r \le r_n = 2n^2 a_0. \quad (20)$$

The radius r_n determines the classical region for REs with the specified total energy E_n. Note that upon normalization of r to r_n, the distribution function $f(\mathbf{r})$ for REs is universal.

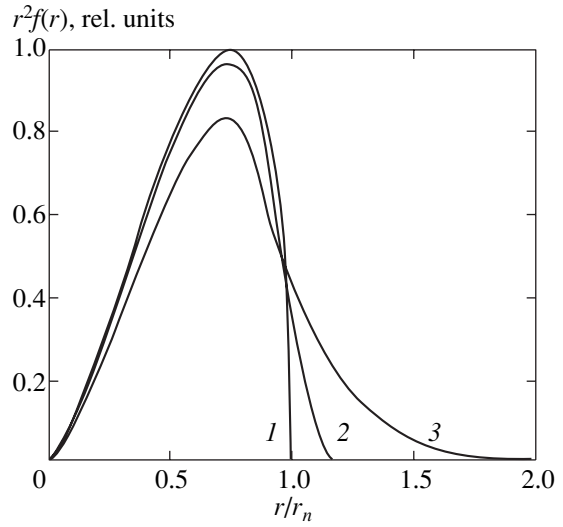

Fig. 1. Radial distribution of the probability of the RE location. Curve *1* corresponds to the immobile RA; curves *2* and *3* correspond to the moving RA for $\alpha = 0.5$ and 1, respectively.

The total distribution function for REs (14) can be represented in the form

$$f(\mathbf{r}, \mathbf{v}) = \frac{2}{\pi^3 r_n^3}\frac{\delta(v^2 - v_n^2(r))}{v_0/n},$$
$$v_n^2(r) = \frac{v_0^2}{n^2}\left[\frac{r_n}{r} - 1\right]. \quad (21)$$

Figure 1 (curve *1*) shows the radial distribution function $f(r) = 4\pi r^2 f(\mathbf{r})$ ($\int f(r)dr = 1$). One can see from this figure, in particular, that the RE is located far from the nucleus on average. The mean distance $\bar{r} = \int r f(r)dr$ proves to be equal to

$$\bar{r} = \frac{5}{8}r_n.$$

After integration of the total distribution function (21) over coordinates $\mathbf{r}$, we obtain the distribution of the RE velocities in RAs:

$$f(v) = \frac{32n^3}{\pi v_0^3}\frac{v^2}{(1 + v^2n^2/v_0^2)^4}, \quad \int_0^\infty f(v)dv = 1. \quad (22)$$

The scale of variation in the function $f(v)$ is specified by the quantity v_0/n, which is close to the mean velocity

$$\bar{v} = \int_0^\infty v f(v)dv = \frac{8}{3\pi}\frac{v_0}{n}.$$

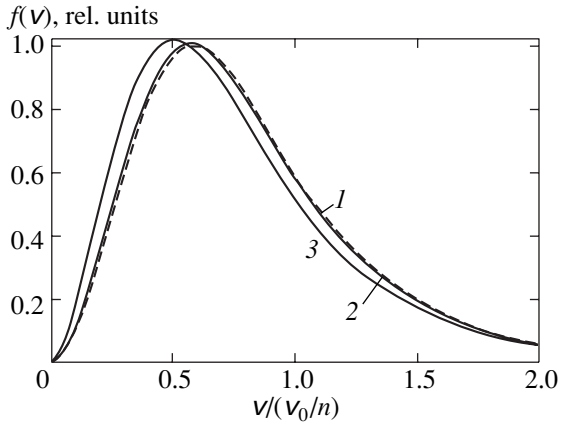

Fig. 2. The RE velocity distribution in the average-volume RA. Curve *1* corresponds to the immobile RA; curves *2* and *3* correspond to the moving RA for $\alpha = 0.5$ and 1, respectively.

This distribution function is shown in Fig. 2 (curve *1*). Note that for $v > v_0/n$, the value of $f(v)$ strongly decreases with increasing v (proportionally to $1/v^6$): the contributions from both small and large velocities to the velocity distribution of REs are small. Similar to $f(r)$, the distribution $f(v)$ for REs is universal (independent of E_n) when v is normalized to v_0/n.

In the classical case, the RE moves along a certain Kepler orbit around the ion core by retaining the magnitude and direction of the angular momentum. The RE trajectory changes in collisions with buffer atoms. Provided the total energy is conserved, this is equivalent to the mixing of states with different values of the angular momentum (l mixing). It is natural that the state of an individual RE can no longer be characterized by the conserved momentum. It is interesting to calculate the distribution of REs over the angular momentum after the l mixing. We decompose the velocity $\mathbf{v}$ in the distribution function (21) into the radial v_r and tangential v_τ components. Then, we consider the combination $f(\mathbf{r}, \mathbf{v})d\mathbf{r}d\mathbf{v}$ and integrate it over angles and the radial velocity (the value of the latter does not affect the value of the angular momentum). As a result, we obtain the combination $f(r, L)drdL$, where

$$f(r, L) = \frac{4}{\pi r_n L_n}\frac{(r/r_n)(L/L_n)}{\sqrt{-(r/r_n)^2 + (r/r_n) - (L/2L_n)^2}}, \quad (23)$$
$$L \equiv m_e v_\tau r, \quad L_n \equiv \hbar n.$$

Here, L is the value of the RE angular momentum, and L_n is the maximum value of L for the specified total energy. The function $f(r, L)$ is the distribution function of REs over the angular momentum and radius. Note that the RE angular momentum is small in the inner and outer regions of the RA, as follows from (23). The maximum value of L is achieved at the point $r = r_n/2$.

For the specified value of L, the function $f(r, L)$ coincides, with an accuracy to a normalization factor, with the square of the modulus of the radial part of a quasiclassical wave function (see, for example, [15]) averaged over spatial oscillations. This coincidence is quite obvious and confirms the validity of expression (23).

By integrating function (23) over r, we obtain the distribution function of REs over the angular momentum:

$$f(L) \equiv \int_0^\infty f(r, L)dr = 2\frac{L}{L_n^2}, \quad 0 \le L \le L_n, \quad (24)$$
$$\int_0^{L_n} f(L)dL = 1.$$

The distribution over L represents a linear function with a sharp cutoff at $L = L_n$. The mean value $\bar{L}$ of the RE angular momentum is

$$\bar{L} \equiv \int_0^{L_n} L\, f(L)dL = \frac{2}{3}\hbar n, \quad (25)$$

which is equal to 2/3 of the maximum value of L. The function $f(L)$ coincides, as it should, with the quantum-mechanical result. In the latter case, the result is obtained without any calculations—it is sufficient only to assume that the complete l mixing occurs and to take into account the statistical weight $(2l + 1)$ of the level with the quantum number l.

For a particle moving in a potential representing a homogeneous function of coordinates, the virial theorem is valid in both classical and quantum mechanics. In particular, the kinetic energy $\bar{T}$ averaged over the period of motion of the RE and the mean potential energy $\bar{U}$ in the Coulomb attraction potential $U_0(r) = -e^2/r$ are related by the known expression

$$\bar{U} = -2\bar{T}. \quad (26)$$

The distribution (21) allows us to calculate the mean values of the kinetic and potential energies of the RE,

$$\bar{T} \equiv \frac{m_e}{2}\int v^2 f(\mathbf{r}, \mathbf{v})d\mathbf{v}d\mathbf{r} = \frac{R_\infty}{2n^2},$$
$$\bar{U} \equiv -e^2\int\frac{1}{r} f(\mathbf{r}, \mathbf{v})d\mathbf{v}d\mathbf{r} = -\frac{R_\infty}{n^2}, \quad (27)$$

in complete agreement with the virial theorem (26) for the RE motion in the Coulomb potential.

Note in conclusion of this section that, after l-selective excitation of a Rydberg state (upon laser excitation from deep energy states, the initial value of l is small), the complete l mixing occurs for the time of the order of $(\nu_e^{tr})^{-1}$ if the RA size does not strongly exceed the

electron mean free path. This follows from both the general physical considerations and the Euler equation (9), taking into account relation (13) between the frictional force and the flux. This time is substantially shorter than the energy diffusion time for REs and the mean free time of the RA (the latter is characterized by its own transport collision frequency; see below). This justifies the separation of the intermediate stationary stage in the total relaxation process for the RE gas.

4. DIRECTIONALLY MOVING RYDBERG ATOMS

Consider a flux of Rydberg atoms moving at the velocity $\mathbf{u} \neq 0$ in buffer gas. Before solving stationary hydrodynamic equations (8) and (9), taking into account expression (13) for the frictional force, we present some important qualitative considerations. Let us discuss the part of the frictional force (13) that is caused by the directional movement of RAs:

$$\mathbf{F}_u(\mathbf{r}) = -\mathbf{u} m_e \nu_e^{\mathrm{tr}}(v_n(\mathbf{r}))\, f(\mathbf{r}). \quad (28)$$

This force causes the displacement of the electron cloud relative to the ion core ("blowing off" of electrons by the buffer gas). If the velocity $\mathbf{u}$ is not very high, the RA is conserved as a whole but the electron density is no longer spherically symmetric. Note that, for the transport collision frequency $\nu_e^{\mathrm{tr}}(v)$ dependent on the velocity, the frictional force $\mathbf{F}_u(\mathbf{r})/f(\mathbf{r})$ acting on a RE is not a potential force ($\mathrm{curl}[\mathbf{F}_u(\mathbf{r})/f(\mathbf{r})] \neq 0$). This means that the electron flux $\mathbf{j}$ that appeared at the initial instant of time under stationary conditions does not vanish even when the RA is conserved as a whole but has the spatial inhomogeneity corresponding to the circulation of the electron "gas" in the RA.

The problem is substantially simplified when the dependence of the transport collision frequencies on the velocity can be neglected ($\nu_e^{\mathrm{tr}}(v) \equiv \nu_e^{\mathrm{tr}}$). In this case, the force $\mathbf{F}_u(\mathbf{r})$ can be written in the potential form

$$\mathbf{F}_u(\mathbf{r}) = -m_e \nu_e^{\mathrm{tr}} f(\mathbf{r}) \nabla(\mathbf{u} \cdot \mathbf{r}). \quad (29)$$

This means that, in the reference system coupled with the RA, the additional potential energy

$$U_{\mathrm{fr}}(\mathbf{r}) = m_e \nu_e^{\mathrm{tr}} \mathbf{u} \cdot \mathbf{r}$$

is produced for the electron due to frictional forces. Therefore, the evolution of the RE "gas" occurs in the effective potential

$$U_{\mathrm{tot}}(\mathbf{r}) = U_0(r) + U_{\mathrm{fr}}(\mathbf{r}) = -\frac{e^2}{r} + m_e \nu_e^{\mathrm{tr}} \mathbf{u} \cdot \mathbf{r}. \quad (30)$$

Because this potential is no longer spherically symmetric, the established electron density also will not be spherically symmetric (blowing off by the buffer gas), and neither will the kinetic energy of REs, for which the relation

$$\frac{m_e v_n^2(\mathbf{r})}{2} = E_n - U_{\mathrm{tot}}(\mathbf{r}) = E_n + \frac{e^2}{r} - m_e \nu_e^{tr} \mathbf{u} \cdot \mathbf{r} \quad (31)$$

is now valid when the total energy is specified.

Under stationary conditions and neglecting the energy diffusion, the distribution function $f(\mathbf{r}, \mathbf{v})$ has the same form (14), taking into account that v_n is no longer a spherically symmetric function of coordinates but is determined by expression (31), i.e.,

$$v_n(\mathbf{r}) = \frac{v_0}{n} \sqrt{\frac{r_n}{r} - \frac{\alpha}{4}\frac{z}{r_n} - 1}, \quad \alpha = (2n)^4 \frac{\nu_e^{tr} u}{\nu_0 v_0}. \quad (32)$$

We directed the z axis of the cylindrical coordinate system along the vector $\mathbf{u}$.

Let us substitute expression (14) with $v_n(\mathbf{r})$ from (32) into expression (7) for the pressure tensor and into Eq. (9) under stationary conditions (taking into account that for the frictional force of the potential type (29) the flux $\mathbf{j}$ vanishes at each point). As a result, we obtain the differential equation for the spatial distribution of the electron density in the RA, which coincides with Eq. (17) after the replacement of $v_n(r)$ and $U_0(r)$ by $v_n(\mathbf{r})$ and $U_{\mathrm{tot}}(\mathbf{r})$, respectively. This equation can be transformed to Eq. (18) in the same way by retaining the above substitution. The solution to this equation (which now has only cylindrical symmetry) is

$$f(\mathbf{r}) = C' v_n(\mathbf{r}) = C' \frac{v_0}{n} \sqrt{\frac{r_n}{r} - \frac{\alpha}{4}\frac{r}{r_n}\cos\theta - 1}, \quad (33)$$

where θ is the rotation angle between the vectors $\mathbf{u}$ and $\mathbf{r}$, so that $r\cos\theta = z$. The integration constant C' is determined by the normalization condition

$$(C')^{-1} \equiv \int v_n(\mathbf{r}) d\mathbf{r} = 2\pi \frac{v_0}{n} r_n^3 \varphi_{02}(\alpha). \quad (34)$$

We introduced functions $\varphi_{km}(\alpha)$, which are useful for further analysis and are determined by the expression

$$\varphi_{km}(\alpha) = \int_{-1}^{1} t^k dt \times \int_0^1 dx\, x_0^{-m-1/2} x^{m-1/2} \sqrt{(1-x)(1+\eta x)}, \quad (35)$$

where

$$x_0 = \frac{1 + \sqrt{1+\alpha t}}{2}, \quad \eta = \frac{\alpha t}{(1+\sqrt{1+\alpha t})^2}.$$

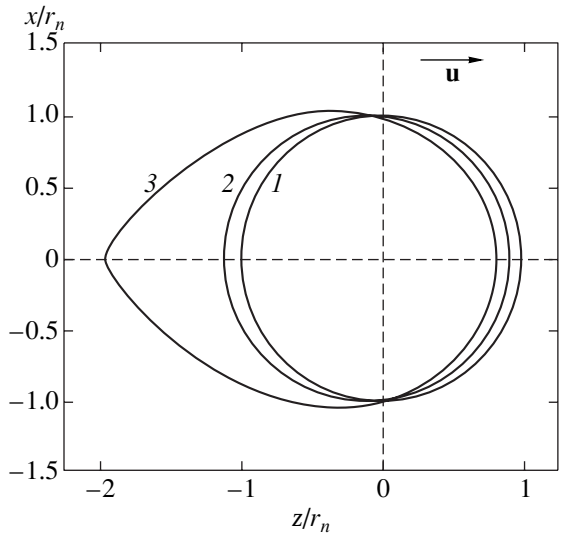

Fig. 3. Cross sections of classically accessible regions of the RE movement (37) by a plane passing through the *z* axis. Curve *1* corresponds to the immobile RA; curves *2* and *3* correspond to the RA moving along the *z* axis for $\alpha = 0.4$ and 1, respectively.

The integrals in (35) can be reduced to hypergeometric functions; however, the integral representation of the function $\varphi_{km}(\alpha)$ proved to be more convenient for numerical calculations. Taking into account the first terms of the expansion in α, we have

$$\varphi_{km}(\alpha) = \frac{2}{k+1}\frac{\Gamma(m+1/2)\Gamma(3/2)}{\Gamma(m+2)}\left[\left(\frac{1+(-1)^k}{2}\right)\right.$$
$$+\left(\frac{1-(-1)^k}{2}\right)\frac{k+1}{k+2}\frac{(m+1/2)(m+3/2)}{m+2}\frac{\alpha}{4}$$
$$+\frac{1}{2}\left(\frac{1+(-1)^k}{2}\right)\frac{k+1}{k+3} \qquad (36)$$
$$\left.\times\frac{(m+1/2)(m+3/2)(m+5/2)(m+7/2)}{(m+2)(m+3)}\left(\frac{\alpha}{4}\right)^2\right].$$

Here, $\Gamma(s)$ is the gamma function. By calculating C' and other characteristics, one should remember that the integration region is limited by the classical condition $E_n - U_{\text{tot}}(\mathbf{r}) \geq 0$. This region is not spherically symmetric and is determined by the inequality

$$\frac{r_n}{r} - \frac{\alpha}{4}\frac{r}{r_n}\cos\theta - 1 \geq 0,$$

namely,

$$0 \leq \frac{r}{r_n} \leq \frac{2}{1+\sqrt{1+\alpha\cos\theta}}, \quad 0 \leq \theta \leq \pi. \qquad (37)$$

This condition determines the boundaries of the RA. For $\theta = 0$, the boundary value of r is smaller than r_n, whereas for $\theta = \pi$, on the contrary, the boundary value of r is greater than r_n. If $\alpha > 1$, the radicand in (37) becomes negative for $\theta = \pi$. Physically, this means that the RA loses its integrity due to ionization (electron blowing off) caused by the frictional force produced by the buffer gas.

Figure 3 shows the boundaries of the RA in the *xz* plane according to expression (37) for several values of the parameter α. The case $\alpha = 0$ ($u = 0$) corresponds to the spherically symmetric solution (21). The case $\alpha = 0.4$ demonstrates a comparatively weak deformation of the region of motion of REs produced by the frictional force caused by the directional motion of RAs. The maximum distortion of the region of finite motion is achieved for $\alpha = 1$. In this case, the attraction force of the ion core is equal to the frictional force at the point $z = -2r_n$, which is the most remote from the nucleus (the so-called Lagrange point in classical mechanics).

Consider the characteristic values of the parameter α under real conditions. The transport cross section for the polarization interaction potential is described by the expression [16]

$$\sigma^{\text{tr}} = 2.21\pi\sqrt{\frac{\beta e^2}{\mu v_{\text{rel}}^2}}, \qquad (38)$$

where β is the polarizability of a neutral collision partner of a charged particle (with the charge e), μ is the reduced mass, and v_{rel} is the relative velocity. By using formula (38), we obtain for the transport collision frequency for REs

$$\nu_e^{\text{tr}} \equiv N_b\langle\sigma^{\text{tr}} v_{\text{rel}}\rangle$$
$$= 2.21\pi N_b\sqrt{\frac{\beta e^2}{m_e}} = 2.21\pi N_b v_0\sqrt{\beta a_0}. \qquad (39)$$

Here, N_b is the concentration of buffer particles, and a_0 and v_0 are the atomic units introduced above. Thus, we have

$$\alpha = (2n)^4 \times 2.21\pi\frac{N_b u\sqrt{\beta a_0}}{\nu_0}. \qquad (40)$$

We can assume for estimates that $\beta \sim a_0^3$. Then, for the buffer gas pressure equal to 1 Torr at room temperature, we obtain ($N_b \sim 3\times10^{16}$ cm^{-3}, $u \sim 10^5$cm/s)

$$\alpha \sim 2\times10^{-10}n^4.$$

Recall that the parameter α determines the degree of violation of the spherical symmetry in the region (37). This parameter is small in rather realistic situations. For example, for $n < 100$, we have $\alpha < 10^{-2}$. For this reason, the first terms of the expansion of physical characteristics in this parameter are important. On the other hand, because the value of α rapidly increases with increasing n, the value of α becomes comparable with or greater than unity already for $n > 300$. This means that in this case the RA is efficiently ionized due to the blowing off

of REs. The distance to the ionization limit for the immobile RA at $n = 300$ is about 10^{-4} eV, which is considerably lower than the mean thermal energy of gas particles. Therefore, it is most likely that the ionization of the RA will be mainly determined by other mechanisms rather than by the electron blowing off.

The function (33) characterizes the electron density of the RA. The function $f(r)$ normalized by the relation $\int f(r)\,dr = 1$ is also useful. This function gives the probability for an electron to be at the distance r from the nucleus and is described by the expressions

$$\begin{aligned} f(r) &= 2\pi\int_{-1}^{1} r^2 f(\mathbf{r})d\cos\theta, \\ 0 \le r &\le \frac{2r_n}{1+\sqrt{1+\alpha}}, \\ f(r) &= 2\pi\int_{-1}^{\cos\theta_0} r^2 f(\mathbf{r})d\cos\theta, \\ \frac{2r_n}{1+\sqrt{1+\alpha}} &\le r \le \frac{2r_n}{1+\sqrt{1-\alpha}}, \end{aligned} \tag{41}$$

where

$$\cos\theta_0 = \frac{4r_n}{\alpha r}\left(\frac{r_n}{r} - 1\right).$$

Curves *2* and *3* in Fig. 1 are plotted using these expressions for $\alpha = 0.5$ and 1, respectively. These curves demonstrate the influence of the blowing-off effect on the radial distribution of the probability of the electron location.

Due to the blowing-off effect, the effective potential energy U_{tot} [see (30)] for REs is no longer a uniform function of coordinates and, hence, the virial theorem is not valid. The mean potential energy $\bar{U}_{\text{tot}}$ calculated using the distribution function (33) has the form

$$\bar{U}_{\text{tot}} = -\frac{e^2}{r_n}\frac{\varphi_{01}(\alpha) - \alpha\varphi_{13}(\alpha)/4}{\varphi_{02}(\alpha)}. \tag{42}$$

The dependence of $\bar{U}_{\text{tot}}$ on α is presented in Fig. 4a. Within the entire interval of variation in α where the RA integrity is conserved, the value of $\bar{U}_{\text{tot}}$ varies weakly (by no more than 6%) compared to its change predicted by the virial theorem. Therefore, we can assume that the virial theorem remains valid with a sufficient accuracy. Note also that the expression

$$\bar{U}_{\text{tot}} = 2E_n\left(1 - \frac{21}{2^9}\alpha^2\right) \approx 2E_n(1 - 0.041\alpha^2)$$

based on the first terms of the expansion of $\varphi_{km}(\alpha)$ [see (36)] represents a good approximation of $\bar{U}_{\text{tot}}$.

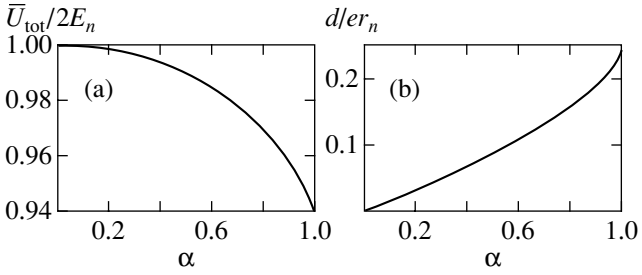

Fig. 4. Dependence of the mean potential energy (a) and the induced dipole moment (b) on the RA velocity (on the parameter α).

Taking the above consideration into account, the total distribution function $f(\mathbf{r}, \mathbf{v})$ is described by the expression

$$f(\mathbf{r}, \mathbf{v}) = \frac{C'}{2\pi}\delta(v^2 - v_n^2(\mathbf{r})), \tag{43}$$

where the velocity $v_n(\mathbf{r})$ is defined by expression (32).

After integration of expression (43) over coordinates, we obtain the velocity distribution of REs

$$\begin{aligned} f(v) &= 32\pi C' r_n^3 \frac{a-1}{\alpha} \\ &\times\left[\frac{1}{\left(\sqrt{a^2-\alpha}+a\right)^2} - \frac{1}{\left(\sqrt{a^2+\alpha}+a\right)^2}\right], \\ \int f(v)dv &= 1, \quad a \equiv 1 + \frac{v^2 n^2}{v_0^2}. \end{aligned} \tag{44}$$

Curves *2* and *3* in Fig. 2 represent the velocity distributions of REs for $\alpha = 0.5$ and 1, respectively. Note that the velocity distribution function is distorted negligibly over the entire interval of variation in α (when the RA integrity is conserved). This fact is rather unexpected because the size and shape of the RA itself strongly change due to the blowing-off effect for $\alpha \approx 1$.

5. COLLISION-INDUCED DIPOLE MOMENT OF THE RYDBERG ATOM

The asymmetry of the density distribution of REs along the direction of the vector $\mathbf{u}$ means that the RA has the nonzero electric dipole moment

$$\mathbf{d} = -e\int \mathbf{r} f(\mathbf{r})d\mathbf{r} \neq 0.$$

The integration with the distribution function (33), taking expression (34) into account, gives the result

$$\mathbf{d} = -\frac{\mathbf{u}}{u} e r_n \frac{\varphi_{13}(\alpha)}{\varphi_{02}(\alpha)}. \tag{45}$$

The dependence of d/er_n on α is shown in Fig. 4b. According to the result obtained, the dipole moment of

the RA reaches the value $d_{\max} \approx er_n/4$, which is a huge value at the atomic scale ($d_0 = ea_0$). In the linear approximation in α, which, as one can see from Fig. 4b, is valid over almost all values of α under study, we can obtain, using (36)

$$d = er_n\frac{21}{128}\alpha \approx er_n\frac{\alpha}{6} = d_0\frac{n^2}{3}\alpha, \qquad (46)$$

where d_0 is the natural atomic unit for measuring the dipole moment. According the above estimate of α, the induced dipole moment begins to exceed substantially the value of d_0 for $n = 100$.

The presence of unidirectional dipole moments for individual atoms means the existence of the macroscopic polarization of the medium. If the RA gas is in equilibrium with the buffer gas, it is clear that the macroscopic polarization of the medium is absent due to the symmetry. However, we point out that the so-called latent polarization takes place, namely, the polarization of a subensemble of RAs moving in the reference system coupled with the buffer gas. This polarization can be revealed in velocity-selective physical processes.

The macroscopic polarization of the RA gas can also be produced. In particular, a velocity-selective source of RAs can be created using laser excitation of atoms to Rydberg states. In this case, the selectivity over velocities is provided by the Doppler effect. Under appropriate conditions, only such RAs will be produced that have the projection of the velocity on the specified direction (the x axis) near some (resonance) value u_{x0}. In the approximation linear in α, the macroscopic polarization of the medium appears along the x axis:

$$P = er_n\alpha N_R \quad \left(\alpha = (2n)^4\frac{\nu_e^{\mathrm{tr}}u_{x0}}{\nu_0 v_0}\right). \qquad (47)$$

Here, N_R is the concentration of the RA flux. The polarization of the medium can be manifested as optical activity and other physical effects.

If Rydberg states are excited by pulsed laser radiation, then the creation (and subsequent relaxation) of polarization of the medium will result in the appearance of a bias current, which can be directly detected in experiments. Let us make some relevant estimates. The dipole moment of the RA is formed during the time of the order of $(\nu_e^{\mathrm{tr}})^{-1}$. For the buffer gas pressure of about 1 Torr and $\beta \sim a_0^3$, we have, according to (39),

$$(\nu_e^{\mathrm{tr}})^{-1} \sim 10^{-8}\ \mathrm{s}.$$

It follows from this estimate that the duration of pulses emitted by existing pulsed lasers is suitable for achieving the maximum effect. The relaxation time of the induced polarization coincides with the relaxation time of the directional motion of RAs and is determined by the value of $(\nu_R^{\mathrm{tr}})^{-1}$, where ν_R^{tr} is the transport collision frequency for RAs. We will show below that this value is smaller by a factor of $\sqrt{M_R/m_e}$ than ν_e^{tr} (M_R is the RA mass). Therefore, the bias current is maximal at the stage of polarization formation, when it is determined by the relation

$$i \equiv \frac{dP}{dt} \sim P\nu_e^{\mathrm{tr}} = \frac{16}{3}(2.21\pi)^2 N_R e u_{x0} \times (N_b\sqrt{\beta a_0}a_0 n^3)^2 \approx N_R e u_{x0}(16 N_b n^3 a_0^3)^2. \qquad (48)$$

For the values of parameters used above and for $N_R \sim 10^{13}$ cm^{-3}, we have

$$i \sim 10^{-3}\ \mathrm{A/cm^2}.$$

This value can be measured experimentally. The value of i increases with increasing N_b and n; however, it is limited by the value

$$i = eN_R u_{x0} \qquad (49)$$

when the RA integrity is conserved. For $N_R \sim 10^{13}$ cm^{-3} and $u_{x0} \sim 10^5$ cm/s, we obtain $i \sim 0.16$ A/cm^2.

Note that the disturbance of the RA integrity caused by the blowing-off effect results not in the disappearance of the electric current but in some modification of the current, which is now not a bias current but a usual current caused by the motion of the ion core. The latter loses its directional velocity much slower than the ejected electron. This current can exist in a continuous regime as well, and its magnitude is described by expression (49), in which N_R is the concentration of directionally moving ion cores. The physical nature of the ion current is equivalent to that of a photoinduced current (see, for example, [17] and references therein). In this case, the velocity-selective ionization is caused by the electron blowing-off effect.

6. CONTRIBUTION OF RYDBERG ELECTRONS TO THE TRANSPORT COLLISION FREQUENCY OF RYDBERG ATOMS

Deceleration of the RE "gas" in directionally moving RAs results in deceleration of RAs themselves due to the Coulomb force caused by the electron blowing off, which acts on the ion core. On the other hand, deceleration of RAs in the buffer gas is characterized by an important kinetic characteristic, the transport collision frequency. Consider the contribution of REs to this characteristic.

The total frictional force acting on the RA from the buffer gas is $\mathbf{F}_R = \mathbf{F}_I + \mathbf{F}_e$, where $\mathbf{F}_I$ is the frictional force caused by collisions of the ion core with buffer particles and $\mathbf{F}_e$ is the additional force caused by the friction of

the electron gas, which, according to (13), is described by the expression

$$\mathbf{F}_e = \int \mathbf{F}(\mathbf{r})d\mathbf{r} = -m_e\mathbf{u}\nu_e^{\mathrm{tr}}(n, u),$$
$$\nu_e^{\mathrm{tr}}(n, u) = \int \nu_e^{\mathrm{tr}}(v(\mathbf{r}))\, f(\mathbf{r})d\mathbf{r}. \quad (50)$$

Here, we took into account that the concentration of the electron "gas" in the RA has already become stationary in accordance with the velocity $\mathbf{u}$ of its directional movement, so that the integral electron flux relative to the RA vanishes. The frictional force $\mathbf{F}_R$ can be written in the form

$$\mathbf{F}_R = -(\nu_I + \nu_R^e)M_R\mathbf{u}, \quad \nu_R^e = \frac{m_e}{M_R}\nu_e^{\mathrm{tr}}(n, u), \quad (51)$$

where ν_I is the transport collision frequency for the ion core and ν_R^e is the addition to the transport frequency of the RA caused by the RE. This addition contains the factor $m_e/M_R \ll 1$, which reduces its contribution. If we assume that the interaction of the RE and ion core with a buffer particle is described by the polarization mechanism, then the relation between the contributions from the ion and electron components to the transport frequency of the RA will be determined only by the mass ratio:

$$\frac{\nu_I}{\nu_R^e} = \sqrt{\frac{M_R(M_R + M_b)}{m_e M_b}}. \quad (52)$$

Here, M_b is the mass of the buffer-gas particle. One can see from this expression that, when M_R, $M_b \geq 10$ amu, the contribution of the electron component to the transport collision frequency of the RA does not exceed one percent and can be neglected in many cases. The exclusion is the problems related to the photoinduced drift of RAs excited by radiation in resonance with transitions between Rydberg states of the atoms. Because the photoinduced drift can be detected even when the transport characteristics of the combining states differ only slightly, the corrections caused by the contribution from REs can be measured. In this case, the results obtained in this paper can be important.

Thus, the transport characteristics of RAs, which determine transfer processes, are almost completely related to the ion core, which is quite obvious without any calculations. Therefore, a change in the transport frequency of collisions between atoms upon excitation of an electron to the Rydberg state is caused by a change in the interaction with a collision partner: instead of collisions between two neutral particles, we deal with collisions between a charged ion core and a neutral buffer particle. It is obvious that the transport collision cross section σ^{tr} is higher in the latter case. Assuming that $\sigma_a^{\mathrm{tr}} \approx 4\pi a_0^2$ for an unexcited atom and using expression (38) for the transport cross section σ_I^{tr} for the ion core, we obtain

$$\frac{\sigma_I^{\mathrm{tr}}}{\sigma_a^{\mathrm{tr}}} \approx 0.5\frac{v_0}{u}\sqrt{\frac{m_e\beta}{\mu a_0^3}}, \quad \mu = \frac{M_R M_b}{M_R + M_b}. \quad (53)$$

For $\beta \sim a_0^3$ and $u \sim 10^5$ cm/s, we have $\sigma_I^{\mathrm{tr}}/\sigma_a^{\mathrm{tr}} \sim 10$; i.e., upon excitation of an atom from the ground state to the Rydberg states, its transport cross section for collisions with neutral particles increases approximately by an order of magnitude.

7. CONCLUSIONS

We have considered the internal characteristics and the kinetics of RAs in a buffer gas using the kinetic Boltzmann equation directly for electrons in the Coulomb field of the atomic core. Such a description of the behavior of bound electrons was earlier demonstrated by Pitaevsky [12], who studied recombination processes in a plasma. The results obtained in our paper have shown that this approach is also efficient for studying the properties of individual RAs, which are energy-selectively excited from the deep states, and of the RA gas mixed with the buffer gas.

The kinetics of the RE "gas" exhibits two distinct stages after excitation. At the first stage, the relaxation of the momentum (and of the angular momentum) of the RE occurs; and at the second stage, a slow energy diffusion takes place. In this paper, we considered only the first stage and obtained a number of interesting results, in our opinion, at this stage. We found the stationary distribution function of REs over velocities and intra-atomic coordinates for both the immobile RA and the RA moving in the buffer gas, the distribution of the electron density over the intra-atomic coordinates, and the mean velocity distribution. We demonstrated the practical applicability of the virial theorem and found and described the effect of electron blowing off during the RA movement. This effect results in the latent polarization of the RA gas. Upon velocity-selective excitation (for example, by a laser), macroscopic polarization appears, which is manifested as the bias-current pulse. When the RA integrity is lost due to the blowing-off effect, the bias current transforms to a usual electric current, which can exist in the stationary regime.

The latent and macroscopic polarizations, as well as the bias current, represent the macroscopic kinetic properties of the RA gas. Thus, the approach used in this paper allowed us to study not only internal characteristics of individual RAs but also the properties of the RA gas. Another example of this kind is the problem of the transport collision frequency for the RA, which determines transfer processes in the RA gas. We found the RE contribution to the transport collision frequency for the RA.

The next stage of the RE gas kinetics (energy diffusion) will result in the deformation of the distribution function of REs. At this stage, some new processes (ionization, recombination, escape to deeper energy levels, etc.) should be taken into account. However, some results of the above analysis will not change significantly. In particular, this concerns the latent and macroscopic polarizations, as well as the RA transport collision frequency.

ACKNOWLEDGMENTS

This work was supported by the Russian Foundation for Basic Research (project no. 01-02-17433) and by the "Physics of Quantum and Wave Processes" program of the Ministry of Industry and Science.

REFERENCES

1. *Rydberg States of Atoms and Molecules*, Ed. by R. F. Stebbings and F. B. Dunning (Cambridge Univ. Press, Cambridge, 1983; Mir, Moscow, 1985).
2. W. Demtröder, *Laser Spectroscopy. Basic Concepts and Instrumentation* (Springer-Verlag, Berlin, New York, 1996).
3. T. F. Gallagher, *Rydberg Atoms* (Cambridge Univ. Press, New York, 1994).
4. T. F. Gallagher, Rep. Prog. Phys. **51**, 143 (1988).
5. A. P. Hickman, R. E. Olson, and J. Pascale, in *Rydberg States of Atoms and Molecules*, Ed. by R. F. Stebbings and F. B. Dunning (Cambridge Univ. Press, Cambridge, 1983; Mir, Moscow, 1985), p. 187.
6. M. Matsuzawa, in *Rydberg States of Atoms and Molecules*, Ed. by R. F. Stebbings and F. B. Dunning (Cambridge Univ. Press, Cambridge, 1983; Mir, Moscow, 1985), p. 267.
7. I. M. Beterov and P. B. Lerner, Usp. Fiz. Nauk **159**, 665 (1989) [Sov. Phys. Usp. **32**, 1084 (1989)].
8. I. M. Beterov and I. I. Ryabtsev, Proc. SPIE **3485**, 275 (1998).
9. J. H. Hoogenraad and L. D. Noordam, Phys. Rev. A **57**, 4533 (1998).
10. I. Sh. Averbukh and N. F. Perel'man, Usp. Fiz. Nauk **161** (7), 41 (1991) [Sov. Phys. Usp. **34**, 572 (1991)].
11. E. Fermi, Nuovo Cimento **11**, 157 (1934).
12. L. P. Pitaevskiĭ, Zh. Éksp. Teor. Fiz. **42**, 1326 (1962) [Sov. Phys. JETP **15**, 919 (1962)].
13. S. G. Rautian and A. M. Shalagin, *Kinetic Problems of Nonlinear Spectroscopy* (North-Holland, Amsterdam, 1991).
14. A. A. Radtsig and B. M. Smirnov, *Reference Data on Atoms, Molecules, and Ions* (Énergoatomizdat, Moscow, 1986; Springer-Verlag, Berlin, 1985).
15. L. D. Landau and E. M. Lifshitz, *Course of Theoretical Physics*, Vol. 3: *Quantum Mechanics: Non-Relativistic Theory* (Nauka, Moscow, 1989, 4th ed.; Pergamon, New York, 1977, 3rd ed.).
16. B. M. Smirnov, *Physics of Weakly Ionized Gases* (Nauka, Moscow, 1972; Mir, Moscow, 1981).
17. S. N. Atutov, K. A. Nasyrov, S. P. Pod'yachev, *et al.*, Phys. Rev. A **54**, 4279 (1996).

Translated by M. Sapozhnikov

Journal of Experimental and Theoretical Physics, Vol. 94, No. 3, 2002, pp. 509–515.
Translated from Zhurnal Éksperimental'noĭ i Teoreticheskoĭ Fiziki, Vol. 121, No. 3, 2002, pp. 596–602.

NUCLEI, PARTICLES, AND THEIR INTERACTION

Ising Exchange Interaction of Two-level Optical Systems

A. R. Kessel* and I. S. Donskaya

Zavoĭskiĭ Physicotechnical Institute, Kazan Scientific Center, Russian Academy of Sciences, Sibirskiĭ trakt 10/7, Kazan 29, 420029 Tatarstan, Russia

**e-mail: kessel@dionis.kfti.knc.ru*

Received July 10, 2001

Abstract—It is shown that the indirect coupling between two-level optical systems through a radiation field has the form of the Ising exchange interaction if the coupling between atoms and the field is conducted through electric quadrupole interactions. The manifestation of the paired interaction between two-level systems in the form of a nonuniform optical transition width and in the kinetics of nonequilibrium optical processes is considered. © *2002 MAIK "Nauka/Interperiodica".*

1. INTRODUCTION

A situation when optical transitions are excited between a certain pair of energy levels of an atom (usually, between the ground level E_g and one of the excited levels E_e), while the remaining energy levels do not participate in physical processes, is often encountered in optics. Such situations can be described conveniently using the concepts of a two-level system and a pseudospin. In this case, the pair of energy levels of an individual atom under investigation is defined as eigenvalues and eigenstates of a certain Hamiltonian

$$H_S^j = \hbar\omega_0^j \hat{S}_j^z, \quad \hbar\omega_0^j = E_e^j - E_g^j, \tag{1}$$

having the form of the Zeeman energy operator for a particle with the effective pseudospin $S_j = 1/2$ [1].

It follows from parity considerations (the states ψ_g and ψ_e under investigation usually possess different parities) that the projection of the electric dipole moment operator $\mathbf{d}_j = e\mathbf{r}_j$ of the atom on the states of a two-level system may contain only nondiagonal matrix elements. For an atom in an axisymmetric electric crystal field of the lattice, we can assume that $\mathbf{d}_j = \mathbf{d}S_j^x$. In such a case, the two-particle dipole–dipole interaction between atoms contains only the products of nondiagonal terms of the type $\hat{S}_j^x\hat{S}_k^x$ [2].

Dipole–dipole effects are reflected in the generalized Maxwell–Bloch equations. The required changes in the equations are made phenomenologically through the replacement of external (relative to atoms) electric fields by the local fields created by neighboring atoms of the two-level system [3, 4]. In particular, a number of nonlinear optical effects which can be attributed to the dipole–dipole interactions between optical atoms are listed in [4].

It will be shown below, however, that in addition to what has been said above, the Ising-type exchange interaction between pseudospins $\hat{S}_j^z\hat{S}_k^z$ also exists. It will be derived as an indirect interaction between the diagonal energy components of pseudospins through the electromagnetic field of vacuum. These results were reported preliminarily in [5].

2. METHOD OF DERIVATION OF THE PAIR INTERACTION OPERATOR

The structure of the Hamiltonian of two subsystems in the problem of indirect interaction can be presented in the general form as

$$H = H_0 + V_{Sf}, \quad H_0 = H_S + H_f, \tag{2}$$

where H_S is the Hamiltonian of the dynamic subsystem consisting of noninteracting particles, H_f is the Hamiltonian of the interaction-carrier field, and V_{Sf} is the operator of interaction between particles of the two subsystems.

The method of calculation of indirect interactions [6, 7] includes two stages and is constructed on the assumption that the following inequality holds for the matrix elements of the operators:

$$|V_{Sf}| \ll |H_0|.$$

The first stage is the transition to a new representation using the unitary transformation $U = \exp\{-L\}$, where L is an anti-Hermitian operator satisfying the condition

$$V_{Sf} + [H_0, L] = 0. \tag{3}$$

In this new representation, Hamiltonian H assumes the form

$$H \longrightarrow \tilde{H} = H_S + H_f + \frac{1}{2}[V_{Sf}, L] + O(V_{Sf}^3); \tag{4}$$

i.e., it does not contain terms linear in V_{Sf}. The solution of the operator equation (3) has the form

$$L = \frac{1}{i\hbar}\lim_{\varepsilon \to 0}\int_{-\infty}^{0} e^{\varepsilon t} V_{Sf}(t)\,dt,$$
$$V_{Sf}(t) = \exp\frac{i(H_S + H_f)t}{\hbar} V_{Sf} \exp\frac{-i(H_S + H_f)t}{\hbar}. \quad (5)$$

Thus, the generator of the unitary linear transformation L *i*s on the order of magnitude

$$L \sim \frac{|V_{Sf}|}{|H_0|}.$$

The second stage involves the averaging of expression (4) for $\tilde{H}$ over the states of the interaction-carrier field so that the second-order term

$$W_{SS} = \frac{1}{2}\langle [V_{Sf}, L]\rangle \quad (6)$$

of perturbation theory in expansion (4) becomes independent of the variables of the carrier of interaction, but preserves the dependence on the dynamic variables for different particles and, hence, acquires the meaning of the operator of their indirect interaction. In most cases, there is no need to carry out this averaging since the second-order terms in expansion (4) do not contain field operators.

3. HAMILTONIAN OF THE PROBLEM UNDER CONSIDERATION

In order to simplify the notation, we assume that the energy levels of a two-level system are determined by the atomic shell containing one electron; e, m, and $\mathbf{p}$ are the electron charge, mass, and momentum. The Hamiltonian of the jth atom in the radiation field has the form [8]

$$H^j = H_0^j + H_1^j + H_2^j, \quad (7)$$

where

$$H_0^j = H_{e0}^j + H_{ph}^0, \quad H_{e0}^0 = \frac{\mathbf{p}_j^2}{2m} + eV(\mathbf{R}_j), \quad (8)$$

$$H_1^j = -\mathbf{d}_j \mathbf{E}(\mathbf{R}_j, t), \quad H_2^j = Q_j \nabla_R \mathbf{E}(\mathbf{R}_j). \quad (9)$$

Here, we have used the multiplet expansion, where H_1 and H_2 correspond to the electric dipole and quadrupole interaction, respectively; H_{e0}^j is the principal Hamiltonian of the jth atom (henceforth, we will use only the "projection" of this Hamiltonian on the states of the two-level system in form (1)); $\mathbf{d}_j = e\mathbf{r}_j$ and $Q_j = e\mathbf{r}_j \cdot \mathbf{r}_j/2$ are the operators of the dipole and quadrupole moments of the jth atom; and $\mathbf{R}_j$ and $\mathbf{r}_j$ are the radius vectors of the nucleus and of the electron in the jth atom, respectively. Using the definition of the electromagnetic field strength,

$$\mathbf{E}(\mathbf{R}, t) = -\frac{1}{c}\frac{\partial \mathbf{A}(\mathbf{R}, t)}{\partial t},$$

we can present H_2^j in the form

$$H_2^j = -\frac{e}{2c}\sum_{\alpha,\beta} \mathbf{r}_\alpha^j \mathbf{r}_\beta^j \frac{\partial^2 A_\alpha(\mathbf{R}_j, t)}{\partial R_\beta \partial t}. \quad (10)$$

Formula (9) for H_1 was derived in the dipole approximation. An analysis of Hamiltonian H_1 using the method described in the previous section leads to the well-known expression for the dipole–dipole coupling operator containing pair operators of the form $S_i^x S_j^x$ and $S_i^y S_j^y$ [2].

In many cases, operator H_2 could be neglected. It will be proved below that the contribution from this interaction to the paired coupling of two-level systems is significant and may affect the observed physical properties.

Substituting the expression for the vector potential in the interaction representation, i.e.,

$$\mathbf{A}(\mathbf{R}, t) = \sqrt{\frac{2\pi\hbar c^2}{V}} \times \sum_{\mathbf{k},\mu} \frac{\mathbf{e}_{\mathbf{k}\mu}}{\sqrt{\omega_k}} \{a_{\mathbf{k}\mu}(t) e^{i\mathbf{k}\cdot\mathbf{R}} + a_{\mathbf{k}\mu}^+(t) e^{-i\mathbf{k}\cdot\mathbf{R}}\},$$

into the expression for H_2^j, we obtain

$$H_2^j = -\frac{e}{2}\sqrt{\frac{2\pi\hbar}{V}}\sum_{\mathbf{k},\mu} \omega_k^{1/2} \{a_{\mathbf{k}\mu}(t) - a_{-\mathbf{k}\mu}^+(t)\} \times \sum_{\alpha,\beta} (\mathbf{r}_\alpha^i \mathbf{e}_{\mathbf{k}\mu}^\alpha)(\mathbf{r}_\beta^j \mathbf{k}_\beta) e^{i\mathbf{k}\cdot\mathbf{R}_j}. \quad (11)$$

Here, $a_{\mathbf{k}\mu}^+$ and $a_{\mathbf{k}\mu}$ are the creation and annihilation operators for a photon of polarization μ ($\mu = 1, 2$) with the energy $\hbar\omega_k$ and the wave vector $\mathbf{k}$; $\mathbf{e}_{\mathbf{k}\mu}^\alpha$ is the αth component of the polarization vector; and V is the quantization volume of the radiation field.

Since the eigenstates ψ_g and ψ_e possess different parities (see above), the operators which are even relative to spatial inversion contain only diagonal matrix elements, which enables us to present the product $\mathbf{r}_\alpha^j \mathbf{r}_\beta^j$ for an two-level optical system in the form of the matrix (see the Appendix)

$$\|\mathbf{r}_\alpha^j \mathbf{r}_\beta^j\| = (\rho_\alpha^j \hat{S}_z^j + \rho^{j'} \hat{E})\delta_{\alpha\beta},$$

$$\hat{S}_z = \frac{1}{2}\begin{vmatrix} 1 & 0 \\ 0 & -1 \end{vmatrix}, \quad \hat{E} = \begin{vmatrix} 1 & 0 \\ 0 & 1 \end{vmatrix}, \tag{12}$$

$$\rho_\alpha^j = \langle \psi_e | (\mathbf{r}_\alpha^j)^2 \psi_e \rangle - \langle \psi_g | (\mathbf{r}_\alpha^j)^2 \psi_g \rangle.$$

The term proportional to the operator unity $\hat{E}$ does not generate the observed effects and, hence, will not be considered here. Since the choice of the principal Hamiltonian to be proportional to the z component of pseudospin breaks the spherical symmetry, we must assume that, generally, $\rho_x = \rho_y \neq \rho_z$. Such a symmetry breaking emerges as a result of the interaction between an atom and the electric field of the crystal lattice. The z axis of the reference frame is determined by this choice and cannot be oriented arbitrarily.

Let us now consider a system of two-level atoms. Substituting the first relation from formula (12) into expression (11) and carrying out summation over all atoms of the sample, we can present the Hamiltonian of two-level systems interacting with the field in the form

$$H_2 = -e\sqrt{\frac{\pi\hbar}{2V}}\sum_j S_j^z \sum_{\mathbf{k},\mu} G_{\mathbf{k}\mu}(\mathbf{R}_j) D_{\mathbf{k}\mu}(t),$$

$$D_{\mathbf{k}\mu}(t) = (a_{\mathbf{k}\mu}(t) - a^+_{-\mathbf{k}\mu}(t)), \tag{13}$$

$$G_{\mathbf{k}\mu}(\mathbf{R}_j) = \sqrt{\omega_k}\sum_\alpha (k_\alpha \mathbf{e}^\alpha_{\mathbf{k}\mu})\boldsymbol{\rho}_\alpha e^{i\mathbf{k}\cdot\mathbf{R}_j}.$$

The operator of the electromagnetic field energy in the secondary quantization representation is known to be

$$H_f = \hbar\sum_{\mathbf{k},\mu}\omega_k\left(a^+_{\mathbf{k}\mu}a_{\mathbf{k}\mu} + \frac{1}{2}\right). \tag{14}$$

Finally, operator H_{0e}^j may have a large set of eigenstates ψ_α^j from which we choose a pair ψ_g^j and ψ_e^j as a two-level optical system, which is characterized by Hamiltonian (1) in the pseudospin representation.

4. PAIRED INTERACTION OF TWO-LEVEL OPTICAL SYSTEMS

Using the formulas from Section 2, we will calculate the paired interaction operator for the physical system described in Section 3. The role of the Hamiltonians H_S, H_F, and V_{Sf} in the problem under investigation is played by operators (1), (14), and (13). In this case, the generator of the transformation has the form

$$L = e\sqrt{\frac{\pi}{2V\hbar}}\sum_j S_j^z \sum_{\mathbf{k},\mu} G_{\mathbf{k}\mu}(\mathbf{R}_j) I_{\mathbf{k}\mu},$$
$$I_{\mathbf{k}\mu} = -\lim_{\varepsilon\to 0}\left\{\frac{a_{\mathbf{k}\mu}}{\omega_k + i\varepsilon} + \frac{a^+_{-\mathbf{k}\mu}}{\omega_k - i\varepsilon}\right\}. \tag{15}$$

Substituting this expression into Eq. (6), we obtain the following expression for the operator of interaction between two-level systems:

$$W_{SS} = \hbar\sum_{ij} U_2(\mathbf{R}_{ij}) S_i^z S_j^z, \tag{16}$$

$$U_2(\mathbf{R}_{ij}) = -\frac{e^2}{2\hbar}\frac{\pi}{V}$$
$$\times \sum_{k,\mu}\left[\sum_\alpha (k_\alpha e^2_{\mathbf{k}\mu})\rho_\alpha\right]^2 e^{i\mathbf{k}\cdot(\mathbf{R}_i - \mathbf{R}_j)}, \tag{17}$$

where $\mathbf{R}_{ij} = (\mathbf{R}_i - \mathbf{R}_j) \equiv \mathbf{R}$. Thus, the mechanism considered by us here has led to the exchange interaction between two-level systems of the Ising type. To our knowledge, this type of interaction has not been considered before as applied to two-level optical systems.

Let us simplify the expression for the interaction potential $U_2(\mathbf{R})$. We first find the sum over polarizations,

$$\sum_\mu\left[\sum_\alpha (k_\alpha e^\alpha_{\mathbf{k}\mu})\rho_\alpha\right]^2 = |k|^2(\rho_z - \rho_x)^2\cos^2\theta_k\sin^2\theta_k, \tag{18}$$

where θ_k and φ_k are the polar and azimuthal angles of vector $\mathbf{k}$ in the chosen system of coordinates.

Passing from summation over the wave vector to integration according to the formulas

$$\sum_{\mathbf{k}} \longrightarrow \frac{V}{(2\pi)^3}\int_0^\infty k^2 dk \int_0^\pi \sin\theta_k d\theta \int_0^{2\pi} d\varphi_k$$

and using the representation of the exponential with the scalar product in the exponent in the form of an expansion in spherical Bessel functions $j_l(kR)$,

$$e^{i(\mathbf{k}\cdot\mathbf{R})} = 4\pi\sum_{l,m} i^l j_l(kR) Y_{lm}(\theta_R, \varphi_R) Y_{lm}(\theta_k, \varphi_k),$$

we calculate the integrals with respect to angular variables of vector $\mathbf{k}$. Then, we expand all functions of the angular variables θ_k and φ_k into series in the spherical harmonics $Y_{lm}(\theta_k, \varphi_k)$ and calculate the corresponding integrals using the orthogonality properties of spherical

functions. After these calculations, we can pass to the following expression for the interaction potential:

$$U_2(R) = \frac{e^2(\rho_z - \rho_x)^2}{2\pi\hbar}$$

$$\times \int_0^{k_{\max}} k^4 \left\{ \frac{1}{15} j_0(kR) P_0(\cos\theta_R) - \frac{1}{21} j_2(kR) P_2(\cos\theta_R) \right. \tag{19}$$

$$\left. - \frac{4}{35} j_4(kR) P_4(\cos\theta_R) \right\} dk.$$

Here, $P(\cos\theta_R)$ are the Legendre polynomials, and θ_R is the polar angle between the crystal axis z and vector $\mathbf{R}$.

Unfortunately, the upper integration limit $k_{\max}$ cannot go to infinity since, for wavelengths smaller than the atomic size, the atom cannot be regarded as a point particle, and the form of interaction V_{Sf} chosen above can hardly be valid. In our case, it is expedient to carry out integration to $k_{\max} = 2\pi/r_a$, where r_a is the atomic radius.

Finally, the condition $k_{\max} r > 1$ holds, which means that the atomic spacing in the crystal is larger than the linear size of an atom. This allows us to use the approximation

$$j_l(z) = \frac{1}{z} \cos\left(z - \frac{\pi}{2}(l+1) \right),$$

which is applicable for large values of the argument.

Under these conditions, we have

$$J_0 = \int_0^{\infty} j_0(kR) k^4 dk \approx -\frac{a^3}{R^5} \cos a, \quad a = \frac{2\pi R}{r_a} \gg 1.$$

As a result of this simplification, we obtain

$$U_2(R) = \hbar^{-1} \left[\frac{2\pi e(\rho_z - \rho_x)}{R} \right]^2 \times \frac{\cos(2\pi R/r_a)}{2r_a^3} \cos^2\theta_R \sin^2\theta_R. \tag{20}$$

Thus, the oscillating potential (20) decreases as R_{ij}^{-2}. Such a decrease is associated with a decrease at point R_j in the number density of photons interacting with the two-level system at point R_i. A periodic dependence is inherent in many types of indirect interactions, the most familiar of which being the interaction of nuclear spins through conduction electrons in metals [7].

The paired interaction integral (16) together with expression (20) for potential is the final result of our analytic derivation of the operator of indirect interaction between two-level systems. This operator has the form of the Hamiltonian of the Ising exchange interaction with a potential depending on the distance and direction between the interacting two-level systems.

The paired interaction in form (16) can also be obtained if we characterize the contact between an atom and the field by choosing the term in the Pauli Hamiltonian, which is quadratic in the vector potential:

$$H_3 = \frac{e^2}{2mc^2} \mathbf{A}^2$$

(this term is usually employed for describing weak diamagnetism of atoms). After a certain unitary transformation, this operator acquires the form [9]

$$H_3 = -\frac{e^2}{2mc^2} \sum_{\alpha\beta\gamma} \mathbf{r}_\alpha^j \mathbf{r}_\beta^j \frac{\partial A_\alpha}{\partial \mathbf{r}_\gamma} \frac{\partial A_\beta}{\partial \mathbf{r}_\gamma}, \quad \alpha, \beta, \gamma = x, y, z,$$

which enables us to apply directly the algorithm of the derivation of operator W_{SS} from the previous section. This leads to an operator of the form (16), whose potential is given by

$$U_3(R) = \left(\frac{e^2}{2\pi m} \right)^2 J_{00} \left\{ \rho_x^2 (1 + \cos^4\theta_R) \right.$$

$$\left. + \rho_z^2 \sin^4\theta_R + \frac{1}{2} \rho_x \rho_z \sin^2(2\theta_R) \right\}, \tag{21}$$

$$J_{00} = 0.26 \frac{1}{c^3 R^3} \left(\frac{\pi}{r_a} \right)^4 \sin\left(a + 4\frac{\cos a}{a} \right).$$

In order to simplify this expression, we have used the same approximations as for calculating the potential $U_2(R)$ (20).

Finally, as was mentioned in the Introduction, the expression for H_1^j from (9) leads to an indirect interaction between transverse pseudospin components with the potential [10]

$$U_1(R) = \frac{d^2}{R^3} (3\cos^2\theta_R - 1), \quad \frac{\omega_0 R}{c} \longrightarrow 0,$$

where $d = |\mathbf{d}|$.

5. ESTIMATION OF THE EXCHANGE INTERACTION POTENTIAL OF TWO-LEVEL SYSTEMS

Let us estimate the potential of the Ising interaction (17). In order to obtain an order-of-magnitude estimate for the quantity ρ_α (12), we calculate the matrix element r_α^2 in the simplest particular case. For states ψ_g and ψ_e, we choose the states (1, 0, 0) and (2, 1, 1) of the hydrogen atom (triads of quantum numbers (n, l, m) are indicated in [1]). If we use the known functions of

state $\psi_{2,1,1}$ and $\psi_{1,0,0}$ for hydrogen, we obtain $\rho_x = \rho_y = 5r_B^2$ and $\rho_z = 11r_B^2$, where r_B is the Bohr radius. Having chosen the values $r_a \sim 10^{-8}$ cm and $R \sim 10^{-6}$ cm for other parameters, we obtain the following value of the Ising exchange interaction potential: $U_2(R) \approx 10^{12}$ rad/s.

In the same approximations and for the same values of parameters, the other potentials are found to be

$$U_1(R) \approx 10^8 \text{ rad/s}, \quad U_3(R) \approx 10^6 \text{ rad/s}.$$

Finally, the natural line width of spontaneous emission is defined by the formula [11]

$$\gamma = \frac{2d^2\omega_0^2}{3\hbar c^3};$$

for optical frequencies $\omega_0/2\pi \sim 3 \times 10^{14}$ Hz, the value of γ is approximately equal to 2×10^5 Hz. Thus, the indirect interaction potential (20) is much higher than potentials of another origin and exceeds the spontaneous emission line width.

The question arises: Why is potential U_2 higher than all the remaining potentials? This question can be formulated in a more stringent form: Why is the coupling U_2 between two-level systems through the second-order multipole moment stronger than the coupling U_1 through the first-order multipole moment? The reason lies in the features of interactions H_1 and H_2 and also in the nature of the quantum-mechanical perturbation theory. Operator W_{SS} from Eq. (16) is a second-order correction to the energy operator. In accordance with perturbation theory, such a correction must be on the order of $V_{Sf}^2(\Delta E \pm \hbar\omega_k)^{-1}$, where ΔE is the difference in the energy levels of a dynamic system, between which the matrix element of the perturbation operator V_{Sf} is calculated. In the case of the dipole coupling between an atom and the field, the operator $V_{Sf} = H_1$ contains only nondiagonal matrix elements in the pseudospin space and $\Delta E = \hbar\omega_0$, where ω_0 is the optical transition frequency. In the case of the coupling through interaction H_2, operator V_{Sf} contains only diagonal matrix elements and $\Delta E = 0$. It is the larger value of the ratio $V_{Sf}/\hbar\omega_k$ as compared to $V_{Sf}^2(\Delta E \pm \hbar\omega_k)^{-1}$ that determines the numerical superiority of U_2 over U_1. The smallness of potential U_3 and of the spontaneous line width associated with interactions of other origins could be predicted beforehand.

6. POSSIBLE MANIFESTATIONS OF PAIRED INTERACTION BETWEEN TWO-LEVEL SYSTEMS

Let us consider the manifestations of interaction (16) in optical properties of active substances.

In the case of a random distribution of two-level systems in a substance, interaction W_{SS} may lead to the so-called nonuniform broadening of the optical transition since it generates at each jth atom the shift of the resonant frequency ω_0,

$$\Delta\omega_j = \sum_i U_2(R_{ij})\langle S_j^z\rangle, \tag{22}$$

which is a random quantity. The mean $\langle S_j^z\rangle$ in this expression corresponds to the molecular field approximation for pseudospin operators, which is often used for estimating the resonance line shifts. The width can be characterized by the root-mean-square value

$$\overline{\Delta\omega_j} = \frac{\sqrt{2n}}{3\sqrt{35}}\left[\left(\frac{2\pi}{r_a}\right)^3\frac{e^2(\rho_z-\rho_x)^2}{\hbar}\right]\frac{\cos(2\pi R_0/r_a)}{\sqrt{\pi R_0}}\langle S_j^z\rangle,$$

where $\langle S_j^z\rangle$ is the temperature-averaged value of the z component of the pseudospin of the jth atom at the experimental temperature, which can generally be regarded as independent of the point; R_0 is the shortest possible distance between two-level systems; and n is their concentration. For $n = 10^{17}$ cm^{-3}, we have $\overline{\Delta\omega_j} \approx 10^{12}$ rad/s.

A more interesting manifestation of the Ising interaction can be expected in the case of an ordered distribution of two-level systems in the crystal lattice. It is well known that an Ising magnet exhibits additional resonant peaks if the exchange integral is larger than the natural line width [12]. Under these conditions, the quantities $\Delta\omega_j$ are not random any longer and assume several definite values in accordance with the number of nonequivalent positions in which neighboring exchange-coupled two-level systems can occur. This gives rise to additional absorption peaks. The number of peaks is determined by the number of exchange-coupled atoms. For example, a linear Ising system with exchange interaction between nearest neighbors spaced by distance R_0 from one another is characterized by three resonance frequencies: ω_0 and $\omega_0 \pm U_2(R_0)$ [12].

The integral intensities of these lines exhibit a typical temperature dependence; in particular, all the lines (except one whose intensity increases) are frozen out as the temperature decreases to zero. Unfortunately, the separation $E_e - E_g$ between the optical energy levels is so large that the zero-temperature limit is realized in equilibrium virtually in all cases. Consequently, additional peaks should be sought under nonequilibrium conditions.

Experiments of this kind are well known in the field of physics studying the magnetic resonance. When a strong narrowband varying field acts on a uniformly broadened EPR line, the subsequent passage of another weak field through the line profile singles out a broad

profile with a "burnt-out hole" [13]. The EPR line profile undergoes complex transformations during restoration of equilibrium; the kinetics of this process reflects the relaxation properties of the object under investigation.

Let us consider another example: as a result of intense narrow-frequency saturation of a uniformly broadened EPR line, its profile varies intricately until it acquires segments with negative absorption. The complex kinetics of this process associated with the existence of a reservoir of magnetic dipole–dipole interactions has been studied extensively by experimental methods [13].

In order to observe experimentally the Ising exchange interaction between two-level optical systems, the thermodynamic equilibrium of the physical system must be disturbed, for example, by applying a π pulse or subjecting it to an intense static irradiation followed by scanning of the wide optical line of a two-level system by a monochromatic frequency-tuned laser beam. In this situation, we can expect the emergence of additional peaks reflecting a complex kinetics. The spectral burning of dips in a nonuniformly broadened optical line was observed experimentally in [14].

APPENDIX

The concept of pseudospin (or effective spin) has been permanently used in the theory of paramagnetic resonance since the beginning of the 1950s [15] for a concise description of the dynamics and kinetics of paramagnetic ions possessing a small low-lying group of n energy levels under the conditions when the remaining levels do not participate in these processes. Higher lying levels are empty at moderate temperatures and are not involved in the resonant transitions induced by a comparatively low-frequency (on the order of 10^{10} Hz) ac field used in the EPR.

Any operators in the form of square $n \times n$ matrices can be projected onto the set of low-lying states. It is well known that $n \times n$ matrices stretch the linear space of dimension n^2 and, hence, possess a basis such that any $n \times n$ matrix can be expressed in terms of linear combinations of its components. The role of such a basis can be played, for example, by unit (or projective) matrices $\|p_{mn}\|$ such that all matrix elements of the matrix $\|p_{mn}\|$ are equal to zero except the single element p_{mn}, which is equal to unity.

Pseudospin operators can also serve as the basis of the $n \times n$ space formed on the Hilbert n-dimensional space of physical states; for the n-dimensional space, the pseudospin operator is $S = (n - 1)/2$. For example, if we consider a pair of energy levels (as is the case in the present work), it suffices to take $2^2 = 4$ operators: the unity operator E and the three components S_α of the pseudospin $S = 1/2$. The subspace of 3×3 matrices must have a basis of 9 independent matrices. This basis is constructed from the components of the pseudospins $S = 1$. It consists of four elements of the basis of the 1/2 pseudospin and five operators $Y_2^m(S)$ constructed from the pseudospin components S_α in the form of quadratic combinations transformed under rotation as the mth component ($m = 0, \pm 1, \pm 2$) of a second-rank tensor. For the four-dimensional space of physical states, use should be made of the pseudospin $S = 3/2$, and the 4×4 basis of the matrix space is constructed as the basis of a three-dimensional space and includes components of the $Y_3^m(S)$ tensor, and so on.

In the case of projecting onto the low-lying group of energy levels, the "correctly" written operator of a physical quantity can be expressed in terms of the pseudospin operators. The features of a specific problem are reflected in effective coefficients (gyromagnetic ratios, dipole moments, etc.) which may acquire a queer form. For example, for the two-level optical systems considered here, the static energy can be expressed in terms of the **z** component of pseudospin 1/2; the "Zeeman" frequency ω_0 in expression (1) is independent of the magnetic field, being generated by the splitting of optical energy levels in the electric field of the crystal. The "gyromagnetic" ratio (or Lande factor) has a definite value for the "transverse" direction of the ac field and is equal to zero for a "parallel" field, and so on. In particular, it follows from symmetry considerations that the matrix elements of the operators $\mathbf{r}_\alpha \mathbf{r}_\beta$ can only be diagonal and, hence, can be expressed in terms of the unity operator and the z component of pseudospin (see formula (12)).

ACKNOWLEDGMENTS

The authors are thankful to K.M. Salikhov and V.N. Lisin for fruitful discussions.

REFERENCES

1. L. Allen and J. H. Eberly, *Optical Resonance and Two-Level Atoms* (Wiley, New York, 1975; Mir, Moscow, 1978).
2. A. R. Kessel' and V. A. Popov, Opt. Spektrosk. **88**, 270 (2000) [Opt. Spectrosc. **88**, 232 (2000)].
3. M. E. Crenshow and C. M. Bowden, Phys. Rev. A **53**, 1139 (1996).
4. C. M. Bowden and J. P. Dowling, Phys. Rev. A **47**, 1247 (1993).
5. A. R. Kessel' and I. S. Donskaya, Pis'ma Zh. Éksp. Teor. Fiz. **74**, 283 (2001) [JETP Lett. **74**, 255 (2001)].
6. H. Frohlich, Phys. Rev. **79**, 845 (1950).
7. M. A. Ruderman and C. Kittel, Phys. Rev. **96**, 99 (1954).
8. R. Loudon, *The Quantum Theory of Light* (Clarendon, Oxford, 1973; Mir, Moscow, 1976).
9. W. H. Louisell, *Radiation and Noise in Quantum Electronics* (McGraw-Hill, New York. 1964; Nauka, Moscow, 1972).

10. G. S. Agarwal, *Quantum Optics*, Springer Tracts in Modern Physics (Springer-Verlag, Berlin, 1974), Vol. 70, p. 95.

11. A. N. Oraevskiĭ, Usp. Fiz. Nauk **164**, 415 (1994) [Phys. Usp. **37**, 393 (1994)].

12. A. R. Kessel' and G. O. Berim, *Magnetic Resonance of Ising Magnetics* (Nauka, Moscow, 1982); G. O. Berim, M. M. Zaripov, and A. R. Kessel', Zh. Éksp. Teor. Fiz. **66**, 734 (1974) [Sov. Phys. JETP **39**, 355 (1974)]; Fiz. Tverd. Tela (Leningrad) **17**, 2622 (1975) [Sov. Phys. Solid State **17**, 1744 (1975)].

13. V. A. Atsarkin, *Dynamic Nuclear Polarization in Solid Dielectrics* (Nauka, Moscow, 1980).

14. M. Drobizhev, A. Korotki, and A. Rebane, Chem. Phys. Lett. **334**, 76 (2001).

15. A. Abragam and M. H. L. Pryce, Proc. R. Soc. London, Ser. A **205**, 135 (1951).

Translated by N. Wadhwa

Journal of Experimental and Theoretical Physics, Vol. 94, No. 3, 2002, pp. 516–520.
Translated from Zhurnal Éksperimental'noĭ i Teoreticheskoĭ Fiziki, Vol. 121, No. 3, 2002, pp. 603–608.

PLASMA, GASES

Effect of a Longitudinal Magnetic Field on the Excitation of Plasma Wake Waves

A. G. Khachatryan
Yerevan Physical Institute, Yerevan, 375036 Armenia
e-mail: khachatr@moon.yerphi.am
Received May 4, 2001

Abstract—The effect of a longitudinal magnetic field on the linear wake fields excited by a relativistic electron bunch in a cold homogeneous plasma is considered. The obtained results prove that the presence of an external magnetic field leads to a dependence of the wake wavelength on the transverse coordinate, to a change in the wave amplitude with increasing distance from the bunch, and to the emergence of anharmonicity. It is found that a strong magnetic field reduces the wave amplitude significantly for narrow bunches and changes the amplitude insignificantly for broad bunches. © *2002 MAIK "Nauka/Interperiodica".*

1. INTRODUCTION

Plasma waves excited by relativistic electron bunches or high-intensity laser pulses (wake waves) may create abnormally strong accelerating and focusing fields. The results of theoretical and experimental studies show that the acceleration rate in a wake wave may reach up to several tens of GeV/m, which is three orders of magnitude higher than the rates attained in traditional accelerators (see the review in [1] and the literature cited therein). The plasma methods of acceleration are being developed intensely at present.

In experiments, a plasma is usually placed in a magnetic field for its confinement and for the suppression of various types of instabilities. It can be assumed that when the electron gyrofrequency $\omega_H = eH_0/m_ec$ becomes comparable to or higher than the plasma frequency $\omega_p = \sqrt{4\pi n_p e^2/m_e}$ (here, H_0 is the magnetic field strength and n_p is the unperturbed electron number density in the plasma), the magnetic field may noticeably affect the excitation of wake fields. Thus, we can choose as a natural parameter of the problem the dimensionless frequency

$$\Omega_H \equiv \frac{\omega_H}{\omega_p} = 3.12 \times 10^5 \frac{H_0[\text{kG}]}{\sqrt{n_p[\text{cm}^{-3}]}}.$$

For example, for $n_p = 10^{12}$ cm^{-3} (which is typical of experiments on the excitation of wake waves by relativistic electron bunches [2]), $\Omega_H = 1$ for $H_0 \approx 3.2$ kG. When wake waves are excited by a high-intensity laser pulse, the required density of the plasma is 10^{16}–10^{18} cm^{-3}. Such values of plasma density are determined by the length of high-intensity laser pulses, which in turn must be equal approximately to half the plasma wavelength. For $n_p = 10^{17}$ cm^{-3}, we have $\Omega_H = 1$ for $H_0 \approx 1$ MG, which is much higher than magnetic fields attainable by conventional methods. Megagauss magnetic fields can be generated in a plasma by a laser beam (see, for example, [3]). For example, a strong longitudinal magnetic field can be created in a plasma by a circularly polarized laser pulse due to the inverse Faraday effect [4, 5]; however, such a field is localized in a region occupied by the laser pulse and is equal to zero in the wake. For this reason, we will confine our subsequent analysis to the wake fields excited by electron bunches.

The linear theory of plasma wake waves in an isotropic plasma was applied earlier both for laser pulses (see references in [1]) and for electron bunches [6, 7]. In the latter case, regular potential plasma oscillations whose amplitude depends on the parameters of a source are excited behind this source. The effect of a finite longitudinal magnetic field on the excitation of three-dimensional wake fields by a relativistic electron bunch was considered for the first time (to our knowledge) by Balakirev *et al.* in [8]. They discovered that, in a strong magnetic field for which $\Omega_H \gg 1$, the amplitude of a wake wave at the axis decreases with increasing distance from the bunch. In the present work, we will obtain an analytic solution to the linear problem of excitation of wake waves in an external magnetic field, which is valid for arbitrary values of Ω_H and for an arbitrary distribution of electrons in the bunch, and will give numerical results.

2. FORMULATION OF THE PROBLEM AND GENERAL SOLUTION TO INITIAL EQUATIONS

We consider a cylindrical homogeneous (in energy) electron bunch with density $n_b(Z - v_b t, r)$, flying along the Z axis at velocity v_b in a homogeneous plasma. As usual, we assume that plasma ions are stationary owing to their large mass. We disregard the thermal motion of electrons in the plasma, assuming that $v_{Te} \ll v_b$, which

is observed virtually in all cases under laboratory conditions. We also disregard the dynamics of electrons in the bunch, which is justified for time intervals $t < t_d \sim \gamma_b/\omega_p$ [9], where $\gamma_b = 1/\sqrt{1-(v_b/c)^2}$ is the relativistic factor of the bunch. For convenience of subsequent calculations, we introduce the following dimensionless quantities. We normalize the electric $\mathbf{E}(E_r, E_\theta, E_Z)$ and magnetic $\mathbf{H}(H_r, H_\theta, H_Z)$ fields excited by the bunch to the nonrelativistic wave breaking field $E_{WB} = m_e c\omega_p/e$ ($E_{WB}[\mathrm{V/cm}] \propto \sqrt{n_p[cm^{-3}]}$), while spatial coordinates are normalized to v_b/ω_p. Then, the Maxwell equations and the equation of motion for electrons in the plasma can be written in the form

$$\nabla\times\mathbf{H} = V_b\frac{\partial\mathbf{E}}{\partial\tau} - \mathbf{V}_e - N_b\mathbf{V}_b,$$

$$\nabla\times\mathbf{E} = -V_b\frac{\partial\mathbf{H}}{\partial\tau}, \quad (1)$$

$$\frac{\partial\mathbf{V}_e}{\partial\tau} = -V_b\mathbf{E} - \mathbf{V}_e\times\mathbf{\Omega}_H,$$

where $\tau = \omega_p t$, $N_b = n_b/n_p$, $\mathbf{V}_b = \mathbf{v}_b/c$, and $\mathbf{V}_e(V_r, V_\theta, V_Z) = \mathbf{v}_e/c$ are the dimensionless velocities of the bunch and of plasma electrons, $\mathbf{\Omega}_H = e\mathbf{H}_0/m_e c$, $\mathbf{H}_0$ being the external magnetic field strength.

Let the external magnetic field be directed along the Z axis: $\mathbf{H}_0 = H_0\mathbf{e}_Z$, $H_0 = \mathrm{const}$. We will consider ultrarelativistic bunches and assume that $V_b \approx 1$ ($\gamma_b \gg 1$). Owing to the axial symmetry of the problem, the field is independent of azimuth angle θ. In this case, for steady-state wake fields (i.e., the fields depending only on $z = Z - \tau$ and r), we obtain from system (1)

$$\frac{\partial H_\theta}{\partial z} = \frac{\partial E_r}{\partial z} + V_r, \quad (2a)$$

$$\frac{\partial H_r}{\partial z} - \frac{\partial H_Z}{\partial r} = -\frac{\partial E_\theta}{\partial z} - V_\theta, \quad (2b)$$

$$\nabla_\perp H_\theta = -\frac{\partial E_Z}{\partial z} - N_b - V_Z, \quad (2c)$$

$$\frac{\partial E_\theta}{\partial z} = -\frac{\partial H_r}{\partial z}, \quad (2d)$$

$$\frac{\partial E_r}{\partial z} - \frac{\partial E_Z}{\partial r} = \frac{\partial H_\theta}{\partial z}, \quad (2e)$$

$$\nabla_\perp E_\theta = \frac{\partial H_Z}{\partial z}, \quad (2f)$$

$$\frac{\partial V_r}{\partial z} = E_r + \Omega_H V_\theta, \quad (2g)$$

$$\frac{\partial V_\theta}{\partial z} = E_\theta - \Omega_H V_r, \quad (2h)$$

$$\frac{\partial V_Z}{\partial z} = E_Z, \quad (2i)$$

where $\nabla_\perp = \partial/\partial r + 1/r$. It follows from Eq. (2d) that $E_\theta = -H_r$. In this case, the force exerted by the wake wave on relativistic electrons flying behind the exciting bunch is $\mathbf{F}(eE_{WB}(H_\theta - E_r), 0, -eE_{WB}E_Z)$. In accordance with Eq. (2e), we have

$$\frac{\partial E_Z}{\partial r} = -\frac{\partial(H_\theta - E_r)}{\partial z} \equiv -\frac{\partial f_r}{\partial z}. \quad (3)$$

It can easily be seen that the field of forces $\mathbf{F}$ is of the potential type; i.e., we can write $\mathbf{F} = \nabla\Phi$, which also holds for nonlinear wave waves. It should also be noted that Eqs. (2a) and (2e) lead to

$$V_r = -\frac{\partial E_Z}{\partial r}. \quad (4)$$

In order to solve the system of equations (2), we will use the approach applied in [10]. In Eqs. (2), we pass to the Fourier transforms in z and to the Hankel transformation in the transverse coordinate in accordance with the formulas (see, for example, [11])

$$Y(z, r) = \frac{1}{\sqrt{2\pi}}\int_{-\infty}^{\infty}\int_{0}^{\infty} Y_{\lambda\xi}\exp(i\lambda z)\xi J_n(\xi r)d\xi d\lambda, \quad (5a)$$

$$Y_{\lambda\xi} = \frac{1}{\sqrt{2\pi}} \times \int_{-\infty}^{\infty}\int_{0}^{\infty} Y(z', r')\exp(-i\lambda z')r' J_n(\xi r')dr'dz', \quad (5b)$$

where J_n are Bessel functions; $n = 1$ for the quantities equal to zero on the axis ($r = 0$), namely, for $E_{r,\theta}$, $H_{r,\theta}$, and $V_{r,\theta}$; and $n = 0$ for E_Z, H_Z, V_Z, and N_b. Then, Eqs. (2) are reduced to a system of algebraic equations, which gives

$$E_{Z,\lambda\xi} = \frac{i\lambda N_{b,\lambda\xi}}{(1+\xi^2)(\lambda^2 - w^2)},$$
$$w = \sqrt{1 + \left(\frac{\Omega_H\xi^2}{1+\xi^2}\right)^2} \geq 1. \quad (6)$$

We present the number density of electrons in the bunch in the form $N_b(z, r) = N_{b0}g_1(z)g_2(r)$. Substituting now Eqs. (6) into Eq. (5a) and integrating with respect to λ, we obtain

$$E_Z(z, r) = N_{b0}\int_0^\infty \frac{\xi J_0(\xi r)}{1+\xi^2} G_1 G_2 d\xi, \quad (7)$$

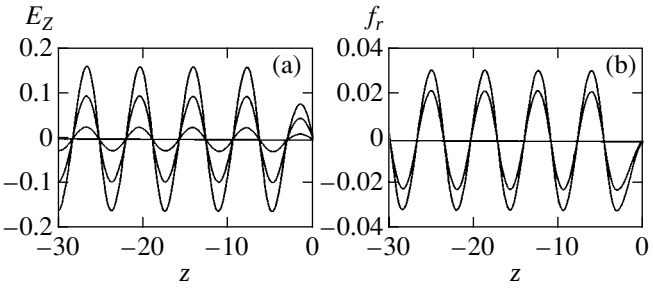

Fig. 1. Wake wave in a plasma in zero external magnetic field. Here and in all the remaining figures, electron bunches are homogeneous with a length equal to half the plasma wavelength in an isotropic plasma: $d = \pi$. The dimensionless radius and the radius of the bunch are $r_b = 1$ and $N_b = 0.2$. (a) Longitudinal electric field of a wake wave; the normalized distance r from the axis is equal to 0, 1, and 2 in order of decreasing amplitude. (b) Focusing force, $r = 1$ and 2 in order of decreasing amplitude of the oscillations.

where

$$G_1 = \int_z^\infty g_1(z')\cos[w(z-z')]dz',$$

$$G_2 = \int_0^\infty g_2(r')r'J_0(\xi r')dz'.$$

While evaluating the integral with respect to λ, we bypassed the poles $\lambda_{1,2} = \pm w$ on the complex plane from above [10]. This is equivalent to the introduction of an infinitely small damping and is associated with the fact that the initial equations "are not aware" of the plasma stability, i.e., that the plasma tends to the equilibrium state for $t \longrightarrow \infty$. Indeed, if we introduce from the very outset a dissipative term into the equations (e.g., the collision term into the equation of motion), the poles would occur outside the integration path and can be bypassed "correctly."

Thus, we obtain the general solution (7) for the longitudinal field. For the known E_Z, we can also calculate the remaining quantities in the system of equations (2). For example, V_Z and V_r can be evaluated from Eqs. (2i) and (4), respectively. The focusing field f_r can be determined from relations (3). For $\Omega_H = 0$ ($w = 1$), the integral with respect to ξ in expression (7) can be evaluated easily and we arrive at the well-known solution for an isotropic plasma [7, 10]. It should also be noted that since the external magnetic field appears in expression (7) in the form H_0^2, the magnetic field directions parallel and antiparallel to the direction of motion of the electron bunch are equivalent from the physical point of view.

In the case of a homogeneous bunch having the density

$$N_b = \begin{cases} N_{b0}, & -d < z \le 0, \quad r \le r_b, \\ 0, & z \le -d, \quad r > r_b, \end{cases}$$

where d and r_b are the bunch length and radius, the expressions for E_Z and f_r assume the form

$$E_Z = N_{b0}r_b\int_0^\infty \frac{J_0(\xi r)J_1(\xi r_b)}{(1+\xi^2)w}Ld\xi, \tag{8}$$

$$f_r = -N_{b0}r_b\int_0^\infty \frac{\xi J_1(\xi r)J_1(\xi r_b)}{(1+\xi^2)w^2}L'd\xi, \tag{9}$$

where

$$L = \begin{cases} -\sin(wz), & -d < z \le 0, \\ 2\sin(wd/2)\cos[w(z+d/2)], & z \le -d, \end{cases}$$

$$L' = \begin{cases} 1-\cos(wz), & -d < z \le 0, \\ -2\sin(wd/2)\sin[w(z+d/2)], & z \le -d. \end{cases}$$

Although the evaluation of integrals with respect to ξ in Eqs. (7)–(9) for arbitrary values of Ω_H is a complicated problem, it can be seen that a finite magnetic field effectively leads to the emergence of field components with wavelengths smaller that the plasma wavelength in an isotropic plasma or, which is the same, with frequencies higher than ω_p. It is well known that a cold magnetically active plasma with stationary ions is characterized by two vibrational eigenmodes. The frequency of one of these modes increases monotonically with the angle between the wave vector and the direction of the magnetic field, attaining its maximum value $\omega_p\sqrt{1+\Omega_H^2}$ in the case of transverse propagation [12]. Obviously, it is the waves propagating at finite angles to the magnetic field (and having a finite group velocity) that make a contribution to the wake wave components having a frequency $\omega > \omega_p$. In contrast to the case of an isotropic plasma, the wake wave is not plane any longer. It will be demonstrated below that, according to Balakirev *et al.* [8], the finiteness of the group velocity of the wake wave leads to the transfer of the wake field energy in the radial direction and to a decrease in the field amplitude in the vicinity of the axis upon an increase in the distance from the bunch as a result of the absence of dissipation.

3. NUMERICAL RESULTS FOR A HOMOGENEOUS BUNCH

In this section, we consider the numerical results for a homogeneous bunch. The bunch length is chosen equal to half the length of a wake wave in an isotropic plasma: $d = \pi$. Figure 1 shows by way of an example a wake wave excited in a plasma in zero external magnetic field ($\Omega_H = 0$). Figure 2 illustrates a typical behavior of a wake wave in a finite magnetic field; the bunch parameters are the same as in Fig. 1. It can be seen that the presence of an external field leads (a) to a depen-

dence of the wake wavelength on the transverse coordinate; (b) to a change in the wave amplitude upon an increase in the distance from the bunch; and (c) to the emergence of anharmonicity in field oscillations or, which is the same, to the emergence of harmonics. The reason for these effects was considered above. It should be noted that the field in the vicinity of the axis is subjected to the strongest "deformation". For $r < r_b$, the amplitude of the wake wave decreases noticeably with increasing distance from the bunch. The case of a narrow bunch ($r_b < 1$) is illustrated in Fig. 3. A distinguishing feature here is a nonmonotonic decrease in the wave amplitude behind the bunch. It can easily be seen that the change in the wake wavelength with the distance r from the axis leads to a distortion of the phase front of the wave, which becomes stronger with increasing distance from the bunch, and to a nonmonotonic variation of the field in the transverse direction. The latter is depicted in Fig. 4, which also shows that the region occupied by the wake field expands in the transverse direction upon an increase in the distance from the bunch. This occurs due to a finite group velocity of plasma oscillations being excited (see also [8]). In turn, the wake field amplitude decreases in the vicinity of the axis since the total energy of the wave must be conserved.

It is interesting to note that the dependence of the wake wavelength on the transverse coordinate and the wave front bending take place for $H_0 = 0$ in the plasma channel also (see, for example, [13]) in the case of a nonlinear mode in a homogeneous plasma [14]. In these two cases, the wavelength attains its maximum value at the axis and decreases upon an increase in the distance r from the axis. In the case under investigation, when a wake wave is excited in the presence of a longitudinal magnetic field, the wavelength at the axis immediately behind the bunch has the minimum value and increases with r (see Figs. 2 and 3). Consequently, one could try to compensate the undesirable wave front bending in the case of a nonlinear wake wave by applying a longitudinal magnetic field.

The obtained numerical results prove that the presence of a weak magnetic field ($\Omega_H \ll 1$) affects linear wake waves only insignificantly (at least, at distances on the order of ten wavelengths behind the source). The case of a strong magnetic field ($\Omega_H \gg 1$) is illustrated in Fig. 5. Here, the amplitude of the longitudinal electric field for a narrow bunch ($r_b = 1$) is more than an order of magnitude smaller than in zero magnetic field (cf. Figs. 5a and 1a); the focusing force is smaller by two orders of magnitude. Thus, in the case of a narrow bunch, when the dimensionless bunch radius is smaller than or on the order of unity, a strong magnetic field considerably reduces the amplitude of the wake wave, which in the given case cannot be used for an effective acceleration and focusing of charged bunches.

Behind a broad bunch ($r_b \gg 1$; see Fig. 5b), the amplitude of the wake wave is comparable to that in an

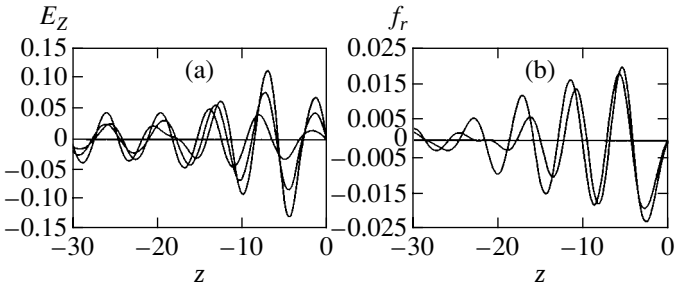

Fig. 2. Wake wave excited in the presence of a finite magnetic field, $\Omega_H = 1$. The bunch parameters are the same as in Fig. 1. (a) $E_Z(z)$: $r = 0$, 1, and 2 in order of decreasing amplitude immediately behind the bunch. (b) $f_r(z)$: $r = 1$, 2 in order of decreasing amplitude immediately behind the bunch.

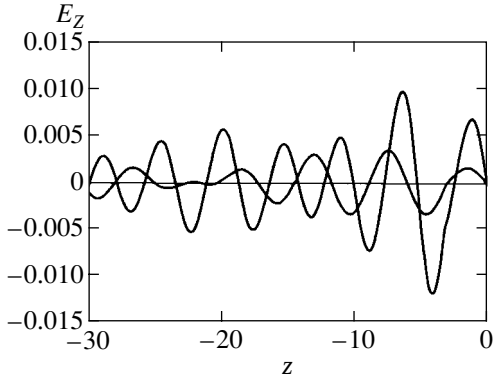

Fig. 3. Longitudinal electric field of a wake wave excited by a narrow bunch, $\Omega_H = 1$, $r_b = 0.2$, and $N_b = 0.2$, $r = 0$, 1 in order of decreasing amplitude.

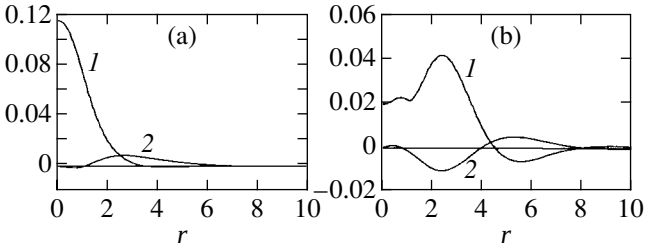

Fig. 4. Radial behavior of the wake field presented in Fig. 2: (a) $E_Z(z = -7, r)$ (*1*); $f_r(z = -7, r)$ (*2*); (b) $E_Z(z = -20, r)$ (*1*); $f_r(z = -20, r)$ (*2*).

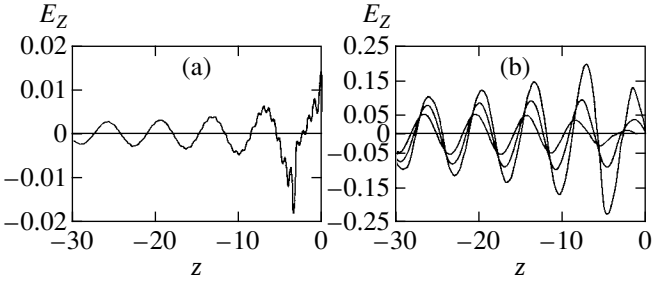

Fig. 5. Excitation of a wake field in a strong magnetic field, $\Omega_H = 0$. (a) Longitudinal electric field of a wake wave at the axis; the bunch parameters are $r_b = 1$, $N_b = 0.2$. (b) Broad bunch, $r_b = 10$, $N_b = 0.1$, $r = 0$, 10, and 15 in order of decreasing amplitude.

isotropic plasma. This is due to the fact that in the case of a broad bunch, the motion of electrons for $r < r_b$ is predominantly longitudinal. The latter statement is true of arbitrary values of Ω_H and leads to the closeness of the amplitude of the longitudinal component of the electric field created by a wake wave in a magnetized plasma to that in the 1D theory, while the transverse components (including the focusing force also) are negligibly small as compared to the longitudinal field. This is in accord with the theory of wake fields in an isotropic plasma and with the well-known result in the theory of plasma that a longitudinal magnetic field does not affect the propagation of 1D plasma waves.

4. CONCLUSION

Thus, qualitatively new properties of 3D wake waves excited in a plasma in the presence of a longitudinal magnetic field have been observed, including a change of the amplitude with the transverse coordinate and an increase in the wavelength with the distance from the axis. The latter effect can be used for compensating the undesirable bending of the wave front in the nonlinear 3D case. These features of wake fields in the presence of a longitudinal magnetic field are associated with the properties of eigenmodes of a magnetically active plasma, namely, an increase in their frequency with the angle between the wave vector and the magnetic field and with their nonzero group velocity.

ACKNOWLEDGMENTS

The author is grateful to S. Élbakyan for fruitful discussions.

This work was partly financed by the International Center of Science and Technology (project no. A-405).

REFERENCES

1. E. Esarey, P. Sprangle, J. Krall, and A. Ting, IEEE Trans. Plasma Sci. **24**, 252 (1996).
2. J. B. Rosenzweig, P. Schoessow, B. Cole, *et al.*, Phys. Rev. A **39**, 1586 (1989); H. Nakanishi, A. Emomoto, A. Ogata, *et al.*, Nucl. Instrum. Methods Phys. Res. A **328**, 596 (1993); A. K. Berezin, Ya. B. Faĭnberg, V. A. Kiselev, *et al.*, Fiz. Plazmy **20**, 663 (1994) [Plasma Phys. Rep. **20**, 596 (1994)].
3. S. V. Bulanov, T. Zh. Esirkepov, M. Lontano, *et al.*, Phys. Rev. Lett. **76**, 3562 (1996); L. Gorbunov, P. Mora, and T. M. Antonsen, Jr., Phys. Rev. Lett. **76**, 2495 (1996); M. Borghesi, A. J. Mackinon, R. Gaillard, *et al.*, Phys. Rev. Lett. **80**, 5137 (1998).
4. V. Yu. Bychenkov, V. I. Demin, and V. T. Tikhonchuk, Zh. Éksp. Teor. Fiz. **105**, 118 (1994) [JETP **78**, 62 (1994)].
5. L. M. Gorbunov and R. R. Ramazashvili, Zh. Éksp. Teor. Fiz. **114**, 849 (1998) [JETP **87**, 461 (1998)].
6. P. Chen, J. M. Dawson, R. W. Huff, and T. Katsouleas, Phys. Rev. Lett. **54**, 693 (1985); R. D. Ruth, A. W. Chao, P. L. Morton, and P. B. Wilson, Part. Accel. **17**, 171 (1985).
7. R. Keinigs and M. E. Jones, Phys. Fluids **30**, 252 (1987).
8. V. A. Balakirev, I. V. Karas', and G. V. Sotnikov, Fiz. Plazmy **26**, 948 (2000) [Plasma Phys. Rep. **26**, 889 (2000)].
9. K. V. Lotov, Phys. Plasmas **5**, 785 (1998).
10. A. G. Khachatryan, A. Ts. Amatuni, É. V. Sekhposyan, and S. S. Élbakyan, Fiz. Plazmy **22**, 638 (1996) [Plasma Phys. Rep. **22**, 576 (1996)].
11. I. H. Sneddon, *The Use of Integral Transforms* (McGraw-Hill, New York, 1972).
12. A. I. Akhiezer, I. A. Akhiezer, R. V. Polovin, *et al.*, *Plasma Electrodynamics* (Nauka, Moscow, 1974; Pergamon, Oxford, 1975), Chap. 5; V. L. Ginzburg and A. A. Rukhadze, *Waves in Magnetoactive Plasmas* (Nauka, Moscow, 1975), Para. 8.
13. N. E. Andreev, L. M. Gorbunov, V. I. Kirsanov, *et al.*, Phys. Plasmas **4**, 1145 (1997).
14. A. G. Khachatryan, Phys. Rev. E **60**, 6210 (1999).

Translated by N. Wadhwa

Journal of Experimental and Theoretical Physics, Vol. 94, No. 3, 2002, pp. 521–524.
Translated from Zhurnal Éksperimental'noĭ i Teoreticheskoĭ Fiziki, Vol. 121, No. 3, 2002, pp. 609–613.

PLASMA, GASES

Cooperative Formation of Dust Structures in Plasma

L. M. Vasilyak*, S. P. Vetchinin, D. N. Polyakov, and V. E. Fortov

Institute for High Energy Densities, Associated Institute for High Temperatures, Russian Academy of Sciences, ul. Izhorskaya 13/19, Moscow, 127412 Russia

** e-mail: lab852@ihed.ras.ru*

Received September 6, 2001

Abstract—The formation and destruction of ordered dust structures in glow discharges are investigated experimentally. The initial construction phase of an ordered structure is related to the construction of its cooperative field and is determined by the number of particles and by the existence of crystallization centers. After the structure has been constructed, it influences the local plasma properties and the discharge current–voltage characteristics. The recovery of the structure after weak exposure takes place at local equilibrium, while, after intense exposure to high-voltage nanosecond pulses, it is determined by the fluctuation level and the degree of chaotization in the system. *© 2002 MAIK "Nauka/Interperiodica".*

Plasma with charged dust particles is an object with a strong Coulomb coupling that yields record high parameters of nonideality,

$$\gamma = Z^2 e^2 n^{1/3}/kT \sim 10^5,$$

through a significant macroparticle charge Z. The formation of structures from micron-sized dust particles was experimentally observed in a low-pressure nonequilibrium plasma in high-frequency and glow discharges [1], as well as under intense ultraviolet and radioactive radiation [2]. The particles acquire a large negative charge (10^5–10^6 electron charges) that corresponds to the floating plasma potential, and the dissipative dust structures can form a Coulomb crystal [1]. The external conditions and the ambient-plasma properties under which ordered plasma–dust structures can be produced have currently been studied. It is not yet known how the ordering of dust particles with a strong Coulomb coupling and plasma condensation proceed; the transition from chaos to order in such systems is not understood and has been investigated neither experimentally nor theoretically. The appearing stable structure must, in turn, change the local properties of the ambient plasma, the distribution of parameters in it, the electric fields, and the charged particle fluxes. Previously, most authors have assumed the background-plasma properties to be virtually constant. Here, our goal is to experimentally investigate the formation and destruction of charged macroparticle structures, the action of force on these structures, and the changes in plasma properties.

We investigated the structures composed of Al_2O_3 particles (3–5 μm in size), polydisperse MgO particles (5–20 μm in size), and hollow glass spheres (20–60 μm in size) in glow discharges in helium, argon, nitrogen, air, and their mixtures. The experiments were carried out in cylindrical discharge tubes of 1 and 2 cm in diameter, as well as in a conical 50-cm-long discharge tube with a variable diameter from 1.5 to 4 cm [3]. Since the similarity rule, according which the reduced electric-field strength E/P is determined by the product Pd (where d is the discharge tube diameter and P is the gas pressure), holds for a positive gas discharge column, the longitudinal electric field in the conical tube changes along its length: it is at a maximum in its lower narrow part and decreases as one rises in height. Therefore, particles with different masses can find a suitable field, causing the localization of different particles in different cross sections of the discharge tube and the particle separation in size, charge, and mass along the tube. When using the cylindrical tube of 2 cm in diameter, we pasted two metal rings of the same diameter spaced 5 cm apart in its walls. We used these rings to measure the average field in the discharge and applied high-voltage nanosecond pulses to them to act on the dust structures. The particle structures were examined with a videocamera through their illumination by two perpendicular laser "knifes" with a 0.63-μm wavelength and a 150-μm caustic. The particles were imaged along and across the tube. The structures were also examined with an optical microscope. We measured the average field along the discharge column with probes, the voltage between the metal rings, the current and voltage on the discharge tube, and the geometric parameters of the dust structure as a function of the discharge current and gas pressure.

A distinct three-dimensional dust structure is formed in strata at $Pd < 1$ torr cm. The number of particles in the structure depends on conditions and can vary from several tens to several thousand. The characteristic distances between the strata are 150–250 μm. The horizontal distances between the particles in the stratum are typically a factor of 1.5 or 2 larger and increase with particle size, tube diameter, and passing current. In air,

1063-7761/02/9403-0521$22.00 © 2002 MAIK "Nauka/Interperiodica"

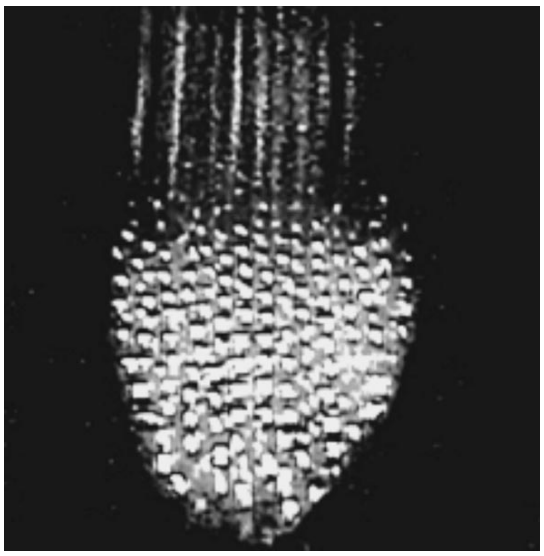

Fig. 1. Luminous jets above an ordered dust structure. The cross section is longitudinal, the glow discharge is in air, and the current is 0.5 mA.

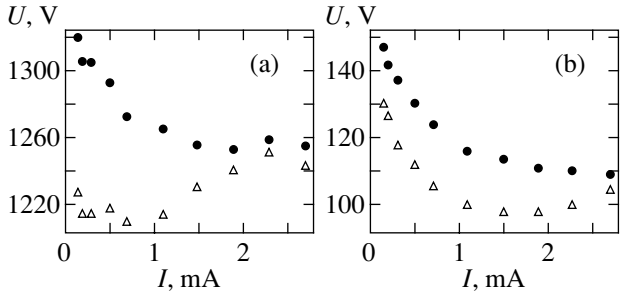

Fig. 2. The current–voltage characteristics of (a) a glow discharge and (b) a stratified discharge column between the rings with (dots) and without (triangles) glass microspheres. The air pressure is 0.2 Torr.

the conditions for the formation of an ordered crystal are fairly stringent; the range of discharge currents at a pressure of 0.2 torr is 0.3–1 mA, while, in air–argon mixtures at pressures of 0.1–0.5 Torr, it is 0.3–3 mA. As the current rises further to several milliamperes, the crystal is disordered and resembles a liquid. In this case, the particles retreat to the walls of the discharge tube and ring-shaped structures suspended in strata are observed [3, 4].

In general, a distinct spatial structure is formed when several particles are initially aligned in the stratum and then the remaining particles sequentially line up with them. The initial particles act as the crystallization centers. These are localized in the undisturbed field of the stratum and are aligned in its potential pit [4]. As the number of dust particles gradually increases, they sequentially fill the entire stratum volume to produce a spatially ordered structure. The collective field of this structure is a superposition of the stratum electric field and the spatial fields of individual dust particles. Adding several particles distorts this collective field only slightly, and these line up with the structure. The spatial order of the particle arrangement in the formed plasma–dust structure is determined by Coulomb forces, although the Debye screening length calculated from the background plasma parameters is severalfold smaller than the interparticle separation. The cooperative field of the dust structure is comparable in strength to the stratum field. Therefore, if many randomly moving dust particles whose average field greatly fluctuates and distorts the local stratum field are simultaneously injected into the stratum, then no stable ordered structures are formed. In this case, although the particles are confined to the stratum, they randomly move through its entire volume.

The cooperative behavior that facilitates the formation of a plasma–dust structure is consistent with the standard principles of nonequilibrium thermodynamics when the formation and self-organization of dissipative structures have a threshold character [5]. In a thermodynamic equilibrium, the probability that a macrosopic number of particles are spontaneously organized into a regular stream or a phased collective is negligible. A system can form ordered structures only because the external restrictions (temperature gradient, electric field, and radiation field) maintain the system in a nonequilibrium state. The new structure results from the growth of instability and arises from fluctuations [5].

The collective action of the dust grain field on the processes in the stratum can be significant, because the grain charge per unit volume is comparable to the electron number density in the stratum itself (10^8–10^9 cm^{-3}). An ordered crystal changes not only the electric fields in the stratum itself but also the properties of the adjacent plasma at distances comparable to the crystal size. When a current passes through a macrocrystal, the formation of luminous plasma jets above the crystal from the anode is observed (Fig. 1). When moving along the channels formed by neighboring parallel chains of charged macroparticles, the electrons apparently undergo grazing collisions and mirror reflections and are confined to these channels. The channeled electrons are accelerated when passing through the crystal, much as they are in a solid [6], and produce an additional plasma disturbance in the form of luminous fibers above the crystal.

The formed dust structures also affect other discharge properties, in particular, the current–voltage characteristics. We measured the current–voltage characteristics of a positive column with stationary strata at an air pressure of 0.2–0.5 Torr with structures with and without glass microspheres between the metal rings in the discharge tube of 2 cm in diameter. At all pressures, the voltage between the rings in the presence of macroparticles is higher than that in the discharge without particles (Figs. 2a and 2b). The difference between the two current–voltage characteristics at a fixed current for

a small number of particles in the structure is 5–10 V. For a large number of particles in the structure, it increases to 20–30 V, which is apparently attributable to the additional electron death on particles. The electron death on macroparticles at small currents can cause the discharge to be quenched. At the minimum possible discharge current, we detected a relaxation discharge glow when the discharge periodically went out and ignited with a period of about one second. The oscillation period decreases with increasing discharge current. These oscillations can be explained as follows: an additional channel of the electron death on particles appears when the particles enter into the discharge, a voltage higher than the available one is required to maintain the discharge, and the discharge goes out. The dust particles fall and retreat to the walls. The discharge ignites again. In the discharge, the particles are charged, the dust structure is recovered, and the process is repeated.

When the dust structure is destroyed, its recovery depends on the type of exposure. For slow weak exposure, for example, a thermal [4] or electric [7] one, the structure shifts in space; part of it can be deformed or destroyed. After the exposure, the destroyed part of the structure gradually lines up with its preserved part. If the disturbing processes are less intense than the processes that produce an equilibrium of the dust structure, then a local equilibrium is maintained in the system with a certain accuracy. Otherwise, for intense exposure, the structure is completely destroyed and chaotized. The recovery of the structure from chaos is no longer determined by the local equilibrium alone. If there is no initial seed with which the structure lines up, then the formation of an ordered structure will depend on the fluctuation level. One or more sufficiently intense macrosopic fluctuations are needed for a new ordered structure to emerge in the wake of instability.

The ordered dust structure was intensely exposed to nanosecond high-voltage pulses. Since the pulse duration is very short, the particle displacement in the structure in the exposure time of the pulsed electric field is negligible. The dust structure was produced in the stratum between the two metal rings in the cylindrical discharge tube (Fig. 3a). High-voltage pulses of negative polarity, 40 ns in duration and 10 kV in amplitude, with a repetition frequency of 1–100 Hz were applied to the rings through blocking capacitors. After exposure to a single pulse, the particles slightly oscillated about their stable state. After pulse-periodic exposure with a frequency of about 10 Hz, the order in the structure broke down, while, at a higher frequency, the particles scattered over the entire volume and began to randomly move with large velocities (Fig. 3b). After the nanosecond voltage was removed, the particles gathered in the stratum in several seconds. The number of particles in the new structure always exceeded their initial number, which stems from the fact that a larger number of particles were drawn into the construction process. The number of returning particles increases with exposure intensity. When the number of particles after the exposure to nanosecond pulses ended was smaller than some critical number, the particles gradually formed an ordered structure in several seconds (Figs. 3c and 3d). If their number was too large, then the particles were confined to the structure but they were not aligned into an ordered structure; the dust structure resembled in form a boiling liquid with randomly moving particles. Such a chaotic state could be stable for a long period.

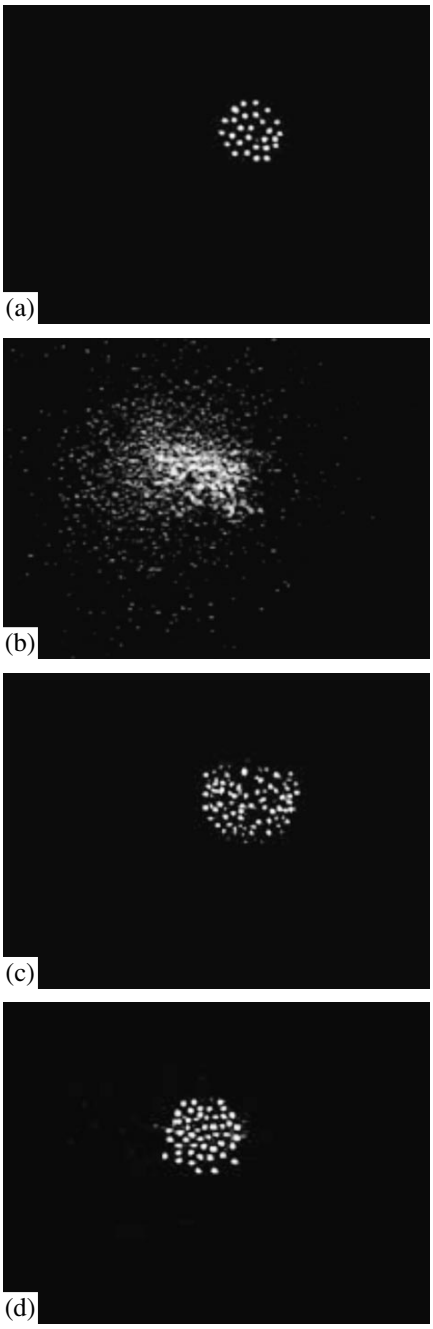

Fig. 3. Exposure of a dust crystal in a glow discharge in air (cross section) to nanosecond pulses: (a) before the exposure, (b) during the exposure with a pulse repetition frequency of 40 Hz, (c) recovery of the structure after the exposure, and (d) an ordered structure after the exposure.

The destruction of the structure and the scatter of particles under nanosecond exposure primarily result from an increase in their charge. High-voltage nanosecond pulses produce many high-energy electrons (with energies of several hundred eV [8]) in plasma that rapidly increase the dust-particle charge, which is proportional to the electron energy. The surplus negative charge is neutralized much more slowly, because this neutralization is determined by the ion flux. The action of this surplus charge results in their Coulomb repulsion. Chaotization proceeds gradually from pulse to pulse. If the system of dust particles does not completely return to its initial ordered state in the time between pulses and if this time depends on the extent of the structure destruction and is several seconds for complete chaotization, then the structure falls apart, which is observed in the experiment.

Thus, the initial construction phase of an ordered structure is related to the construction of its cooperative field. It is determined by the initial electric-field distribution in plasma, the number of particles, the degree of their chaotization, and the existence of crystallization centers. After the structure has been constructed, it influences the local plasma and discharge properties. After weak exposure, the structure is recovered at local equilibrium, while after intense exposure, it is determined by the fluctuation level and the degree of chaotization in the system.

REFERENCES

1. A. P. Nefedov, O. F. Petrov, and V. E. Fortov, Usp. Fiz. Nauk **167**, 1215 (1997) [Phys. Usp. **40**, 1163 (1997)].
2. V. E. Fortov, V. I. Molotkov, A. P. Nefedov, and O. F. Petrov, Phys. Plasmas **6**, 1759 (1999).
3. L. M. Vasilyak, S. P. Vetchinin, A. P. Nefedov, and D. N. Polyakov, Teplofiz. Vys. Temp. **38**, 701 (2000).
4. V. V. Balabanov, L. M. Vasilyak, S. P. Vetchinin, *et al.*, Zh. Éksp. Teor. Fiz. **119**, 99 (2001) [JETP **92**, 86 (2001)].
5. A. I. Osipov, *Self-Organization and Chaos* (Znanie, Moscow, 1986).
6. M. W. Thompson, Usp. Fiz. Nauk **99**, 297 (1969).
7. A. Melzer, T. Trottenberg, and A. Piel, Phys. Lett. A **191**, 301 (1994).
8. L. M. Vasilyak, S. V. Kostyuchenko, N. N. Kudryavtsev, and I. V. Filyugin, Usp. Fiz. Nauk **164**, 263 (1994) [Phys. Usp. **37**, 247 (1994)].

Translated by V. Astakhov

Journal of Experimental and Theoretical Physics, Vol. 94, No. 3, 2002, pp. 525–533.
Translated from Zhurnal Éksperimental'noĭ i Teoreticheskoĭ Fiziki, Vol. 121, No. 3, 2002, pp. 614–623.

PLASMA, GASES

Single-Photon Double Ionization of an Atom in a Strong Radiation Field

E. A. Volkova, A. M. Popov, and O. V. Tikhonova*

Skobel'tsyn Research Institute of Nuclear Physics, Moscow State University, Moscow, 119899 Russia

**e-mail: ovt@mics.msu.su*

Received September 19, 2001

Abstract—Double ionization is studied by direct numerical integration of the time-dependent Schrödinger equation for a model two-electron system in the field of an electromagnetic wave in the case when the photon energy exceeds the energy required for the removal of both electrons of the atom. The probabilities of single-electron and double ionization are obtained as functions of the radiation intensity. The energy spectra and double pulse distributions of photoelectrons are analyzed. It is shown that single-photon ionization plays a significant role only in the limiting cases of weak and strong fields. The obtained results are used in an analysis of the contributions from different channels to the double-ionization process (in particular, for clarifying the role of the electron–electron interaction). The results of numerical calculations are compared with the analytic model of the phenomenon. *© 2002 MAIK "Nauka/Interperiodica".*

1. INTRODUCTION

The development of high-power laser sources of electromagnetic radiation has resulted in the discovery and analysis of the effect of multielectron ionization of atoms in strong light fields [1]. The most significant feature of the effect is an anomalously large yield of doubly charged ions as compared to the model treating the double-ionization process as a sequence of the acts of ionization of an atom and a singly charged positive ion [2, 3]. None of the models proposed for explaining this feature of the effect ("shaking" [2], "rescattering" [4], and collective tunneling [5] models) provides an adequate description of the entire body of experimental data [1].

The process of formation of doubly charged ions in the laser radiation field has also been widely investigated recently by the method of direct numerical integration of the time-dependent Schrödinger equation describing a model two-electron system in an external electromagnetic field [6–13]. Although such calculations make it possible to visualize the detailed space and time pattern of the single- and double-ionization process, the contributions of various mechanisms to the probability of simultaneous photodetachment of two electrons remain unclear.

First experiments on double photoionization of atoms had been made long before high-power laser sources of radiation were created. The photoionization of atoms of inert gases by short-wave electromagnetic radiation was studied in [14, 15] under the conditions when the photon energy exceeded the energy of simultaneous photodetachment of two electrons from the outer shell of an atom. Under such conditions, two electrons can be removed upon the absorption of a single photon, the probability of this process being determined by the intensity of the correlation energy exchange between the electrons. A detailed theoretical analysis of single-photon double ionization was carried out in [16]. However, this analysis is in fact confined to perturbation theory and the self-consistent field approximation for atomic electrons. In strong electromagnetic fields, where multiphoton processes occur together with single photon processes, such approximations are obviously insufficient. It should also be noted that, according to [8, 17], the self-consistent field approximation based on the time-dependent Hartree or Hartree–Fock equations cannot be used for describing the multiphoton double ionization even on a qualitative level.

In the present work, the process of single and double photoionization of a model two-electron quantum system is investigated by the method of direct numerical integration of the time-dependent Schrödinger equation in the case when the energy $\hbar\omega$ of a quantum is sufficient for the removal of both electrons from the atom. The obtained results are used for studying various channels of double ionization. The results of calculations are compared with the analytical model of the effect.

2. NUMERICAL MODEL

In this work, we confine our analysis to a 1D two-electron quantum system simulating a negative hydrogen ion H^- and studied in detail in [9, 18, 19]. The Hamiltonian of the system was given in the form

$$H_0 = \sum_{i=1}^{2} (T_i + V(x_i)) + V_{12}(x_1, x_2), \qquad (1)$$

Table

n	1	2	3	4	5	6	7	8	9
E_n, eV	–11.45	–6.05	–3.85	–2.52	–1.74	–1.26	–0.96	–0.60	–0.41

where T_i is the kinetic energy of the ith electron,

$$V(x_i) = -\frac{e^2}{\sqrt{\alpha^2 + x_i^2}}$$

is the energy of its interaction with the nucleus, and

$$V_{12} = \frac{e^2}{\sqrt{\alpha^2 + (x_1 - x_2)^2}}$$

is the energy of the electron–electron interaction. For the value of the smoothing parameter $\alpha = 0.92$ Å, the energies required for the removal of the first and second electrons are $I_1 \approx 1.11$ eV and $I_2 \approx 11.45$ eV, respectively.

A detailed analysis of the model of a negative hydrogen ion under investigation and of its relation to 3D models was carried out in [9]. Among other things, it was proved in [9] that the system has a single bound state characterized by different sizes of the regions of spatial localization for the electrons. Indeed, if we try to present the wave function of the steady state of the system in the form of the symmetrized product of one-electron wave functions,

$$\varphi_0(x_1, x_2) = N[u(x_1)v(x_2) + u(x_2)v(x_1)]$$

(N is the normalization factor and $u(x) \neq v(x)$), we must assume that the coordinate dispersions calculated on the basis of functions u and v are different.[1] This means that the electron density of one of the electrons (the identity principle does not allow us to specify the electron exactly) is localized closer to the attracting center than that of the other electron. In other words, the model under investigation is a system with an expelled electron. In this sense, we will speak of the "outer" and "inner" electrons.

All excited states of our system belong to the continuum; among these states, we can single out the states of one- and two-electron continua. Following [9], we will approximately describe the states of the one-electron continuum by a symmetrized wave function of the form

$$\varphi_{nk}(x_1, x_2) = \frac{1}{\sqrt{2}} \times \left\{ \Phi_n(x_1)\frac{\exp(ikx_2)}{\sqrt{2\pi}} + \Phi_n(x_2)\frac{\exp(ikx_1)}{\sqrt{2\pi}} \right\}. \quad (2)$$

Here, $\Phi_n(x)$ is the wave function describing a one-electron (hydrogen) atom in the nth stationary state (the corresponding values of energy E_n are given in the table), and k is the wave vector of the electron in the continuum, which is connected with the energy through the relation $E = \hbar^2k^2/2m$.

An analysis of the temporal dynamics of the model H^- ion in the field of a wave was carried out on the basis of direct numerical integration of the time-dependent Schrödinger equation for the wave function of the system. In the dipole approximation, the interaction of the system with the field of an electromagnetic wave is determined by the operator

$$W = -e(x_1 + x_2)\varepsilon(t)\cos(\omega t), \quad (3)$$

where ε and ω are the amplitude and frequency of the field of the electromagnetic wave. In analogy with [9, 12, 13], the envelope $\varepsilon(t)$ has a smoothed trapezoidal shape, the durations of the generation pulse fronts and plateau being $t_f = 5T$ and $t_{pl} = 10T$, $T = 2\pi/\omega$.

The frequency of the external field was chosen corresponding to $\hbar\omega = 15$ eV, which is sufficient for single photon ionization of both atomic electrons. The mesh parameters and the size of the counting region were chosen in analogy with [12, 13]; this enabled us to calculate the wave function of the system over the entire pulse length in the absence of the probability flux absorption in the vicinity of the boundaries. The latter circumstance is important for calculating the energy spectra and the momentum distributions for photoelectrons.

All physical parameters of the system were calculated by using the function $\psi(x_1, x_2, t_0)$ obtained as a result of numerical integration of the time-dependent Schrödinger equation at instant t_0 corresponding to the end of the radiation pulse. In particular, the probability of finding the system in the bound state was defined as

$$W_0(t) = |C_0(t)|^2 = \left|\int \psi(x_1, x_2, t)\varphi_0(x_1, x_2)dx_1dx_2\right|^2, \quad (4)$$

where $\varphi_0(x_1, x_2)$ is the wave function of the ground state of the system.

The probabilities of single-electron ionization and the energy and momentum distributions for electrons were calculated using the function

$$\tilde{\psi}(x_1, x_2, t) = \psi(x_1, x_2, t) - C_0(t)\varphi_0(x_1, x_2)\exp\left\{-\frac{i}{\hbar}E_0t\right\} \quad (5)$$

[1] In the 3D case, such a situation is described, for example, by the Chandrasekhar wave function (see [9] and the literature cited therein).

(E_0 is the energy of the stationary state $\varphi_0(x_1, x_2)$) describing the state of the system in the one- and two-electron continua. The technique of the corresponding computations was considered in detail in [9].

For an analysis of the electron–electron energy exchange contribution to the ionization of the system, some of the calculations were made in the "passive" electron approximation which was used earlier to analyze double ionization by radiation in the visible frequency range [12, 13]. In this approximation, the interaction with an external field can be written in the form

$$W = -ex_1\varepsilon(t)\cos(\omega t), \qquad (6)$$

the ionization of the "passive" electron occurring only as a result of its interaction with the "active" electron.

3. DISCUSSION

Figure 1 shows the distributions of the probability density $|\psi(x_1, x_2)|^2$ at the instant corresponding to the end of a laser pulse for three values of radiation intensity. The results presented in the figure indicate that double ionization under the given conditions occurs mainly as a result of absorption of two field quanta by the system; we can assume that each electron absorbs only one quantum. Indeed, the structure of the electron density distribution $|\psi(x_1, x_2)|^2$ in the region corresponding to double ionization indicates that the ratio of the velocities of the photoelectrons is

$$v_2 : v_1 \approx 2 : 1,$$

which correlates well with the expression

$$\frac{E_2}{E_1} = \frac{v_2^2}{v_1^2} = \frac{\hbar\omega - I_1}{\hbar\omega - I_2} \approx 4 : 1,$$

obtained under the assumption of independent photoionization of the "outer" and "inner" electrons. Here, we assume that the energy required for the removal of the inner electron is equal to the ionization potential $I \approx$ 11.45 eV of a model hydrogen atom; i.e., this quantity is virtually independent of the presence of the outer electron. It should be noted that the process occurs consecutively in time: first, the outer electron is ionized, which leads to the emergence of a fast electron in the continuum and to the formation of a "cross" on the distribution $|\psi(x_1, x_2)|^2$, followed by the ionization of the inner electron. In this case, the continuum acquires an electron with a comparatively low energy $E_2 \approx \hbar\omega - I_2 \approx$ 3.5 eV, and a probability flux moving away from both coordinate axes is formed on the $|\psi(x_1, x_2)|^2$ distribution. The results presented in Fig. 1 lead to the conclusion that, at the instant of ionization of the second (inner) electron, the first electron is separated from the attracting center by approximately 10 Å and, hence, the delay in the emission of the second electron can be estimated at 0.3 fs. Such a delay corresponds to the duration of an optical cycle. It should be noted that, nevertheless, double ionization is a correlated process: the electrons fly apart only in opposite directions (this feature of the emission was also noted in [16]), which

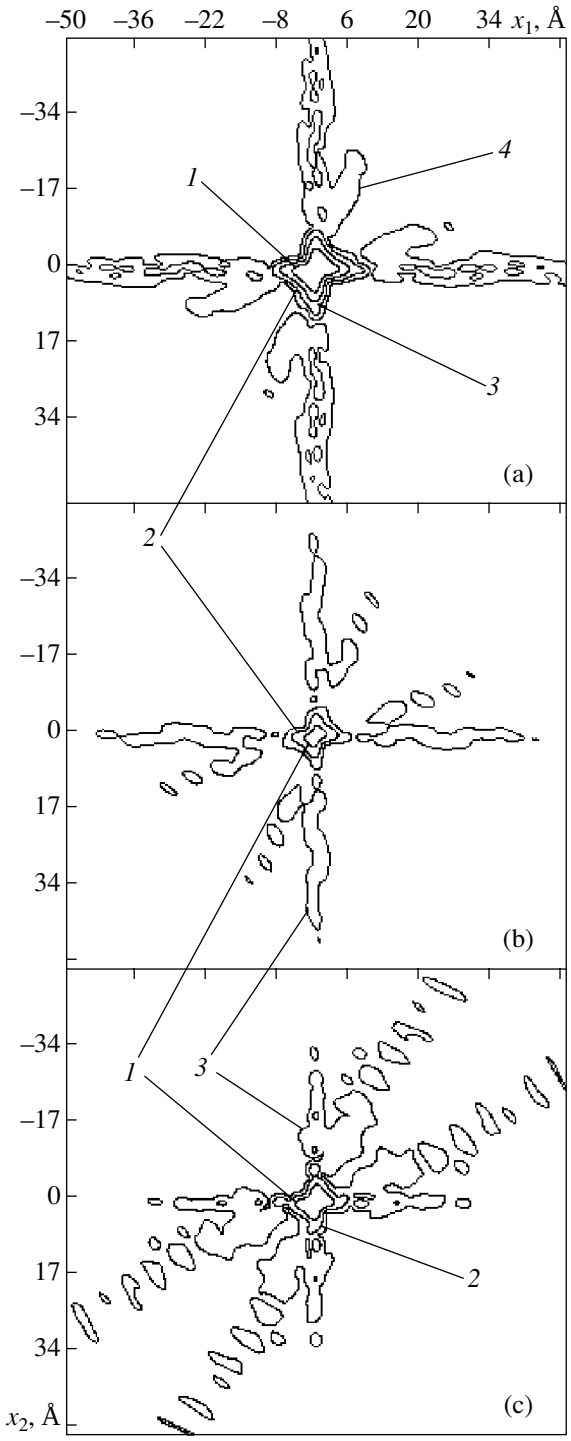

Fig. 1. Spatial distribution of the two-electron density $|\psi(x_1, x_2)|^2$ at the instant of termination of the external action for the radiation intensities (a) 10^{15}, (b) 10^{16}, and (c) 10^{17} W/cm^2. The level lines correspond to the following values: 10^{-2} (*1*), 10^{-3} (*2*), 10^{-4} (*3*), and 10^{-5} (*4*).

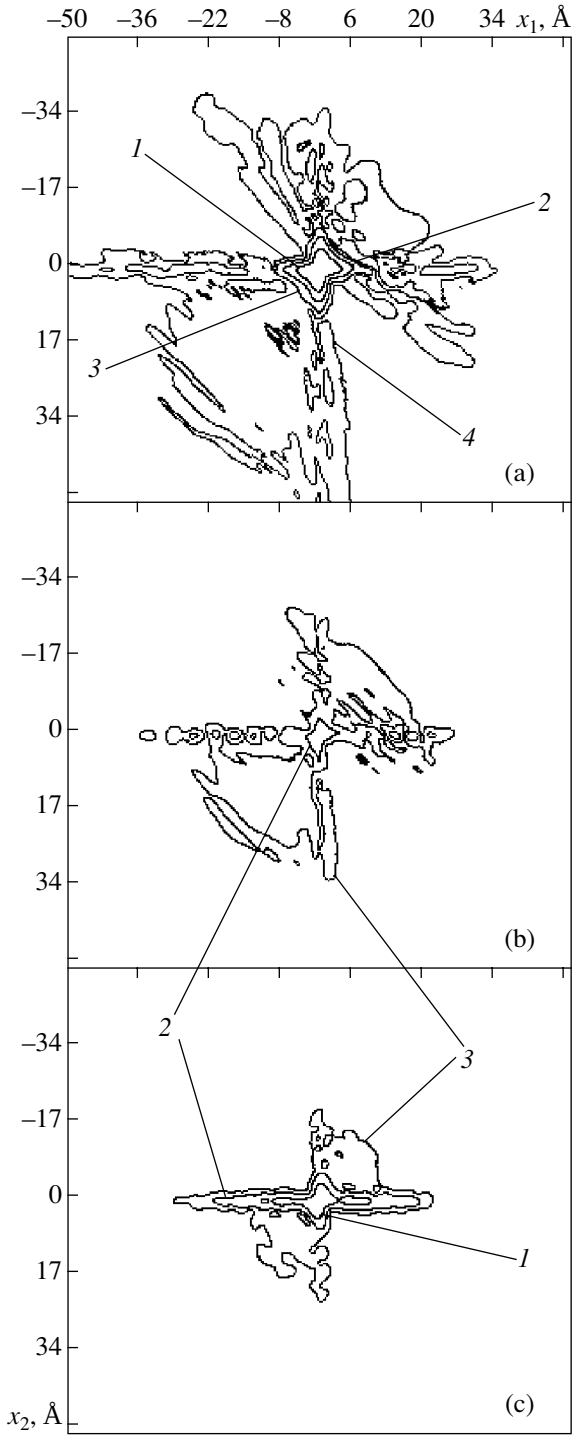

Fig. 2. The same as in Fig. 1, but in the "passive" electron approximation.

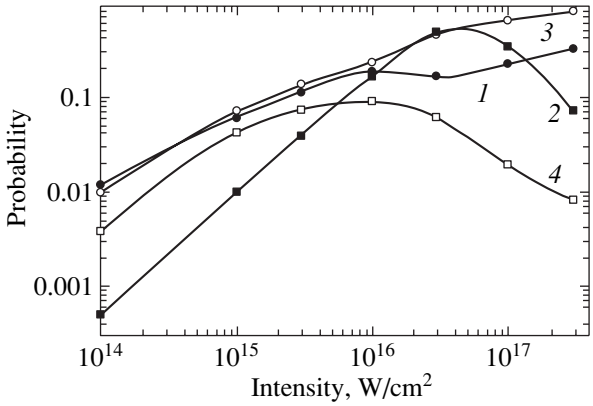

Fig. 3. Probabilities of single (*1*, *3*) and double (*2*, *4*) ionization of the system during a pulse as functions of the radiation intensity, obtained in exact calculations (*1*, *2*) and in the "passive" electron approximation.

necessitates the inclusion of the electron–electron interaction in the course of the photodetachment of the electrons.

Similar $|\psi(x_1, x_2)|^2$ distributions obtained in the "passive" electron approximation are presented in Fig. 2. These distributions indicate an intense energy exchange between electrons. By the instant of cessation of the action of the wave field, the absorbed energy is distributed between the electrons so that the obtained distributions $|\psi(x_1, x_2)|^2$ virtually cannot be used to determine which of the electrons was subjected to the external action. The only exception is the case of extremely strong fields (see Fig. 2c), in which the intensity of energy exchange proved to be noticeably lower, leading to predominant ionization of the "active" electron.

The probabilities of single and double ionization as functions of the radiation intensity, which were obtained from the solution of the Schrödinger equation (exact calculations and calculations in the "passive" electron approximation) are shown in Fig. 3. It should be noted that, in the region where single-electron ionization dominates $P \le 10^{16}$ W/cm^2), the probabilities of single-electron ionization in the "passive" electron model and in exact calculations virtually coincide. On the contrary, the probability of double ionization in the "passive" electron model is several times higher than in exact calculations. Thus, we can draw the following conclusion: in moderate fields, double ionization occurs as a result of the electron–electron energy exchange, while the action of the field of a wave on both electrons "hampers" the process. In the "passive" electron model, the action of the wave field on the bound "active" electron is apparently stronger than in exact calculations. As a result, the energy of vibrational motion of the active electron turns out to be higher, leading to an increase in the probability of ionization of the passive electron by an electron impact. Such a pattern of the process corresponds to the widely discussed "rescattering" model [4]. Thus, we can assume that, in the case under investigation, the action of the field on both electrons partly suppresses the effect of "rescattering."

On the other hand, in the region of strong fields ($P \ge 10^{16}$ W/cm^2), the probability of double ionization in the "passive" model decreases upon an increase in the

intensity, indicating a decreasing role of the energy exchange between the electrons. In exact calculations, double ionization turns out to be considerably stronger than in the "passive" electron approximation. However, a decrease in the total (single and double) ionization probability upon an increase in the intensity is also observed in exact calculations in the region $P \geq 10^{17}$ W/cm^2: the effect of stabilization relative to the ionization process takes place. Since the electron–electron interaction in this intensity range is weak, the stabilization effect is apparently of the one-electron origin and can be explained in the framework of the Kramers–Hennenberger formalism [20, 21].

The distribution over the quantum states of the remaining electron (Fig. 4), which was calculated for single-electron ionization, may serve as an additional confirmation of the fact that the system contains an "inner" and an "outer" electron ionized by an external field almost independently. The second peak for $n = 5$ appears as a result of the photodetachment of the inner electron, the probability of this process increasing with the radiation intensity.

The energy spectra of photoelectrons calculated as a result of expansion of the wave function $\tilde{\psi}(x_1, x_2)$ in functions (2) also indicate the independent photodetachments of the outer and inner electrons (see Fig. 5). The main peak *1* corresponds to the photodetachment of the outer electron; the hydrogen atom formed as a result of photoionization remains in the ground state. Peak *2* corresponds to the detachment of the inner electron, the hydrogen atom being in an excited state ($n = 4$, 5, 6). As the radiation intensity increases, this peak becomes higher. The presence of peak *3* corresponds to the photodetachment of an electron accompanied by the excitation of the remaining electron to the state with $n = 2$. The origin of this peak cannot be explained in the model of independent photoionization of the outer and inner electrons; it is associated with the correlation energy exchange between the electrons. Indeed, in the case under investigation, the energy absorbed by the system in the form of a quantum $\hbar\omega$ is distributed in a certain proportion between the electrons. As the radiation intensity increases, the role of this correlation process becomes smaller and the correlation peak *3* virtually vanishes for $P = 10^{17}$ W/cm^2.

Let us now analyze the momentum distributions of photoelectrons formed as a result of double ionization. These distributions were calculated at the instant of termination of the laser radiation action on the basis of the formula

$$W(k_1, k_2) = |\tilde{\psi}(k_1, k_2)|^2 \propto \left|\frac{1}{2}\int \tilde{\psi}(x_1, x_2)[\exp(-i(k_1x_1 + k_2x_2)) + \exp(-i(k_1x_2 + k_2x_1))]dx_1dx_2\right|^2. \quad (7)$$

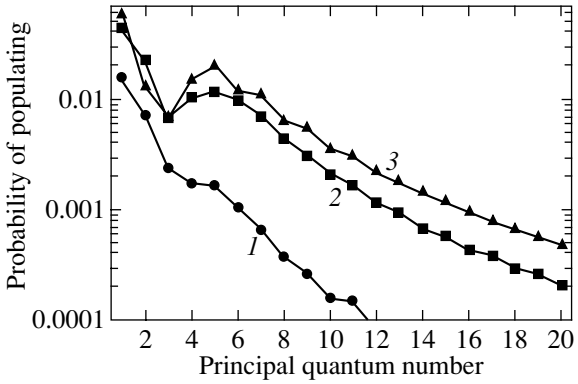

Fig. 4. Probabilities of populating various stationary states of the one-electron atom formed as a result of single-electron ionization of a two-electron system. The radiation intensities are 10^{15} (*1*), 10^{16} (*2*), and 10^{17} (*3*) W/cm^2.

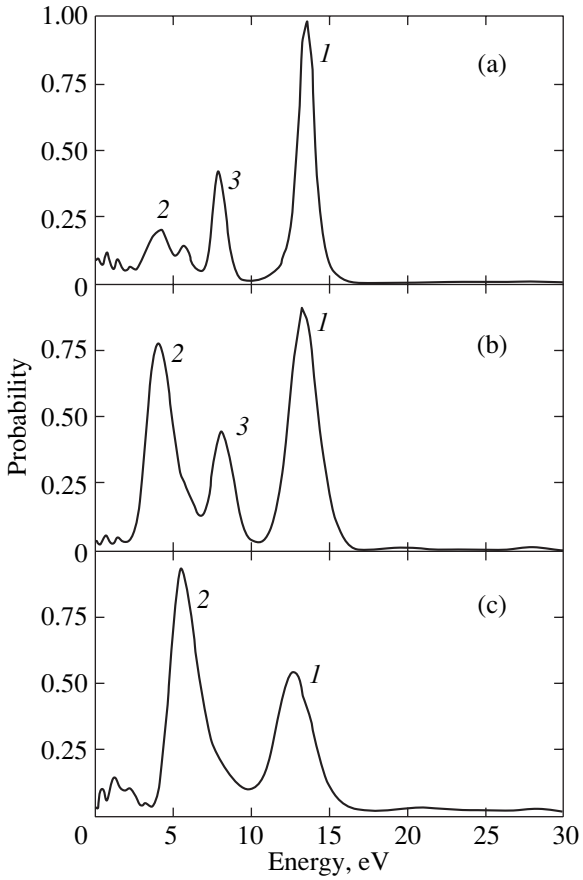

Fig. 5. Energy spectra of photoelectrons (in relative units) for radiation intensities (a) 10^{15}, (b) 10^{16}, and (c) 10^{17} W/cm^2. The numbers on the peaks are explained in text.

It was mentioned above that the momentum distributions take into account the states of one- and two-electron continua. The distributions obtained for various values of intensity are presented in Fig. 6. The electron densities corresponding to single-electron ionization

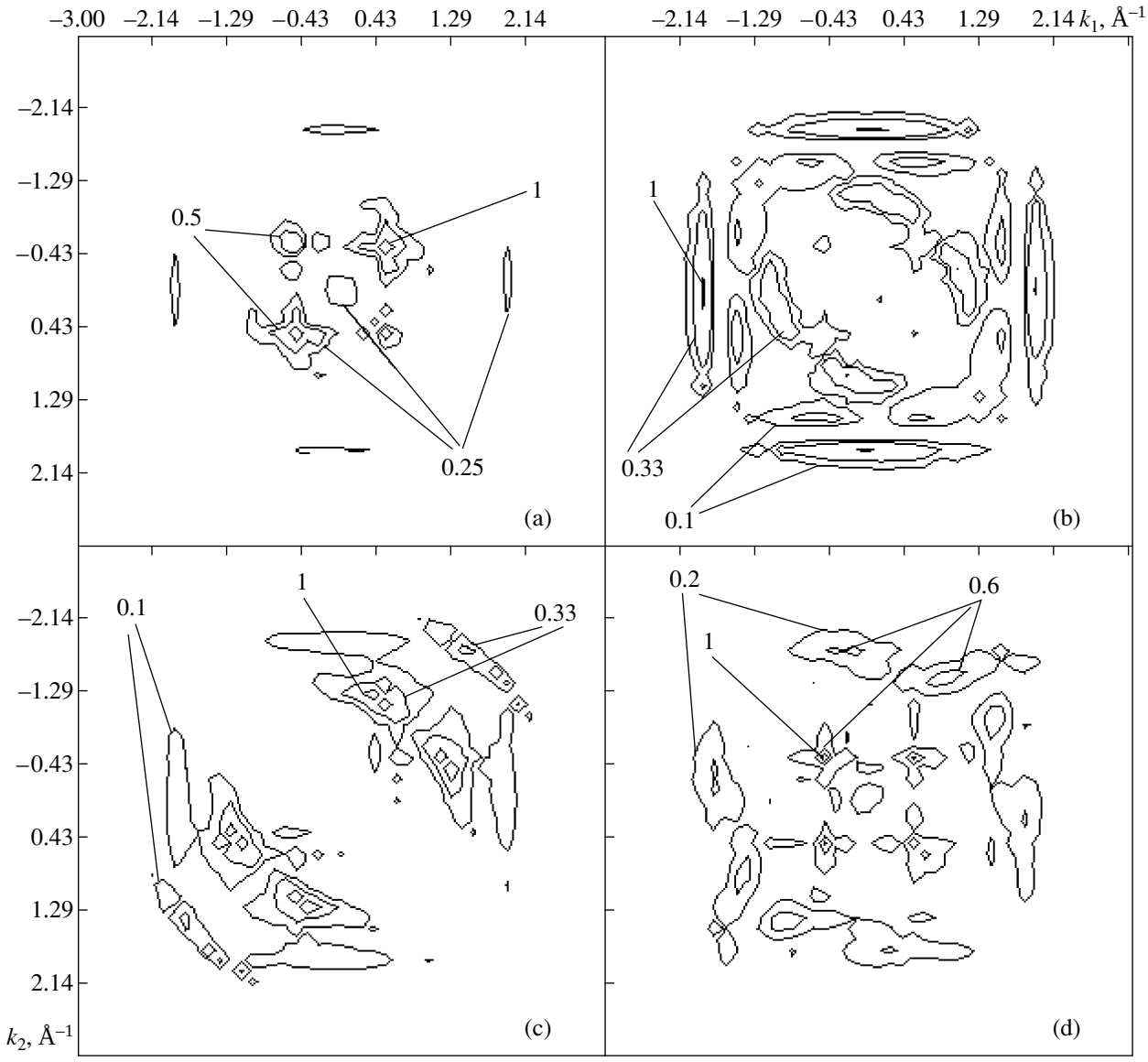

Fig. 6. Double momentum distributions $W(k_1, k_2)$ for electrons in the superposition of states of the one- and two-electron continua by the end of a pulse. The intensities are (a) 10^{14}; (b) 10^{15}; (c) 10^{17}; and (d) 3×10^{17} W/cm^2. The level lines (in relative units) are given in each figure.

determine the characteristic rectangular structure (which is manifested most clearly in Fig. 6b) formed due to the fact that one (bound) electron has a broad momentum distribution with zero average value, while the other (free) electron is characterized by the momentum

$$p = \sqrt{2m(\hbar\omega - |E_n|)}, \quad (8)$$

where E_n is the energy of the bound electron in the atom. For $P = 10^{15}$ W/cm^2 (Fig. 6b), the peaks corresponding to $n = 1, 2$ are manifested clearly. The double ionization corresponding to the absorption of two field quanta is obviously responsible for local peaks on the $W(k_1, k_2)$ distribution, which are at considerable distances from both coordinate axes. Such peaks emerge indeed (see Figs. 6b and 6c). At the same time, in extremely weak ($P = 10^{14}$ W/cm^2) and extremely strong ($P = 3 \times 10^{17}$ W/cm^2) fields, two slow electrons emerge in the continuum with a certain probability (see Figs. 6a and 6d). Obviously, these electrons cannot appear as a result of two-quantum absorption and are associated with the existence of the two-electron single-quantum process of photoionization. The distributions presented in the figures convincingly indicate that such a process is virtually absent in the intermediate intensity range ($P = 10^{15}$–10^{17} W/cm^2).

Similar conclusions also follow from the total momentum ($K = k_1 + k_2$) distributions for two electrons, which can be obtained from function $W(k_1, k_2)$ as a result of integration with respect to the relative momentum $k = k_1 - k_2$. These $W(K)$ distributions are presented in Fig. 7. The bifurcated structure of the peaks at $P = 10^{15}$ and 10^{17} W/cm^2 (see Figs. 7b and 7c) emerges as a result of single electron ionization: in this case, one electron has zero momentum on the average, and the total momentum is determined by the momentum of the electron in the continuum. As the radiation intensity increases (Fig. 7d), the role of double ionization becomes larger, and the position of the peak is determined by the difference in the absolute values of the photoelectron momenta (it should be recalled that the electrons fly apart in opposite directions). This leads to a displacement of the peak towards smaller values of K. At the same time, the structure of the function $W(K)$ in weak fields ($P = 10^{14}$ W/cm^2) is different in principle: slow electrons formed as a result of single-photon double ionization dominate in the distribution. A similar increase in the role of slow electrons is observed in extremely strong fields ($P = 3 \times 10^{17}$ W/cm^2). In this case, we can apparently speak of the competition of single- and double-photon double-ionization processes.

Let us analyze qualitatively the results obtained on the probabilities of single- and double-photon processes of double ionization. In the case of weak fields, when perturbation theory is applicable [16, 22], the expression for the amplitude of single-photon double ionization can be written in the form

$$M_{fi}^{(1)} \propto \sum_{kn}\left(\frac{\langle k_1, k_2|u|\varphi_{nk}\rangle\langle\varphi_{nk}|d\varepsilon|\varphi_0\rangle}{E_{kn} - E_0 - \hbar\omega} + \frac{\langle k_1, k_2|d\varepsilon|\varphi_{nk}\rangle\langle\varphi_{kn}|u|\varphi_0\rangle}{E_{kn} - E_0}\right). \quad (9)$$

Here, d is the dipole operator, $u = e^2/x_{12}$ is the electron–electron interaction operator, φ_0 and φ_{nk} are the wave functions of the ground state and of the one-electron continuum, E_0 and E_{kn} are the corresponding energies, and $|k_1, k_2\rangle$ are the states of the two-electron continuum.

Similarly, for the amplitude of a double-photon process, we have

$$M_{fi}^{(2)} \propto \sum_{kn}\left(\frac{\langle k_1, k_2|d\varepsilon|\varphi_{nk}\rangle\langle\varphi_{nk}|d\varepsilon|\varphi_0\rangle}{E_{kn} - E_0 - \hbar\omega}\right). \quad (10)$$

The first process, (9), is linear in the wave field strength, while the second, (10), is quadratic; consequently, single-photon ionization must dominate in weak fields. The ratio of the amplitudes of the process under investigation is determined by the ratio of the energy $d\varepsilon$ of interaction between an electron and the field to the energy $u = e^2/x_{12}$ of the electron–electron interaction. Assuming that $x_{12} \approx 4a_0$ and $d \approx 4ea_0$ for our system (a_0 is the Bohr radius), we obtain $M_{fi}^{(2)}/M_{fi}^{(1)} \approx 1$ for $P \approx 3 \times 10^{14}$ W/cm^2, which is in good agreement with the results of numerical calculations. Surprisingly, in extremely strong fields, the contribution of single-photon double ionization increases again. This fact is apparently associated with the stabilization relative to ionization in strong electromagnetic fields. Indeed, if the condition $d\varepsilon \gg e^2/x_{12}$ is satisfied, the motion of elec-

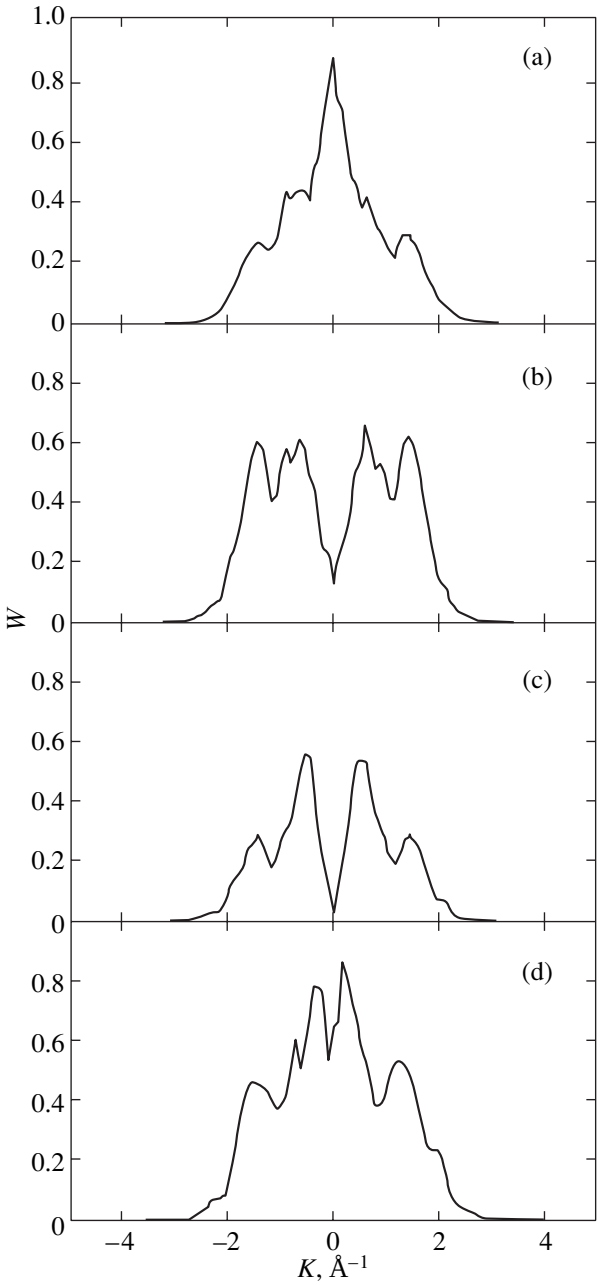

Fig. 7. Total momentum distribution $W(K)$ for two electrons in the superposition of the states of the one- and two-electron continua, corresponding to the instant of pulse termination. The intensities are (a) 10^{14}, (b) 10^{15}, (c) 10^{17}, and (d) 3×10^{17} W/cm^2.

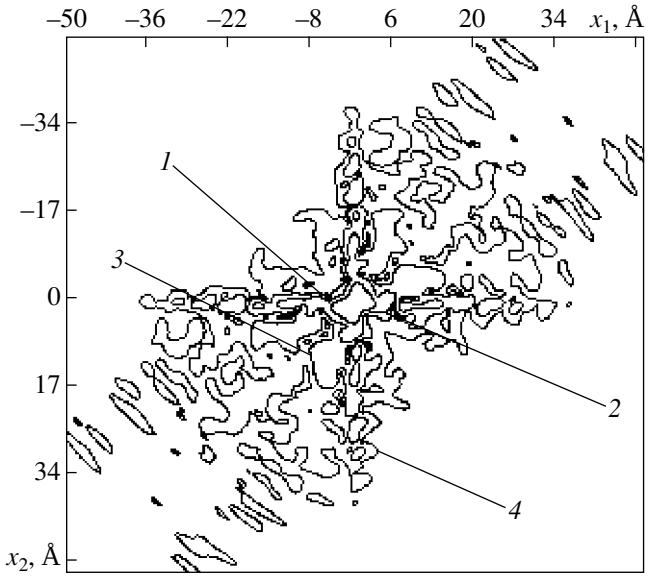

Fig. 8. Same as in Fig. 1, for a radiation intensity of 3×10^{17} W/cm^2.

trons in the first approximation can be regarded as independent. Under such conditions, double ionization can be regarded as a combination of two processes of single-electron ionization. If the stabilization threshold is exceeded, the probability of these two processes decreases upon an increase in the lasing intensity. Against such a background, the role of the electron–electron energy exchange increases again and, hence, the probability of single-photon double ionization also increases. In ultrastrong fields, when the amplitude of free electron vibrations in the field of the wave is larger than the characteristic atomic size, this energy exchange between the electrons can be interpreted in terms of the rescattering concept. The electron density distribution $|\psi(x_1, x_2)|^2$ obtained at the instant of termination of a radiation pulse of intensity $P \approx 3 \times 10^{17}$ W/cm^2 may serve as a qualitative confirmation of the change in the mechanism of double ionization in extremely strong fields (see Fig. 8). In addition to the characteristic structure indicating the presence of a fast and a slow electron (see the data presented in Fig. 1), photoelectrons with almost identical momenta and with an energy approximately equal to 1 eV also appear. In addition, along with the ejection of electrons in opposite directions, the probability of emission in the same direction becomes appreciable; this was considered in [23–25] as a confirmation of the "rescattering" effect.

4. CONCLUSIONS

In this work, the double ionization of a system under the conditions when the energy of a quantum exceeds the total binding energy of both electrons in the atom is considered. It is shown that, in a wide range of radiation intensities, double ionization occurs as a result of consecutive correlated absorption of two field quanta and is accompanied by the ejection of electrons in opposite directions. The strictly single-quantum process of double ionization is realized only in relatively weak fields, when the energy of interaction of an electron with the field of the wave is much lower than the energy of the electron–electron interaction. It is shown that, in extremely strong fields, the relative contribution of the energy exchange between the electrons to the double-ionization process also increases, leading to an increase in the probability of photodetachment of two electrons upon the absorption of a single quantum of the laser field. In the case of extremely strong fields, the vibrational energy of an electron is sufficient for ionizing the atomic electron by an electron impact, which can be regarded as a manifestation of the rescattering effect.

ACKNOWLEDGMENTS

This work was supported by the CRDF (grant no. RP1-2259) and the Russian Foundation for Basic Research (projects nos. 00-02-16046 and 00-15-96554).

REFERENCES

1. Opt. Express **8** (2001).
2. D. N. Fittinghoff, P. R. Bolton, B. Chang, and K. C. Kulander, Phys. Rev. Lett. **69**, 2642 (1992).
3. B. Walker, B. Sheehy, L. F. DiMauro, *et al.*, Phys. Rev. Lett. **73**, 1227 (1994).
4. P. B. Corcum, Phys. Rev. Lett. **71**, 1994 (1993).
5. U. Eichman, M. Dörr, H. Maeda, *et al.*, Phys. Rev. Lett. **84**, 3550 (2000).
6. R. Grobe and J. H. Eberly, Phys. Rev. Lett. **68**, 2905 (1992).
7. R. Grobe and J. H. Eberly, Phys. Rev. A **48**, 4664 (1993).
8. D. Bauer, Phys. Rev. A **56**, 3028 (1997).
9. E. A. Volkova, A. M. Popov, and O. V. Tikhonova, Zh. Éksp. Teor. Fiz. **114**, 1618 (1998) [JETP **87**, 875 (1998)].
10. W.-C. Liu, J. H. Eberly, S. L. Haan, and R. Grobe, Phys. Rev. Lett. **83**, 520 (1999).
11. M. Lein, E. K. U. Gross, and V. Engel, J. Phys. B **33**, 433 (2000).
12. E. A. Volkova, A. M. Popov, and O. V. Tikhonova, Zh. Éksp. Teor. Fiz. **118**, 816 (2000) [JETP **91**, 706 (2000)].
13. A. M. Popov, O. V. Tikhonova, and E. A. Volkova, Laser Phys. **11**, 236 (2001).
14. T. A. Carlson, Phys. Rev. **156**, 142 (1967).
15. J. A. R. Samson and G. N. Haddad, Phys. Rev. Lett. **33**, 875 (1974).
16. M. Ya. Amus'ya, *The Photoelectric Effect in Atoms* (Nauka, Moscow, 1987), Chap. 8.

17. A. M. Popov, O. V. Tikhonova, and E. A. Volkova, Laser Phys. **9**, 124 (1999).

18. A. I. Artemiev, R. Grobe, and J. H. Eberly, in *Proceedings of the 4th NATO Advanced Research Workshop on Super-Intense Laser-Atom Physics, SILAP-IV, Moscow, 1995*, Ed. by H. G. Muller and M. V. Fedorov (Kluwer, Dordrecht, 1996), p. 285.

19. S. L. Haan, R. Grobe, and J. H. Ebergy, Phys. Rev. A **50**, 378 (1994).

20. M. Pont and M. Gavrila, Phys. Rev. Lett. **65**, 2362 (1990).

21. A. M. Popov, O. V. Tikhonova, and E. A. Volkova, Laser Phys. **5**, 1029, 1184 (1995).

22. M. Ya. Amysia, Comments At. Mol. Phys., No. 10 (4), 155 (1981).

23. Th. Weber, M. Weckenbrock, A. Staudte, *et al.*, Phys. Rev. Lett. **84**, 443 (2000).

24. R. Moshammer, B. Feuerstein, W. Schmitt, *et al.*, Phys. Rev. Lett. **84**, 447 (2000).

25. S. P. Goreslavski and S. V. Popruzhenko, Opt. Express **8**, 395 (2001); J. Phys. B **34**, L239 (2001).

Translated by N. Wadhwa

Journal of Experimental and Theoretical Physics, Vol. 94, No. 3, 2002, pp. 534–544.
Translated from Zhurnal Éksperimental'noĭ i Teoreticheskoĭ Fiziki, Vol. 121, No. 3, 2002, pp. 624–636.

FLUIDS

Exact Solutions of the Equations of Motion of Liquid Helium with a Charged Free Surface

N. M. Zubarev

Institute of Electrophysics, Ural Division, Russian Academy of Sciences, ul. Komsomol'skaya 34, Yekaterinburg, 620016 Russia

e-mail: nick@ami.uran.ru

Received August 15, 2001

Abstract—The dynamics of the development of instability of the free surface of liquid helium, which is charged by electrons localized above it, is studied. It is shown that, if the charge completely screens the electric field above the surface and its magnitude is much larger than the instability threshold, the asymptotic behavior of the system can be described by the well-known 3D Laplacian growth equations. The integrability of these equations in 2D geometry makes it possible to describe the evolution of the surface up to the formation of singularities, viz., cuspidal point at which the electric field strength, the velocity of the liquid, and the curvature of its surface assume infinitely large values. The exact solutions obtained for the problem of the electrocapillary wave profile at the boundary of liquid helium indicate the tendency to a change in the surface topology as a result of formation of charged bubbles. © *2002 MAIK "Nauka/Interperiodica".*

1. INTRODUCTION

It is well known [1, 2] that the liquid helium surface may be charged to high values of the surface density of a negative electric charge. This is due to the fact that, on the one hand, electrons are attracted to the surface by weak electrostatic image forces and, on the other hand, the liquid helium boundary is a potential barrier for electrons, which prevents their penetration in the bulk. An important feature of liquid helium as a dielectric with a low polarizability is the relative weakness of the image forces, as a result of which the mean distance between localized electrons and the surface is much larger than the atomic spacing. Consequently, the electrons are not bound to individual atoms of the substance and form a two-dimensional conducting system.

The ability of electrons to move freely over the surface of liquid helium ensures the equipotential nature of this surface over characteristic hydrodynamic times and scales. A charged surface of a conducting liquid also possesses this property, the only difference being that the electric field cannot penetrate into a conducting medium, while liquid helium is not subjected to such a limitation. This enabled Gor'kov and Chernikova [3, 4] to extend a number of classical results from the theory of instability of a liquid metal surface in an external electric field [5–7] to the case of the charged boundary of liquid helium (the geometry of the system is shown schematically in Fig. 1). For example, a natural generalization of the dispersion relation for linear waves on the surface of a conducting liquid is the following dispersion relation for liquid helium:

$$\omega^2 = gk + \frac{\alpha}{\rho}k^3 - \frac{E^2 + E'^2}{4\pi\rho}k^2, \qquad (1)$$

where ω is the frequency, k is the wave number, g is the acceleration due to gravity, α is the surface tension, ρ is the density of the medium, and E' and E are the electric field strengths above the liquid and in the bulk of it, respectively ($E = 0$ for a conducting medium). It follows hence that for

$$E'^2 + E^2 < E_c^2 = 8\pi\sqrt{g\alpha\rho}$$

the inequality $\omega^2 > 0$ holds for any k and, hence, small perturbations of the surface do not build up with time. In the case when the sum of the squares of the fields $E'^2 + E^2$, which plays the role of an extrinsic controlling parameter, exceeds the critical value E_c^2, a region of wave numbers k for which $\omega^2 < 0$ is formed. This corresponds to an aperiodic instability of the liquid boundary.

The buildup of perturbations of the surface inevitably transforms the system to a state in which its evolution is determined by nonlinear processes. The nature

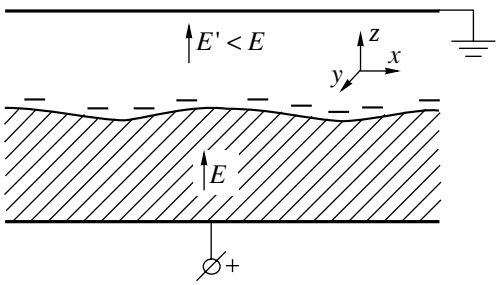

Fig. 1. Schematic diagram of the surface of liquid helium, charged by electrons, in a parallel-plate capacitor.

of their effect can be estimated most easily in the vicinity of the instability threshold, i.e., for a small supercriticality

$$\varepsilon = \frac{E^2 + E'^2 - E_c^2}{E_c^2},$$

when only perturbations with wave numbers close to $k_0 = \sqrt{g\rho/\alpha}$ increase and we can pass to envelopes in the equations of motion. For example, Gor'kov and Chernikova [8] proved that, in the case of the 2D symmetry of the problem, the complex amplitude $A(x, t)$ of perturbation of the surface obeys the nonlinear Klein–Gordon equation

$$(gk_0)^{-1}A_{tt} = 2\varepsilon A + k_0^{-2}A_{xx} + \left(2S^2 - \frac{5}{8}\right)A|A|^2, \quad (2)$$

where

$$S = \frac{E^2 - E'^2}{E_c^2}$$

is the dimensionless parameter characterizing the surface charge density. It can be seen from Eq. (2) that, depending on the value of parameter S, the nonlinearity either saturates the instability, or, conversely, facilitates a burst of the perturbation amplitude. A similar conclusion can also be drawn in the general (3D) case with a correction taking into account the fact that the nonlinearity in the first nonvanishing order plays a destabilizing role due to the interaction of three waves forming the hexagonal structure. As in the 2D case, cubic nonlinearities produce a stabilizing effect for small values of S [9, 10]. Consequently, for a low surface charge density (when the values of E and E' are close), a steady-state relief of the liquid helium boundary may be formed. In this case, the standard perturbation theory in the small parameter, viz., the characteristic slope of the surface, can be used for studying the structures being generated (see [11] and the literature cited therein).

The processes occurring in the supercritical region of electric fields and for relatively large electron surface charge screening the field above the liquid surface to a considerable extent have not been investigated in detail theoretically. This is due to the fact that, in these cases, the development of instability violates the small-angle approximation. For example, the analysis of the behavior of the charged boundary of liquid helium by high-speed microphotography carried out by Volodin *et al.* [12] proved that the dimples appearing on the surface are sharpened over a finite time (the bubbles which are subsequently formed at the tips carry the charge from the helium surface to the positive plate of the capacitor). In view of the considerable nonlinearity of such processes, their description requires the construction of solutions to the fundamental equations of the electrohydrodynamics of liquid helium.

In the present work, it will be shown that, when the condition $E \gg E'$, which corresponds to complete screening of the field above the liquid by the surface electron charge, is satisfied along with the condition that the electric field strength considerably exceeds the critical value, $E \gg E_c$, the equations of motion of liquid helium have an infinitely large number of exact analytic solutions. Their analysis has facilitated a considerable advance in the analysis of unsolved problems in the electrohydrodynamics of liquids with a free surface, which are associated with the formation of singularities (cusps) and with considerable changes in the surface geometry (formation of bubbles).

In Section 2, the equations of a vortex-free flow of liquid helium with a free surface charge are considered. In the limit of a strong electric field, when the effect of the force of gravity and capillary forces can be neglected, the approach to an analysis of the liquid helium dynamics proposed in our earlier work [13] is developed. This approach is based on the separation of two branches corresponding to solutions increasing and decreasing with time in the equations of motion. In Section 3, it is shown that the asymptotic behavior of the system is given by the well-known equations describing the Laplacian growth in the 3D geometry (the motion of the equipotential boundary with the velocity determined by the normal derivative of the harmonic potential). Section 4 is devoted to an analysis of the dynamics of the formation of cuspidal dimples on the helium surface in 2D geometry, when the Laplacian growth equations have an unlimited number of exact nontrivial solutions. The propagation of nonlinear surface waves in the short-wave region in which the surface pressure must be taken into account along with the electrostatic pressure is considered in Section 5. It is shown that the problem of the profile of a progressive electrocapillary wave at the liquid helium boundary has exact analytic solutions similar to the Crepper solutions for capillary waves [14]. These solutions are used for obtaining a nonlinear dispersion relation for surface waves of an arbitrary amplitude, whose analysis led to a number of conclusions concerning the stability of the charged surface of liquid helium to finite-amplitude perturbations and the domain of the existence of wave solutions to the electrohydrodynamic equations. In Section 6, the simplest axisymmetric solutions of the equations of motion, describing the pulling of the surface into the bulk of the liquid at a constant rate, are analyzed.

2. INITIAL EQUATIONS: THE LIMIT OF A STRONG FIELD

Let us consider the potential motion of an ideal dielectric liquid (liquid helium) with a free surface charged by electrons in an electric field. We assume that, in the unperturbed state, the boundary of the liquid is a flat horizontal surface $z = 0$ and the field vector is directed along the z axis of our system of coordinates

(Fig. 1). We introduce a function $\eta(x, y, t)$ specifying the deviation of the boundary from the plane. Then, the shape of the perturbed surface of liquid helium is described by the equation $z = \eta(x, y, t)$. The velocity potential Φ for an incompressible liquid satisfies the Laplace equation

$$\nabla^2\Phi = 0, \tag{3}$$

which must be supplemented with the dynamic boundary condition

$$\Phi_t + \frac{(\nabla\Phi)^2}{2} = \frac{E^2 - (\Delta\varphi)^2}{8\pi\rho} + \frac{\alpha}{\rho}\nabla_\perp\frac{\nabla_\perp\eta}{\sqrt{1 + (\nabla_\perp\eta)^2}} - g\eta, \tag{4}$$
$$z = \eta(x, y, t),$$

where φ is the electric potential in the liquid (we assume that the charge completely screens the field above the helium surface). The first term on the right-hand side of the time-dependent Bernoulli equation (4) is responsible for electrostatic pressure, the second is responsible, for the capillary pressure, and the third takes into account the effect of the field of gravity. We assume that the characteristic spatial scale of surface perturbations is smaller than the size of the region occupied by the liquid. In this case, we can write

$$\Phi \longrightarrow 0, \quad z \longrightarrow -\infty; \tag{5}$$

i.e., the motion of the liquid attenuates at infinity. The time evolution of the free surface is determined by the kinematics relation (the condition that the liquid does not flow through its boundary):

$$\eta_t = \Phi_z - \nabla_\perp\eta\nabla_\perp\Phi, \quad z = \eta(x, y, t). \tag{6}$$

Finally, the electric potential φ in the absence of space charges satisfies the Laplace equation

$$\nabla^2\varphi = 0, \tag{7}$$

which must be solved under the condition that the liquid helium boundary is equipotential and the field is uniform at an infinitely large distance from the surface:

$$\varphi = 0, \quad z = \eta(x, y, t), \tag{8}$$

$$\varphi \longrightarrow -Ez, \quad z \longrightarrow -\infty. \tag{9}$$

It should be noted that, in zero electric field ($E = 0$ and, hence, $\nabla\varphi = 0$), the above equations coincide with the equations of motion for a thick layer of liquid in the field of gravity.

Let the electric field strength exceed considerably its critical value ($E \gg E_c$) and let the following relation hold for the characteristic wavelength λ of surface waves:

$$\alpha E^{-2} \ll \lambda \ll \frac{E^2}{g\rho}.$$

It follows from the dispersion relation (1) that, in an analysis of small-amplitude surface perturbations, we can disregard the effect of both the capillary forces and the force of gravity. In Section 4, we will prove that this statement also holds for finite-amplitude surface perturbations. This means that we can omit the last two terms on the right-hand side of the boundary condition (4) and take into account the electrostatic pressure alone.

Now we pass to the dimensionless notation, assuming that the unit of length is equal to λ, the unit of electric field strength is E, and the unit of time is $\lambda E^{-1}(4\pi\rho)^{1/2}$. In this case, the equation of motion (3)–(9) assume the form

$$\nabla^2\varphi = 0, \quad \nabla^2\Phi = 0, \tag{10}$$

$$\Phi_t + (\nabla\Phi)^2/2 + (\nabla\varphi)^2/2 = 1/2, \quad z = \eta(x, y, t), \tag{11}$$

$$\eta_t = \Phi_z - \nabla_\perp\eta\cdot\nabla_\perp\Phi, \quad z = \eta(x, y, t), \tag{12}$$

$$\varphi = 0, \quad z = \eta(x, y, t), \tag{13}$$

$$\Phi \longrightarrow 0, \quad z \longrightarrow -\infty, \tag{14}$$

$$\varphi \longrightarrow -z, \quad z \longrightarrow -\infty. \tag{15}$$

Let us write these equations in the form which does not contain function η explicitly and introduce the perturbed harmonic potential $\tilde{\varphi} = \varphi + z$ attenuating at infinity ($\tilde{\varphi} \longrightarrow 0$ as $z \longrightarrow -\infty$). At the boundary, we have

$$\tilde{\varphi}|_{z=\eta} = \eta.$$

This readily leads to the relations

$$\eta_t = \left.\frac{\tilde{\varphi}_t}{1 - \tilde{\varphi}_z}\right|_{z=\eta}, \quad \nabla_\perp\eta = \left.\frac{\nabla_\perp\tilde{\varphi}}{1 - \tilde{\varphi}_z}\right|_{z=\eta},$$

which allow us to eliminate η from Eq. (12). The kinematic and dynamic boundary conditions (11) and (12) can be transformed to

$$\tilde{\varphi}_t - \Phi_z = -\nabla\tilde{\varphi}\cdot\nabla\Phi, \quad z = \eta(x, y, t),$$

$$\Phi_t - \tilde{\varphi}_z = -\frac{(\nabla\Phi)^2}{2} - \frac{(\nabla\tilde{\varphi})^2}{2}, \quad z = \eta(x, y, t).$$

Adding and subtracting these equations, we obtain

$$(\tilde{\varphi} + \Phi)_t - (\tilde{\varphi} + \Phi)_z = -\frac{(\nabla(\tilde{\varphi} + \Phi))^2}{2}, \quad z = \eta(x, y, t),$$

$$(\tilde{\varphi} - \Phi)_t + (\tilde{\varphi} - \Phi)_z = \frac{(\nabla(\tilde{\varphi} - \Phi))^2}{2}, \quad z = \eta(x, y, t);$$

i.e., the boundary conditions can be specified separately for the sum and the difference of the harmonic poten-

tials $\tilde{\varphi}$ and Φ. It is convenient to introduce a pair of auxiliary potentials

$$\phi^{(\pm)}(x, y, z, t) = \frac{\tilde{\varphi} \pm \Phi}{2}.$$

Using these potentials, we can write the equations of motion in the following symmetric form:

$$\nabla^2 \phi^{(\pm)} = 0, \tag{16}$$

$$\phi_t^{(\pm)} = \pm \phi_z^{(\pm)} \mp (\nabla \phi^{(\pm)})^2, \quad z = \eta(x, y, t), \tag{17}$$

$$\phi^{(\pm)} \longrightarrow 0, \quad z \longrightarrow -\infty, \tag{18}$$

while the shape of the liquid helium boundary is determined from the relation

$$\eta = (\phi^{(+)} + \phi^{(-)})\big|_{z = \eta}. \tag{19}$$

Thus, the equations of motion can be split into two systems of equations for potentials $\phi^{(+)}$ and $\phi^{(-)}$, the relation between which is given by the implicit equation for the shape of the surface (19). It is important that these equations are compatible with the condition $\phi^{(-)} = 0$ or with the condition $\phi^{(+)} = 0$. In the next section, we will show that the former condition corresponds to the solutions of the problem whose amplitude increases with time, while the latter (which is of no interest to us), to damped solutions.

The possibility of separating equations into individual branches is due to the symmetries of the electrohydrodynamic equations, which can be easily seen when the Hamilton formalism is used. Indeed, the equations of motion (10)–(15) for a liquid with a free surface possess a Hamilton structure, the functions $\eta(x, y, t)$ and $\psi(x, y, t) = \Phi|_{z = \eta}$ being canonically conjugate quantities [15],

$$\psi_t = -\frac{\delta H}{\delta \eta}, \quad \eta_t = \frac{\delta H}{\delta \psi},$$

where the Hamiltonian H coincides to within constants with the total energy of the system:

$$H = K + P, \quad K = \int\limits_{z \le \eta} \frac{(\nabla \Phi)^2}{2} d^3 r,$$

$$P = \int\limits_{z \le \eta} \frac{1 - (\nabla \varphi)^2}{2} d^3 r = -\int\limits_{z \le \eta} \frac{(\nabla \tilde{\varphi})^2}{2} d^3 r.$$

It should be recalled that the harmonic potentials Φ and $\tilde{\varphi}$ attenuate for $z \longrightarrow -\infty$ and their values on the surface are defined by the functions ψ and η, respectively. Consequently, if $\psi = \eta$, then $\Phi = \tilde{\varphi}$, and the kinetic energy functional K coincides, except for the sign, with the potential energy functional P. This allows us to write the Hamilton equations of motion using the functional K alone:

$$\psi_t = -\frac{\delta K}{\delta \eta} + \left(\frac{\delta K}{\delta \eta} + \frac{\delta K}{\delta \psi}\right)\Bigg|_{\psi = \eta}, \quad \eta_t = \frac{\delta K}{\delta \psi}.$$

It can be seen that, if we set $\psi = \eta$ in these equations, they will coincide. This means that the condition $\psi = \eta$ or (which is the same) the condition $\phi^{(-)} = 0$ is compatible with the equations of motion for liquid helium. Similarly, we can prove that the Hamilton equations coincide for $\psi = -\eta$, which corresponds to the condition $\phi^{(+)} = 0$. It should also be noted that the equations describing the evolution of the system on the branches $\phi^{(+)} = 0$ and $\phi^{(-)} = 0$ coincide except for the substitution $t \longrightarrow -t$, which is associated with the time reversibility in the Hamilton equations of motion. In this case, the conditions $\phi^{(\pm)} = 0$ single out the solutions of the problem for which H is equal to zero.

3. INCREASING BRANCH: STABILITY

In the linear approximation whose applicability is limited by the condition of the smallness of the slopes of the surface $|\nabla_\perp \eta| \ll 1$, the boundary conditions (17) assume the form

$$\phi_t^{(\pm)} = \pm \phi_z^{(\pm)}, \quad z = 0,$$

and Eqs. (16)–(19) split into two independent systems. The dispersion relations for these systems can be found by substituting potentials in the form

$$\phi^{(\pm)} \propto \exp(kz + i\mathbf{k} \cdot \mathbf{r}_\perp - i\omega t).$$

This gives

$$\omega^{(\pm)} = \pm ik$$

(the same result follows directly from the dispersion relation (1) considered in the strong field limit). It can be seen that, for one branch, small periodic perturbations of the surface increase exponentially with the characteristic times k^{-1}, while, for the other branch, these perturbations attenuate. In this case, for large periods of time, we can assume that $\phi^{(-)} = 0$ and consider only the equations for potential $\phi^{(+)}$. Let us prove that this statement is also valid in the general case, when the evolution of the surface is described by the nonlinear equations (16)–(19).

We assume that, in the nonlinear equations of motion (16)–(19),

$$\phi^{(+)} = \varphi + z, \quad \phi^{(-)} = 0,$$

which, in accordance with the results of linear analysis, isolates the solutions increasing with time. Passing to the moving fame of reference $\{x, y, z'\} = \{x, y, z - t\}$ in which the plane unperturbed surface of the liquid moves downwards (i.e., in the direction opposite to the

z' axis) at a constant velocity, after simple transformations, we obtain

$$\nabla^2\varphi = 0, \tag{20}$$

$$\eta'_t = \partial_n\varphi\sqrt{1 + (\nabla_\perp\eta')^2}, \quad z' = \eta'(x, y, t), \tag{21}$$

$$\varphi = 0, \quad z' = \eta'(x, y, t), \tag{22}$$

$$\varphi \longrightarrow -z', \quad z' \longrightarrow -\infty, \tag{23}$$

where $\eta'(x, y, t) = \eta - t$ and ∂_n denotes the derivative along the normal to the boundary of the liquid. These equations define explicitly the motion of the free charged surface of liquid helium $z' = \eta'(x, y, t)$. They coincide with the equations describing the so-called Laplacian growth, viz., the motion of the phase boundary with a velocity directly proportional to the normal derivative of a certain harmonic scalar field (φ in our case). Depending on the chosen frame of reference, this field may have the meaning of temperature (Stefan's problem in the quasi-stationary limit), electrostatic potential (electrolytic deposition), or pressure (flow through a porous medium).

Let us prove that the solutions of Eqs. (10)–(15) corresponding to system (20)–(23) are stable to small perturbations of potential $\phi^{(-)}$. It should be noted that the motion of the liquid boundary described by Eqs. (20)–(23) is always directed inwardly; this is associated with the principle of the extremum for harmonic functions. Let function η' at the initial instant $t = 0$ be a single-valued function of variables x and y. In this case, for $t > 0$, the following inequality holds:

$$\eta'(x, y, t) \le \eta'(x, y, 0).$$

In the original notation, we have

$$\eta(x, y, t) \le \eta(x, y, 0) + t \tag{24}$$

for any x and y. This inequality remains valid for small perturbations of $\phi^{(-)}$ also, when the effect of potential $\phi^{(-)}$ in relation (19) can be disregarded as compared to the effect of potential $\phi^{(+)}$, and the motion of the boundary is described by the same Eqs. (20)–(23).

As regards the evolution of potential $\phi^{(-)}$, it is described, for small $|\nabla\phi^{(-)}|$, by Eqs. (16)–(18), where it is sufficient to consider the condition (17) at the boundary in the linear approximation:

$$\phi_t^{(-)} = -\phi_z^{(-)}, \quad z = \eta(x, y, t).$$

Let us suppose that, at the initial instant $t = 0$, the potential distribution is described by the following expression:

$$\phi^{(-)}\big|_{t=0} = \phi_0(x, y, z),$$

where ϕ_0 is a certain function which is harmonic for $z \le \eta(x, y, 0)$ and attenuating for $z \longrightarrow -\infty$. In this case, the temporal dynamics of potential $\phi^{(-)}$ is described by the expression

$$\phi^{(-)} = \phi_0(x, y, z - t).$$

It can be seen from this expression that the singularities of the function $\phi^{(-)}$ are displaced in the direction of the z axis and can exist only in the region

$$z > \eta(x, y, 0) + t. \tag{25}$$

A comparison of this inequality with (24) shows that the singularities of potential $\phi^{(-)}$ do not approach the liquid helium boundary $z = \eta(x, y, t)$ and, hence, the value of the potential at the surface does not increase with time. It should be noted that, otherwise, the solution obtained by us for $\phi^{(-)}$ would be inapplicable.

In view of incompressibility of the liquid, the level of its surface (the value of function η averaged over the spatial variables) is not displaced. On the other hand, the boundary of the region defined by inequality (25) and averaged over x and y, in which the singularities of the function $\phi^{(-)}$ occur, moves upwards at a constant velocity. This means that the singularities move away from the surface of liquid helium and the perturbation of $\phi^{(-)}$ relaxes to zero.

Thus, we have proved that, as $t \longrightarrow \infty$, we have

$$\varphi(x, y, z, t) + z \longrightarrow \Phi(x, y, z, t),$$

and Eqs. (20)–(23) describe the asymptotic behavior of liquid helium with a charged surface in a strong electric field.

4. SOLUTIONS OF 2D EQUATIONS OF MOTION

In the previous section, we proved that the analysis of the 3D potential motion of liquid helium in a strong electric field can be reduced to an analysis of Eqs. (20)–(23) describing the three-dimensional Laplacian growth. The exact solvability of these equations in the 2D geometry will allow us to effectively study the dynamics of the development of instability of the charged surface of a liquid, including the formation of singularities in it.

We assume that, in the system of equations (20)–(23), all quantities are independent of variable y (variable y'). We introduce the function $w = v - i\varphi$ of the complex argument $Z = x + iz'$, which is analytic for $z' \le \eta'(x, t)$ (this is the so-called complex potential of the field correct to a constant factor). Here, v is a function harmonically conjugate to φ and such that the condition $v = \text{const}$ defines the lines of force of the electric field in the medium. Clearly, $w \longrightarrow Z$ as $Z \longrightarrow x - i\infty$.

It is convenient for the subsequent analysis to pass to a system of coordinates in which the role of the independent variable is played by quantity w and the role of the unknown function is played by function Z which is analytic in the lower half-plane of the complex variable

w (i.e., for $\varphi > 0$). It follows from condition (23) that the following condition holds at infinity:

$$Z \longrightarrow w, \quad w \longrightarrow v - i\infty. \tag{26}$$

We can also obtain the condition for Z at the boundary $\varphi = 0$ of the half-plane. The profile of the liquid helium surface can be specified by the parametric relations

$$z' = z'(v, t) = \eta'(x(v, t), t), \quad x = x(v, t).$$

Using these relations, we can easily express the normal velocity of the surface and the electric field strength appearing in formulas (21) in terms of the functions $z'(v, t)$ and $x(v, t)$:

$$\frac{\eta'_t}{\sqrt{1+\eta'^2_x}} = \frac{z'_t x_v - x_t z'_v}{\sqrt{z'^2_t + x^2_v}}, \quad \partial_n\varphi = -\frac{1}{\sqrt{z'^2_v + x^2_v}}.$$

Substituting these relations into the condition (21) at the surface, we obtain

$$z'_t x_v - x_t z'_v = -1,$$

or, which is the same,

$$\mathrm{Im}(Z^*_t Z_w) = 1, \quad w = v. \tag{27}$$

Thus, we arrive at the problem of determining the function Z, which is analytic in the lower half-plane of the complex variable w and satisfies conditions (26) and (27). The nonlinear condition (27) is the so-called Laplacian growth equation which is widely used for describing the 2D motion of the boundary between two liquids with noticeably different viscosities [16, 17], the evolution of the free surface of a liquid in the field of gravity [18, 19], and so on. The Laplacian growth equation is integrable in the sense that it has an infinitely large number of particular solutions of the form [20]

$$\begin{aligned} Z(w) = w - it - i\sum_{n=1}^{N} a_n \ln(w - w_n(t)) \\ + i\left(\sum_{n=1}^{N} a_n\right)\ln(w - w_0(t)). \end{aligned} \tag{28}$$

Here, a_n are complex constants, and the function of time w_n satisfies the condition $\mathrm{Im}(w_n) > 0$ (singularities of the function Z can only be in the upper half-plane of the complex variable w). The last term in expression (28) was supplemented to ensure the fulfillment of condition (26) and, hence, the condition of localization of the perturbation of the surface in a certain region: $\eta \longrightarrow 0$ for $|x| \longrightarrow \infty$. We can set $\mathrm{Im}(w_0) \gg \mathrm{Im}(w_n)$; in this case, the effect of this term on the evolution of the surface is negligibly small.

Substituting expression (28) into Eq. (27) and decomposing the obtained expression into simple fractions, we obtain a system of N ordinary differential equations for $w_n(t)$:

$$\dot{w}_n + i + i\sum_{m=1}^{N} a^*_m \frac{\dot{w}_n - \dot{w}^*_m}{w_n - m^*_m} = 0.$$

Integration with respect to t leads to the following N transcendental equations:

$$w_n + it + i\sum_{m=1}^{N} a^*_m \ln(w_n - w^*_m) = C_n,$$

where C_n are arbitrary complex constants.

Let us consider the simplest solutions of this type, which correspond to $N = 1$, $\mathrm{Re}(w_1) = 0$, and $a_1 = \pm 1$:

$$Z(w) = w - it \mp i\ln(w - iq(t)), \tag{29}$$

$$q(t) \pm \ln q(t) = 1 + t_c - t, \tag{30}$$

where $q = \mathrm{Im}(w_1)$ and t_c is a real constant. The form of a solitary perturbation corresponding to Eqs. (29) and (30) is specified by the parametric expressions

$$z(v, t) = z'(v, t) + t = \mp\ln\sqrt{v^2 + q^2(t)},$$

$$x(v, t) = v \pm \arctan\frac{v}{q(t)}.$$

Let us suppose that $a_1 = +1$ and we are dealing with a solitary perturbation of the surface, which is directed "upwards." It can be seen from Eq. (30) that for large values of t, the quantity $q \sim e^{-t}$ and, hence, the surface perturbation amplitude increases linearly with time: $z|_{v=0} \longrightarrow t$ as $t \longrightarrow \infty$. This is the "one-finger" solution of the Laplacian growth equation (see Fig. 2). It can easily be proved that similar solutions are possible in the 3D case also. It can be seen from Eqs. (20)–(23) describing the three-dimensional Laplacian growth that, if the surface initially contains a region in which the field strength $\partial_n\varphi$ is small (e.g., in the vicinity of the apex of a 3D fingerlike perturbation of the surface), its velocity in the coordinates $\{x, y, z'\}$ is also small. In the laboratory reference frame, this corresponds to a jet flowing at a constant velocity in the direction of the z axis.

Let us now consider a solitary perturbation of the surface, which is directed "downwards" ($a_1 = -1$, $q(t) \geq 1$). This solution exists only during a finite period of time, leading to the formation of a singularity on the liquid surface, viz., cuspidal point of the first kind (Fig. 3), at instant $t = t_c$. Indeed, expanding z and x into a power series in v and τ taking into account the fact that the function $q(t)$ in the vicinity of t_c satisfies the relation

$$q(t) \approx 1 + \sqrt{2}\tau, \quad \tau = t_c - t,$$

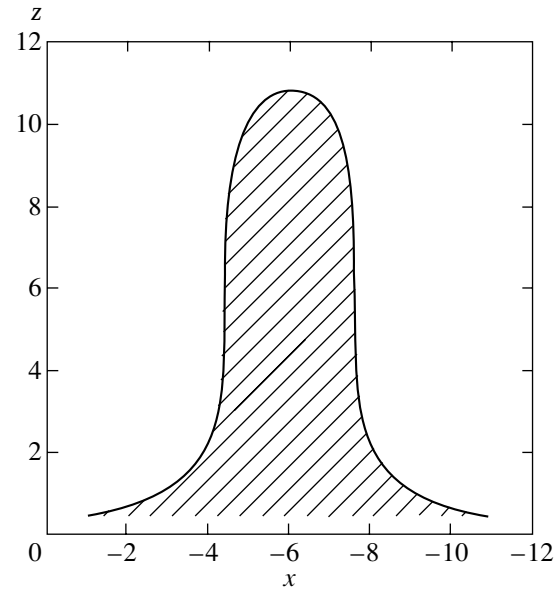

Fig. 2. The profile of the liquid helium surface, corresponding to the "one-finger" solution of the Laplacian growth equation; $a_1 = 1$, $q = 10^{-4}$, and $w_0 = 5i$.

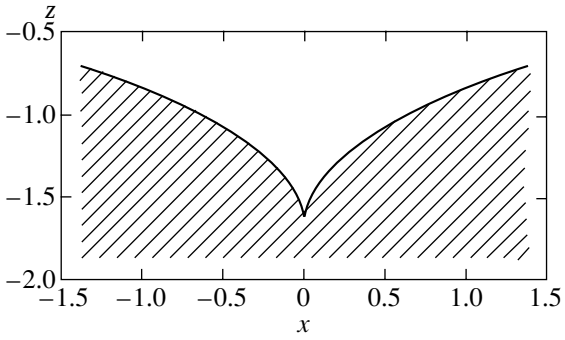

Fig. 3. The profile of the liquid helium surface at the instant of formation of a singularity (cusp); $a_1 = -1$, $q = 0.8$, and $w_0 = 4i$.

we obtain the following expressions in the main order:

$$z = \frac{v^2}{2} + \sqrt{2\tau}, \quad x = \frac{v^3}{3} + v\sqrt{2\tau}. \tag{31}$$

It can be seen that, at instant $\tau = 0$ (i.e., for $t = t_c$), the shape of the surface in the vicinity of a singular point is defined by the relation $2z = |3x|^{2/3}$, which corresponds to a cusp.[1] It was indicated in [17, 23] that the singularities of $z^3 \propto x^2$ are general-position singularities for processes described by the Laplacian growth equation. Similar solutions of the equations of motion for liquid helium with the charged boundary reflect the experimentally observed tendency [12, 24] to the emergence of dimples on the surface, which become sharpened over a finite time. From the mathematical point of view, the emergence of a singularity on the liquid surface is associated with vanishing of the Jacobian of the transformation $\{x, z'\} \longrightarrow \{v, \varphi\}$ for $\varphi = v = \tau = 0$. At a cusp, the electric field strength increases indefinitely along with the velocity of the surface over a finite time interval:

$$|\nabla\varphi| \sim x_v^{-1}\big|_{v=0} \propto \tau^{-1/2}, \quad |\nabla\Phi| \propto z_t\big|_{v=0} \propto \tau^{(-1/2)}.$$

It is important to note that the singular solution of the problem described by expressions (31) is also valid in the case when the field above the surface is not screened completely; i.e., the condition $E' \ll E$ does not hold. As a matter of fact, in the vicinity of a singularity, the condition of the smallness of the field above the surface as compared to the field in the bulk of the liquid naturally holds. In addition, the condition $\lambda \ll E^2/g\rho$ is not necessary. This is due to the fact that the amplitude of surface perturbations remains finite, and the effect of the gravity forces is always negligibly small in the vicinity of the cusp.

Let us now consider the capillary effects. The surface and electrostatic pressures in the vicinity of a singularity can be estimated easily:

$$P_S \propto \alpha\eta_{xx} \propto \alpha\rho^{1/2}E^{-1}\tau^{-1},$$

$$P_E \propto (\nabla\varphi)^2 \propto \lambda\rho^{1/2}E\tau^{-1}.$$

Here, we have returned to the dimensional notation. It can be seen from these expressions that, when the condition $\lambda \gg \alpha E^{-2}$ is satisfied, the capillary forces are small as compared to electrostatic forces and, hence, can be disregarded at the stage of formation of cusps. This is the only necessary condition of the applicability of the Laplacian growth equation and its solutions (31) in the vicinity of singularities.

5. ELECTROCAPILLARY WAVES

Let us consider the case when the characteristic length of surface waves is comparable with the value of αE^{-2} and the capillary effects must be taken into consideration. We assume that condition $E \gg E_c$ is satisfied; in this case, the effect of the force of gravity can be neglected. The dispersion relation (1) for electrocapillary waves at the charged boundary of liquid helium for $E' = 0$ in the dimensionless notation introduced in Section 2 assumes the form

$$\omega^2(k) = k^3 - k^2, \tag{32}$$

where the value of $\lambda = 4\pi\alpha E^{-2}$ is taken for unit length. It can be seen from Eq. (32) that $\omega^2 < 0$ for $k < 1$ and, hence, an aperiodic electrohydrodynamic instability of the liquid surface develops. If, however, the condition

[1] On the charged surface of a conducting liquid, for which $E = 0$ and $E' \neq 0$, in the limit of a strong field, weak root singularities of the type $z \propto |x|^{3/2}$ are formed, for which the curvature is equal to infinity, while the surface itself remains smooth [21, 22].

$k > 1$ holds, the frequency ω is real-valued, which corresponds to the propagation of linear dispersive waves.

The approach to the study of the evolution of a charged liquid surface based on the analysis of relation (32) is obviously applicable only in the case of small-amplitude perturbations of the boundary: $A \ll k^{-1}$. For finite-amplitude waves, the nonlinear effect may consist in the dependence of the dispersion relation on A (see, for example, [25]):

$$\omega = \omega(k, A).$$

The amplitude dependence of frequency is usually sought in the form of a power series in A (Stokes expansion), which limits the analysis to the weak-nonlinearity limit. Let us prove that, for electrocapillary waves, an exact solution to the nonlinear dispersion relation can be found.

The equations describing a progressive wave (whose profile does not change in the reference frame attached to the wave) can be obtained from the electrohydrodynamic equations (3)–(9) with the help of the following substitutions:

$$\varphi = \varphi(x', z), \quad \Phi = \Phi'(x', z) + Cx', \quad \eta = \eta(x'),$$

where $x' = x - Ct$ and constant C has the meaning of the velocity of a wave moving in the direction of the x axis. This gives

$$\Phi'_{x'x'} + \Phi'_{zz} = 0, \tag{33}$$

$$\varphi_{x'x'} + \varphi_{zz} = 0, \tag{34}$$

$$\frac{\Phi'^2_{x'} + \Phi'^2_z - C^2}{2} + \frac{\varphi^2_{x'} + \varphi^2_z - 1}{2} = \frac{\eta_{x'x'}}{(1 + \eta^2_{x'})^{3/2}}, \tag{35}$$

$$z = \eta(x'),$$

$$\Phi'_x = \eta_{x'}\Phi'_{x'}, \quad z = \eta(x'), \tag{36}$$

$$\varphi = 0, \quad z = \eta(x'), \tag{37}$$

$$\Phi' \longrightarrow -Cx', \quad z \longrightarrow -\infty, \tag{38}$$

$$\varphi \longrightarrow -z, \quad z \longrightarrow -\infty. \tag{39}$$

These equations can be simplified by introducing the function of current $\Psi(x', z)$, which is harmonically conjugate to potential Φ':

$$\Psi_{x'} = -\Phi'_z, \quad \Psi_z = \Phi'_{x'}.$$

This function satisfies the Laplace equation

$$\Psi_{x'x'} + \Psi_{zz} = 0 \tag{40}$$

with the boundary conditions

$$\Psi = 0, \quad z = \eta(x'), \tag{41}$$

$$\Psi \longrightarrow -Cz, \quad z \longrightarrow -\infty, \tag{42}$$

which follow from relations (36) and (38). It can easily be seen that Eqs. (40)–(42) coincide with the Eqs. (34), (37), and (39) for the electric potential. Consequently, the following functional relation exists:

$$\Psi = C\varphi.$$

Using this relation, we can considerably simplify the Bernoulli equation (35), which assume the form

$$\frac{C^2 + 1}{2}(\varphi^2_{x'} + \varphi^2_z - 1) = \frac{\eta_{x'x'}}{(1 + \eta^2_{x'})^{3/2}}, \tag{43}$$

$$z = \eta(x').$$

In combination with relations (34), (37), and (39), this condition completely defines the shape of a wave propagating in the coordinate system $\{x', z\}$.

Equations (34), (37), (39), and (43) coincide except for constant factors with the equations describing the shape of a progressive capillary wave [14] and an equilibrium configuration of the charged surface of a liquid metal [26]. These equations have exact periodic solutions for which the boundary of the liquid is defined by the parametric expressions

$$z = \frac{4k^{-2}}{2(C^2 + 1)^{-1} + A\cos(kp)} + z_0, \tag{44}$$

$$x' = p - \frac{2Ak^{-1}\sin(kp)}{2(C^2 + 1)^{-1} + A\cos(kp)} + x'_0, \tag{45}$$

where z_0 and x'_0 are constants, p is a parameter (the value of p changes over a period by $2\pi/k$), and the quantity A has the meaning of the amplitude of a surface perturbation; i.e., $A = (z_{max} - z_{min})/2$. The dependence of A on k and C is specified by the relation

$$A = \left[\frac{4}{(C^2 + 1)^2} - \frac{4}{k^2}\right]^{1/2}. \tag{46}$$

It was mentioned in [14] that solutions (44) and (45) exist only for

$$1 \le \frac{k}{C^2 + 1} \le \gamma,$$

where $\gamma \approx 1.52$.

Considering that C is the phase velocity of the wave, we set $C = \omega/k$ in relation (46). Solving the obtained equation for frequency ω, we arrive at the exact nonlinear dispersion relation

$$\omega^2(k, A) = \frac{k^3}{\sqrt{1 + A^2k^2/4}} - k^2 \tag{47}$$

and the conditions of its applicability

$$k^3\gamma^{-1} \le \omega^2 - k^2 \le k^3. \tag{48}$$

It can be seen that, in the limit of infinitely small amplitudes ($A \longrightarrow 0$), expression (47) is transformed into the linear dispersion relation (32). Let us consider the con-

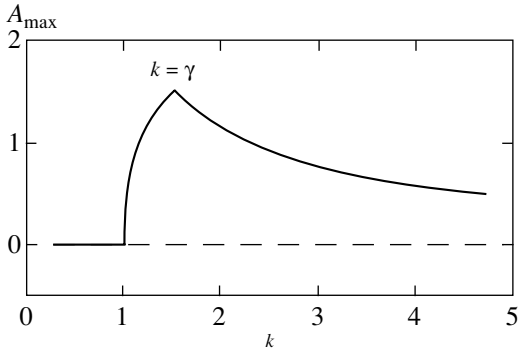

Fig. 4. The maximum value of amplitude A_{max} of an electrocapillary wave on the charged surface of liquid helium as a function of the wave number k. For $k < \gamma$, the peak corresponds to the value of $\omega = 0$, while, for $k > \gamma$, the frequency differs from zero.

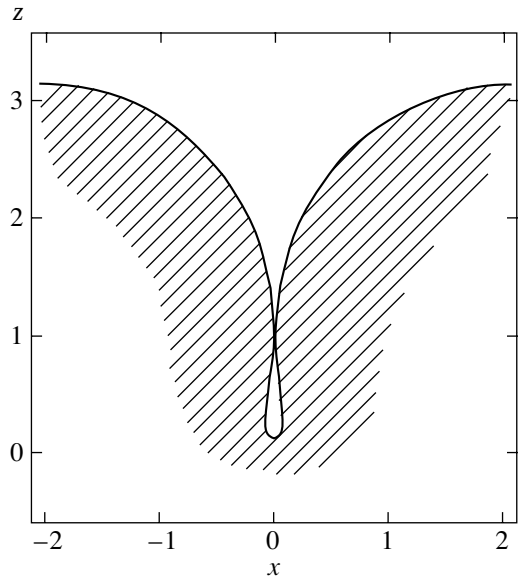

Fig. 5. A period of the steady-state profile of a charged surface of liquid helium for $k = \gamma$. For this value of the wave number, the amplitude of the electrocapillary wave attains its maximum value.

sequences of this nonlinearity. It can be seen from relation (47) that, for a fixed wave number $k \geq 1$, the maximum value of the surface perturbation amplitude $A_{max}(k)$ corresponds to the minimum possible value of ω^2. It follows from conditions (48) that, for $1 \leq k \leq \gamma$, the value of $\omega_{min}^2 = 0$, which corresponds to a wave with zero velocity. In this case, expressions (44) and (45) define the solution of the problem on the steady-state profile of the charged surface of liquid helium. For $k > \gamma k_1$, the amplitude has the maximum value for electrocapillary waves propagating at the velocity

$$C = \sqrt{k\gamma^{-1} - 1};$$

in this case,

$$\omega_{min}^2 = k^3\gamma^{-1} - k^2.$$

This gives

$$A_{max}(k) = \begin{cases} 0, & 0 \leq k < 1, \\ 2\sqrt{1 - k^{-2}}, & 1 \leq k \leq \gamma, \\ 2k^{-1}\sqrt{\gamma^2 - 1}, & k > \gamma \end{cases}$$

(the curve describing this dependence is presented in Fig. 4). If the amplitude exceeds this value, expressions (44) and (45) describe a self-intersecting surface, which cannot be realized from the physical considerations, or $\omega^2 < 0$, which corresponds to an incorrectly formulated problem in the context of wave propagation. This leads to the assumption that the condition $A(k) > A_{max}(k)$ is the criterion of hard excitation of electrohydrodynamic instability of a plane charged surface of liquid helium, which generalizes the simplest linear instability criterion $k < 1$ to the case of finite-amplitude perturbations.

It should be noted that the peak of the function $A_{max}(k)$ corresponds to $k = \gamma$. The shape of the liquid surface corresponding to this value of the wave number is depicted in Fig. 5. It can be seen that the liquid acquires cavities. Such solutions reflect the tendency to the formation of charged bubbles (referred to as bubblons in the experimental work [12]) on cuspidal dimples of the liquid helium boundary. The main mechanism of departure of electrons from the surface is associated with the generation of such bubbles.

6. AXISYMMETRIC SOLUTIONS

Let us consider the evolution of the charged surface of liquid helium in an important case of the axial symmetry of the problem. The equations of motion (20)–(23) corresponding to the increasing branch of the solutions to system (10)–(15) in the cylindrical coordinates $\{r, z'\} = (r, z - t)$ assume the form

$$\varphi_{rr} + r^{-1}\varphi_r + \varphi_{z'z'} = 0,$$

$$\eta_t' = -(\varphi_r^2 + \varphi_{z'}^2)^{1/2}(1 + \eta_r'^2)^{1/2}, \quad z' = \eta'(r, t),$$

$$\varphi = 0, \quad z' = \eta'(r, t),$$

$$\varphi \longrightarrow -z', \quad z' \longrightarrow -\infty.$$

Here, $r = \sqrt{x^2 + y^2}$ and we have taken into account the fact that $\partial_n\varphi = -|\nabla\varphi|$ at the equipotential boundary in condition (21).

At essentially nonlinear stages of the formation of a dimple on the surface of a liquid, we can assume that the electric field in the region of a large curvature of the surface is much stronger than the external field, $|\nabla\varphi| \gg 1$. In this case, the dynamics of the boundary $\eta' = \eta - t$ is

completely determined by the intrinsic field rapidly attenuating with increasing distance, which allows us to use the condition $|\nabla\varphi| \longrightarrow 0$ for $z \longrightarrow -\infty$ instead of the condition of field uniformity. We will also assume that the velocity of the liquid surface is considerably higher than the velocity of the origin in the laboratory reference frame (i.e., $|\eta_t| \gg 1$). In this case, we can substitute η for η' and z for z' in the equations of motion. This gives

$$\varphi_{rr} + r^{-1}\varphi_r + \varphi_{zz} = 0, \quad z < \eta(r, t), \tag{49}$$

$$\varphi_t = -\varphi_r^2 - \varphi_z^2, \quad z = \eta(r, t), \tag{50}$$

$$\varphi = 0, \quad z = \eta(r, t), \tag{51}$$

$$\varphi_r^2 + \varphi_z^2 \longrightarrow 0, \quad r^2 + z^2 \longrightarrow \infty. \tag{52}$$

In relations (50), we have used the following conditions at the boundary of the liquid:

$$\eta_t = -\frac{\varphi_t}{\varphi_z}, \quad \eta_r = -\frac{\varphi_r}{\varphi_z}.$$

The conditions for the applicability of this approximation will be considered at the end of this section.

A particular solution of Eqs. (49)–(52) can be obtained by using a substitution similar to that used in [27] for constructing the axisymmetric solutions of the Stefan problem:

$$\varphi(r, z, t) = f(u(r, z, t)), \tag{53}$$

$$u(r, z, t) = -z - Vt + \sqrt{r^2 + (z + Vt)^2}, \tag{54}$$

where the constant V has the meaning of the inward-directed velocity of the liquid surface. It can easily be seen that the equipotential surfaces corresponding to Eqs. (53) and (54) form a family of confocal paraboloids of revolution:

$$r^2 = 2u(z + Vt) + u^2 \tag{55}$$

with the focus at the point $r = 0$ and $z = -Vt$.

Substituting expressions (53) and (54) into Eq. (49), we arrive at the following ordinary differential equation:

$$uf_{uu} + f_u = 0. \tag{56}$$

It follows from Eqs. (50) and (51) that the boundary conditions to this equation have the form

$$f_u(u_0) = \frac{V}{2}, \quad f(u_0) = 0. \tag{57}$$

Here, u_0 is the value of parameter u at the surface of the liquid. Henceforth, we will use the quantity $K = 1/u_0$ which, in accordance with Eq. (55), defines the curvature of the liquid surface at the symmetry axis. Solving Eqs. (56) and (57), we obtain

$$f(u) = \frac{V\ln(Ku)}{2K}, \tag{58}$$

which, together with Eqs. (53) and (54), describes the time evolution of the electric potential. It should be noted that condition (52) is naturally satisfied. The shape of the surface for the given exact solution of the equations of motion (49)–(52) is defined by the relation

$$\eta(r, t) = \frac{Kr^2}{2} - Vt - (2K)^{-1}, \tag{59}$$

which corresponds to a needle-shaped dimple pulled into the bulk of the liquid at velocity V. Such a geometry of the surface perturbation can be regarded as the simplet (paraboloidal) approximation of the shape of the liquid boundary at essentially nonlinear stages of the development of instability of the charged boundary of the liquid.

It should be recalled that the applicability of approximation (49)–(52) of the initial system (20)–(23) is limited by the conditions

$$|\eta_t| \gg 1 \text{ and } |\nabla\varphi| \gg 1.$$

Since $\eta_t = -V$ in solutions (59) for any r and t, the first condition is reduced to the inequality $V \gg 1$ (in the dimensional notation, $V \gg E\sqrt{4\pi\rho}$). As regards the second condition, we can find the characteristic size D of the region in which the electric field created by a charged paraboloidal surface exceeds the external field. It follows from relations (53), (54), and (58) that the field distribution in the liquid is described by the relation

$$|\nabla\varphi| = \frac{V}{K\sqrt{2Ru}}.$$

Here, $R = \sqrt{r^2 + (z + Vt)^2}$ is the distance to the focus of the paraboloid; i.e., the field attains it maximum value equal to V at the point $r = 0$ and $z = -Vt - (2K)^{-1}$. Since the field strength generally decreases in proportion to R^{-1} with increasing distance from the focus, the scale of D can be estimated as $D \propto V/K$. It should be noted that such a conclusion makes sense only if the value of D is much larger than the radius of the curvature K^{-1} of the surface perturbation. This requirement again leads us to the inequality $V \gg 1$.

Thus, we have obtained partial axisymmetric solutions to the equations of motion of liquid helium with a charged surface, which describe the evolution of a localized perturbation of the surface with a considerable curvature, and have determined the conditions of their applicability. However, the obtained solutions should not be regarded as general-position solutions. In all probability, solutions of the burst type, for which the surface becomes indefinitely cuspidate over a finite time interval, will dominate as in the 2D case.

7. CONCLUDING REMARKS

In the absence of a surface charge, the equations of electrohydrodynamics of liquid helium considered by us are transformed into the well-known equations of a vortex-free flow of an incompressible liquid with a free boundary. These equations are extremely difficult to analyze, and the methods for their solution have not been developed at present. In this work, we succeeded in proving that the inclusion of the electrostatic pressure does not complicate the analysis of these equations. On the contrary, the emergence of an additional term in the dynamic boundary condition introduces a certain symmetry into the equations so that they become compatible with the conditions $\varphi + z = \pm\Phi$. The emerging functional relation between the potentials of velocity and of the electric field makes it possible to reduce by half the number of equations required for describing the motion of the surface and, in the long run, to find a wide class of exact solutions of the equations of motion of liquid helium with the boundary charged by electrons. It is important that the solutions obtained by us are not limited by the condition of the smallness of surface perturbations; they describe the evolution of the liquid boundary up to the formation of cuspidal points in it.

The dynamics of the formation of singularities in the case when the characteristic scale λ of surface perturbations is comparable with the value of αE^{-2} and the capillary effects must be taken into consideration has not been considered by us here. In 2D geometry, such an analysis can be carried out using the methods of investigations of 2D potential flows with a free boundary, which was proposed in [28, 29] and is based on conformal mapping of the region occupied by the liquid to a half-plane. In terms of the present work, such a transformation corresponds to the use of the field potential φ and its harmonically conjugate function v as independent variables. In the case of the axial symmetry of the problem (such a geometry reflects the experimentally observed phenomena [12, 24] most correctly), the formation of singularities can be described by self-similar solutions of the electrohydrodynamic equations, which are analogous to those considered in the recent publication [30] devoted to the formation of conic tips on the surface of a liquid metal in an external electric field. In accordance with the self-similar scenario of the development of instability, conical dimples with an angle of 98.6° appear on the surface over a finite time. A detailed analysis of these processes calls for further investigations.

ACKNOWLEDGMENTS

The author is grateful to V.E. Zakharov and E.A. Kuznetsov for their interest in this research.

This work was supported by the Russian Foundation for Basic Research (project no. 00-02-17428), INTAS (grant no. 99-1068), and the Russian Academy of Sciences (Sixth Competition of Projects Presented by Young Scientists in 1999, grant no. 63).

REFERENCES

1. M. W. Cole and M. H. Cohen, Phys. Rev. Lett. **23**, 1238 (1969).
2. V. B. Shikin, Zh. Éksp. Teor. Fiz. **58**, 1748 (1970) [Sov. Phys. JETP **31**, 936 (1970)].
3. L. P. Gor'kov and D. M. Chernikova, Pis'ma Zh. Éksp. Teor. Fiz. **18**, 119 (1973) [JETP Lett. **18**, 68 (1973)].
4. D. M. Chernikova, Fiz. Nizk. Temp. **2**, 1374 (1976) [Sov. J. Low Temp. Phys. **2**, 669 (1976)].
5. L. Tonks, Phys. Rev. **48**, 562 (1935).
6. Ya. I. Frenkel', Zh. Éksp. Teor. Fiz. **6**, 347 (1936).
7. L. D. Landau and E. M. Lifshitz, *Course of Theoretical Physics*, Vol. 8: *Electrodynamics of Continuous Media* (Nauka, Moscow, 1982; Pergamon, New York, 1984).
8. L. P. Gor'kov and D. M. Chernikova, Dokl. Akad. Nauk SSSR **228**, 829 (1976) [Sov. Phys. Dokl. **21**, 328 (1976)].
9. H. Ikezi, Phys. Rev. Lett. **42**, 1688 (1979).
10. D. M. Chernikova, Fiz. Nizk. Temp. **6**, 1513 (1980) [Sov. J. Low Temp. Phys. **6**, 737 (1980)].
11. V. B. Shikin and Yu. P. Monarkha, *Two-Dimensional Charged Systems in Helium* (Nauka, Moscow, 1989).
12. A. P. Volodin, M. S. Khaĭkin, and V. S. Édel'man, Pis'ma Zh. Éksp. Teor. Fiz. **26**, 707 (1977) [JETP Lett. **26**, 543 (1977)].
13. N. M. Zubarev, Pis'ma Zh. Éksp. Teor. Fiz. **71**, 534 (2000) [JETP Lett. **71**, 367 (2000)].
14. G. D. Crapper, J. Fluid Mech. **2**, 532 (1957).
15. V. E. Zakharov, Prikl. Mekh. Tekh. Fiz., No. 2, 86 (1968).
16. P. Ya. Polubarinova-Kochina, Dokl. Akad. Nauk SSSR **47**, 254 (1945).
17. D. Bensimon, L. P. Kadanoff, Sh. Liang, *et al.*, Rev. Mod. Phys. **58**, 977 (1986).
18. A. I. D'yachenko, V. E. Zakharov, and E. A. Kuznetsov, Fiz. Plazmy **22**, 916 (1996).
19. V. E. Zakharov and A. I. Dyachenko, Physica D (Amsterdam) **98**, 652 (1996).
20. M. B. Mineev-Weinstein and S. P. Dawson, Phys. Rev. E **50**, R24 (1994).
21. N. M. Zubarev, Phys. Lett. A **243**, 128 (1998).
22. N. M. Zubarev, Zh. Éksp. Teor. Fiz. **114**, 2043 (1998) [JETP **87**, 1110 (1998)].
23. S. D. Howison, SIAM J. Appl. Math. **46**, 20 (1986).
24. V. S. Édel'man, Usp. Fiz. Nauk **130**, 675 (1980) [Sov. Phys. Usp. **23**, 227 (1980)].
25. G. B. Whitham, *Linear and Nonlinear Waves* (Wiley, New York, 1974; Mir, Moscow, 1977).
26. N. M. Zubarev, Zh. Éksp. Teor. Fiz. **116**, 1990 (1999) [JETP **89**, 1078 (1999)].
27. G. P. Ivantsov, Dokl. Akad. Nauk SSSR **58**, 567 (1947).
28. A. I. Dyachenko, E. A. Kuznetsov, M. D. Spector, and V. E. Zakharov, Phys. Lett. A **221**, 73 (1996).
29. A. I. D'yachenko, Dokl. Akad. Nauk **376**, 27 (2001).
30. N. M. Zubarev, Pis'ma Zh. Éksp. Teor. Fiz. **73**, 613 (2001) [JETP Lett. **73**, 544 (2001)].

Translated by N. Wadhwa

Journal of Experimental and Theoretical Physics, Vol. 94, No. 3, 2002, pp. 545–551.
Translated from Zhurnal Éksperimental'noĭ i Teoreticheskoĭ Fiziki, Vol. 121, No. 3, 2002, pp. 637–643.

SOLIDS
Structure

Formal Determination of the Nucleation Probabilities in Binary Alloys: A Hyperfinite Approach and Thermodynamic Justification of the Lattice Models

I. B. Krasnyuk* and V. M. Yurchenko

Donetsk Physicotechnical Institute, National Academy of Sciences of Ukraine, Donetsk, 83114 Ukraine
**e-mail: kras@host.dipt.donetsk.ua*

Received July 9, 2001

Abstract—We obtained an equation of the Burgers type modeling the glass transition process in binary alloys with inhomogeneous inclusions. The proposed equation is thermodynamically justified; conditions are indicated under which this equation converts into the classical Cahn–Hillard equation. © *2002 MAIK "Nauka/Interperiodica".*

1. INTRODUCTION

As is well known, polymers in the glassy state represent a system of randomly distributed regions of increased and decreased density with not very clearly pronounced space and time scales: in the thermodynamic approximation, the space scale is much greater than the monomer unit length but much smaller than the system size. There are hydrodynamic models of glass transition in polymers under these conditions, which are based on the continuum approximation (see [1]). In an alloy with the characteristic length l of the spatial variation of the concentration (density) $c_i = \langle n_i \rangle = c(r_i, t)$ comparable to the spatial scale of the interaction between "adjacent" fluctuations, the phase transition is usually described in terms of the nearest neighbor interaction model [2–7]. Below, we will consider this situation using a nonstandard method of probability analysis [5]. On an intuitive level, this implies that we differentiate between the rates of convergence of the trajectories of random processes $n_i(t, \omega)$, where $\omega \in \Omega$ is a measure space of random events with a certain probability measure (in particular, mean).[1] Examples in which this approach leads to positive results in real problems of mathematical physics are given in [8].

Below, we describe a new formal approach to modeling of the structural evolution of nonequilibrium alloys. It should be recalled that (see, e.g., [1]) the local concentration $c_i = c(r_i, t)$ in the ith cell of a lattice is, generally speaking, a random process; typical examples are offered by the well-known Ising lattice models [2, 3]. This situation takes place provided that the characteristic scale l of variation of the concentration c_i in the ith cell is not greater than the lattice parameter a ($l \le a$), otherwise the mean (i.e., the mathematical expectation) of some random process is $\langle n_i \rangle = c_i = c(r_i, t)$ in the thermodynamic sense.

The questions as to what the "real" structure of a random process $n_i(t, \omega)$ is and how to define strictly the space of elementary events $\omega \in \Omega$ were formulated long ago by Kac [4]. Since then, considerable progress has been achieved in this respect: Benassi and Fouque [5] showed that $n_i(t, \omega)$ can be defined as a random process of the Poisson clock type. For $a \longrightarrow +0$, the mean $\langle n_i \rangle$ satisfies the ordinary diffusion equation only provided that the probabilities $p^{\pm}$ of transitions from ith to the neighboring $(i \pm 1)$th cell are $p^+ = p^- = 1/2$.

For $p \neq 1/2$, we obtain thermodynamic equations of an absolutely different type—the Burgers equations [5, 6], the solutions to which have the form of concentration waves showing a tendency to "triggering" within a finite time. Thus, selecting a model even on the microscopic level is a nontrivial problem.

This paper can be divided into two parts. In Section 2, we derive a relationship for calculating the probability density of transitions in binary alloys in terms of the nearest neighbor model. This model is a simple consequence of the formal results [8] and physical data [1]. We do not know whether an analogous formula can be derived within the framework of the classical probability analysis. In Section 3, we have to make a recourse to the classical (thermodynamic) equations for binary alloys (Cahn– Hillard model) in order to show that fluctuations in the vicinity of an equilibrium state (there can be several such sates) satisfy the Burgers equation with a "viscosity" term. Then, we will demonstrate that a linearized Burgers equation in the case of an "ideal" liquid corresponds to a random process of the Poisson clock type, which breaks the symmetry of transitions ($p \neq 1/2$) on the nearest neighbor lattice. Taking into account the viscosity and assuming that $\nu \ll 1$, where ν is the

[1] In contrast to the classical analysis, where the quantities $1/n$ and $1/n^2$ are of the same order of smallness, in the nonstandard case $1/n^2 \ll 1/n$ [8].

flow (polymer chain) velocity, we obtain a diffusion equation the solution to which represents a mathematical expectation of an ordinary (classical) random process with a normal (Gaussian) distribution for $p = 1/2$ (or with a close distribution for $p \approx 1/2$).

From this standpoint, the Burgers equation can be considered (in the vicinity of an equilibrium state of the classical system) as a "deterministic" model for binary alloys with chaotic nucleation. We did not consider the case of a simultaneous mismatch between velocity and viscosity ($\nu \neq 0$ and $\gamma \neq 0$).

2. ABSTRACT MODEL OF HYPERRANDOM WALK ON LATTICE

Let us consider the random concentration dynamics of a binary alloy on a hyperfinite lattice. For this purpose, it is necessary to analyze the density of probability of transitions from ith to $(i \pm 1)$th cell for all $i \in Z^+ = \{0, 1, \ldots\}$. The simplest hyperfinite model is just the nearest neighbor model [8].

Let Λ_δ be the lattice

$$\Lambda_\delta = \{u_\delta \in \Lambda \subset R^d, u \in Z^d\},$$

where Z^d is an integer lattice of the dimension $d \geq 1$. For each $i \in \Lambda_\delta$ we define the set of nearest neighbors of the ith site on the Λ_δ set:

$$N_i = \{j \in \Lambda_\delta : |i - j| = \delta\}.$$

Therefore, $|N_i|$ is the number of elements in this set. Obviously, $|N_i| = 2d$, except for the case ($i = s$) when the ith site occurs on the lattice boundary.

Let us assume that $c_i(t, \omega)$ is a hyperfinite Markov process. According to [8, p. 540], this process is generated by an infinitesimal generator $-\Delta_\delta/2 + m^2$, where

$$\Delta_\delta f(i) = \delta^{-2}\left(\sum_{j \in N_i} f(i) - |N_i| f(i)\right),$$

δ is the lattice period (step), and f_i is the function corresponding to the concentration c_i to be determined.

Following [1], where the alloy concentrations were calculated based on the Ising model, we introduce the relaxation time $t \propto k_{CH}^{-2}$. Here, k_{CH} is the wave vector taking into account the amplitude of the fluctuation decay depending on the wavelength $\lambda = 2\pi k_{CH}/L$, and L is the sample size (we restrict the consideration to the one-dimensional case). In addition, we define a potential for the finite binary alloy under consideration [1]:

$$\nu(r) = \begin{cases} -A\exp(-a^2/\sigma^2) & \text{for } r \leq a \sim \delta, \\ 0 & \text{for } r > a, \end{cases}$$

where A is a constant factor determined below and σ is the variance. It should be noted that this model coincides with that considered by Kac [4] for a one-dimensional (continuous) gas. Since (by definition) we consider the probability densities of the concentration randomly distributed on a lattice, below we will take $a = \delta$.

Let us select the dimensionless time in the form $t = t'\gamma^{-1}\sigma^2$, where γ is related to the mobility $M(c)$ in the spinodal decomposition theory [1]. The relaxation time in the cell is

$$t_{CH} \propto \frac{\sigma^2}{\gamma k_{CH}^2},$$

and we may formally consider the quantity

$$m = -\frac{\sigma^2 A}{\gamma k_{CH}^2}\exp\left\{-\frac{\delta^2}{2\sigma^2}\right\}$$

as the constant of interaction between nearest neighbors, so that the hyperfinite random process under consideration is a local Markov process [3].

Now consider a hyperdiscrete line

$$T = \{k\Delta t | k \in N^* \cup \{0\}\},$$

where N^* is the expanded natural universum (see [8, p. 541]) and Δt is a certain positive fixed infinitesimal value (in contrast to the period δ, which will be standard in some cases and infinitesimal in the hyperfinite sense in other cases). Finally, to render the analysis formally strict, we add a "trap" $\square$ (or an "absorbing" state) so that the space of states of the hyperfinite lattice is $\Lambda_\square = \Lambda_\delta \cup \{\square\}$.

Usually, the unknown probabilities of transitions between cells are set *a priori* in the form of a transition matrix generating by the Kolmogorov reconstruction theory (see, e.g. [9]) a certain discrete Markov chain [3]. Below, we will calculate these transition probabilities for a binary alloy model based on the data reported in [1]. Consider a nucleus occasionally formed at a certain time instant. At the next instant, the nucleus may occur in any of the neighboring states (see formulas in [8, p. 541]) $j \in N_i$ at a probability

$$\begin{aligned} P_{i \neq j} &\approx \frac{\Delta t}{2\delta^2} = \frac{1}{2}\frac{t}{\delta^2} \\ &\approx \frac{1}{2}\left(\frac{\sigma}{\delta}\right)^2\frac{4\pi^2}{\lambda^2} = 2\pi^2\left(\frac{\sigma}{\delta}\right)^2\frac{1}{\lambda^2}. \end{aligned} \quad (1)$$

Note that, by virtue of the local Markovian character of the random process under consideration (proved in [7]), this probability is independent of the nucleation probability.

Since $0 \leq P \leq 1$, we obtain

$$\lambda > \sqrt{2\pi}\left(\frac{\sigma}{\delta}\right). \quad (2)$$

This inequality has a simple physical meaning: for large variance, we can (and must) take into account only the long-wave fluctuations (at a given period δ), while the ratio σ/δ can be considered as the scattering of the random process on the lattice.

Formula (1), following from the aforementioned mathematical model (see [8, p. 541]) and the physical model [1], implies that (i) the binary alloy most probably features short-wave fluctuations and (ii) the growth of the nucleus depends on the square ratio of variance to the wavelength $(\sigma/\lambda)^2$.

The nucleus can remain in the ith state at a probability

$$P_{i=j} \approx 1 - \left[\frac{|N_i|}{2\delta^2} + m^2\right]\Delta t. \qquad (3)$$

This relationship also admits a clear physical interpretation. Indeed, formula (3) readily yields a restriction on the amplitude of the interaction potential,

$$m^2(A) \le \gamma\left(\frac{k}{\sigma}\right)^2,$$

which merely indicates that, provided A is sufficiently large (i.e., the interaction is strong), a nucleus appearing in the ith cell will never reside in this cell. It should be recalled that, although we restricted the consideration to a simple case of $\sigma \ll \delta$, the general case is also readily analyzed.

A less trivial requirement is that

$$2d \le \frac{1}{4\pi^2}\left(\frac{\lambda}{\sigma}\right)^2 - \sigma^2 m^2$$

for the lattice dimension d (recall that $2d = |N_i|$). This condition implies limitations (i) on the magnitude of the nearest neighbor interaction

$$m^2(A) \le \frac{1}{4\pi\sigma^2}\left(\frac{\lambda}{\sigma}\right)^2;$$

and (ii) on the magnitude of fluctuations (remaining within a given cell) depending on the lattice dimension

$$2\pi\sqrt{2d} \le \left(\frac{\lambda}{\sigma}\right).$$

The latter restrictions can be more conveniently written as

$$V \ge \frac{\sigma}{\omega}\sqrt{2d},$$

where V is the volume of an occasionally formed nucleus. This inequality has a simple physical meaning: the greater the space dimension, the larger the size necessary for a nucleus to reside (after spontaneous appearance) in a given cell of this space. From the standpoint of phase transitions, the situation is even more clear. Indeed, it is known [3] that no phase transitions take place in the one-dimensional Ising model, while the probability of such transitions in the models with $d \ge 2$ usually increases with the space dimension.

3. CLASSICAL APPROACH

Let us write the free energy $f = \beta F$ ($\beta = 1/T$) for an inhomogeneous alloy in the following form:

$$f = \sum_i (c_i \ln c_i + c_i' \ln c_i') + \frac{1}{2}\sum_{i,j} \beta v_{ij} c_i c_j.$$

Then, the ordinary differential equation describing evolution of the concentration c_i in the ith cell is [1]

$$\frac{dc_i}{dt} = \sum_s A_{is}\left[\exp\left(\frac{\partial f}{\partial c_s}\right) - \exp\left(\frac{\partial f}{\partial c_i}\right)\right], \qquad (1')$$

where $A_{is} = A_{si} > 0$ owing to the Onsager condition. In an equilibrium state, all $f_i = \partial f/\partial c_i$ values are equal to the chemical potential and the right-hand part of Eq. (1') vanishes.

For a multicomponent alloy, the corresponding equations are as follows:

$$\frac{dc_{p_i}}{dt} = \sum_{q_s} v_{i,s}^{p,q}[\exp(f_{ps} + f_{qi}) - \exp(f_{pi} + f_{qs})], \qquad (2')$$

where

$$f = \sum_{p_i} c_{p_i} \ln c_{p_i} + \frac{1}{2}\beta v_{i,\gamma}^{p,q} c_{p_i} c_{q_\gamma}.$$

These relationships will be employed below.

In the case of an alloy with inhomogeneous density distribution, we will use the Cahn–Hillard equation [1]

$$\frac{\partial c_i}{\partial t} = \mathrm{div}\left\{M(c_i)\left[\frac{\nabla c_i}{c_i c_i'} + \nabla(\beta v c)_i\right]\right\}, \qquad (3')$$

where

$$M(c) = \gamma c c' \exp[\beta(uc)_i]$$

is the mobility, β is proportional to the probability of jumping from ith to $(i+1)$th cell, γ is the quantity defined above, $c' = 1 - c$, and u is the value determining the interaction potential in the Kac theory (see above).

Let us assume that Eq. (3') is averaged with respect to i (in the sense of [1], see also the Introduction). The corresponding equation can be written in the following form:

$$\frac{\partial c}{\partial t} = \frac{\partial M(c)}{\partial x}\left[\frac{\nabla c}{cc'} + \beta v \nabla c\right]$$

$$+ M(c)\frac{\partial}{\partial x}\left[\frac{\nabla c}{cc'} + \beta v \nabla c\right].$$

Linearizing this expression in a certain equilibrium state (there can be several such states), we obtain an equation for the perturbations:

$$\frac{\partial c}{\partial t} = M'(c_0)\left[\frac{(\nabla c)^2}{c_0 c_0'} + \beta v \nabla^2 c + \beta \nabla v \nabla c\right] + \frac{\nabla^2 c c_0 c_0' - \nabla c \nabla (c c')}{(c_0 c_0')^2} + \beta \nabla v \nabla c + \beta v \nabla^2 c.$$

Applying the method of "frozen coefficients" (see, e.g., [10]) to this last equation and taking into account that the term $\nabla c \nabla (cc')$ on the order of ε^3 can be ignored, we obtain

$$\frac{\partial c}{\partial t} = [M'(c_0)\beta \nabla v + \beta \nabla v]\nabla c + \frac{M'(c_0)}{c_0 c_0'}(\nabla c)^2 + \left[M'(c_0)\beta v + \frac{1}{c_0 c_0'} + \beta v\right]\nabla^2 c.$$

Since this is the equation for perturbations, the strict form should be as follows:

$$\varepsilon \frac{\partial c}{\partial t} = \varepsilon a_1 \nabla c + \varepsilon^2 a_2 (\nabla c)^2 + \varepsilon^2 a_3 \nabla^2 c, \qquad (3'')$$

where the meaning of coefficients a_i ($i = 1, 2, 3$) is obvious. Equation (3'') has a simple physical sense. Indeed, if the gradient

$$\nabla v(x) = 2A\frac{x}{\sigma^2}e^{-x^2/\sigma^2}$$

is small, the term with the coefficient a_1 can be ignored and we arrive at an equation of the Burgers type

$$\varepsilon \frac{\partial c}{\partial t} + \frac{1}{2}a_2 \varepsilon^2 \left(\frac{\partial c}{\partial x}\right)^2 - \frac{1}{2}a_3 \varepsilon^2 \frac{\partial^2 c}{\partial x^2} = 0, \qquad (4')$$

albeit written in a somewhat unusual form: a solution u to the equation

$$\frac{\partial u}{\partial t} = \frac{a_3}{2}\frac{\partial^2 u}{dx^2} \quad \left(t' = \frac{t}{\varepsilon}, \quad x' = \frac{x}{\varepsilon}\right)$$

yields the function $c = -a_3 \ln u$ which is a solution to Eq. (4'). In the standard writing, the Burgers equation is obtained from (4') by differentiating with respect to x and substituting $u = \partial c/\partial x$. In what follows, we will bear this in mind and consider the Burgers equation in the commonly accepted form:

$$\frac{\partial u}{\partial t} + a_2 u \frac{\partial u}{\partial x} = a_3 \frac{\partial^2 u}{\partial x^2}. \qquad (4'')$$

Since the potential $v(r)$ is small both for $r \le \sigma^2$ and for $r \gg \sigma$], Eq. (4'') is valid in the latter case as well. The intermediate situation $r \sim \sigma$ corresponds to a simple equation

$$\frac{\partial c}{\partial t} = \beta \nabla v(x)(1 + M'(c_0))\frac{\partial c}{\partial x}, \qquad (5)$$

which can be written as

$$\frac{dc}{dt} = 0 \text{ for } \frac{dx}{dt} = a_1(x), \qquad (6)$$

where

$$a_1(x) = -2\beta A \frac{x}{\sigma^2}e^{-x^2/\sigma^2}(1 + M'(c_0)).$$

Introducing the notation $y = x/\sigma$ and expanding the function $\exp(y^2)$ into a Taylor series, we obtain an equation (for sufficiently small y^2)

$$\sigma \frac{\partial y}{\partial t} = -2\beta \frac{A}{\sigma} y,$$

which has an integral

$$\ln y = -2\beta \frac{A}{\sigma^2} t + \text{const}. \qquad (7)$$

This expression implies that the function $c(x, t)$ remains constant along the curve determined by a solution to Eq. (6). In particular, any initial δ-like perturbation propagates along this curve without changing in shape, which is analogous to a solution of the soliton type. These perturbations propagate at a phase velocity determined by the function $a_1(x)$. It is convenient to consider the perturbations existing in a "phase tube" with a radius of $|x| = \sigma$, for which

$$v_c \sim -2\beta \frac{A}{\sigma}(1 + M'(c_0)).$$

This formula has an obvious physical meaning.

Note that, upon "eliminating" the parameter ε from Eq. (4') by means of substitution $x = x'/\varepsilon$ and $t = t'/\varepsilon$, we arrive at Eq. (4''). On the contrary, upon "returning" to the initial variables in Eq. (4''), the left-hand part of this equation possesses the order of ε^2, while the right-hand part acquires the order of ε^2 and, hence, can be ignored. As a result, we arrive at the Burgers equation

$$\frac{\partial u}{\partial t} + a\frac{\partial G(u)}{\partial x} = 0, \qquad (5')$$

where $G(u) = u^2$ and $a = a_2/2$ (it should be recalled that $a_2 = M'(c_0)/c_0(1 - c_0)$.

Let us select the following boundary conditions for Eq. (5'):

$$u(\cdot, 0) = u_0. \qquad (5'')$$

According to [5–7], a solution to Eq. (5') with this boundary condition can be written for $\varepsilon \longrightarrow +0$ in the following form:

$$u_t^\varepsilon = E\{X_t^\varepsilon(x)\} = E\{X_{t/\varepsilon}([x/\varepsilon])\},$$

where $\varepsilon > 0$ plays the role of the lattice period and $E\{\cdot\}$ denotes the operation of taking mathematical expectation of the random process $X_t^\varepsilon(\cdot)$.

In this case, the convergence takes place in any sense [3]

$$\lim_{\varepsilon \to +0} \int_x^y E\{x_t^\varepsilon(z)\}dz = \int_x^y u(z, t)dz,$$

and, hence,

$$u(z, t) = \lim_{\varepsilon \to +0} E\{X_t^\varepsilon(z)\}$$

for almost all $z \in R$. Here,

$$\{X_t = \{X_t(k)\}, k \in Z\}, t \geq 0\}$$

is a standard Markov Process (in the narrow sense) of the Poisson clock type (for detail, see [3, 5–7]), which is continuous on the right and possesses finite limits on the left. A generator of this random process is determined on a set of cylindrical functions from a certain measure space $\mathscr{E}$ (for the definition see, e.g., [3, 8]) by the relationship

$$Lf(\eta) = \sum_{k, l \in Z} p(l)g(\eta(k))[f(\eta^{k, k+l}) - f(\eta)],$$

where

$$\eta^{k, k+l}(m)$$

$$= \begin{cases} \eta(m), & \text{for } m \neq k \text{ and } m \neq k + l \text{ or } \eta(k) = 0, \\ \eta(m) - 1, & \text{for } m = k \text{ and } \eta(k) \geq 1, \\ \eta(m) + 1, & \text{for } m = k + l \text{ and } \eta(k) \geq 1, \end{cases}$$

the function $g(\cdot)$ is generated by the function $G(\cdot)$ (see Eq. (5')), and

$$a = \sum_{l \in Z^+} lp(l) \neq 0.$$

Thus, the quantity a determines the mean velocity of the perturbation flow moving from left to right for $a > 0$ and right to left for $a < 0$.

The system must obey the following entropy conditions for $a < 0$ [8],

$$u^-(x, t) = \lim_{y \to x} u(y, t) \geq u^+(x, t) = \lim_{y \to x} u(y, t),$$

while, for $a > 0$,

$$u^-(x, t) \leq u^+(x, t).$$

These conditions are obviously satisfied because u is a decreasing function of the coordinate x:

$$u(x, t) = \begin{cases} \alpha, & \text{for } x < a\dfrac{G(\beta) - G(\alpha)}{\beta - \alpha} \\ \beta, & \text{for } x > a\dfrac{G(\beta) - G(\alpha)}{\beta - a}, \end{cases}$$

where $u_0(x, 0) = \alpha$ for $x = 0$ and $u_0(x, 0) = \beta$ for $x > 0$.[2]

For $a > 0$, the continuous function $G'(\cdot)$ is strictly decreasing and we obtain

$$aG'(\alpha) \leq aG'(\cdot) \leq aG'(\beta).$$

According to the method of characteristics for hyperbolic equations (see [10]),

$$x > aG'(\beta)t \Longrightarrow u(x, t) = u_0(x - aG'(u)t) = \beta$$

and

$$x < aG'(\alpha)t \Longrightarrow u(x, t) = u_0(x - aG'(u)t) = \alpha.$$

In the general case,

$$u(x, t) = \begin{cases} \alpha, & \text{for } x \leq aG'(\alpha)t, \\ (G')^{-1}\left(\dfrac{x}{at}\right), & \text{for } aG'(\alpha)t \leq x \leq aG'(\beta)t, \\ \beta, & \text{for } x \geq aG'(\beta)t, \end{cases}$$

which is the well-known representation of a solution to the Burgers equation. The case of a leftward motion is considered by analogy.

Thus, we have demonstrated that perturbations of a solution to the Cahn–Hillard equation in the vicinity of a certain equilibrium state have the form of a traveling wave, which propagates at a phase velocity $v(x, t) = aG'(u(x(t), t))$ for any preset solution u. As is known (see, e.g., [10]), each point on the profile of such a wave travels by its own characteristic trajectory (at its own velocity); since these characteristics are nonparallel, the wave profile changes (expands or contracts). This leads to the appearance of a break representing a region of infinitely rapid variation of the perturbation amplitudes (within a given approximation).

When a sufficiently narrow region featuring a rapid variation of the perturbation amplitude appears in the vicinity of an equilibrium state, a significant role is played by the high-frequency dissipation and dispersion. When the action of these factors compensates for the effect of nonlinearity, the shape of the wave virtually ceases to change (not considering a weak damping); that is, a quasi-stationary shock wave is formed in the system. In this wave, the region containing a large number of breaks propagates at a finite velocity v_c. As is known, the value of this velocity is determined by the

[2] Here and below, we assume that the initial nucleus can be considered as a "step."

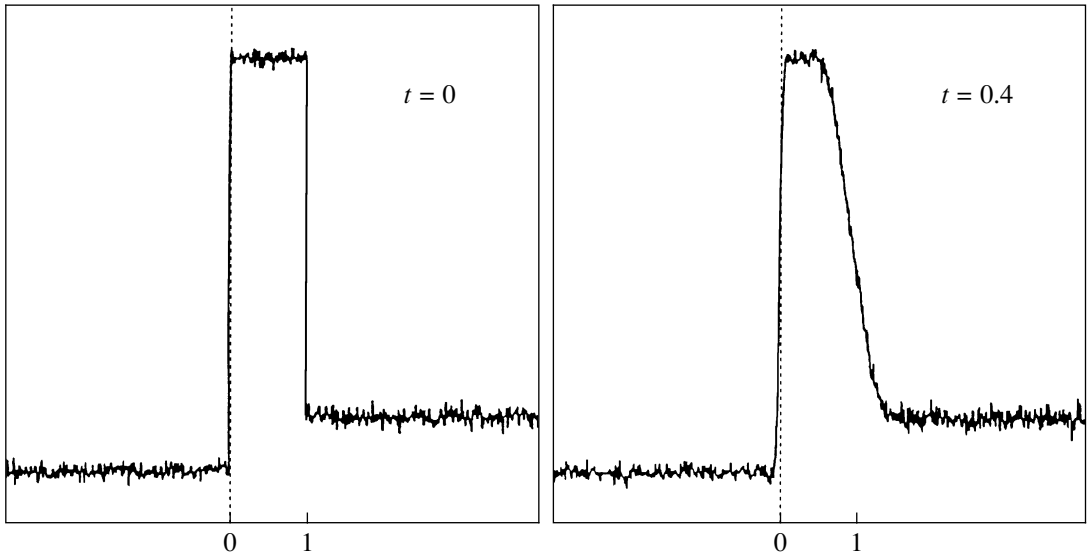

Dynamics of the probability distribution for an elementary quasiequilibrium fluctuation in the vicinity of a spinodal decomposition point in the nearest neighbor model.

boundary conditions at the break; in the situation under consideration, these conditions are as follows:

$$(\beta - \alpha) v_c = a[G(\beta) - G(\alpha)],$$

where the α and β values refer to the amplitudes before and after the break at the shock wave front.

An example of the numerical modeling results obtained by the Monte Carlo method is presented in the figure for random walk on a lattice with a distribution density of the "step" type. Note that the Burgers problem with an arbitrary (sufficiently general) boundary condition (nucleus shape) may also possess piecewise linear periodic solutions of the traveling wave type (over the self-similar variable; see [10]). In such a case, it is unknown which random process corresponds to the Burgers equation derived above. Thus, an experiment is necessary in order to "extend" the result obtained in this study to the general initial distributions of the nuclei. This situation is analogous to that taking place for the well-known Ginzburg–Landau equation in superconductivity theory: strictly proved only for $T = T_c$ (the critical temperature), this equation is nevertheless experimentally confirmed over a finite temperature interval far from the critical point.

4. CONCLUSIONS

We have proved the following statements:

(i) Upon reducing the Cahn–Hillard equations (in the vicinity of an equilibrium state) to the Burgers equation with a viscosity term, we may formally use the results [5–7] indicating the class of random processes averaged on a lattice (in the sense of mathematical expectation). Thus, in the limit of a continuous medium, we obtain a Cauchy problem for the Burgers equation. Using such (strictly indicated) random process, we can model the process of nucleation in binary alloys.

(ii) Using the hyperfinite approach [8] and the corresponding data from [1], it is possible to exactly calculate the probabilities of transitions from one cell to another with an allowance for the relaxation.

(iii) The lattice model proposed above for the density fluctuations, describing the process of nucleation in binary alloys according to the Cahn–Hillard theory [11], can be strictly methodologically justified.

ACKNOWLEDGMENTS

The authors are grateful to L.I. Stefanovich for reading the manuscript and valuable remarks.

This study was supported by the Ministry of Education and Science of Ukraine (project no. 2M/71-2000).

REFERENCES

1. V. G. Vaks, S. V. Beiden, and V. Yu. Dobretsov, Pis'ma Zh. Éksp. Teor. Fiz. **61**, 65 (1995) [JETP Lett. **61**, 68 (1995)].
2. A. G. Sinaĭ, *Theory of Phase Transitions. Strict Results* (Nauka, Moscow, 1980).
3. Th. Liggett, *Interacting Particle Systems* (Springer-Verlag, New York, 1985; Mir, Moscow, 1989).
4. M. Kac, *Probability and Related Topics in Physical Sciences* (Interscience, New York, 1957; Mir, Moscow, 1965).
5. A. Benassi and J. P. Fouque, Ann. Inst. Henri Poincaré, Sect B **24**, 198 (1988).

6. J. P. Fouque, in *Proceedings of the AMS-SIAM Summer Seminar on Mathematics of Random Media, Virginia, 1989* (American Mathematical Society, Providence, 1991).
7. A. Benassi and J. P. Fouque, Ann. Prob. **15**, 2 (1987).
8. S. Albeverio, J. E. Fenstad, R. Höegh-Krohn, and T. Lindström, *Nonstandard Methods in Stochastic Analysis and Mathematical Physics* (Academic, Orlando, 1986; Mir, Moscow, 1980).
9. *Lecture Notes in Mathematics*, Vol. 1055: *Quantum Probability and Applications to the Quantum Theory of Irreversible Processes: Proceedings of the International Workshop, Villa Mondragone, 1982*, Ed. by L. Accardi, A. Frigerio, and V. Gorini (Springer-Verlag, Berlin, 1984).
10. R. Z. Sagdeev, D. A. Usikov, and G. M. Zaslavsky, *Nonlinear Physics: from Pendulum to Turbulence and Chaos* (Nauka, Moscow, 1988; Harwood, Chur, 1988).
11. J. W. Cahn, Trans. Metall. Soc. AIME **242**, 166 (1968).

Translated by P. Pozdeev

Journal of Experimental and Theoretical Physics, Vol. 94, No. 3, 2002, pp. 552–567.
Translated from Zhurnal Éksperimental'noĭ i Teoreticheskoĭ Fiziki, Vol. 121, No. 3, 2002, pp. 644–662.

SOLIDS
Structure

A Study of the Structural Phase Transition in Strontium Titanate Single Crystal by Coherent and Incoherent Second Optical Harmonic Generation

E. D. Mishina[a], A. I. Morozov[a, *], A. S. Sigov[a, **], N. E. Sherstyuk[a, *], O. A. Aktsipetrov[b], V. V. Lemanov[c], and Th. Rasing[d]**

[a]*Moscow State Institute of Radio Engineering, Electronics, and Automation (Technical University), pr. Vernadskogo 78, Moscow, 117454 Russia*
[b]*Moscow State University, Vorob'evy gory, Moscow, 119899 Russia*
[c]*Ioffe Physicotechnical Institute, Russian Academy of Sciences, ul. Politekhnicheskaya 26, St. Petersburg, 194021 Russia*
[d]*Institute of Materials, University of Neimegen, Netherlands*
**e-mail: mor-alexandr@yandex.ru*
***e-mail: sigov@exodus.mirea.ac.ru*
****e-mail: nesherstuk@mail.ru*
Received July 24, 2001

Abstract—The surface phase transition in a $SrTiO_3$ crystal was studied by second optical harmonic generation. Nonlinear optical response singularities were observed at temperature $T^* = 145$ K, which was 40 K higher than the T_c structural phase transition temperature in the crystal volume. Nonlinear critical opalescence in the crystal volume caused by the presence of point defects was studied. The second harmonic field and the intensity of critical opalescence were calculated based on the phenomenological model of nonlinear optical processes with the use of the Landau theory of phase transitions. *© 2002 MAIK "Nauka/Interperiodica".*

1. INTRODUCTION

The strontium titanate $SrTiO_3$ (STO) single crystal is an example of crystals with perovskite structures. The same structure is characteristic of many other materials that are extensively used in modern technology such as ferroelectric and piezoelectric materials, high-T_c superconductors, and materials with giant magnetoresistance. During the past three decades, STO crystals have been studied in detail by dielectric, IR, and Raman spectroscopy and X-ray and neutron diffraction (see review [1]). STO is a potential ferroelectric material in which the ferroelectric transition is suppressed by quantum fluctuations [1]. At $T_q \approx 40$ K, the STO crystal experiences the transition to the quantum paraelectric state [2, 3]. At $T_c = 105$ K, a structural phase transition from the high-temperature cubic phase (point group $m3m$) to the low-temperature tetragonal phase (point group $4/mmm$) is observed in the crystal. This phase transition is close to second-order transitions and is caused by the softening of the transverse optical phonon mode at the R point at the boundary of the Brillouin zone. Soft modes are nonoverdamped and are observed fairly close to the phase transition point [4].

The revival of interest in STO first and foremost stems from the discovery of some new anomalies in its dielectric and optical properties, especially those observed close to T_q and T_c. In particular, optical scattering studies at $T < T_q$ showed that the structure of the central peak became more complex in this temperature region than at high temperatures. This peak contained several spectral components, in particular, components forbidden by selection rules [5]. X-ray and neutron diffraction exhibited unusual features in the structural phase transition region [6, 7]. Two scales appeared in scattering indicatrices, namely, a narrow ($\Delta\theta \approx 1°$–$2°$) peak was observed in the immediate vicinity of T_c against the background of the usual fairly wide peak ($\Delta\theta \approx 10°$–$20°$). The broad peak with a small correlation length corresponded to bulk material, and the narrow peak, to the subsurface region. The unusual features of the optical phonon peak observed in thin STO films were studied as a function of film thickness [8].

Size effects in phase transitions in the bulk and on the surface have been studied since the 1950s. In the past decade, the progress in technologies for the preparation of high-quality thin films of technologically important materials such as ferromagnets and ferroelectrics (see review [9]) revived interest in studying these phenomena. The difference of the phase transition temperatures on the surface and in the bulk was for the first time predicted for magnetic [10] and then for structural phase transitions [11]. The shift of the surface phase transition temperature depends on the quality of

the surface (the presence of defects, dislocations, adsorbed molecules, and stresses). This shift is, however, nonzero even on an ideal crystal surface [12].

The principal experimental techniques sensitive to the structure of the surface are scanning microscopies, slow electron diffraction, X-ray diffraction at glancing angles, and second optical harmonic generation. We will only mention several works published in recent years and concerned with surface phase transitions. Scanning tunnel microscopy was used in [13] to study the mechanism of growth of 7×7 domains from the 1×1 phase on the surface of Si(111). In [14], the special features of the phase transition on the (111) diamond surface including kinetic and electronic structure characteristics were studied by slow electron diffraction. X-ray diffraction at glancing angles was employed to study the surface phase transition in the ND_4Cl crystal [15].

It should, however, be borne in mind that each of the methods mentioned above is characterized by a probing depth specific to it and different from those of the other methods. The results obtained in studying surface phase transitions by different methods may therefore be different. It should also be taken into account that an ideal surface (the surface of an infinite crystal "cut" by a plane) cannot be prepared experimentally. Even in a vacuum, dangling bonds formed in such a "cutting" interact with each other or with adsorbed atoms, which results in surface reconstruction. A certain contradiction arises; namely, methods sensitive to the properties of the upper atomic layer study reconstructed surfaces, whereas penetrating methods study subsurface layers whose thickness is method-dependent.

The method based on second harmonic generation has certain special features. Depending on the object of study and the experimental configuration, this method may be sensitive either to the structure of the upper crystal layer one–two lattice parameters deep (that is, to the surface proper), or to the structure of several (about ten) subsurface atomic layers, or to the bulk phase. This circumstance was used to study phase transitions of various types. For instance, surface reconstruction was studied in [16, 17] by second harmonic generation. In [18, 19], this method was used to study a ferroelectric phase transition in the bulk of a film. The orientation transition in a monolayer on the surface of water [20, 21] and the phase transition in a superthin (two monolayers) PVC film [22] were also studied by second harmonic generation.

Generally, an analysis of a second harmonic signal for obtaining structural information is based on examining the dependence of coherent second harmonic intensity $I^{2\omega}$ on the orientation of electric field vectors of incident and detected radiation with respect to some symmetry-selected directions on the surface or in the bulk, which are characterized by the azimuthal angle of the sample. The selected directions may be, for instance, crystallographic axes in single crystals and directions of structure formation in thin (Langmuir deposited) films. Depending on the orientation that remains unchanged and the orientation that changes in the laboratory frame of reference (wave or crystal electric field orientation), either polarization dependences at a given sample orientation or azimuthal dependences of second harmonic intensity in various polarization configurations are studied. If the medium is spatially nonuniform, incoherent alongside coherent second harmonic generation occurs. These two components are separated by studying the scattering indicatrix (the dependence of the second harmonic intensity on the polar angle).

In this work, we suggest a method for separating the surface and volume contributions to the second harmonic intensity in a centrally symmetrical medium. The temperature dependences of the volume coherent second harmonic contribution are shown to have singularities near T_c. Similar singularities in the surface coherent second harmonic contribution are observed at a different T^* temperature. We assign these singularities to the surface phase transition, and the T^* temperature is treated as the surface phase transition temperature. As an extension to [23], we study the configurations in which the volume contribution is suppressed and configurations in which both volume and surface contributions are present. We also study nonlinear optical light scattering (the incoherent contribution to the second harmonic intensity) in the STO crystal near the structural phase transition. Following Gorelik [24], we use the term "critical hyperopalescence" to combine two phenomena, hyper-Raman and hyper-Rayleigh scattering. From the point of view of nonlinear optics, it is important that both high- and low-temperature phases of the transition under consideration are centrally symmetrical, that is, second harmonic generation is forbidden in the dipole approximation. We suggest a method for calculating the intensity of critical hyperopalescence for the phase transition with second harmonic generation only permitted in the quadrupole approximation in both phases. Note that critical hyperopalescence is for the first time studied for a nonferroelectric (structural) phase transition. The corresponding phenomenon for a ferroelectric phase transition was studied in [24, 25].

This paper is organized as follows. The second section describes a method for separating the volume and surface contributions to the second harmonic intensity. The phenomenological models of the temperature dependences of coherent and incoherent second harmonic fields are considered in Sections 3 and 4, respectively. The experimental unit is described in Section 5. Sections 6–8 contain the results of second harmonic generation studies of the volume and surface phase transitions and of the nonlinear critical hyperopalescence phenomenon.

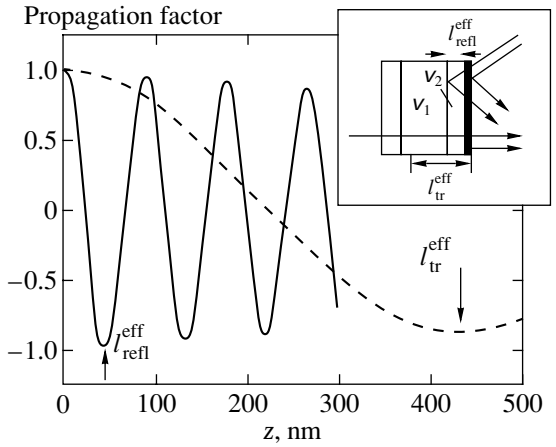

Fig. 1. Dependences of the factor of second harmonic wave propagation in transmission (dashed line) and reflection (solid line) geometries. Shown in the inset are the characteristic second harmonic wave generation regions: surface S (thick solid line) and volumes V_1 and V_2, different in transmission and reflection measurements.

2. A NONLINEAR OPTICS-BASED PROCEDURE FOR SEPARATING THE SURFACE AND VOLUME CONTRIBUTIONS TO SECOND HARMONIC GENERATION INTENSITY

The nonlinear optics-based procedure for separating the surface and volume contributions to second harmonic generation is based on the key role played by medium symmetry in the arising of nonlinear polarization and on the special features of second harmonic wave propagation.

A phenomenological description of nonlinear polarization is based on expanding nonlinear polarization $\mathbf{P}(2\omega)$ in multipoles,

$$\mathbf{P}(2\omega) = \mathbf{P}^D(2\omega) + \mathbf{P}^Q(2\omega) + \dots . \quad (1)$$

The first term in (1) is the dipole polarization

$$P_i^D(2\omega) = \chi_{ijk}^{(2)D} E_j(\omega) E_k(\omega), \quad (2)$$

and the second term describes the quadrupole polarization,

$$P_i^Q(2\omega) = \frac{\partial}{\partial x_j}(\chi_{ijkl}^{(2)Q} E_k(\omega) E_l(\omega)). \quad (3)$$

Here, $\chi_{ijk}^{(2)D}$ and $\chi_{ijkl}^{(2)Q}$ are the quadratic dipole and quadrupole susceptibility tensor components, and $\mathbf{E}(\omega)$ is the incident wave electric field strength. Every successive term in Eq. (1) for nonlinear polarization is much smaller than the preceding one. In particular,

$$\chi^{(2)Q} \sim (r_0/\lambda)\chi^{(2)D},$$

where r_0 is the Bohr radius and λ is the fundamental frequency radiation wavelength.

In the volume of a centrally symmetrical medium, dipole polarization is absent and $\chi^{(2)D} = 0$. The introduction of a boundary essentially changes the symmetry, because surface atoms have different environments on the sides of the bulk and the vacuum. In addition, several subsurface layers have unit cells deformed along the normal to the surface because of the difference in interactions with outside (surface side) and inside (volume phase side) atoms. Surface layers of all, even centrally symmetrical, crystals are therefore noncentrally symmetrical. The volume of a centrally symmetrical medium is described by quadrupole polarization, and the surface layers are described by the dipole polarization

$$P_i^{surf}(2\omega) = \chi_{ijk}^{(2)surf} E_j(\omega) E_k(\omega).$$

This means that volume second harmonic generation in such a medium is comparatively weak, and surface generation is comparatively strong (per unit medium volume). The volumes described by surface (dipole) and bulk (quadrupole) susceptibilities also differ by several orders of magnitude, and the signals from the surface and bulk substance are therefore comparable, which makes it possible to diagnose a surface layer several lattice periods thick (1–5 nm). The surface and volume regions of a crystal described by dipole and quadrupole susceptibilities are schematically shown in the inset in Fig. 1.

The relative contributions of the volume and surface to the second harmonic intensity are determined not only by the medium symmetry but also by the geometry of measurements. The passage from transmission to reflection measurements can additionally increase the relative surface contribution to the second harmonic intensity by one order of magnitude. Generally, the field at the frequency of the second harmonic generated by a semi-infinite centrally symmetrical medium is described by the equations (see [26])

$$\begin{aligned} E_i^{bulkQ}(2\omega) &= \int_0^\infty G_{ij}^{BQ}(z') P_j^{bulkQ}(z') dz' \\ &\approx f_{2\omega} f_\omega^2 (\chi_{ilm}^{(2)bulkQ}) \frac{k_{z,\omega}}{2k_{z,\omega} \pm k_{z,2\omega}} \\ &\times \{\exp[i(2k_{z,\omega} \pm k_{z,2\omega}) l^{eff}] - 1\} E_{0l}^\omega E_{0m}^\omega. \end{aligned} \quad (4)$$

Here, E_{0l}^ω and E_{0m}^ω are the amplitudes of the corresponding incident wave components, f_ω and $f_{2\omega}$ are Fresnel factors defined in [5], sign "+" corresponds to reflection, and sign "–" corresponds to transmission through the medium. The $G^{BQ}(z)$ Green's function multiplied by the exponential factor $\exp[i(2k_{z,\omega} \pm k_{z,2\omega})z]$ forms the so-called "propagation factor," which is an oscillating coordinate function (see Fig. 1). If the medium absorption is weak, an unbalanced contribution to the resultant second harmonic field is generated

from the subsurface region of effective thickness l^{eff} equal to half the distance at which second harmonic field is balanced. For weak absorption, the effective thickness is given by

$$l^{\text{eff}} = \frac{\pi}{2k_\omega \pm k_{2\omega}} = \frac{\lambda_\omega}{4(n_\omega \pm n_{2\omega})}$$

with "–" and "+" signs corresponding to transmission and reflection, respectively. For the STO crystal at λ_ω = 739 nm, the $l^{\text{eff}}_{\text{refl}}$ value equals 40 nm in the reflection geometry and $l^{\text{eff}}_{\text{tr}}$ = 420 nm in the transmission geometry. This means that the contribution of bulk substance to the second harmonic intensity is two orders of magnitude larger in the transmission geometry than in the reflection geometry. The relative contribution of the surface is therefore two orders of magnitude larger in the reflection geometry. Precisely for this reason, if surface diagnostics are possible for a given material, it can much more effectively be performed by reflection measurements.

It was shown in [27] that, in a medium with nonlinear polarization $\mathbf{P}(2\omega)$ fluctuations (spatial and/or time), coherent second harmonic $I^{2\omega}_{\text{coh}}$ generation is accompanied by the generation of an incoherent, or diffuse, second harmonic $I^{2\omega}_{\text{scat}}$,

$$I^{2\omega} = I^{2\omega}_{\text{scat}} + I^{2\omega}_{\text{coh}}.$$

The incoherent second harmonic intensity is determined by the $\Phi_{i,j}(r_1, r_2)$ nonlinear polarization correlation function [28],

$$I^{2\omega}_{\text{scat}}(\mathbf{q}) \propto \iint d\mathbf{r}_1 d\mathbf{r}_2 \exp[i\mathbf{q}(\mathbf{r}_1 - \mathbf{r}_2)]\Phi_{i,j}(\mathbf{r}_1, \mathbf{r}_2), \quad (5)$$

where

$$\Phi_{i,j}(\mathbf{r}_1, \mathbf{r}_2) = \langle(\langle P^{(2\omega)}_i\rangle - P^{(2\omega)}_i(\mathbf{r}_1))(\langle P^{(2\omega)}_j\rangle - P^{(2\omega)}_j(\mathbf{r}_2))\rangle \quad (6)$$

(symbol $\langle\rangle$ denotes statistical averaging including averaging over disorder realizations).

Coherent radiation is generated as a mirror image of incident radiation; that is, its angular diagram is only determined by the angular divergence of laser beams (1–2 degrees). The angular width of scattered radiation depends on the ratio between inhomogeneity size Δ and wavelength λ and can vary from π ($\Delta \ll \lambda$) to a value comparable with laser beam divergence ($\Delta \geq \lambda$) [27]. The procedure for separating coherent and incoherent contributions is based on examining the scattering indicatrix.

Because incoherent radiation has a random phase, its propagation does not lead to field compensation. Scattered radiation at the exit from the crystal is therefore the sum of second harmonic intensities (rather than fields) over the whole crystal volume, and no nonlinear optical probing of the crystal in depth occurs in incoherent second harmonic generation. On the other hand, the intensity of backscattering is much lower than the intensity of scattering along the beam direction. For this reason, the fraction of scattered radiation is much lower when the reflection rather than transmission geometry is used. Clearly, no matter what geometry, the contribution of the crystal volume to the incoherent second harmonic intensity far exceeds the contribution of the surface. We will therefore only consider the volume contribution in discussing incoherent second harmonic generation.

3. A PHENOMENOLOGICAL DESCRIPTION OF THE COHERENT SECOND HARMONIC FIELD NEAR THE PHASE TRANSITION

Determining the temperature dependences of the second harmonic intensity near the phase transition requires calculating the temperature dependences of nonlinear susceptibilities. In the Landau theory of phase transitions, the equation for the nonlinear susceptibility in the low-temperature phase takes the form

$$\chi^{Q4mmm}_{ijkl} = \chi^{Qm3m}_{ijkl} + \Delta\chi^{Q4mmm}_{ijkl}, \quad (7)$$

where

$$\Delta\chi^{Q4mmm}_{ijkl} = \theta_{ijklmn}\eta_m\eta_n, \quad (8)$$

χ^{Qm3m}_{ijkl} is the nonlinear susceptibility, θ_{ijklmn} is the sixth-rank tensor (both correspond to the high-temperature phase), and η is the volume order parameter. In the STO crystal, order parameter η_i is the angle of oxygen octahedron rotation about the ith crystallographic axis (see Fig. 2). The first nonvanishing additional term in χ^{Qm3m}_{ijkl} is quadratic in the order parameter. Note that such a susceptibility representation is in principle similar to the linear susceptibility representation suggested in [29]. At the same time, the authors of [29] disregard the tensor character of the additional susceptibility term, which should be taken into account for both linear and nonlinear susceptibilities. Otherwise, it is, for instance, impossible to distinguish between the longitudinal and transverse (with respect to the tetragonal axis) linear susceptibilities in the low-temperature STO phase.

The temperature dependence of the order parameter is determined by the free energy, which, in the volume of an ideal crystal, has the form [1]

$$F_B = F_0 + \int dV\left(\frac{A}{2}\sum_{i=1}^{3}\eta_i^2 + \frac{D}{2}\sum_{i=1}^{3}(\nabla\eta_i)^2 + \frac{B}{4}\left(\sum_{i=1}^{3}\eta_i^2\right) - \frac{B_1}{4}\sum_{i=1}^{3}(\eta_i^4)\right), \quad (9)$$

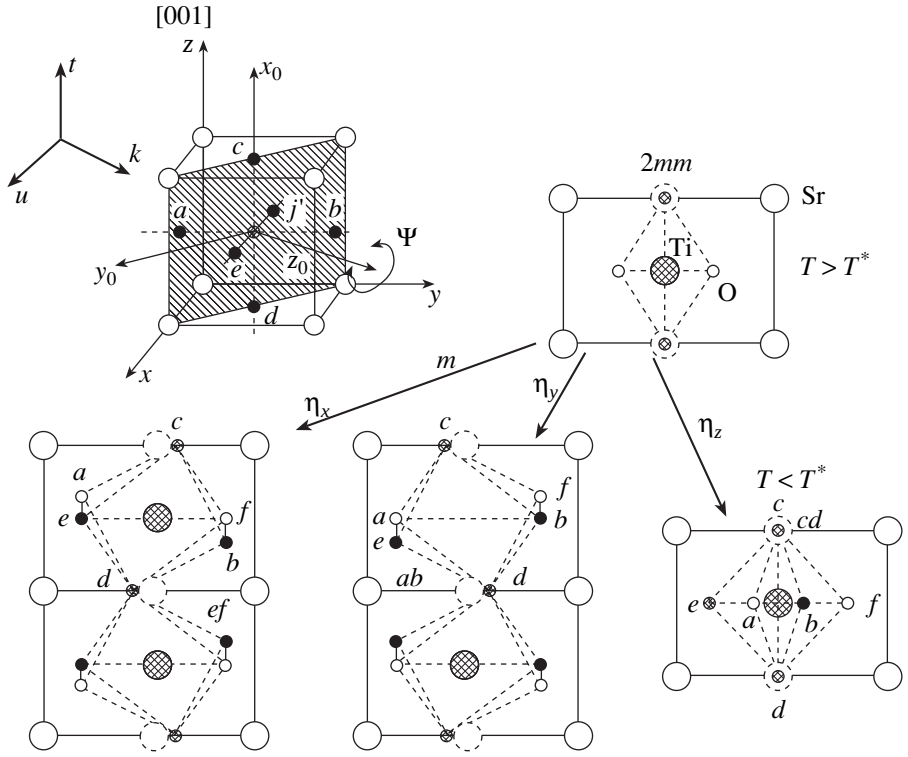

Fig. 2. STO crystal unit cell structure in the high-temperature phase (at the top left). Solid circles are oxygen atoms constituting an oxygen tetrahedron. The angle of rotation of the tetrahedron about one of crystal axes (*x*, *y*, or *z*) equals the corresponding order parameter component at the structural phase transition point; $x_0y_0z_0$ is the (110) surface system of coordinates; *tuk* is the laboratory system of coordinates; Ψ is the azimuthal angle between axis *t* of the laboratory frame of reference and the (001) crystal axis (or the x_0 axis of the surface coordinate system), that is, the angle of crystal rotation about the normal to its surface. Shown at the bottom is the arrangement of atoms in the unit cell of the surface layer in the low-temperature phase when the oxygen tetrahedron rotates about axes (from left to right) *x*, *y*, and *z*; the same is shown at the top right for the high-temperature phase. For convenience of comparing the volume and surface unit cells, oxygen atoms are also labeled by letters.

where

$$A = a(T - T_c), \quad B > B_1 > 0,$$

and *a* and *D* are the Landau expansion constants. For the STO crystal, $a = 5.4 \times 10^{-3}$ eV K^{-1} and $D = 3.7 \times 10^{-15}$ eV cm^2 [30].

We have $\eta = 0$ above T_c and $\eta \propto \tau^{1/2}$ below T_c ($\tau = |T_c - T|/T_c$ is the reduced temperature). It follows that, below T_c, the temperature dependence of the additional nonlinear susceptibility term and, therefore, the additional second harmonic field term is linear in temperature,

$$E^{2\omega} \propto \chi_{ijkl}^{Qm3m} + \Delta\chi_{ijkl}^{Q4mmm} \propto \chi_{ijkl}^{Qm3m} + \alpha(T_c - T), \quad (10)$$

where α is a constant. In the high-temperature phase, $\Delta\chi_{ijkl}^{Q4mmm} = 0$. The temperature dependence of χ_{ijkl}^{Qm3m} unrelated to the phase transition can be included as a second order polynomial of $T_c - T$; that is, in a way similar to that used for the index of refraction in [31]. It follows that the temperature dependence of nonlinear susceptibility has a kink at $T = T_c$; a kink should therefore be present also in the temperature dependence of the second harmonic field.

The presence of a surface causes the appearance of the additional F_{surf} term in the equation for the free energy. If the presence of a surface only results in the arising of a single order parameter component, η can be written without indices, and F_{surf} takes the form [12]

$$F_{surf} = \int \frac{d_0\tilde{A}}{2}\eta_0^2\, dS, \quad (11)$$

where η_0 is the order parameter value on the surface, $\tilde{A} < 0$ and $d_0 > 0$ are constants, and the integration is performed over the surface of the crystal. The $\tilde{A}$ value describes coefficient *A* changes close to the surface, and d_0 is the thickness of the layer within which $\tilde{A}$ varies. For a plane surface coinciding with the $z = 0$ surface of the Cartesian coordinate system, $\eta_0 = \text{const}$, and the order parameter in the volume only depends on coordinate *z*. Varying Eq. (9) for the free energy with respect to the order parameter yields

$$A\eta + (B - B_1)\eta^3 = D\frac{d^2\eta}{dz^2}. \quad (12)$$

At $T > T_c$, when the order parameter equals zero far from the surface, the solution to (12) has the form

$$\eta = \eta_0\left[\sqrt{1 + \frac{(B - B_1)\eta_0^2}{2A}}\sinh\frac{z}{r_c} + \cosh\frac{z}{r_c}\right]^{-1}, \quad (13)$$

which in turn gives

$$\eta = \eta_0\exp(-z/r_c), \quad (14)$$

if

$$\eta_0^2 \ll A/(B - B_1).$$

Here, $r_c = \sqrt{D/A}$ is the correlation radius for the order parameter. Substituting the equation for the free energy into (13) and minimizing the resulting equation with respect to η, we obtain temperature T^* at which a nonzero component of the surface order parameter appears; that is, the temperature of the surface phase transition,

$$T^* = T_c + \frac{(\tilde{A}d_0)^2}{aD}. \quad (15)$$

Assuming that d_0 equals the lattice parameter and $\tilde{A} \approx aT_c$, we obtain

$$T^* = T_c + 20^{\mathrm{K}} = 125\ \mathrm{K}.$$

For order–disorder phase transitions (for instance, magnetic phase transitions), $\tilde{A} > 0$, and the order parameter near the surface is suppressed compared with its value in the volume, because the number of nearest neighbors and, therefore, the effective field created by them for a spin situated close to the surface are lower than in the bulk. For displacement transitions, additional lattice softening caused by the absence of neighbors near the surface may occur; this corresponds to the condition $\tilde{A} < 0$. If this condition is met, the phase transition on the surface occurs earlier than in the bulk as temperature decreases.

If

$$0 < T^* - T \ll T - T_c,$$

the surface order parameter is described by the equation

$$\eta_0^2 = -\frac{8(Ar_c + d_0\tilde{A})}{Br_c} \propto (T^* - T). \quad (16)$$

To calculate nonlinear susceptibility, consider the symmetry of subsurface layers in the high- and low-temperature phases. The arrangement of atoms in the unit cell of the (110) STO crystal surface is schematically shown in Fig. 2. The surface has 2*mm* symmetry in the high-temperature phase. In the low-temperature phase, the order parameter can be oriented along any crystallographic axis. However, surface unit cells have *m* symmetry in any event.

By analogy with the volume nonlinear susceptibility, the nonlinear susceptibility of the surface can be written as

$$\chi_{ijk}^{Dm} = \chi_{ijk}^{D2mm} + \Delta\chi_{ijk}^{Dm}, \quad (17)$$

where

$$\Delta\chi_{ijk}^{Dm} = \theta_{ijklm}\eta_{0l}\eta_{0m}. \quad (18)$$

As in the bulk, the surface phase transition causes the appearance of a kink in the temperature dependence of the second harmonic field. We therefore have

$$E^{2\omega} \propto \chi_{ijk}^{D2mm} + \Delta\chi_{ijk}^{Dm} \propto \chi_{ijk}^{D2mm} + \alpha'(T - T^*) \quad (19)$$

for $T < T^*$, where α' is a constant.

In both transmission and reflection measurements, the second harmonic field is determined by the mutual orientation of pumping wave and second harmonic field vectors and the sample crystallographic axes, on the one hand, and by the Frensel factors, which, in turn, depend on the incidence angle, on the other.

The azimuthal angle at which the surface component can be observed was selected based on model calculations of the azimuthal dependences of the surface and volume contributions to the second harmonic intensity at various symmetry properties of the volume and surface corresponding to different temperature regions (Fig. 3). At temperature $T > T^*$, *p*-polarized second harmonic field components (the **E** vector lies in the incidence plane) generated in the volume and on the surface of a sample are described by the equations

$$E^{\mathrm{bulk}}(2\omega) \propto P^{\mathrm{bulk}}(2\omega) = b_1 + b_2\cos(2\Psi) + b_3\cos(4\Psi), \quad (20a)$$

$$E^{\mathrm{surf}}(2\omega) \propto P^{\mathrm{surf}}(2\omega) = s_1 + s_2\cos(2\Psi), \quad (20b)$$

where b_i are the linear combinations of the quadrupole nonlinear susceptibility tensor χ_{ijkl}^{Q} components and s_i are the linear combinations of the dipole nonlinear susceptibility tensor χ_{ijk}^{D} components determined by symmetry of the corresponding phase and the polarization of pumping radiation. These second harmonic field components always have a constant constituent. Here and throughout, the Ψ angle is counted from the (001) crystallographic axis. S-polarized field components (the **E** vector is perpendicular to the plane of incidence) from both volume

$$E^{\mathrm{bulk}}(2\omega) \propto P^{\mathrm{bulk}}(2\omega) = b_4\sin(2\Psi) + b_5\sin(4\Psi)$$

and surface

$$E^{\mathrm{surf}}(2\omega) \propto P^{\mathrm{surf}}(2\omega) = s_3\sin(2\Psi)$$

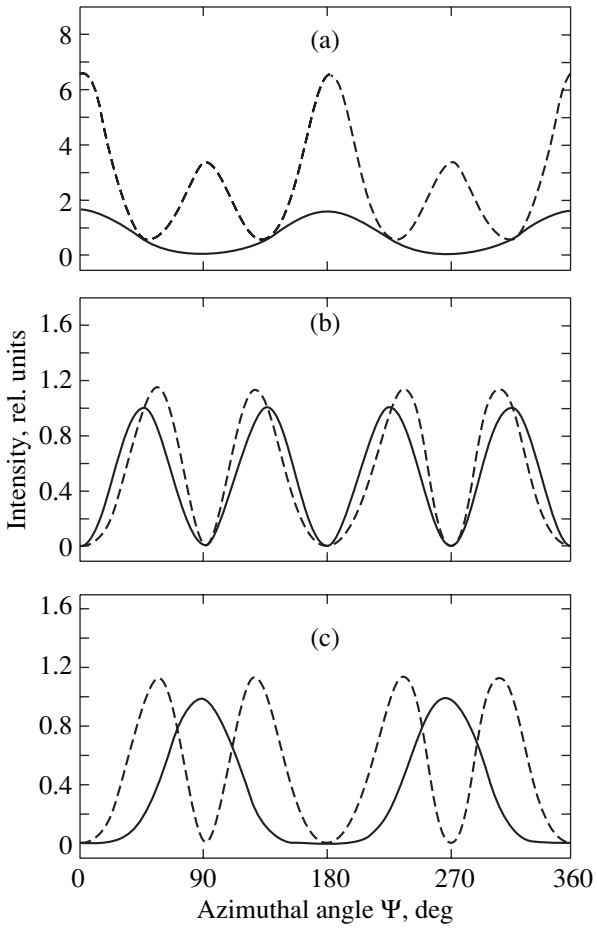

Fig. 3. Qualitative azimuthal angle dependences of the intensity of second harmonics generated in the bulk (dashed lines) and on the surface (solid lines): (a) $T > T_c$, T^*, polarization combinations *pp* and *sp*; (b) $T > T_c$, T^*, polarization combinations *ps* and *ss*; and (c) $T_c < T < T^*$, polarization combinations *ps* and *ss* [see (21) and (22)].

have minima at equal azimuthal angle values. It follows that, at $T > T^*$, there is no such (110) surface azimuthal angle at which the surface contribution can be observed while the volume contribution is zero. In the $T_c < T < T^*$ temperature region, the surface is in the low-temperature and the volume in the high-temperature phase. For the *s*–*s* polarization combination (the α–β combination denotes the α polarization of pumping radiation and the β polarization of second harmonic radiation), the surface contribution can be observed against zero volume contribution. Indeed, for such a polarization combination, the azimuthal dependences of volume and surface second harmonic fields are described by

$$E^{\text{bulk}}(2\omega) \propto P^{\text{bulk}}(2\omega) = b_4 \sin(2\Psi) + b_5 \sin(4\Psi), \quad (21)$$

$$E^{\text{surf}}(2\omega) \propto P^{\text{surf}}(2\omega) = s_4 \sin(\Psi) + s_5 \sin(3\Psi). \quad (22)$$

According to these equations and Fig. 3, the necessary condition for surface second harmonic observation is met at the $\Psi = \pi/2$ azimuthal angle. We selected two azimuthal angles for measurements, namely, $\Psi = \pi/2$ and $\Psi = \pi/4$. At $\Psi = \pi/2$, the surface contribution should be maximum. At $\Psi = \pi/4$, both surface and volume contributions should be observed. An interesting problem is to find whether or not the surface contribution can be identified against the background of a nonzero volume contribution.

4. A PHENOMENOLOGICAL DESCRIPTION OF INCOHERENT SECOND HARMONIC FIELD IN THE PHASE TRANSITION REGION

The characteristics of light scattering in the critical region have been extensively studied in works concerned with ferroelectric phase transitions. The corresponding data on the structural phase transition in the STO crystal are, however, scarce, because the soft mode at the boundary of the Brillouin zone is inactive in first-order Raman spectra [1]. That is, both first-order Raman scattering at the soft mode frequency and first-order Rayleigh scattering are forbidden in the high-temperature phase. Processes allowed in the high-temperature phase are second-order processes.

Unlike linear scattering, scattering at the doubled frequency, that is, hyper-Rayleigh and hyper-Raman scattering, has not been studied in detail for structural phase transitions. Generally, the selection rules for hyper processes are less stringent. Even if Raman or Rayleigh scattering at the fundamental frequency is not observed, it can be observed at the doubled frequency; the more so if the corresponding processes at the fundamental frequency are allowed.

Quite a different picture was, however, observed in experiments. The elastic light scattering peak at the fundamental frequency was observed for STO crystals in [32]. Light scattering at the doubled frequency was studied in [33] in a wide temperature range 40–300 K, but no singularity was detected at $T_c = 105$ K.

The central light scattering peak near the phase transition point appears because of the presence of thermal fluctuations and defects. Generally, processes of different types are characterized by different temperature dependences of light scattering intensity [34]. Order parameter thermal fluctuations give a central quasi-elastic scattering peak and side Raman scattering branches at the soft mode frequency. Defects are elastic scattering sources. According to the estimates made in [35], linear (fundamental frequency) scattering on defects may be comparable in intensity with scattering on fluctuations even in a "pure" crystal with a 10^{18} cm^{-3} concentration of defects. The nature of the central peak can be determined by studying the temperature dependences of scattering intensity.

According to (5), we must first calculate the nonlinear polarization correlation function in the nonuniform medium to determine the incoherent second harmonic intensity. For this purpose, consider the equation for the

free energy containing a term taking into account the presence of defects, F_{def} [35],

$$F_{\text{def}} = -\sum_{i=1}^{3}\sum_{m} h_i^{(m)}\eta_i\delta(\mathbf{r}-\mathbf{R}_m), \tag{23}$$

where the summation over m is over the defects, $\mathbf{R}_m$ are radii vectors determining the positions of chaotically distributed defects, and

$$h_i^{(m)} = h_0(-1)^{z_m}\delta_{i,t_m}.$$

Here, z_m is a random variable which equiprobably takes on the values 0 and 1 (the case of unpolarized defects), and t_m is a random variable which equiprobably takes on the values 1, 2, and 3 (depending on the defect). Equation (23) only takes into account the contribution of so-called *s* defects of the "random field" type; it was shown in [35] that precisely these defects made the predominant contribution to the intensity of quasi-elastic scattering.

By analogy with linear scattering [29], the intensity of light scattered at the doubled frequency is given by the equation

$$\begin{aligned} I(\mathbf{q}) &= \frac{u}{V^2}\Big\langle\iint d\mathbf{r}_1 d\mathbf{r}_2 e^{i\mathbf{q}\cdot(\mathbf{r}_1-\mathbf{r}_2)} e_j^{2\omega}\theta_{jlmnps}k_l^{2\omega}e_m^{\omega}e_n^{\omega} \\ &\times e_\beta^{2\omega}\theta_{\beta\gamma\delta\mu\nu\xi}k_\gamma^{2\omega}e_\delta^{\omega}e_\mu^{\omega}\eta_p(\mathbf{r}_2)\eta_s(\mathbf{r}_2)\eta_\nu(\mathbf{r}_1)\eta_\xi(\mathbf{r}_1)\Big\rangle \\ &= u\Pi_{ps\nu\xi}\Big(4\langle\eta_\nu\rangle\langle\eta_p\rangle\langle\tilde\eta_s(\mathbf{q})\tilde\eta_\xi(-\mathbf{q})\rangle \\ &+\Big\langle\sum_{\mathbf{Q}}\tilde\eta_p(\mathbf{Q})\tilde\eta_s(\mathbf{q}-\mathbf{Q})\sum_{\mathbf{Q}'}\tilde\eta_\nu(-\mathbf{Q}')\tilde\eta_\xi(\mathbf{Q}'-\mathbf{q})\Big\rangle\Big) \\ &= I_1(\mathbf{q}) + I_2(\mathbf{q}), \end{aligned} \tag{24}$$

where

$$\Pi_{ps\nu\xi} = e_j^{2\omega}\theta_{jlmnps}k_l^{2\omega}e_m^{\omega}e_n^{\omega}e_\beta^{2\omega}\theta_{\beta\gamma\delta\mu\nu\xi}k_\gamma^{2\omega}e_\delta^{\omega}e_\mu^{\omega};$$

$\mathbf{k}^{2\omega}$ is the wave vector of the second harmonic wave; $\mathbf{e}^{\omega}$ and $\mathbf{e}^{2\omega}$ are the unit vectors in the directions of the electric field vectors of pumping and second harmonic waves, respectively; and

$$\mathbf{q} = \mathbf{k}^{2\omega} - 2\mathbf{k}^{\omega}, \quad \tilde\eta_p = \eta_p - \langle\eta_p\rangle.$$

The summation is over the Brillouin zone in the second term in (24), and $u = V^2 f_{2\omega}^2 f_{\omega}^4$, where V is the scattering volume.

The first and second terms in (24) determine the intensity of critical hyperopalescence of the first and second orders, respectively. The temperature dependence of the intensity of scattering is determined by the Fourier transform of the correlation function. For thermal order parameter fluctuations, this function will be denoted by $F_f\delta_{ik}$, and for static order parameter fluctuations caused by the presence of defects, by $F_d\delta_{ik}$. For definiteness, set $\langle\eta_i\rangle \equiv \bar\eta\,\delta_{i,x}$ at $T < T_c$. The Fourier transform of the correlation function for the *s*th order parameter component then takes the form

$$F_f(s, x, \mathbf{q}) = \frac{T}{V} \times\begin{cases}(A + 3(B-B_1)\bar\eta^2 + Dq^2)^{-1}, & s = x,\\ (A + B\bar\eta^2 + Dq^2)^{-1}, & s \neq x,\end{cases} \tag{25}$$

$$F_d(s, x, \mathbf{q}) = \frac{Nh_0^2}{3V} \times\begin{cases}(A + 3(B-B_1)\bar\eta^2 + Dq^2)^{-2}, & s = x,\\ (A + B\bar\eta^2 + Dq^2)^{-2}, & s \neq x.\end{cases} \tag{26}$$

The 1/3 factor appears because the number of defects with a given random field direction equals one-third of the total number of defects.

As a result, we obtain

$$I_1(\mathbf{q}) = 4u\Pi_{xsxs}\bar\eta^2 F(s, x, \mathbf{q}) \tag{27}$$

for first-order scattering. At $T > T_c$, $\bar\eta$ is zero, and the $I_f^{(1)}(\mathbf{q})$ and $I_d^{(1)}(\mathbf{q})$ scattering intensities of both types are therefore zero in the high-temperature phase. At $T < T_c$, substituting F_f into (27) gives the intensity of scattering on thermal fluctuations

$$I_f^{(1)}(0) \propto \begin{cases}(B-B_1)^{-1}, & s = x,\\ B_1^{-1}, & s \neq x,\end{cases}$$

in the $qr_c \ll 1$ approximation; that is, the intensity of scattering on thermal fluctuations is independent of temperature. For scattering on defects, substituting F_d into (27) yields

$$I_d^{(1)}(0) \propto \begin{cases}[|A|(B-B_1)]^{-1}, & s = x,\\ \dfrac{B-B_1}{|A|B_1^2}, & s \neq x.\end{cases}$$

The intensity of scattering on defects is therefore proportional to τ^{-1}.

Note that the contribution of domains with one order parameter orientation to scattering intensity differs from the contribution of domains with another orientation.

Consider second-order scattering.

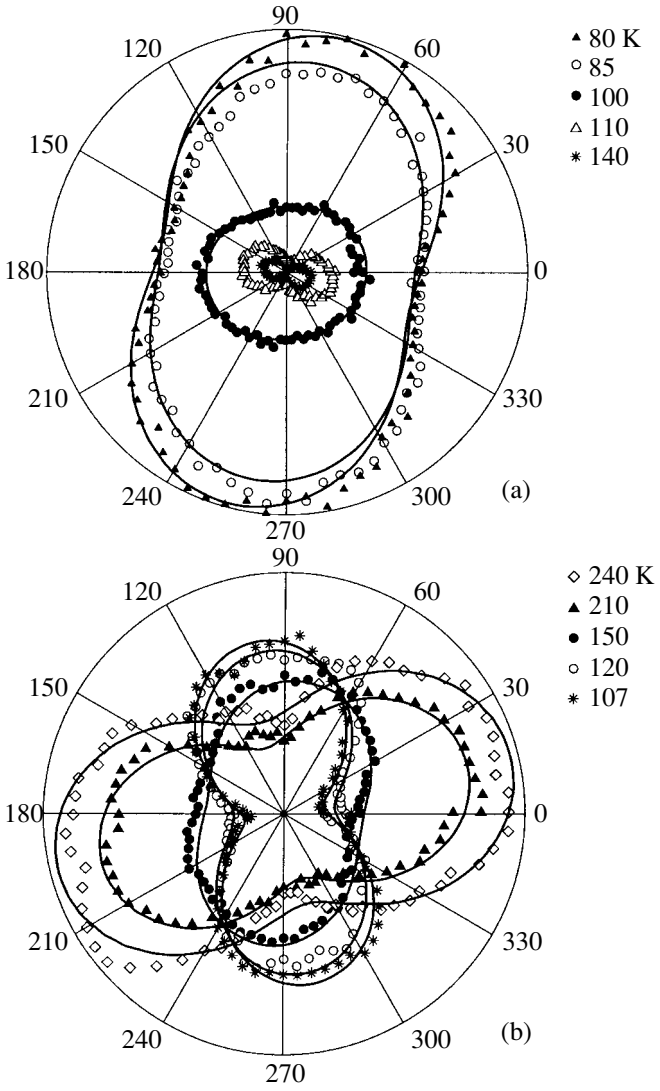

Fig. 4. Dependences of second harmonic intensity on the angle of analyzer rotation (deg) at various sample temperatures in (a) transmission and (b) reflection geometries.

For thermal fluctuations, (24) yields (see [29])

$$I_2(\mathbf{q}) = 2u\Pi_{psps}V \times \int \frac{d^3\mathbf{Q}}{(2\pi)^3} F_f(p, x, \mathbf{Q}) F_f(s, x, \mathbf{q}-\mathbf{Q}) \propto \Pi_{psps}\left(\frac{T}{D}\right)^2 r_c \propto \Pi_{psps}\tau^{-1/2}, \quad T > T_c, \quad qr_c \ll 1. \tag{28}$$

The presence of the coefficient Π_{psps} in (28) is indicative of the anisotropic character of scattered radiation, that is, of the dependence of the intensity of scattered radiation on the azimuthal angle of the crystal at fixed polarization combinations of incident and second harmonic waves.

For defects, applying the approximation of quasi-isolated defects and (24) yields (cf. [34])

$$I_2(\mathbf{q}) = u\Pi_{psps}V \times \left(2\int \frac{d^3\mathbf{Q}}{(2\pi)^3} F_d(p, x, \mathbf{Q}) F_d(s, x, \mathbf{q}-\mathbf{Q}) + \frac{Nh_0^4}{3T^2}\left(\int \frac{d^3\mathbf{Q}}{(2\pi)^3} F_f(p, x, \mathbf{Q}) F_f(p, x, \mathbf{q}-\mathbf{Q})\right) z(p, s)\right), \tag{29}$$

where $z(p, s) = \delta_{p, s}$. At $qr_c \ll 1$ and $T > T_c$, we obtain

$$I_{2d} \propto \Pi_{psps}\frac{Nr_c^2}{D^4}(2\pi Nr_c^3 + 1). \tag{30}$$

The first term in (29) is proportional to $N^2 r_c^5$, and the second term is proportional to Nr_c^2. Either the first or the second term may be predominant depending on the concentration of defects. In both cases, we obtain a power dependence of scattering intensity on reduced temperature,

$$I_{2d} \propto \Pi_{psps}\tau^{-\gamma},$$

where $\gamma = 1$ at $2\pi Nr_c^3 \ll 1$ and $\gamma = 5/2$ at $2\pi Nr_c^3 \gg 1$. In the whole range where the theory of quasi-isolated defects [35] applies, that is, if

$$\frac{BNh_0^2 r_c^3}{4\pi D^3} \ll 1, \tag{31}$$

first-order scattering intensity exceeds second-order scattering intensity at $T < T_c$. The observation of second-order scattering is therefore only possible in the high-temperature phase.

The results of the calculations described above are summarized in the table.

Note that the equations for the temperature dependences of the intensity of scattering on defects at the second harmonic frequency coincide with the equations for the temperature dependences of linear scattering intensities obtained in [34]. These equations contain different coefficients, which, in particular, depend on the directions of incident and scattered wave polarizations and on the azimuthal angle of the crystal.

5. EXPERIMENTAL PROCEDURE

The STO crystal that we used was grown by optical zone melting, polished to an optical quality, and oriented by the (110) plane accurate to ±0.05°. The crystal was placed into an optical helium cryostat (Oxford Instruments, 5–300K).

In nonlinear optical experiments, we used titanium-sapphire laser pumping radiation, radiation wavelength =

739 nm, pulse width = 100 fs, pulse frequency = 82 MHz, and mean power = 100 mW. Radiation was focused onto a spot about 100 μm in diameter. The incidence angle was 45° in reflection measurements and 0° (normal incidence) in transmission measurements.

Pumping radiation polarization was changed by rotating a half-wave plate, and second harmonic radiation polarization, by rotating a polaroid film. By rotating the polaroid, we obtained polarization curves at various sample temperatures, that is, the dependences of second harmonic intensity on the angle of analyzer rotation $I_{2\omega}(\varphi)$ (Figs. 4a, 4b). The $\varphi = 0$ angle corresponded to the vertical orientation of the second harmonic field vector (output *s* polarization in reflection measurements).

The azimuthal dependence of second harmonic intensity $I_{2\omega}(\Psi)$ was measured in the mirror direction when the sample was rotated with respect to normal *z* to the surface of the crystal (*utk* is the laboratory immobile frame of reference, and $x_0y_0z_0$ is the mobile surface coordinate system; azimuthal angle Ψ was measured between axes *u* and x_0—see Fig. 2). An example of azimuthal anisotropy in reflection measurements is given in Fig. 5. The azimuthal dependences of second harmonic intensity qualitatively coincided with the theoretical dependences shown in Fig. 3.

The second harmonic scattering indicatrix was measured when the recording system was rotated about vertical axis *t* (Fig. 2). The reference point for counting polar angle θ was selected in such a way that the θ angle equaled zero in the direction of the normal to the surface of the crystal and was negative in the direction of pumping radiation. An example of the scattering indicatrix in reflection measurements is shown in Figs. 6a and 6b. The receiving aperture equaled 2°. In all experiments, we measured second harmonic radiation intensities at $I^{2\omega}_{\theta=0^\circ}$ and $I^{2\omega}_{\theta=5^\circ}$ at polar θ angle values $\theta = 0^\circ$ and 5°, respectively. The $I^{2\omega}_{\theta=5^\circ}$ second harmonic intensity was assigned to scattered radiation. The angular width of all measured scattering indicatrices was substantially larger than the angular width of the mirror maximum (see Fig. 6) and the 5° detuning value. For this reason, the $I^{2\omega}_{\theta=5^\circ}$ intensity could be considered equal to the scattering radiation intensity at $\theta = 0^\circ$. This allowed us to assign the $I^{2\omega}_{\theta=0^\circ} - I^{2\omega}_{\theta=5^\circ}$ difference to coherent second harmonic radiation.

6. AN EXPERIMENTAL STUDY OF VOLUME PHASE TRANSITION BASED ON COHERENT SECOND HARMONIC GENERATION IN THE TRANSMISSION GEOMETRY

The polarization curves of second harmonic intensity measured in the transmission geometry at normal incidence and various temperatures are shown in Fig. 4a. An analysis of these dependences shows that a second harmonic signal is observed at $T > T_c$, but its intensity is insignificant. At $T = 105$ K, second harmonic intensity sharply increases, and the predominant polarization direction changes. The temperature dependences of the angle of predominant polarization are shown in Figs. 7a and 7b for two azimuthal angles.

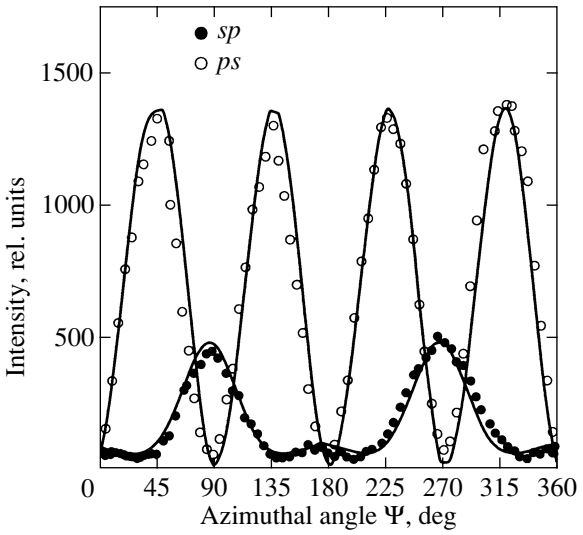

Fig. 5. Experimental azimuthal dependences of second harmonic intensity in reflection geometry at room temperature. Solid lines correspond to approximation by the suggested model.

Second harmonic radiation is incoherent above the phase transition point. After subtracting the intensity of incoherent radiation from the total intensity, the coherent component intensity as a function of the angle of analyzer rotation can be written as

$$I(\varphi) \propto \left(E^{\parallel}_{2\omega}\cos\varphi + E^{\perp}_{2\omega}\sin\varphi\right)^2. \qquad (32)$$

The temperature dependences of the parallel (with respect to the pumping field) $E^{\parallel}_{2\omega}$ and perpendicular

Table

	Fluctuations		Defects	
	$T > T_c$	$T < T_c$	$T > T_c$	$T < T_c$
First order	I = 0	I = const	$I = 0$	$I \propto \tau^{-1}$
Second order	$I \propto \tau^{-1/2}$	$I \propto \tau^{-1/2}$	$2\pi N r_c^3 \ll 1$	
			$I \propto \tau^{-1}$	$I \propto \tau^{-1}$
			$2\pi N r_c^3 \gg 1$	
			$I \propto \tau^{-5/2}$	$I \propto \tau^{-5/2}$

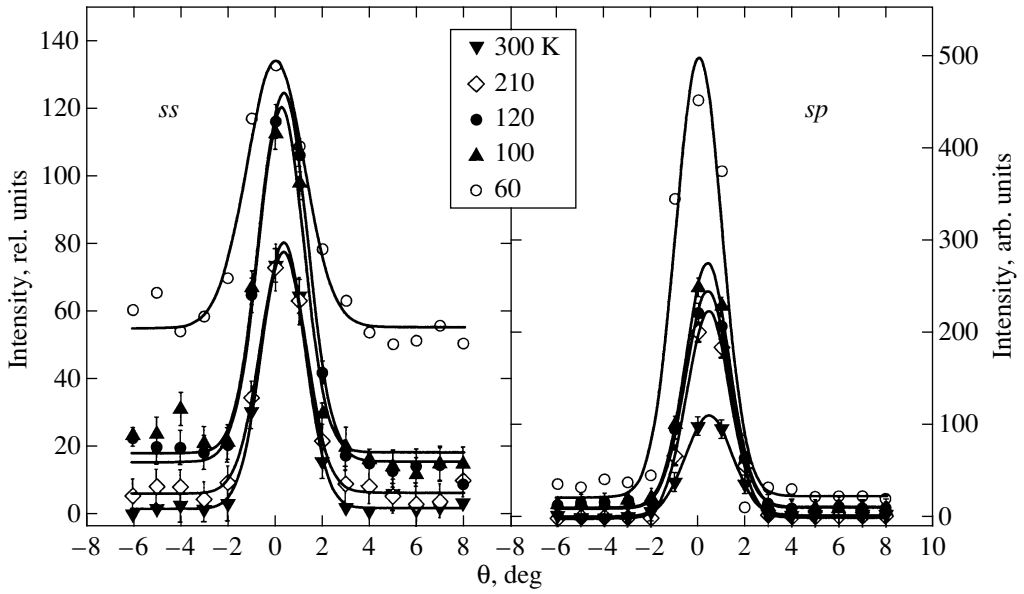

Fig. 6. Experimental polar angle dependences of second harmonic intensity (scattering indicatrices) in reflection geometry for (a) *ss* and (b) *sp* polarization combinations. Crystal azimuthal angle $\Psi = \pi/4$.

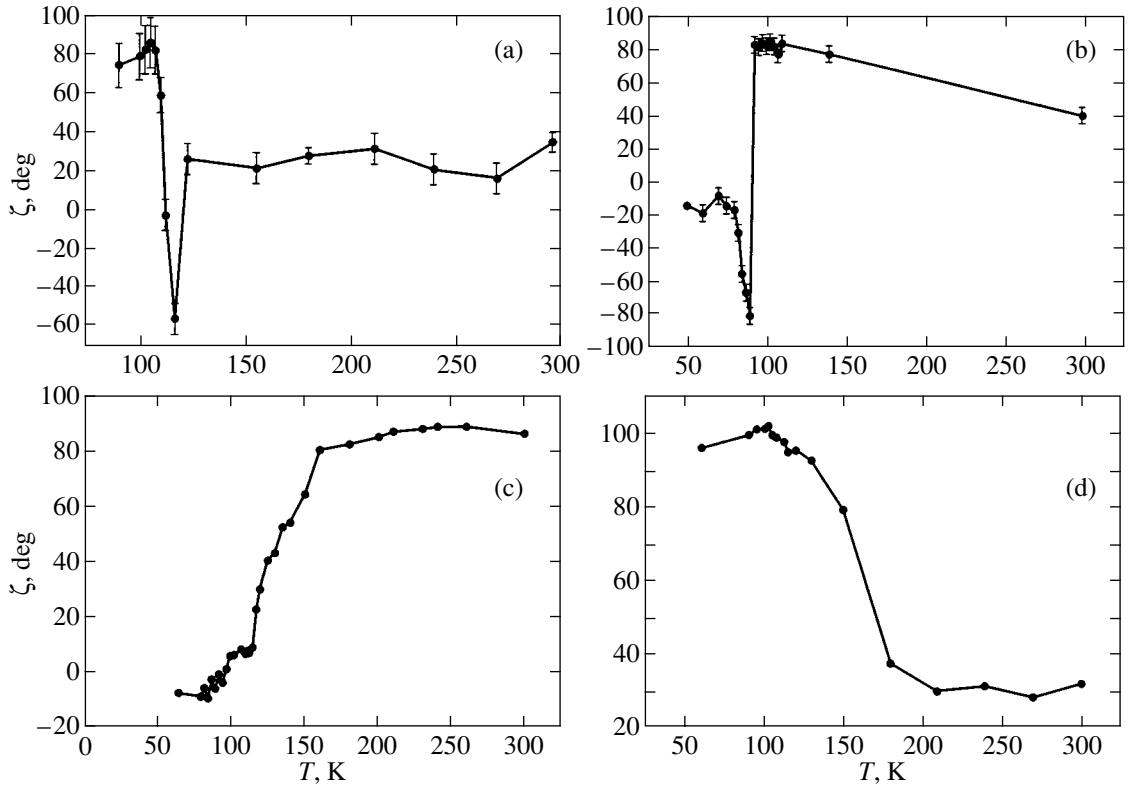

Fig. 7. Temperature dependences of angle ζ of predominant second harmonic radiation polarization at various azimuthal angles in transmission geometry, Ψ = (a) $\pi/4$ and (b) $\pi/2$, and in reflection geometry, Ψ = (c) $\pi/2$ and (d) $\pi/4$.

$E_{2\omega}^{\perp}$ second harmonic field components for the $\Psi = \pi/2$ crystal azimuthal angle are shown in Fig. 8; these dependences were obtained by approximating the experimental polarization curves according to (32). At $T > T_c$, the coherent second harmonic was absent within the error of measurements, in agreement with the model that we use (see Section 3). At $T < T_c$, we observed an increase in both perpendicular and parallel

field components for the $\Psi = \pi/4$ azimuthal angle and in the perpendicular second harmonic field component for the $\Psi = \pi/2$ azimuthal angle. In agreement with our calculations, the parallel field component was absent for this azimuthal angle. Within the framework of our model, such a behavior of the second harmonic intensity means that only second harmonic generation in the crystal volume was observed in the transmission geometry. Below the phase transition point, the temperature dependences of nonzero field components could be approximated by a linear function, in agreement with (10).

It follows that the structural phase transition to the low-symmetry phase manifests itself by coherent second harmonic generation, that is, by the appearance of the corresponding field at the transition point. This field linearly changes as a function of temperature, in agreement with the phenomenological description.

7. AN EXPERIMENTAL STUDY OF THE SURFACE PHASE TRANSITION BASED ON COHERENT SECOND HARMONIC GENERATION IN THE REFLECTION GEOMETRY

The polarization curves for the second harmonic intensity measured in the reflection geometry at various temperatures are shown in Fig. 4b. The intensity of the coherent component (after subtracting the intensity of the incoherent component) can be written in the form

$$I^{\alpha}(\varphi) = (E_{2\omega}^{\alpha, s}\cos\varphi + E_{2\omega}^{\alpha, p}\sin\varphi)^2 \qquad (33)$$

($\alpha = p, s$), which indicates the orientation of the incident wave field vector. The experimental temperature dependences of second harmonic fields $E_{2\omega}^{\alpha, s}$ and $E_{2\omega}^{\alpha, p}$ obtained for the $\Psi = \pi/2$ and $\pi/4$ azimuthal angles are shown in Figs. 9 and 10, respectively. As in transmission measurements, these dependences pass temperature $T^* = 145$ K at which the character of the temperature dependence of second harmonic field changes. Note that the direction of predominant polarization changes at the same temperature T^* (see Fig. 7).

For the $\Psi = \pi/2$ azimuthal angle, the second harmonic s component at all pumping polarizations and the p component at p pumping polarization are zero as temperature decreases from room temperature to T^*. Decreasing temperature below T^* causes an increase (in magnitude) in the second harmonic field until temperature T_c is reached. Further, the character of the dependence again changes. Under p pumping, a constant constituent of the second harmonic p component should always be present. The equality of this component to zero observed experimentally at $T > T^*$ may be explained by the smallness of the $b_1 - b_2 + b_3$ and $s_1 - s_2$ linear combinations [see (20)]. In the temperature range $T_c < T < T^*$, the surface is already in the low-temperature phase, whereas the volume is in the high-temperature phase. An increase in the second harmonic field is then only related to the surface contribution and can, according to (19), be approximated by a linear function. For s pumping at $\Psi = \pi/2$ and all polarization combinations at $\Psi = \pi/4$, the volume contribution to the second harmonic p component is nonzero in the high-temperature phase. As a result, the temperature dependences of the second harmonic field become much more complex. In particular, these dependences contain a trivial (unrelated to the phase transition) temperature dependence of volume nonlinear susceptibilities $\chi_{ijk}^{D2mm}(T)$ and $\chi_{ijkl}^{Qm3m}(T)$ [see (10) and (19)], which can be taken into account by a polynomial second-order in temperature, as was done for the index of refraction in [30]. This trivial dependence does not change as temperature passes the phase transition point. The addition to the second harmonic field caused by the phase transition can be determined as the difference between the temperature dependences of low-temperature phase second harmonic field and of the field obtained by approximating the experimental temperature dependence for the high-temperature phase by the second-

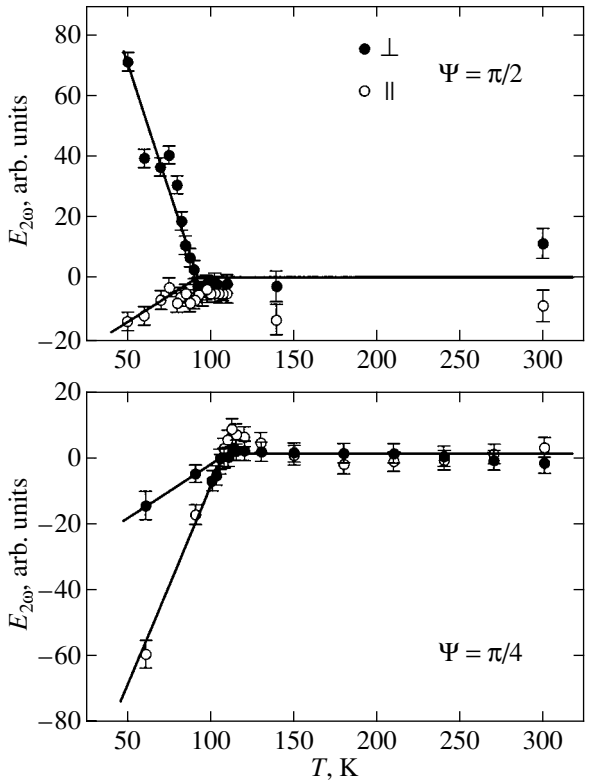

Fig. 8. Temperature dependences of parallel (with respect to pumping field) $E_{2\omega}^{\parallel}$ and perpendicular $E_{2\omega}^{\perp}$ second harmonic components at various crystal azimuthal angles in transmission geometry.

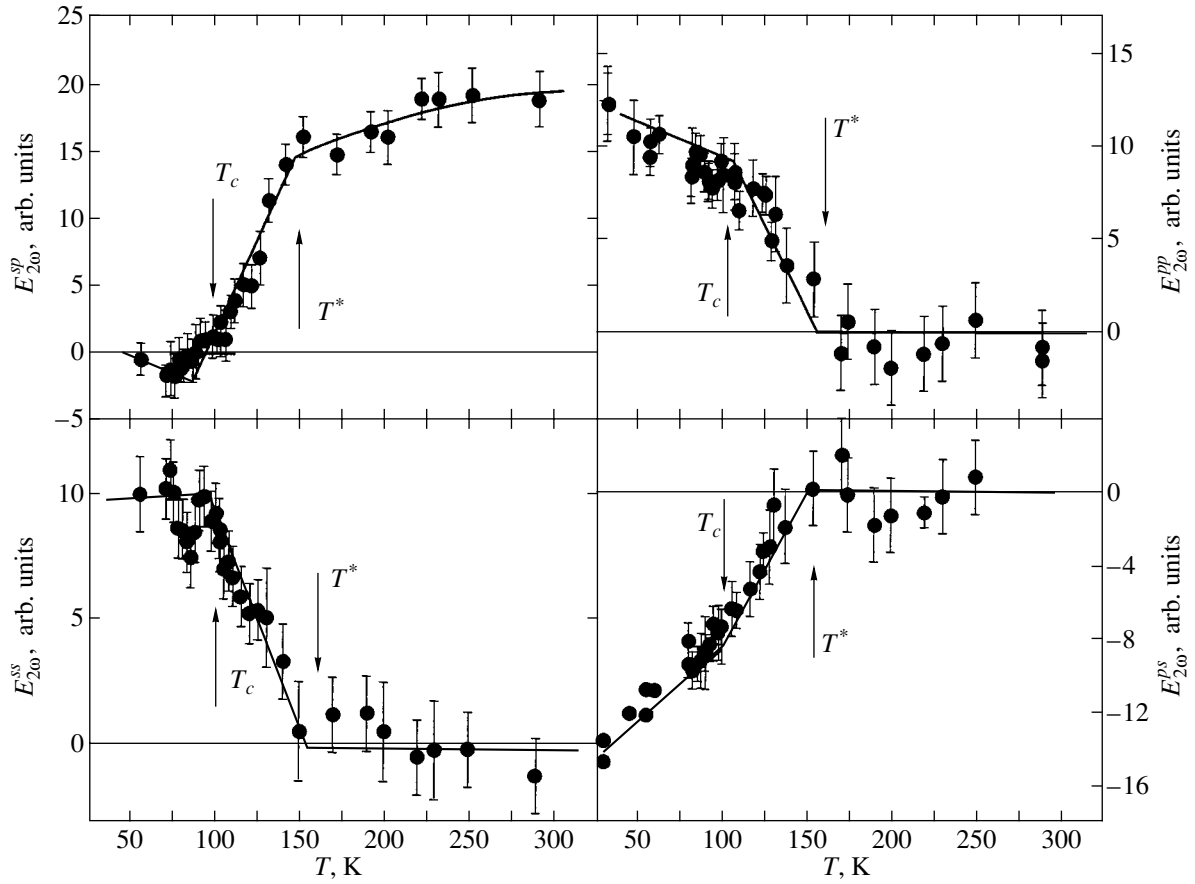

Fig. 9. Temperature dependences of second harmonic field for various polarization combinations in reflection geometry. Solid lines were obtained as approximations by the suggested model. Crystal azimuthal angle $\Psi = \pi/2$.

order polynomial. The temperature dependences of the additional second harmonic field obtained by this procedure are shown in the inset in Fig. 10.

Clearly, the surface contribution may only be qualitatively identified in this situation (Fig. 10). Nevertheless, the results of such an analysis do not contradict the data obtained at $\Psi = \pi/2$. The polarization change at T^* can only be related to the appearance of a surface contribution and can, based on (19), be described by a dependence of the type

$$\frac{a + b\Delta T}{c + d\Delta T},$$

where a, b, c, and d are constants.

The experimental data allowed us to determine the surface phase transition temperature, $T^* = 145 \pm 5$ K.

8. AN EXPERIMENTAL STUDY OF NONLINEAR OPTICAL OPALESCENCE IN THE STRUCTURAL PHASE TRANSITION REGION

The incoherent second harmonic component was measured in both reflection and transmission geometries.

The incoherent second harmonic component intensity measured in the reflection geometry smoothly increased at small polar angles ($\theta = 5°$) as temperature decreased (see Fig. 11).

Such an increase was also observed in [33] and assigned to scattering into the second harmonic as temperature approached the potential ferroelectric phase transition point (such a transition was assumed to occur as $T \longrightarrow 0$). This dependence can be approximated by the expression [33]

$$I_{2\omega}^{\text{scatt}} \propto \omega_{TO}^{-4}(T) = \left(b\frac{\coth(\hbar\bar{\Omega}/2k_BT)}{\bar{\Omega}} - a\right)^{-2}, \quad (34)$$

where ω_{TO} is the phonon TO mode frequency and a, b, and $\bar{\Omega}$ are constants.

In the transmission geometry, a singularity at the T_c volume phase transition point was observed in addition to a low-temperature increase in incoherent second harmonic radiation. The intensity of the incoherent second harmonic, $\Delta I_{2\omega}$, obtained by subtracting the intensity of the second harmonic related to the low-temperature intensity growth [approximation by (34) based on

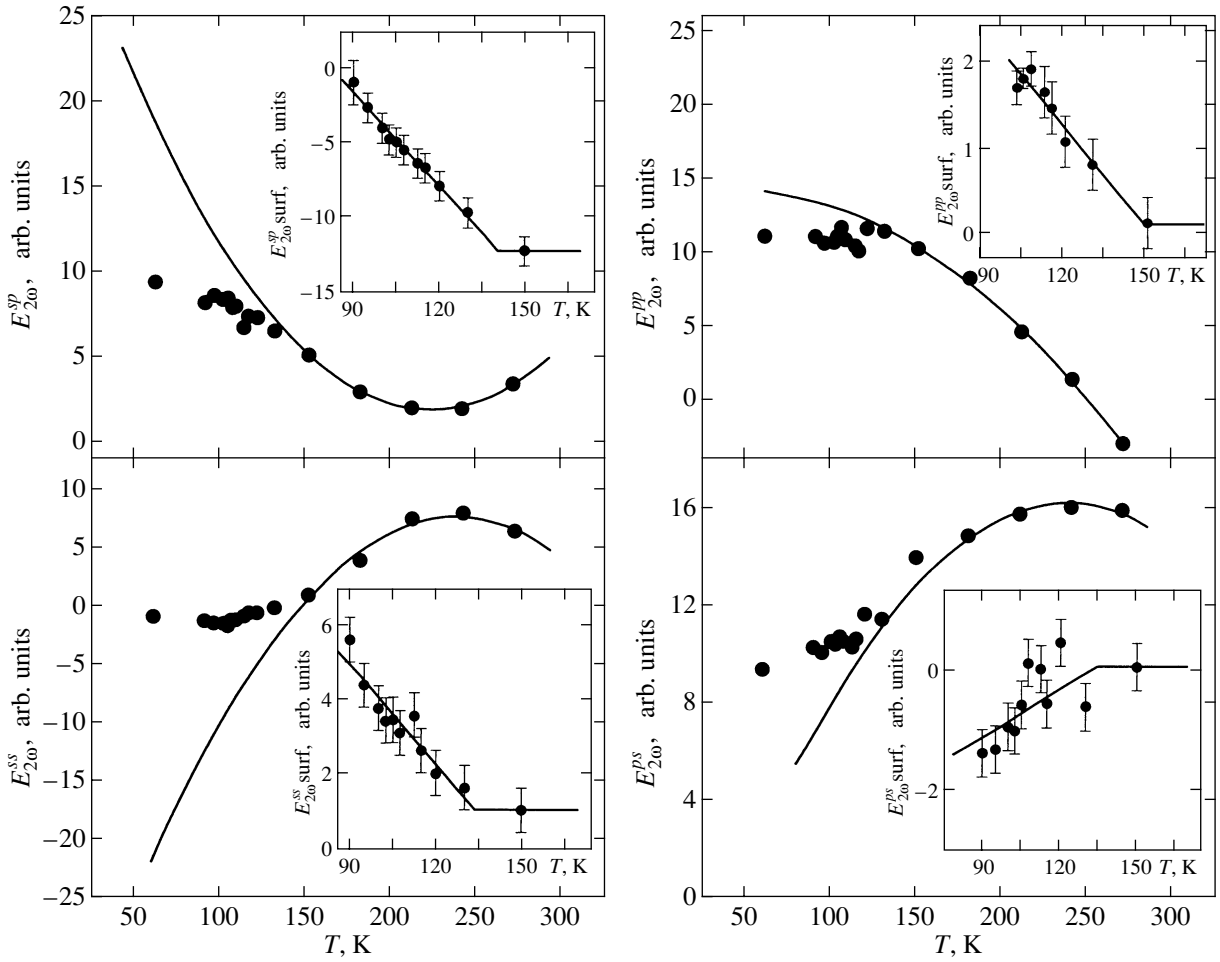

Fig. 10. Temperature dependences of second harmonic field in reflection geometry for various polarization combinations. Crystal azimuthal angle $\Psi = \pi/4$. Solid lines are approximations by the suggested model. Shown in the insets are the same curves less trivial temperature dependences of nonlinear susceptibilities unrelated to the phase transition.

points situated far from T_c ($\tau > 0.1$)] is shown in Fig. 12 on a logarithmic scale as a function of reduced temperature for two crystal azimuthal angle values. This intensity can be used to determine the critical index γ of the dependence

$$I_{2\omega} \propto \tau^{-\gamma}.$$

For the $\Psi = \pi/4$ azimuthal angle, we obtained the critical index $\gamma = 1.08 \pm 0.13$, and for the $\Psi = \pi/2$ angle, this index was $\gamma = 1.2 \pm 0.3$. These values refer to the high-temperature phase. The number of experimental points was insufficient to determine critical index values for the low-temperature phase.

The critical index values obtained in our experiments coincide with the theoretical $\gamma = 1$ value within the error of measurements. This is evidence of the predominance of the contribution of hyper-Rayleigh scattering on defects over the contribution of hyper-Raman scattering on thermal fluctuations ($I_{2d}^{T>T_c} \gg I_{2f}^{T>T_c}$); in addition,

$$2\pi N r_c^3 \ll 1.$$

These two conditions allow the concentration of defects in the crystal to be estimated.

The second condition gives the upper bound for the concentration of defects,

$$N \ll \frac{1}{2\pi r_c^3} = 5 \times 10^{19}\ \text{cm}^{-3}$$

for

$$t_c = 2.6\ \text{nm} \quad (\tau \sim 0.1).$$

The lower bound follows from the predominance of scattering on defects. Indeed, it follows from a comparison of (28) and (29) that $N > 10^{18}$ cm^{-3}. This is a fairly high concentration of defects, which may be related to oxygen vacancies.

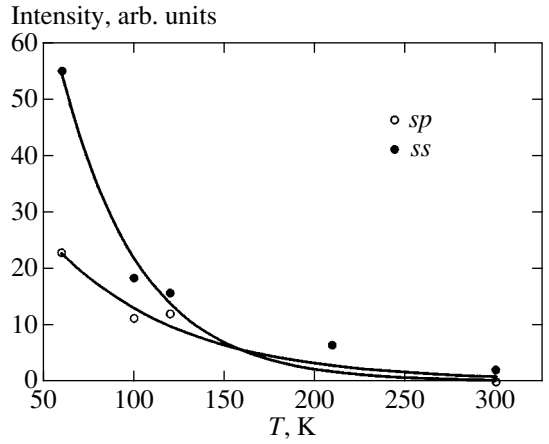

Fig. 11. Temperature dependence of scattered incoherent component intensity in reflection geometry. Crystal azimuthal angle $\Psi = \pi/4$.

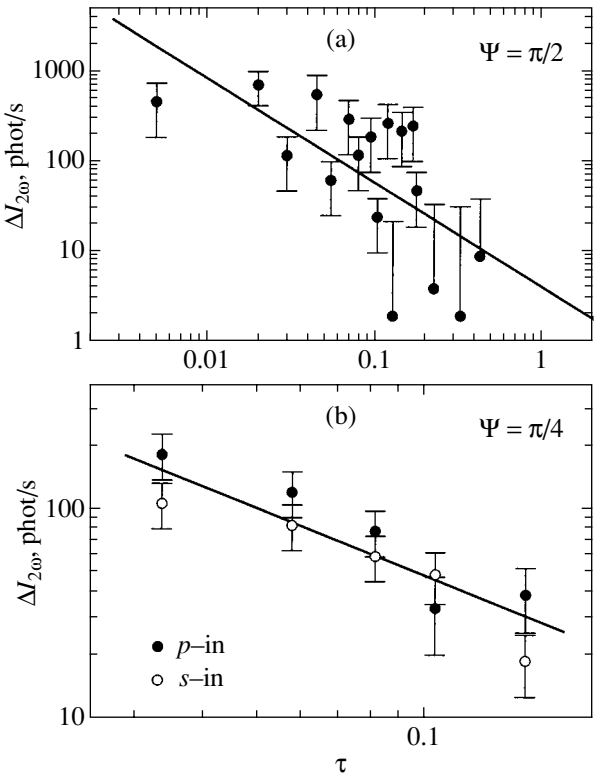

Fig. 12. Temperature dependence of incoherent second harmonic component radiation intensity in transmission geometry for Ψ = (a) $\pi/2$ and (b) $\pi/4$ on logarithmic scale.

9. CONCLUSION

In this work, we continued studies of the surface phase transition in the STO crystal, which was discovered by us in [23], by the method of second optical harmonic generation. The linear character of the temperature dependences of the second harmonic field in the low-temperature (for the surface) phase proves that the surface transition under consideration is a second-order phase transition.

The methods for separating, first, coherent and incoherent contributions and, second, surface and volume coherent contributions suggested in this work enabled us to study the properties of the surface. We were able to separate surface and volume coherent contributions by simultaneously studying the angular, polarization, and temperature dependences of the second harmonic in the reflection geometry. We showed that there existed azimuthal angle values at which second harmonic generation was caused solely by the surface contribution at temperatures above the volume phase transition point but below the surface phase transition point. Studies of the second harmonic characteristics at the phase transition point in the transmission geometry, in which the volume contribution was predominant, were used as reference.

The study of the special features of the temperature dependences of the incoherent second harmonic near the volume phase transition point allowed us to relate this phenomenon to scattering on defects.

Both coherent and incoherent second harmonic field components were described within the framework of the Landau theory of phase transitions taking into account the tensor character of the relations between nonlinear susceptibilities and order parameter.

ACKNOWLEDGMENTS

This work was financially supported by the Russian Foundation for Basic Research (project no. 00-02-16557) and the NWO Scientific Foundation of the Netherlands (grant NFO 1604-1999).

REFERENCES

1. M. E. Lines and A. M. Glass, *Principles and Applications of Ferroelectrics and Related Materials* (Oxford Univ. Press, Oxford, 1977; Mir, Moscow, 1981).
2. K. A. Muller, W. Berlinger, and E. Tossati, Z. Phys. B **84**, 277 (1991).
3. R. Mizaras and A. Loidl, Phys. Rev. B **56**, 10726 (1997).
4. G. Shirane and Y. Yamada, Phys. Rev. **177**, 858 (1969).
5. B. Hehler, A.-L. Perou, E. Courtens, and R. Vacher, Phys. Rev. Lett. **75**, 2416 (1995).
6. R. Wang, Y. Zhu, and S. M. Shapiro, Phys. Rev. Lett. **80**, 2370 (1998).
7. K. Hirota, J. P. Hill, S. M. Shapiro, and G. Shirane, Phys. Rev. B **52**, 13195 (1995).
8. A. A. Sirenko, I. A. Akimov, J. R. Fox, *et al.*, Phys. Rev. Lett. **82**, 4500 (1999).
9. *Ultrathin Magnetic Structure 1: An Introduction to the Electronic, Magnetic, and Structural Properties*, Ed. by J. A. C. Bland and B. Heinrich (Springer-Verlag, Berlin, 1994).
10. D. L. Mills, Phys. Rev. B **3**, 3885 (1971).
11. K. Binder and P. C. Hohenberg, Phys. Rev. B **9**, 2194 (1974).

12. A. P. Levanyuk and S. A. Minyukov, Fiz. Tverd. Tela (Leningrad) **25**, 2617 (1983) [Sov. Phys. Solid State **25**, 1506 (1983)].
13. M. Chida, Y. Tanishiro, H. Minoda, and K. Yagi, Surf. Sci. **423**, L236 (1999).
14. J. B. Cui, J. Ristein, and L. Ley, Phys. Rev. B **59**, 5847 (1999).
15. O. H. Seeck, D. Hupfeld, H. Krull, *et al.*, Phys. Rev. B **59**, 3474 (1999).
16. S. Chandola and J. F. McGilp, Phys. Status Solidi A **175**, 189 (1999).
17. D. Lim, M. C. Downer, J. G. Ekerdt, *et al.*, Phys. Rev. Lett. **84**, 3406 (2000).
18. O. A. Aktsipetrov, S. A. Apukhtina, A. A. Nikulin, *et al.*, Pis'ma Zh. Éksp. Teor. Fiz. **54**, 562 (1991) [JETP Lett. **54**, 563 (1991)].
19. T. V. Misuryaev, T. V. Murzina, O. A. Aktsipetrov, *et al.*, Solid State Commun. **115**, 605 (2000).
20. Th. Rasing, Y. R. Shen, M. W. Kim, and S. Grubb, Phys. Rev. Lett. **55**, 2903 (1985).
21. S. Lin and S. R. Meech, Langmuir **16**, 2893 (2000).
22. O. A. Aktsipetrov, T. V. Misuryaev, T. V. Murzina, *et al.*, Opt. Lett. **25**, 411 (2000).
23. E. D. Mishina, T. V. Misuryaev, N. E. Sherstyuk, *et al.*, Phys. Rev. Lett. **85**, 3664 (2000).
24. V. S. Gorelik, Ferroelectrics **170**, 243 (1995).
25. H. Vogt, Phys. Rev. B **58**, 9916 (1998).
26. J. E. Sipe, D. J. Moss, and H. M. van Driel, Phys. Rev. B **35**, 1129 (1987).
27. A. A. Nikulin and A. V. Petukhov, Dokl. Akad. Nauk SSSR **304**, 87 (1989) [Sov. Phys. Dokl. **34**, 48 (1989)].
28. O. A. Aktsipetrov, A. A. Fedyanin, D. A. Klimkin, *et al.*, Ferroelectrics **190**, 143 (1997).
29. V. L. Ginzburg, A. P. Levanyuk, and A. A. Sobyanin, Phys. Rep. **57**, 151 (1980).
30. F. Schwabl and U. C. Tauber, Phys. Rev. B **43**, 11112 (1991).
31. T. Toyoda and M. Yabe, J. Phys. D **16**, L251 (1983).
32. E. F. Steigmeier, H. Auderset, and G. Harbeke, Solid State Commun. **12**, 1077 (1973).
33. W. Prusseit-Elffroth and F. Schwabl, Appl. Phys. A **51**, 361 (1990).
34. N. I. Lebedev, A. P. Levanyuk, A. I. Morozov, and A. S. Sigov, Fiz. Tverd. Tela (Leningrad) **25**, 2979 (1983) [Sov. Phys. Solid State **25**, 1719 (1983)].
35. N. I. Lebedev, A. P. Levanyuk, A. I. Morozov, and A. S. Sigov, Fiz. Tverd. Tela (Leningrad) **25**, 2975 (1983) [Sov. Phys. Solid State **25**, 1716 (1983)].

Translated by V. Sipachev

Journal of Experimental and Theoretical Physics, Vol. 94, No. 3, 2002, pp. 568–580.
Translated from Zhurnal Éksperimental'noĭ i Teoreticheskoĭ Fiziki, Vol. 121, No. 3, 2002, pp. 663–677.

SOLIDS
Electronic Properties

A New Class of the Surface Shear Magnetoacoustic Waves in Antiferromagnetic Crystals

S. V. Tarasenko

Galkin Institute of Physics and Technology, National Academy of Sciences of Ukraine, Donetsk, 83114 Ukraine
e-mail: tarasen@host.dipt.donetsk.ua

Received April 12, 2001

Abstract—It is shown that the hybridization of magnetoelastic and dipolar interactions may give rise (even in a zero magnetic field) to a new type of surface shear magnetoacoustic waves near a mechanically free or an acoustically continuous interface between uniaxial ferromagnetic and nonmagnetic media. The effect of the conductivity of the nonmagnetic medium on the localization conditions of this surface mode is studied. © *2002 MAIK "Nauka/Interperiodica".*

1. INTRODUCTION

Despite a sufficiently large number of works devoted to the analysis of conditions for the formation of surface shear magnetoacoustic waves near a mechanically free surface of ferro- and antiferromagnetic crystals [1], only one class of surface shear horizontal (SH) phonons, a dipolar Bleustein–Gulyaev wave [2–5], has been traditionally analyzed. The existence of this wave is known to be associated with the fact that a bulk shear elastic wave (SH wave) propagating at a grazing angle along a mechanically free surface of a crystal may completely satisfy the elastic boundary conditions (a exceptional volume wave) [6–9]. As a result, a small variation in the boundary conditions may transform this wave into a surface shear acoustic wave. For example, if a bulk SH phonon is a dipolar wave, a linear coupling between certain components of the elastic strain tensor u and the magnetic field $\mathbf{H}$ can serve as such a perturbation. In this case, a transverse elastic SH wave traveling along a mechanically free surface of a crystal will be transformed into a surface shear magnetoacoustic wave. In ferro- and antiferromagnetic crystals, even in the absence of a constant external magnetic field $\mathbf{H}_0$, such a coupling between u_{ik} and $\mathbf{H}$ can be induced by the long-range magnetic ordering [1, 10].

Conditions for the formation of a surface magnetoacoustic SH wave were first considered in [2] by an example of an elastically and magnetically isotropic ferromagnetic half-space with a mechanically free surface that was uniformly magnetized by an external magnetic field $\mathbf{H}_0$ ($\mathbf{H}_0 \parallel z$, $\mathbf{n} \parallel x$, $\mathbf{k}_\perp \parallel y$, $\mathbf{u} \parallel z \perp \mathbf{n}$, where $\mathbf{n}$ is a normal to the surface of the magnetic material, $\mathbf{k}_\perp$ is the wave vector directed along the propagation direction of the elastic wave, and $\mathbf{u}$ is the vector of elastic displacements). The generalization of the results of [2] to the case of an acoustically continuous interface between ferromagnetic and nonmagnetic dielectrics was carried out in [11]. The effect of the dynamic magnetoelastic interaction on the structure of the spectrum of a surface SH wave near the stability boundary of this magnetic state (the presence of a magnetoelastic gap in the spectrum of a soft magnon mode) was properly taken into account in [1] for a mechanically free interface between a ferromagnetic material and vacuum. The results obtained in [1, 2, 11] imply that a surface shear magnetoelastic SH wave (the Parekh wave) is not a direct analogue of the Bleustein–Gulyaev wave in a nonmagnetic crystal or in the paramagnetic phase ($T > T_C$, where T_C is the Curie point) of a magnetically ordered crystal because of the following circumstances:

(1) In the paramagnetic phase ($T > T_C$), this type of surface SH waves is formed when $\mathbf{H}_0 \parallel z$, $\mathbf{k}_\perp \parallel y$, $\mathbf{n} \parallel x$, and $\mathbf{u} \parallel z$ due to the hybridization of dipolar and magnetoelastic interactions in a bounded magnetic material, whereas the results of [1, 2, 11] imply that, when $T < T_C$ (even when the dipolar interaction is neglected[1]), the surface shear elastic wave under consideration is delocalized neither in the case of a mechanically free nor in the case of an acoustically continuous interface between ferromagnetic and nonmagnetic dielectric media.

(2) In contrast to the case of $T > T_C$, when $T < T_C$, the type of surface magnetoacoustic SH waves under consideration exists on both a mechanically free and an acoustically continuous interface between superconducting and ferromagnetic materials (by its elastic properties, a nonmagnetic medium is assumed to be magnetically harder than a magnetic medium; i.e., the Love wave cannot be formed, and there are no boundary capillary phenomena).

In [12], it was shown that the formation of a surface SH wave on a mechanically free interface between

[1] To this end, one has to formally pass to the limit as $4\pi \longrightarrow 0$ in the relevant formulas in [1, 2, 11].

magnetic and superconducting materials in the absence of a dipolar interaction is attributed to the fact that, for the propagation plane of the elastic SH wave ($\mathbf{k} \in xy$), the magnetic medium under consideration (an easy-axis ferromagnet with the easy axis z) is acoustically gyrotropic. As a result, even in the absence of a dipolar interaction, the spectrum of such a surface magnetoacoustic SH wave ($\mathbf{H}_0 \parallel z$, $\mathbf{k}_\perp \parallel y$, $\mathbf{n} \parallel x$, and $\mathbf{u} \parallel z$), first, is nonreciprocal with respect to the inversion of the propagation direction of the wave, $\omega(k_\perp) \neq \omega(-k_\perp)$, and, second, consists of several branches separated by forbidden frequency bands.

If we make another formal passage to the limit, $B_{44} \longrightarrow 0$ (we neglect the coupling between the spin and elastic subsystems; B_{44} is the constant of magnetoelastic interaction) in the relevant formulas in [1, 2, 11], then, for the same relative orientation of the vectors $\mathbf{n}$, $\mathbf{H}_0$, and $\mathbf{k}_\perp$, these formulas describe (in the magnetostatic approximation) the dispersion law of a surface magnetic TE polariton (the Damon–Eshbach wave) and a homogeneous bulk SH wave.

However, because magnetoelastic effects are relatively small as compared with dipolar ones, the contribution of the magnetoelastic mechanism to the localization of transverse phonons on the spectrum of a surface magnetoacoustic SH wave in a ferromagnetic material is negligible. At the same time, it is well known [10] that the exchange amplification of the magnetoelastic and exchange damping of dipolar interactions occur simultaneously in antiferromagnetic materials; this makes the consideration of the magnetoelastic mechanism of the formation of a surface shear magnetoacoustic SH wave more topical, first of all, for this class of magnetic crystals.

When the magnetoelastic interaction is neglected, the conditions for the formation and propagation of surface magnetic TE polaritons in easy-axis ferromagnetic materials both with and without regard to electromagnetic delay phenomena were studied in sufficient detail in [13–15].

The possibility of localization of elastic shear waves near the mechanically free surface of an antiferromagnet or the acoustically continuous interface between antiferromagnetic and nonmagnetic media due to the magnetoelastic interaction but without regard to the dipolar interaction was investigated in [12, 16, 17]. As regards the simultaneous effect of the magnetoelastic and dipolar interactions on the formation and propagation of a surface magnetoacoustic SH wave near the surface of an antiferromagnet, such a problem has not yet been considered.

One should expect that, in this case, the localization conditions for a shear magnetoacoustic wave propagating along the surface of an easy-axis antiferromagnet for $|\mathbf{H}_0| = 0$ may essentially differ from those studied earlier in [1, 2, 11] by an example of an easy-axis ferromagnet. This is associated with the fact that, conventionally, only a piezomagnetic interaction [1, 3–5] was considered as a mechanism inducing a linear coupling between u_{ik} and H (and, hence, a mechanism inducing the instability of a homogeneous exceptional volume SH wave traveling along the mechanically free surface of the magnetic material), in spite of the fact that the existence of a magnetoelastic interaction in an antiferromagnetic crystal, in contrast to a piezomagnetic crystal, does not require certain special symmetry criteria [10]. In addition, up to the present, normal spin waves [1, 3–5] that exist in the same range of frequencies ω and wave numbers $k_\perp$ have been neglected in calculating the spectrum of surface magnetoacoustic SH phonons in antiferromagnetic media. For an arbitrary value of the wave number $k_\perp$, this fact is justified for high-temperature antiferromagnetic materials ($T_N > T_D$, where T_N (T_D) is the Néel (Debye) temperature) [18] but is not valid for low-temperature antiferromagnetic materials ($T_N < T_D$).

Of special interest here is the analysis of the effect of the magnetoelastic mechanism of linear coupling between elastic u_{ik} and magnetic H fields on the propagation conditions for a exceptional volume magnetoacoustic SH wave along a mechanically free or acoustically continuous interface between an easy-axis antiferromagnet in the collinear phase ($H_0 = 0$) and a superconductor ($\mathbf{n} \parallel x$, $\mathbf{k} \in xy$, $\mathbf{u} \parallel \mathbf{l} \parallel z$; l is the antiferromagnetic vector). This interest is stimulated by the following factors.

(1) In contrast to the ferromagnet [1, 2, 11], for $|\mathbf{H}_0| = 0$, the antiferromagnet in the collinear phase is not simultaneously optically and acoustically active.

(2) As follows from [13–15], the presence of a superconducting coating makes the formation of a surface magnetostatic wave impossible in an easy-axis antiferromagnet ($|\mathbf{H}_0| = 0$).

(3) A dipolar Bleustein–Gulyaev wave induced by a piezomagnetic interaction [19, 20] cannot exist on a mechanically free interface between a piezomagnetic and superconducting (superdiamagnetic) material.

Thus, the aim of this work is to determine the necessary conditions under which the hybridization of magnetoelastic and dipolar interactions gives rise to a new class of surface shear magnetoacoustic waves for $|\mathbf{H}_0| = 0$ on both a mechanically free and an acoustically continuous interface between antiferromagnetic and nonmagnetic media (either a dielectric or a superconductor can be chosen as the nonmagnetic medium).

The paper consists of several sections. In Section 2, we present the basic relations and determine the conditions under which a simultaneous effect of a magnetoelastic and dipolar interactions gives rise to a new type of surface magnetoacoustic SH waves near a mechanically free interface between an easy-axis antiferromagnet and a nonmagnetic medium. In this section, we also study the dispersion characteristics of this

surface wave as a function of the conductivity of the nonmagnetic medium (either dielectric or superconductor). The characteristic features of the dispersion relations of the shear magnetoacoustic wave under consideration for an acoustically continuous interface between an easy-axis antiferromagnet and a nonmagnetic medium are considered in Section 3. In Section 4, we discuss the possibility of the formation of a new type of gap magnetoelastic SH waves by an example of an antiferromagnet–nonmagnetic medium–antiferromagnet three-layer structure. In Section 5, we show a relation between the spectrum of the gap magnetoacoustic SH wave determined for the antiferromagnet–nonmagnetic medium–antiferromagnet structure and the spectrum of a surface shear magnetoacoustic wave propagating along an elastically isotropic antiferromagnetic slab both of whose surfaces have a continuous acoustic contact with identical nonmagnetic halfspaces. Section 6 is devoted to the analysis of the characteristic features of the localization and propagation of the surface magnetoacoustic SH wave under consideration that are induced by the spatial dispersion of the magnetic medium (by the inhomogeneous-exchange interaction). In the Conclusion, we summarize the results obtained.

2. BASIC RELATIONS: MECHANICALLY FREE INTERFACE BETWEEN ANTIFERROMAGNETIC AND NONMAGNETIC MEDIA

Assume that an antiferromagnetic medium occupies a lower half-space ($x < 0$) with the normal to the interface $\mathbf{n} \parallel [100]$. As an example, consider a two-sublattice model ($\mathbf{M}_{1,2}$ are the saturation magnetizations of respective sublattices, and $|\mathbf{M}_1| = |\mathbf{M}_2| = M_0$) of an easy-axis exchange-collinear antiferromagnet (with the easy axis z). For simplicity and obviousness of calculations, assume that the magnetoelastic and elastic properties of the antiferromagnet are isotropic. The density of the thermodynamic potential can be represented in terms of ferromagnetic ($\mathbf{m}$) and antiferromagnetic ($\mathbf{l}$) vectors as follows [10]:

$$W = 0.5\delta\mathbf{m}^2 - 0.5bl_z^2 - \mathbf{m}\cdot\mathbf{h}_m + \gamma l_i l_k u_{ik} + \mu(u_{ik} - \delta_{ik}u_{ll}/3)^2 + 0.5Ku_{ll}^2, \quad (1)$$
$$\mathbf{m} = (\mathbf{M}_1 + \mathbf{M}_2)/2M_0, \quad \mathbf{l} = (\mathbf{M}_1 - \mathbf{M}_2)/2M_0.$$

Here, b, δ, and γ are the constants of magnetic anisotropy, homogeneous-exchange interaction, and magnetoelastic interaction, respectively; K and μ are the compression and shear moduli, respectively; $\mathbf{h}_m$ is the magnetic dipole field; and δ_{ik} is the Kronecker delta. If we assume that electromagnetic waves propagate at infinite velocity in the magnetic material, the dynamics of model (1) is described by a closed system of equations involving the Landau–Lifshits equations for the vectors $\mathbf{m}$ and $\mathbf{l}$, the basic equation of continuum mechanics, and the equations of magnetostatics:

$$\frac{1}{g}\frac{\partial\mathbf{m}}{\partial t} = \mathbf{m}\times\mathbf{H}_m + \mathbf{l}\times\mathbf{H}_l,$$
$$\frac{1}{g}\frac{\partial\mathbf{l}}{\partial t} = \mathbf{m}\times\mathbf{H}_l + \mathbf{l}\times\mathbf{H}_m, \quad (2)$$
$$\mathrm{div}\mathbf{B} = 0, \quad \rho\frac{\partial^2 u_i}{\partial t^2} = \frac{\partial\sigma_{ik}}{\partial x_k},$$

where $\mathbf{B}$ is the magnetic flux density, $\mathbf{u}$ is the vector of lattice displacements, ρ is the mass density, σ_{ik} is the elastic strain tensor, g is the gyromagnetic ratio, and $\mathbf{H}_r \equiv \delta W/\delta r$ is the effective field with $r = \mathbf{m}, \mathbf{l}$.

Since our aim is to analyze the conditions for the formation of a surface magnetoacoustic wave localized near the interface between antiferromagnetic and nonmagnetic media ($x = 0$), the system of dynamic equations considered must be supplemented with appropriate elastic and electromagnetic boundary conditions. If the interface is mechanically free, then such a system of boundary conditions can be represented as [19, 20]

$$\sigma_{ix} = 0 \quad (x = 0), \quad u(x \longrightarrow -\infty) \longrightarrow 0, \quad (3)$$

$$\mathbf{B}_1\cdot\mathbf{n} = -\beta k_\perp\phi_1 \quad (x = 0), \quad \phi_1(x \longrightarrow -\infty) \longrightarrow 0. \quad (4)$$

Here, $k_\perp$ is the wave number; ϕ is the magnetostatic potential ($\mathbf{h}_m \equiv -\nabla\phi$); and subscripts 1 and 2 correspond to magnetic and nonmagnetic media, respectively. Everywhere below, we assume that the permeability of the nonmagnetic medium is equal to unity. In formula (4), depending on the conductivity of the nonmagnetic medium, $\beta \equiv 0$ for a perfect metal or a superdiamagnetic material [20], $\beta \equiv 1$ for vacuum, and $\beta \equiv \tanh(k_\perp\lambda)$ for a superconductor with the London penetration depth λ.

Calculations show that, if $b > 0$ in (1), then, in the equilibrium state with $|\mathbf{H}_0| = 0$, $\mathbf{l} \parallel z$ and $|\mathbf{m}| = 0$ (the collinear phase). Hence, when the propagation direction of the shear wave with $\mathbf{u} \parallel z$ coincides with the axis y ($\mathbf{k} \in xy$), the characteristic equation for the boundary value problem (1)–(4) can be represented as

$$\left(\alpha^2 - 1 + \frac{\omega^2}{s_{1t}^2\bar{c}_{55}k_\perp^2}\right)(\alpha^2 - 1) = 0,$$
$$k_x^2 \equiv -\alpha^2 k_\perp^2, \quad \bar{c}_{55} = \frac{\omega_0^2 - \omega^2}{\Delta}, \quad (5)$$
$$\mu_{xx} = \mu_{yy} = \frac{(\omega_0^2 + \omega_{me}^2)\epsilon}{\Delta} + 1,$$

where

$$\omega_0^2 \equiv g^2M_0^2\delta b, \quad \omega_{me}^2 \equiv \frac{g^2M_0^4\delta\gamma^2}{\mu_1}, \quad s_{1t}^2 \equiv \frac{\mu_1}{\rho_1},$$

$$\Delta \equiv \omega_0^2 + \omega_{me}^2 - \omega^2, \quad \epsilon \equiv \frac{16\pi}{\delta}.$$

Thus, the elastic SH wave in this case is one-partial with respect to the elastic displacement and is nonmagnetic-dipole-active in the bulk of the crystal. Following the standard calculation technique and taking into account (5), we can represent the dispersion relation for the spectrum of the appropriate surface shear magnetoacoustic wave ($\mathbf{u} \parallel \mathbf{l} \parallel z, \mathbf{k} \in xy$) traveling along the mechanically free interface ($x = 0$) between antiferromagnetic and nonmagnetic media (expressions (1)–(4)) as follows (for all values of β considered in the electromagnetic boundary value problem (4)):

$$\bar{c}_{55}\alpha_1 = -D(\beta), \quad \alpha_1^2 \equiv 1 - \frac{\omega^2}{s_{1t}^2 \bar{c}_{55} k_\perp^2},$$
$$D(\beta) \equiv \frac{\epsilon_* \omega_{me}^2 \omega^2}{\Delta((\omega_0^2 + \omega_{me}^2)\epsilon_* + \Delta)}, \quad \epsilon_* \equiv \frac{\epsilon}{1+\beta}. \tag{6}$$

The analysis of Eqs. (5) and (6) shows that the dispersion law of a exceptional volume SH wave is determined from (5) by the relation $\alpha = 0$, while the necessary condition for the existence of a surface SH wave is given by the inequalities

$$\omega_0^2 < \omega^2 < \omega_0^2 + \omega_{me}^2.$$

Here, one should emphasize that the formation of the surface shear magnetoacoustic wave on the mechanically free interface between antiferromagnetic and nonmagnetic media (conditions (3) and (4)) can be satisfied only due to the hybridization of the magnetoelastic ($\gamma \neq 0$) and dipolar ($\epsilon \neq 0$) interactions. In the general case, the analysis of the dispersion relations (5) and (6) can be carried out only by numerical methods; therefore, below, we restrict the analysis to certain particular cases. For example, it follows from (5) and (6) that, in the long-wavelength limit ($k_\perp \longrightarrow 0$), the dispersion law for the surface shear magnetoacoustic wave can be obtained from the relation

$$k_\perp^2 \approx \frac{\omega^2 \bar{c}_{55} s_{1t}^{-2}}{\bar{c}_{55}^2 - D^2(0)}, \tag{7}$$

i.e., the surface wave in question is a forward wave ($\partial\Omega_s(k_\perp)/\partial k_\perp > 0$) irrespective of the conductivity of the nonmagnetic medium (irrespective of the type of β). In the short-wavelength (elastostatic) limit, when $\omega/s_{1t} \ll k_\perp$, the dispersion law of the surface magnetoacoustic SH wave (5), (6) is determined by the following relation:

$$\Omega_s^2(k_\perp) = \omega_0^2(1 + \epsilon_*). \tag{8}$$

Thus, it follows from (8) that, if the nonmagnetic halfspace is occupied by a superconductor with the London penetration depth λ ($\beta \equiv \tanh(k_\perp \lambda)$), then the surface wave (5), (6) with the dispersion law $\Omega_s(k_\perp)$ in the short-wavelength limit (8) is a backward wave ($\partial\Omega_s(k_\perp)/\partial k_\perp < 0$). In the general case, a simultaneous analysis of formulas (5)–(8) shows that the dispersion curve of the surface shear magnetoacoustic wave (5), (6) under this type of electromagnetic boundary conditions may have an extremum for $k_\perp \neq 0$. The presence of this extremum depends, in particular, on the London penetration depth λ (Fig. 1, curve *1*). If the electromagnetic boundary conditions (4) on the mechanically free surface of the antiferromagnet (1) are such that $\beta \equiv 0$ or $\beta \equiv 1$, then, as follows from (5)–(8), the dispersion characteristics of the surface wave considered will primarily be determined by the acoustic-delay phenomenon (Fig. 1, curves *2* and *3*, respectively).

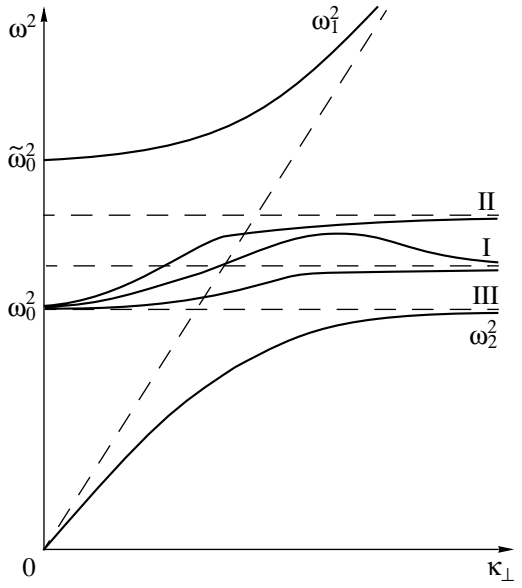

Fig. 1. The structure of the spectrum of a surface shear magnetoacoustic wave (5), (6) on the mechanically free interface (3), (4) between antiferromagnetic and nonmagnetic media;

(*1*) $\beta = \tan(k_\perp \lambda)$ and $\Omega_s^2(k_\perp \gg 1) \approx \omega_0^2(1 + \epsilon/2)$;

(*2*) $\beta = 0$ and $\Omega_s^2(k_\perp \gg 1) \approx \omega_0^2(1 + \epsilon)$; and

(*3*) $\beta = 1$ and $\Omega_s^2(k_\perp \gg 1) \approx \omega_0^2(1 + \epsilon/2)$; $\tilde{\omega}_0^2 \equiv \omega_0^2 + \omega_{me}^2$;

the frequencies $\omega_{1,2}^2$ are determined from (5) with $\alpha = 0$.

In view of the extensive study of multilayer magnetic structures based on antiferromagnetic and nonmagnetic materials [21, 22], the following question is of undoubted interest: How will the spectrum of the surface magnetoacoustic SH wave change if the elastic conditions on the interface between antiferromagnetic and nonmagnetic media correspond to an acoustically continuous (rigid) contact between these media rather than to a mechanically free surface (3)?

3. A RIGID CONTACT BETWEEN ANTIFERROMAGNETIC AND NONMAGNETIC MEDIA

When, as before, the antiferromagnetic medium (medium 1) occupies the lower half-space $x < 0$ and the nonmagnetic medium (medium 2) represents a layer of thickness f ($f > \lambda$) whose external surface $x = f$ is mechanically free and is coated by an infinitely thin perfectly superconducting film ($\mathbf{B}_2 \cdot \mathbf{n} = 0$ for $x = f$), the system of elastic and electromagnetic boundary conditions for a dipolar SH wave ($\mathbf{u} \parallel z \parallel \mathbf{l}$, $\mathbf{k} \in xy$) takes the following form instead of (3), (4):

$$\sigma_{ix1} + \mu_1 a k_\perp u_{z1} = 0 \quad (x = 0), \qquad u_{z1,2}(x \longrightarrow -\infty) \longrightarrow 0, \tag{9}$$

$$\mathbf{B}_1 \cdot \mathbf{n} = -\beta k_\perp \phi_1 \quad (x = 0), \qquad \phi_{1,2}(x \longrightarrow -\infty) \longrightarrow 0, \tag{10}$$

where

$$a \equiv \frac{\mu_2}{\mu_1}\alpha_2 \tanh(\alpha_2 k_\perp f), \quad \alpha_2^2 \equiv 1 - \frac{\omega^2 \rho_2}{k_\perp^2 \mu_2}.$$

The corresponding dispersion relation for the spectrum of a surface magnetoacoustic SH wave guided by the acoustically continuous interface between antiferromagnetic (1) and nonmagnetic (9), (10) media can be rewritten, with regard to (5), (6), as ($\mathbf{k} \in xy$, $\mathbf{n} \parallel x$, $\mathbf{l} \parallel z$)

$$\bar{c}_{55}\alpha_1 + a + D(\beta) = 0. \tag{11}$$

In the limit as $\mu_2 \longrightarrow 0$, relation (11) coincides with (6); i.e., combined with (5), relation (11) describes the dispersion law for the surface magnetoacoustic SH wave localized near the mechanically free interface between magnetic and nonmagnetic media. If we pass to the limit as $f \longrightarrow \infty$ in (5) and (11), we obtain a dispersion relation for the surface magnetoacoustic SH wave propagating along the acoustically continuous interface between antiferromagnetic and nonmagnetic half-spaces. The analysis of Eqs. (5) and (11) implies that, when $f < \infty$, the necessary condition for the existence of the surface magnetoacoustic SH wave is given, as before, by the inequalities

$$\omega_0^2 < \omega^2 < \omega_0^2 + \omega_{me}^2.$$

In the case of a nonmagnetic half-space for $x > 0$ ($f \longrightarrow \infty$), in addition to the above constraint on the frequency of the surface wave, it is required that the inequality $\mu_2\rho_1 < \mu_1\rho_2$ should be satisfied. However, one should stress that the formation of the surface shear elastic wave in the case of a rigid contact between antiferromagnetic and nonmagnetic media (see (9)) is possible when the dipolar interaction is neglected ($\epsilon/\gamma \longrightarrow 0$) and only the magnetoelastic interaction is taken into account ($\gamma \neq 0$); this result coincides with the results of [12]. Since a full analysis of relations (5) and (11) can be carried out only by numerical techniques, we will only consider certain particular cases. For example, it follows from (5) and (11) that, when $\mu_2\rho_1 > \mu_1\rho_2$, the spectrum of the surface wave in the long-wavelength limit ($k_\perp \longrightarrow 0$) has the following endpoint:

$$k_{\min}^2 \equiv \omega_0^2 \rho_1/\mu_1, \quad \Omega_s(k_{\min}) = \omega_0;$$

in the neighborhood of this point, the surface wave under consideration is a forward wave ($\partial\Omega_s(k_\perp)/\partial k_\perp > 0$) irrespective of the conductivity (the form of β) of the nonmagnetic medium and the elastic properties of the nonmagnetic coating. The comparison of (6) and (11) shows that the effect of the nonmagnetic coating on the spectrum of the surface SH wave under consideration is manifested most clearly in the short-wavelength (elastostatic) limit $\omega/s_{1t} \ll k_\perp$.

As a result, the dispersion law of the surface magnetoacoustic SH wave (5), (11), is rewritten as

$$\Omega_s^0(k_\perp) = [\omega_0^2 + \omega_{me}^2 a_*/(1 + a_*)](1 + \epsilon_*), \tag{12}$$

where

$$a_* \equiv \frac{\mu_2}{\mu_1}\tanh(k_\perp f).$$

Thus, in contrast to the case of a mechanically free interface between magnetic and nonmagnetic media (5) and (6), even if the nonmagnetic layer is a dielectric ($\beta = 0$) or a perfect superconductor ($\beta = 0$), the presence of a rigid contact at $x = 0$ gives rise to the dispersion of the surface mode considered even in the short-wavelength limit. In this case, the dispersion curve (12) corresponds to a forward wave ($\partial\Omega_s(k_\perp)/\partial k_\perp > 0$) for both $\beta = 0$ and $\beta = 1$. If the nonmagnetic medium ($0 < x < f$) is a superconductor with the London penetration depth λ ($\beta \equiv \tanh(k_\perp\lambda)$), then, as follows from (12), the dispersion curve of the surface magnetoacoustic SH wave of the type under consideration may have an extremum point for $k_\perp \neq 0$ even in the elastostatic limit ($\omega/s_{1t} \ll k_\perp$). In particular, a necessary condition for the existence of a minimum is the inequality $\lambda < f$.

Both for a mechanically free (3) and for an acoustically continuous (9) interface between magnetic and nonmagnetic media, the conditions for the formation of the surface magnetoacoustic SH wave (5), (6) or (5), (11) prove to be closely related to the reflection conditions of a normal dipolar shear elastic wave from the surface of an antiferromagnetic crystal ($x = 0$).

Calculations show that the reflection coefficient R of a bulk transverse wave polarized perpendicular to the plane of incidence ($\mathbf{k} \in xy$, $\mathbf{u} \parallel \mathbf{l} \parallel z$) for the acoustically continuous interface between ferromagnetic ($x < 0$, medium 1) and nonmagnetic ($x > 0$, medium 2) half-spaces ($\mathbf{n} \parallel x$) that is defined by relations (9) and (10) for $f \longrightarrow \infty$ and $\phi_2(x \longrightarrow \infty) \longrightarrow 0$, $u_{z2}(x \longrightarrow \infty) \longrightarrow 0$ can be represented as

$$R = (i\bar{c}_{55}\cos\theta_1 - h)(i\bar{c}_{55}\cos\theta_1 + h)^{-1},$$
$$h \equiv \frac{\epsilon\omega^2\omega_{me}^2}{(\mu_{xx}+\beta)\Delta^2}\sin\theta_1 - \tilde{a}\cos\theta_2, \quad k_1^2 \equiv \frac{\omega^2}{s_{1t}^2\bar{c}_{55}}, \quad (13)$$
$$k_2^2 \equiv \frac{\omega^2\rho_2}{\mu_2}, \quad \tilde{a} \equiv \frac{\mu_2 k_2}{\mu_1 k_1}, \quad \tan\theta \equiv k_y/k_x,$$

irrespective of the conductivity of the nonmagnetic medium; here, the angles θ_1 and θ_2 define the directions of the wave vector k_1 of the incident SH wave in the antiferromagnetic medium ($\pi \le \theta_1 \le 3\pi/2$) and the wave vector k_2 of the refracted wave in medium 2 ($0 \le \theta_2 \le \pi/2$), respectively. In a particular case of $\mu_2 = 0$, the relation obtained corresponds to the reflection coefficient of a bulk magnetoacoustic SH wave from a mechanically free surface of the antiferromagnetic crystal (3), (4).

Thus, it follows from (13) that the character of reflection of a bulk magnetoacoustic SH wave from a mechanically free interface between antiferromagnetic and nonmagnetic media is qualitatively similar to the reflection of a shear SH wave from a mechanically free surface of a cubic piezocrystal [23, 24]. In particular, the total internal reflection ($|R| = 1$) occurs for any angle of incidence of a normal elastic SH wave onto the surface of the antiferromagnet. In addition, in this case, the hybridization of the magnetoelastic and dipolar interactions ($\epsilon \neq 0$, $\gamma \neq 0$) makes impossible the propagation of a bulk magnetoacoustic SH wave along the surface of the magnetic crystal at a grazing angle (when $\theta_1 \longrightarrow \pi$, $R \longrightarrow -1$). Otherwise ($\epsilon/\gamma \longrightarrow 0$ or $\gamma/\epsilon \longrightarrow 0$), formula (13) implies that $R = 1$ for $\pi \le \theta_1 \le 3\pi/2$; i.e., a exceptional volume SH wave can propagate along a mechanically free surface of the antiferromagnetic crystal ($\mu_2 = 0$) in the absence of a dipolar ($\epsilon/\gamma \longrightarrow 0$) or magnetoelastic ($\gamma/\epsilon \longrightarrow 0$) interactions. Upon the substitution $ik_1\cos\theta_1 \longrightarrow \alpha_1 k_\perp$, $k_1\sin\theta_1 \longrightarrow k_\perp$, the pole of the reflection coefficient R (13) coincides with the dispersion relations for the spectrum of a surface shear magnetoacoustic wave (5), (6) or (5), (11). It should be noted that, if the interface between antiferromagnetic and nonmagnetic media is acoustically continuous, (9) and (10), then formula (13) implies that, according to (5), (11), a sufficient condition for the impossibility of propagation of a homogeneous SH wave along the interface between magnetic and nonmagnetic media ($R(\theta_1 \longrightarrow \pi/2) \longrightarrow -1$) for $\mu_2 \neq 0$ is fulfilled even in the absence of the dipolar interaction ($\epsilon/\gamma \longrightarrow 0$). This result agrees with the aforementioned fact that, in such a structure, a surface SH wave can propagate in this direction due to the magnetoelastic interaction alone ($\gamma \neq 0$). The corresponding dispersion relation is determined from (13) by the equation

$$R^{-1} = 0$$

for $\epsilon/\gamma \longrightarrow 0$ and upon the substitutions

$$ik_1\cos\theta_1 \longrightarrow \alpha_1 k_\perp, \quad k_1\sin\theta_1 \longrightarrow k_\perp,$$
$$ik_2\cos\theta_2 \longrightarrow -\alpha_2 k_\perp.$$

Calculations show that, when a normal bulk SH wave is reflected from the surface of antiferromagnet (1), not only the amplitude of the reflection coefficient R but also its phase ψ ($R = |R|\exp(i\psi)$) shows anomalous behavior. Since $h \neq 0$, both for $\mu_2 \longrightarrow 0$ and $\epsilon/\mu_2 \longrightarrow 0$, the phase of the reflected shear wave differs from the phase of the incident elastic SH wave for both a mechanically free surface of antiferromagnet (1) and an acoustically continuous interface between antiferromagnetic and nonmagnetic half-spaces. In the general case, the phase shift considered depends not only on the frequency ω and the wave number $k_\perp$ of the incident elastic wave but also on the elastic properties (μ_2) and the conductivity (λ) of the nonmagnetic medium. One of the practically important consequences of the total reflection is the Schoch effect, which consists in the shift of a beam of reflected elastic waves along the boundary [25]. If $k_\perp$ is the wave number of the beam, then, according to [25, 26], its shift Δ_s upon reflection from the boundary is determined by the relation

$$\Delta_s = -\frac{\partial\psi}{\partial k_\perp}. \quad (14)$$

It follows from (13) and (14) that the shift Δ_s depends on the sign and the magnitude of the ratio $h/\bar{c}_{55}$. In this case, depending on the relation between the parameters entering in this ratio, the shift Δ_s may be either positive or negative. In particular, Δ_s attains its maximum when the condition $\mu_{xx} + \beta = 0$ is satisfied, which corresponds to the frequency of a magnetostatic surface wave propagating along the interface between antiferromagnetic and nonmagnetic media [22].

Taking into account the results of this and the preceding sections, one can expect that the localization mechanism of a surface magnetoacoustic SH wave will work even in the case of a magnetic-sandwich-type structure, which represents two identical antiferromagnetic half-spaces separated by a nonmagnetic layer of a dielectric or superconducting medium. In view of this fact, we devote the following section to the study of the conditions for the formation of a new type of gap magnetoacoustic SH waves induced by the hybridization of dipolar and magnetoelastic interactions for such a structure.

4. ANTIFERROMAGNET–NONMAGNETIC LAYER–ANTIFERROMAGNET-TYPE STRUCTURE

Suppose that the upper and lower half-spaces ($x < -d$ and $x > d$) are occupied by antiferromagnet (1), the spacing between them ($-d < x < d$) is occupied by a nonmagnetic medium (medium 2), and both interfaces

($x = \pm d$) of this structure are mechanically free. If, as before, $\mathbf{l} \parallel z \parallel \mathbf{u}$ and $\mathbf{k} \in xy$, then the system of elastic and electromagnetic boundary conditions corresponding to the elastic SH wave localized near the nonmagnetic layer can be represented as

$$\sigma_{ix1} = 0 \quad (x = \pm d), \quad u_{z1}(x \longrightarrow \pm\infty) \longrightarrow 0, \quad (15)$$

$$\left.\begin{aligned} &\mathbf{B}_1 \cdot \mathbf{n} = \mathbf{B}_2 \cdot \mathbf{n}, \\ &\phi_1 = \phi_2, \end{aligned}\right\} \quad x = \pm d, \quad \phi_1(x \longrightarrow \pm\infty) \longrightarrow 0. \quad (16)$$

Calculations show that a shear gap magnetoacoustic SH wave with $\mathbf{k}_\perp \parallel y$ can propagate in such a three-layer structure along the interface between the magnetic and nonmagnetic media. This wave is formed as a result of hybridization of two surface shear magnetoacoustic waves in each half-space due to the indirect interaction between these oscillations through a magnetostatic field in the nonmagnetic layer separating these antiferromagnetic half-spaces ($-d < x < d$). The dispersion law of such a gap shear magnetoacoustic wave consists of two branches, $\Omega_\pm(k_\perp)$, whose spectra, with regard to (5), (6), are determined by

$$\bar{c}_{55}\alpha_1 = -D(\beta_\pm), \quad (17)$$

where

$$D(\beta_\pm) \equiv \frac{\epsilon_\pm \omega_{me}^2 \omega^2}{\Delta[(\omega_0^2 + \omega_{me}^2)\epsilon_\pm + \Delta]},$$

$$\epsilon_\pm \equiv \frac{\epsilon}{1 + \beta_\pm},$$

$$\beta_+ \equiv \tanh(k_\perp d) \quad \text{for} \quad \Omega_+(k_\perp),$$

$$\beta_- \equiv \coth(k_\perp d) \quad \text{for} \quad \Omega_-(k_\perp).$$

Just as in the case (5), (6), the necessary condition for the existence of a gap magnetoacoustic SH wave (5), (17) is given by the inequalities

$$\omega_0^2 < \omega^2 < \omega_0^2 + \omega_{me}^2$$

and a simultaneous consideration of the magnetoelastic and ($\gamma \neq 0$) and magnetostatic ($\epsilon \neq 0$) interactions.

In the long-wavelength limit as $k_\perp \longrightarrow 0$, the branch $\Omega_+(k_\perp)$ of the dispersion law of the shear gap magnetoacoustic wave coincides with (7), while the branch $\Omega_-(k_\perp)$ is given by the relation

$$k_\perp^2 \approx \frac{\omega^2 \bar{c}_{55} s_{1t}^{-2}}{\bar{c}_{55}^2 - D^2(\infty)}. \quad (18)$$

In the elastostatic limit ($\omega/s_{1t}k_\perp \ll 1$), both branches of the spectrum of shear gap magnetoacoustic wave (5), (17) are dispersive and are determined by relation (8) with $\beta = \beta_+$ for $\Omega_+(k_\perp) = \Omega_s(k_\perp)$ and $\beta = \beta_-$ for $\Omega_-(k_\perp) = \Omega_s(k_\perp)$. Thus, in the three-layer structure under consideration, the "low-frequency" branch of the spectrum of shear gap magnetoacoustic waves is a forward wave ($\partial\Omega_+(k_\perp)/\partial k_\perp > 0$), while the "high-frequency" branch represents a backward wave ($\partial\Omega_-(k_\perp)/\partial k_\perp < 0$) even for the interface between an antiferromagnet and a nonmagnetic dielectric. When $k_\perp d \longrightarrow \infty$, the dispersion curves of these waves tend to the same limit given by the relation

$$\Omega_\pm(k_\perp \longrightarrow \infty) = \omega_0\sqrt{1 + \epsilon/2}.$$

The spectrum of the gap magnetoacoustic SH waves of the type under consideration exhibits additional features when the three-layer structure (two identical antiferromagnetic half-spaces and a nonmagnetic layer) is acoustically continuous, while the nonmagnetic layer itself is a perfect superconductor ($\lambda = 0$). In this case, the corresponding system of elastic and electromagnetic boundary conditions can be represented as

$$\left.\begin{aligned} &\sigma_{ix1} = \sigma_{ix2}, \\ &\mathbf{u}_1 = \mathbf{u}_2, \end{aligned}\right\} \quad x = \pm d, \quad \mathbf{u}_1(x \longrightarrow \pm\infty) \longrightarrow 0, \quad (19)$$

$$\mathbf{B}_1 \cdot \mathbf{n} = 0 \quad (x = \pm d), \quad \phi_1(x \longrightarrow \pm\infty) \longrightarrow 0. \quad (20)$$

As a result, for $\mathbf{k} \in xy$, $\mathbf{n} \parallel x$, $\mathbf{l} \parallel z \parallel \mathbf{u}$, $|\mathbf{H}_0| = 0$, the spectrum of the gap magnetoacoustic SH wave under consideration also consists of two branches: symmetric and antisymmetric ones. Unlike (5), (17), the classification of the branches of the spectrum for this type of gap waves is based on the character of distribution of elastic displacements $\mathbf{u} \parallel z$ in the nonmagnetic layer with respect to the midplane $x = 0$. Calculations show that the formation of the gap SH wave is attributed to the hybridization of two surface shear magnetoacoustic waves in each half-space due to the indirect interaction of these oscillations through the field of elastic displacements ($\mathbf{u} \parallel z$) in the nonmagnetic superconducting layer separating the two antiferromagnetic half-spaces ($-d < x < d$). Taking into account (5), (6), we can represent the dispersion equation for the spectrum of the gap magnetoacoustic SH wave in the case (19), (20) as

$$\bar{c}_{55}\alpha_1 + a_\pm = -D(0), \quad (21)$$

where

$$a_+ \equiv (\mu_2/\mu_1)\alpha_2 \tanh(\alpha_2 k_\perp d) \quad \text{for} \quad \Omega_+(k_\perp),$$

$$a_- \equiv (\mu_2/\mu_1)\alpha_2 \coth(\alpha_2 k_\perp d) \quad \text{for} \quad \Omega_-(k_\perp).$$

The simultaneous analysis of (5), (6), and (21) shows that, as expected, the structure of the branch $\Omega_+(k_\perp)$ is qualitatively similar to the case of a rigid contact (5), (11), considered above, between an antiferromagnetic half-space and a superconducting layer of thickness d with the London penetration depth $\lambda = 0$. The corresponding dispersion curve represents a forward wave ($\partial\Omega_+(k_\perp)/\partial k_\perp > 0$). As regards the branch $\Omega_-(k_\perp)$ of the gap SH wave (5), (21) under consideration, its most distinctive feature induced by the rigid contact between magnetic and nonmagnetic media is that the relation

$\partial\Omega_-(k_\perp)/\partial k_\perp < 0$ holds even in the elastostatic limit. Due to the finiteness of the acoustic delay, a maximum appears on this dispersion curve for $k_\perp \neq 0$. For $k_\perp d \longrightarrow \infty$, we have

$$\Omega_\pm^2(k_\perp \longrightarrow \infty) = \left(\omega_0^2 + \frac{\omega_{me}^2}{1+\mu_1/\mu_2}\right)(1+\epsilon).$$

In the cases (5), (17) and (5), (21), the lower branch $\Omega_+(k_\perp)$ of the spectrum of the gap magnetoacoustic wave coincides, for $2d \longrightarrow \infty$, with the above expressions for the spectrum of a surface magnetoacoustic SH wave traveling, respectively, along a mechanically free and an acoustically continuous interface between the antiferromagnetic and superconducting half spaces. To compare with the cases (5), (17) or (5), (21), one should assume in (5), (6) that $\beta = 1$ or $\beta = 0$, respectively.

The analysis shows that, in both cases (15)–(17) and (19)–(21), the spectrum of the gap magnetoelastic SH wave for the antiferromagnet–nonmagnetic layer–antiferromagnet structure investigated above is closely related to the spectrum of the surface wave formed in the structure of the type nonmagnetic material–antiferromagnet–nonmagnetic material.

5. SPECTRUM OF A MAGNETOACOUSTIC SH WAVE IN AN ANTIFERROMAGNETIC SLAB

Consider an antiferromagnetic (medium 1) slab of thickness $2d$ assuming that both of its surfaces ($x = \pm d$) have a continuous acoustic contact with the nonmagnetic (medium 2) half-space ($x > d$ and $x < -d$) and, as before, $\mathbf{n} \parallel x$, $\mathbf{k} \in xy$, and $\mathbf{l} \parallel \mathbf{u} \parallel z$. The corresponding system of boundary conditions has the form

$$\left.\begin{aligned}\sigma_{ix1} &= \sigma_{ix2},\\ \mathbf{u}_1 &= \mathbf{u}_2,\end{aligned}\right\} \quad x = \pm d, \quad \mathbf{u}_2(x \longrightarrow \pm\infty) \longrightarrow 0, \tag{22}$$

$$\begin{aligned}\mathbf{B}_1 \cdot \mathbf{n} &= \mathbf{B}_2 \cdot \mathbf{n} \quad (x = \pm d),\\ \phi_2(x \longrightarrow \pm\infty) &\longrightarrow 0.\end{aligned} \tag{23}$$

Taking into account (5), we can seek a solution to this boundary value problem in the form

$$\begin{aligned}u_{z1} &= [u_+\exp(-\alpha_1 k_\perp x) + u_-\exp(\alpha_1 k_\perp x)]\\ &\quad\times \exp(i\omega t - ik_\perp y),\\ \phi_1 &= [\phi_+\exp(-k_\perp x) + \phi_-\exp(k_\perp x)]\\ &\quad\times \exp(i\omega t - ik_\perp y)\end{aligned} \tag{24}$$

for $-d \le x \le d$;

$$u_{z2} = u_0\exp(-\alpha_2 k_\perp x)\exp(i\omega t - ik_\perp y),$$

$$\phi_2 = \phi_0\exp(-k_\perp x)\exp(i\omega t - ik_\perp y)$$

for $x > d$; and

$$u_{z2} = u_0\exp(\alpha_2 k_\perp x)\exp(i\omega t - ik_\perp y),$$

$$\phi_2 = \phi_0\exp(k_\perp x)\exp(i\omega t - ik_\perp y)$$

for $x < -d$. As a result, the calculation of the spectrum of shear magnetoelastic waves shows that, in this case, two types of normal magnetoelastic SH waves can propagate simultaneously and independently with the same wave number $k_\perp$; the distribution of the vector of elastic displacements $\mathbf{u} \parallel \mathbf{l} \parallel z$ in these waves can be either symmetric or antisymmetric with respect to the midplane $x = 0$ of the slab ($\lambda < 2d$ is the penetration depth of a magnetic field into the nonmagnetic superconducting medium, and $\bar a \equiv \mu_2\alpha_2/\mu_1$):

$$\begin{aligned}u_+ &= u_-, \quad \phi_+ = -\phi_-,\\ &[\bar c_{55}\alpha_1\tanh(\alpha_1 k_\perp d) + \bar a][\mu_{xx}\coth(k_\perp d) + \beta]\\ &\quad + \epsilon\omega_{me}^2\omega^2/\Delta^2 = 0,\end{aligned} \tag{25}$$

$$\begin{aligned}u_+ &= -u_-, \quad \phi_+ = \phi_-,\\ &[\bar c_{55}\alpha_1\coth(\alpha_1 k_\perp d) + \bar a][\mu_{xx}\tanh(k_\perp d) + \beta]\\ &\quad + \epsilon\omega_{me}^2\omega^2/\Delta^2 = 0.\end{aligned} \tag{26}$$

It follows from (25) and (26) that, in the short-wavelength limit ($\alpha_{1,2} \longrightarrow 1$), the spectrum of the gap magnetoelastic SH waves for the acoustically continuous antiferromagnet–superconductor–antiferromagnet structure coincides with the spectrum of surface magnetoelastic SH waves traveling along an acoustically continuous nonmagnetic medium–antiferromagnet–nonmagnetic medium structure. Moreover, such a correspondence holds both when all interfaces are mechanically free, $\mu_2 = 0$ [see Eqs. (15)–(17)], and when both structures are acoustically continuous, $\beta/\mu_2 \longrightarrow 0$ [see Eqs. (19)–(21)].

Up to now, the spatial dispersion has been neglected in the analysis; in the magnetic medium, this dispersion is primarily attributed to the inhomogeneous-exchange interaction ($\delta_* > 0$ is the inhomogeneous-exchange constant). As a result, the term $0.5\delta_*(\nabla\mathbf{l})^2$ has not been taken into account when calculating the spectrum of surface magnetoacoustic SH phonons in the thermodynamic potential density (1) (it was assumed that $|\mathbf{m}| \ll |\mathbf{l}|$ in the exchange-collinear antiferromagnet for $|\mathbf{H}_0| = 0$). A simultaneous consideration of the dipolar, magnetoelastic, and inhomogeneous-exchange interactions substantially complicates the boundary value problem, because, in addition to the elastic and electromagnetic boundary conditions, one has to take into account additional exchange-induced boundary conditions that determine the behavior of the magnetic moment on the surface of the magnetic medium.

The analysis of the influence of the inhomogeneous-exchange interaction on the formation conditions and the dispersion characteristics of surface magnetoacoustic SH waves is described in the next section as applied to a ferromagnetic with the Néel temperature T_N less than the Debye temperature T_D.

6. EFFECTS OF INHOMOGENEOUS-EXCHANGE INTERACTION

Neglecting the effects of surface magnetic reconstruction, in this study, we choose the Rado–Weertman [27] exchange boundary conditions as additional boundary conditions; this choice corresponds to the surface ($x = 0$) of a magnetic with completely free spins:

$$\frac{\partial \tilde{\mathbf{l}}}{\partial x} = \frac{\partial \tilde{\mathbf{m}}}{\partial x} = 0, \quad x = 0,$$
$$\tilde{l}(x \longrightarrow -\infty) \longrightarrow 0, \quad \tilde{m}(x \longrightarrow -\infty) \longrightarrow 0, \tag{27}$$

here, $\tilde{\mathbf{m}}$ and $\tilde{\mathbf{l}}$ describe small deviations of the ferromagnetic $\mathbf{m}$ and antiferromagnetic $\mathbf{l}$ vectors from their respective equilibrium orientations.

If, as before, $\mathbf{n} \parallel x$, $\mathbf{k} \in xy$, and $\mathbf{l} \parallel \mathbf{u} \parallel z$, then the consideration in (1) of the additional term $0.5\delta_*(\nabla \mathbf{l})^2$, induced by the inhomogeneous-exchange interaction, substantially complicates the corresponding characteristic equation:

$$\{[s_{1t}^2(k_\perp^2 - q^2) - \omega^2][\Delta + c^2(k_\perp^2 - q^2)] - \omega_{me}^2 - \omega^2\omega_{me}^2\}$$
$$\times [\Delta + c^2(k_\perp^2 - q^2)][k_\perp^2 - q^2] = 0, \tag{28}$$

where $k_x^2 \equiv -q^2$, $k_y^2 \equiv k_\perp^2$, and $c^2 = g^2 M_0^2 \delta\delta_*$. It follows from (28) that the spatial dispersion ($\delta_* \neq 0$) gives rise to additional partial waves (two waves for an easy-axis ferromagnet) that take part in the formation of a normal magnetoacoustic SH wave. As a result, for $\delta_* \neq 0$, a shear magnetoacoustic wave with $\mathbf{u} \parallel \mathbf{l} \parallel z$, $\mathbf{k} \in xy$, and $\mathbf{n} \parallel x$ propagating in an easy-axis antiferromagnet is a four-partial wave.

Calculations show that, in the case of (28) with $\delta_* \neq 0$ (without taking dissipation into account), the dispersion law of the surface SH mode $\Omega_s(k_\perp)$ determined from (3), (4), and (27) or from (9), (10), and (27), depending on the type of acoustic contact at the interface between magnetic and nonmagnetic media, will have both real $\Omega_{sR}(k_\perp)$ and imaginary $\Omega_{sI}(k_\perp)$ parts:

$$\Omega_s(k_\perp) = \Omega_{sR}(k_\perp) + i\Omega_{sI}(k_\perp), \quad \mathrm{Im}\Omega_{sR,I}(k_\perp) = 0.$$

For $\delta_* \longrightarrow 0$, we have

$$\Omega_{sI}(k_\perp) \longrightarrow 0, \quad \Omega_{sR}(k_\perp) \longrightarrow \Omega_s(k_\perp).$$

This fact suggests that, in the case of a magnetic halfspace with $\delta_* \neq 0$, the surface magnetoacoustic SH wave under consideration transforms into a leaky wave. It follows from (28) that the physical mechanism of the leakage of this surface mode is associated with the fact that the spatial dispersion in the magnetic medium (the inhomogeneous-exchange interaction) gives rise to additional partial waves that take part in the formation of a normal shear magnetoacoustic wave. One of these additional partial waves in the domain of existence of an exchange-free ($\delta_* \longrightarrow 0$) surface magnetoacoustic SH wave (5), (6) or (5), (11) is a wave of trigonometric type; therefore, the energy of the surface magnetoacoustic SH wave traveling along the interface between magnetic and nonmagnetic media is pumped into the bulk of the magnetic material.

As the wave number $k_\perp$ increases, the contribution of the exchange mechanism to the dynamic properties of the magnetic medium increases, and, in the short-wavelength limit, the dispersion curves for the spectrum of the surface magnetoacoustic SH wave will always correspond to a forward wave ($\partial\Omega_{sR}(k_\perp)/\partial k_\perp > 0$). In particular, in the case of an easy-axis antiferromagnet with $\delta_* \neq 0$, the expression for $\Omega_{sR}(k_\perp)$ in the elastostatic limit ($\omega/s_{1t} \ll k_\perp$) will be determined, as before, by (5), (6) upon the substitution $\omega_0^2 \longrightarrow \omega_0^2 + c^2 k_\perp^2$. As a result, the dispersion curve of the surface magnetoacoustic SH wave with $\delta_* \neq 0$ that travels along the mechanically free interface between an easy-axis antiferromagnet and a superconductor may have a minimum for $k_\perp \neq 0$ even when the acoustic delay is neglected, provided that the London penetration depth λ of a magnetic field into the superconductor is different from zero (i.e., $\beta \equiv \tanh(k_\perp\lambda) \neq 0$ in (4)).

However, this does not exhaust the phenomena associated with the effect of the spatial dispersion of the magnetic medium (inhomogeneous-exchange interaction) on the spectrum and the conditions for the formation of the surface magnetoacoustic SH wave of the type considered. The analysis shows that the consideration of the inhomogeneous-exchange interaction ($0.5\delta_*(\nabla \mathbf{l})^2$) in (1) may also be essential for the transformation of a exceptional volume magnetoacoustic SH wave into a surface shear wave traveling along the mechanically free surface of a magnetically ordered crystal.

As an example, consider a semi-infinite easy-axis antiferromagnet (1) with the mechanically free surface (3). Let a normal vector $\mathbf{n}$ to the surface be collinear to the easy axis z of the antiferromagnet and the sagittal plane coincide with the plane xz ($\mathbf{k} \in xz$). Calculations show that, in such a configuration, when the spatial dispersion of the magnetic medium is neglected ($\delta_* \longrightarrow 0$), the formation of a surface magnetoacoustic SH wave ($\mathbf{u} \parallel y$) due to the hybridization of the dipolar and magnetoelastic interactions is impossible. We will assume that, together with the additional (exchange) boundary conditions (27), the elastic boundary conditions (3) and the electromagnetic boundary conditions (4)[2] with $\beta = \infty$ are satisfied simultaneously on the mechanically free surface $z = 0$. Possible physical mechanisms for the realization of such an electromagnetic condition

[2] In this case, one has to make the changes $x \longrightarrow z$ and $u_z \longrightarrow u_y$ in (3), (4), and (27).

are described, for example, in [20]. If $\mathbf{k} \in xz$, $\mathbf{l} \parallel z$, and $\mathbf{u} \parallel y$ then the corresponding dispersion equation is given by

$$(s_{1t}^2\mathbf{k}^2 - \omega^2)\left(\Delta + c^2\mathbf{k}^2 + \frac{\omega^2 k_x^2}{\mathbf{k}^2 + \epsilon k_x^2}\right) - \omega_{me}^2 s_{1t}^2 k_z^2 = 0. \quad (29)$$

The simultaneous analysis of (29) and (13) shows that, when $\mathbf{n} \parallel z$, the inhomogeneous-exchange interaction is neglected ($\delta_* \longrightarrow 0$), and $\beta = \infty$, a homogeneous bulk magnetoacoustic SH wave ($\mathbf{u} \parallel y$) can propagate at a grazing angle to the surface of the magnetic crystal in this configuration; hence, the localization of a shear dipolar wave on the mechanically free surface of the antiferromagnet is impossible. If we take into account the spatial dispersion in the magnetic medium ($\delta_* \neq 0$ in (29) and the additional boundary condition (27)), then the calculations show that the inhomogeneous exchange makes impossible the propagation of a bulk homogeneous two-partial magnetoacoustic SH wave ($\mathbf{u} \parallel y$, $\mathbf{l} \parallel z$, $\mathbf{k} \in xz$) along the surface with $\mathbf{n} \parallel z$ and $\beta = \infty$. This is a necessary condition for the formation of a three-partial surface shear magnetoacoustic wave in the magnetic medium ($z < 0$). As a result, the spatial structure, for example, of the vector of elastic displacements $\mathbf{u} \parallel y$ in this wave can be represented as

$$u_{y1} = \sum_{i=1}^{3} A_i \exp(q_i z)\exp(i\omega t - ik_\perp x), \quad (30)$$

where q_{1-3} ($k_\perp^2 \equiv k_y^2$) are only those of the six roots of Eq. (29) that satisfy the localization condition for the SH wave under consideration near the surface of the antiferromagnet:

$$u_{y1}(z \longrightarrow -\infty) \longrightarrow 0, \quad \phi_1(z \longrightarrow -\infty) \longrightarrow 0,$$
$$\tilde{l}_y(z \longrightarrow -\infty) \longrightarrow 0, \quad \tilde{m}_x(z \longrightarrow -\infty) \longrightarrow 0.$$

This makes it possible to study, on the basis of (29) and (30), the effect of the inhomogeneous-exchange interaction on the degree of localization of the magnetoacoustic SH wave traveling along the surface of the antiferromagnetic crystal ($z = 0$) under the assumption that the frequency ω and the wave number $k_\perp$ are prescribed external parameters. It follows from (29) that, in the elastostatic limit ($\omega/s_{1t} \ll k_\perp$), up to $\epsilon^2 \ll 1$, $q_1^2 \approx (1 + \epsilon)k_\perp^2$, while $q_{2,3}^2$ are the roots of the equation

$$q^4 - P_1 q^2 + P_2 = 0, \quad (31)$$

where

$$P_1 = \frac{1}{c^2}(\omega_0^2 + 2c^2k_\perp^2 - \omega^2),$$

$$P_2 = \frac{k_\perp^2}{c^2}[\omega_0^2 + c^2k_\perp^2 + \omega_{me}^2 - \omega^2(1 - \epsilon)].$$

The simultaneous analysis of Eqs. (30), (31) shows that, depending on the frequency ω and the wave vector $k_\perp$, two types of traveling three-partial surface magnetoacoustic SH waves can be formed that differ by the character of their spatial localization near the surface of the antiferromagnetic crystal:

I. A surface magnetoacoustic SH wave ($q_{1-3}^2 > 0$)

$$k_1 > k_\perp, \quad \omega_+^2(k_\perp) < \omega^2 < \frac{\omega_0^2 + \omega_{me}^2 + c^2k_\perp^2}{1 - \epsilon}, \quad 0 < k_\perp < k_2, \quad \omega^2 < \omega_-^2(k_\perp); \quad (32)$$

II. A generalized surface magnetoacoustic SH wave ($q_1^2 > 0$ and $q_2^2 = (q_3^2)^*$, where the asterisk denotes complex conjugation)

$$\omega_-^2(k_\perp) < \omega^2 < \omega_+^2(k_\perp); \quad (33)$$

III. A bulk magnetoacoustic SH wave of type *A* ($q_1^2 > 0$ and $q_{2,3}^2 < 0$)

$$0 < k_\perp < k_1, \quad \omega_+^2(k_\perp) < \omega^2 < \frac{\omega_0^2 + \omega_{me}^2 + c^2k_\perp^2}{1 - \epsilon}; \quad (34)$$

IV. A bulk magnetoacoustic SH wave of type *B* ($q_{1,2}^2 > 0$ and $q_3^2 < 0$)

$$(\omega_0^2 + \omega_{me}^2 + c^2k_\perp^2)/(1 - \epsilon) < \omega^2. \quad (35)$$

Here, $\omega_\pm^2(k_\perp)$ are the positive roots of the equation $P_1^2 = 4P_2$, and $k_{1,2}$ are determined by the relations

$$k_1^2 \equiv (\epsilon\omega_0^2 + \omega_{me}^2)/(1 - 2\epsilon), \quad \omega_-^2(k_2) = 0.$$

The analysis of expressions (30)–(33) shows that one of characteristic features of the spectrum of magnetoacoustic SH waves induced by the inhomogeneous exchange in this configuration ($\mathbf{u} \parallel y$, $\mathbf{k} \in xz$, $\mathbf{n} \parallel z$) is the presence of "high-frequency" and "low-frequency" regions of existence of surface shear magnetoacoustic waves in the plane of parameters ω and $k_\perp$.

Using relations (30)–(33), we can now proceed to a more detailed analysis of the possibility of formation, due to the inhomogeneous-exchange interaction, of a shear three-partial surface magnetoacoustic wave with $\mathbf{k} \in xz$, $\mathbf{u} \perp \mathbf{l} \parallel z$, and $\mathbf{n} \parallel z$ near the mechanically free surface of an antiferromagnet (see (3) and (4) with $\beta = \infty$). Calculations show that the spectrum of this three-partial shear magnetoacoustic wave can be determined in the explicit form if we restrict the analysis to

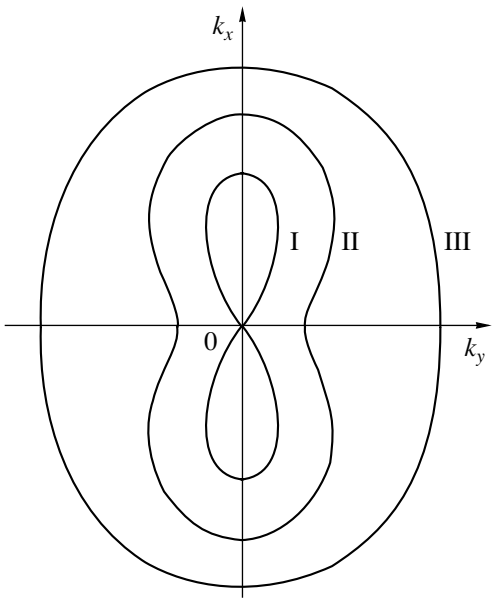

Fig. 2. The structure of the surface of wave vectors for a normal magnetoacoustic SH wave in the easy-axis antiferromagnet (38): (I) $\omega_0^2 < \omega^2 < (\omega_0^2 + \omega_{me}^2)/(1-\epsilon)$; (II) $((\omega_0^2 + \omega_{me}^2)/(1-\epsilon) < \omega^2 < (\omega_0^2 + \omega_{me}^2 + c^2k_1^2)/(1-\epsilon)$; and (III) $\omega^2 > (\omega_0^2 + \omega_{me}^2 + c^2k_1^2)/(1-\epsilon)$.

the elastostatic approximation. The corresponding dispersion equation is

$$q_2^2 + q_3^2 + q_2q_3 - k_\perp^2 = 0. \quad (36)$$

Hence, taking into account (30) and (31), we obtain the following dispersion law for the surface magnetoacoustic SH wave induced by the inhomogeneous-exchange interaction:

$$\Omega_s^2(k_\perp) = 0.5N_1 + \sqrt{0.25N_1^2 - N_2}, \quad (37)$$

where

$$N_1 = 2\omega_0^2 + c^2k_\perp^2(1-\epsilon),$$

$$N_2 = (\omega_0^2 + c^2k_\perp^2)^2 - c^2k_\perp^2(\omega_0^2 + c^2k_\perp^2 + \omega_{me}^2).$$

The juxtaposition of (36), (37) with inequalities (32), (33) shows that, if $0 < k_\perp < k_{**}$ (k_{**} is determined from the equation $\Omega_s^2(k_{**}) = \omega_+^2(k_\perp)$ with the use of (32)–(37)), then the surface shear mode under consideration is a three-partial magnetoacoustic SH wave ($q_1^2 > 0$, $q_2^2 = (q_3^2)^*$) whose dispersion curve transforms into that of a three-partial surface magnetoacoustic SH wave ($q_{1-3}^2 > 0$) at $k_\perp = k_{**}$. It follows from (36) and (37) that this type of localized magnetoelastic excitations is not realized without taking into account the inhomogeneous-exchange interaction ($\delta_* \longrightarrow 0$).

This conclusion can also be confirmed by calculating the reflection coefficient R of a shear elastic wave ($\mathbf{u} \parallel y$, $\mathbf{k} \in xz$) from the surface of antiferromagnet (26) with $\mathbf{n} \parallel z$ and the boundary conditions (3), (27), and (4) for $\beta = \infty$. In particular, if $k_z \longrightarrow 0$, then $R \longrightarrow -1$ for $\delta_* \neq 0$ and $R \longrightarrow 1$ for $\delta_* = 0$.

The analysis shows that, for an easy-axis antiferromagnet (29) with the spatial dispersion of the medium (the inhomogeneous-exchange interaction) taken into account, the conditions for the formation of a surface magnetoacoustic SH wave prove to be related not only to the amplitude characteristics of the incident and reflected shear normal magnetoacoustic waves (to the reflection coefficient) but also to the local geometry of its isofrequency surface constructed in the elastostatic approximation.

As an example, consider a two-sublattice model of easy-axis antiferromagnet (1) under the conditions $\mathbf{u} \parallel y$, $\mathbf{k} \in xz$, and $\mathbf{n} \parallel z$. In this case, if we neglect the acoustic delay ($\omega/(s_{1t}k_\perp) \longrightarrow 0$), the cross section of the isofrequency ($\omega = \text{const}$) surface, in the $\mathbf{k}$ space, of a normal magnetoacoustic SH wave in an unbounded crystal ($\tilde{l}_y$, $\tilde{m}_x$, $u_y \neq 0$) by the sagittal plane xz is determined from (29) by the equation ($\tan\theta = k_x/k_z$)

$$c^2k^2 = \omega^2\left(1 - \frac{\epsilon\sin^2\theta}{1 + \epsilon\sin^2\theta}\right) - \omega_0^2 - \omega_{me}^2\sin^2\theta. \quad (38)$$

Calculations show that, with allowance for (32)–(35), the condition under which regions with negative Gaussian curvature appear on the curve (38) can be represented as

$$\omega^2 < \frac{\omega_0^2 + c^2k_\perp^2 + \omega_{me}^2}{1-\epsilon}. \quad (39)$$

It follows from (39) that, for (38), a region with negative Gaussian curvature is realized for $\theta = \pi/2$ (Fig. 2). Juxtaposing this result with the existence conditions for the surface magnetoacoustic SH wave that were obtained above with regard to the inhomogeneous-exchange interaction, we can conclude that a region with negative curvature on curve (38) is a necessary condition for the transformation of this type of normal oscillations into an appropriate surface magnetoacoustic SH wave. Here, it is required that the direction of the normal $\mathbf{n}$ to the surface of the magnetic medium should be perpendicular to the direction in which the above region with the maximum negative curvature is formed.

It should be noted that, for the given geometry ($\mathbf{n} \parallel \mathbf{l} \parallel z$, $\mathbf{u} \parallel y$, $\mathbf{k} \in xz$), the hybridization of dipolar, magnetoelastic, and inhomogeneous-exchange interactions may lead to the localization of the magnetoacoustic SH wave near the surface of antiferromagnet (1) even when the surface is rigidly fixed. Suppose, as before, that the

antiferromagnetic medium occupies the lower half-space ($z < 0$) and the following system of boundary conditions holds on the surface:

$$\left.\begin{aligned} &\frac{\partial \tilde{\mathbf{l}}}{\partial z} = \frac{\partial \tilde{m}}{\partial z} = 0, \\ &u_{y1} = 0, \\ &\mathbf{B}_1 \cdot \mathbf{n} = -\beta k_\perp \phi_1, \end{aligned}\right\} \quad z = 0, \tag{40}$$

$$u_{y1}(z \longrightarrow -\infty), \quad \phi_1(z \longrightarrow -\infty).$$

Since the dispersion relation for the shear wave is determined by (29) as before, the surface wave under consideration is three-partial again (30). Calculations show that, in the short-wavelength limit under the condition that $\beta \ll 1$ in (40), the spectrum of the magnetoacoustic SH wave traveling along the surface of the antiferromagnet can be represented as

$$\Omega_s^2(k_\perp) \approx (\omega_0^2 + c^2 k_\perp^2 + \omega_{me}^2)(1 + \epsilon) - \frac{\epsilon^2 \beta^2}{c^2 k_\perp^2}(\omega_0^2 + c^2 k_\perp^2 + \omega_{me}^2)^2. \tag{41}$$

Using (32)–(35), one can verify that this type of oscillations corresponds to a surface shear three-partial ($q_{1-3}^2 > 0$) wave.

7. CONCLUSIONS

In this work, we determined conditions under which the magnetoelastic mechanism of linear coupling between the oscillations of the magnetostatic potential ϕ and the lattice may give rise, even in a zero external magnetic field, to a new type of surface shear magnetoacoustic waves near both a mechanically free and an acoustically continuous interface between a uniaxial antiferromagnet and a nonmagnetic medium. In particular, we demonstrated that

(1) this type of surface shear waves cannot be formed for a mechanically free interface between a uniaxial antiferromagnet and a perfect superconductor when either only magnetoelastic or only dipolar interaction is taken into account;

(2) the conductivity of the nonmagnetic medium may essentially affect the structure of the spectrum of the surface magnetoacoustic SH wave obtained;

(3) in an easy-axis antiferromagnet, this type of surface waves is dipolar only on the surface of the magnetic crystal but not in the bulk;

(4) in the case of a rigid contact between antiferromagnetic and nonmagnetic media, the formation of the surface SH wave with allowance for the magnetoelastic interaction is possible even in the absence of the dipolar interaction;

(5) there exists a close relationship between the conditions for the formation of the surface magnetoacoustic SH waves obtained and the conditions for the propagation of a shear bulk magnetoacoustic wave at a grazing angle along the surface of the magnetic medium;

(6) conditions for the reflection of a normal magnetoacoustic SH wave from the surface of the antiferromagnet essentially depend on the frequency and the wave number of the incident wave, as well as on the conductivity and the elastic properties (in the case of a rigid contact) of the adjoining nonmagnetic medium;

(7) in the short-wavelength (elastostatic) limit, the spectrum of a gap magnetoacoustic SH wave in the antiferromagnet–nonmagnetic layer–antiferromagnet structure coincides with the spectrum of a surface shear magnetoacoustic traveling along an antiferromagnetic slab in the structure of the type nonmagnetic medium–antiferromagnet–nonmagnetic medium;

(8) a consistent consideration of the spatial dispersion induced by the inhomogeneous-exchange interaction in the antiferromagnet may give rise to both a leaky and a surface three-partial magnetoacoustic SH wave even in the case when the surface of the magnetic material is rigidly fixed;

(9) the analysis of the local geometry of the surface of wave vectors of the normal bulk magnetoacoustic SH wave in an antiferromagnetic crystal allows one to determine the necessary conditions under which a surface three-partial magnetoacoustic SH wave can propagate along the interface between magnetic and nonmagnetic media.

Despite the fact that we considered a model of a uniaxial antiferromagnet with isotropic magnetoelastic and elastic interactions, one can easily verify that all the results obtained are qualitatively the same when the antiferromagnetic crystal is cubic, tetragonal, or hexagonal, provided that the equilibrium antiferromagnetic vector **l** is directed along the higher order axis (or along the edges of a cube in the case of a cubic crystal). Moreover, all the above solutions remain valid when the elastic boundary conditions at the interface between antiferromagnetic and nonmagnetic media (3) correspond to a grazing-type condition rather than to a mechanically free boundary [28].

ACKNOWLEDGMENTS

I am grateful to V.E. Tarasenko and V.M. Yurchenko for supporting the idea of this work and useful discussions.

REFERENCES

1. Yu. V. Gulyaev, I. E. Dikshteĭn, and V. G. Shavrov, Usp. Fiz. Nauk **167**, 735 (1997) [Phys. Usp. **40**, 701 (1997)].
2. J. P. Parekh, Electron. Lett. **5**, 322 (1969).
3. Yu. V. Gulyaev, Yu. A. Kuzavko, I. N. Oleĭnik, and V. G. Shavrov, Zh. Éksp. Teor. Fiz. **87**, 674 (1984) [Sov. Phys. JETP **60**, 386 (1984)].

4. M. I. Kaganov and Yu. A. Kosevich, Poverkhnost, No. 6, 148 (1986).
5. Yu. A. Kosevich and E. S. Syrkin, Fiz. Tverd. Tela (Leningrad) **28**, 248 (1986) [Sov. Phys. Solid State **28**, 134 (1986)].
6. P. Chadwick and G. D. Smith, Adv. Appl. Mech. **17**, 303 (1977).
7. J. Lothe and V. I. Al'shits, Kristallografiya **22**, 906 (1977) [Sov. Phys. Crystallogr. **22**, 519 (1977)].
8. V. I. Al'shits and J. Lothe, Kristallografiya **24**, 1122 (1979) [Sov. Phys. Crystallogr. **24**, 644 (1979)].
9. V. I. Al'shits and V. N. Lyubimov, Kristallografiya **30**, 213 (1985) [Sov. Phys. Crystallogr. **30**, 123 (1985)].
10. E. A. Turov and V. G. Shavrov, Usp. Fiz. Nauk **140**, 429 (1983) [Sov. Phys. Usp. **26**, 593 (1983)].
11. R. E. Camley and A. A. Maradudin, Appl. Phys. Lett. **38**, 610 (1981).
12. S. V. Tarasenko, Fiz. Tverd. Tela (St. Petersburg) **42**, 694 (2000) [Phys. Solid State **42**, 712 (2000)].
13. J. Barnas, Acta Phys. Pol. A **59**, 449 (1981).
14. R. E. Camley and D. L. Mills, Phys. Rev. B **26**, 1280 (1982).
15. B. Luthi, D. L. Mills, and R. E. Camley, Phys. Rev. B **28**, 1475 (1983).
16. A. L. Sukstanskiĭ and S. V. Tarasenko, Zh. Éksp. Teor. Fiz. **105**, 928 (1994) [JETP **78**, 498 (1994)].
17. S. V. Tarasenko, Fiz. Tverd. Tela (St. Petersburg) **40**, 299 (1998) [Phys. Solid State **40**, 272 (1998)].
18. V. I. Ozhogin and V. L. Preobrazhenskiĭ, Usp. Fiz. Nauk **155**, 593 (1988) [Sov. Phys. Usp. **31**, 713 (1988)].
19. V. I. Al'shits and V. N. Lyubimov, Zh. Éksp. Teor. Fiz. **106**, 663 (1994) [JETP **79**, 364 (1994)].
20. V. I. Alshits, A. N. Darinskii, and J. Lothe, Wave Motion **16**, 265 (1992).
21. R. E. Camley, Surf. Sci. Rep. **7**, 103 (1987).
22. K. Abraha and D. R. Tilley, Surf. Sci. Rep. **24**, 125 (1996).
23. M. K. Balakirev and I. A. Gilinskiĭ, *Waves in Piezoelectric Crystals* (Nauka, Novosibirsk, 1982).
24. Yu. A. Kosevich and E. S. Syrkin, Kristallografiya **33**, 1347 (1988) [Sov. Phys. Crystallogr. **33**, 801 (1988)].
25. L. M. Brekhovskikh, *Waves in Layered Media* (Nauka, Moscow, 1973; Academic, New York, 1980).
26. L. M. Lyamshev and N. S. Shevyakov, Akust. Zh. **21**, 951 (1975) [Sov. Phys. Acoust. **21**, 581 (1975)].
27. A. G. Gurevich and G. A. Melkov, *Magnetic Oscillations and Waves* (Nauka, Moscow, 1994).
28. V. A. Krasil'nikov and V. V. Krylov, *Introduction to Physical Acoustics* (Nauka, Moscow, 1984).

Translated by I. Nikitin

Journal of Experimental and Theoretical Physics, Vol. 94, No. 3, 2002, pp. 581–592.
Translated from Zhurnal Éksperimental'noĭ i Teoreticheskoĭ Fiziki, Vol. 121, No. 3, 2002, pp. 678–691.

SOLIDS
Electronic Properties

The Nonlinear Magnetic Properties of the Pseudocubic $Nd_{0.77}Ba_{0.23}MnO_3$ Single Crystal in the Critical Paramagnetic Region and Phase Separation

V. A. Ryzhov[a, *], A. V. Lazuta[a], I. D. Luzyanin[a], I. I. Larionov[a], V. P. Khavronin[a], Yu. P. Chernenkov[a], I. O. Troyanchuk[b, **], and D. D. Khalyavin[b]

[a]*Institute of Nuclear Physics, Russian Academy of Sciences, Gatchina, Leningrad oblast, 188350 Russia*
[b]*Institute of Solid-State and Semiconductor Physics, Belarussian Academy of Sciences, ul. Brovki 17, Minsk, 220072 Belarus*
**e-mail: ryzhov@omrb.pnpi.spb.ru*
***e-mail: troyan@ifttp.bas-net.by*
Received June 15, 2001

Abstract—The second magnetization harmonic was studied for a moderately doped $Nd_{0.77}Ba_{0.23}MnO_3$ neodymium manganite single crystal in parallel constant and harmonic magnetic fields in the critical paramagnetic region. According to the neutron and X-ray diffraction data, the crystal was crystallographically single-phase and had a pseudocubic structure both at room temperature and below the Curie point T_C = 124.1 K. Although the specific resistance of this compound had a singularity near T_C and exhibited giant magnetoresistance, it remained an insulator in the ferromagnetic state. Nonlinear response measurements in the $T_C < T < T_* \approx 146.7$ K paramagnetic region were indicative of the existence of two magnetic phases. Above T_*, the crystal was magnetically single-phase, and its critical behavior was well described by dynamical similarity theory for isotropic 3D ferromagnets. The unexpected appearance of a new magnetic phase in the structurally homogeneous crystal was discussed based on phase separation ideas; such a phase separation could occur in moderately doped cubic manganites experiencing orbital ordering. *© 2002 MAIK "Nauka/Interperiodica".*

1. INTRODUCTION

The appearance of ferromagnetic ordering in $LMnO_3$ manganites, where L is a trivalent rare-earth metal ion, is a consequence of doping them with a divalent alkaline-earth metal (Ca, Sr, or Ba) [1]. Doping results in the formation of mobile holes and, above a certain level, causes the transition to the ferromagnetic metallic state by the double exchange mechanism [2, 3]. Usually, an isotropic insulating ferromagnetic phase is formed in the transition from the antiferromagnetic dielectric to the ferromagnetic metallic state as the level of doping increases; this phase cannot be described by the double exchange mechanism [1]. The interactions responsible for the ferromagnetic transition in doped compounds are fairly complex in character (e.g., see [4]). In [4], an important example of interactions in cubic manganites was considered; these interactions included double exchange for e_g electrons in the presence of orbitally degenerate states, superexchange caused by electron correlation, and antiferromagnetic exchange for spins of localized t_{2g} electrons. The spin and orbital degrees of freedom were interrelated in such interactions. As a result, a complex phase diagram was obtained, which included phase separation regions with the coexistence of phases that differed in magnetic or (and) orbital order. The authors were able to correlate the formation of a ferromagnetic insulating phase and the appearance of an antiferromagnetic-type orbital order observed in $La_{0.88}Sr_{0.12}MnO_3$ below the Curie temperature [5].

Among the manganites that have been studied, only $L_{1-x}Ba_xMnO_3$ compounds moderately doped with barium ($0.15 < x < 0.5$) have very weak structural distortions for most of the rare-earth metals [6, 7]. This circumstance allows these compounds to be treated as manganites with the predominance of electronic interactions and their properties to be compared with those predicted by the model suggested in [4]. Note that the $La_{0.88}Sr_{0.12}MnO_3$ compound is characterized by static cooperative Jahn–Teller deformations, which develop at $T_{JT} \approx 291$ K > $T_C \approx 172$ K and persist up to the orbital ordering temperature $T_{oo} \approx 145$ K [5].

One of the important aspects of the magnetic properties of manganites is their critical behavior in the vicinity of the ferromagnetic transition, which has not been studied in detail. In spite of the complexity of magnetic interactions resulting in ferromagnetism in manganites, it can be expected that, by virtue of the universality of second-order phase transitions, their critical static behavior depends not on all interaction details but only on such characteristics as symmetry, the number of order parameter components, and the dimension

of the system. Apart from these properties, the universality of dynamic behavior is determined by the laws of conservation in the system and permutation relations between the operators of strongly fluctuating values [8]. This universality arises because the physics of critical phenomena is determined by interaction of large-scale fluctuations, whose correlation radii substantially exceed interatomic distances.

The interactions that result in ferromagnetism in cubic manganites are isotropic in the spin space. If the universality hypothesis is valid for these systems, it is natural to assume that their critical behavior should not differ from the behavior of a magnet described by the Heisenberg Hamiltonian. A similar assertion applies to changes in the critical properties when dipole forces, which are the most important anisotropic spin interactions in isotropic magnets, are taken into account. Usually negligibly weak influence of single-ion cubic anisotropy, which, according to estimates, can also be ignored for cubic manganites, was considered in [9].

In this work, we studied critical dynamics of the $Nd_{0.77}Ba_{0.23}MnO_3$ single crystal in the paramagnetic region. According to the neutron and X-ray diffraction data, the crystal was pseudocubic both above and below the Curie temperature. Although the specific resistance of this manganite has a singularity near T_C, the ferromagnetic transition occurred without a change in its dielectric state, and the crystal exhibited giant magnetoresistance [10].

In [11], we used the temperature dependence of nonlinear response at low frequencies (1–100 kHz) to reliably determine the ferromagnetic ordering temperature T_C = 124.1 K of the single crystal under study. Above T_C, the critical exponents for linear susceptibility χ and the third magnetization harmonic in zero constant magnetic field and also for the real second magnetization harmonic component M_2 (f = 15.7 MHz) in the presence of a weak constant field (see below) were determined. Their values agreed with the predictions of similarity theory for isotropic 3D ferromagnets in the temperature range $\tau = (T - T_C)/T_C > 0.12$.

In this work, most attention is given to the nonlinear dynamic response to alternating magnetic field actions. The temperature and field dependences of the second magnetization harmonic $M_2(T, H)$ and, especially, its imaginary component allowed us to determine the temperature boundary $T_* \approx 146.7$ K of the appearance of the second magnetic phase. In addition, these data were used to analyze the spin dynamics based on the isotropic ferromagnet model. As a result, we obtained the temperature dependence of spin relaxation rate Γ for uniform magnetization and determined spin diffusion coefficient D in the region $T > T_*$. Below this temperature, the appearance of the second magnetic phase prevented us from performing a quantitative analysis of the $M_2(T, H)$ data. The relative volume of the new phase, whose critical behavior was radically different from that of a classic isotropic ferromagnet, increased as temperature approached T_C. It was assumed that the formation of the new phase was related to orbital ordering, because, at 110 K (below T_C), no structural changes were observed in the crystal compared with room temperature.

The paper is organized as follows. Section 2 briefly considers second magnetization harmonic generation in an isotropic ferromagnet and contains equations necessary for quantitatively analyzing data. The sample is characterized and the procedure for measurements is described in Section 3. Section 4 contains experimental results, which are discussed in Section 5. Lastly, the most important results are summarized in the Conclusion.

2. SECOND CUBIC FERROMAGNET MAGNETIZATION HARMONIC IN THE CRITICAL PARAMAGNETIC NEIGHBORHOOD OF T_C

It has been shown [11] that the linear and nonlinear static magnetic properties of the $Nd_{0.77}Ba_{0.23}MnO_3$ crystal in the critical paramagnetic region not too close to T_C are described by the isotropic 3D ferromagnet model. As we study second harmonic M_2 generation in this region, we will briefly describe this model.

The second magnetization harmonic, which is induced in a magnet by a harmonic magnetic field $h(t) = h\sin\omega t$ parallel to the constant field if $M_2 \propto h^2$, is described by second-order dynamic susceptibility $\chi_\parallel^{(2)}$. In ferromagnets, where the transition to the magnetically ordered state is caused by fairly strong interactions isotropic in the spin space, there exists a temperature region above T_C in which weak anisotropic spin interactions responsible for uniform magnetization relaxation can be taken into account by perturbation theory [9, 12]. The nonlinear response to a uniform harmonic magnetic field is then described by the relaxation time approximation, and the corresponding expression for $\chi_\parallel^{(2)}$ has the form [13]

$$\chi_\parallel^{(2)}(\omega) = \frac{\Gamma_\parallel}{-2i\omega + \Gamma_\parallel}\chi_\parallel^{(2)} - i\omega\frac{(\partial/\partial\omega_0)\Gamma_\parallel}{(-2i\omega + \Gamma_\parallel)(-i\omega + \Gamma_\parallel)}\chi_\parallel^{(1)}. \quad (1)$$

Here,

$$\chi_\parallel^{(1)} = \chi_\parallel^{(1)}(\tau, H) = \frac{\partial M(\tau, H)}{\partial H};$$

$$\chi_\parallel^{(2)} = \chi_\parallel^{(2)}(\tau, H) = \frac{1}{2}\frac{\partial^2 M(\tau, H)}{\partial H^2};$$

$\chi_\parallel^{(1)}$ and $\chi_\parallel^{(2)}$ are the first- and second-order static longitudinal susceptibilities, respectively; and $\Gamma_\parallel = \Gamma_\parallel(H, \omega_0, \tau)$ is the longitudinal magnetization relaxation rate.

The first term in (1) is caused by the nonlinear dependence of M on H. The second term takes into account alternating field influence on relaxation processes. This is a purely dynamic part of the response, which vanishes at $\omega = 0$. In $\Gamma_\parallel$, the dependences on H and $\omega_0 = g\mu H$ are separated in accordance with static and dynamic influence of H on the properties of the isotropic magnet [12, 13]. Note also that $\chi_\parallel^{(2)}(\omega)$ is, in accordance with the common properties of susceptibilities, an odd function of H, which vanishes at $H = 0$ [14]. In the frequency region $\omega < \Gamma_\parallel$, the first term in (1) [a consequence of the nonlinearity of the $M(H)$ dependence] makes the major contribution to $\mathrm{Re}\chi_\parallel^{(2)}(\omega)$, whereas the second term [a consequence of the influence of $H(t)$ on uniform magnetization relaxation rate] makes the major contribution to $\mathrm{Im}\chi_\parallel^{(2)}(\omega)$.

The most important anisotropic spin interactions in a cubic ferromagnet are caused by dipole forces, which are taken into account by perturbation theory in the temperature region in which $4\pi\chi < 1$ (exchange region) and $\chi = \chi_\parallel^{(1)}$ ($H = 0$). These forces change the dynamics of fluctuations and cause uniform magnetization relaxation (Hewber damping) at the rate [9, 15]

$$\Gamma_d = \frac{\gamma_d \omega_d^2}{T_C \tau} = \gamma_{d1}(4\pi\chi)^2 \Omega(\tau). \qquad (2)$$

Here, $\omega_d = 4\pi(g\mu)^2/V_0$ is the characteristic dipole energy (V_0 is the magnetic unit cell volume), $\gamma_d \sim \gamma_{d1} \sim 1$ are multipliers, and $\Omega(\tau) = T_C\tau^{5/3}$ is the characteristic energy of critical fluctuations (we ignore Fisher index η, which is small for 3D systems). Complete change in the critical behavior occurs in the dipole region ($4\pi\chi > 1$) [9, 16]. Note that dipole crossover at $4\pi\chi \approx 1$ was observed in manganites in only one work concerned with spin relaxation of muons in $Nd_{0.5}Sr_{0.5}MnO_3$ [17].

Consider the critical behavior of an isotropic three-dimensional ferromagnet in a magnetic field. The influence of H on its static properties is determined by the characteristic energy of critical fluctuations $\Omega(\tau)$. The field is considered weak (strong) if $g\mu H/\Omega(\tau) \ll (\gg) 1$. We are interested in the case of a weak field, when

$$4\pi\chi_\parallel^{(1)}(\tau, H) \approx 4\pi\chi(\tau) = C_\chi(\omega_d/T_C)\tau^{-4/3}. \qquad (3)$$

Here, factor C_χ is usually close to $S(S+1)/3$, where S is the magnetic center spin value. The $\chi_\parallel^{(2)}$ function can conveniently be written as

$$\frac{\chi_\parallel^{(2)}(\tau, H)}{\chi(\tau)} = -\frac{C_\parallel^{(2)} g\mu H}{\Omega^2(\tau)}, \qquad (4)$$

where the $C_\parallel^{(2)}$ coefficient is determined from the expansion of M in powers of H. The dependence of $\Gamma_\parallel$ on ω and ω_0 in a weak field is determined by the decay of a uniform mode into two hydrodynamic modes caused by dipole forces [9, 12]. Because of the existence of spin diffusion, the characteristic scale of $\Gamma_\parallel$ variations is a value substantially smaller than $\Omega(\tau)$, namely, magnetization relaxation rate Γ at $\omega = \omega_0 = 0$. Virtually the same processes determine the dependence of the EPR signal width on H. This circumstance was used to determine spin diffusion coefficient $D(\tau)$ under weak field conditions for $\omega_0 \gg \Gamma$ in studying the critical dynamics of the cubic Heisenberg ferromagnets $CdCr_2Se_4$ and $CdCr_2S_4$ [18]. Under the conditions of interest to us, when $\omega \ll \omega_0 \ll \Gamma$, an important dispersion correction to Γ appears. This $\Delta\Gamma_\parallel(\tau, \omega_0) \propto D^{-3/2}$ correction, for which the diffusion mode is responsible [12], can be written in the form

$$\Delta\Gamma_\parallel(\tau, \omega_0) = \Gamma(\tau) - \Gamma_\parallel(\tau, \omega_0) = C_{\Gamma_\parallel}\Gamma_d\omega_0^2(\Omega(\tau)\Gamma^3)^{-1/2}. \qquad (5)$$

Here, the dipole damping scale $\Gamma_d = \gamma_d\omega_d^2/T_C\tau$ is singled out. The numerical factor is described by the equation

$$C_{\Gamma_\parallel} \approx \frac{C_\chi}{120\pi C_D^{3/2}},$$

in which the C_D multiplier is determined by the spin diffusion coefficient,

$$D(\tau) = C_D T_C d^2 \tau^{1/3} = D_0 \tau^{1/3}, \qquad (6)$$

where d is the magnetic lattice constant. Diffusion correction (5) is the main term determining the $\Gamma_\parallel(\omega_0)$ dependence in a weak field. If we know C_χ, determining this correction allows C_D and, through this, the spin diffusion coefficient to be found.

In addition to dipole forces, other interactions can contribute to damping Γ. Of these, the most important ones in cubic ferromagnets with spin $S > 1/2$ are interactions with phonons. The corresponding noncritical $\Gamma_{nc}(\tau)$ contribution varies as $\chi^{-1} \propto \tau^{4/3}$ [12]. We eventually obtain

$$\Gamma(\tau) = \Gamma_d(\tau) + \Gamma_{nc}(\tau) = \Gamma_d^*(\tau^{-1} + \Lambda\tau^{4/3}). \qquad (7)$$

For convenience of further use, we factored out here the $\Gamma_d^* = \gamma_d\omega_d^2/T_C$ dipole contribution amplitude and introduced dimensionless parameter Λ, which describes the relative noncritical component value.

Next, consider the ratio between $\mathrm{Re}\chi_\parallel^{(2)}(\omega)$ and $\mathrm{Im}\chi_\parallel^{(2)}(\omega)$. We will see that the relations

$$\Delta\Gamma_\parallel/\Gamma \ll 1, \quad 2\omega/\Gamma_\parallel \approx 2\omega/\Gamma \ll 1$$

hold in the whole range of τ and H variations that we consider. Accordingly, we find from (1) and (4) for conditions linear in H that

$$\mathrm{Re}\chi_{\parallel}^{(2)}(\omega) \approx \chi_{\parallel}^{(2)}(0) \propto \tau^{-14/3}. \quad (8)$$

Under the same conditions, (1) and (5) give the imaginary component in the form

$$\begin{aligned}\mathrm{Im}\chi_{\parallel}^{(2)}(\omega) &\approx -\frac{\omega}{\Gamma^2(\tau)}\chi(\tau)\frac{\partial\Gamma_{\parallel}(\tau, \omega, \omega_0)}{\partial\omega_0} \\ &= 2C_{\Gamma_{\parallel}}\frac{\omega}{\Gamma(\tau)}\frac{\Gamma_d(\tau)}{\Gamma(\tau)}\frac{\omega_0}{\Gamma(\tau)}\frac{\chi(\tau)}{\sqrt{\Omega(\tau)\Gamma(\tau)}}.\end{aligned} \quad (9)$$

Taking into account (8) and (9), the ratio between the imaginary and real M_2 components can be written as

$$\begin{aligned}R(\omega, \tau) &= \frac{\mathrm{Im}M_2(\omega)}{\mathrm{Re}M_2(\omega)} = \frac{\mathrm{Im}\chi_{\parallel}^{(2)}(\omega)}{\mathrm{Re}\chi_{\parallel}^{(2)}(\omega)} \\ &= C_{\Gamma}\frac{\omega}{\Gamma(\tau)}\frac{\Gamma_d(\tau)}{\Gamma(\tau)}\left(\frac{\Omega(\tau)}{\Gamma(\tau)}\right)^{3/2}.\end{aligned} \quad (10)$$

Here, $C_{\Gamma} = 2G_{\Gamma_{\parallel}}/C_{\parallel}^{(2)}$ is a factor of the order of one. It will be shown that, although the $\omega/\Gamma \ll 1$ ratio is small in (10), the inequality $R > 1$ can be satisfied in the exchange region because, in this region, $\Omega(\tau)/\Gamma(\tau) \gg 1$. This inequality cannot be met at $\omega/\Gamma \ll 1$ for linear susceptibility described by a Lorentzian. In our problem, such a ratio arises as a consequence of the existence of two contributions of different natures to $\chi_{\parallel}^{(2)}(\omega)$. The H dependence of one of them is controlled by $\Omega(\tau)$ and of the other, by $\Omega(\tau)$ and $\Gamma(\tau)$ [see (4) and (5)].

Increasing H requires including terms of a higher order in ω_0/Γ in the equation for $\mathrm{Im}\chi_{\parallel}^{(2)}(\omega)$. According to [12], the $\partial\Gamma_{\parallel}(\tau, \omega_0)/\partial\omega_0$ function present in (1) and (9) is then proportional to

$$\frac{\partial\Gamma_{\parallel}(\tau, \omega_0)}{\partial\omega_0} \propto x\varphi(x) = x\sqrt{\frac{\sqrt{1+x^2}}{1+\sqrt{1+x^2}}}, \quad (11)$$

where $x = \omega_0/\Gamma(\tau)$. As a result, Eq. (9) for $\mathrm{Im}\chi_{\parallel}^{(2)}$ is multiplied by the $\varphi(x)$ function.

Lastly, note that M_2, which is an even function of h, is an odd function of H in the paramagnetic region as a pseudovector, and $M_2 = 0$ at $H = 0$. For this reason, this function is sensitive to the appearance of spontaneous moment M_{sp} in the sample because $M_2 \propto M_{sp}$ at $H = 0$. As a result, the $M_2(H)$ dependence changes in a jump as H passes zero. This jump corresponds to a change in the direction of M_{sp} [19]. Such a hysteresis-free behavior is possible at a vanishingly small coercive force. Otherwise, a hysteresis with $M_2 \neq 0$ at $H = 0$ would be observed.

3. EXPERIMENTAL

The $Nd_{0.77}Ba_{0.23}MnO_3$ single crystal ($m \approx 54.5$ mg, $2 \times 2 \times 3$ mm^3) was taken from the same portion of material as the single crystals studied in [10, 11]. The neutron and X-ray diffraction data showed that the sample remained pseudocubic at 293 and 110 K. Within the resolving power and transmission characteristics of standard four-circle diffractometers (neutron and X-ray) used in this study, Jahn–Teller crystal lattice distortions were undetectable. Nor were weak (of 10^{-3}–10^{-2} of the intensity of Bragg reflections) diffuse superstructure peaks observed in the characteristic [100], [110], and [111] crystallographic directions. The lattice parameter $a = 3.899 \pm 0.002$ Å measured at room temperature equaled that reported in [10]. Note that a ferromagnetic contribution to Bragg reflections was observed below T_C. At the same time, no reflections corresponding to some antiferromagnetic phase were detected either above or below T_C.

The single crystal was used to study the temperature and field behaviors of the second nonlinear response harmonic in parallel constant and harmonic magnetic fields,

$$H(t) = H + h\sin 2\pi ft, \quad f = 15.7 \text{ MHz}.$$

Alternating field amplitude h equaled 35 Oe at high temperatures and was decreased to 0.1 Oe as signal intensity increased at low temperatures to prevent signal distortions by the receiver, on the one hand, and to satisfy the $M_2 \propto h^2$ condition, on the other. The latter condition allows second-order susceptibility to be used in describing the response; for second-order susceptibility, we have explicit theoretical expression (1). The experimental data were recalculated to one alternating field amplitude value. Both signal phase components, $\mathrm{Re}M_2(H, T)$ and $\mathrm{Im}M_2(H, T)$, were recorded simultaneously as functions of constant magnetic field H at various sample temperatures. The appearance of long-range magnetic order could conveniently be controlled by detecting field hysteresis of M_2. For this purpose, constant magnetic field scans were symmetrical with respect to the $H = 0$ point (±400 Oe). The error of sample temperature measurements was smaller than 0.2 K. The experimental unit and the method for isolating phase components were described in more detail in [13, 20]; unit sensitivity was 10^{-9} G or higher.

4. EXPERIMENTAL RESULTS

4.1. Linear Susceptibility and Transport Properties

The temperature dependence of the real linear susceptibility part, $\mathrm{Re}\chi(T) = \chi'(T)$, obtained in [11] is plotted in Fig. 1. The analysis performed in [11] shows that the behavior of $\chi'(\tau)$ is close to that predicted for the isotropic 3D ferromagnet in the τ range $0.07 \leq \tau \leq 1$(133 K $\leq T <$ 250 K). The $\mathrm{Re}M_2(\tau)$ dependence also satisfies the power law for cubic ferromagnets; devia-

tions from this law began below $\tau \approx 0.12$ ($T \approx 139$ K). The deviations of the linear and nonlinear susceptibilities from the characteristic power laws starting with τ specified above are difficult to explain by the known dipole crossover [9, 11, 16], because the crossover temperature $\tau_d \approx 4.3 \times 10^{-2}$ ($T_d \approx 129.4$ K) determined by the equality $4\pi\chi(\tau_d) = 1$ is lower. Indeed, in usual cubic ferromagnets ($CdCr_2Se_4$ and $CdCr_2S_4$), the linear susceptibility ceases to satisfy the $\chi'(\tau) \propto \tau^{-\gamma}$ scaling law ($\gamma \approx 4/3$) at $4\pi\chi \geq 10$, that is, at temperatures much lower than the dipole crossover temperature [21], whereas, in the compound under consideration, this phenomenon is observed even at $4\pi\chi \approx 0.5$.

The temperature dependences of specific resistance ρ and magnetoresistance of the single crystal under study obtained in [10] are shown in Fig. 2. The $\rho(T)$ curve has a singularity near T_C, and, although the metal–dielectric transition is absent, giant magnetoresistance is observed. As follows from Fig. 2, the $\rho(T)$ dependence is satisfactorily described by the conductivity model with a variable carrier jump length [22] in the temperature range $T \approx 145$–265 K,

$$\rho(T) = \rho_0 \exp(T_0/T)^{1/4}.$$

The temperature dependence of the $T_0 = T\{\ln[(\rho(T)/\rho_0)]\}^4$ parameter obtained from the experimental data on the assumption that this model is applicable is shown in the inset in Fig. 2. According to these results, the T_0 and, accordingly, $\rho(T)$ values become lower than those predicted by the model below 147 K. The polaron mechanism describes the $\rho(T)$ dependence substantially worse above 147 K. Note that the experimental $\rho(T)$ values below 147 K are much lower than those predicted by the polaron mechanism too.

4.2. The Second Magnetization Harmonic

The temperature and field dependences of the second magnetization harmonic phase components, $\mathrm{Im}M_2$ and $\mathrm{Re}M_2$, were studied in the temperature range 119 K < $T \leq 204$ K. The $\mathrm{Im}M_2$ and $\mathrm{Re}M_2$ values were recorded as constant field functions at various crystal temperatures. Typical experimental $\mathrm{Re}M_2(H)$ and $\mathrm{Im}M_2(H)$ curves are shown in Fig. 3 for several temperatures. Shown in Figs. 3a and 3c–3h are the $\mathrm{Re}M_2(H)$ and $\mathrm{Im}M_2(H)$ dependences obtained in forward and backward constant field scans both above and below T_C. The experimental and theoretical [calculated by (12)] $\mathrm{Im}M_2(H)$ dependences at $T = 168.8$ K are shown in Fig. 3b.

The $\mathrm{Re}M_2(H)$ phase component dependence is close to linear in the scan range (±400 Oe) at T from 204 to 146.7 K ($0.64 \geq \tau \geq 0.18$), in agreement with the $\mathrm{Re}\chi_2(T, H)$ dependence described by (4) in the weak field region. The condition of field weakness for the maximum $H = 400$ Oe value is well satisfied also at the lowest τ temperature, $\tau \approx 0.18$ ($g\mu H/\Omega(0.18) \approx 7.5 \times 10^{-3}$). According to the estimate made from the $g\mu H \approx T_C\tau_H^{5/3}$ scaling relation, the transition to strong field conditions at $H = 400$ Oe occurs much nearer to T_C, at $\tau_H \approx 10^{-2}$ ($T_H \approx 125$ K). The $\mathrm{Re}M_2(H)$ signal at $T = 168.8$ K is shown in Fig. 3a. The response changes

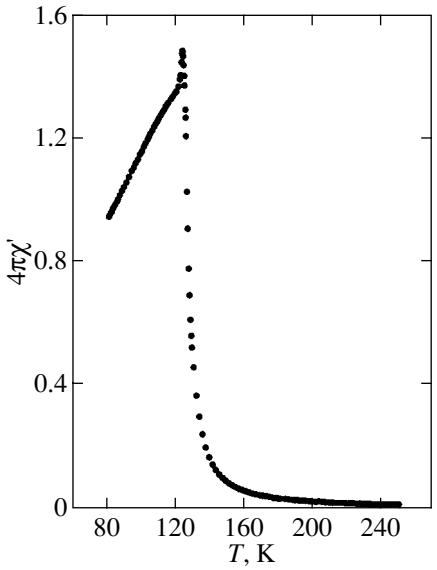

Fig. 1. Temperature dependence of $4\pi\chi'$; $T_C = 124.1$ K, $H = 0$.

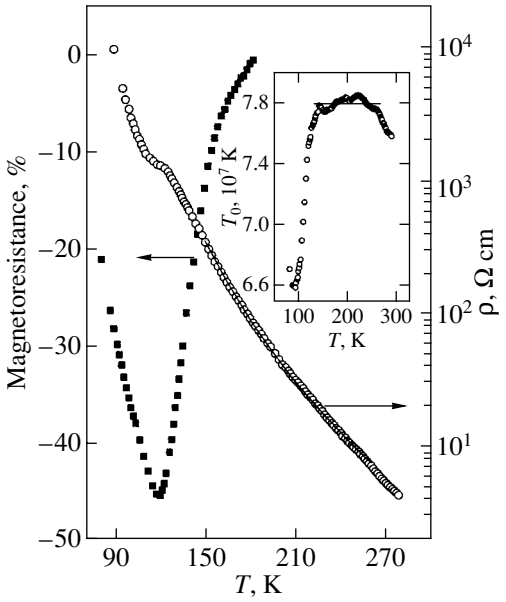

Fig. 2. Temperature dependences of specific resistance ρ and magnetoresistence defined as $([R(H = 9\text{ kOe}) - R(H = 0)]/R(H = 0)) \times 100\%$ (symbols). Specific resistance values in the temperature range $T = 145$–265 K were approximated by the $\rho(T) = \rho_0 \exp(T_0/T)^{1/4}$ theoretical dependence (solid curve). The experimental and theoretical ($T_0 = 7.8 \times 10^7$ K, $\rho_0 = 6.1 \times 10^{-10}$ Ω cm) dependences are plotted in the inset in different coordinates, $T_0 = T\{\ln[\rho(T)/\rho_0]\}^4$ versus T.

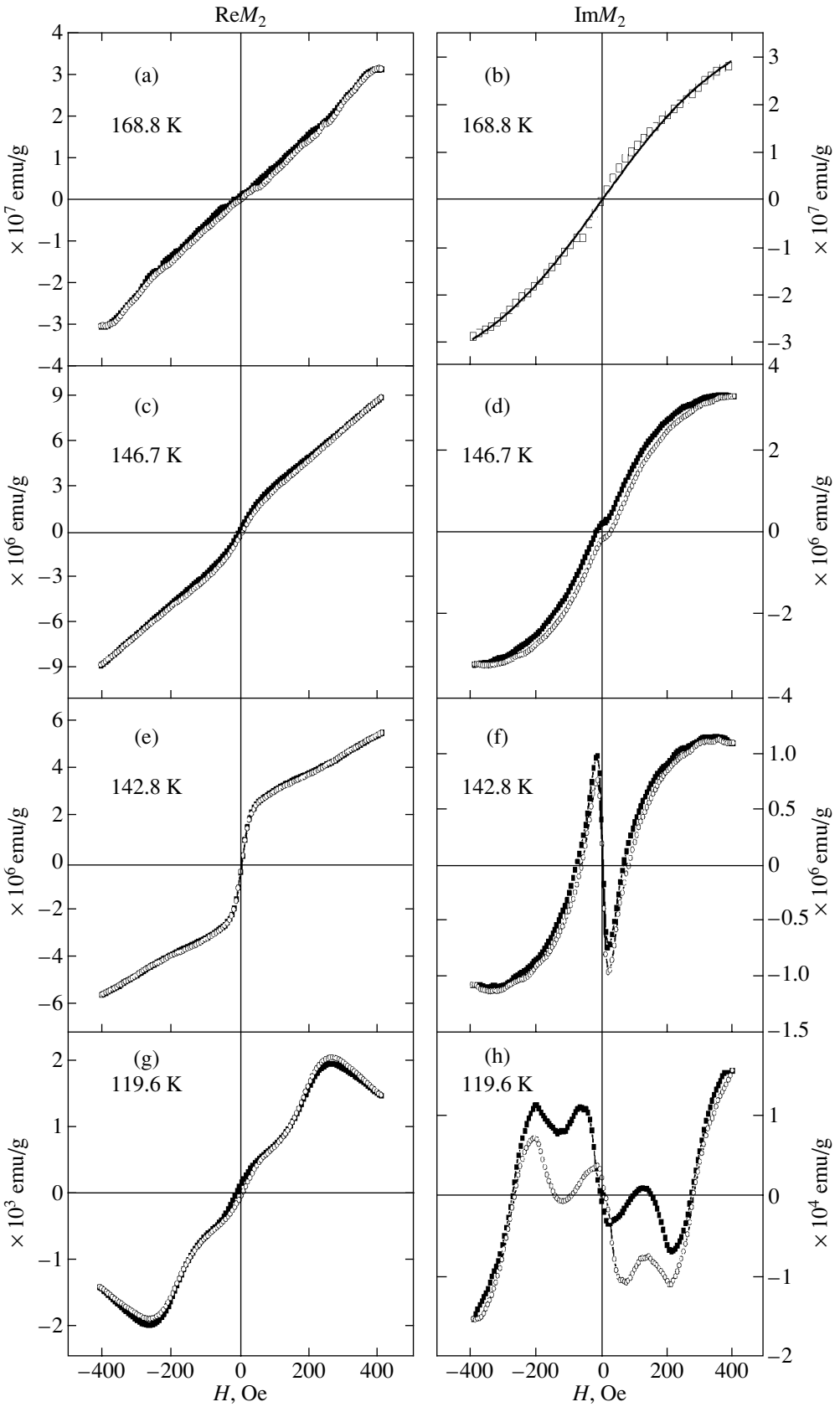

Fig. 3. Experimental (a, c, e, g) Re$M_2(H)$ and (b, d, f, h) ImM_2(H) curves at T = 168.8, 146.7, 142.8, and 119.6 K, respectively. Shown in Fig. 3b are the experimental (symbols) and theoretical (solid curve) Im$M_2(H)$ dependences at T = 168.8 K; the theoretical curve is described in text. The other figures contain curves for forward (solid symbols) and backward (open symbols) magnetic field scans.

in the temperature range 139 K < $T \le T_* \approx 146.7$ K (Figs. 3c, 3e), and there appear two intervals with different linear behaviors separated by a sharp crossover region, which is virtually a point ($H \approx 30$ Oe). The $\mathrm{Re}M_2(\tau)$ dependence in the field range 30 Oe < H < 400 Oe follows the scaling law for an isotropic 3D ferromagnet also below T_* down to T < 139 K [11]. At the same time, in weak fields H < 30 Oe, a linear dependence with a larger slope is observed. At T < 139 K, linear behavior in the 30 Oe < H < 400 Oe interval changes to nonlinear. As the boundary temperature of strong field conditions for an isotropic ferromagnet determined above ($T_H \approx 125$ K for H = 400 Oe) is obviously lower than 139 K, this nonlinearity cannot be explained in terms of the usual critical behavior. The changes in $\mathrm{Re}M_2(H)$ below T_* described above correlate with the appearance of a minimum of the second phase component $\mathrm{Im}M_2(H)$ in a weak $H \approx 20$ Oe field (Figs. 3d, 3f).

Probable reasons for the observed transformation of the M_2 signal caused by temperature lowering are (1) a change in the magnetic properties of the whole phase responsible for the signal, while the sample remains homogeneous, and (2) the formation of an inhomogeneous state caused by the arising of a new magnetic phase in some part of the sample which gives a signal with a field dependence uncharacteristic of cubic ferromagnets; this signal is summed with the signal from the remaining initial phase. If signal change at weak fields H < 30 Oe (Figs. 3c–3f) is caused by the appearance of a new magnetic phase, it is reasonable to suggest that the special features of the temperature behavior of signal intensity and the positions of the signal extrema (if any) at H < 30 Oe should noticeably differ from the temperature behavior at H > 30 Oe. Clearly, such special features cannot appear in a magnetically uniform isotropic ferromagnet. Note also that two $M_2(H, T)$ signals with different temperature dependences were observed for $Sm_{0.6}Sr_{0.4}MnO_4$ [19]; it was shown that two different magnetic phases were responsible for these signals.

To elucidate the problem, we measured (1) $\mathrm{Re}M_2(H, T)$ and $\mathrm{Im}M_2(H, T)$ values at two constant field values, H_1 = 22 Oe [close to the minimum of $\mathrm{Im}M_2(H)$ in a weak field] and H_2 = 198.4 Oe (far from this minimum), and (2) the magnetic field H_m positions of the extrema of both phase components at H < 30 Oe and H > 30 Oe.

The $\mathrm{Im}M_2(T, H_i)$ (i = 1, 2) temperature dependences are shown in Fig. 4. According to this figure, the curves have different signal signs and intensities. The $\mathrm{Im}M_2(T, H_1)$ curve contains a sharp minimum at $T \approx T_C$.

The temperature dependences of the positions of extrema, H_m, for both phase components are plotted in Fig. 5. The figure shows that the position of the $\mathrm{Im}M_2(H)$ minimum in weak fields ($H \le 30$ Oe) (this minimum appears at $T \le T_*$) is independent of temperature virtually to $T \approx T_C$, whereas the positions of the maxima of both $\mathrm{Im}M_2(H)$ and $\mathrm{Re}M_2(H)$ in fields H > 30 Oe are temperature-dependent. Note that the maximum of $\mathrm{Re}M_2(H)$ becomes observable in the H scan range only below 130 K, and its position corresponds to the minimum at $T \approx T_C$.

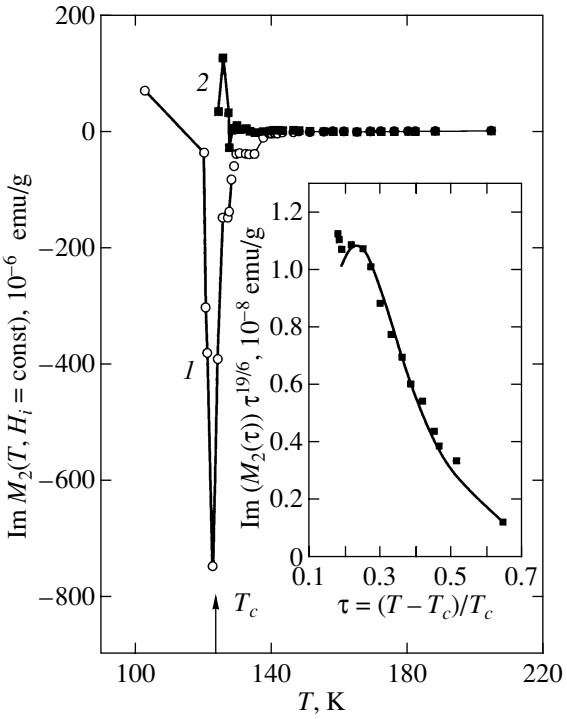

Fig. 4. (*1*) $\mathrm{Im}M_2(T, H_1$ = 22 Oe) and (*2*) $\mathrm{Im}M_2(T, H_2$ = 198.4 Oe) temperature dependences. Shown in the inset is the approximation to $\mathrm{Im}M_2(\tau, H_2)$ at temperatures T > 146.7 K (see text); the experimental values are shown by solid squares; H = 198.4 Oe, Λ = 23.63.

Let us summarize the differences between the temperature behaviors of $\mathrm{Im}M_2(T, H)$ at H < 30 Oe and H > 30 Oe.

(1) The signs of $\mathrm{Im}M_2(T, H_1)$ and $\mathrm{Im}M_2(T, H_2)$ are opposite (Figs. 3, 4), and the $\mathrm{Im}M_2(T, H_1)$ value increases much faster as temperature decreases (Fig. 4).

(2) The position of the minimum of $\mathrm{Im}M_2(T, H)$ in weak fields H < 30 Oe ($H_m \approx 20$ Oe) is virtually independent of temperature from its appearance at T_* to T_C (Fig. 5), in contrast to the temperature behaviors of the maxima of $\mathrm{Im}M_2(T, H)$ and $\mathrm{Re}M_2(T, H)$ at H > 30 Oe.

The invariability of the character of the field dependence of $\mathrm{Im}M_2$ in weak fields as temperature changes, which manifests itself especially well by the constant extremum position H_m, is at variance with the traditional critical behavior, according to which $H_m \propto \tau^{5/3}$. On the other hand, this invariability can be explained on the assumption that a new phase, which is in the critical state, is responsible for the low-field signal below T_*. If

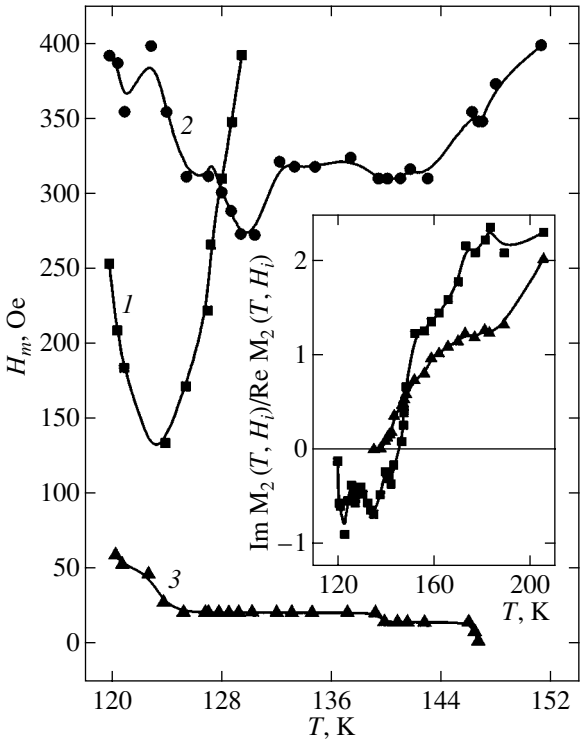

Fig. 5. Temperature dependences of the positions of signal extrema H_m for ReM_2(H) [one extremum (max), curve *1*] and ImM_2(H) [two extrema, max (*2*) and min (*3*)] (T_C = 124.1 K). Temperature dependences of the $R(T, H_i)$ = Im$M_2(T, H_i)$/Re$M_2(T, H_i)$ ratio, i = 1, 2, in fields H_1 = 22 Oe (squares) and H_2 = 198.4 Oe (triangles) are shown in the inset.

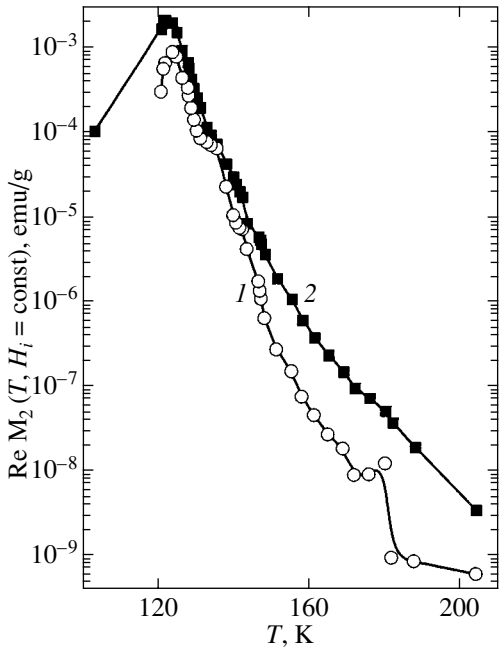

Fig. 6. (*1*) Re$M_2(T, H_1$ = 22 Oe) and (*2*) Re$M_2(T, H_2$ = 198.4 Oe) dependences; T_C = 124.1 K.

the magnetic correlation length of fluctuations that develop in such a phase is larger than the typical size of new phase fragments, the signal intensity can increase sharply without changes in the shape of the signal (in particular, without extremum shifts) because of an increase in the phase volume not accompanied by changes in its critical properties [23]. Such a behavior can be observed if the new phase has a certain spatial distribution (if a large number of its comparatively small-sized fragments are formed within the initial phase). This suggestion also allows the nonlinear character of Re$M_2(H)$ variations at $H > 30$ Oe, which appears below 139 K (see above), to be explained in a natural way by relating this peculiarity to a substantial nonlinear contribution of the newly formed phase.

Note also that the $M_2(H)$ signal at $H < 30$ Oe below T_* is accompanied by the arising of a small field hysteresis (Figs. 3d and 3f, T = 146.7 and 142.8 K, respectively), although the ferromagnetic ordering temperature is much lower (124.1 K).

To summarize, the differences between the temperature dependences of $M_2(T, H_i)$ and $H_m(T)$ at $H < 30$ Oe and $H > 30$ Oe lead us to conclude that a second magnetic phase with critical properties uncharacteristic of isotropic ferromagnets is formed in the crystal below $T_* \approx 147$ K.

In addition, it will be shown that the behavior of the Im$M_2(\tau)$ function, which much more strongly depends on τ than Re$M_2(\tau)$, closely corresponds to the critical behavior of an isotropic ferromagnet only at temperatures of 204 K to T_*.

The Re$M_2(T, H_1$ = 22 Oe) and Re$M_2(T, H_2$ = 198.4 Oe) dependences are shown in Fig. 6. Both functions have maxima at $T \approx T_C$. It follows that, below T_*, the temperature dependences of both phase components of the low-field and initial signals and the positions of their extrema $H_m(T)$ have singularities at $T \approx T_C$. This is evidence of the arising of ferromagnetic ordering in both magnetic phases virtually at the same temperature. Below, the low-field signal and the corresponding magnetic phase will be called anomalous, and the high-field signal observed above T_* and the corresponding phase, usual.

As mentioned above, the appearance of the anomalous signal in the paramagnetic region is accompanies by a field hysteresis of ImM_2 and a weak (coercive force $H_c \approx 6$ Oe) hysteresis of the ReM_2 component (Figs. 3c, 3d). This phenomenon at temperatures higher than T_C can be caused by the character of fragmentation of the anomalous phase; namely, the characteristic size of the arising fragments may be smaller than the magnetic correlation radius in this phase. Actually, the magnetic state of the anomalous phase remains unchanged to T_C. As the surrounding usual phase is in the critical state, the creation of magnetization in the sample by an

external field can cause the formation of a comparatively long-lived metastable ferromagnetic state of the anomalous phase.

In classic cubic ferromagnets, the field hysteresis of $\mathrm{Re}M_2(H)$ with $\mathrm{Re}M_2(0) \neq 0$, which is evidence of the appearance of a spontaneous moment, develops directly below T_C [13]. The behavior of $Nd_{0.77}Ba_{0.23}MnO_3$ is more complex. The hysteresis of such a kind that develops in $\mathrm{Re}M_2(H)$ at $T \approx T_*$ decreases to zero at $T \approx$ 139.9 K and then again increases ($H_c \approx 1.5$ Oe at 130.2 K, the ascending and descending branches then changing places) and is preserved approximately to 123.7 K. A further increase in hysteresis is only observed at $T \approx 122.6$ K ($H_c \approx 5$ Oe), below T_C (see Fig. 3g for a close temperature). As temperature decreases further, the hysteresis loop gradually opens, which is evidence of a small coercive force near T_C and its increase as T lowers.

5. DISCUSSION

First, consider the $T > T_*$ temperature region, where only one signal is observed for M_2. A quantitative analysis of the temperature behavior of the corresponding usual magnetic phase was only performed in this temperature region based on the experimental data on $\mathrm{Im}M_2(H, T)$.

Note from the outset that, in [11], the $0.12 \leq \tau \leq 0.64$ region (from 139 K to a maximum $T = 204$ K temperature at which the signal was still observed) was established within which the $\mathrm{Re}M_2(\tau) \propto \mathrm{Re}\chi_2(\tau) \propto \tau^{-\gamma_2}$ power dependence with the critical index $\gamma_2 = 5.2 \pm 0.2$ was in satisfactory agreement with scaling result (8) for isotropic 3D ferromagnets ($\gamma_2 \approx 14.3$).

The experimental data on $\mathrm{Im}M_2(T, H_2)$(see Fig. 4) were used to analyze spin dynamics. The $\Gamma \approx 990$ Oe value (g factor ≈ 2.05, $\Delta g \approx 0.12$) was found from the EPR spectrum ($f_{EPR} = 8.34$ GHz) of the sample at $T =$ 204 K ($\tau \approx 0.64$). This value was used to independently check the $2\omega/\Gamma \ll 1$ condition, whose fulfillment is necessary for Eqs. (7)–(10) used to analyze the $\mathrm{Im}M_2(T)$ dependence to be applicable. EPR measurements were performed at the highest temperature of M_2 measurements, because field influence on the critical behavior and on Γ decreased as the distance from the transition point increased. A comparison of the obtained Γ value with the frequency used in our experiments ($\omega \approx 5.77$ Oe in field units) gives $2\omega/\Gamma \approx 1.2 \times 10^{-2}$.

Let us turn to the $\mathrm{Im}\chi_{\parallel}^{(2)}(\tau)$ dependence determined by (9) with damping $\Gamma(\tau)$ in form (7). Note that the relation

$$\mathrm{Im}\chi_{\parallel}^{(2)}(\tau) \propto \Gamma_d(\tau)\Omega^{-1/2}(\tau)\chi(\tau) \propto \tau^{-19/6}$$

contains a strongly changing power factor τ, which worsens the accuracy of determining Λ from the experimental data. We therefore found Λ by forming an array of $\tau^{19/6}\mathrm{Im}M_2(\tau)$ values for which the approximation was performed.

Next, consider $\mathrm{Im}M_2(H)$ at a fixed $T = 168.8$ K temperature. A comparison of $\mathrm{Re}M_2(H) \propto H$ (Fig. 3a) and $\mathrm{Im}M_2(H)$ (Fig. 3b) shows that these dependences are different and $\mathrm{Im}M_2(H)$ is not a linear field function in the whole range of field variations. As the $2\omega/\Gamma$ ratio is small, this leads us to conclude that the contribution of the first term in (1) to $\mathrm{Im}M_2$ is insignificant. The reason for the difference between the field dependences of M_2 components is therefore the dynamic contribution to $\mathrm{Im}M_2$, which arises because of the influence of $h(t)$ on the rate of uniform magnetization relaxation. This conclusion also follows from the experimental $R(H, T) = \mathrm{Im}M_2(T, H)/\mathrm{Re}M_2(T, H)$ dependence shown in the inset in Fig. 5. According to this plot, $R(T, H)$ is larger than one in the high-temperature region 156 K $\leq T \leq$ 204 K in spite of the smallness of $2\omega/\Gamma \ll 1$. As follows from Eq. (10) for R, the smallness of ω/Γ can be compensated by a large value of the $(\Omega(\tau)/\Gamma(\tau))^{3/2}$ multiplier; we may then have $R > 1$. To be more definite, we have $R = 1.16$ at $T = 168.8$ K ($\tau \approx 0.36$) and $H = 198.4$ Oe. According to the $\Gamma(\tau)$ dependence (see below), $\Gamma(0.36) \approx 600$ Oe and $2\omega/\Gamma \approx 2 \times 10^{-2}$ at this point.

The nonlinearity of the $\mathrm{Im}M_2(H)$ dependence requires that the terms of higher orders in ω_0/Γ should accurately be taken into account. The approximation was therefore performed using (9) with multiplier φ from (11),

$$\mathrm{Im}M_2(\tau, H)\tau^{19/6} = C_{M_2}\Gamma^{-5/2}(\tau) \times \frac{\omega_0}{\Gamma(\tau)}\sqrt{\frac{\sqrt{1 + (\omega_0/\Gamma(\tau))^2}}{1 + \sqrt{1 + (\omega_0/\Gamma(\tau))^2}}}, \quad (12)$$

where C_{M_2} is the normalization constant. The approximation was performed in the temperature range $0.19 < \tau < 0.64$ above T_*. The $\Gamma_{EPR} \approx 990$ Oe value found at $T = 204$ K ($\tau \approx 0.64$) was used to express one of two independent parameters in (7) Γ_d^* through the other,

$$\Gamma_d^* = \frac{\Gamma_{\mathrm{EPR}}}{(0.64)^{-1} + \Lambda(0.64)^{4/3}};$$

one free dimensionless parameter Λ was found from the experimental data. The inset in Fig. 4 shows that such a one-parameter equation allows the $\mathrm{Im}M_2(\tau)\tau^{19/6}$ dependence to be described fairly well at $\Lambda = 23.4 \pm 0.7$. If we know Λ, we can calculate $\Gamma_d^* = 68.5 \pm 1.0$ Oe. In the inset, three experimental points ($T = 146$, 146.4, and 146.7 K) not used in the adjustment are given, and the theoretical curve is extended to this region. The plot shows that the experimental $\mathrm{Im}M_2(\tau)\tau^{19/6}$ value again begins to grow at these points instead of the descent

predicted by the theory. According to the arguments presented above, the reason for the discrepancy is the appearance of the new magnetic phase below T_*.

The obtained Γ_d^* value can be used to determine the γ_d coefficient in (2) for Hewber damping. As $\omega_d = 4\pi(g\mu)^2/d^3 \approx 0.53$ K at $d \approx 3.9$ Å, the $\Gamma_d^* = \gamma_d\omega_d^2/T_C \approx 68.5$ Oe value gives $\gamma_d \approx 4$.

According to (5) and (9), $C_{M_2} \propto C_{\Gamma_\parallel}C_\chi \propto C_\chi^2 C_D^{-3/2}$. We can therefore find C_D from C_{M_2} and C_χ. The $C_\chi \approx 1.9$ value was determined using the data on the critical static susceptibility of the crystal reported in [10]. This gave $C_D \approx 0.02$. The C_D value allows the D_0 constant in Eq. (6) for the spin diffusion coefficient to be found. We have $d \approx 3.9$ Å, and (6) yields $D_0 \approx 3.3$ meV Å^2. The obtained C_D and D_0 values can be compared with those characteristic of classic cubic ferromagnets, namely, $C_D \approx 0.045$ and $D_0 \approx 5.4$ meV Å^2 in $CdCr_2S_4$ ($T_C \approx 84$ K, $d \approx 4.07$ Å) and $C_D \approx 0.07$ and $D_0 \approx 15$ meV Å^2 in $CdCr_2Se_4$ ($T_C \approx 129$ K, $d \approx 4.27$ Å) [18]. The C_D values for classic ferromagnets are fairly different. According to [18], the $C_D\gamma_d$ product only remains approximately constant; it equals 6.5×10^{-2} ($\gamma_d \approx 1.45$) for $CdCr_2S_4$ and 5.9×10^{-2} ($\gamma_d \approx 0.84$) for $CdCr_2Se_4$. We also obtained a similar magnetic moment, $C_D\gamma_d \approx 8 \times 10^{-2}$.

Recall that Γ (in zero field) was set equal to the half-width of the EPR line. This was justified because the ω_0-dependent diffusion correction to $\Gamma_\parallel$ did not exceed 15% at the selected $\tau \approx 0.64$ value and given frequency.

As $\Gamma_d(\tau) \propto \tau^{-1}$, $\Gamma_{nc} \propto \tau^{4/3}$, and, usually, $\Gamma_{nc} > \Gamma_d$ for $\tau = 1$, a characteristic minimum at some τ_{min} is observed in dependence (7) for $\Gamma(\tau)$. Such a minimum was observed not only in cubic ferromagnets with localized spins [18] but also in several doped manganites with virtually cubic structures studied by the EPR method [24]. This is direct evidence of the influence of dipole forces on spin relaxation processes in isotropic manganites; this influence was virtually undetectable in the present work. In [24], experiments were performed for compounds with doping levels at which the dielectric–metal transition temperature was $T_{IM} \approx T_C$. Measurements at different resonance frequencies showed that magnetic field strongly changed the temperature dependence of Γ at $\tau \leq \tau_{min}$. An analysis shows that field effects in these manganites cannot be fully reduced to the known change in the critical behavior that occurs in classic ferromagnets and is related to the transition to strong field conditions [9, 12, 13]. The difference can be explained by the closeness of T_C and T_{IM}, that is, by the "metallization" of holes.

The $\Gamma(\tau)$ function obtained in this work is also nonmonotonic and has a minimum $\Gamma_{min} \approx 520$ Oe at $\tau_{min} \approx 0.23$. The $\Gamma_d(\tau_{min})/\Gamma_{nc}(\tau_{min})$ ratio equals 4/3; that is, the dipole contribution to Γ exceeds the noncritical contribution at τ_{min}. This leads us to conclude that the Γ_d^* and Λ values were determined fairly reliably, although the interval of τ values accessible to analysis was fairly small.

Lastly, the theoretical $\mathrm{Im}M_2(H)$ dependence at a fixed temperature $T = 168.8$ K is shown in Fig. 3b. This dependence was described by (12) with $\Gamma(\tau) = 600$ Oe determined above and did not contain free parameters. Close agreement between the experimental values and the theoretical curve is an important test for the reliability of the obtained $\Gamma(\tau)$ value and consistency of the approach that we use.

The results described above show that the magnetic behavior of the $Nd_{0.77}Ba_{0.23}MnO_3$ single crystal is quantitatively similar to that of classic Heisenberg ferromagnets in the $T > T_* \approx 146.7$ K critical exchange region. As stated in the Introduction, such a similarity at equal numbers of order parameter components and equal system dimensions is a consequence of the universality of second-order transitions.

Let us turn to the experimental results obtained below T_*. According to the neutron and X-ray diffraction data, the structure of the crystal virtually does not change in cooling from 293 to 110 K and remains pseudocubic. The appearance of structural changes can hardly be expected in this temperature interval. It is therefore unlikely that the appearance of the new phase may be related to lattice rearrangement. Thus, the whole body of data indicates that two coexisting phases appear below T_* irrespective of the structural transformation. Like the usual phase, the anomalous phase experiences ferromagnetic ordering at $T \approx T_C$. One of the most probable physical reasons for this phenomenon is different types of orbital states in the phases.

A theoretical analysis of cubic manganites shows that phases in different orbital or (and) magnetic states can exist in these compounds at moderate doping levels [4]. In the case of the paramagnetic and ferromagnetic states at finite temperatures that we are interested in, three orbital order types are considered, namely, antiferromagnetic (*G*), paramagnetic (*P*), and ferromagnetic (*F*). In the ferromagnetic state, phase separation arises because of competition of ferromagnetic interactions of two types, superexchange caused by electron correlation and double exchange. These interactions are responsible for different orbital order types. As the degree of doping increases, the *G* type with the predominance of superexchange changes to the *F* type with the predominance of double exchange. Uniform ferromagnetic states with *G*- and *F*-type orbital orders were present in the low-temperature region at $x \leq 0.06$ and $0.4 < x < 0.5$, respectively. In addition, in the $0.2 < x \leq 0.3$ region of doping at $T = 0$, two orbitally ordered phases that had lower orbital symmetries than those characteristic of the *G*- and *F*-type orbital orders were observed in the ferromagnetic state. These phases were not taken into account in analyzing phase separation at

finite temperatures, it appears, because of the very high complexity of the ensuing phase diagram.

The *P*-type–*G*-type orbital ordering transition was directly observed by resonance X-ray scattering in lightly doped $La_{0.88}Sr_{0.12}MnO_3$ at $T_{oo} \approx 145$ K [5]. The ferromagnetic phase above T_{oo} was in the metallic state, $d\rho/dT < 0$, whereas the phase below T_{oo} was dielectric. A more complex picture was observed for $La_{0.75}Ca_{0.25}MnO_3$ studied by the NMR method [25]. A mixture of metallic and dielectric phases existed in the temperature intervals 160 K < T < $T_C \approx$ 250 K and 3.2 K < T < 20 K, whereas only the metallic phase signal was present at intermediate temperatures. The result obtained in the low-temperature region was interpreted as evidence of the occurrence of a mixture of orbital *G* and *P* states caused by electron correlations. It was assumed that the same mixture of orbital states was responsible for the two-phase state of the system in the other temperature region. Orbital ordering was related to strong interactions with Jahn–Teller phonons.

It is clear from the aforesaid that there are reasons to relate the appearance of the anomalous phase in the manganite under study to its orbital ordering. Orbital ordering can strengthen ferromagnetic interactions in this phase. As a result, the magnetic correlation radius can prove to be larger than the characteristic size of orbitally ordered regions that appear in the orbitally paramagnetic usual phase, as follows from the experimental data. It can be suggested that the type of orbital ordering in the anomalous phase is intermediate between *G* and *F*. The point is that the experimentally observed *G* type corresponded to a phase with a larger specific resistance than that characteristic of the *P* type, and the *P* type corresponded to a phase with metallic conductivity. The crystal studied in this work remained in the dielectric state below T_C, and the $\rho(T)$ dependence only contained a plateau in a narrow temperature interval below T_C. If this specific resistance singularity is related to the appearance of the anomalous phase, the conductivity of this phase should be higher than that of the *P*-type orbital phase. Bearing in mind that there is a tendency to metallization accompanied by the *G*-type–*F*-type orbital order transition as the degree of doping increases, we can expect the existence of an intermediate type of orbital ordering in our crystal, for instance, one of the two types observed at $T = 0$ K [4]. If this suggestion is correct, the fraction of the anomalous phase should increase at higher doping levels.

Nevertheless, we cannot rule out the variant with *G*-type orbital ordering in the anomalous phase; that is, we do not exclude the possibility of the formation of the orbital phase characteristic of light doping. The observed $\rho(T)$ singularity is then caused by the behavior of the main phase, and the volume of the anomalous phase with a higher specific resistance should decrease as the level of doping increases.

6. CONCLUSION

The study of the longitudinal nonlinear response of the $Nd_{0.77}Ba_{0.23}MnO_3$ single crystal with a pseudocubic structure both in the paramagnetic region and below the Curie temperature revealed the existence of two temperature intervals separated by the boundary temperature $T_* \approx 146.7$ K ($T_C = 124.1$ K). Above this temperature, the system is structurally and magnetically single-phase. Its behavior in the critical exchange region above T_* closely agrees with dynamic similarity theory for isotropic ferromagnets and gives critical parameters close to the theoretical values, which is a consequence of the universality of second-order phase transitions. Below T_*, the system is structurally single-phase and magnetically heterophase. A possible reason for this may be orbital ordering, which causes the appearance of the anomalous phase with magnetic correlation properties and conductivity different from those of the usual phase. As mentioned above, a study of samples with a high doping level may provide insight into the nature of the fairly unusual heterophase magnetic state in this system, which remains dielectric at $T < T_C$.

ACKNOWLEDGMENTS

The authors thank I.A. Kiselev, Ya.V. Greshneva, and I.R. Metskhvarishvili for help with experiments and S.V. Maleev and S.M. Dunaevskiĭ for useful discussions. This work was financially supported by the Russian Foundation for Basic Research (project nos. 00-02-16729 and 00-02-81205 Bel2000–a).

REFERENCES

1. Yu. A. Izyumov and Yu. N. Skryabin, Usp. Fiz. Nauk **171**, 121 (2001).
2. C. Zener, Phys. Rev. **82**, 403 (1951).
3. P. G. de Gennes, Phys. Rev. **118**, 141 (1960).
4. S. Okamoto, S. Ishihara, and S. Maekawa, Phys. Rev. B **61**, 451 (2000).
5. Y. Endoh, K. Hirota, S. Ishihara, *et al.*, Phys. Rev. Lett. **82**, 4328 (1999).
6. A. Barnabe, F. Millange, A. Maignan, *et al.*, Chem. Mater. **10**, 252 (1998).
7. I. O. Troyanchuk, I. M. Kolesova, H. Szymczak, and A. Nabialek, J. Magn. Magn. Mater. **176**, 267 (1997).
8. A. Z. Patashinskiĭ and V. L. Pokrovskiĭ, *Fluctuation Theory of Phase Transitions* (Nauka, Moscow, 1982; Pergamon, Oxford, 1979), Chap. 3.
9. S. V. Maleev, Sov. Sci. Rev., Sect. A **8**, 1229 (1987).
10. I. O. Troyanchuk, D. D. Khalyavin, S. V. Trukhanov, and H. Szymczak, J. Phys.: Condens. Matter **11**, 8707 (1999).
11. I. D. Luzyanin, V. P. Khavronin, V. A. Ryzhov, *et al.*, Pis'ma Zh. Éksp. Teor. Fiz. **73**, 369 (2001) [JETP Lett. **73**, 327 (2001)].

12. A. V. Lazuta, S. V. Maleev, and B. P. Toperverg, Zh. Éksp. Teor. Fiz. **81**, 2095 (1981) [Sov. Phys. JETP **54**, 1113 (1981)].
13. A. V. Lazuta, I. I. Larionov, and V. A. Ryzhov, Zh. Éksp. Teor. Fiz. **100**, 1964 (1991) [Sov. Phys. JETP **73**, 1086 (1991)].
14. A. V. Lazuta and V. A. Ryzhov, in *Proceedings of the First Workshop on Nonlinear Physics Theory and Experiment, Italy*, Ed. by E. Alfinito, M. Boiti, L. Martina, and F. Pempinelli (World Scientific, Singapore, 1995), p. 406.
15. D. L. Huber, J. Phys. Chem. Solids **32**, 2145 (1971).
16. S. V. Maleev, Zh. Éksp. Teor. Fiz. **66**, 1809 (1974) [Sov. Phys. JETP **39**, 889 (1974)].
17. V. V. Krishnamurthy, I. Watanabe, K. Nagamine, *et al.*, Phys. Rev. B **61**, 4060 (2000).
18. V. N. Berzhansky, V. I. Ivanov, and V. A. Lazuta, Solid State Commun. **44**, 77 (1982).
19. L. D. Luzyanin, V. A. Ryzhov, D. Yu. Chernyshov, *et al.*, Phys. Rev. B **64**, 094432 (2001).
20. V. A. Ryzhov, I. I. Larionov, and V. N. Fomichev, Zh. Tekh. Fiz. **66** (6), 183 (1996) [Tech. Phys. **41**, 620 (1996)].
21. I. D. Luzyanin and V. P. Khavronin, Zh. Éksp. Teor. Fiz. **87**, 2129 (1984) [Sov. Phys. JETP **60**, 1229 (1984)].
22. N. F. Mott, *Metal–Insulator Transition* (Taylor & Francis, London, 1990).
23. M. M. Barber, in *Phase Transition and Critical Phenomena*, Ed. by S. Domb and J. L. Lebovitz (Academic, London, 1983), Vol. 8, p. 153.
24. M. T. Causa, M. Tovar, A. Caniero, *et al.*, Phys. Rev. B **58**, 3233 (1998).
25. G. Papavassiliou, M. Fardis, M. Belesi, *et al.*, Phys. Rev. Lett. **84**, 761 (2000).

Translated by V. Sipachev

Journal of Experimental and Theoretical Physics, Vol. 94, No. 3, 2002, pp. 593–602.
Translated from Zhurnal Éksperimental'noĭ i Teoreticheskoĭ Fiziki, Vol. 121, No. 3, 2002, pp. 692–702.

SOLIDS
Electronic Properties

Resonant Acceptor States in Uniaxially Strained Semiconductors

M. A. Odnoblyudov[a, b], A. A. Prokofiev[b, *], and I. N. Yassievich[b]

[a]*Division of Solid State Theory, Department of Physics, Lund University, SE-223 62 Lund, Sweden*
[b]*Ioffe Physicotechnical Institute, Russian Academy of Sciences, Politekhnicheskaya ul. 26, St. Petersburg, 194021 Russia*
**e-mail: lxpro@pop.ioffe.rssi.ru*

Received July 12, 2001

Abstract—A new approach to calculating the parameters of resonant states is proposed, which also makes it possible to determine the probabilities of the resonant scattering and capture probabilities at the resonant state. This approach is based on the application of the method of configuration interaction, which was proposed for the first time by Fano for an analysis of field ionization of the helium atom. Following Fano, use is made of two different Hamiltonians of the initial approximation for the states of continuum and the initial local state. Following Dirac, the wave functions are constructed in the same way as in the general theory of scattering. A detailed analysis and specific calculations are made for resonant acceptor states in uniaxially strained germanium under a pressure directed along the [001] and [111] axes. © *2002 MAIK "Nauka/Interperiodica".*

1. INTRODUCTION

Quasi-stationary (resonant) states have been much studied in atomic physics. Semiconductors proved to be another system in which quasi-stationary states play a significant role in physical processes. Resonant states are formed, for example, as a result of doping of gapless semiconductors with a shallow acceptor impurity [1, 2] or in the spectrum of 2D holes for energies exceeding the potential well depth [3]. The resonant states induced by a shallow acceptor impurity in uniaxially stressed germanium are of special interest in connection with the possibility of generation of radiation in the THz region [4–6].

In semiconductors with the zinc blende structure (gallium arsenide, germanium, and silicon), the top of the valence band is fourfold degenerate; accordingly, the acceptor ground state is also degenerate (see, for example, [7]). Under strain, the top of the valence band splits into two doubly degenerate subbands, and the fourfold degeneracy of acceptor levels is removed. In the limit of high pressures, a series of energy levels falls into the continuous spectrum and forms the resonant states. In this situation, effective optical transitions between resonant and local states of the same impurity become possible. In electric fields above the impurity breakdown threshold, virtually all holes are in the valence band. Under these conditions, the population of resonant states may lead to the creation of intracenter population inversion forming the basis for the generation of radiation in the THz region [8, 9].

For this reason, it is important to find the hole distribution function in strained *p*-Ge in external electric fields taking into account resonant scattering and to calculate the population of resonant states. To this end, it is necessary to develop a method permitting one not only to find the position and width of the resonance, but also to calculate the probabilities of capture and ejection to the resonance level. Such a method will be proposed in this paper and applied to resonant acceptor states in uniaxially strained *p*-Ge.

Resonant acceptor states in strained semiconductors were studied in the model of zero-radius potential [10] or using the Dirac approach in the case of the Coulomb potential [11]. The numerical method of analysis of resonant states on the basis of the continuous spectrum discretization was used in [12]. The application of the Dirac approach requires construction of the Hamiltonian in the initial approximation in which the initial local states can be obtained on the background of the continuous spectrum [13], which is normally difficult to do directly. In [11], the diagonal component of the Luttinger Hamiltonian was used as the initial Hamiltonian, while its nondiagonal component was treated as a perturbation leading to the decay of local states. Such an approach, however, is suitable for local states related to the split-off band, but in the case of continuous spectrum, it is valid only for small quasimomenta.

In this work, we propose a new approach for calculating the parameters of resonant states as well as the probabilities of resonant scattering and capture into the resonant state. This approach is based on the application of the method of configuration interaction, which was proposed for the first time by Fano for analyzing the field ionization of the helium atom [14]. Following Fano, we will use two different Hamiltonians of the initial approximation for the states of the continuum and for the initial local state. On the other hand, wave functions will be constructed, following Dirac, in the same

way as in the general theory of scattering. A detailed analysis and specific calculations are made for resonant acceptor states in uniaxially stressed germanium under a pressure applied along the [001] and [111] axes.

In Section 2, a general approach is described adopting the spherical approximation for the Luttinger Hamiltonian and then, generalized to the case of the cylindrical approximation for a strain directed along the [001] axis. The results of calculations of the probabilities of elastic scattering and capture into the resonant acceptor state in *p*-Ge strained along the [001] axis are presented in Section 3. In Section 4, a generalization is made to the case of straining along the [111] axis.

2. CONFIGURATION INTERACTION APPROXIMATION FOR RESONANT ACCEPTOR STATES

The Luttinger Hamiltonian for a cubic-symmetry semiconductor has the form

$$\hat{H}_L(\mathbf{k}) = -\frac{\hbar^2}{2m_0}\begin{bmatrix} \hat{a}_+ & \hat{b} & \hat{c} & 0 \\ \hat{b}^* & \hat{a}_- & 0 & \hat{c} \\ \hat{c}^* & 0 & \hat{a}_- & -\hat{b} \\ 0 & \hat{c}^* & -\hat{b}^* & \hat{a}_+ \end{bmatrix}, \tag{1}$$

where the matrix elements are given by

$$\begin{aligned} \hat{a}_+ &= -(\gamma_1 - 2\gamma_2)\hat{k}_z^2 - (\gamma_1 + \gamma_2)(\hat{k}_x^2 + \hat{k}_y^2), \\ \hat{a}_- &= -(\gamma_1 + 2\gamma_2)\hat{k}_z^2 - (\gamma_1 - \gamma_2)(\hat{k}_x^2 + \hat{k}_y^2), \\ \hat{b} &= 2\sqrt{3}\gamma_3(\hat{k}_x - i\hat{k}_y)\hat{k}_z, \\ \hat{c} &= \sqrt{3}\gamma_2(\hat{k}_x^2 - \hat{k}_y^2) - i\gamma_3 2\sqrt{3}\hat{k}_x\hat{k}_y. \end{aligned} \tag{2}$$

Here, the operators $\hat{\mathbf{k}} = -i\nabla$, and the kinetic energy of holes is assumed to be positive. Hamiltonian (1) is written in the basis of Bloch functions

$$\begin{aligned} u_{+3/2} &= -\frac{1}{\sqrt{2}}(X + iY)\uparrow, \\ u_{-3/2} &= \frac{1}{\sqrt{2}}(X - iY)\downarrow, \\ u_{+1/2} &= \frac{1}{\sqrt{6}}[-(X + iY)\downarrow + 2Z\uparrow], \\ u_{-1/2} &= \frac{1}{\sqrt{6}}[(X - iY)\uparrow + 2Z\downarrow]. \end{aligned} \tag{3}$$

In the presence of strain, the Hamiltonian acquires a correction H_ε which depends on the strain tensor components ε_{ij} in the same way as H_L depends on the product $k_i k_j$:

$$\hat{H}_\varepsilon = \begin{bmatrix} \hat{p}_+ & \hat{s} & \hat{r} & 0 \\ \hat{s}^* & \hat{p}_- & 0 & \hat{r} \\ \hat{r}^* & 0 & \hat{p}_- & -\hat{s} \\ 0 & \hat{r}^* & -\hat{s}^* & \hat{p}_+ \end{bmatrix}, \tag{4}$$

where

$$\begin{aligned} \hat{p}_+ &= (a + b)\varepsilon_{zz} + (a - 0.5b)(\varepsilon_{xx} + \varepsilon_{yy}), \\ \hat{p}_- &= (a - b)\varepsilon_{zz} + (a + 0.5b)(\varepsilon_{xx} + \varepsilon_{yy}), \\ \hat{s} &= \sqrt{3}d(\varepsilon_{xz} - i\varepsilon_{yz}), \\ \hat{r} &= 0.5\sqrt{3}b(\varepsilon_{xx} - \varepsilon_{yy}) - i0.5\sqrt{3}d\varepsilon_{xy}, \end{aligned} \tag{5}$$

and *a*, *b*, and *d* are the strain potentials. In the presence of a Coulomb acceptor center, the complete Hamiltonian has the form

$$\hat{H} = \hat{H}_L(\mathbf{k}) + \hat{H}_\varepsilon - \hat{V}_c(r), \tag{6}$$

where

$$\hat{V}_c(r) = \frac{e^2}{\kappa r}\begin{bmatrix} 1 & 0 & 0 & 0 \\ 0 & 1 & 0 & 0 \\ 0 & 0 & 1 & 0 \\ 0 & 0 & 0 & 1 \end{bmatrix}, \tag{7}$$

e is the electron charge, and κ is the dielectric constant.

We will describe the application of the configuration interaction method to the problem of scattering and capture into the resonant acceptor state in a strained semiconductor using the spherical approximation for the Luttinger Hamiltonian. In this approximation, γ_2 and γ_3 are replaced by $\gamma = (2\gamma_2 + 3\gamma_3)/5$, and the matrix elements of the Hamiltonian $\hat{H}_L$ acquire the form

$$\begin{aligned} \hat{a}_+ &= -(\gamma_1 - 2\gamma)\hat{k}_z^2 - (\gamma_1 + \gamma)(\hat{k}_x^2 + \hat{k}_y^2), \\ \hat{a}_- &= -(\gamma_1 + 2\gamma)\hat{k}_z^2 - (\gamma_1 - \gamma)(\hat{k}_x^2 + \hat{k}_y^2), \\ \hat{b} &= 2\sqrt{3}\gamma(\hat{k}_x - i\hat{k}_y)\hat{k}_z, \\ \hat{c} &= \sqrt{3}\gamma(\hat{k}_x - i\hat{k}_y)^2. \end{aligned} \tag{8}$$

We assume that pressure is applied along the [001] axis. In this case, the strain tensor has the form

$$\begin{aligned} \varepsilon_{xx} &= \varepsilon_{yy} = S_{12}P, \\ \varepsilon_{zz} &= S_{11}P, \\ \varepsilon_{xy} &= \varepsilon_{xz} = \varepsilon_{zy} = 0, \end{aligned} \tag{9}$$

where S_{ij} are the components of the elastic moduli tensor and P is the pressure. In this case, only the diagonal components of the Hamiltonian $\hat{H}_\varepsilon$ differ from zero.

Disregarding terms of the form $a\mathrm{Tr}\hat{\varepsilon}$ describing the shift of the top of the valence band, we can conveniently write Hamiltonian $\hat{H}_\varepsilon$ in the form

$$\hat{H}_\varepsilon = \frac{\hbar^2}{2m_0}\begin{bmatrix}\zeta & 0 & 0 & 0\\ 0 & -\zeta & 0 & 0\\ 0 & 0 & -\zeta & 0\\ 0 & 0 & 0 & \zeta\end{bmatrix}, \qquad (10)$$

where parameter ζ is associated with the strain tensor components and with the strain potential b through the relations

$$\frac{\hbar^2\zeta}{2m_0} = b(\varepsilon_{zz}-\varepsilon_{xx}) = b(S_{11}-S_{12})P. \qquad (11)$$

A uniaxial strain along the [001] axis leads to the splitting of the fourfold degenerate top of the valence band into two doubly degenerate levels separated by the energy interval

$$E_{\mathrm{def}} = 2\frac{\hbar^2\zeta}{2m_0} = \alpha P, \qquad (12)$$

where $\alpha = 2b(S_{11} - S_{12})$ (α = 6 meV/kbar for germanium stressed along the [001] axis).

The energy spectrum in this case consists of two subbands, whose states will be characterized by the values of the components of the total momentum M at point Γ, and is defined by the formulas

$$\varepsilon_{\mathbf{k}} = \frac{\hbar^2}{2m_0}[\gamma_1 k^2 \pm \sqrt{\zeta^2 - 2\gamma\zeta(3k_z^2 - k^2) + 4\gamma^2 k^4}], \qquad (13)$$

where the plus sign corresponds to the upper subband ($M = \pm 3/2$) and the minus sign, to the lower subband ($M = \pm 1/2$); see Fig. 1.

The fourfold degenerate acceptor ground state also splits similarly. Under high pressure, the doubly degenerate state corresponding to the upper subband ($M = \pm 3/2$) lies in the continuous spectrum of the lower subband; as a result, their wave functions are hybridized and a resonant state is formed.

In order to find the initial approximation for the local state $\varphi^{\pm 3/2}$, we will use the diagonal component of the complete Hamiltonian (6). Such an approximation is fully justified for small k ($k^2 \ll \zeta$), i.e., in the limit when E_{def} is larger than the binding energy E_A.

The corresponding wave functions of the initial doubly degenerate local state can be determined using the variational method and can be presented in basis (3) in the form [15]

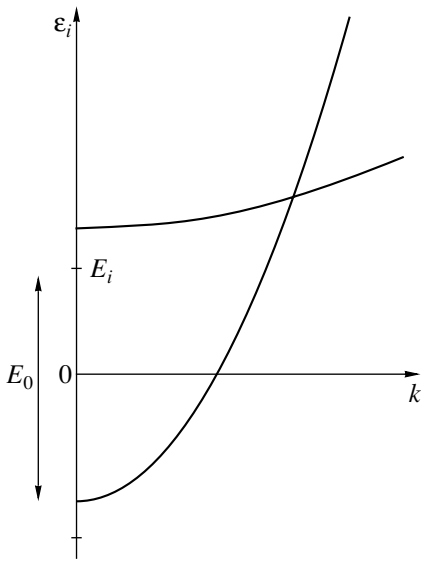

Fig. 1. Valence band of uniaxially stressed Ge in the direction of strain. Acceptor levels are indicated.

$$\varphi^{3/2}(\mathbf{r}) = \begin{bmatrix}1\\0\\0\\0\end{bmatrix}\varphi(\mathbf{r}), \quad \varphi^{-3/2}(\mathbf{r}) = \begin{bmatrix}0\\0\\0\\1\end{bmatrix}\varphi(\mathbf{r}), \qquad (14)$$

where

$$\varphi(\mathbf{r}) = \frac{1}{\sqrt{\pi a^2 b}}\exp\left(-\sqrt{\frac{\rho^2}{a^2}+\frac{z^2}{b^2}}\right), \qquad (15)$$

and the variational parameters a and b are connected with the binding energy E_A counted from the bottom of the upper subband (see [15]).

In the case of germanium, the solution of the corresponding variational problem gives a = 114 Å, b = 61.8 Å, and E_A = 4.68 meV.

As the initial approximation for the wave functions of the continuous spectrum, we choose the eigenfunctions of the Luttinger Hamiltonian for free holes with an allowance for the pressure:

$$[\hat{H}_L + \hat{H}_\varepsilon]\psi_{\mathbf{k}}^{\pm 1/2} = \varepsilon_{\mathbf{k}}\psi_{\mathbf{k}}^{\pm 1/2}, \qquad (16)$$

$$\psi_{\mathbf{k}}^{1/2} = \frac{1}{N_l(\mathbf{k})}\frac{e^{i\mathbf{kr}}}{\sqrt{V}}\begin{bmatrix}-b\\ d_+\\ 0\\ -c^*\end{bmatrix}, \quad \psi_{\mathbf{k}}^{-1/2} = \frac{1}{N_l(\mathbf{k})}\frac{e^{i\mathbf{kr}}}{\sqrt{V}}\begin{bmatrix}-c\\ 0\\ d_+\\ b^*\end{bmatrix}, \qquad (17)$$

$$\varepsilon_{\mathbf{k}} = \frac{\hbar^2}{2m_0}[\gamma_1 k^2 - \sqrt{\zeta^2 - 2\gamma\zeta(3k_z^2 - k^2) + 4\gamma^2 k^4}], \qquad (18)$$

$$b = 2\sqrt{3}\gamma(k_x - ik_y)k_z,$$
$$c = \sqrt{3}\gamma(k_x - ik_y)^2,$$
$$d_+ = a_+ + \frac{2m\varepsilon_{\mathbf{k}}}{\hbar^2}, \tag{19}$$
$$N_l^2(\mathbf{k}) = |b(\mathbf{k})|^2 + |c(\mathbf{k})|^2 + d^2(\mathbf{k}).$$

Following Dirac [13], we will seek the solution of the Schrödinger equation with the complete Hamiltonian

$$\hat{H}\Psi_{\mathbf{k}}^{\pm 1/2} = E_{\mathbf{k}}\Psi_{\mathbf{k}}^{\pm 1/2} \tag{20}$$

in the form

$$\Psi_{\mathbf{k}}^{1/2} = \psi_{\mathbf{k}}^{1/2} + a_{\mathbf{k}}^{1/2,\,3/2}\varphi^{3/2}(\mathbf{r}) + a_{\mathbf{k}}^{1/2,\,-3/2}\varphi^{-3/2}(\mathbf{r}) + \sum_{\mathbf{k}'}\frac{t_{\mathbf{k}\mathbf{k}'}^{1/2,\,1/2}}{\varepsilon_{\mathbf{k}} - \varepsilon_{\mathbf{k}'} + i\gamma}\psi_{\mathbf{k}'}^{1/2} + \sum_{\mathbf{k}'}\frac{t_{\mathbf{k}\mathbf{k}'}^{1/2,\,-1/2}}{\varepsilon_{\mathbf{k}} - \varepsilon_{\mathbf{k}'} + i\gamma}\psi_{\mathbf{k}'}^{-1/2}, \tag{21}$$

as it is usually done in the general theory of scattering. Here, we neglect the effect of the potential of one impurity on the states of the continuous spectrum: $E_{\mathbf{k}} = \varepsilon_{\mathbf{k}}$. The wave function $\Psi_{\mathbf{k}}^{1/2}$ describes the scattering of a particle located at a large distance from the center in the state $\psi_{\mathbf{k}}^{1/2}$, which is accompanied by transitions to the states $\psi_{\mathbf{k}'}^{\pm 1/2}$ and by capture into the states $\varphi^{\pm 3/2}(\mathbf{r})$. The scattering of a particle from the initial state $\psi_{\mathbf{k}}^{-1/2}$ is considered similarly.

Substituting relation (21) into Eq. (20), multiplying it by $(\varphi^{\pm 3/2}(\mathbf{r}))^*$ or $(\psi_{\mathbf{k}}^{\pm 1/2})^*$, and integrating with respect to d$\mathbf{r}$, we obtain a system of equations for the capture coefficient $a_{\mathbf{k}}^{1/2,\,\pm 3/2}$ and the scattering amplitudes $t_{\mathbf{k}\mathbf{k}'}^{1/2,\,\pm 1/2}$. The solution of this system leads to the following expressions:

$$a_{\mathbf{k}}^{1/2,\,3/2} = \frac{1}{\sqrt{V}}\frac{1}{\varepsilon_{\mathbf{k}} - (E_i + \Delta E) + i\Gamma/2}A_{\mathbf{k}}^{1/2,\,3/2},$$
$$a_{\mathbf{k}}^{1/2,\,-3/2} = \frac{1}{\sqrt{V}}\frac{1}{\varepsilon_{\mathbf{k}} - (E_i + \Delta E) + i\Gamma/2}A_{\mathbf{k}}^{1/2,\,-3/2}, \tag{22}$$

$$t_{\mathbf{k}\mathbf{k}'}^{1/2,\,1/2} = -\frac{\tilde{V}_{\mathbf{k}'\mathbf{k}}^{1/2,\,1/2}}{V} - \frac{W_{\mathbf{k}'}}{\sqrt{V}}\frac{\hbar^2}{2m_0}\frac{d_+}{N_l(\mathbf{k}')} \times [b^*(\mathbf{k}')a_{\mathbf{k}}^{1/2,\,3/2} + c(\mathbf{k}')a_{\mathbf{k}}^{1/2,\,-3/2}],$$
$$t_{\mathbf{k}\mathbf{k}'}^{1/2,\,-1/2} = -\frac{\tilde{V}_{\mathbf{k}'\mathbf{k}}^{-1/2,\,1/2}}{V} - \frac{W_{\mathbf{k}'}}{\sqrt{V}}\frac{\hbar^2}{2m_0}\frac{d_+}{N_l(\mathbf{k}')} \times [c^*(\mathbf{k}')a_{\mathbf{k}}^{1/2,\,3/2} - b(\mathbf{k}')a_{\mathbf{k}}^{1/2,\,-3/2}]. \tag{23}$$

The expressions for coefficients $A_{\mathbf{k}}^{1/2,\,\pm 3/2}$ and the matrix elements $W_{\mathbf{k}}$ and $\tilde{V}_{\mathbf{k}}^{\pm 1/2,\,1/2}$ are given in Appendix A. The expressions for Γ and ΔE are presented in Appendix B. The resonant nature of capture and scattering is determined by the presence of the denominator $\varepsilon_{\mathbf{k}} - (E_i + \Delta E) + i\Gamma/2$ in the expressions (22) for the capture coefficients. Expressions (23) for scattering amplitudes were derived taking into account the Coulomb potential scattering in the Born approximation. This scattering corresponds to the first terms in formulas (23). The remaining terms in these formulas describe the resonant scattering which is a result of capture followed by ejection.

It can be seen that as a result of configuration interaction, the energy level of the initial local state is displaced by ΔE and acquires the width $\Gamma/2$, which corresponds to a finite lifetime of a particle in this quasi-local state. The values of ΔE and $\Gamma/2$ are functions of energy $\varepsilon_{\mathbf{k}}$ (see Appendix B). Consequently, it is natural to determine the position of resonance E_0 as the energy for which the real part of the resonance denominator is equal to zero:

$$E_0 - E_i - \Delta E(E_0) = 0. \tag{24}$$

In this case, the resonance half-width is defined as the value of $\Gamma/2$ calculated by formula (59) from Appendix B for the resonant energy E_0.

It should be noted that the spherical approximation for the Luttinger Hamiltonian is quite rough and does not permit an analysis of the effect of anisotropy in the spectrum of the light hole subband on the parameters of the resonant state. The anisotropy effects can be taken into account by using the cylindrical approximation for the Luttinger Hamiltonian. A transition to this approximation is carried out by the replacement of γ_2 and γ_3 in the nondiagonal elements of Hamiltonian (1) by their mean value $\gamma_c = 0.5(\gamma_2 + \gamma_3)$. In this case, the dispersion relation in the light hole subband becomes

$$\varepsilon_{\mathbf{k}} = \frac{\hbar^2}{2m_0}[\gamma_1(k_\perp^2 + k_z^2) - [\zeta^2 + 2\gamma_2\zeta(k_\perp^2 - 2k_z^2) + (\gamma_2^2 + 3\gamma_c^2)k_\perp^4 + 4\gamma_2^2k_z^4 + 4(3\gamma_c^2 - \gamma_2^2)k_\perp^2k_z^2]^{1/2}], \tag{25}$$

where $k_\perp^2 = k_x^2 + k_y^2$. The results of calculations of the position of the resonance and its half-width for *p*-Ge stressed along the [001] axis are presented in Figs. 2 and 3.

Figure 3 also shows the results of calculations of the resonance level half-width $\Gamma/2$ in the spherical approximation of the Luttinger Hamiltonian.

The inset to Fig. 3 shows that, for low resonant energies ($E_0 \ll E_{def}$), the $\Gamma(E_0)$ dependence has the form $E_0^{5/2}$ in accordance with the general theory [11].

3. PROBABILITIES OF CAPTURE INTO THE RESONANT STATE AND RESONANT ELASTIC SCATTERING

The representation of the wave function in the form (21) makes it possible to derive expressions for the probability $W_{\mathbf{kk'}}^{1/2}$ of resonant elastic scattering and the probability of capture into the resonant state $W_{\mathbf{k}r}^{1/2}$, which are related to the capture coefficients $a_{\mathbf{k}}^{1/2,\pm 3/2}$ and the scattering amplitudes $t_{\mathbf{kk'}}^{1/2,\pm 1/2}$ through the following relations [11]:

$$W_{\mathbf{k}r}^{1/2} = \left|a_{\mathbf{k}}^{1/2,3/2}\right|^2 + \left|a_{\mathbf{k}}^{1/2,-3/2}\right|^2, \quad (26)$$

$$W_{\mathbf{kk'}}^{1/2} = \frac{2\pi}{\hbar}\left(\left|t_{\mathbf{kk'}}^{1/2,1/2}\right|^2 + \left|t_{\mathbf{kk'}}^{1/2,-1/2}\right|^2\right)\delta(\varepsilon_{\mathbf{k}} - \varepsilon_{\mathbf{k'}}). \quad (27)$$

It should be noted that resonant scattering is elastic by nature when no phasebreaking takes place during the lifetime $\hbar/\Gamma$ in the resonant state; i.e., the capture is followed by a coherent ejection. In the opposite case, resonant scattering becomes inelastic and $\delta(\varepsilon_{\mathbf{k}} - \varepsilon_{\mathbf{k'}})$ in Eq. (27) should be replaced by the Lorentzian factor [8, 11].

Considering the scattering of a particle in the $\psi_{\mathbf{k}}^{-1/2}$ state, we can easily prove that $W_{\mathbf{kk'}}^{1/2} = W_{\mathbf{kk'}}^{-1/2}$ and $W_{\mathbf{k}r}^{1/2} = W_{\mathbf{k}r}^{-1/2}$. Accordingly, the hole distribution functions $f_{\mathbf{k}}^{\pm 1/2}$, which must be determined from the solution of the kinetic equation taking into account elastic resonant scattering, are also equal.

The population f_r of the resonant state is defined by the formula [11]

$$f_r = \sum_{\mathbf{k}} W_{\mathbf{k}r}^{1/2} f_{\mathbf{k}}^{1/2} + \sum_{\mathbf{k}} W_{\mathbf{k}r}^{-1/2} f_{\mathbf{k}}^{-1/2}. \quad (28)$$

It is convenient to present the capture probability (26) in a form similar to the simple isotropic Breit–Wigner model [16, 17] by isolating the resonance factor and the dimensionless factor $w(\theta, \varepsilon_{\mathbf{k}})$ specifying the angular dependence. In view of the resonant nature of the capture process, this factor can easily be evaluated for the hole energy $\varepsilon_{\mathbf{k}} = E_0$:

$$W_{\mathbf{k}r}^{1/2} = \frac{1}{V}\frac{\Gamma}{(\varepsilon_k - E_0)^2 + \Gamma^2/4}\frac{\pi}{4\sqrt{E_0}} \times \left\{\left[\frac{1}{k_\perp}\frac{\partial\varepsilon_{\mathbf{k}}}{\partial k_\perp} + \frac{1}{k_z}\frac{\partial\varepsilon_{\mathbf{k}}}{\partial k_z}\right]^{3/2}\right\}\Bigg|_{\varepsilon_{\mathbf{k}} = E_0} w(\theta, E_0), \quad (29)$$

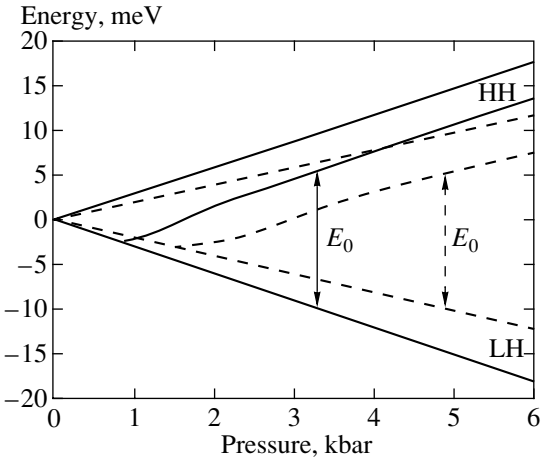

Fig. 2. Energy diagram of the dependence of the splitting of light and heavy hole subbands and also of the position of the resonance level on the applied pressure. Solid curves corresponds to the [001] direction of strain, and dashed curves, to the [111] direction.

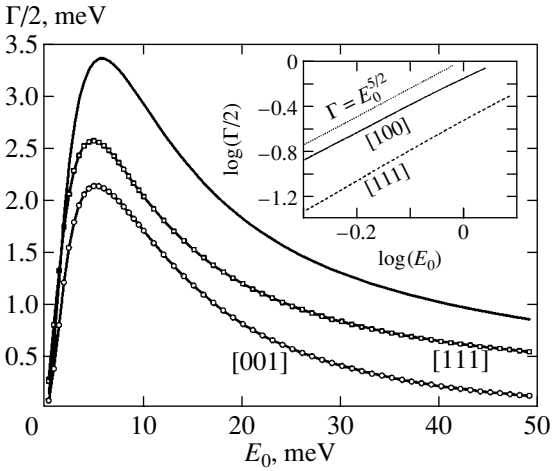

Fig. 3. Dependence of the half-width of the resonance level on its position E_0 in the cylindrical and spherical (solid curve) approximations for two directions of the applied pressure: [001] and [111]. The inset shows the proportionality of the obtained dependences to for $E_0^{5/2}$ at small energies.

$$w(\theta, E_0) = \frac{4\sqrt{E_0}}{\pi\Gamma}\left\{\left(\left|A_{\mathbf{k}}^{1/2,3/2}\right|^2 + \left|A_{\mathbf{k}}^{1/2,3/2}\right|^2\right) \times \left(\frac{1}{k_\perp}\frac{\partial\varepsilon_{\mathbf{k}}}{\partial k_\perp} + \frac{1}{k_z}\frac{\partial\varepsilon_{\mathbf{k}}}{\partial k_z}\right)^{-3/2}\right\}\Bigg|_{\varepsilon_{\mathbf{k}} = E_0}. \quad (30)$$

The results of numerical calculations of $w(\theta, E_0)$ as a function of the angle θ between the wave vector and the direction of pressure (z axis) for germanium stressed along the [001] axis are presented in Fig. 4. It can easily be proved that $w(\theta, E_0) = w(\pi - \theta, E_0)$; for

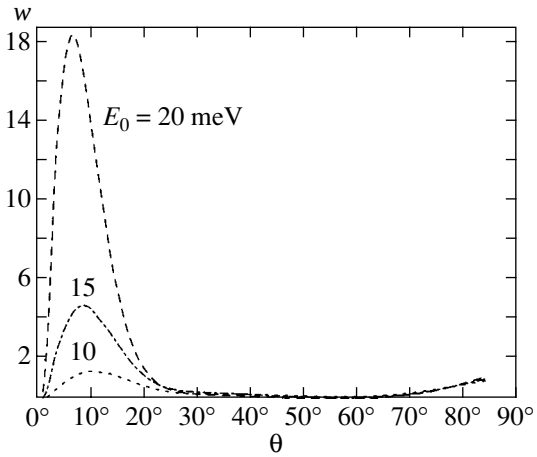

Fig. 4. Angular dependence of the coefficient $w(\theta, E_0)$ in the capture probability (see relation (29)). Angle $\theta = \arctan(k_\perp/k_z)$, E_0 = 10, 15, and 20 meV. The pressure is applied along the [001] axis (cylindrical approximation).

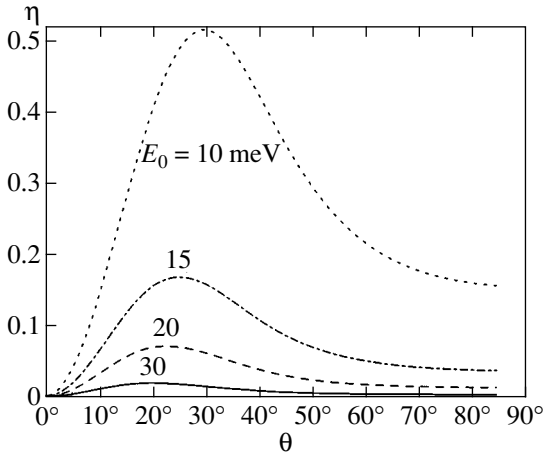

Fig. 5. Angular dependence of the coefficient $\eta(\theta', E_0)$ in the ejection probability (see relation (32)). Angle $\theta' = \arctan\left(k'_\perp/k'_z\right)$, E_0 = 10, 15, 20, and 30 meV. The pressure is applied along the [001] axis (cylindrical approximation).

this reason, the curves are plotted in the interval $0 < \theta < \pi/2$.

The expression for the elastic scattering probability derived on the basis of formulas (22), (23), and (27) splits into two terms corresponding to the potential Coulomb scattering (Born approximation) and to the resonant scattering. It is convenient to present the resonant component of the elastic scattering probability $\tilde{W}^{1/2}_{\mathbf{kk'}}$ by introducing the resonant scattering cross section $\sigma^{1/2}_{\mathbf{kk'}}$:

$$\tilde{W}^{1/2}_{\mathbf{kk'}} = \frac{2\pi}{\hbar}\sigma^{r}_{\mathbf{kk'}}\frac{1}{V^2}\frac{\pi}{4}\left(\frac{1}{k_\perp}\frac{\partial\varepsilon_\mathbf{k}}{\partial k_\perp} + \frac{1}{k_z}\frac{\partial\varepsilon_\mathbf{k}}{\partial k_z}\right)^2\delta(\varepsilon_\mathbf{k} - \varepsilon'_\mathbf{k}). \quad (31)$$

Using relations (22) and (23) and separating the resonant factor, we can write $\sigma^{1/2}_{\mathbf{kk'}}$ in the form

$$\sigma^{1/2}_{\mathbf{kk'}} = \pi a^2 b\frac{\Gamma}{(\varepsilon_\mathbf{k} - E_0)^2 + \Gamma^2/4} \times E_0^{3/2}\left\{\left(\frac{1}{k_\perp}\frac{\partial\varepsilon_\mathbf{k}}{\partial k_\perp} + \frac{1}{k_z}\frac{\partial\varepsilon_\mathbf{k}}{\partial k_z}\right)^{-1/2}\right\}\Bigg|_{\varepsilon_\mathbf{k} = E_0} w(\theta, E_0)\eta(\theta', E_0), \quad (32)$$

where a and b define the size of the localized state (15), and the dimensionless factor $\eta(\theta', E_0)$, which is a function of the angle of scattering relative to the stress axis (z axis), is defined as

$$\eta(\mathbf{k'}) = \left\{\frac{64}{[1 + b^2 k_z'^2 + a^2 k_\perp'^2]^4}\frac{|b(\mathbf{k'})|^2 + |c(\mathbf{k'})|^2}{N_l(\mathbf{k'})^2} \times\left[\frac{\hbar^2}{2mE_0}a_+(\mathbf{k'}) + 1\right]^2\right\}\Bigg|_{\varepsilon'_\mathbf{k} = E_0}. \quad (33)$$

The theoretical dependence of the factor $\eta(\theta, E_0)$ for germanium strained along the [001] axis is shown in Fig. 5.

It can be seen that particles moving along the z axis have zero probabilities of capture and scattering. This result can be obtained from an analysis of expressions for $W_\mathbf{kr}$ without resorting to calculations. This is due to the fact that the capture takes place if the states of the light hole subband contain an admixture of states of the heavy hole subband, i.e., if the wave function (17) contains nonzero components for the Bloch functions $u_{\pm 3/2}$. In the case when the wave vector of a particle is directed along the z axis, the states in both subbands are "pure," i.e., contain contributions of their own subbands only. In this case, the transverse wave vector component and the nondiagonal elements of the Luttinger Hamiltonian (1) vanish and functions (17) acquire the form $\psi^{\pm 1/2}_\mathbf{k} = e^{i\mathbf{kr}}/\sqrt{V}u_{\pm 1/2}$. Thus, a particle in the state $\psi^{\pm 1/2}_\mathbf{k}$ does not interact with the local sates (14), and no capture into this state takes place. The capture probability increases with the component of the wave vector of the particle, which is perpendicular to pressure. If particles move in an electric field directed along the strain axis in the complete absence of scattering (streaming mode), the distribution function for the particles is extended in the direction of the field and the probability of the particles being captured into the resonant state is extremely low. This leads to a decrease in the population of the center. Conversely, in the diffusion mode which is characterized by a broad angular distribution of particles, the capture probability increases for most particles, thus increasing the population of the center. The population of the resonance state of an impurity center in the diffusion mode was considered in [9].

According to the results of calculations (see Figs. 4 and 5), the capture probability has the highest value for particles with a wave vector directed at an angle on the order of 10° to the direction of straining, while elastic scattering mainly takes place at an angle of approximately 20°.

4. STRAINING ALONG THE [111] AXIS

Let us now consider a generalization of the method of configuration interaction for resonant acceptor states emerging under strain along the [111] axis. In this case, the strain tensor has the form

$$\varepsilon_{xx} = \varepsilon_{yy} = \varepsilon_{zz} = \frac{(S_{11} + 2S_{12})}{3}P,$$
$$\varepsilon_{xy} = \varepsilon_{xz} = \varepsilon_{zy} = \frac{S_{44}}{12}P. \quad (34)$$

Eliminating the terms describing the shift of the top of the valence band in analogy with the case of straining along the [001] axis, we can present Hamiltonian $\hat{H}_\varepsilon$ in the following convenient form:

$$\hat{H}_\varepsilon = -\frac{\hbar^2}{2m_0}\begin{bmatrix} 0 & \hat{h} & \hat{j} & 0 \\ \hat{h}^* & 0 & 0 & \hat{j} \\ \hat{j}^* & 0 & 0 & -\hat{h} \\ 0 & \hat{j}^* & -\hat{h}^* & 0 \end{bmatrix}, \quad (35)$$

where

$$\hat{h} = -\frac{\sqrt{3}}{3}\zeta(1-i),$$
$$\hat{j} = \frac{i\sqrt{3}}{3}\zeta. \quad (36)$$

The splitting of the top of the valence band is described by

$$E_{\text{def}} = 2\frac{\hbar^2\zeta}{2m_0} = 6d\varepsilon_{xy} = \frac{S_{44}}{2}dP = \alpha P, \quad (37)$$

where α = 4 meV/kbar. The dispersion relations have the form

$$\varepsilon^{(h)} = \frac{\hbar^2}{2m_0}[(\gamma_1 - 2\gamma_3)k^2 + \zeta],$$
$$\varepsilon^{(l)} = \frac{\hbar^2}{2m_0}[(\gamma_1 + 2\gamma_3)k^2 - \zeta] \quad (38)$$

for $\mathbf{k} \parallel [111]$ and

$$\varepsilon^{(h)} = \frac{\hbar^2}{2m_0}[(\gamma_1 + \gamma_3)k^2 + \zeta],$$
$$\varepsilon^{(l)} = \frac{\hbar^2}{2m_0}[(\gamma_1 - \gamma_3)k^2 - \zeta] \quad (39)$$

for $\mathbf{k}$ lying in a plane perpendicular to the [111] axis (e.g., directed along $[11\bar{2}]$ axis). In order to find the initial approximation Hamiltonian for local acceptor states under the heavy hole band, we pass to the coordinate basis ($x'y'z'$) with the z' axis directed along [111], the y' axis directed along $[1\bar{1}0]$, and the z' axis directed along $[11\bar{2}]$. The coordinates of vector $\mathbf{k}$ in the old and rotated frames of reference are connected through the linear transformation $\mathbf{k} = \hat{T}\mathbf{k}'$, where

$$\hat{T} = \begin{bmatrix} -\frac{1}{\sqrt{2}} & \frac{1}{\sqrt{6}} & \frac{1}{\sqrt{3}} \\ \frac{1}{\sqrt{2}} & \frac{1}{\sqrt{6}} & \frac{1}{\sqrt{3}} \\ 0 & -\frac{2}{\sqrt{6}} & \frac{1}{\sqrt{3}} \end{bmatrix}. \quad (40)$$

With such a rotation of the system of coordinates, basis (3) and Hamiltonian (6) are transformed through the linear transformation $\hat{D}$. The matrix of this transformation can be composed from the eigenvectors of Hamiltonian (6), in which vector $\mathbf{k}$ is replaced by a unit vector directed along the new quantization axis $z' \parallel [111]$:

$$\hat{D} = \frac{1}{\sqrt{2}} \times \begin{bmatrix} 1 & \frac{\sqrt{3}}{3}(1-i) & -\frac{\sqrt{3}}{3}i & 0 \\ \frac{\sqrt{3}}{3}(1+i) & -1 & 0 & -\frac{\sqrt{3}}{3}i \\ \frac{\sqrt{3}}{3}i & 0 & -1 & -\frac{\sqrt{3}}{3}(1-i) \\ 0 & \frac{\sqrt{3}}{3}i & -\frac{\sqrt{3}}{3}(1+i) & 1 \end{bmatrix}. \quad (41)$$

It should be noted that the coordinate axes of the rotated frame of reference coincide with the principal axes of the strain tensor under a pressure directed along the [111] axis. Transformation $\hat{D}$ converts $\hat{H}_\varepsilon$ in relation (35) to a diagonal form similar to (10), while the Coulomb interaction Hamiltonian remains unchanged. In order to find the wave functions of local states under the heavy hole band, we will use as the initial approxima-

tion Hamiltonian the diagonal component of Hamiltonian (6) transformed with the help of matrix $\hat{D}$:

$$[\hat{\tilde{H}}_0 - \hat{V}_c]\varphi^{\pm 3/2\prime}(\mathbf{r}) = E_i\varphi^{\pm 3/2\prime}(\mathbf{r}), \tag{42}$$

where

$$\hat{\tilde{H}}_0 = -\frac{\hbar^2}{2m_0}\begin{bmatrix} \hat{\tilde{a}}_+ & 0 & 0 & 0 \\ 0 & \hat{\tilde{a}}_- & 0 & 0 \\ 0 & 0 & \hat{\tilde{a}}_- & 0 \\ 0 & 0 & 0 & \hat{\tilde{a}}_+ \end{bmatrix} \tag{43}$$

with the matrix elements

$$\begin{aligned} \hat{\tilde{a}}_+ &= -\gamma_1(\hat{k}_x^2 + \hat{k}_y^2 + \hat{k}_z^2) + 2\gamma_3(\hat{k}_x\hat{k}_y + \hat{k}_x\hat{k}_z + \hat{k}_y\hat{k}_z) - \zeta, \\ \hat{\tilde{a}}_- &= -\gamma_1(\hat{k}_x^2 + \hat{k}_y^2 + \hat{k}_z^2) \\ &\quad - 2\gamma_3(\hat{k}_x\hat{k}_y + \hat{k}_x\hat{k}_z + \hat{k}_y\hat{k}_z) + \zeta. \end{aligned} \tag{44}$$

The eigenfunctions of this Hamiltonian in the transformed basis $u'_{\pm 3/2}$, $u'_{\pm 1/2}$ look similar to functions (14) in basis (3). It should be borne in mind, however, that the variables z and ρ in the expression for the envelope of the wave function (15) are connected with the rotated coordinate basis with the z axis directed along [111]. The variational parameters are now a = 110 Å and b = 49.9 Å, while the energy of state E_A = 5.05 meV. It is convenient to carry out subsequent calculations in basis (3). We transform both sides of Eq. (42) to this basis using the inverse transformation

$$\hat{H}_{0h}\varphi^{\pm 3/2}(\mathbf{r}) = E_A\varphi^{\pm 3/2}(\mathbf{r}), \tag{45}$$

where $\hat{H}_{0h} = \hat{D}\hat{\tilde{H}}_0\hat{D}^+ - \hat{V}_c$ and

$$\begin{aligned} \varphi^{3/2}(\mathbf{r}) &= \hat{D}\varphi^{3/2\prime}(\mathbf{r}) = \begin{bmatrix} 1 \\ \frac{\sqrt{3}}{3}(1+i) \\ \frac{\sqrt{3}}{3}i \\ 0 \end{bmatrix}\frac{\varphi(\mathbf{r})}{\sqrt{2}}, \\ \varphi^{-3/2}(\mathbf{r}) &= \hat{D}\varphi^{-3/2\prime}(\mathbf{r}) = \begin{bmatrix} 0 \\ -\frac{\sqrt{3}}{3}i \\ -\frac{\sqrt{3}}{3}(1-i) \\ 1 \end{bmatrix}\frac{\varphi(\mathbf{r})}{\sqrt{2}}, \end{aligned} \tag{46}$$

$\varphi(\mathbf{r})$ is defined by relation (15), and

$$\hat{D}\tilde{H}_0\hat{D}^+ = -\frac{\hbar^2}{2m_0} \times \begin{bmatrix} \hat{q} & \frac{\sqrt{3}}{3}(1-i)\hat{g} & -\frac{\sqrt{3}}{3}i\hat{g} & 0 \\ \frac{\sqrt{3}}{3}(1+i)\hat{g} & \hat{q} & 0 & -\frac{\sqrt{3}}{3}i\hat{g} \\ -\frac{\sqrt{3}}{3}i\hat{g} & 0 & \hat{q} & -\frac{\sqrt{3}}{3}(1-i)\hat{g} \\ 0 & \frac{\sqrt{3}}{3}i\hat{g} & -\frac{\sqrt{3}}{3}(1+i)\hat{g} & \hat{q} \end{bmatrix}, \tag{47}$$

where

$$\begin{aligned} \hat{q} &= \frac{\hat{\tilde{a}}_+ + \hat{\tilde{a}}_-}{2}, \\ \hat{g} &= \frac{\hat{\tilde{a}}_+ - \hat{\tilde{a}}_-}{2}. \end{aligned} \tag{48}$$

We add to and subtract from Hamiltonian (6) the term $\hat{D}\hat{\tilde{H}}_0\hat{D}^+$; then, the complete Hamiltonian $\hat{H}$ can be presented in the form

$$\hat{H} = \hat{H}_{0h} + \hat{U}_h, \tag{49}$$

where

$$\hat{U}_h = \hat{H}_L + \hat{H}_\varepsilon - \hat{D}\hat{\tilde{H}}_0\hat{D}^+ \tag{50}$$

is the Hamiltonian of perturbation for local states under the bottom of the heavy hole subband.

As in the case of straining along the [001] direction, we choose as the initial approximation for the wave functions of the light hole subband the solutions of the Schrödinger equation with a free Luttinger Hamiltonian taking the strain into consideration: $\hat{H}_L + \hat{H}_\varepsilon$.

A procedure completely analogous to the case of straining along the [001] direction again leads to expressions (59) and (60) for the displacement of the position of the local state and its broadening. However, the components of vector $\mathbf{k}$ in expressions (53) used for calculating the matrix elements $W_\mathbf{k}$ and $V_\mathbf{k}$ are associated with the frame of reference in which the z axis is directed along the [111] axis. Accordingly, the wave vector components in expressions (44) for $a_+(\mathbf{k})$ and $a_-(\mathbf{k})$ as well as in the dispersion relation $\varepsilon_\mathbf{k}$ for the light hole band must be transformed to the same coordinate basis with the help of the linear transformation T (40). As a result, the expressions for $a_+(\mathbf{k})$, $a_-(\mathbf{k})$, and $\varepsilon_\mathbf{k}$ used for

evaluating the integrals in expressions (59) and (60) now take the form

$$\begin{aligned} a_+^{\sim}(\mathbf{k}) &= -(\gamma_1 - 2\gamma_3)k_z^2 - (\gamma_1 + \gamma_3)(k_x^2 + k_y^2) - \zeta, \\ a_-^{\sim}(\mathbf{k}) &= -(\gamma_1 + 2\gamma_3)k_z^2 - (\gamma_1 - \gamma_3)(k_x^2 + k_y^2) + \zeta, \\ \varepsilon_{\mathbf{k}} &= \frac{\hbar^2}{2m_0}[\gamma_1(k_\perp^2 + k_z^2) - (\zeta^2 + 2\gamma_3\zeta(k_\perp^2 - 2k_z^2) \\ &\quad + (\gamma_2^2 + 3\gamma_3^2)k_\perp^4 + 8\gamma_2^2k_\perp^2k_z^2 + 4\gamma_3^2k_z^4)^{1/2}]. \end{aligned} \tag{51}$$

The expression for $\varepsilon_{\mathbf{k}}$ corresponds to the cylindrical approximation for the spectrum in the light hole subband relative to direction [111]. Figures 2 and 3 show the results of calculations of the position of the resonance and its half-width under a pressure applied along the [111] direction. It can be seen that the form of the $\Gamma(E_0)$ dependence in this case remains almost the same as for strain along [001].

5. CONCLUSION

A method of configuration interaction is proposed for studying the parameters of the resonant states emerging in a doped *p*-type semiconductor under uniaxial stress. Concrete calculations of the position of the lowest resonance level, the lifetime in this resonant state, and the probabilities of elastic scattering and capture into this state were carried out for *p*-Ge subjected to uniaxial stress along the [001] and [111] directions.

It is shown that elastic scattering at resonant states induced by shallow acceptors in uniaxially strained *p*-Ge is strongly anisotropic. The same property is also characteristic of the coefficients of capture into resonant states. This anisotropy considerably influences the dependence of the occupancy of the resonant state on the electric field and temperature and affects the conditions for the emergence of population inversion of resonant states relative to local states (see [9]).

The obtained results make it possible to develop a computer model of a THz laser operating on resonant states in uniaxially strained *p*-Ge.

It should be noted that the method developed by us here can be used for analyzing the kinetics in the presence of other types of resonant states also, which emerge in semiconductors and semiconducting nanostructures. Among other things, this method makes it possible to study the features of the kinetics of hot 2D carriers due to capture and ejection at the resonant states induced by impurities in the barriers of nanostructures [18].

ACKNOWLEDGMENTS

This work was supported financially by the Russian Foundation for Basic Research (project nos. 01-02-16265, 00-15-96768, and 00-02-17429) and NorFa. I.N. Yassievich also thanks the STINT Fellowships Programme (contract no. 99/527(00)) for financial assistance, and A. A. Prokofiev expresses his gratitude to the Swedish Institute for offering a grant under the New Visby Programme.

APPENDIX A

Expressions for Matrix Elements

$$A_{\mathbf{k}}^{1/2,\,3/2} = \left[V_{\mathbf{k}} \frac{b(\mathbf{k})}{N_l(\mathbf{k})} - \frac{1}{V}\sum_{\mathbf{k}'} \frac{b(\mathbf{k}')\tilde{V}_{\mathbf{k}'\mathbf{k}}^{1/2,\,1/2} + c(\mathbf{k}')\tilde{V}_{\mathbf{k}'\mathbf{k}}^{-1/2,\,1/2}}{N_l(\mathbf{k}')} W_{\mathbf{k}'} \right], \tag{52a}$$

$$A_{\mathbf{k}}^{1/2,\,-3/2} = \left[V_{\mathbf{k}} \frac{c^*(\mathbf{k})}{N_l(\mathbf{k})} - \frac{1}{V}\sum_{\mathbf{k}'} \frac{c^*(\mathbf{k}')\tilde{V}_{\mathbf{k}'\mathbf{k}}^{1/2,\,1/2} - b^*(\mathbf{k}')\tilde{V}_{\mathbf{k}'\mathbf{k}}^{-1/2,\,1/2}}{N_l(\mathbf{k}')} W_{\mathbf{k}'} \right]; \tag{52b}$$

$$W_{\mathbf{k}} = \langle \varphi(\mathbf{r}) | e^{i\mathbf{k}\mathbf{r}} \rangle = \frac{8\sqrt{\pi a^2 b}}{[1 + (k_z b)^2 + (k_\perp a)^2]^2}, \tag{53}$$

$$V_{\mathbf{k}} = \langle \varphi(\mathbf{r}) | \hat{V}_c(\mathbf{r}) | e^{i\mathbf{k}\mathbf{r}} \rangle = \frac{4\sqrt{\pi a^2 b}e^2}{\kappa a} V_1(\mathbf{k}), \tag{54}$$

$$V_{\mathbf{k}'\mathbf{k}} = \langle e^{-i\mathbf{k}'\mathbf{r}} | \hat{V}_c(\mathbf{r}) | e^{i\mathbf{k}\mathbf{r}} \rangle = \frac{4\pi e^2}{\kappa |\mathbf{k}' - \mathbf{k}|^2}, \tag{55}$$

$$\tilde{V}_{\mathbf{k}'\mathbf{k}}^{-1/2,1/2} = V_{\mathbf{k}'\mathbf{k}} \frac{b(\mathbf{k})c^*(\mathbf{k}') - b(\mathbf{k}')c^*(\mathbf{k})}{N_l(\mathbf{k}')N_l(\mathbf{k})}, \tag{56}$$

$$\tilde{V}_{\mathbf{k}'\mathbf{k}}^{1/2,\,1/2} = V_{\mathbf{k}'\mathbf{k}} \frac{b(\mathbf{k})b^*(\mathbf{k}') + c^*(\mathbf{k})c(\mathbf{k}') + d(\mathbf{k})d(\mathbf{k}')}{N_l(\mathbf{k}')N_l(\mathbf{k})}, \tag{57}$$

$$V_1(\mathbf{k}) = \int_0^{+\infty} r e^{-r} dr \int_0^1 \frac{\cos(bk_z r t) J_0(ak_\perp r\sqrt{1-t^2})}{\sqrt{1 - t^2(1 - b^2/a^2)}} dt, \tag{58}$$

J_0 being a zeroth-order Bessel function.

APPENDIX B

Expressions for Γ and ΔE

$$\frac{\Gamma}{2} = -\frac{1}{8\pi^2}\int d^3k' \times \frac{\left(\frac{\hbar^2}{2m_0}a_+(\mathbf{k}') + \varepsilon_{\mathbf{k}'} - \varepsilon_{\mathbf{k}} + E_0\right)\left(\frac{\hbar^2}{2m_0}a_-(\mathbf{k}') + \varepsilon_{\mathbf{k}'}\right)}{\frac{\hbar^2}{2m_0}(a_+(\mathbf{k}') + a_-(\mathbf{k}')) + 2\varepsilon_{\mathbf{k}'}} \times W_{\mathbf{k}'}V_{\mathbf{k}'}\delta(\varepsilon_{\mathbf{k}'} - \varepsilon_{\mathbf{k}}), \tag{59}$$

$$\Delta E = -\frac{1}{8\pi^2}\int d^3k' \times \frac{\left(\frac{\hbar^2}{2m_0}a_+(\mathbf{k}') + \varepsilon_{\mathbf{k}'} - \varepsilon_{\mathbf{k}} + E_0\right)\left(\frac{\hbar^2}{2m_0}a_-(\mathbf{k}') + \varepsilon_{\mathbf{k}'}\right)}{\frac{\hbar^2}{2m_0}(a_+(\mathbf{k}') + a_-(\mathbf{k}')) + 2\varepsilon_{\mathbf{k}'}} W_{\mathbf{k}'}^2 - \frac{1}{8\pi^2}P\int d^3k' \times \frac{\left(\frac{\hbar^2}{2m_0}a_+(\mathbf{k}') + \varepsilon_{\mathbf{k}'} - \varepsilon_{\mathbf{k}} + E_0\right)\left(\frac{\hbar^2}{2m_0}a_-(\mathbf{k}') + \varepsilon_{\mathbf{k}'}\right)}{\frac{\hbar^2}{2m_0}(a_+(\mathbf{k}') + a_-(\mathbf{k}')) + 2\varepsilon_{\mathbf{k}'}} \frac{W_{\mathbf{k}'}V_{\mathbf{k}'}}{\varepsilon_{\mathbf{k}} - \varepsilon_{\mathbf{k}'}}. \quad (60)$$

REFERENCES

1. S. A. Nemov and Yu. I. Ravich, Usp. Fiz. Nauk **168**, 817 (1998) [Phys. Usp. **41**, 735 (1998)].
2. M. I. D'yakonov and B. L. Gel'mont, Zh. Éksp. Teor. Fiz. **62**, 713 (1972) [Sov. Phys. JETP **35**, 377 (1972)].
3. M. V. Vergelis and I. A. Merkulov, Fiz. Tekh. Poluprovodn. (St. Petersburg) **26**, 1784 (1992) [Sov. Phys. Semicond. **26**, 999 (1992)].
4. I. V. Altukhov, E. G. Chirkova, M. S. Kagan, *et al.*, Zh. Éksp. Teor. Fiz. **101**, 756 (1992) [Sov. Phys. JETP **74**, 404 (1992)].
5. I. V. Altukhov, E. G. Chirkova, M. S. Kagan, *et al.*, Zh. Éksp. Teor. Fiz. **115**, 89 (1999) [JETP **88**, 51 (1999)].
6. Yu. P. Gousev, I. V. Altukhov, K. A. Korolev, *et al.*, Appl. Phys. Lett. **75**, 757 (1999).
7. G. L. Bir and G. E. Pikus, *Symmetry and Strain–Induced Effects in Semiconductors* (Nauka, Moscow, 1972; Wiley, New York, 1974).
8. M. A. Odnoblyudov, I. N. Yassievich, M. S. Kagan, *et al.*, Phys. Rev. Lett. **83**, 644 (1999).
9. M. A. Odnoblyudov, I. N. Yassievich, M. S. Kagan, *et al.*, Phys. Rev. B **62**, 15291 (2000).
10. M. A. Odnoblyudov, V. M. Chistyakov, and I. N. Yassievich, Fiz. Tekh. Poluprovodn. (St. Petersburg) **31**, 1180 (1997) [Semiconductors **31**, 1014 (1997)].
11. M. A. Odnoblyudov, I. N. Yassievich, V. M. Chistyakov, *et al.*, Phys. Rev. B **62**, 2486 (2000).
12. V. Ya. Aleshkin, B. A. Andreev, V. I. Gavrilenko, *et al.*, Nanotechnology **11**, 348 (2000).
13. P. A. M. Dirac, *Principles of Quantum Mechanics* (Clarendon, Oxford, 1981, 4th ed.).
14. U. Fano, Phys. Rev. B **124**, 1866 (1961).
15. M. A. Odnoblyudov and V. M. Chistyakov, Semiconductors **32**, 799 (1998).
16. L. D. Landau and E. M. Lifshitz, *Course of Theoretical Physics*, Vol. 3: *Quantum Mechanics: Non-Relativistic Theory* (Nauka, Moscow, 1989, 4th ed.; Pergamon, New York, 1977, 3rd ed.).
17. A. A. Prokof'ev, M. A. Odnoblyudov, and I. N. Yassievich, Fiz. Tekh. Poluprovodn. (St. Petersburg) **35**, 586 (2001) [Semiconductors **35**, 565 (2001)].
18. I. N. Yassievich, A. Blom, A. A. Prokofiev, *et al.*, submitted to Physica B (Amsterdam).

Translated by N. Wadhwa

Journal of Experimental and Theoretical Physics, Vol. 94, No. 3, 2002, pp. 603–626.
Translated from Zhurnal Éksperimental'noĭ i Teoreticheskoĭ Fiziki, Vol. 121, No. 3, 2002, pp. 703–727.

SOLIDS
Electronic Properties

The Electric Conductivity of a Laminated Metal System (Alternating Magnetic and Nonmagnetic Layers)

V. Ya. Kravchenko

Institute of Solid-State Physics, Russian Academy of Sciences, Chernogolovka, Moscow oblast, 142432 Russia
e-mail: krav@issp.ac.ru

Received August 1, 2001

Abstract—A set of kinetic equations for the distribution functions of carriers differing both by the energy spectrum and by the spin projection is used to investigate the conductivity of a multilayer sample (alternating layers of magnetic (*m*) and nonmagnetic (*n*) metals). The boundary conditions on the interlayer surfaces are derived in an approximation in which the surface scattering is divided into "specular" and "diffuse" scattering and is characterized by scattering parameters (reflection and transmission) which are related to each other by relations dependent on spin projections and on the type of spectrum. The problem on the longitudinal (with respect to the layers) current is treated; situations are analyzed in which the variation in conductivity due to the change of mutual orientation of magnetization in successive *m* layers from antiparallel to parallel may be of the order of the values of the conductivity proper (the so-called giant magnetoresistance effect). This is possible only in the case of thin (compared with the free path) *n* layers (in *m* layers, the ratios of the characteristic dimensions may be arbitrary) and in the mandatory presence of specular surface scattering. Results are given for different possible ratios of Fermi momenta of electron groups and for different fractions of specular and diffuse scattering. The possibility of realizing the effects of both signs is demonstrated. © *2002 MAIK "Nauka/Interperiodica".*

1. INTRODUCTION

The problem of electron transport in laminated conductors has been attracting particular interest in the last decade in view of studies into the so-called giant negative magnetoresistance (GNMR) effect. This effect involves a marked decrease in the electric resistance under the effect of relatively weak magnetic fields (the characteristic magnitude of relative variation of resistance may be as high as tens of percent in fields of up to several kilooersteds). The GNMR effect is realized in systems of alternating layers of ferromagnetic (*m* layers) and nonmagnetic (*n* layers) metals; the drop of resistance occurs during the change of orientation of magnetizations in successive *m* layers from the initial antiparallel (AP) to parallel (P) orientation, this change being due to the effect of an external magnetic field (which is weaker than the field exhibiting galvanomagnetic effects in uniform samples of the metals of which the multilayer systems are made up). The first experiments into the GNMR were reported in [1, 2]; tens of publications a year have been made since then; reviews of relevant studies are found in [3–6]. To date, numerous experimental investigations have been performed using different multilayer samples. Numerous theoretical publications are devoted to revealing the mechanisms of the GNMR effect.

In a number of theoretical papers, this phenomenon was analyzed (according to the terminology of their authors) "from the first principles" [7–12]. These studies involved the simulation of the electronic structure of a multilayer sample for concrete cases of packing of monatomic planes into layers with different structures of the transition regions between *n* and *m* layers, for defects of different types and their arrangement in the bulk and on the surfaces, and so on. In this manner, a number of features of electron states were revealed for concrete structures made up of thin (several atomic planes) layers, in particular, the emergence of specific electron modes localized at the interfaces, sensitive to the type of magnetic ordering, and capable of manifesting themselves in electron transport and causing a drop of resistance upon transition from the AP to P order, i.e., as in the case of the GNMR effect. However, investigations of this kind (based on selecting models, followed by verification using numerical methods) can hardly reveal the general physical pattern of the GNMR effect. For example, the situation involving thicker layers (tens of or more interatomic spacings) and very frequently observed in experiments calls for different treatment: in this case, the surface modes cannot make a determining contribution to the processes of electron transport, so that their variation is incapable of providing for a "giant" variation in the electric resistance.

Another approach appears to be promising, which is not based on revealing the special features of quantum electron states in the case of multilayer packing of unlike atoms, but utilizes an ordinary quasi-classical description of delocalized electrons involving the spectral properties of the "parent" *n* and *m* metals of which the layers are made up. In this case, the characteristics of interlayer interactions, which bring about AP ordering in the absence of an external magnetic field, are not

treated: it is assumed that these interactions do not play an important part in the formation of transport properties (this assumption is justified, in particular, by the realizations of the GNMR effect on the so-called spin valves, i.e., structures in which both the AP and P polarizations of layers are imposed from without [11, 13, 14]). In studies based on this approach, the conductivity of the system is calculated using either the Green function formalism [15–18] or kinetic equations [19–24]; in a quasi-classical approximation, these procedures are equivalent [25]. When the Boltzmann formalism is used, the transition regions between layers are approximated by the interfaces on which the boundary conditions that relate the values of the electron distribution functions in neighboring layers with one another must be valid on both sides of the boundary.

A number of theoretical studies performed within the foregoing concepts produced results which were used to estimate the variation of the resistance in concrete structures (Co/Cu, Fe/Cr, and so on [9, 11, 17, 22, 26]); the fitting of correlations between the determining parameters made it possible to reveal options leading to agreement with experiment. In our opinion, however, the theoretical analysis was inconsistent and incomplete and, in a number of cases, incorrect. Serious comments need to be made in relation to the approximations used in formulating the boundary conditions. The problem of boundary conditions on the interface still attracts the theorists' attention, especially, in the case of the current normal to the layers. In studies in the field under consideration, these conditions are usually formulated by analogy with the known approximations of Fuchs [27] and Sondheimer [28], i.e., with the processes of surface scattering divided into "specular" (retaining the longitudinal momentum) and "diffuse" (fully isotropic scattering) processes and with the introduction of "specular reflection" and "diffusion" coefficients corresponding to the fractions of electron flow normal to the surface and scattered on the latter; in addition to the reflection parameters of Fuchs, parameters are introduced which characterize the penetration of electrons through interfaces.

Such an approximation simplifies considerably the theoretical treatment of the problem on the formation of conductivity with due regard for scattering by interlayer surfaces and, in principle, may enable one to determine the mechanisms of its "giant" variation during the change of the pattern of the distribution of magnetizations over layers. In this case, it is important to correctly include the correlations between the coefficients of transitions (from the *m* layers to *n* layers and back). The values of these parameters are related by the principle of detailed balance (and the sets of these parameters must satisfy the normalization rules following from the conditions of conservation of normal flows), and their correlations are sensitive, in particular, to differences in the spectra of electrons of the *m* and *n* layers. This fact *per se* must cause the spin dependence of the parameters of transitions and, consequently, the possibility of the effect of the type of distribution of magnetization over layers on the conductivity of a multilayer system. However, in a number of studies, the coefficients of direct and reverse transitions were assumed to coincide with each other (and to do so in the entire range of variation of momenta [20, 24]); in some studies, this equality was associated with the diffuse parts, while simplified optical analogs were used for the specular parts [22, 29]. The contributions made to the scattering potentials by exchange or other spin-sensitive perturbations were invoked for interpreting the spin dependence of the scattering parameters (in particular, of the free paths) [21, 30]. These contributions may be appreciable (especially if the *s–d* interaction plays an important part); however, the densities of final states (to which the probabilities of transitions upon scattering are proportional) serve as spin-dependent factors along with the above-identified contributions (and, in numerous critical situations, predominantly): this fact must always be taken into account.

The above-identified studies lack analysis which would enable one to understand the physical mechanisms of the effect on the qualitative level: the relative importance of *n* and *m* electrons in the formation of orientationally dependent contributions to conductivity was not estimated; it was not found what the ratio of the specular and diffuse parts of surface scattering must be for the giant effect to be realized, what influence is made by bulk scattering, and which factors define the sign of the effect (the latter is important, in particular, in view of experimental discovery of positive magnetoresistance as well—the so-called inverse effect of giant magnetoresistance [31–35]).

This paper deals with the theoretical analysis of the problem under consideration associated with singularities of propagation of current in a sample made up of metal *n* and *m* layers, i.e., in a conductor that is nonuniform as regards both the material and the distribution of magnetization orientation. The mechanisms peculiar to ferromagnetics, which affect the magnetoresistance (for example, manifestations of magnetopolaron coupling [36], scattering by magnetization fluctuations [37], etc.), are not included (for marked involvement of such processes, external fields are required that are much higher than those at which the giant magnetoresistance effect is realized). A set of kinetic equations is used to describe the electron behavior. The derivation of the boundary conditions for the distribution functions of layers on interfaces is suggested, as well as the approximation of these relations using the generalized Fuchs–Sondheimer parameters expressed in terms of surface scattering probabilities. The problem on longitudinal current is analyzed. A study is made into the dependence of the variation of electric conductivity on the parameters defining the properties of carriers in the *n* and *m* layers, and the factors are revealed on which the magnitude and sign of the effect depend.

2. PROBLEM EQUATIONS

Following is the kinetic equation for the distribution function component $f_p^s(z)$ describing electrons of momentum $\mathbf{p}$, energy ε_p^s, and spin projection s (the z axis is directed on a normal to the layers, and $s = \pm 1$ indicates the sign of spin projection onto the quantization axis):

$$\frac{\partial \varepsilon_p^s}{\partial p_z}\frac{\partial f_p^s}{\partial z} - \nabla(e\varphi + \varepsilon_p^s)\frac{\partial f_p^s}{\partial \mathbf{p}} = \mathrm{St}^s(f). \tag{2.1}$$

Here, φ is the potential of the current-exciting external field, and $\mathrm{St}^s(f)$ is the collision integral. The expression for $\mathrm{St}(f)$ must include both the contributions due to collisions in the bulk of layers with fairly uniformly distributed scatterers and the contributions due to electronic transitions caused by the effect of the intermediate region between adjacent layer structures and by defects localized in this gap. The observed nonuniformity of scatterers manifests itself as the coordinate dependence of the transition probabilities appearing in the expression for $\mathrm{St}(f)$ as a result of their proportionality to the concentrations of the respective scattering centers (for the case of laminated system being treated, the transition from the Dyson equations to kinetic equations with coordinate-dependent collision terms was demonstrated in [23]).

In the case when the thicknesses of the transition regions are much less than those of the layers, one can restrict oneself to solving Eqs. (2.1) within the layers, while retaining in the collision integrals only the parts responsible for intrabulk scattering. As to the presence and effect of boundary regions, they will be expressed by relations relating the distribution functions in neighboring layers with one another; it is these relations, defined by the form of Eqs. (2.1) and by the surface parts of the collision integral $\mathrm{St}(f)$, that are the boundary conditions which must be valid on the interfaces. The derivation of such relations and their simplified form are given in Appendix A.

We will now turn to concretely defining the problem within the layers and agree to use the subscripts j to indicate the nonmagnetic layers n_j and the magnetic layers m_j. For definiteness, we will assume that the external surfaces of a sample are n layers and will denote a sequence of three layers as n_{j-1}, m_j, n_j, with $j = 1, \ldots, K$. We will further assume that the layer thickness is the same for each sort and equal to d_n, d_m, so that the total sample thickness is

$$D = D_m + D_n, \quad D_m = Kd_m, \quad D_n = (K+1)d_n. \tag{2.2}$$

In what follows, we will restrict ourselves to a simple parabolic spectrum of carriers and will use in the n layers

$$\varepsilon_{n_j p}^s = \varepsilon_{np} = \frac{p^2}{2m_n} + \varepsilon_n, \quad \varepsilon_n = \varepsilon_{n0} + e\varphi_0 \tag{2.3}$$

and in the m-layers

$$\varepsilon_{m_j p}^s = \frac{p^2}{2m_m} + \varepsilon_m - \Omega_j s, \qquad \varepsilon_m = \varepsilon_{m0} + e\varphi_0, \quad \Omega_j = \frac{1}{2}\mu_0 H_j. \tag{2.4}$$

Here, the origins for spectra in massive n and m samples, ε_{n0} and ε_{m0}, are identified. In Eq. (2.4), the presence of magnetization is expressed in the form of Zeeman spin energy in the internal magnetic field H_j (μ_0 denotes the product of the Bohr magneton and the g factor); it is assumed that the directions of magnetization in the layers are collinear, so that, in the case of P packing, all values of H_{m_j} are identical, and, in the case of AP packing, H_{m_j} changes its sign when the subscript j is changed by unity. The expressions for energy include the potential $\varphi_0(z)$ arising as a result of redistribution of the electron densities (initially related to the chemical potentials μ_n and μ_m of isolated materials) when the layers are combined in a single sample of total chemical potential μ. The Poisson equation with the uncompensated charge density defined by the difference of local electron concentrations between a multilayer system and initial materials readily yields the following expressions for φ_0:

$$\varphi_0(z) = \varphi_{0n} + (\varphi_{0m} - \varphi_{0n})\frac{2R_n^D}{R_n^D + R_m^D} \times \exp\left(-\frac{d_n}{2R_n^D}\right)\cosh\frac{z - \bar{z}_j}{R_n^D},$$
$$\varphi_0(z) = \varphi_{0m} + (\varphi_{0n} - \varphi_{0m})\frac{2R_m^D}{R_n^D + R_m^D} \times \exp\left(-\frac{d_m}{2R_m^D}\right)\cosh\frac{z - \bar{z}_j}{R_m^D} \tag{2.5}$$

for the n and m layers, respectively ($\bar{z}_j$ denotes the middles of the respective layers). In the end layers (for definiteness, here and below, we will assume them to be nonmagnetic), we have

$$\varphi_0(z) = \varphi_{0n} + 2R_n^D\frac{\varphi_{0m} - \varphi_{0n}}{R_n^D + R_m^D}\exp\left(-\frac{d_n}{R_n^D}\right) \times \begin{cases} \cosh(z/R_n^D), & z \geq 0, \\ \cosh[(z-D)/R_n^D], & z \leq D. \end{cases} \tag{2.6}$$

In Eq. (2.6), $R^D_{n,m}$ denotes the Debye screening radii in the layers; it is assumed that $d_{n,m} \gg R^D_{n,m}$. The quantity $e\varphi_{0,j} \approx \mu_{0j} - \mu$; i.e., it is equal to the difference between the electron work function of the material of a separate isolated layer and that of a unified multilayer sample.

We will write the electron distribution function in an arbitrary layer $i = (n_j, m_j)$ in the regular form,

$$f^s_i = f^s_{0i} + \frac{\partial f^s_{0i}}{\partial \varepsilon^s_{ip}} \chi^s_i, \tag{2.7}$$

where $f^s_{0i} = f_0(\varepsilon^s_{ip} - \mu)$ is the equilibrium Fermi function (the system is taken to be degenerate, so that we assume in what follows that $\partial f^s_{0i}/\partial \varepsilon^s_{ip} = -\delta(\mu - \varepsilon^s_{ip})$. In the linearized equation for the nonequilibrium addition $\chi^s_i(\mathbf{p})$, we will restrict ourselves to writing the collision integral (its volume part) in terms of the relaxation times,

$$v_z \frac{\partial \chi^s_i}{\partial z} + \frac{\chi^s_i - \bar{\chi}^s_i}{\tau^s_{si}} + \frac{\chi^s_i - \bar{\chi}^{-s}_i}{\tau^s_{-si}} = e\mathbf{v} \cdot \nabla\varphi, \tag{2.8}$$

where $\bar{\mathbf{v}}$ is the electron velocity, and the notation

$$\bar{F}^s_i = \frac{\langle F^s_i \rangle^s_i}{\langle 1 \rangle^s_i}, \quad \langle F^s_i \rangle^s_i = -\int \frac{d^3p}{(2\pi\hbar)^3} F^s_i(p) \frac{\partial f^s_{0i}}{\partial \varepsilon^s_{ip}},$$
$$\langle 1 \rangle^s_i = \frac{m^{3/2}(\mu - \varepsilon^s_i)^{1/2}}{\sqrt{2}\pi^2\hbar^3} = \nu^s_{iF} \tag{2.9}$$

is introduced. In the expression for the partial density of states at the Fermi level, $\nu^s_{iF} = \nu^s_i(\mu)$; ε^s_i in the case of $i = n_j$ must be given by ε_n from Eq. (2.3), and, in the case of $i = m_j$, by the set $\varepsilon_m - s\Omega_j$ from Eq. (2.4). We will introduce the notation convenient for further use,

$$p_{si} = p_i\sqrt{\Gamma_{si}}, \quad p_i = \sqrt{2m_i(\mu - \varepsilon_i)},$$
$$\Gamma_{si} = 1 + s\frac{\Omega_i}{\mu - \varepsilon_m}. \tag{2.10}$$

For $i = n_j$, the quantity $p_{si} = p_n$ is the Fermi momentum of n electrons; in the case of $i = m_j$, Fermi momenta of separate s groups arise. The parameter Γ_{sj} (important for further analysis) characterizes the differences between the energy shifts of s groups, which are observed for m electrons alone (for n electrons, $\Gamma_{sn} = 1$). When Eqs. (2.10) are used, the expressions for electron momenta on a Fermi sphere (i.e., at $\varepsilon^s_i = \mu$) and for the densities of states take the form

$$p^2 = p_z^2 + p_\parallel^2 = p^2_{si}, \quad \nu^s_{iF} = \frac{p_{si}m_i}{2\pi^2\hbar^3}, \tag{2.11}$$

where $\mathbf{p}_\parallel$ is the electron momentum component parallel to the layer surfaces.

In writing the volume collision integral, Eq. (2.8) takes into account the possibility of emergence of nonequilibrium variations of carrier concentration, as expressed by the terms $\bar{\chi}^s_i$. In the problem being treated, the redistribution of the concentrations between groups of s electrons must be taken into account in analyzing the current transverse with respect to the layers.

Equation (2.8) includes a set of relaxation times: τ^s_{si} corresponds to scattering with conservation of spin projection, and τ^s_{-si}, to scattering with spin flip. Here and in what follows, the superscripts indicate the initial state, and the subscripts indicate the final state. The times of flip transitions, τ^s_{-s} and τ^{-s}_s, are related by the condition of cancellation of the total collision integral, $\sum_s \langle \mathrm{St}^s(f) \rangle^s = 0$, which defines their correlation in accordance with the principle of detailed balance,

$$\frac{\nu^s_F}{\tau^s_{-s}} = \frac{\nu^{-s}_F}{\tau^{-s}_s}. \tag{2.12}$$

For further discussion, it is important to have information about the dependence of the relaxation times on the spin index s. We will restrict ourselves to the situation in which the mechanisms of bulk scattering are dominated by elastic scattering by point defects (δ-like interaction potential). The general expression for the relaxation frequency must include the density of final states at the level of chemical potential, ν^s_i in Eq. (2.11), which contains the dependence on s for m electrons. Other reasons for the emergence of the spin dependence of relaxation frequency may be associated only with the involvement of spin-dependent potentials in the scattering. The simplest (and most realistic) case is that of scattering by defects with a potential in the form of the sum of two parts, of which one contains spin operators [21, 30, 38]. In this case, it is necessary that the linear contribution made by the spin part to the total scattering cross section would not be canceled upon averaging over the set of defects of a given type; this is, in principle, feasible in the m material, in which the sign of spin addition in the scattering potential may be fixed by the internal magnetic field. In order to take into account the foregoing cases, it is convenient to perform the following redesignation of the relaxation times:

$$\frac{1}{\tau^s_{si}} = \frac{\sqrt{\Gamma_{si}}}{\tau_{si}}, \quad \frac{1}{\tau^s_{-si}} = \frac{\sqrt{\Gamma_{-si}}}{\tau_{fi}}. \tag{2.13}$$

Here, the pattern of the s dependence associated with the density of final states is clearly identified, and the "nominal" times τ_{si} and τ_{fi} are introduced. In the case

described above, the s dependence of the nominal time τ_{si} is possible only in the m layers. As to scattering with a change of spin, τ_{fi} is insensitive to the index s by virtue of relations (2.12).

The boundary conditions on the surface between the layers are formulated in Appendix A.

3. LONGITUDINAL CURRENT: GENERAL EXPRESSIONS

We will treat the problem on the electron kinetics in a laminated system in the presence of a potential difference applied along the layers, i.e., under the effect of a uniform electric field $E_x = -\partial\varphi/\partial x$ directed along the x axis. By virtue of the inference about the proportionality of the nonequilibrium parts of the distribution functions χ_i^s to the velocity component v_x (which is obvious for this geometry), the terms with nonequilibrium concentrations drop out from kinetic equations (2.8), so that the equations are simplified,

$$v_z\frac{\partial\chi_i^s}{\partial z} + \frac{\chi_i^s}{\tilde\tau_{si}} = -eE_x v_x, \tag{3.1}$$

where

$$\frac{1}{\tilde\tau_{si}} = \frac{\sqrt{\Gamma_{si}}}{\tau_{si}} + \frac{\sqrt{\Gamma_{-si}}}{\tau_{fi}} \tag{3.2}$$

(relations (2.13) are used). We will write the solutions of (3.1) in the m_j layer and in the adjoining n_j layer (the left-hand and right-hand boundaries of the m_j layer are $z_{m_j}^l = z_{n_{j-1}}^r$ and $z_{m_j}^r = z_{n_j}^l$, respectively),

$$\chi_{m_j}^{s>} = -eE_x v_x\tilde\tau_{sm_j}\times\left[1-(1-\alpha_{m_j}^s)\exp\left(-\frac{z-z_{m_j}^l}{v_z\tilde\tau_{sm_j}}\right)\right],\quad v_z\geq 0,$$
$$\chi_{m_j}^{s<} = -eE_x v_x\tilde\tau_{sm_j}\times\left[1-(1-\beta_{m_j}^s)\exp\left(-\frac{z-z_{m_j}^r}{v_z\tilde\tau_{sm_j}}\right)\right],\quad v_z\leq 0, \tag{3.3}$$

$$\chi_{n_j}^{s>} = -eE_x v_x\tilde\tau_n\times\left[1-(1-\alpha_{n_j}^s)\exp\left(-\frac{z-z_{n_j}^l}{v_z\tilde\tau_n}\right)\right],\quad v_z\geq 0,$$
$$\chi_{n_j}^{s<} = -eE_x v_x\tilde\tau_n\times\left[1-(1-\beta_{n_j}^s)\exp\left(-\frac{z-z_{n_j}^r}{v_z\tilde\tau_n}\right)\right],\quad v_z\leq 0. \tag{3.4}$$

The formulas for χ on other boundaries differ from those written above by the layer indices. Expressions (3.3) and (3.4) are written so that the values of $\chi^>$ ($\chi^<$) on the left-hand (right-hand) boundary of the layer are proportional to the parameters α (β) in terms of which the effect of scattering on the left-hand (right-hand) interface on the electron distribution is expressed. The values of the parameters α and β must be found from the boundary conditions given by Eq. (A.12). On the surfaces separating the m_j layer from the neighboring n layers, these conditions take the form (for both sides of the respective interfaces)

$$\begin{aligned}
&\beta_{n_{j-1}}^s - \sum_{s'}\left[\alpha_{n_{j-1}}^{s'}R_{s(r)}^{s'n_{j-1}}(p) + \frac{\beta_{m_j}^{s'}}{\kappa_{s'j}}T_{sn_{j-1}}^{s'm_j}(p)\right]\\
&\quad = \sum_{s'}\left[\hat g_n r_{sc(r)}^{s'n_{j-1}p} + \frac{\hat g_{m_j}^{s'}}{\kappa_{s'j}}t_{sn_{j-1}c}^{s'm_jp}\right],\\
&\frac{\alpha_{m_j}^s}{\kappa_{sj}} - \sum_{s'}\left[\frac{\beta_{m_j}^{s'}}{\kappa_{s'j}}R_{s(l)}^{s'm_j}(p) + \alpha_{n_{j-1}}^{s'}T_{sm_j}^{s'n_{j-1}}(p)\right]\\
&\quad = \sum_{s'}\left[\frac{\hat g_{m_j}^{s'}}{\kappa_{s'j}}r_{sc(l)}^{s'm_jp} + \hat g_n t_{sm_jc}^{s'n_{j-1}p}\right],\\
&\frac{\beta_{m_j}^s}{\kappa_{sj}} - \sum_{s'}\left[\frac{\alpha_{m_j}^{s'}}{\kappa_{s'j}}R_{s(r)}^{s'm_j}(p) + \beta_{n_j}^{s'}T_{sm_j}^{s'n_j}(p)\right]\\
&\quad = \sum_{s'}\left[\frac{\hat g_{m_j}^{s'}}{\kappa_{s'j}}r_{sc(r)}^{s'm_jp} + \hat g_n t_{sm_jc}^{s'n_jp}\right],\\
&\alpha_{n_j}^s - \sum_{s'}\left[\beta_{n_j}^{s'}R_{s(l)}^{s'n_j}(p) + \frac{\alpha_{m_j}^{s'}}{\kappa_{s'j}}T_{sn_j}^{s'm_j}(p)\right]\\
&\quad = \sum_{s'}\left[\hat g_n r_{sc(l)}^{s'n_jp} + \frac{\hat g_{m_j}^{s'}}{\kappa_{s'j}}t_{sn_jc}^{s'm_jp}\right].
\end{aligned} \tag{3.5}$$

Here,

$$\begin{aligned}
&\hat g_n = 1-\exp\left(-\frac{d_n}{\tilde\tau_n\hat v_{zn}}\right),\\
&\hat g_{m_j}^s = 1-\exp\left(-\frac{d_m}{\tilde\tau_{sm_j}\hat v_{zm}}\right),\\
&\hat v_{zn} = \frac{\sqrt{p_n^2-p_l^2}}{m_n},\quad \hat v_{zm} = \frac{\sqrt{p_{sm}^2-p_l^2}}{m_m},\\
&\kappa_{sj} = \frac{m_m\tilde\tau_n}{m_n\tilde\tau_{sm_j}} = \frac{M_n}{M_{m_j}^s}.
\end{aligned} \tag{3.6}$$

The definitions given by Eqs. (3.6) imply restrictions on the ranges of variation of the longitudinal momentum that are dictated by the specular parameters t and r in Eqs. (A.9), which appear in Eqs. (3.5) along with the quantities g. Further,

$$\begin{aligned} R_s^{s'n_j}(p) &= r_{sc}^{s'n_jp}(1-\hat{g}_n), \\ R_s^{s'm_j}(p) &= r_{sc}^{s'm_jp}(1-\hat{g}_{m_j}^{s'}), \\ T_{sm_j}^{s'n_j}(p) &= t_{sm_jc}^{s'n_jp}(1-\hat{g}_n), \\ T_{sn_j}^{s'm_j} &= t_{sn_jc}^{s'm_jp}(1-\hat{g}_{m_j}^{s'}). \end{aligned} \tag{3.7}$$

The subscripts (r) and (l) in Eqs. (3.5) indicate the surfaces of the respective layer, i.e., right-hand or left-hand, to which the reflection coefficients belong. No contributions by the diffuse parts of expression (A.12) are present in Eqs. (3.5): in the problem on longitudinal current, at $\chi \propto v_x$, these contributions are zero. Note that the parameters α and β depend on the specular components of surface scattering alone, so that, in the absence of specular scattering, in accordance with Eqs. (3.5), every $\alpha = \beta = 0$. When canceling in the boundary relations the velocities v_x appearing in formulas (3.3) and (3.4) for χ, we take into account the condition of conservation of longitudinal momentum during specular transitions. As a result, the parameters κ_{sj} appear in Eqs. (3.5), which are equal to the ratios of electron mobilities in the n and m layers, M_n and $M_{m_j}^s$.

The expression for the s component of the current density in the m_j layer (for $z_{lj} \le z \le z_{rj}$) has the form

$$J_{m_j}^s(z) = -e\langle v_x \chi_{m_j}^s \rangle = \sigma_{m_j}^s(z) E_x, \tag{3.8}$$

where

$$\begin{aligned} \sigma_{m_j}^s(z) = \sigma_{0m_j}^s \Bigg\{ 1 - \frac{3}{4p_{sm_j}^3} \int_0^{p_{sm_j}} dp_z (p_{sm_j}^2 - p_z^2) \\ \times \Bigg[(1-\alpha_{m_j}^s) \exp\left(-\frac{z-z_{il}}{v_z \tilde{\tau}_{sm_j}} \right) \\ + (1-\beta_{m_j}^s) \exp\left(-\frac{z_{jr}-z}{v_z \tilde{\tau}_{sm_j}} \right) \Bigg] \Bigg\}, \end{aligned} \tag{3.9}$$

and the notation

$$\sigma_{0m_j}^s = \frac{e^2 \tilde{\tau}_{sm_j} n_{m_j}^s}{m_m}, \quad n_{m_j}^s = \frac{p_{sm_j}^3}{6\pi^2} \tag{3.10}$$

is introduced for the partial conductivity of a group of m electrons with spin projection s, which would characterize a massive sample in the case of partial concentration $n_{m_j}^s$. The total current density at point z of the m_j layer is found by summation of (3.8) with respect to s. The formula for the current density in the n_j layer differs from expressions (3.8) and (3.9) by the change of indices (in so doing, $\Gamma_{sn} = 1$). In order to characterize the entire sample, we will use, as usual, the average current density and, accordingly, the conductivity σ averaged over the entire sample thickness D,

$$\sigma = \frac{1}{D} \int_0^D dz \sum_s \sigma_i^s(z) = \sigma_{bd} + \sigma_c. \tag{3.11}$$

Two components of average conductivity are identified in Eq. (3.11). The first of these components, σ_{bd}, is formed by the contributions from (3.9) in the absence of α and β and corresponds to the value of the conductivity of a multilayer sample under conditions of fully diffuse surface scattering. The quantity σ_{bd} is written in the form of the difference

$$\sigma_{bd} = \sigma_b - \sigma_d, \tag{3.12}$$

where σ_b is made up of the conductivities of massive materials,

$$\begin{aligned} \sigma_b &= \sigma_{bn} + \sigma_{bm}, \quad \sigma_{bn} = \frac{D_n}{D}\sigma_{0n}, \\ \sigma_{bm} &= \frac{D_m}{D}\sigma_{0m}, \quad \sigma_{0n,m} = \sum_s \sigma_{0n,m}^s, \end{aligned} \tag{3.13}$$

and σ_d describes the reduction of the bulk conductivity, which would be performed under conditions of fully diffuse surface scattering reducing the bulk free paths to appropriate effective values,

$$\begin{aligned} \sigma_d &= \sigma_d(n) + \sigma_d(m), \\ \sigma_d(n) &= \frac{3D_n}{2D} \sum_s \sigma_{0n}^s Y_n\left(\frac{u_n g_n \tilde{l}_n}{d_n} \right), \\ \sigma_d(m) &= \frac{3D_m}{2D} \sum_s \sigma_{0m}^s Y_m\left(\frac{u_m g_m^s \tilde{l}_m}{d_m} \right). \end{aligned} \tag{3.14}$$

Here,

$$\begin{aligned} Y_i(x_i) &= \int_0^1 du_i (1-u_i^2) x_i, \\ u_i &= \frac{p_z}{p_{si}}, \quad g_i = 1 - \exp\left(-\frac{d_i}{u_i \tilde{l}_i} \right), \\ \tilde{l}_i &= v_{si}\tilde{\tau}_i, \quad v_{si} = \frac{p_{si}}{m_i} \end{aligned} \tag{3.15}$$

($\tilde{l}$ denotes the free paths, and the relaxation times $\tilde{\tau}$ are introduced in Eq. (3.2)). The summation with respect to

s of expressions dependent only on the local properties of a given (*n* or *m*) layer, which appears in Eqs. (3.13) and (3.14), points to the absence of interlayer correlations in σ_{bd} and, consequently, to the independence of this part of conductivity given by Eq. (3.11) of the type of magnetic order in the sample.

The second component of average conductivity given by Eq. (3.11), σ_c is defined by the "specular" transitions on the layer interfaces,

$$\sigma_c = \sigma_c(m) + \sigma_c(n), \tag{3.16}$$

where

$$\sigma_c(n) = \frac{3}{4D}\sum_s\sum_{j=0}^{K}\tilde{l}_n\sigma_{0n}^s Y_n[u_n g_n(\alpha_{n_j}^s + \beta_{n_j}^s)],$$

$$\sigma_c(m) = \frac{3}{4D} \tag{3.17}$$

$$\times\sum_s\sum_{j=1}^{K}\tilde{l}_{sm_j}\sigma_{0m}^s Y_{m_j}^s[u_{m_j} g_{m_j}^s(\alpha_{m_j}^s + \beta_{m_j}^s)].$$

The part played by contributions to the conductivity due to specular scattering usually consists in compensating for the above-mentioned diffuse reduction associated with σ_d from Eq. (3.12); the degree of this compensation depends on the values of the parameters α and β defined by the boundary conditions given by Eqs. (3.5). Of chief interest in our case is the dependence of the "specular" corrections of σ_c on the pattern of ordering of magnetic layers; it is this dependence that must define the scale of corresponding variations of conductivity.

We will analyze expressions for σ_c in the P and AP configurations. Assume that the structure of all boundaries between the *n* and *m* layers is the same, so that the nonequivalence of their scattering properties may be due only to the differences in the orientation of magnetizations of the *m* layers adjoining the interfaces. Therefore, the parameters of penetration *t* and reflection *r* on different boundaries must be related by certain relations. Consider the case of parallel polarization of all *m* layers (P packing), when the following obvious equalities must be valid:

$$\begin{aligned}
\Gamma_{sm_j} &= \Gamma_{sm_{j\pm1}} \equiv \Gamma_s,\\
\tilde{l}_{sm_j} &= \tilde{l}_{sm_{j\pm1}} \equiv \tilde{l}_{sm}, \quad \kappa_{sj} \equiv \kappa_s,\\
r_{s(r)}^{s'n_j p} &= r_{s(l)}^{s'n_j p} = r_{s(r,\,l)}^{s'n_{j\pm1}p} \equiv r_s^{s'np},\\
t_{sm_j}^{s'n_j p} &= t_{sm_j}^{s'n_{j-1}p} = t_{sm_{j+1}}^{s'n_j p} \equiv t_{sm}^{s'np},\\
r_{s(r)}^{s'm_i p} &= r_{s(l)}^{s'm_j p} = r_{s(r,\,l)}^{s'm_{j\pm1}p} \equiv r_s^{s'mp},\\
t_{sn_{j-1}}^{s'm_j p} &= t_{sn_j}^{s'm_j p} = t_{sn_j}^{s'm_{j+1}p} \equiv t_{sn}^{s'mp}.
\end{aligned} \tag{3.18}$$

The exception is provided by the external surfaces of the n_0th and n_Kth layers; for these layers, it should be assumed that $t = 0$ and $r_{s(l)}^{s'n_0} = r_{s(r)}^{s'n_K} \equiv r_{s0}^{s'}$.

By virtue of relations (3.18), the set of equations (3.5) breaks down into sets of pairs of equations with identical coefficients at α and β and identical right-hand parts except for the equations which contain the external surface parameters r_0. If not for this exception, the set of linking equations for α and β would have been reduced to equations for two neighboring layers with simple correlations of $\alpha_{n_j}^s = \beta_{n_j}^s$ and $\alpha_{m_j}^s = \beta_{m_j}^s$. As a result of the presence of external boundaries, the equality of the parameters α and β is disturbed; the difference between these parameters must depend on the layer number and will apparently be the smaller, the larger the distance from the layers to the sample surfaces. We will represent the sought parameters in the form

$$\begin{aligned}
\alpha_{n_j}^s &= A_n^s + a_{n_j}^s, \quad \beta_{n_j}^s = A_n^s + b_{n_j}^s,\\
\alpha_{m_j}^s &= A_m^s + a_{m_j}^s, \quad \beta_{m_j}^s = A_m^s + b_{m_j}^s,
\end{aligned} \tag{3.19}$$

and use the set of equations (3.5), given the validity of relations (3.18), to derive the following equations for the quantities A:

$$\begin{aligned}
A_n^s - \sum_{s'}[R_s^{s'n}(p)A_n^{s'} + T_{sn}^{s'm}(p)A_m^{s'}/\kappa_{s'}] &= \sum_{s'}[r_{sc}^{s'np}\hat{g}_n + t_{snc}^{s'mp}\hat{g}_m^{s'}/\kappa_{s'}],\\
A_m^s/\kappa_s - \sum_{s'}[R_s^{s'm}(p)A_m^{s'}/\kappa_{s'} + T_{sm}^{s'n}(p)A_n^{s'}] &= \sum_{s'}[r_{sc}^{s'mp}\hat{g}_m^{s'}/\kappa_{s'} + t_{smc}^{s'np}\hat{g}_n].
\end{aligned} \tag{3.20}$$

For the quantities *a* and *b*, we have, for the external left-hand layer,

$$\begin{aligned}
a_{n_0}^s - \sum_{s'}R_{s0}^{s'n}(p)b_{n_0}^{s'} &= \sum_{s'}[r_{sc0}^{s'np}\hat{g}_n + R_{s0}^{s'n}(p)A_n^{s'}] - A_n^s,\\
b_{n_0}^s - \sum_{s'}[R_s^{s'n}(p)a_{n_0}^{s'} + T_{sn}^{s'm}(p)b_{m_1}^{s'}/\kappa_{s'}] &= 0;
\end{aligned} \tag{3.21}$$

for the internal layers,

$$a^s_{m_j}/\kappa_s - \sum_{s'}[R^{s'm}_s(p)b^{s'}_{m_j}/\kappa'_s + T^{s'n}_{sm}(p)a^{s'}_{n_{j-1}}] = 0,$$

$$b^s_{m_i}/\kappa_s - \sum_{s'}[R^{s'm}_s(p)a^{s'}_{m_j}/\kappa_{s'} + T^{s'n}_{sm}(p)b^{s'}_{n_j}] = 0,$$

$$a^s_{n_j} - \sum_{s'}[R^{s'n}_s(p)b^{s'}_{n_j} + T^{s'm}_{sn}(p)a^{s'}_{m_j}/\kappa_{s'}] = 0, \tag{3.22}$$

$$b^s_{n_j} - \sum_{s'}[R^{s'n}_s(p)a^{s'}_{n_j} + T^{s'm}_{sn}(p)b^{s'}_{m_{j+1}}/\kappa_{s'}] = 0,$$

$$1 \le j \le K-1;$$

and for the external right-hand layer,

$$a^s_{n_K} - \sum_{s'}[R^{s'n}_s(p)b^{s'}_{n_K} + T^{s'm}_{sn}(p)a^{s'}_{m_K}/\kappa_{s'}] = 0,$$

$$b^s_{n_K} - \sum_{s'}R^{s'n}_s(p)a^{s'}_{n_K} = \sum_{s'}[r^{s'np}_{sc0}\hat{g}_n + R^{s'n}_{s0}(p)A^{s'}_n] - A^s_n. \tag{3.23}$$

The number of independent equations in the set of equations (3.22) is reduced when the symmetry relative to the middle of the multilayer sample is taken into account. For definiteness, we will restrict ourselves to the case where the $n_{k'}$ layer is the middle one (an even number of m layers, $k' = K/2$). In the case of P packing, obvious relations

$$a^s_{n_{k'}} = b^s_{n_{k'}}, \quad a^s_{n_j} = b^s_{n_{K-j}}, \quad a^s_{m_j} = b^s_{m_{K-j+1}} \tag{3.24}$$

must be valid, so that in Eqs. (3.22) it is sufficient to retain the equations up to the subscript $j = k'$, with the last one of the retained equations having the form

$$a^s_{n_{k'}} - \sum_{s'}[R^{s'n}_s(p)a^{s'}_{n_{k'}} + T^{s'm}_{sn}(p)a^{s'}_{m_{k'}}/\kappa_{s'}] = 0. \tag{3.25}$$

In the case of antiparallel polarization of neighboring m layers (AP packing), it is convenient to use in all layers the values of spin projections s relative to a single axis, namely, the same axis which was used when relations (3.18) were written in the case of P packing. We will use the subscript i to indicate the numbers of layers in which the directions of magnetization are the same as in the P layers; the $(i \pm 1)$ layers are polarized oppositely. We will express the parameters of the ith and $(i \pm 1)$th layers in terms of the same quantities which appear in Eqs. (3.18),

$$\begin{gathered}
\Gamma_{sm_i} = \Gamma_s, \quad \Gamma_{sm_{i\pm1}} = \Gamma_{-s}, \\
\tilde{l}_{sm_i} = \tilde{l}_{sm}, \quad \tilde{l}_{sm_{i\pm1}} = \tilde{l}_{-sm}, \\
\kappa_{s,\,i\pm1} = \kappa_{-s}, \quad \kappa_{s,\,i} = \kappa_s, \\
r^{s'n_ip}_{s(l)} = r^{s'n_{i-1}p}_{s(r)} = r^{-s'n_ip}_{-s(l)} = r^{-s'n_{i+1}p}_{-s(l)} = r^{s'np}_s, \\
t^{s'n_ip}_{sm_i} = t^{s'n_{i-1}p}_{sm_i} = t^{-s'n_ip}_{-sm_{i+1}} = t^{-s'n_{i+1}p}_{-sm_{i+1}} = t^{s'np}_{sm}, \\
r^{s'm_ip}_{s(l)} = r^{s'm_ip}_{s(r)} = r^{-s'm_{i\pm1}p}_{-s(l)} = r^{-s'm_{i\pm1}p}_{-s(l)} = r^{s'mp}_s, \\
t^{s'm_ip}_{sn_i} = t^{s'm_ip}_{sn_{i-1}} = t^{-s'm_{i+1}p}_{-sn_i} = t^{-s'm_{i+1}p}_{-sn_{i+1}} = t^{s'mp}_{sn}.
\end{gathered} \tag{3.26}$$

The quantities α and β may be conveniently represented as binomials of the following form:

$$\begin{gathered}
\alpha^s_{n_i} = A^s_{1n} + a^s_{1n_i}, \quad \beta^s_{n_i} = A^{-s}_{1n} + b^{-s}_{1n_i}, \\
\alpha^s_{n_{i\pm1}} = A^{-s}_{1n} + a^{-s}_{1n_{i\pm1}}, \quad \beta^s_{n_{i\pm1}} = A^s_{1n} + b^s_{1n_{i\pm1}}, \\
\alpha^s_{m_i} = A^s_{1m} + a^s_{1m_i}, \quad \beta^s_{m_i} = A^s_{1m} + b^s_{1m_i}, \\
\alpha^s_{m_{i\pm1}} = A^{-s}_{1m} + a^{-s}_{1m_{i\pm1}}, \quad \beta^s_{m_{i\pm1}} = A^{-s}_{1m} + b^{-s}_{1m_{i\pm1}}.
\end{gathered} \tag{3.27}$$

As follows from the set of equations (3.5) with relations (3.26), the equations for A_1, a_1, and b_1 are written similarly to Eqs. (3.20)–(3.23), with the quantities A, a, and b replaced by A_1, a_1, and b_1; in so doing, in the sums with respect to s', the quantities $A^{s'}_n$, $a^{s'}_n$, and $b^{s'}_n$ must be replaced by $A^{-s'}_{1n}$, $a^{-s'}_{1n}$, and $b^{-s'}_{1n}$; in the case of other replacements, the spin indices are retained. In the set of equations written in this manner, the subscript j indicates any layer (it is assumed that the magnetization in the m_1 layer is parallel to the magnetization observed in the case of P packing).

So, in order to calculate the contributions due to specular scattering to the conductivity σ_c given by Eq. (3.16), one must find the values of A, a, and b from Eqs. (3.20)–(3.23) for the P configuration and A_1, a_1, and b_1 from the respective equations for the AP configuration. The variation of the electric conductivity in the case of change of the type of configuration from P to AP orientation of magnetizations in successive m layers is determined using the difference parameters of the following form in formulas (3.17):

$$\begin{gathered}
\delta A^s_n = A^s_n - A^{-s}_{1n}, \quad \delta a^s_{n_j} = a^s_{n_j} - a^{-s}_{1n_j}, \\
\delta b^s_{n_j} = b^s_{n_j} - b^{-s}_{1n_j}
\end{gathered} \tag{3.28}$$

in n components and

$$\begin{gathered}
\delta A^s_m = A^s_m - A^s_{1m}, \quad \delta a^s_{m_j} = a^s_{m_j} - a^s_{1m_j}, \\
\delta b^s_{m_j} = b^s_{m_j} - b^s_{1m_j}
\end{gathered} \tag{3.29}$$

in m components. These difference quantities may be found from the following equations:

$$\begin{gathered}
\delta A^s_n - \sum_{s'}[R^{s'n}_s(p)\delta A^{s'}_n + T^{s'm}_{sn}(p)\delta A^{s'}_m/\kappa_{s'}] = A^{as}_{1n}, \\
\delta A^s_m/\kappa_s - \sum_{s'}[R^{s'm}_s(p)\delta A^{s'}_m/\kappa_{s'} + T^{s'n}_{sm}(p)\delta A^{s'}_n] = 0.
\end{gathered} \tag{3.30}$$

For δa and δb, we have,

for the external layer,

$$\delta a^s_{n_0} - \sum_{s'} R^{s'n}_{s0}(p)\delta b^{s'}_{n_0}$$

$$= \sum_{s'} R^{s'n}_{s0}(p)\delta A^{s'}_n - \delta A^s_n + A^{as}_{1n} + a^{as}_{1n_0}, \qquad (3.31a)$$

$$\delta b^s_{n_0} - \sum_{s'}[R^{s'n}_s(p)\delta a^{s'}_{n_0} + T^{s'm}_{sn}(p)\delta b^{s'}_{m_1}/\kappa_{s'}] = b^{as}_{1n_1};$$

for the intermediate layers,

$$\delta a^s_{n_i} - \sum_{s'}[R^{s'n}_s(p)\delta b^{s'}_{n_i} + T^{s'm}_{sn}(p)\delta a^{s'}_{m_i}/\kappa_{s'}] = a^{as}_{1n_i},$$

$$\delta b^s_{n_i} - \sum_{s'}[R^{s'n}_s(p)\delta b^{s'}_{n_i} + T^{s'm}_{sn}(p)\delta b^{s'}_{m_{i+1}}/\kappa_{s'}] = b^{as}_{1n_i}, \qquad (3.31b)$$

$$\delta a^s_{m_i}/\kappa_s - \sum_{s'}[R^{s'm}_s(p)\delta b^{s'}_{m_i}/\kappa_{s'} + T^{s'n}_{sm}(p)\delta a^{s'}_{n_{i-1}}] = 0,$$

$$\delta b^s_{m_i}/\kappa_s - \sum_{s'}[R^{s'm}_s(p)\delta a^{s'}_{m_i}/\kappa_{s'} + T^{s'n}_{sm}(p)\delta b^{s'}_{n_i}] = 0;$$

and for the central layer,

$$\delta a^s_{n_{k'}} - \sum_{s'}[R^{s'n}_s(p)\delta a^{s'}_{n_{k'}} + T^{s'm}_{sn}(p)\delta a^{s'}_{m_{k'}}/\kappa_{s'}] = a^{as}_{1n_{k'}}. \qquad (3.31c)$$

Here, the following notation is introduced for the difference of parameters characterized by the opposite values of spin projection:

$$F^{as} = F^s - F^{-s} \quad (F^a = F^+ - F^-). \qquad (3.32)$$

According to Eqs. (3.30) and (3.31), the parameters δA, δa, and δb depend on the differences between the surface corrections to the distribution functions of n electrons, A^{as}_{1n}, a^{as}_{1n}, and b^{as}_{1n}, and go to zero in their absence. These differences characterize the asymmetry of the scattering properties of the surfaces of an n layer surrounded by oppositely polarized m layers, which, in accordance with the physical pattern described in this paper, must define the effect of variation of conductivity in the case of the AP $\longrightarrow$ P reorientation.

4. ANALYSIS OF BOUNDARY RELATIONS

It is the objective of further analysis to reveal the conditions of realization of such values of boundary parameters at which the specular part of conductivity given by Eq. (3.16) and its variation in the case of the AP $\longrightarrow$ P reorientation make up a significant fraction of the total conductivity of the system σ given by Eq. (3.11). We will eliminate from treatment the situations in which this is *a priori* impossible. First of all, this is the case of "thick" layers defined by the inequalities

$$d_n \gg \tilde{l}_n, \quad d_m \gg \tilde{l}_m. \qquad (4.1)$$

When inequalities (4.1) are valid, both the diffuse, σ_d (3.14), and specular, σ_c (3.16), corrections are insignificant: the parameters $g_n \approx g_m \approx 1$ and the integrals $Y_n \sim Y_m \sim l/d$, so that the surface scattering causes the conductivity σ to vary by values on the order of $\sigma(l/d)$. Similarly, the case of thick n, but "thin" m, layers, when the conditions

$$d_n \ll \tilde{l}_n, \quad d_m \ll \tilde{l}_m \qquad (4.2)$$

are valid, appears to be unpromising. When conditions (4.2) are valid, marked "specular" contributions to the conductivity in the m layers are possible (with a minor variation in the n components); however, their differences for the cases of P and AP packings must be negligibly small. This follows from Eqs. (3.30) and (3.31), according to which the quantities δA^s_m, δa^s_m, and δb^s_m are proportional to the specular parameters T^n in Eqs. (3.7) that are exponentially small at $d_n \gg l_n$.

A substantially different situation arises when "thin" n layers are used, when the mutual (and combined) influence of the m layers (of arbitrary thickness) separated by these n layers is permissible. We will further analyze the possibilities associated with different options of such systems with a simplification of no fundamental importance, which, nevertheless, enables one to do away with excess awkwardness of computations and formulas, namely, under conditions of negligibly weak processes of scattering with variation of the spin state $s \longrightarrow -s$ (flip transitions). The conservation of spin projection during transitions between layers contributes to the manifestation of correlations in the behavior of electrons, which are due to the coincidence or difference in the magnetic order between neighboring layers, so that an analysis performed in the absence of flip processes must enable one to estimate the possible effect of maximal variation of conductivity. Further, strictly in order to simplify the analysis, we will restrict ourselves to treating the problem under the following conditions (which are of no fundamental importance): let the s dependence of the bulk relaxation frequencies $1/\tau^s_{is'}$ be related mainly to the density of final states, and let the contributions made by s-dependent potentials to scattering be less significant so that they may be omitted. Then, the "nominal" times τ_{si} in Eqs. (2.13) in both m and n-layers may be assumed to be independent of s, and the index s may be omitted from the notation. In so doing, the free paths given by Eqs. (3.15) also lose their

dependence on s, and the notation of a number of parameters is simplified,

$$\tilde{l}_{sm} = l_m = v_m\tau_m, \quad \tilde{l}_{sn} = l_n = v_n\tau_n,$$
$$\kappa_s = \kappa\sqrt{\Gamma_s}, \quad \kappa = \frac{l_n p_m}{l_m p_n},$$
$$\sigma^s_{0m_j} = \frac{1}{2}\sigma_{0m}\Gamma_{js}, \quad \sigma^s_{0n} = \frac{1}{2}\sigma_{0n}, \tag{4.3}$$
$$\sigma_{0i} = e^2 n_i \frac{\tau_i}{m_i}, \quad n_i = \frac{p_i^3}{3\pi^2\hbar^3}.$$

Before starting an analysis of the importance of various factors defining the magnitude of the "specular" part of conductivity of the system being treated, one must clear up the question of the ratio of the quantities identified in the surface parameters α and β for describing the contributions (A) identical for all layers of a given sort and for describing additions dependent on the location of the layer (a and b, see Eqs. (3.19)). This part of analysis is given in Appendix B, where it is demonstrated that, in multilayer samples at $K \gg 1$, the parameters a and b may be ignored. Therefore, in what follows, the specular contribution to the conductivity given by Eq. (3.16) is estimated (in terms of parameters A and δA) as

$$\sigma_c^P(n) \approx \frac{3}{4}\sigma_{bn}\sum_s Y_n(u_n l_n g_n A_n^s/d_n),$$
$$\sigma_c^P(m) \approx \frac{3}{4}\sigma_{bm}\sum_s Y_m(u_m l_m g_m^s \Gamma_s A_m^s/d_m), \tag{4.4}$$

and its variation is estimated as

$$\delta\sigma_c \approx \sigma_c^P - \sigma_c^{AP} = \delta\sigma_c(n) + \delta\sigma_c(m). \tag{4.5}$$

The expressions for $\delta\sigma$ differ from Eqs. (4.4) in that the quantities A in the arguments of the integrals Y_n and Y_m in Eqs. (3.15) are replaced by δA. The equations from which the determining parameters for Eqs. (4.4) are found have the form

$$[T_m^{sn}(p) + G_n^s]A_n^s - \frac{T_n^{sm}(p)A_m^a}{\kappa_s} = r^{snp}\hat{g}_n + \frac{t_{cn}^{smp}\hat{g}_m^s}{\kappa_s},$$
$$\frac{[T_n^{sm}(p) + G_m^s]A_m^s}{\kappa_s} - T_m^{sn}(p)A_n^s = \frac{r_c^{smp}\hat{g}_m^s}{\kappa_s} + t_{cm}^{snp}\hat{g}_n, \tag{4.6}$$

and those from which the determining parameters for Eq. (4.5) are found have the form

$$[T_m^{sn}(p) + G_n^s]\delta A_n^S - \frac{T_n^{sm}(p)\delta A_m^s}{\kappa_s} = A_{1n}^{as} \equiv \delta A_n^{as} - A_n^{as},$$
$$\frac{[T_n^{sm}(p) + G_m^s]\delta A_m^s}{\kappa_s} - T_m^{sn}(p)\delta A_n^s = 0. \tag{4.7}$$

In Eqs. (4.6) and (4.7),

$$G^s = \hat{g}^s + \zeta^s(1 - \hat{g}^s), \quad T^s + R^s + G^s = 1. \tag{4.8}$$

Here, the designation G^s is introduced for the complete diffuse component of scattering (surface and bulk), and the sum rule is written out, which is a result of determinations of the parameters T and R in Eqs. (3.7), G in Eqs. (4.8), and of normalization relations in the absence of flip transitions,

$$t_{cm}^{snp} + r_c^{snp} + \zeta_n^s = 1, \quad t_{cn}^{smp} + r_c^{smp} + \zeta_m^s = 1. \tag{4.9}$$

It will be recalled that the transition parameters t_c include in their definition given by Eq. (A.9) the restrictive factors defining the range of coincidence of longitudinal momenta. The dependence on the transverse component of momentum, with respect to which the integration in Eqs. (3.15) is performed, is determined from relations (2.11) for the n and m parameters, respectively, i.e., from the condition of conservation of energy and its coincidence with the chemical potential. The functions $\hat{g}_n^s$ and $\hat{g}_m^s$ characterizing the scattering during the passage of electrons through the respective layers are given by expressions (3.6).

The difference between the ranges of existence of individual terms in Eqs. (4.6) and (4.7) brings about an additional (apart from that associated with the presence of the functions $\hat{g}$) momentum dependence of solutions of these equations. We will select characteristic concrete options of correlations between the Fermi momenta of m_s and n electrons, p_{sm} and p_n, and detail this dependence for subsequent analysis of the behavior of solutions in typical situations.

Option 1:

$$p_{sm} > p_n. \tag{4.10}$$

In this case, the parameters characterizing the n layers in the $I_s(1n)$ interval, $0 \le p_z \le p_n$ ($0 \le p_\parallel \le p_n$), assume the form

$$A_n^s = \frac{Q_n^s}{\Delta_s}, \quad \delta A_n^s = \frac{(1 - R_m^s)A_n^{as}}{\Delta_s\Delta_0},$$
$$\Delta_0 = \sum_s \frac{1 - R_m^s}{\Delta_s} - 1, \tag{4.11}$$
$$\Delta_s = t_c^s[(1 - \hat{g}_n)G_m^s + (1 - \hat{g}_m^s)G_n^s] + G_m^s G_n^s,$$
$$Q_n^s = t_c^s[\hat{g}_m^s/\kappa_s + \hat{g}_n(1 - \hat{g}_m^s)(1 - \zeta_n^s)] + r_{cn}^s g_n G_m^s.$$

The contribution by the m layers in the $I_{s,1}(1m)$ interval, $0 \le p_z \le \sqrt{p_{sm}^2 - p_n^2}$ ($p_n \le p_\parallel \le p_{sm}$), takes the form

$$A_m^s = g_m^s r_{cm}^s/G_m^s, \quad \delta A_m^s = 0, \tag{4.12}$$

and in the $I_{s,2}(1m)$ interval, $\sqrt{p_{sm}^2 - p_n^2} \le p_z \le p_{sm}$ ($0 \le p_\parallel \le p_n$),

$$A_m^s = \frac{Q_m^s}{\Delta_s}, \quad \delta A_m^s = \frac{\kappa_s t_c^s A_n^{as}}{\Delta_s \Delta_0}, \tag{4.13}$$
$$Q_m^s = t_c^s[\hat{g}_n \kappa_s + g_m^s(1-\hat{g}_n)(1-\zeta_m^s)] + r_{cm}^s g_m^s G_n^s.$$

The foregoing formulas include the "nominal" (see Eqs. (A.9)) coefficients t and r which are the same for direct and reverse specular transitions and constant in the regions of realization of such transitions.

For other options of correlations between Fermi momenta (namely, $p_{+m} > p_n > p_{-m}$ and $p_n > p_{sm}$), we will restrict ourselves to treating simple but typical situations realized in the case of limiting asymmetry of the s branches of m electron spectrum, when the states of m electrons with the projection $s = -1$ may be totally ignored (for example, the density of states of such carriers at the Fermi level is $\nu_m^- \sim p_{-m} \longrightarrow 0$). This restriction may be realized in the so-called magnetic semimetals, but is unfit for d metals. It will be used strictly to simplify the description: as a result of this choice, all physical factors defining the special features of the effect being investigated are retained, and its maximal scale is revealed. So, all of the options of correlations between Fermi momenta that differ from Eq. (4.10) will be restricted to the application to systems in which only electrons with the spin projection $s = +1$ are involved in transport in m layers magnetized in parallel. In nonmagnetic layers, electrons with both projections are involved.

Option 2:

$$p_n < p_{+m}. \tag{4.14}$$

For nonmagnetic layers in the $I_s(1n)$ interval, $0 \le p_z \le p_n$ ($0 \le p_\parallel \le p_n$), we have

$$A_n^+ = \frac{Q_n^+}{\Delta_-}, \quad A_n^- = \frac{\hat{g}_n r_n^-}{G_n^-}, \quad \delta A_n^+ = \frac{(1-R_m^+)A_n^a}{\Delta_+ \Delta_1},$$
$$\delta A_n^- = -\frac{A_n^a}{G_n^- \Delta_1}, \quad \Delta_1 = \frac{1-R_m^+}{\Delta_+} + \frac{1}{G_n^-} - 1, \tag{4.15}$$

and for magnetic layers in the $I_{+,1}(1m)$ interval, $0 \le p_z \le \sqrt{p_{+m}^2 - p_n^2}$ ($p_n \le p_\parallel \le p_{+m}$),

$$A_m^+ = \hat{g}_m^+ r_m^+ / G_m^+, \quad \delta A_m^+ = 0, \tag{4.16}$$

and in the $I_{+,2}(1m)$ interval, $\sqrt{p_{+m}^2 - p_n^2} \le p_z \le p_{+m}$ ($0 \le p_\parallel \le p_n$),

$$A_m^+ = \frac{Q_m^+}{\Delta_+}, \quad \delta A_m^+ = \frac{\kappa_+ t_c^+ A_n^a}{\Delta_+ \Delta_1}. \tag{4.17}$$

The same notation is used for the parameters as that in the respective ranges in Eqs. (4.11)–(4.13).

Option 3:

$$p_n > p_{+m}. \tag{4.18}$$

The contribution by the m_+ carriers in the $I_+(3m)$ interval, $0 \le p_z \le p_{+m}$ ($0 \le p_\parallel \le p_{+m}$, takes the form

$$A_m^+ = \frac{Q_m^+}{\Delta_+}, \quad \delta A_m^+ = \frac{\kappa_+ t_c^+ A_{3n}^a}{\Delta_+ \Delta_1}. \tag{4.19}$$

The contribution by the n electrons in the $I_{s,1}(3n)$ interval, $0 \le p_z \le \sqrt{p_n^2 - p_{+m}^2}$ ($p_{+m} \le p_\parallel \le p_n$), takes the form

$$A_n^s = \frac{\hat{g}_n r_n^s}{G_n^s}, \quad \delta A_n^s = \frac{A_n^{as}}{G_n^s \Delta_2}, \quad \Delta_2 = \sum_s \frac{1}{G_n^s} - 1, \tag{4.20}$$

and in the $I_{s,2}(3n)$ interval, $\sqrt{p_n^2 - p_{+m}^2} \le p_z \le p_n$ ($0 \le p_\parallel \le p_{+m}$),

$$A_n^+ = \frac{Q_n^+}{\Delta_+}, \quad A_n^- = \frac{\hat{g}_n r_n^-}{G_n^-},$$
$$\delta A_n^+ = \frac{(1-R_m^+)A_n^a}{G_n^s \Delta_1}, \quad \delta A_n^- = -\frac{A_n^a}{G_n^- \Delta_1}. \tag{4.21}$$

In Eqs. (4.19), the parameter A^a has the subscript $3n$, which points to the $I_{s,2}(3n)$ interval of the variable p_z, in which this quantity is determined.

The formulas for options 1–3 express the dependence of the "specular" surface corrections A_n^s and A_m^s to the distribution functions of n and m electrons on the parameters of specular transmission t_c and reflection r_c. For the quantities δA_n^s and δA_m^s, which characterize the effect of variation of conductivity being investigated, their proportionality to the value of $A_n^{as} = A_n^s - A_n^{-s}$ is shown. It is natural that, in the case of m electrons, the parameters δA_m^s arise only in the case of specular transitions between n and m layers.

The foregoing results are then used in systems in which one can expect the specular fractions of conductivity to play an important part, namely, in multilayer samples containing thin nonmagnetic layers.

5. THE CONDUCTIVITY OF A MULTILAYER SYSTEM WITH THIN NONMAGNETIC LAYERS

We will start with the case in which the magnetic layers are thick,

$$l_n \gg d_n, \quad l_m \ll d_m. \tag{5.1}$$

Under conditions (5.1), the contribution made by the m layers to the total conductivity given by Eq. (3.11)

reduces to the quantity $\sigma_b(m)$ (3.13) defined by the bulk conductivity; the corrections due to the diffuse and specular m parts are small to the extent of smallness of the ratio l_m/d_m. The contribution by the n layers to σ_{bd} given by Eq. (3.12) experiences, at $d_n/l_n \ll 1$, the well-known size-dependent reduction

$$\sigma_{bd}(n) \approx \sigma_{bn}\lambda_n, \quad \lambda_n = \frac{3d_n}{4l_n}\ln\frac{l_N}{d_n}. \tag{5.2}$$

It is necessary to reveal the situations in which the values of specular additions $\sigma_c(n)$ (3.17) are of the order of σ_{bn} in Eqs. (3.13), i.e., they do not contain the small factor λ_n appearing in Eqs. (5.2) and may introduce a contribution comparable with σ_{bm} to the total conductivity given by Eq. (3.11). This requires that the value of the integral Y_n in (3.17) be of the order of unity. Because it is the realization of "giant" variation of conductivity, i.e., of the quantities $\delta\sigma_c(n) \approx \sigma_c^P(n)$, which is of prime interest, one must find the conditions at which

$$\sum_s \delta A_n^s \approx \sum_s A_n^s.$$

We will take into account the fact that, because of the presence of the size-dependent function g_n in the integrands in Y_n, the main contribution to the integral is made by the region beginning with the values of u_n of the order of d/l. In this region, for performing estimations, it is permissible to replace the function g_n by its argument. One can readily see that, in satisfying conditions (5.1), the situation in which the specular factors dominate the scattering parameters is favorable,

$$t_c^s, t_c^s \gg \zeta^s, \quad d_n/l_n. \tag{5.3}$$

Under conditions of option 1 as given by Eq. (4.10), we find

$$A_n^s \approx \frac{1}{\kappa_s},$$
$$\delta A_n^s \approx -\frac{\Gamma_{as}t_c^{-s}}{\sqrt{\Gamma_+\Gamma_-}\sum_s \kappa_s\left[\sum_s t_c^s - t_c^+ t_c^-\right]}. \tag{5.4}$$

The respective specular fractions of conductivity are

$$\sigma_c^P(n) \approx \frac{\sigma_{bn}}{2}\sum_s \kappa_s^{-1},$$
$$\delta\sigma_c(n) \approx \frac{\sigma_{bn}\Gamma_a t_c^a}{2\sqrt{\Gamma_+\Gamma_-}\sum_s \kappa_s\left(\sum_s t_c^s - t_c^+ t_c^-\right)}. \tag{5.5}$$

The results for option 2 given by Eq. (4.14) are as follows:

$$A_n^+ \approx \frac{1}{\kappa_+}, \quad A_n^- \approx \frac{g_n}{g_n + \zeta_n^-},$$
$$\delta A_n^+ \approx \frac{(g_n + \zeta_n^-)}{t_c^+}\left[\frac{1}{\kappa_+} - 1 + \frac{\zeta_n^-}{g_n + \zeta_n^-}\right], \tag{5.6}$$
$$\delta A_n^- \approx 1 - \frac{1}{\kappa_+} - \frac{\zeta_n^-}{g_n + \zeta_n^-},$$

so that

$$\sigma_c^P(n) \approx \frac{\sigma_{bn}}{2\kappa_+}\begin{cases}\kappa_+ + 1, & \zeta_n^- \ll d_n/l_n,\\ 1, & \zeta_n^- \gg d_n/l_n,\end{cases} \tag{5.7}$$

$$\delta\sigma_c(n) \approx \frac{\sigma_{bn}}{2\kappa_+}\begin{cases}\kappa_+ - 1, & \zeta_n^- \ll d_n/l_n,\\ -1, & \zeta_n^- \gg d_n/l_n.\end{cases} \tag{5.8}$$

Under conditions of option 3, it is only the contribution according to Eqs. (4.21), made by the $I_{s,2}(3n)$ region in which the expressions for A_n^+ and δA_n^s coincide with Eqs. (5.6), that may turn out to be important for $\delta\sigma_c$. In this case, we find

$$\sigma_c^P(n) \approx \frac{\sigma_{bn}}{\kappa_+} \times \begin{cases}\kappa_+ + \frac{3}{4}(1-\kappa_+)Y'(\sqrt{1-q_+^2}, 1), & \zeta_n^s \ll d_n/l_n,\\ \frac{3}{4}Y'(\sqrt{1-q_+^2}, 1), & \zeta_n^s \gg d_n/l_n,\end{cases} \tag{5.9}$$

$$\delta\sigma_c(n) \approx \frac{3\sigma_{bn}}{4\kappa_+}Y'(\sqrt{1-q_+^2}, 1) \times \begin{cases}\kappa_+ - 1, & \zeta_n^- \ll d_n/l_n,\\ -1, & \zeta_n^- \gg d_n/l_n,\end{cases} \tag{5.10}$$

where the notation

$$Y'(a, b) = \int_a^b du(1-u^2), \quad q_s = \frac{p_{sm}}{p_n} \tag{5.11}$$

is used.

Then, we perform calculations for a multilayer system in which the layers of both types are thin,

$$l_m \gg d_m, \quad l_n \gg d_n. \tag{5.12}$$

In this case, the m parts of σ_{bd} given by Eq. (3.12) decrease similarly to (5.2),

$$\sigma_d(m) \approx \sigma_{bm}\lambda_m, \quad \lambda_m = \frac{3d_m}{4l_m}\ln\frac{l_m}{d_m}, \tag{5.13}$$

so that, along with specular n contributions, specular m contributions may become significant as well. For giant effects to be realized, it is now sufficient that the values of specular additions according to Eq. (3.16) correspond to reduced values of conductivities given by Eq. (3.12) (in addition to the fact that σ_c^P and $\delta\sigma_c$ are close to each other). However, the conditions are quite permissible in which the specular additions according to Eq. (3.16) take values of the order of σ_{bn} and σ_{bm} and define the total conductivity of the sample. We will start with treating this case which is realized under conditions of extremely weak diffuse surface scattering,

$$t_c^s, r_{cn}^s, r_{cm}^s \gg d_n/l_n, \quad d_m/l_m \gg \zeta_n^s, \zeta_m^s. \tag{5.14}$$

Under conditions of option 1 in the $I_s(1n)$ interval, Eqs. (4.11)–(4.13) yield

$$A_n^s \approx \frac{g_n + \hat{g}_m^s/\kappa_s}{g_n + \hat{g}_m^s}, \quad \sum_s \delta A_n^s \approx -\frac{A_n^a \hat{g}_m^a}{\sum_s (g_n + \hat{g}_m^s)}; \tag{5.15}$$

in the $I_{s,1}(1m)$ interval,

$$A_m^s \approx 1, \quad \delta A_m^s \approx 0; \tag{5.16}$$

and in the $I_{s,2}(1m)$ interval,

$$A_m^s \approx \frac{\kappa_s \hat{g}_n + g_m^s}{\hat{g}_n + g_m^s}, \quad \delta A_m^s \approx \frac{\kappa_s(\hat{g}_n + g_m^{-s})A_n^{as}}{\sum_s (\hat{g}_n + g_m^s)}. \tag{5.17}$$

In estimating the conductivity $\sigma_c^P(n)$ according to Eqs. (4.4), it is permitted to use the values of A_n^s according to Eqs. (5.15) in which the functions g are taken at the upper limit of integration in Y_n. In order to calculate $\delta\sigma_c(n)$, one needs to estimate the sum $\sum_s \delta A_n^s$ more exactly, because Eqs. (5.15) include the cofactor

$$\hat{g}_m^a \approx \frac{d_m}{l_m}\left(\frac{p_{+m}}{\sqrt{p_{+m}^2 - p_\parallel^2}} - \frac{p_{-m}}{\sqrt{p_{-m}^2 - p_\parallel^2}}\right),$$

which goes to zero at the upper limit $p_z = p_n$. Used for further estimations is its approximate value,

$$g_m^a \approx -\frac{d_m p_\parallel^2 \Gamma_a}{2l_m p_m^2 \Gamma_+ \Gamma_-},$$

obtained from the exact value by isolating the factor $p_\parallel^2$ and replacing p_z by p_n in the remaining terms. As a result, we find

$$\sigma_c^P(n) \approx \sigma_{bn}\frac{\delta + \sum_s \kappa_s^{-1/2}/2}{1+\delta}, \quad \delta\sigma_c(n) \approx -\frac{\sigma_{bn}\Gamma_a^2}{10\kappa\sum_s \Gamma_s^{-1/2}\Gamma_+^2\Gamma_-^2 q^2(1+\delta)^2}. \tag{5.18}$$

Here, the notation

$$\delta = d_n l_m / d_m l_n \tag{5.19}$$

is introduced (the quantity δ estimates the ratio of the functions g_n and g_m at the upper limit of the integration variable).

The contribution to the conductivity from the m layers is introduced by the intervals $I_{s,1}(1m)$ (4.12) and $I_{s,2}(1m)$ (4.13). We use Eqs. (5.16) and (5.17) to find

$$\sigma_c(m) \approx \sigma_{bm} \times \left[1 + \frac{3\delta}{4(1+\delta)}\sum_s \Gamma_s(\kappa_s - 1)Y'(\sqrt{1-q_s^{-2}}, 1)\right], \quad \delta\sigma_c(m) \approx -\frac{3\sigma_{bm}}{8} \times \frac{\sum_s \Gamma_{as}\Gamma_s(1+\kappa_s\delta)Y'(\sqrt{1-q_s^{-2}}, 1)}{(1+\delta)^2\kappa\sqrt{\Gamma_+\Gamma_-}\sum_s \sqrt{\Gamma_s}}. \tag{5.20}$$

If the parameters defining the differences between the spectra of n and m electrons are such that $q_s^2 \gg 1$, the value of the integral in Eqs. (5.20) will be

$$Y'(\sqrt{1-q_s^{-2}}, 1) \approx 1/4q_s^4 \ll 1$$

and the conductivity variation $\delta\sigma_c(m)$ proves to be insignificant compared with $\sigma_c(m)$. A favorable situation will be the situation in which $q_+^2 \gg 1$ and $q_-^2 \approx 1$; then, the integral $Y' \approx 2/3$ for $s = -1$, which makes the $\delta\sigma_c(m)$ contribution quite appreciable.

The estimations made for option 2 given by Eq. (4.14) under conditions (5.14) of negligibly weak diffuse scattering lead to

$$A_n^+ \approx \frac{g_n + \hat{g}_m^+/\kappa_+}{g_n + \hat{g}_m^+}, \quad A_n^- \approx 1, \quad \delta A_n^+ \approx \frac{\delta}{1+2\delta}A_n^a, \quad \delta A_n^- \approx -\frac{1+\delta}{1+2\delta}A_n^a, \tag{5.21}$$

in the $I_s(1n)$ interval;

to

$$A_m^+ \approx 1, \quad \delta A_m^+ \approx 0, \tag{5.22}$$

in the $I_{+,1}(1m)$ interval; and to

$$A_m^+ \approx 1 + \frac{(\kappa_+ - 1)\delta}{1+\delta}, \qquad \delta A_m^+ \approx \frac{\delta(1-\kappa_+)}{(1+\delta)(1+2\delta)} \tag{5.23}$$

in the $I_{+,2}(1m)$ interval.

As a result, Eqs. (4.4) and (4.5) yield

$$\sigma_c^P(n) \approx \sigma_{bn}\left[1 + \frac{(1-\kappa_+)}{2\kappa_+(1+\delta)}\right], \qquad \delta\sigma_c(n) \approx \frac{\sigma_{bn}(\kappa_+ - 1)}{2\kappa_+(1+\delta)(1+2\delta)},$$
$$\sigma_c^P(m) \approx \sigma_{bm}^+\left[1 + \frac{\delta(\kappa_+ - 1)}{(\delta+1)}\right], \qquad \delta\sigma_c(m) \approx \frac{\sigma_{bm}^+(1-\kappa_+)\delta}{(1+\delta)(1+2\delta)}. \tag{5.24}$$

Equations (5.24) give the value of $\delta\sigma_c(m)$ at the maximal value of the respective integral $Y'(\sqrt{1-q_+^{-2}}, 1) \approx 2/3$, which is realized at $q_+^2 = 1 + \epsilon$, $\epsilon \ll 1$, with the notation

$$\sigma_{bm}^+ = \frac{D_m}{D}\sigma_{0m}^+, \tag{5.25}$$

where the quantity σ_{0m}^+ in Eqs. (4.3) is the bulk conductivity of the m layer with the condition of absence of carriers with $s = -1$ adopted above.

In the case of option 3, given by Eq. (4.18), and conditions (5.14), we have

$$A_m^+ \approx \frac{\hat{g}_n\kappa_+ + g_m^+}{\hat{g}_n + g_m^+} \approx \frac{1+\kappa_+\delta}{1+\delta}, \qquad \delta A_m^+ \approx \frac{\kappa_+\delta}{1+2\delta}A_n^a; \tag{5.26}$$

in the $I_{s,1}(3n)$ interval,

$$A_n^s \approx 1, \quad \delta A_n^s \approx 0; \tag{5.27}$$

and in the $I_{s,2}(3n)$ interval,

$$A_n^+ \approx \frac{g_n + \hat{g}_m^+/\kappa_+}{g_n + \hat{g}_m^+}, \quad A_n^- \approx 1, \qquad \delta A_n^+ \approx \frac{g_n A_n^a}{2g_n + \hat{g}_m^+}, \quad \delta A_n^- \approx -\frac{(g_n + \hat{g}_m^+)A_n^a}{2g_n + \hat{g}_m^+}. \tag{5.28}$$

Here, we will also restrict ourselves to estimation for situations with the maximum possible values of $\delta\sigma_c$, namely, with the maximal width of the $I_{s,2}(3n)$ interval according to Eqs. (5.28), which is realized on condition that $q_+^2 = 1 - \epsilon$, $\epsilon \ll 1$. In this case, Eqs. (4.4) and (4.5) yield expressions for conductivity close to Eqs. (5.28).

The foregoing examples exhaust the possibilities of finding the bulk conductivity values under conditions (5.12). We will now turn to analyzing the problem for the situations in which the values of σ_c and $\delta\sigma_c$ depend significantly on the diffuse components of surface scattering and are of the order of the values yielded by Eqs. (5.2) and (5.13). This is primarily the case in which, under conditions of general prevalence of specular factors, diffuse surface scattering turns out to be more important than bulk scattering,

$$t_c, r_c \gg \zeta \gg \lambda \tag{5.29}$$

(in this situation, the characteristic values of the functions g are estimated by the values of λ).

As in the case of Eqs. (5.14) above, we will illustrate the case given by (5.29) by examples which correspond to the maximal effects of conductivity variation. For option 1 according to Eqs. (4.11)–(4.13), we have, in the $1_s(1n)$ interval,

$$A_n^s \approx \frac{g_n + \hat{g}_m^s/\kappa_s}{\zeta_n^s + \zeta_m^s}, \qquad \sum_s \delta A_n^s \approx -\frac{\zeta_n^a + \zeta_m^a}{\sum_s(\zeta_n^s + \zeta_m^s)}A_n^a; \tag{5.30}$$

in the $I_{s,1}(1m)$ interval,

$$A_m^s \approx g_m^s/\zeta_m^s, \quad \delta A_m^s = 0; \tag{5.31}$$

and in the $1_{s,2}(1m)$ interval,

$$A_m^s \approx \frac{\kappa_s\hat{g}_n + g_m^s}{\zeta_n^s + \zeta_m^s}, \qquad \delta A_m^s \approx \frac{\kappa_s(\zeta_n^{-s} + \zeta_m^{-s})A_n^a}{\sum_s(\zeta_n^s + \zeta_m^s)}. \tag{5.32}$$

The functions $\hat{g}$ are present here only in the numerators and define the size reduction of conductivity. We will recall a significant detail: an important part is played by the logarithmic factor $\ln(l/d) \gg 1$ (included in the definition of the parameter λ according to Eqs. (5.2) and (5.13)) which is due to the contribution by the electrons incident on the surfaces at small angles θ ($\theta < d/l \ll 1$). One can readily see that this factor is introduced only by regions of integration with respect to p_z which begin with $p_z = 0$, in the presence in integrands of the func-

tions g with an argument proportional to $1/p_z$. In Eqs. (5.30), these are the terms with g_n, which appear in the integrals Y_n when calculating $\sigma_c(n)$ and $\delta\sigma_c(n)$ according to Eqs. (4.4) and (4.5), and the terms with g_m^s in the $I_{s,1}(1m)$ interval according to Eqs. (5.31) of the integral Y_{sm} defining $\sigma_c(m)$. The contributions made by other terms containing the functions $\hat{g}$ include only factors of the order of d/l without logarithmic multiplication and may be omitted.

By way of illustration of the maximum possible effect, we will use the above-identified case of close values of the Fermi momenta $p_{-,m}$ and p_n, in which the ranges of integration with respect to p_z in Y_n and the $I_{-,2}(1m)$ interval in Y_{-m} almost coincide. Then, for the n layer from Eqs. (5.30)–(5.32) and (4.4) and (4.5), we have ($q_+ - 1 \gg d/l$, $q_- - 1 \leq d/l$)

$$\sigma_c(n) \approx \sigma_{bn}\left[\lambda_m \sum_s \frac{1}{\zeta_n^s + \zeta_m^s} + \frac{\lambda_m}{\kappa_-(\zeta_n^- + \zeta_m^-)}\right],$$

$$\delta\sigma_c(n) \approx \sigma_{bn}\frac{\zeta_n^a + \zeta_m^a}{(\zeta_n^- + \zeta_m^-)\sum_s(\zeta_n^s + \zeta_m^s)} \times \left[\frac{\lambda_n(\zeta_n^a + \zeta_m^a)}{\zeta_n^+ + \zeta_m^+} + \frac{\lambda_m}{\kappa_-}\right]. \quad (5.33)$$

For the m layer under the same conditions, we have

$$\sigma_c(m) \approx \sigma_{bm}\left[\lambda_m\left(\frac{\Gamma_+}{\zeta_m^+} + \frac{\kappa_-\Gamma_-}{\zeta_n^- + \zeta_m^-}\right) + \lambda_n \sum_s \frac{\kappa_s\Gamma_s}{(\zeta_n^s + \zeta_m^s)}\right],$$

$$\delta\sigma_c(m) \approx \sigma_{bm}\frac{\kappa_-\Gamma_-(\zeta_n^+ + \zeta_m^+)}{(\zeta_n^- + \zeta_m^-)\sum_s(\zeta_n^s + \zeta_m^s)} \times \left[\frac{\lambda_m}{\kappa_-} + \frac{\lambda_n(\zeta_n^a + \zeta_m^a)}{\zeta_n^+ + \zeta_m^+}\right]. \quad (5.34)$$

If the conditions $q_s - 1 \gg d/l$ are valid for both quantities q_s, the expressions for conductivity vary as follows: in the formulas written above for $\sigma_c(n)$ and $\delta\sigma_c(n)$, the terms with λ_m must be omitted, and in those for $\sigma_c(m)$, the term with λ_n must be omitted; as to the quantity $\delta\sigma_c(m)$, it should be ignored in the approximation used (it does not contain the logarithmic factor $\ln(d/l) \gg 1$).

In the case of option 2 given by Eq. (4.14), we have, for the parameters A in the $I_s(1n)$ interval,

$$A_n^+ \approx \frac{g_n + \hat{g}_m^+/\kappa_+}{\zeta_n^+ + \zeta_m^+}, \quad A_n^- \approx \frac{g_n}{\zeta_n^-},$$

$$\delta A_n^+ \approx \frac{\zeta_n^- A_n^a}{\zeta_m^+ + \sum_s \zeta_n^s}, \quad \delta A_n^- \approx -\frac{(\zeta_n^+ + \zeta_m^+)A_n^a}{\zeta_m^+ + \sum_s \zeta_n^s}; \quad (5.35)$$

in the $I_{+,1}(1m)$ interval,

$$A_m^+ \approx \frac{g_m^+}{\zeta_m^+}, \quad \delta A_m^+ \approx 0; \quad (5.36a)$$

and in the $I_{+,2}(1m)$ interval,

$$A_m^+ \approx \frac{\kappa_+\hat{g}_n + g_m^+}{\zeta_n^+ + \zeta_m^+}, \quad \delta A_m^+ \approx \frac{\kappa_+\zeta_n^- A_n^a}{\zeta_m^+ + \sum_s \zeta_n^s}. \quad (5.36b)$$

It follows from this and from Eqs. (4.4) and (4.5) that, with an almost complete intersection of the ranges of determination of the n and m_+ states of the carriers, the maximal values of conductivity are observed ($q_+^2 - 1 \leq d/l$),

$$\sigma_c(n) \approx \frac{\sigma_{bn}}{\kappa_+(\zeta_n^+ + \zeta_m^+)}\left[\frac{\kappa_+\lambda_n\left(\zeta_m^+ + \sum_s \zeta_n^s\right)}{\zeta_n^-} + \lambda_m\right],$$

$$\delta\sigma_c(n) \approx \frac{\sigma_{bn}(\zeta_n^+ + \zeta_m^+)}{(\zeta_n^+ + \zeta_m^+)\left(\zeta_m^+ + \sum_s \zeta_n^s\right)}\left[\frac{\lambda_n(\zeta_n^a + \zeta_m^+)}{\zeta_n^-} - \frac{\lambda_m}{\kappa_+}\right], \quad (5.37)$$

$$\sigma_c(m) \approx \frac{\sigma_{bm}^+}{\zeta_n^+ + \zeta_m^+}(\lambda_m + \kappa_+\lambda_n),$$

$$\delta\sigma_c(m) \approx -\frac{\sigma_{bm}^+\zeta_n^-}{(\zeta_n^+ + \zeta_m^+)\left(\zeta_m^+ + \sum^s \zeta_m^s\right)} \times \left[-\lambda_m + \frac{\kappa_+\lambda_n(\zeta_n^a + \zeta_m^+)}{\zeta_n^-}\right].$$

With q_+ being markedly different from unity ($q_+ - 1 \gg d/l$), the quantities $\sigma_c(n)$ and $\delta\sigma_c(n)$ are described by formulas (5.37), from which the terms with λ_m must be omitted; the quantities $\sigma_c(m)$ coincide with those in Eqs. (5.37) in the absence of the term with λ_n; as to the variation of $\delta\sigma_c(m)$, it may be ignored, as is the case in the previous example.

For option 3 given by Eq. (4.18), we find, in the $I_{+1}(3m)$ interval,

$$A_m^+ \approx \frac{\kappa_+ \hat{g}_n + g_m^+}{\zeta_n^+ + \zeta_m^+}, \quad \delta A_m^+ \approx \frac{\kappa_+ \zeta_n^- A_{2n}^a}{\zeta_m^+ + \sum_s \zeta_n^s}; \tag{5.38}$$

in the $I_{s,1}(3n)$ interval,

$$A_n^s \approx \frac{g_n}{\zeta_n^s}, \quad \delta A_n^s \approx -\frac{g_n \zeta_n^{as}}{\zeta_n^s \left(\sum_s \zeta_n^s \right)}; \tag{5.39a}$$

and in the $I_{s,2}(3n)$ interval,

$$A_n^+ \approx \frac{g_n + \hat{g}_m^+/\kappa_+}{\zeta_n^+ + \zeta_m^+}, \quad A_n^- \approx \frac{g_n^-}{\zeta_n^-},$$
$$\delta A_n^+ \approx \frac{\zeta_n^- A_n^a}{\zeta_m^+ + \sum_s \zeta_n^s}, \quad \delta A_n^- \approx -\frac{(\zeta_m^+ + \zeta_n^+) A_n^a}{\zeta_m^+ + \sum_s \zeta_n^s}, \tag{5.39b}$$

which, in the limiting case of coincidence of the $I_{s,2}(3n)$ and $I_{s,1}(3m)$ regions for the n_s and m_+ spectra, leads to the following ($1 - q_+ \le d/l$):

$$\sigma_c^P(n) \approx \frac{\sigma_{bn}}{\kappa_+(\zeta_n^+ + \zeta_m^+)} \left[\kappa_+ \lambda_n \frac{\zeta_m^+ + \sum_s \zeta_n^s}{\zeta_n^-} + \lambda_m \right],$$

$$\sigma_c^P(m) \approx \frac{\sigma_{bm}^+}{\zeta_n^+ + \zeta_m^+} (\lambda_m + \kappa_+ \lambda_n),$$

$$\delta\sigma_c(n) \approx \sigma_{bn} \frac{\zeta_n^a + \zeta_m^+}{\kappa_+(\zeta_m^+ + \zeta_n^+) \left(\zeta_m^+ + \sum_s \zeta_n^s \right)} \times \left[\lambda_n \kappa_+ \frac{\zeta_n^a + \zeta_m^+}{\zeta_n^-} - \lambda_m \right], \tag{5.40}$$

$$\delta\sigma_c(m) \approx \sigma_{bm}^+ \frac{\zeta_n^-}{(\zeta_m^+ + \zeta_n^+) \left(\zeta_m^+ + \sum_s \zeta_n^s \right)} \times \left[\lambda_m - \kappa_+ \lambda_n \frac{\zeta_n^a + \zeta_m^+}{\zeta_n^-} \right].$$

If the ranges of variation of the variable p_z in Eqs. (3.15) for the n and m_+ contributions diverge considerably, the values of conductivity vary ($1 - q_+ \gg d/l$),

$$\sigma_c^P(n) \approx \sigma_{bn} \lambda_n \sum_s \frac{1}{\zeta_n^s}, \quad \sigma_c(m) \approx \frac{\sigma_{bm}^+ \lambda_m}{\zeta_n^+ + \zeta_m^+},$$
$$\delta\sigma_c(n) \approx \frac{\sigma_{bn} \lambda_n (\zeta_n^a)^2}{\zeta_n^+ \zeta_n^- \sum_s \zeta_n^s}, \tag{5.41}$$
$$\delta\sigma_c(m) \approx \frac{\sigma_{bm}^+ \lambda_m \zeta_n^-}{(\zeta_n^+ + \zeta_m^+) \left(\zeta_m^+ + \sum_s \zeta_n^s \right)}.$$

Note that the estimated values of $\sigma_c^P(n)$ and $\sigma_c^P(m)$ given above differ from the reduced values of conductivity according to Eqs. (5.2) and (5.13) by the factors containing the quantities $1/\zeta > 1$, so that the resultant contributions due to specular scattering, generally speaking, define the total conductivity for conditions (5.29).

In conclusion, we will treat the case in which the surface scattering is largely diffuse, and the parameters ζ exceed both the small quantities d/l and the coefficients of specular transmission and reflection, t_c and r_c,

$$\zeta \gg t_c, r_c, \lambda_{n,m}. \tag{5.42}$$

Under these conditions, the contribution made by the m layers to the variation of conductivity must be *a priori* small (by virtue of the proportionality of the parameters δA_m^s to the coefficients t_c); therefore, it is sufficient to estimate $\delta\sigma_c(n)$ alone. We will now consider the results for option 1. According to Eqs. (4.11) under conditions (5.42),

$$A_n^s \approx \frac{t_c^s \hat{g}_m^s/\kappa_s + r_n^s g_n \zeta_m^s}{\zeta_n^s \zeta_m^s},$$
$$\sum_s \delta A_n^s \approx -\frac{\zeta_n^a A_n^a}{\sum_s \zeta_n^s}, \quad A_n^a \approx -\frac{g_n \zeta_n^a}{\zeta_n^+ \zeta_m^-}. \tag{5.43}$$

In this case, the specular additions σ_c^P proper do not exceed the values according to Eqs. (5.2) and (5.13); as to the variation of conductivity, we find

$$\delta\sigma_c(n) \approx \frac{\sigma_{bn} \lambda_n (\zeta_n^a)^2}{\zeta_n^+ \zeta_n^- \sum_s \zeta_n^s}. \tag{5.44}$$

One can see that, for options 2 and 3, the estimates of the values of $\delta\sigma_c(n)$ coincide with those according to Eq. (5.44).

6. DISCUSSION

Summing up, it will be recalled that our results were obtained within the quasi-classical description of an electron system; the interlayer gaps in the system were simulated by scattering surfaces on which the boundary conditions for the distribution functions were preassigned of the type of Fuchs–Sondheimer conditions with due regard for the possibility of transmission through interfaces involving other electron groups (differing both by the energy spectrum and by the spin state). Theoretical analysis resulted in the demonstration of the possibilities of realizing a giant variation of conductivity (i.e., of the order of magnitude of the conductivity proper) during a change of pattern of alternation of magnetic polarization in the m layer sequence. As was already noted, one can expect this in the following cases:

(a) when at least the n layers are thin, i.e., relations (5.1) or (5.12) are valid; and

(b) when the presence of specular components in the set of parameters responsible for the scattering on the boundaries between layers is imperative.

The magnitude and sign of the effect depend significantly both on the values of the coefficients t_c and r_c of specular transitions and on the correlations between the parameters characterizing diffuse surface (ζ, see Eq. (A. 14)) and bulk (d_i/l_i) scattering. An important part is played by the differences between the spectra of n and m_s electrons, which are expressed by the ratios between the Fermi momenta of electron groups, in other words, between the respective concentrations of carriers (options 1 (4.10), 2 (4.14), and 3 (4.18)).

We will start systematizing the data of Section 4 from the case in which the diffuse surface scattering is of minimal significance,

$$t_c, r_c \gg d_i/l_i \gg \zeta_i \tag{6.1}$$

(in the case of thin layers of both types according to (5.12)).

The results for options 1 and 2, 3 differ substantially. In the case of option 1 ($q_s = p_{ms}/p_n > 1$), the variations of conductivities $\delta\sigma_c(n)$ and $\delta\sigma_c(m)$ turn out to be negative (expressions (5.18) and (5.20)) and depend on the value of the difference parameter $\Gamma_a = \Gamma_+ - \Gamma_-$ according to Eqs. (2.10), which is the measure of asymmetry of the s branches of m electrons. The total value of $\delta\sigma_c = \delta\sigma_c(n) + \delta\sigma_c(m)$ is maximal (in magnitude) at $q_- \approx 1$ and $q_+ \gg 1$. If both parameters $q_s \gg 1$ (this means that $q = p_m/p_n \gg 1$ as well), the effect of conductivity variation will decrease considerably and may drop out of the category of giant effects.

For electron groups with spectra typical of options 2 and 3, the signs of variation of the conductivities $\delta\sigma_c(n)$ and $\delta\sigma_c(m)$ are opposite (see Eqs. (5.24)). If the Fermi momenta p_n and p_{+m} are close to one another in magnitude ($q_+ \approx 1$), the total quantity $\delta\sigma_c$ is positive,

$$\delta\sigma_c \approx \frac{\sigma_{bn}(1 - 1/\kappa_+)^2}{2(1+\delta)(1+2\delta)} \tag{6.2}$$

(the correlations between the parameters according to Eqs. (3.13), (4.3), and (5.19) are used). As to the "extreme" situations, i.e., at $q_+ \gg 1$ (option 2) and $q_+ \ll 1$ (option 3), $\delta\sigma_c(n)$ (5.24) and $\delta\sigma_c(m)$ (5.25) predominate, respectively; the signs of these quantities are opposite and defined by the sign of the factor $\kappa_+ - 1$. Common to all results in the case given by (6.1) is that the specular parameters t_c and r_c are absent from the estimated values of $\delta\sigma_c$.

We will now turn to the situation in which the surface diffuse scattering is more important than bulk scattering, and the quantities λ_n (5.2) and λ_m (5.13) are used as the effective free path,

$$t_c, r_c \gg \zeta \gg \lambda. \tag{6.3}$$

Under conditions (6.3), in contrast to the results in the case given by (6.1), the expressions for $\delta\sigma_c$ depend explicitly on the components of the diffuse parameters $\zeta_{sn,m}$. In the case of option 1, the signs and values of $\delta\sigma_c(n)$ (5.33) and $\delta\sigma_c(m)$ (5.34) are defined by the difference parameters ζ_n^a and ζ_m^a, whose values (and even their signs) are undefined within our analysis; however, generally speaking, it is possible to expect the emergence of a giant quantity $\delta\sigma_c$. In the extreme situation of $q_- \gg 1$, the value of $\delta\sigma_c$ is definitely positive: according to Eqs. (5.33) and (5.34),

$$\delta\sigma_c \approx \delta\sigma_c(n) \approx \frac{\sigma_{bn}\lambda_n(\zeta_n^a + \zeta_m^a)^2}{(\zeta_n^+ + \zeta_m^+)(\zeta_n^- + \zeta_m^-)\sum\limits_s(\zeta_n^s + \zeta_m^s)}. \tag{6.4}$$

Under conditions of options 2 and 3 and close values of Fermi momenta of electron groups ($q_+ \approx 1$), the quantities $\delta\sigma_c(n)$ and $\delta\sigma_c(m)$ in Eqs. (5.37) and (5.40) are quite appreciable, while their signs are indeterminate. In the extreme situation ($q_+ \gg 1$ for option 2),

$$\frac{\delta\sigma_c(n)}{\sigma_{bn}} \approx \frac{\lambda_n(\zeta_n^a + \zeta_m^+)^2}{\zeta_n^-(\zeta_n^+ + \zeta_m^+)\left(\zeta_m^+ + \sum\limits_s \zeta_n^s\right)}, \quad \delta\sigma_c(m) \approx 0, \tag{6.5}$$

the effect of conductivity variation is *a priori* positive. In the case of option 3 with the extreme correlation $q_+ \gg 1$, the conductivity varies both for n electrons (the value coincides with that according to Eqs. (6.5)) and for m_+ electrons,

$$\frac{\delta\sigma_c(m)}{\sigma_{bm}^+} \approx \frac{\lambda_m\zeta_n^-}{(\zeta_n^+ + \zeta_m^+)\left(\zeta_m^+ + \sum\limits_s \zeta_n^s\right)}, \tag{6.6}$$

with an *a priori* positive total result.

Finally, under conditions when the diffuse surface coefficients exceed the specular parameters as well, i.e., at

$$\zeta \gg t_c, r_c, \lambda, \tag{6.7}$$

the conductivity variations reduce to $\delta\sigma_c(n)$ and, for all three options, are positive and close to one another,

$$\frac{\delta\sigma_c(n)}{\sigma_{bn}} \approx \frac{\lambda_n(\zeta_n^a)^2}{\zeta_n^+\zeta_n^-\sum_s \zeta_n^s}. \tag{6.8}$$

According to the sum rule given by Eqs. (4.9), the difference parameter

$$\zeta_n^A = -t_{cm}^{na} - r_c^{na};$$

according to conditions (6.7), the specular differences must be much less than ζ_n^s. Therefore, the scale of conductivity variation under conditions (6.7) may hardly correspond to a giant effect.

Note the distinctions of the situation in which the *m* layers are thick, i.e., relations (5.1) are valid. In this case, only the conditions of prevalence of specular scattering given by (5.3) are promising from the standpoint of realization of giant variations of conductivity, and the contributions to $\delta\sigma_c$ are defined by the *n* electrons alone. For option 1, according to Eqs. (5.5), the conductivity variation $\delta\sigma_c$ is proportional to the difference parameter t_c^a, whose value and sign remain undefined. As to options 2 and 3, here, as in the case given by (6.1), no parameters of surface scattering appear in the resultant formulas. The variations of conductivity are described by simple relations: in the case of extremely weak diffuse surface scattering ($\zeta_n \ll d_n/l_n$), the value and sign of $\delta\sigma_c(n)$, as in the case given by (6.1), depend on $\kappa_+ - 1$,

$$\frac{\delta\sigma_c(n)}{\sigma_{bn}} \approx \frac{\kappa_+ - 1}{2\kappa_+}. \tag{6.9}$$

If the surface diffuse scattering is more significant than bulk scattering, and the conditions $t_c, r_c \gg \zeta_n \gg d_n/l_n$ are valid, the conductivity variation is *a priori* negative and, according to (5.8), it is defined by the parameter κ_+,

$$\frac{\delta\sigma_c(n)}{\sigma_{bn}} \approx -\frac{1}{2\kappa_+}. \tag{6.10}$$

Expressions (6.9) and (6.10) hold for option 2 for any value of $q_+ > 1$. They are also valid for option 3 in the case of $q_+ \approx 1$; however, in the case of extreme correlation $q_+ \ll 1$, the quantity $\delta\sigma_c(n)$, as well as $\delta\sigma_c$, are negligibly small. Note the differences of Eqs. (6.9) and (6.10) from the results for thin *m* layers under analogous conditions of scattering: the quantities $\delta\sigma_c$ in these two cases may differ even by their sign.

The foregoing set of expressions for $\delta\sigma_c$ demonstrates the diversity of the possibilities of attaining giant values of conductivity variation of both signs. As is demonstrated, the result depends on the correlations between quite a number of parameters, and it proves to be rather difficult to interpret or predict the scale and sign of the effect on a qualitative level. In view of this, it appears useful to make remarks concerning the frequently suggested makeshift explanation of the effect of negative magnetoresistance, which was formulated as early as the first papers on the subject [1] and repeatedly used later on (see, for example [15, 39]). It is based on elementary "electrotechnical" considerations concerning the current in two independent *s* channels (the spin projection *s* is registered in a laboratory system) with different resistivities $\rho_s \neq \rho_{-s}$ within the layers. In the case of AP packing, the total resistance over all layers is the same for each channel; in the case of P packing, the channel with $\rho_{\min}$ must predominate, via which the short-circuiting (using the adopted terminology) occurs and, thereby, the GNMR effect is realized. Analogous explanations are suggested for the case of the so-called inverse effect (an increase in the resistance during the AP $\longrightarrow$ P rearrangement): here, the same reasoning is used, and the involvement of magnetic layers of two types with different ρ_+/ρ_- ratios is required [31–35]. No grounds exist, however, for using this simplified scheme to interpret the effect being treated, which is associated with a complex of physical processes. We will only point out some aspects of the problem. In order to introduce the *s*-group resistance of all layers of the sample, it is insufficient to know the values of ρ_s within independent layers: the surface processes are of decisive importance. In the case of fully diffuse surface scattering which, by definition, interrupts the process of distortion of electron distribution by the external field and thus defines the effective free path, the electric currents and respective kinetic characteristics will be formed within individual layers independently and in a like manner for both types of magnetic order. The specular scattering intervenes in these processes and provides for the conservation of the "memory" of variations of the electron distribution during transitions from layer to layer or during reflections from the boundaries; it is this conservation that introduces interlayer and *s*-dependent correlations into the formation of the total conductivity of the sample. The combination of physical effects of this kind, complemented with the possible *s* dependence of electric resistivity within the layers, defines the scale of the effect of variation of total conductivity during the AP $\longrightarrow$ P rearrangement; of course, the estimation of this scale lies outside the limits of the above-mentioned electrotechnical analogs. Note further that the short-circuiting scheme, based on the inequality $\rho_s \neq \rho_{-s}$, leads to the underestimation of the part played by the *n* layers (in which $\rho_s = \rho_{-s}$) in the

formation of $\delta\sigma$, while the contribution made by these layers may be decisive in a number of cases.

For some of the inferences made in this paper concerning the possibility of realizing giant quantities $\delta\sigma$, the physical reasons on a qualitative level appear to be fairly apparent. For example, the need for long free paths in the *n* layers is quite clear, i.e., the requirement of $l_n \gg d_n$ (this condition was pointed out even in the early papers when using arguments based on the interlayer correlations of *m* carriers; see, for example, [40]). The special part played by surface scattering in the formation of $\delta\sigma$ is based on the following simple physical pattern: in an *n* layer, electrons with a fixed spin projection *s* are scattered similarly by both surfaces of the given *n* layer if the neighboring *m* layers are magnetized in parallel; in the case of AP packing of the *m* neighbors, the surface scattering must be different for different surfaces. It is this variation of scattering from a pair of surfaces (the measure of which is provided by the quantities A_n^a in Sections 4 and 5) that is an essential prerequisite to the emergence of $\delta\sigma_n$. As to the *m* layers, both surfaces of every one of them scatter *m* electrons with a fixed value of *s* similarly for any order of magnetization orientations. Therefore, the quantities $\delta\sigma(m)$ arise only due to the penetration of electrons through neighboring layers. We will mention once again the result which must be regarded as one of the main results, namely, that a variation of the order of magnetization orientations causes a variation in the conductivity of the system layers only in the presence of specular components of scattering on interlayer boundaries. In the process, in accordance with the described physical pattern, specular reflections are sufficient in the *n* layers, while the realization of $\delta\sigma(m)$ requires specular components of penetration. In this case, the so-called channeling effect shows up, i.e., restrictions on transitions from layer to layer for a part of carriers due to differences in magnitude of Fermi momenta between respective groups of electrons [15, 22, 41] (according to the method of describing surface scattering in my paper, this fact is included in terms of the *p* dependence of the transition parameters t^p in Eqs. (A.10)), as well as the effect of a possible match between the band parameters in neighboring layers (band matching effect) [42–45]. Qualitative evidence of the contribution due to penetrations is provided by the parameter $\kappa_+ - 1 = (M_n - M_{m+})/M_{m+}$ in Eqs. (5.24): the difference in mobilities characterizes the variation of the electron states in a layer due to the penetration from the neighboring layers and departure to those layers. Similar reasoning is used to explain the emergence of the $\sigma_{bn}/\kappa = eM_m n_n$ combination appearing in Eqs. (5.18): the variation of conductivity in the *n* layer is defined by the mobility in the *m* layer.

Note yet another result which appears to be of importance, namely, the possibility of variation of conductivity of both signs, i.e., of both direct and inverse effects of giant magnetoresistance. In the general case, it is difficult to predict the sign of the effect based on qualitative reasoning. Most apparent, perhaps, is the situation for options 2 (4.14) and 3 (4.18) with predominating specular transmissions through interlayer surfaces. In the case of thick *m* layers but thin *n* layers, when the size reduction of conductivity (more precisely, of mobility) is realized only in the *n* layers (on condition that $\zeta \gg d/l$), the conductivity in the latter layers will be defined by the arrivals from the neighboring *m* layers; in so doing, the unreduced *m* mobility is also "introduced." It is clear that, in this case, the AP configuration will define a higher value of effective conductivity in the *n* layers, because carriers with both spin projections are introduced, while in the case of P packing they are introduced only with one (within adopted restrictions for options 1 and 2) or mostly with one (in a more general case) spin projection. In the final analysis, the quantity $\delta\sigma(n)$ turns out to be negative (see Eqs. (5.8) and (5.10)). In the case of weak diffuse surface scattering ($\zeta \ll l/d$), the mobility in the *n* layers retains its bulk value, so that the departures to the *m* layers become significant as well; in the final analysis, the effective conductivity comes to depend on the differences between the *n* and *m* mobilities (see Eqs. (5.7)–(5.10)). In samples with thin layers of both types, analogous reasoning explains the result given by Eqs. (5.24). As to the situation under conditions of significant diffuse fractions in the surface processes, the results of our analysis demonstrate that, in the case of the AP $\longrightarrow$ P reorientation, one can expect a positive variation of conductivity (i.e., the effect of negative magnetoresistance), even if without *a priori* grounds for a giant magnitude of this variation. Other combinations of the correlations between the scattering parameters and the characteristics of electron groups, which provide for the possibility of giant variations of conductivity, exhibit, as was shown above, a great diversity and require concrete data for estimating the real magnitude and sign of the effect.

The objectives of my study did not include qualitative comparison with experiment. For this purpose, the problem would have to be concretely defined: the data on real energy spectra of laminated metals (for example, from [46–48]) would have to be used instead of parabolic laws of dispersion given by Eqs. (2.3) and (2.4). Note, for example, that a Fe/Cr system corresponds to option 1 according to the classification of possible ratios of Fermi momenta introduced in Section 4; for a Co/Cu system, the data pertaining to options 2 or 3 could be used, under conditions of similarity between the momentum for copper and some Fermi momentum or other for cobalt. In order to describe the surface scattering, one must use the mechanisms and field configurations that fit the situation (as in [9, 22] or, for example, in [49]) and treat samples of a concrete structure, and so on. Some fairly general results of my analysis may be compared with experimental data. In a number of studies, significant variations of the value of giant magnetoresistance were

observed when the interlayer surfaces were subjected to special stimulation; as a result, the specular component in their scattering properties varied, and an increase (decrease) in this component was accompanied by an increase (decrease) in the giant magnetoresistance [49, 50–52]; the dependence of this effect on the layer thickness was investigated, and its decrease with an increase in d_m was observed [53, 54]; an increase in the giant magnetoresistance with the number of *m*–*n* pairs and the saturation of this behavior were demonstrated [53], which may be compared with the results of analysis in Appendix B. Naturally, special-purpose experiments need to be performed. A rather concrete testlike investigation may be suggested: the difference of the results between the cases of thin and thick *m* layers under the same conditions of surface scattering was demonstrated above, i.e., a significant variation of the effect during transition from one type of multilayer sample to another type of the same composition (when the effect is regarded as giant in both cases).

ACKNOWLEDGMENTS

I am grateful to I.F. Voloshin, L.M. Fisher, and V.S. Tsoi for their interest in this study, and to É.I. Rashba for valuable advice.

This study received support from the Russian Foundation for Basic Research (project no. 01-02-16418).

APPENDIX A

Characteristics of Surface Scattering: Boundary Conditions

It is assumed that the kinetic Boltzmann equations are valid in the entire space of a multilayer sample (the conditions of smallness of de Broglie wavelength on the Fermi level with respect to the characteristic dimensional parameters such as thickness and free path are valid). The dependence of the distribution functions f_p^s on *z* arises due to the nonuniformity of the system. First of all, the nonuniformity is due to the variation of the spectral characteristics of electrons from layer to layer. In addition, a nonuniform distribution of scattering fields is observed; it is obvious that, in the situation in which the layers are much thicker than the interlayer gaps, specific potentials localized in narrow intervals with respect to *z* are associated with the latter gaps, so that these gaps are anomalous as regards their scattering properties.

The nonuniformity of the scattering properties shows up in the formalism of kinetic equations in terms of collision integrals, in the form of the *z* dependence of the transition probabilities appearing in those integrals,

$$\mathrm{St}^s(f) = \sum_{s'}\int d\tau_p' W_{s'p'}^{sp}(f_p^{s''} - f_p^s), \quad d\tau_p = \frac{d^3p}{(2\pi\hbar)^3}. \quad \text{(A.1)}$$

Here, *W* is the density (per unit reduced volume of momentum space $d\tau_p$) of the probability of scattering per unit time, which corresponds to the $(sp) \longrightarrow (s'p')$ transitions. We restrict ourselves to the Born approximation for which $W_{s'p'}^{sp} = W_{sp}^{s'p'}$, as well as to elastic scattering.

In Eqs. (A.1), the probabilities of respective bulk scattering appear in one of the layers (over the extent of uniform material), which are described by quantities that are uniform with respect to *z* (are associated with scatterers uniformly distributed in the bulk). For analyzing the behavior of electrons within the layers, it is sufficient (for the purposes of the problem being treated) to resort to the relaxation time approximation, as given in Eq. (2.8). The variation of electron distribution in interlayer gaps, which are assumed to be much thinner than the scattering probabilities locally identified in the interfaces, may be used to find correlations between the values of distribution functions at the edges of these gaps. When the gap thickness is ignored, such correlations will serve the function of boundary conditions relating the solutions of kinetic equations in successive layers *j* and *j*' on both sides of the separating interface $z = z_{jj'}$. This program may be conveniently executed with the aid of overdetermination of the probability density *W* in Eqs. (A.1) and its reduction to the form suitable for describing the scattering by a flat object (see, for example, [55–57]). If, in calculating the transition probability, the wave function of the initial state is normalized to a flux of unit density normal to the surface, we will obtain the probability density of scattering *V* per unit thickness of the range of effect of flat scatterers (rather than per unit time, as in the case of *W*). These characteristics are related as

$$W_{s'p'}^{sp} = |v_z| V_{s'p'}^{sp}. \quad \text{(A.2)}$$

The quantity *V* is used to describe the scattering which is inevitable for the flux incident on the surface. The involvement of all surface scatterers (characterized by the quantity *V* integrated with respect to the interlayer gap thickness) and the inclusion of all possible final states (*s*'*p*') corresponding to the reflections (change of sign of v_z) and transmissions to the neighboring layer, i.e., the summation with respect to *s*' and integration with respect to $d\tau_p'$, provide for reliable realization of departure from the state (*sp*) in the initial layer, as expressed by the normalizing relation

$$\sum_{s'}\int d\tau_p' V_{1s'p'}^{sp} = 1, \quad V_1 = \int V dz \quad \text{(A.3)}$$

(the integral with respect to *dz* covers the range of localization of flat scatterers in the interlayer region).

In treating the boundary region, we will use in the interlayer gap (in the vicinity of $z = z_{jj'}$) the collision integral according to Eqs. (A.1), expressed in terms of the functions *V*. We will write the kinetic equation for

the nonequilibrium addition χ_j^s in Eq. (2.7), divide all terms of the equation by v_z, and integrate with respect to the gap between the layers j and j'. The boundary conditions formally follow from here as the extent of the integration range tends to zero (while retaining the resultant nonzero contribution by the integrals V_1 according to Eqs. (A.3)). For the case of $v_z > 0$, we find

$$\phi_{j'lp}^{s>} - \phi_{jrp}^{s>} = \sum_{s'}\left\{\int_{>} d\tau_p'[V_{1js'p'}^{j'sp}\phi_{jrp'}^{s'>} - V_{1j's'p'}^{jsp}\phi_{jrp}^{s>}] + \int_{<} d\tau_p'[V_{1j's'p'}^{j'sp}\phi_{j'lp'}^{s'<} - V_{1js'p'}^{jsp}\phi_{jrp}^{s>}]\right\}, \quad \phi = \chi - e\varphi \tag{A.4}$$

(here, the factors $\partial f_0/\partial\varepsilon$ are omitted: they are the same with all terms; in the collision integral, this is provided for by the condition of elasticity of scattering). The collision parameters V_1 bear the layer indexes j and j' which correspond to the following types of transitions during scattering: to arrivals to the state (jsp) from the states ($j's'p'$) (transmissions) and ($j's'p'$) (reflections)—positive terms on the right in Eq. (A.4); and to departures from the state (jsp) to the states ($j's'p'$) (transmissions) and ($js'p'$) (reflections)—negative terms in Eq. (A.4). The indexes $r(l)$ indicate that the jth or j'th layer belongs to the right-hand (left-hand) boundary, and the symbols > (<) correspond to the positive (negative) values of the velocity v_z. By virtue of the normalization conditions given by (A.3), the terms with $\phi_{jrp}^{s>}$ in Eq. (A.4) are canceled, and the rest are the boundary condition which relates at point $z_{jj'}$ the values of the distribution functions $\chi_{j'}^{s>}$, $\chi_{j'}^{s'<}$, and $\chi_j^{s>}$. Similar computations for $v_z < 0$ will produce the condition of coupling for $\chi_s^{j<}$, $\chi_j^{s'>}$, and $\chi_{j'}^{s<}$.

In order to introduce the scattering parameters similar to the Fuchs coefficients and use them in the boundary conditions, we will rewrite the normalizing relation (A.3) in the form (for the $v_z > 0$ region)

$$\sum_{s'}(t_{j's'}^{jsp} + r_s^{jsp'}) = 1, \quad t_{j's'}^{jsp} = \int_{>} d\tau_p' V_{1j's'p'>}^{jsp>}, \quad r_s^{jsp'} = \int_{<} d\tau_p' V_{1js'p'<}^{jsp>}. \tag{A.5}$$

By its meaning, the quantity $t_{j's'}^{jsp}$ is the coefficient of electron transmission from the state (sp) in the layer j to the states in the neighboring layer j' with the spin projection s', and the quantity $r_s^{jsp'}$ is the coefficient of electron reflection in the state (sp) from the boundary of the jth layer with transition to the states s' of the same layer (initial states are indicated starting from above). The transition coefficients for the case of $v_z < 0$ are determined analogously. The thus introduced parameters have the meaning of probabilities of the respective transitions; their set generalizes the set of the Fuchs parameters, which relate to reflections alone, to the cases of transmission through boundaries and additionally details the channels of scattering over spin variables. The scheme of introducing the transition parameters may be extended to cover situations involving groups of electrons differing by other than spin characteristics, for example, by the feature of belonging to independent "valleys" of the energy spectrum, as in the case of semimetals or some semiconductors. In this case, the parameters of respective transitions will appear, as well as the additional parts in the boundary conditions, which generalize the relations used in the investigation of anisotropic size effects [58].

In order to reveal the correlations between various transition coefficients and their dependence on spin indexes, which are essential to the problem being investigated, we will resort to a simplified model of scattering (in the spirit of Fuchs approximation) after defining concretely the expressions for the scattering functions V_1. We will identify in $V_{1j's'p'}^{jsp}$ the δ function expressing the conservation of energy, as well as the factor $|v_z'|$ (similarly to the procedure of (A.2)), which will result in recovering, in the remaining part, the symmetry relative to permutation of indexes,

$$V_{1j's'p'}^{jsp} = |v_z'|\delta(\varepsilon_{jp}^s - \varepsilon_{j'p'}^{s'})w_{j's'p'}^{jsp}. \tag{A.6}$$

Then, the parameters of surface scattering assume the form

$$t_{j's'}^{jsp} = \int_{>} d\tau_{p'} v_z \delta(\varepsilon_{j'p'}^{s'} - \mu) w_{j's'p'}^{jsp>} = 2\int_{>} d\tau_{p'} p_z' \delta(p'^2 - p_{j's'}^2) w_{j's'p'>}^{jsp>}, \tag{A.7}$$

$$r_{s'}^{jsp} = 2\int_{<} d\tau_{p'} |p_z'| \delta(p'^2 - p_{js'}^2) w_{js'p'<}^{jsp>}$$

(in writing Eq. (A.7), the presence of the factors $\partial f_{0jp}^s/\partial\varepsilon = -\delta(\varepsilon_{jp}^s - \mu)$ in the nonequilibrium distribution functions was taken into account), which enables one to replace ε_{jp}^s in V_1 by μ and use expressions (2.10) and (2.11) in the δ functions in Eq. (A.7). The next step is to identify, in the scattering characteristic w, the correlated and uncorrelated parts corresponding to the specular and diffuse cases of the Fuchs model. The correlation in this case implies the conservation of

momentum parallel to the surface, which is realized in the presence of a uniform (along the interlayer interface) component of scattering potential (the potential which is periodic in the plane will complement the coupling of longitudinal momenta with reciprocal lattice vectors; we will not take into account the attendant singularities of scattering). We will further take into account the contribution due to scattering fields, which vary randomly in the interlayer planes, and write w in the form

$$w^{jsp}_{j's'p'} = w^{js}_{cj's'} p_j p_{j'} \delta(\mathbf{p}'_\parallel - \mathbf{p}_\parallel) + w^{js}_{dj's'}, \tag{A.8}$$

where, remaining within the Fuchs model, we assume the parameters w_c and w_d to be constant and momentum-independent quantities (in so doing, their differences for the cases of transmission and reflection are retained, as will be indicated by the indexes t and r, respectively). From (A.7) follows

$$\begin{aligned} t^{jsp}_{cj's'} &= t^{j's'p}_{cjs} = t^{js}_{cj's'} \Theta[\min(p_{js}, p_{j's'}) - p_\parallel], \\ r^{jsp}_{cs'} &= r^{js'p}_{cs} = r^{js}_{cs'} \Theta[\min(p_{js}, p_{js'}) - p_\parallel]. \end{aligned} \tag{A.9}$$

Here, Θ is the Heaviside unit function. The parameters

$$\begin{aligned} t^{js}_{cj's'} &= t^{j's'}_{cjs} = w^{js}_{ctj's'} p_j p'_j, \\ r^{js}_{cs'} &= r^{js'}_{cs} = w^{js}_{crs'} p_j^2, \end{aligned} \tag{A.10}$$

symmetric relative to the permutation of indexes, appear in Eqs. (A.9). The parameters of diffuse scattering, which are also assumed to be constant, may be conveniently written as

$$\begin{aligned} t^{jsp}_{dj's'} &= t^{js}_{dj's'} \frac{p^2_{j's'}}{p_j p_{j'}}, \quad r^{jsp}_{ds'} = r^{js}_{ds'} \Gamma_{js'}, \\ t^{js}_{dj's'} &= t^{j's'}_{djs} = w^{js}_{dtj's'} \pi p_j p_{j'}, \\ r^{js}_{ds'} &= r^{js'}_{ds} = w^{js}_{drs'} \pi p_j^2. \end{aligned} \tag{A.11}$$

One can easily check that the principle of detailed balance is automatically valid for each type of transition processes separately $\langle v_z t^{jsp}_{c(d)j's'} \rangle^> = \langle |v'_z| t^{j's'p'}_{c(d)js} \rangle^<$ and so on.

We will turn to the boundary conditions according to Eq. (A.4) and use Eqs. (A.6) and (A.7) to derive

$$\begin{aligned} \phi^{s>}_{j'lp} &= \sum_{s'} [t^{js'p}_{cj's} \phi^{s'>}_{jr}(\tilde{\mathbf{p}}_t(s')) + r^{j's'p}_{cs} \phi^{s'<}_{j'l}(\tilde{\mathbf{p}}_r(s'))] \\ &+ \sum_{s'} \left[t^{js'p}_{dj's} \frac{\langle v'_z \phi^{s'}_{jrh'} \rangle^{s'>}_j}{\langle v_z \rangle^{s>}_{j'}} + r^{j's'p}_{ds} \frac{\langle |v'_z| \phi^{s'}_{j'lp'} \rangle^{s'<}_{j'}}{\langle |v_z| \rangle^{s<}_{j'}} \right]. \end{aligned} \tag{A.12}$$

Here,

$$\tilde{\mathbf{p}}_t(s') = (\mathbf{p}_\parallel, \sqrt{p^2_{js'} - p^2_\parallel}),$$

$$\tilde{\mathbf{p}}_r(s') = (\mathbf{p}_\parallel, -\sqrt{p^2_{j's'} - p^2_\parallel}).$$

The values of distribution functions at $z = z_{jj'}$ are used throughout. The boundary conditions for $\phi^{s<}_{jrp}$ (on the other side of the $z = z_{jj'}$ boundary) are written similarly to (A.11).

APPENDIX B

Assessment of the Part Played by Scattering from External Surfaces in the Formation of Distribution Functions in a Multilayer Sample

We will eliminate $a^s_{m_j}$ and $b^s_{m_j}$ in the equations of set (3.21)–(3.23), from which the coefficients nondiagonal with respect to the spin index s are omitted. We use pairs of neighboring equations containing these parameters (with identical spin indexes) to derive

$$\begin{aligned} a^s_{m_j} &= \frac{\kappa_{sj} T_{sn}}{1 - R^2_{sm}} (a^s_{n_{j-1}} + R_{sm} b^s_{n_j}), \\ b^s_{m_j} &= \frac{T_{sn}}{1 - R^2_{sm}} (a^s_{n_{j-1}} R_{sm} + b^s_{n_j}). \end{aligned} \tag{B.1}$$

Here and in what follows, the notation

$$R^s_{sm,n} = R_{sm,n}, \quad T^{sm}_{sn} = T_{sm}, \quad T^{sn}_{sm} = T_{sn} \tag{B.2}$$

is used.

For the n parameters, we have

$$\begin{aligned} a^s_{n_0} - R_{sn_0} b^s_{n_0} &= v^s_0, \\ b^s_{n_0} - R_s a^s_{n_0} - T_s b^s_{n_1} &= 0, \end{aligned} \tag{B.3}$$

$$\begin{aligned} -T_s a^s_{n_{j-1}} - R_s b^s_{n_j} + a^s_{n_j} &= 0, \\ b^s_{n_j} - R_s a^s_{n_j} - T_s b^s_{n_{j+1}} &= 0, \end{aligned} \tag{B.4}$$

$$\begin{aligned} -T_s a^s_{n_{k'-1}} + (1 - R_s) b^s_{n_{k'}} &= 0, \\ a^s_{n_{k'}} &= b^s_{n_{k'}}, \end{aligned} \tag{B.5}$$

where

$$\begin{aligned} R_s &= R_{sn} + T_s R_{sm}, \quad T_s = \frac{T_{sn} T_{sm}}{1 - R^2_{sm}}, \\ v^s_0 &= g_n r_{scn_0} - A^s_n (1 - R_{sn_0}). \end{aligned} \tag{B.6}$$

We express the parameters b in terms of a (using the boundary conditions (3.6) containing one term with b each) and substitute them into the other equations to derive the following set of equations for the parameters a:

$$\begin{aligned} -(2x_s - y^s_{0a})a^s_{n_0} + a^s_{n_1} &= -\frac{\nu^s_0 R_s}{T_s R_{sn_0}}, \\ a^s_{n_0} - 2x_s a^s_{n_1} + a^s_{n_2} &= 0, \\ a^s_{n_{j-1}} - 2x_s a^s_{n_j} + a^s_{n_{j+1}} &= 0, \\ a^s_{n_{k'-1}} - (2x_s - y^s_{k'a})a^s_{n'_k} &= 0. \end{aligned} \tag{B.7}$$

Here,

$$\begin{aligned} 2x_s = \frac{T_s^2 - R_s^2 + 1}{T_s}, \quad y^s_{0a} = \frac{1 - R_s/R_{sn_0}}{T_s}, \\ y^s_{k'a} = \frac{T_s^2 - R_s^2 + R_s}{T_s}. \end{aligned} \tag{B.8}$$

We act similarly to derive the set of equations for the quantities b,

$$\begin{aligned} -(2x_s - y^s_{0b})b^s_{n_0} + b^s_{n_1} &= -\nu^s_0 R_s/T_s, \\ b^s_{n_0} - 2x_s b^s_{n_1} + b^s_{n_2} &= 0, \\ b^s_{n_{j-1}} - 2x_s b^s_{n_j} + b^s_{n_{j+1}} &= 0, \\ b^s_{n_{k'-1}} - (2x_s - y^s_{k'b})b^s_{n'_k} &= 0, \end{aligned} \tag{B.9}$$

where

$$y^s_{0b} = \frac{T_s^2 - R_s^2 + R_s R_{sn_0}}{T_s}, \quad y^0_{k'b} = \frac{1 - R_s}{T_s}. \tag{B.10}$$

The solutions to Eqs. (B.7) and (B.9) are as follows:

$$\begin{aligned} a^s_{n_j} &= \frac{\nu^s_0}{\Delta(x_s)}[C^1_{k'-j} - y^s_{k'a}C^1_{k'-j-1}(x_s)], \\ b^s_{n_j} &= \frac{\nu^s_0}{\Delta(x_s)}[C^1_{k'-j}(x_s) - y^s_{k'b}C^1_{k'-j-1}(x_s)], \\ \Delta(x_s) &= (1 - R_{sn_0})C^{1'}_k(x_s) \\ &- [T_s + (1 - R_s)(R_s - R_{sn_0})/T_s]C^1_{k'-1}(x_s), \end{aligned} \tag{B.11}$$

where C^1_j are Gegenbauer polynomials of the jth order [57]. We use Eqs. (B.11) to write the sum over the n layers appearing in the expression for $\sigma^P_c(n)$ (3.17),

$$\begin{aligned} \sum_{j=0}^{K}(a^s_{n_j} + b^s_{n_j}) &= \frac{2\nu^s_0}{\Delta(x_s)} \\ \times\left[2\sum_{j=0}^{k'}C^1_{k'-j}(x_s) - \sum_{j=0}^{k'-1}(y^s_{k'a} + y^s_{k'b})C^1_{k'-j-1}(x_s)\right] \\ = \frac{4\nu^s_0}{\Delta(x_s)}\left[\sum_{j=0}^{k'}C^1_j(x_s) - x_s\sum_{j=0}^{k'-1}C^1_j(x_s)\right] \\ = \frac{2\nu^s_0}{\Delta(x_s)}[C^1_{k'}(x_s) + C^1_{k'-1}(x_s) + 1]. \end{aligned} \tag{B.12}$$

The summation was performed using the well-known representation of Gegenbauer polynomials [58]

$$C^1_j(x) = \frac{z_1^{j+1} - z_2^{j+1}}{z_1 - z_2}, \quad z_{1,2} = x \pm \sqrt{x^2 - 1} \tag{B.13}$$

and recurrent relations. The sum according to Eq. (B.12) appears in the expression for the specular part of conductivity $\sigma_c(n)$ (3.17) along with the analogous term $(K+1)A^s_n$. Comparison reveals that the latter is approximately $K+1$ times greater: the parameter x_s in Eqs. (B.8) varies from unity (in the case of purely specular scattering) to a value much greater than unity in the case of prevailing diffuse scattering and T^s_n, $T^s_m \longrightarrow 0$, so that (B.12) is estimated by a quantity of the order of $\nu^s_0 \sim A^s_n$. A similar comparison may be performed for the m parameters, as well as for the quantities δA, δa, and δb, and with the same estimation.

The obtained result has a simple qualitative validation: the special features of the effect of external surfaces on the electron behavior must affect the overall electric conductivity of the entire system the less, the larger the number of conducting layers.

REFERENCES

1. M. N. Baibich, J. M. Broto, A. Fert, *et al.*, Phys. Rev. Lett. **61**, 2472 (1988).
2. G. Binasch, P. Grunberg, F. Sauerbach, *et al.*, Phys. Rev. B **39**, 4828 (1989).
3. P. M. Levy, Solid State Phys. **47**, 367 (1994).
4. M. A. M. Gijs and G. E. W. Bauer, Adv. Phys. **46**, 285 (1997).
5. J.-Ph. Ansermet, J. Phys.: Condens. Matter **10**, 6027 (1998).
6. A. Barthelemy, A. Fert, and F. Petroff, in *Handbook of Magnetic Materials*, Ed. by K. H. J. Buschow (Elsevier, Amsterdam, 1999), Vol. 12.
7. P. Zahn, I. Mertig, M. Richter, *et al.*, Phys. Rev. Lett. **75**, 2996 (1995).
8. W. H. Butler, X.-G. Zhang, D. M. C. Nickolson, *et al.*, Phys. Rev. B **52**, 13399 (1995).
9. M. D. Stiles, J. Appl. Phys. **79**, 5805 (1996).

10. K. Schep, P. J. Kelly, and G. E. Bauer, Phys. Rev. Lett. **74**, 586 (1995); Phys. Rev. B **57**, 8907 (1998).
11. R. Brown, D. M. C. Nickilson, W. H. Butler, *et al.*, Phys. Rev. B **58**, 11146 (1998).
12. C. Blaas, P. Wienberger, L. Szunyogh, *et al.*, Phys. Rev. B **60**, 492 (1999).
13. W. F. Egelhoff, Jr., T. Ha, R. D. K. Misra, *et al.*, J. Appl. Phys. **78**, 273 (1995).
14. H. J. W. Swagten, G. J. Strijker, P. J. H. Bloemen, *et al.*, Phys. Rev. B **53**, 9108 (1996).
15. H. Hasegawa, Phys. Rev. B **42**, 2368 (1990); **43**, 10803 (1991); **47**, 15073 (1993).
16. S. Zhang, P. M. Levy, and A. Fert, Phys. Rev. B **45**, 8689 (1992).
17. W. H. Butler, X.-G. Zhang, T. C. Shulthess, *et al.*, Phys. Rev. B **56**, 14574 (1997).
18. A. Vedyaev, N. Ryzhanova, B. Dieny, *et al.*, Phys. Rev. B **55**, 3728 (1997).
19. R. E. Camley and J. Barnas, Phys. Rev. Lett. **63**, 664 (1989).
20. J. Barnas, A. Fuss, R. E. Camley, *et al.*, Phys. Rev. B **42**, 8110 (1990); J. Magn. Magn. Mater. **140–144**, 497 (1995).
21. J. Inoue, H. Itoh, and S. Maekawa, J. Phys. Soc. Jpn. **60**, 376 (1991).
22. R. Q. Hood and L. M. Falicov, Phys. Rev. B **46**, 8287 (1992).
23. L. Sheng, D. Y. Xing, Z. D. Wang, *et al.*, Phys. Rev. B **55**, 5908 (1997); **58**, 6428 (1998).
24. K. Majamdar, J. Chen, and S. Hershfield, Phys. Rev. B **57**, 2950 (1998).
25. E. M. Lifshitz and L. P. Pitaevskiĭ, *Course of Theoretical Physics*, Vol. 10: *Physical Kinetics* (Nauka, Moscow, 1979; Pergamon, Oxford, 1981).
26. T. H. Todorov, E. Yu. Tsymbal, and D. G. Pettifor, Phys. Rev. B **54**, R12685 (1996).
27. K. Fuchs, Proc. Cambridge Philos. Soc. **34**, 100 (1938).
28. H. Sondheimer, Adv. Phys. **1**, 1 (1952).
29. S. Zhang and P. M. Levy, Phys. Rev. B **57**, 5336 (1998).
30. P. M. Levy, S. Zhang, and A. Fert, Phys. Rev. Lett. **65**, 1643 (1990).
31. S. S. Parkin, Appl. Phys. Lett. **63**, 1987 (1993).
32. J. George, L. Pereira, A. Barthelemy, *et al.*, Phys. Rev. Lett. **72**, 408 (1994).
33. J.-H. Renard, P. Bruno, R. Megy, *et al.*, Phys. Rev. B **51**, 12821 (1995); J. Appl. Phys. **79**, 5270 (1996).
34. R. Y. Gu, Z. D. Wang, and D. Y. Xing, J. Phys. Soc. Jpn. **67**, 255 (1998).
35. K. Rahmouni, A. Dinia, D. Stoeffler, *et al.*, Phys. Rev. B **59**, 9475 (1999).
36. É. A. Nagaev, *Physics of Magnetic Semiconductors* (Nauka, Moscow, 1983); Usp. Fiz. Nauk **166**, 833 (1996) [Phys. Usp. **39**, 781 (1996)].
37. V. Yu. Irkhin and M. I. Katsnel'son, Usp. Fiz. Nauk **164**, 705 (1994) [Phys. Usp. **37**, 659 (1994)].
38. H. Itoh, J. Inoue, and S. Maekawa, Phys. Rev. B **47**, 5809 (1993).
39. P. M. Levy, J. Magn. Magn. Mater. **140–144**, 485 (1995).
40. A. Fert, P. Grunberg, A. Barthelemy, *et al.*, J. Magn. Magn. Mater. **140–144**, 1 (1995).
41. W. H. Butler, X.-G. Zhang, D. C. M. Nickolson, *et al.*, Phys. Rev. Lett. **76**, 3216 (1996).
42. K. B. Hathaway and J. R. Cullen, J. Magn. Magn. Mater. **104–107**, 1840 (1992).
43. W. H. Butler, X.-G. Zhang, D. M. C. Nickolson, *et al.*, J. Magn. Magn. Mater. **151**, 354 (1995).
44. I. Mertig, P. Zahn, M. Richter, *et al.*, J. Magn. Magn. Mater. **151**, 363 (1995).
45. C. T. Yu, K. Westerholt, K. Theis-Brohl, *et al.*, Phys. Rev. B **57**, 2955 (1998).
46. *The Physics of Metals*, Ed. by J. M. Ziman (Cambridge Univ. Press, Cambridge, 1969; Mir, Moscow, 1972), Vol. 1, Chap. 8.
47. A. P. Cracknell and K. C. Wong, *Fermi Surface: Its Concept, Determination, and Use in Physics of Metals* (Clarendon, Oxford, 1973; Atomizdat, Moscow, 1978).
48. D. A. Papaconstantopoulos, *Handbook of the Band Structure of Elemental Solids* (Plenum, New York, 1986).
49. A. K. Zvezdin and S. N. Utochkin, Pis'ma Zh. Éksp. Teor. Fiz. **57**, 418 (1993) [JETP Lett. **57**, 433 (1993)].
50. D. Grieg, M. J. Hall, C. Hamond, *et al.*, J. Magn. Magn. Mater. **110**, 1239 (1992).
51. V. Sato, S. Ishio, and T. Miyazaki, IEEE Transl. J. Magn. Jpn. **9**, 44 (1994).
52. S. Li, C. Yu, W. Lai, *et al.*, J. Appl. Phys. **78**, 405 (1995).
53. L. D. Landau and E. M. Lifshitz, *Course of Theoretical Physics*, Vol. 3: *Quantum Mechanics: Non-Relativistic Theory* (Fizmatgiz, Moscow, 1963; Pergamon, New York, 1977), Chap. 17.
54. V. F. Gantmakher and Y. B. Levinson, *Carrier Scattering in Metals and Semiconductors* (Nauka, Moscow, 1984; North-Holland, New York, 1987), Chap. 11.
55. V. I. Okulov and V. V. Ustinov, Fiz. Nizk. Temp. **5**, 312 (1979) [Sov. J. Low Temp. Phys. **5**, 101 (1979)].
56. É. I. Rashba, Z. S. Gribnikov, and V. Ya. Kravchenko, Usp. Fiz. Nauk **119**, 3 (1976) [Sov. Phys. Usp. **19**, 361 (1976)].
57. I. S. Gradshteyn and I. M. Ryzhik, *Table of Integrals, Series, and Products* (Fizmatgiz, Moscow, 1963; Academic, New York, 1980).
58. L. Brillouin, *Wave Propagation in Periodic Structures* (Dover, New York, 1953; Inostrannaya Literatura, Moscow, 1959).

Translated by H. Bronstein

Journal of Experimental and Theoretical Physics, Vol. 94, No. 3, 2002, pp. 627–636.
Translated from Zhurnal Éksperimental'noĭ i Teoreticheskoĭ Fiziki, Vol. 121, No. 3, 2002, pp. 728–738.

SOLIDS
Electronic Properties

Laser Hyperacoustic Spectroscopy of Single Crystal Germanium

N. V. Chigarev[a], D. Yu. Parashchuk[b, *], Yu. S. Pan[b, **], and V. É. Gusev[c]

[a]*International Laser Center, Moscow State University, Moscow, 119899 Russia*
[b]*Moscow State University, Moscow, 119899 Russia*
**e-mail: paras@polys.phys.msu.su*
***Current address: X.Y. Pan, State Key Laboratory for Artificial Structure and Mesoscopic Physics, Peking University, Beijing 100871, China*
[c]*Laboratoire de Physique de l'Etat Condense, UMR-CNRS 6087, Universite du Maine, 72805, Le Mans, France*

Received August 14, 2001

Abstract—Using a photothermal laser deflection technique the profiles of laser-induced hyperacoustic pulses in single crystal germanium were studied at a subnanosecond time resolution. It is shown that the hyperacoustic pulses are excited due to an electron-deformation interaction of photogenerated carriers with the crystal lattice, which is much more effective than the thermoelastic mechanism of the acoustic wave generation. Evolution of the hyperacoustic pulse profiles related to the diffraction and acoustic absorption effects was studied. An analysis of the hyperacoustic signal profiles allowed us to estimate the coefficient of ambipolar diffusion of the photogenerated charge carriers and the coefficient of hyperacoustic wave damping. It is established that the front of the electron–hole plasma laser-excited in germanium at room temperature propagates at a supersonic velocity. *© 2002 MAIK "Nauka/Interperiodica".*

1. INTRODUCTION

Using picosecond optoacoustic techniques, it is possible to measure the sound velocity in thin films and determine the thicknesses of thin semiconductor [1, 2], dielectric [3], conducting polymer [2, 3], and metal [2, 4] films and interfaces between such films [5]. An analysis of the hyperacoustic signals excited by subpicosecond laser pulses in thin α-SiO_2 films allowed the acoustic absorption to be studied in a frequency range of up to several hundred gigahertz [6]. The picosecond optoacoustics provides for the possibility of tracing the spatiotemporal dynamics of the energy transfer from electrons to coherent phonons (i.e., to the acoustic oscillations) and revealing athermal mechanisms of the hyperacoustic wave excitation [7, 8]. On the other hand, there were attempts at determining the effect of hyperacoustic waves on the electron spectrum. In particular, it was reported that hyperacoustic pulses lift up the symmetry prohibition on the dipole-allowed transitions in conducting polymers [9]. In addition, the picosecond optoacoustic provides for valuable information about the electron structure of solids. For example, detection of the hyperacoustic pulses by measuring changes in the reflection coefficient induced by these pulses allowed the contribution of interband transitions to the acoustic absorption in metal films to be determined [10].

The optical detection schemes have proved to be especially effective in detecting hyperacoustic pulses. The original, and still the most popular, method in picosecond optoacoustics [1] consists in measuring the sample reflection coefficient modulated by a short acoustic pulse [3, 6, 9, 10], which is performed using the well-known excite–probe technique that provides for a time resolution on the level of laser pulse duration; within the framework of the same approach, picosecond optoacoustics employs more direct methods: using the modulated probing beam in the displacement [4] and interference [5, 11] schemes, it is possible to measure the mechanical shift of the sample surface. It should be noted that picosecond optoacoustics typically measures the time of arrival and amplitude of an acoustic signal, while the signal profile could be measured only in a few cases (see, e.g., [10]). This is caused by an insufficient signal-to-noise ratio in most experiments [1–6, 12]. However, the signal profile may carry important information about certain details of the acoustic wave photoexcitation and propagation processes.

The purpose of this study was to develop the method of laser hyperacoustic spectroscopy for measuring the shape of ultrashort acoustic signals and to apply this technique to investigation of the athermal mechanisms of the photoacoustic wave conversion in single crystal semiconductors. We will demonstrate that, within a picosecond time scale, the electron-deformation mechanism of the acoustic wave generation [1, 7, 13] on a moderate excitation level is much more effective than the universal thermoelastic mechanism. By studying features of the acoustic pulse shape, it is possible to

obtain information about the source of excitation—moving nonequilibrium electron–hole plasma, in particular, to determine the plasma diffusion coefficient [14, 15]. For example, using the developed laser hyperacoustic spectroscopy technique, we showed that the front of an expanding photogenerated electron–hole plasma can propagate at a supersonic velocity [14].

In the first part of this paper, we describe a model of hyperacoustic wave photoexcitation and propagation (Section 2) and present the main principles of measurements and their experimental implementation (Section 3). Then, we present the experimental results (Section 4), followed by their analysis and discussion (Section 5). The main results are summarized in the Conclusion.

2. THE MODEL OF HYPERACOUSTIC WAVE PHOTOEXCITATION AND PROPAGATION

In a semiconductor under pulsed optical action, the sources of acoustic waves are the spatiotemporal fields of the lattice temperature T and the nonequilibrium electron–hole plasma density N. These sources are responsible for the thermoelastic and electron-deformation mechanisms of the acoustic wave excitation.[1] We have employed a one-dimensional model of acoustic wave excitation on a mechanically free surface, since the characteristic depths of light absorption, heat transfer, and electron–hole plasma diffusion in our experiments are below 1 μm, while the exciting beam spot diameter on the sample surface is above 20 μm.

An equation describing longitudinal acoustic waves of mechanical displacement U in a semi-infinite homogeneous medium is as follows [7, 8]:

$$U_{tt} - c_a^2 U_{xx} = (dN_x - K\beta T_x)/\rho, \tag{1}$$

where c_a is the longitudinal sound velocity, K is the modulus of dilatation, β is the volumetric expansion coefficient, d is the sum of electron and hole deformation potentials, and ρ is the equilibrium density. The boundary conditions on the free surface is selected in the following form:

$$\begin{aligned} -c_a^2 U_x(t, x = 0) \\ = (dN(t, x = 0) - K\beta T(t, x = 0))/\rho, \end{aligned} \tag{2}$$

where subscripts x and t indicate derivatives with respect to the corresponding coordinate and time, respectively.

On the subnanosecond time scale, we may assume that the absorption of an exciting photon with the energy $h\nu_L$ exceeding the bandgap width E_g leads to the production of an electron–hole pair possessing the energy E_g and the instantaneous (on the same time scale) dissipation of the energy $h\nu_L - E_g$ spent for the lattice heating. The spatiotemporal dynamics of the nonequilibrium electron–hole plasma and lattice temperature are described by the diffusion equations with the corresponding diffusion coefficients D and χ:

$$N_t - DN_{xx} = \frac{(1-R)\alpha I}{h\nu_L}\exp(-\alpha x) f(t/\tau_L), \tag{3}$$

$$\begin{aligned} T_t - \chi T_{xx} = \frac{1-R}{C}(1 - E_g/h\nu_L)\alpha L \\ \times \exp(-\alpha x) f(t/\tau_1), \end{aligned} \tag{4}$$

where R is the coefficient of reflection of the exciting beam from the sample surface, α is the coefficient of light absorption at the excitation wavelength, I is the excitation pulse intensity, $f(t/\tau_L)$ is the laser pulse envelope, τ_L is the pulse duration, and C is the isobaric heat capacity per unit volume. The boundary condition for Eqs. (3) and (4) corresponds to the zero total diffusion flux on the surface $x = 0$.

The above model does not take into account the possible nonlinear effects, the contribution of which was insignificant in our experiments (see Section 4.2) and ignores processes of the electron–hole plasma recombination. An analysis [16] showed that the rates of various recombination processes (surface, linear, and Auger) in Ge single crystals on our time scale (0.1–1 ns) are small and do not influence the profiles of hyperacoustic signals. Note that the surface recombination process can be ignored unless the recombination rate is smaller than the sound velocity; this conclusion follows both from the theory [8] and from the results of experiments on samples with properly prepared surfaces [16].

Now, we present some reference data on the Ge crystal parameters at room temperature, which will be used below: $E_g = 0.65$ eV; $C = 9$ J/(cm^3 K); $\rho = 5.3$ g/cm^3; $c_a = 5.6 \times 10^5$ cm/s (in the [111] direction); $K = 75$ GPa; $\beta = 1.8 \times 10^{-5}$ 1/K; $D = 65$ cm^2/s; $\chi = 0.35$ cm^2/s [17]; $d = -K\partial E_g/\partial P \approx -5$ eV [18]. The optical absorption coefficients for the excitation wavelength employed in the experiments, $\lambda_1 = 1064$ nm and $\lambda_2 = 532$ nm ($h\nu_L = 1.17$ and 2.33 eV, respectively), are $\alpha(\lambda_1) \approx 1.4 \times 10^4$ cm^{-1} [18] and $\alpha(\lambda_2) \approx 5.3 \times 10^5$ cm^{-1} [19]; the reflection coefficient, $R \approx 0.5$. In our experiments, the excitation pulse energy densities were $I\tau_L \le 50$ μJ/cm^2, from which we obtain using Eq. (3) an upper estimate for the electron–hole plasma density: $N \approx 10^{18}$ cm^{-3}.

The hyperacoustic signal profiles were determined by analytically solving Eqs. (1)–(4) in a spectral representation [7, 8], followed by the inverse Fourier transform. For the electron-deformation mechanism, the source of acoustic oscillations is described by Eq. (3) and a solution to the problem (1)–(3) outside the exci-

[1] In piezoelectric semiconductors, the acoustic waves can also be excited through the so-called inverse piezoeffect [8], whereby the photogenerated electron–hole plasma produces screening of the electric field in the sample.

tation region (determined by $\max\{\alpha^{-1}, (D\tau_L)^{1/2}\}$) is as follows [7]:

$$U(\omega) = U_0 \frac{m_D \omega_D}{\omega_D + i\omega} \times \left[\frac{\omega_D}{\omega^2 + m_D^2 \omega^2} + \frac{1}{\sqrt{-i\omega_D}(m_D\sqrt{\omega_D} + \sqrt{-i\omega})} \right] f(\omega), \quad (5)$$

where $\omega_D = c_a^2/D$ is a characteristic frequency for which the wave vectors of the acoustic and diffusion waves are compared; $m_D = \alpha D/c_a$ is the ratio of the time of acoustic wave propagation to the time of carrier diffusion over the region of light absorption (α^{-1}); $f(\omega) = \exp(-\omega^2\tau_L^2)$ is the envelope spectrum of the exciting laser pulse; and $U_0 = (1 - R)dI\tau_L/(h\nu_L\rho c_a^2)$ is a characteristic displacement. As can be seen from expression (5), the spectrum and, hence, the time profile of the acoustic signal are determined by the same sample parameter—the ambipolar diffusion coefficient D of the photogenerated carriers (assuming that the α and c_a values are known).

For the thermoelastic mechanism described by Eq. (4), a solution is given by the same expression (5) in which D is replaced by χ. In this case, the characteristic displacement is $U_0 = -(1 - R)(1 - E_g/h\nu_L)K\beta I\tau_L/(C\rho c_a^2)$. As can be seen from Eq. (1), the ratio of efficiencies of the electron-deformation and thermoelastic mechanisms is $B = N_x d/(K\beta T_x)$. Using Eqs. (3) and (4) and solution (5) and ignoring the transfer of heat and free carriers during the optical excitation time τ_L, this ratio can be expressed as $B = Cd/(K\beta(h\nu_L - E_g))$. For λ_1, this yields $\beta \approx 20$, which indicates that the electron-deformation mechanism in Ge single crystals is significantly more effective than the thermoelastic mechanism. Below, we will demonstrate that our experimental data agree with this estimate. It should be noted that the obtained estimate for B is correct for moderate excitation levels ($N < 10^{19}$ cm^{-3}), that is, until we can neglect the nonlinear recombination processes capable of saturating the linear relationship between N and I.

The effects of propagation of the hyperacoustic signals were taken also into account in the spectral form. The calculated spectrum of displacements in the acoustic wave $U(\omega)$ given by expression (5) was multiplied by the function $K(\omega, x) = K_a(\omega, x)K_d(\omega, x)$ [8] taking into account the absorption and diffraction of the acoustic wave. In this function, the absorption factor is

$$K_a(\omega, x) = \exp(-\gamma\omega^2 x/4\pi^2), \quad (6)$$

where $\gamma = 2.8$ cm^{-1} GHz^{-2} for crystalline Ge in the [111] direction [20]. In the quasi-optical approximation, the diffraction factor can be expressed as [21]

$$K_d(\omega) = \frac{1}{1 + ix/L_d} \exp\left[-\frac{r^2}{a^2(1 + ix/L_d)} \right], \quad (7)$$

where a is the acoustic beam radius (on the $1/e$ level) for $x \longrightarrow 0$ and $L_d = \omega a^2/2c_a$ is the characteristic diffraction length for the spectral component ω. Note that an allowance for the diffraction within the quasi-optical approximation is correct for acoustic wavelengths much shorter than the transverse size of the acoustic beam ($\lambda \ll 2a$).

In addition to the absorption and diffraction effects, an analysis of the hyperacoustic wave propagation in a crystal must take into account the effect of phonon focusing [22], since this phenomenon changes the amplitude–phase relationships between spectral components of the acoustic signal. We have estimated the phonon focusing effect on the hyperacoustic signal profile in experiments with the samples oriented in the focusing and defocusing directions [16]. To within the experimental accuracy, we observed no difference between the profiles measured in these two cases. For this reason, the phonon focusing effect is ignored below.

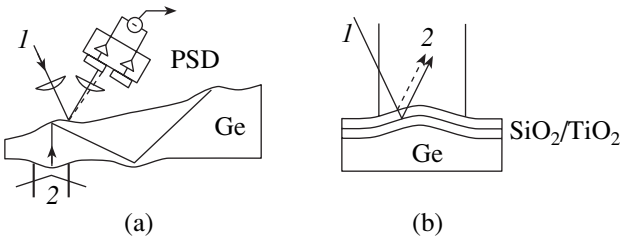

Fig. 1. Schematic diagrams illustrating the laser beam deflection measurements for the sample excited and probed (a) from the opposite sides and (b) from the same side coated with a dielectric mirror film: (*1*) probing beam; (*2*) exciting beam; (PSD) position-sensitive detector.

3. EXPERIMENT: METHOD, SCHEME, SAMPLES

The idea of the photothermal displacement method involving the measurement of small shifts of the surface of a solid sample is as follows [23]. An acoustic beam reaches the sample surface and deforms the material (Fig. 1a). At the same time, a probing light beam focused on the deformed region is mirror-reflected from this surface area. The material straining induces a small deflection of the beam axis in proportion to the slope of the deformed surface and, hence, to the surface displacement. This small deflection is measured by a position-sensitive detector (see, e.g., [24, 25]). There is a significant disadvantage in the originally proposed scheme of measurements: the response signal may contain a contribution not related to the mechanical shift of

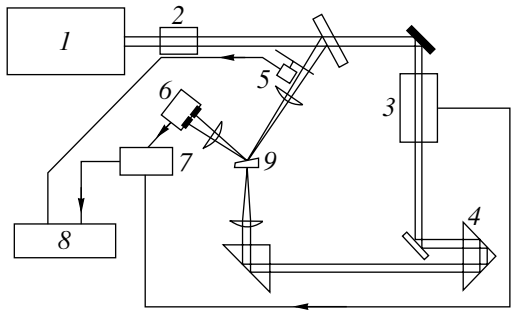

Fig. 2. Schematic diagram of a laser beam deflection spectrometer: (*1*) picosecond laser; (*2*) nonlinear crystal; (*3*) electrooptical modulator; (*4*) delay line; (*5*) mechanical chopper; (*6*) position-sensitive detector; (*7*) frequency converter; (*8*) lock-in detector; (*9*) sample.

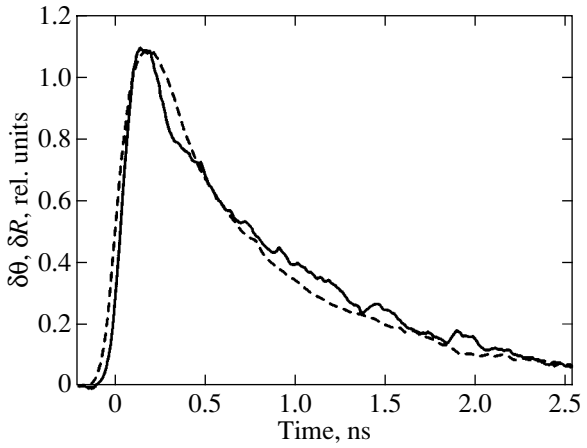

Fig. 3. Dynamics of the deflection signal δθ (solid curve) and reflection coefficient δ*R* (dashed curve) measured in the photoexcitation region.

the sample surface if the excited and probed regions are on the same sample surface [26].

As will be demonstrated below, the propagation effects produce a significant influence on the profile of our hyperacoustic signals only for the pathlengths on the order of $x \sim 100$ μm. For this reason, it was important to measure the hyperacoustic signal profile at a point as close as possible to the region of excitation. For this purpose, we used a scheme with excitation and probing of the same sample surface (Fig. 1b) [27]. In order to eliminate the optical interaction of exciting and probing beams, the sample was coated by a dichroic mirror layer transmitting the former beam and reflecting the latter beam before reaching the excitation region on the Ge crystal surface.

We have developed a method of laser beam deflection measurements with a sensitivity of ~0.1 nrad to the laser beam deflection angle [28], based on the RF lock-in amplification technique. Using this method, it is possible to measure small surface deformations with an amplitude of ~0.1 pm at a time resolution on the level of the laser pulse duration. A scheme of the laser deflection spectrometer is depicted in Fig. 2. The exciting and probing radiation beams were generated by a continuously pumped double-frequency picosecond Nd:YAG laser operating on the wavelengths $\lambda_1 = 1064$ nm and $\lambda_2 = 532$ nm. The λ_1 pulses were produced at a repetition frequency of 100 MHz and had a duration of $\tau_L \approx$ 100 ps. The exciting and probing radiation beams were focused by lenses onto the sample surface, showing spots with a characteristic size of 20–100 and 15–20 μm, respectively. The surface energy density in the exciting beam could be varied from 0 to 5 μJ/cm^2. The photoresponse detection technique is described in detail elsewhere [16, 29, 30].

The samples were [111]-oriented Ge plates cut from an undoped single crystal Ge ingot. The experiments were performed with the samples of three types: (i) ≈5-mm-thick plates polished to an optical quality from one side; (ii) analogous plates with the finished side coated by multilayer dielectric films (dichroic mirrors) (Fig. 1b); and (iii) ≈100-μm-thick wedge-shaped plates (Fig. 1a) polished to an optical quality from both sides. The coated sample had three surface regions with different numbers of sequentially deposited TiO_2 and SiO_2 layers $m = 8$, 18, and 36. These films transmitted well the exciting laser radiation ($\lambda_1 = 1064$ nm) and reflected the probing radiation ($\lambda_2 = 532$ nm), the reflection coefficient being about 90% for the sample surface region with $m = 8$ and ≥99% for the coatings with $m = 18$ and 36. The layer thicknesses were $l_1 =$ 0.18 μm for SiO_2 and $l_2 = 0.12$ μm for TiO_2, as estimated from the optical thickness of $\lambda_2/2$ films. The angle between faces of the wedge-shaped samples was ≈3°, which excluded interference of the acoustic pulse reflected from the crystal–air interface (responsible for the echo signals in the probing channel).

4. EXPERIMENTAL RESULTS

4.1. Hyperacoustic Signal Excitation

In order to probe the hyperacoustic response in the vicinity of the photoexcitation region, we used the scheme presented in Fig. 1b with a sample of the first type (uncoated). The probing channel yielded two signals, including a deflection signal δθ(*t*) and a signal due to the photoinduced reflection δ*R*(*t*). The latter signal was detected by a position-sensitive detector section onto which a probing beam was focused.

Figure 3 shows typical profiles of the δθ(*t*) and δ*R*(*t*) signals. The peak values of the relative variation in the reflection coefficient was $\delta R(t)/R \approx -2 \times 10^{-4}$; the deflection signal δθ(*t*) showed a relative change in the photocurrent on the same level. A characteristic feature of the signals measured is a sharp leading front with a duration of~100 ps observed at the point of coincidence of the exciting and probing radiation pulses. As can be seen from Fig. 3, the two signal profiles virtually coin-

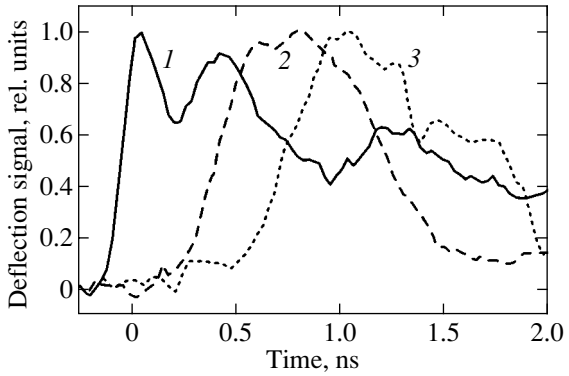

Fig. 4. Time variation of the deflection signal for a sample with dielectric mirror coatings containing various numbers of layers $m = 8$ (*1*), 18 (*2*), and 36 (*3*).

cide in both leading and trailing fronts. Therefore, the deflection signal is related to an optical interaction of the exciting and probing beams on the sample surface, rather than to a mechanical displacement of this surface [26]. As was demonstrated in [16, 26], this deflection signal is due to a transverse phase gradient of the photoinduced complex reflection coefficient.

In order to eliminate the optical interaction of the exciting and probing beams on the sample surface, we performed an experiment with Ge samples coated with dichroic mirror layers. The mirror layer allowed the excited and probed regions to be spatially separated by ~1 μm, thus significantly suppressing the optical interaction of the exciting and probing beams. Figure 4 shows the time variation of the deflection signal for three coatings of different thickness on the same sample. The mirror with $m = 8$ (curve *1*) transmitted about 10% of the probing beam, which produced a deflection signal in the region of zero delay, the profile of which was similar to that of a deflection signal measured in the photoexcitation region (Fig. 3). The second peak in curve *1* of Fig. 4, observed at a delay time of ~0.3 ns relative to the first peak, is due to the dielectric coating being strained by the photoexcited acoustic pulse. The position of each maximum in the acoustic response (the second and third peaks in curve *1* and the peaks in curves *2* and *3*) corresponds to a delay of the acoustic signal propagating in the coating $\tau = lm/c_a$, where $c_a \approx 7 \times 10^5$ cm/s is the average sound velocity in the coating and $l = (l_1 + l_2)/2$ is the average film thickness. The third peak in curve *1*, which is delayed by ~1.3 ns relative to the excitation pulse, is attributed to the acoustic signal traveling three times across the multilayer film. As can be seen from Fig. 4, the acoustic pulse rise and fall times increase with the number of layers in the dielectric coating.

Thus, the experiments with Ge crystal samples excited and probed from the same side coated with dichroic mirror layers showed a displacement of the mirror layers under the action of an acoustic signal excited near the germanium surface.

4.2. Hyperacoustic Signal Propagation

Let us consider the results of experiments with wedge-shaped samples excited and probed from the opposite surfaces (Fig. 1a). Figure 5a (solid curve) shows a deflection signal corresponding to a single passage of the acoustic signal across the sample (pathlength $x \sim 110$ μm). A characteristic peak amplitude of the surface displacement was ~5 pm, which is close to the value calculated within the framework of the electron-deformation mechanism (formula (5)). Also depicted in Fig. 5a are the acoustic signals having passed a length of $x \approx 770$ and 2300 μm. The pathlength traveled by the acoustic signal was calculated using the corresponding delay of the deflection signal relative to the excitation pulse front. The signal that traveled a distance of 110 μm exhibits a bipolar profile; the profile width increases with the path traveled by the acoustic signal (Fig. 5a). It should be noted that the hyperacoustic signal front duration weakly depended on the propagation

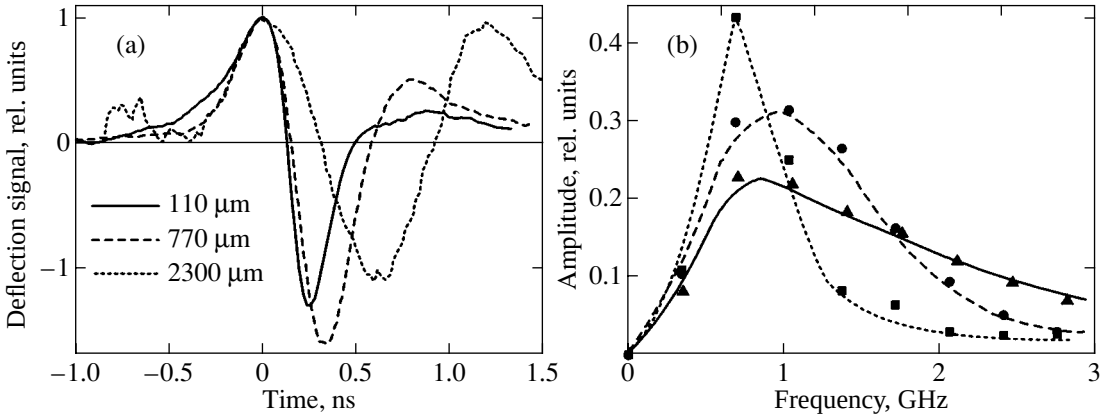

Fig. 5. (a) Deflection signal profiles observed for various acoustic pulse propagation lengths x and (b) the corresponding frequency spectra.

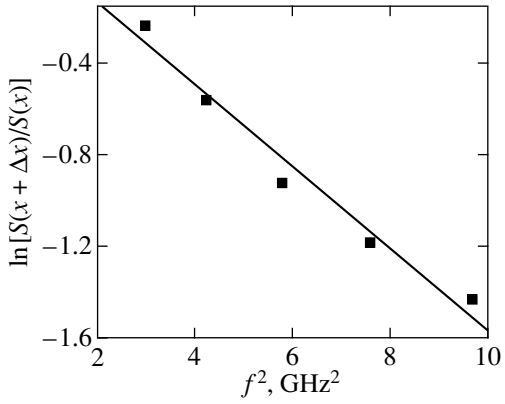

Fig. 6. A plot of the ratio of the high-frequency spectral components (Fig. 5b) versus f^2 for x = 770 and 110 μm (Δx = 660 μm).

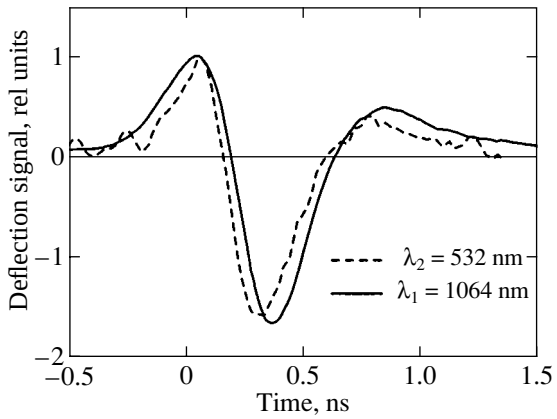

Fig. 7. Profiles of the hyperacoustic signals excited in a wedge-shaped sample at two wavelengths λ_1 and λ_2 and measured for a propagation length of $x \sim 100$ μm.

length and amounted to ~250 ps (on the 1/*e* level). A maximum of the acoustic signal spectrum was close to 1 GHz irrespective of the propagation length (Fig. 5b).

The propagation effects significantly change the acoustic signal profile. As can be seen from Fig. 5b, the acoustic absorption decreases the high-frequency components of the signal spectrum (formula (6)), while diffraction decreases the low-frequency components (formula (7)). As a result, the absorption leads to extension of the leading and trailing fronts of the pulse, while diffraction mostly reduces to differentiation of the signal profile. Indeed, for a given spectral component ω of the signal, formula (7) with $x \gg L_d$ describes differentiation of the profile with respect to time on the beam axis (r = 0). Using the high-frequency (above 1 GHz) spectral components (corresponding to different propagation lengths) of the acoustic signal (Fig. 5b), the absorption coefficient γ was calculated by formula (6) (Fig. 6). This calculation yielded 3 cm^{-1} GHz^{-2} [16], which agrees with the published reference value [20].

The acoustic signal profile did not change when the excitation pulse energy density was varied in the range from 5 to 50 μJ/cm^2, while the signal amplitude increased in proportion to the excitation energy [16]. Therefore, various possible nonlinear effects did not play any significant role for the excitation energy level studied ($N \sim 10^{17}$–10^{18} cm^{-3}).

4.3. Relative Efficiency of the Thermoelastic and Electron-Deformation Mechanisms

Figure 7 shows the hyperacoustic signal profiles for two excitation wavelengths (λ_1 = 1064 nm, λ_2 = 532 nm). As can be seen, the two profiles are very close in shape, which is indicative of an almost identical spatiotemporal localization of the corresponding acoustic sources, although the optical absorption of germanium at these wavelengths differs by more than one order of magnitude: $\alpha^{-1}(\lambda_1) \gg \alpha^{-1}(\lambda_2)$. Indeed, the depth of heat transfer during excitation is $L_T = (\chi\tau_L)^{1/2} \approx 0.1$ μm, while the electron–hole plasma diffusion depth is about ten times as great, $L_N = (D\tau_L)^{1/2} \approx 1$ μm, so that $L_N \approx \alpha^{-1}(\lambda_1)$. Therefore, the regions of localization of the photoexcited electron–hole plasma in the sample excited at λ_1 and λ_2 for the time $\sim\tau_L$ are approximately equal, while the regions of heating determined by $\max(L_T, \alpha^{-1})$ are significantly different. Thus, we may conclude that the main contribution to the hyperacoustic signal excitation for both wavelengths is related to the electron-deformation mechanism.

In order to directly compare efficiencies of the thermoelastic and electron-deformation mechanisms of the optoacoustic response formation, we performed an experiment in which the signal at λ_1 was excited in an Al–Ge sample representing an Al film with a thickness of several tens of nanometers deposited onto a Ge plate surface. The exciting laser beam was incident to the Al-coated surface of the sample. In this experiment, the optoacoustic signal intensity measured in the scheme of Fig. 1a dropped by a factor of 30. Since the Al film was nontransparent, acoustically thin, and (to the first approximation) thermally thin as well, we may suggest that the acoustic signal in the Al–Ge sample is excited due to the near-surface layer of Ge being heated by the Al film [31]. With an allowance for a difference between the reflection coefficients of Ge and Al at the excitation wavelength (λ_1), it was established [31] that the efficiency of the thermoelastic mechanism is lower approximately by one order of magnitude than that of the electron-deformation mechanism (on our time scale). This result agrees with an independent estimate obtained in Section 2.

5. ANALYSIS AND DISCUSSION OF RESULTS

Below we will compare the hyperacoustic signal profiles obtained in the experiment (Section 4) to those calculated within the framework of the model devel-

oped for description of the electron-deformation mechanism of the hyperacoustic wave excitation (Section 2) with an allowance for the diffraction and absorption effects.

5.1. Hyperacoustic Signal Excitation in Multilayer Coatings

Figure 8 shows the hyperacoustic signal profile calculated by formula (5) for a point in the vicinity of the excitation region ($x \longrightarrow 0$). This curve is compared with the deflection signal dynamics observed for a Ge crystal plate coated with a reflecting film containing $m = 18$ layers. A difference between the experimental data and the results of calculation is evident: the measured profile exhibits extended leading and trailing fronts in comparison with the model curve.

The observed time delay and increased duration of the deflection signal (Fig. 4) observed for the sample with multilayer coatings are explained by two factors: optical and acoustic. The former is related to certain features of the probing beam reflection from the multilayer dielectric mirror. Indeed, the probing laser pulse is not only reflected from the outermost layer (distant from the crystal surface), but penetrates into the film as well, to be reflected from deeper layers (up to about ten). The coefficient of reflection of the probing radiation from an SiO_2/TiO_2 interface is rather significant: $(n_1 - n_2)/(n_1 + n_2) = 0.22$, where $n_1 = 1.46$ and $n_2 = 2.3$ are the refractive indices of SiO_2 and TiO_2. Thus, the deflection signal formed due to the probing light reflection from many interfaces contains contributions from several layers, which are separated by the characteristic time interval required for the acoustic pulse to travel through a single layer. For a pair of adjacent SiO_2 and TiO_2 layers, the average delay time per layer is $\tau = l/c_a \approx 40$ ps. Note that the time delay due to the light propagation through the coating is smaller by three orders of magnitude as compared to the acoustic pulse delay and, hence, can be ignored. The second (acoustic) factor is related to interference of the acoustic signal in the multilayer coating, which is caused by a difference in the acoustic impedance of SiO_2 and TiO_2 layers amounting to $Z_1 = 3.4 \times 10^6$ g/(cm^2 s) and $Z_2 = 1.5 \times 10^6$ g/(cm^2 s), respectively. The difference between Z_1 and Z_2 leads to a significant coefficient of reflection of the acoustic signal from the SiO_2/TiO_2 interface: $(Z_1 - Z_2)/(Z_1 + Z_2) \approx 0.4$ (with respect to amplitude). Obviously, both optical and acoustic factors lead to a time delay and broadening of the deflection signal with the characteristic times determined by the acoustic signal propagation across the coating ($m\tau$) and across the depth required for the reflected signal formation (~10τ).

It should also be noted that the model of acoustic signal excitation on the free surface of germanium described by Eqs. (1) and (2) is, generally speaking, valid only for an acoustically thin coating with a thickness of $ml \ll \lambda$, where λ is a characteristic acoustic wavelength. Under the conditions studied, the exciting laser pulse gives rise to a wideband acoustic signal with a maximum spectral density at a wavelength of about 5 μm (see the spectra in Fig. 5b). Therefore, the approximation of acoustically thin film is obeyed, even with a thinnest coating of $m = 8$ layers ($ml \approx 2.4$ μm), only for the longwave components of the hyperacoustic pulse. Thus, the adopted model of the acoustic pulse excitation on the free crystal surface is not quite correct.

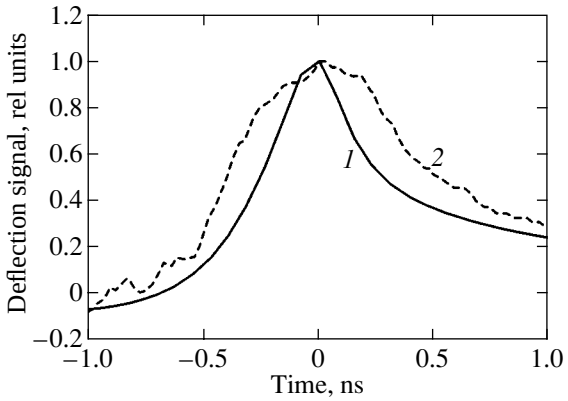

Fig. 8. A comparison of (*1*) the hyperacoustic signal profile calculated for a point in the vicinity of the excitation region and (*2*) the deflection signal dynamics observed for a Ge sample coated with a reflecting film containing $m = 18$ layers.

In addition, note that the experimental signal profiles exhibit an overshoot (Fig. 4) probably related to a complicated mechanism of interaction between the probing pulse and the hyperacoustic response formed in the multilayer coating. A detailed analysis of the measured deflection signal requires taking into account the multibeam interference of both the probing light and the hyperacoustic wave in the multilayer coating, as well as their interaction, which falls outside the scope of this publication.

Thus, the multilayer dielectric coating (a dichroic mirror for the exciting and probing beams) deposited onto the semiconducting crystal sample allows the excitation region to be spatially separated from the region of hyperacoustic signal generation and detection, thus suppressing a spurious deflection signal not related to the mechanical displacement of the sample surface (Fig. 4, the first peak in curve *1*). On the other hand, although the time profile of the measured deflection signal is determined primarily by the hyperacoustic pulse excited in Ge, the effects of optical and acoustic signal interference in the multilayer mirror film does not provide for an adequate profile description within the framework of the model developed in Section 2. Nevertheless, the experiments on a sample with multilayer coating definitely showed that the hyperacoustic signal excited in Ge single crystal is unipolar, whereas the signals measured after traveling through a distance of $x \geq 100$ μm (Fig. 5a) are bipolar. From this, we con-

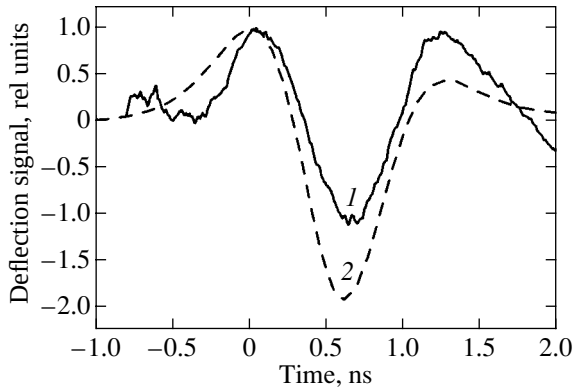

Fig. 9. A comparison of (*1*) the experimental signal to (*2*) the calculated hyperacoustic pulse profile for a propagation length of $x = 2300$ μm.

clude that the propagation effects significantly change the hyperacoustic signal profile even over relatively small distances.

5.2. Hyperacoustic Signal Propagation

Let us compare the calculated hyperacoustic pulse profiles to the experimental signals observed with a wedge-shaped sample. As demonstrated above (Section 4), the acoustic absorption leads to broadening of the experimental profile. An analysis of the signal spectra obtained for various propagation lengths allowed the acoustic absorption coefficient to be estimated at $\gamma \approx 3$ cm^{-1} GHz^{-2}. For this γ value, we may ignore the absorption of low-frequency components (below 1 GHz) of the signal spectrum in the range of propagation lengths studied (<3 mm). Therefore, a significant modification of the signal profile can be related, besides the broadening, to the diffraction effects. Based on the model developed for description of the electron-deformation mechanism, we have calculated the hyperacoustic pulse profiles (see [14, Fig. 3]) with an allowance for both diffraction and absorption (formulas (5)–(7)) for the known parameters of Ge (see the data in Section 2). The results showed good coincidence of the leading fronts of model pulses and experimentally measured signals (Fig. 5a) for various propagation lengths, but the profiles showed not as good a fitting.

The most significant discrepancy was observed for $x = 110$ μm. The calculated profile exhibited a weakly pronounced negative phase, while the experimental signal showed a fast negative phase with a characteristic duration below 0.5 ns. At the same time, the calculated profile acquired a more pronounced negative phase upon taking into account the diffraction effects. However, the duration of this phase was significantly shorter than the experimental value even for large diffraction lengths (see [14, Fig. 3]). We explain these discrepancies by incorrect description of the diffraction of low-frequency components (below 1 GHz) within the framework of the quasi-optical approximation, which is valid for $\lambda = 2\pi c_a/\omega \ll 2a$ (formula (7)). Indeed, the model pulse spectra calculated with neglect of the propagation effects ($x \longrightarrow 0$) show that a characteristic frequency of the energy concentration for the model pulse is ~0.1 GHz, which corresponds to a hyperacoustic wavelength approximately equal to the acoustic beam diameter ($\lambda \approx 2a$).

A comparison of the experimental signal to the profile calculated for a greater propagation length $x = 2300$ μm (Fig. 9) shows a much better agreement than that observed for $x = 110$ μm. We attribute this behavior to the fact that, for large x, the diffraction strongly suppresses the low-frequency components of the spectrum (which are incorrectly described in the quasi-optical approximation). As a result, the quasi-optical approximation provides for a rather adequate description of the remaining spectral components. Thus, we may conclude that the second (negative) phase of the hyperacoustic signal appears as a result of the pulse propagation, rather than during photoexcitation. The same conclusion follows from the results of experiments with the acoustic pulse detection on the excited surface, where the observed signal shows a unipolar profile (Fig. 8). It should be emphasized that such a profile is predicted by the model of acoustic wave excitation at $x \longrightarrow 0$ (see the solid curve in Fig. 8).

5.3. Supersonic Expansion of the Electron–Hole Plasma

Of special interest for us was the leading front duration of a hyperacoustic pulse, since this information helps answering the question concerning the regime of expansion of the photoexcited electron–hole plasma. This question, which has been extensively discussed since the 1980s [32–36], can be briefly formulated as follows: Is it possible to directionally accelerate the charge carriers in a solid up to a hypersonic velocity? The presence of a sound velocity barrier for the expanding electron–hole plasma is related to the possibility of "feedback" of the phonons emitted at the density front of the expanding electron–hole plasma on the velocity of this front.[2] At the beginning of the 1980s, a series of low-temperature experiments with the electron–hole plasma "drops" accelerated up to subsonic velocities were performed with single crystals of Ge [33] and Si [34]. It was demonstrated that these drops could not be accelerated to a supersonic velocity. At the same time, rougher (in our opinion) estimates of the electron–hole plasma velocity, based on an analysis of the Raman scattering line shape of the light emitted from the excited plasma [36], did not point to the presence of such a barrier and suggested that the plasma may propagate at a speed of the order of the Fermi velocity.

[2] An exhaustive review devoted to the problem of sound velocity barrier and the methods for evaluation of the photoexcited electron–hole plasma velocity is given in [31].

Recently [14], we proposed a method for estimating the electron–hole plasma velocity using the duration of the plasma-excited acoustic pulse. The idea of this method is based on the following considerations. Since the acoustic signal is generated at the photoexcited electron–hole plasma density front moving inward the sample, the moment of the acoustic pulse arrival at the rear face of the sample will depend on the plasma propagation velocity. The proposed method can also be applied to an electron–hole plasma propagating in the diffusion regime. In this case [14, 31], the hyperacoustic pulse front will acquire an additional broadening depending on the electron–hole plasma diffusion rate. By this rate, we imply an effective velocity of the electron–hole plasma density front propagation [14], which is equal to $V_D = \alpha D$ immediately upon photoexcitation. Thus, the parameter $m_D = \alpha D/c_a$ introduced in expression (5) has the meaning of a Mach number: m_D is the ratio of the effective plasma diffusion rate immediately upon photoexcitation to the sound velocity. At an excitation wavelength of $\lambda_1 = 1064$ nm, the best coincidence of the model and experimental fronts of the hyperacoustic signals is obtained for $D \approx 50$–70 cm^2/s, which corresponds to the published reference value. This D value corresponds to the Mach number $m_D \approx 1.5$. From this we may conclude that a Ge single crystal at room temperature features a regime of the electron–hole plasma diffusion at a supersonic rate. In this regime, the electron–hole plasma velocity drops down to the velocity of sound within a time period on the order of the hyperacoustic pulse rise time τ_D [14], that is, within ~200 ps. A difference of the experimental pulse front from that calculated for a subsonic diffusion regime can be experimentally observed (see [14, Fig. 3]).

It should be noted that, for the photoexcitation wavelength $\lambda_2 = 532$ nm, the Mach number must be significantly greater than 1.5 because $\alpha(\lambda_2) \gg \alpha(\lambda_1)$. Indeed, the electron–hole plasma excited at λ_2 in a thin layer on the order of $\alpha^{-1}(\lambda_2) \approx 20$ nm diffuses within the excitation pulse duration over the characteristic length $(D\tau_L)^{1/2} \approx 1$ μm. Therefore, the effective velocity of propagation of the electron-hole plasma density front significantly exceeds the sound velocity. The supersonic regime of the electron–hole plasma diffusion in Ge is possible even at room temperature, since the internal pressure Nk_BT (k_B is the Boltzmann constant) in this plasma is higher by three orders of magnitude than the acoustic field pressure $\sim dNU_x \sim dNU/c_a\tau_D$ developed for the typical mechanical displacements (in our experiments, $U \sim 5$ pm). It should be noted that we have also performed analogous experiments in Si and GaAs single crystals [37], where it was found that Si features a subsonic regime of electron–hole plasma diffusion, while GaAs has a supersonic regime. Thus, an analysis of the shape of an acoustic pulse excited by the electron–hole plasma mechanism provides for a correct evaluation of the coefficients of diffusion of the photogenerated charge carriers.

6. CONCLUSION

We have developed a method of laser deflection spectroscopy for studying condensed media, which is based on thorough measurements and analysis of the shape of wideband hyperacoustic pulses in a 0.1–3 GHz frequency range. The proposed technique employs laser beam deflection measurements with a sensitivity limited by photocurrent shot noise. An important conclusion of this study is that, under moderate excitation densities in a semiconductor ($<10^{19}$ cm^{-3}), the electron-deformation mechanism of acoustic wave excitation (rather than the universal thermoelastic mechanism) dominates on a subnanosecond time scale. We have also developed a method for estimating the rate of diffusion of the photoexcited carriers based on the analysis of the related hyperacoustic signal. The most significant physical result of this study is the conclusion about a supersonic velocity of propagation of the photoexcited electron–hole plasma density front in Ge. Note that the fast diffusion of the electron–hole plasma leads to spatial "smearing" of the photoacoustic excitation source (that is, the electron–hole plasma front), thus leading to expansion of the hyperacoustic signals with time.

ACKNOWLEDGMENTS

This work was supported by the INTAS Foundation, grant no. 31680.

REFERENCES

1. C. Thomsen, J. Strait, Z. Vardeny, *et al.*, Phys. Rev. Lett. **53**, 989 (1984).
2. C. Thomsen, H. T. Grahn, H. J. Maris, and J. Tauc, Phys. Rev. B **34**, 4129 (1986).
3. G. S. Kanner, Z. V. Vardeny, and B. C. Hess, Phys. Rev. B **42**, 5403 (1990).
4. O. B. Wright and K. Kawashima, Phys. Rev. Lett. **69**, 1668 (1992).
5. C. J. K. Richardson, M. J. Ehrlich, and J. W. Wagner, J. Acoust. Soc. Am. **107**, 1987 (2000).
6. T. C. Zhu, H. J. Maris, and J. Tauc, Phys. Rev. B **44**, 4281 (1991).
7. S. A. Akhmanov and V. É. Gusev, Usp. Fiz. Nauk **162** (3), 3 (1992) [Sov. Phys. Usp. **35**, 153 (1992)].
8. V. É. Gusev and A. A. Karabutov, *Laser Optical Acoustics* (Nauka, Moscow, 1991).
9. G. S. Kanner, S. Frolov, and Z. V. Vardeny, Phys. Rev. Lett. **74**, 1685 (1995).
10. A. Devos and C. Lerouge, Phys. Rev. Lett. **86**, 2669 (2001).
11. B. Perrin, B. Bonello, J. C. Jeannet, and E. Romatet, Prog. Nat. Sci. **S6**, 444 (1996).

12. O. B. Wright and V. E. Gusev, Appl. Phys. Lett. **66**, 1190 (1995).
13. S. M. Avanesyan, V. E. Gusev, and N. I. Zheludev, Appl. Phys. A **40**, 163 (1986).
14. N. V. Chigarev, D. Yu. Paraschuk, X. Y. Pan, and V. E. Gusev, Phys. Rev. B **61**, 15837 (2000).
15. O. B. Wright, B. Perrin, O. Matsuda, and V. E. Gusev, Phys. Rev. B **64**, 081202(R) (2001).
16. N. V. Chigarev, Candidate's Dissertation in Physics and Mathematics (Mosk. Gos. Univ., Moscow, 1998).
17. *Handbook of Physical Quantities*, Ed. by I. S. Grigoriev and E. Z. Meilikhov (Énergoatomizdat, Moscow, 1991; CRC Press, Boca Raton, 1997).
18. *Landolt-Bernstein: Numerical Data and Functional Relationships in Science and Technology*, Ed. by O. Mandelung, M. Schulz, and H. Weiss (Springer-Verlag, New York, 1982), Group III, Vol. 17a.
19. D. H. Auston and C. V. Shank, Phys. Rev. Lett. **32**, 1120 (1974).
20. *Acoustical Crystals*, Ed. by M. P. Shaskol'skaya (Nauka, Moscow, 1982).
21. M. B. Vinogradova, O. V. Rudenko, and A. P. Sukhorukov, *The Theory of Waves* (Nauka, Moscow, 1990).
22. G. A. Northop and J. P. Wolfe, Phys. Rev. B **22**, 6196 (1980).
23. M. A. Olmstead, N. M. Amer, S. Kohn, *et al.*, Appl. Phys. A **32**, 141 (1983).
24. E. Dieulesaint and D. Royer, *Elastic Wave Propagation*, Ed. by M. F. McCarthy and M. A. Hayes (North-Holland, Amsterdam, 1989), p. 17.
25. H. Sontag and A. C. Tam, IEEE Trans. Ultrason. Ferroelectr. Freq. Control **33**, 500 (1986).
26. J. E. Rothenberg, Opt. Lett. **13**, 713 (1988).
27. N. V. Chigarev, D. Yu. Parashchuk, and Yu. S. Pan, Izv. Ross. Akad. Nauk, Ser. Fiz. **64**, 24 (2000).
28. D. Yu. Parashchuk and N. V. Chigarev, Opt. Spektrosk. **82**, 908 (1997) [Opt. Spectrosc. **82**, 834 (1997)].
29. D. Yu. Paraschuk, T. A. Kulakov, O. Yu. Nedopekin, *et al.*, Rev. Sci. Instrum. **68**, 3989 (1997).
30. N. V. Chigarev, O. Yu. Nedopekin, Yu. S. Pan, and D. Yu. Parashchuk, Prib. Tekh. Éksp. **41**, 111 (1998).
31. S. Yu. Pan, Candidate's Dissertation in Physics and Mathematics (Mosk. Gos. Univ., Moscow, 2000).
32. A. Forchel, H. Schweizer, and G. Mahler, Phys. Rev. Lett. **51**, 501 (1983).
33. M. A. Tamor, M. Greenstein, and J. P. Wolfe, Phys. Rev. B **27**, 7353 (1983).
34. M. A. Tamor and J. P. Wolfe, Phys. Rev. B **26**, 5743 (1982).
35. I. V. Kukushkin and V. D. Kulakovskiĭ, Fiz. Tverd. Tela (Leningrad) **25**, 2360 (1983) [Sov. Phys. Solid State **25**, 1355 (1983)].
36. K. T. Tsen and O. F. Sankey, Phys. Rev. B **37**, 4321 (1988).
37. N. V. Chigarev and D. Yu. Paraschuk, Proc. SPIE 4749 (2002).

Translated by P. Pozdeev

Journal of Experimental and Theoretical Physics, Vol. 94, No. 3, 2002, pp. 637–643.
Translated from Zhurnal Éksperimental'noĭ i Teoreticheskoĭ Fiziki, Vol. 121, No. 3, 2002, pp. 739–746.

SOLIDS
Electronic Properties

Dielectric Properties of Antiferroelectric Liquid Crystals Composed of Banana-Like Molecules

N. M. Shtykov[a], M. I. Barnik[a], S. P. Palto[a, *], L. M. Blinov[a], G. Pelzl[b], and W. Weissflog[b]

[a]*Shubnikov Institute of Crystallography, Russian Academy of Sciences, Moscow, 117333 Russia*
**e-mail: palto@online.ru; lbf@ns.crys.ras.ru*
[b]*Institute of Physical Chemistry, Martin Luther University, 06108, Halle (S), Germany*

Received September 13, 2001

Abstract—The dielectric properties of an antiferroelectric B_2 phase representing a homolog (n = 14) from a series of 4-chloro-1,3-phenylene-bis[4-(4-n-alkylphenyl)aminobenzoates] with banana-like molecules were studied. The temperature dependence of the dielectric relaxation time was measured, and the corresponding activation energy was determined. The kinetics of the dielectric permittivity was studied in the course of the polarization vector variation under the action of a low-slope triangular bias voltage in the entire temperature range of existence of the B_2 phase. Dependence of the dielectric permittivity on the electric field strength (bias voltage) is determined by the presence of two polar subsystems forming the antiferroelectric B_2 phase. *© 2002 MAIK "Nauka/Interperiodica".*

1. INTRODUCTION

In recent years, polar [12], antiferroelectric [2–5], and ferroelectric [6] liquid crystals (LCs) were synthesized, which (in contrast to the previously known chiral ferro- and antiferroelectric LCs [7, 8]) are composed of nonchiral (mirror-symmetric) molecules and are characterized by large spontaneous polarizations [9]. From the basic standpoint, of special interest are new LCs with banana-like molecules [2, 3, 5, 6, 10] capable of spontaneously forming macroscopic domains possessing a chiral structure as a result of local breakage of the mirror symmetry [11]. In addition, these LCs exhibit a fast change of the polarization vector and transparency under the action of an applied electric field, which makes the antiferroelectric B_2 phase composed of the banana-like molecules a promising material for display technology.

A favorable packing in a smectic layer of molecules with bent cores is that for which the convex parts of all these banana-like molecules are oriented in the same direction parallel to the polar axis. In addition, the preferred direction of long axes of these molecules in the plane perpendicular to the polar axis deviates from the normal to the smectic layer. The breakage of mirror symmetry, caused by these two factors of molecular ordering, results in that each smectic layer possesses chiral properties despite the fact that individual molecules are achiral. In this case, chirality appears due to a polar order generated by a special steric packing of banana-like molecules—in contrast to the usual ferroelectric LCs where the polar order is a consequence of the intrinsic molecular chirality.

The antiferroelectric B_2 phase of compounds with banana-like molecules is a tilted smectic phase featuring an isotropic distribution of the mass centers of molecules in the smectic layer [5]. According to a model proposed by Link *et al.* [11], the B_2 phase may contain coexisting antiferroelectric domains of three types: racemic domains and chiral domains of two types (with opposite handedness). The chiral domains with opposite handedness are present in approximately equal amounts [12].

In the absence of an external field (Fig. 1b), the racemic domains (composed of smectic layers of opposite handedness) are characterized by the same azimuthal angles of the tilt planes (determined by the LC director and the layer normal) of molecules in all smectic layers (this synclinic structure is analogous to that existing in smectic C phases), but the spontaneous polarization vectors $\mathbf{P}_S$ of the adjacent smectic layers are antiparallel. When an external electric field $\mathbf{E}$ is applied, the handedness of each smectic layer remains the same but (for the field strength exceeding a certain threshold) the polarization vectors of all smectic layers are aligned in the field direction (Fig. 1c). As a result, the azimuthal angles of the tilt planes of molecules in the adjacent layers differ by ±180° (anticlinic structure).

The chiral domains in the ground state possess an anticlinic structure (Fig. 1d) comprising smectic layers of the same handedness but opposite directions of the spontaneous polarization in the adjacent layers. In a sufficiently strong electric field, the spontaneous polarization vectors of all smectic layers align in the field (Fig. 1e) and the chiral domains acquire a synclinic structure. The azimuthal angles of the tilt planes of

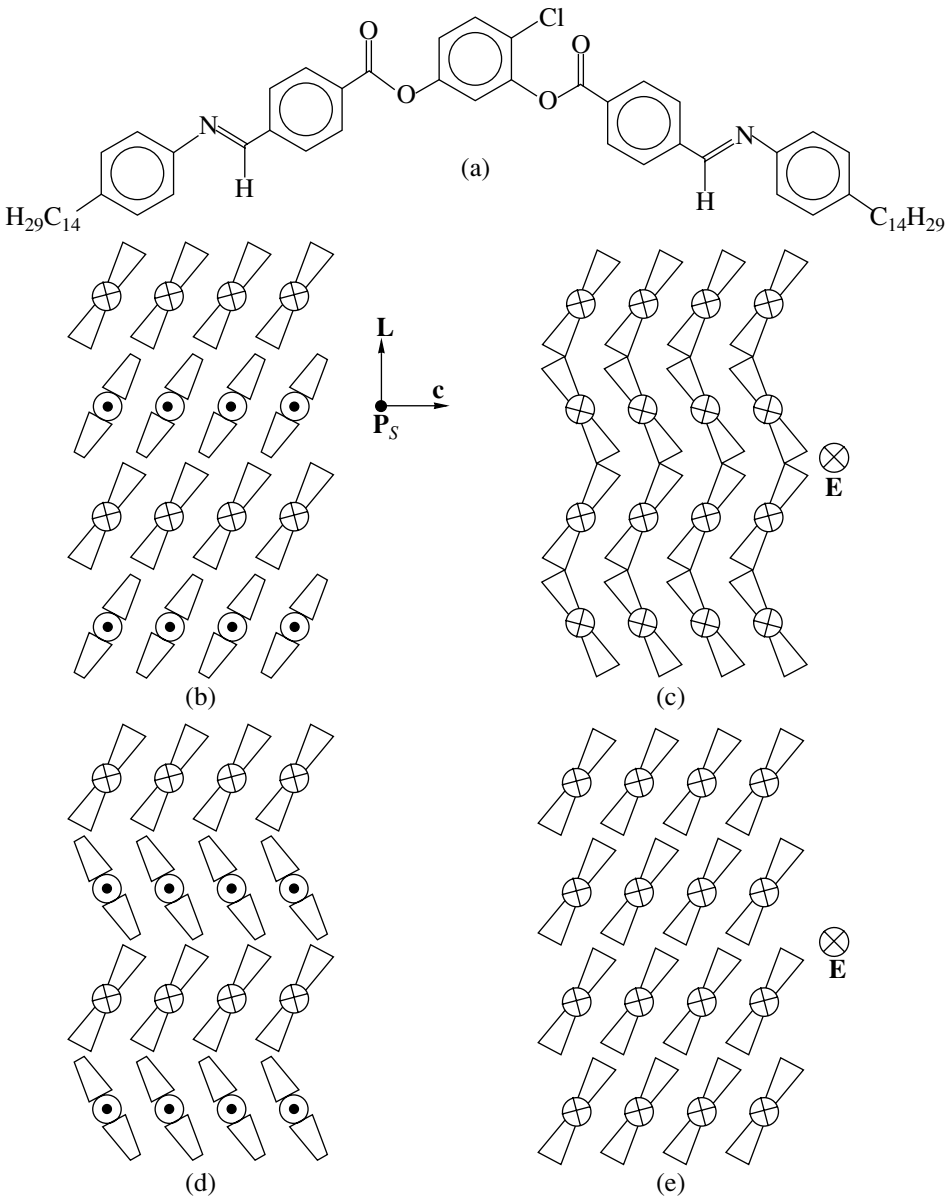

Fig. 1. Schematic diagrams showing (a) chemical structure of a banana-like molecule and the patterns of molecular ordering in (b, d) racemic and (c, e) chiral domains in the ground state for (b, c) $E = 0$ and (d, e) for the applied electric field strength exceeding a threshold value. A vector diagram near the second smectic layer of the racemic domain shows vectors determining the chiral properties: **L** is the normal to the smectic layer, **c** is the projection of the LC director onto the smectic layer plane, and $\mathbf{P}_S$ is the vector of spontaneous polarization of the smectic layer.

molecules in the chiral domains of opposite handedness differ by ±180°. Recently, Kats and Lazherovich [13] gave a theoretical justification of the observed domain structures within the framework of the Landau theory.

In the general case, the dielectric properties of various domains must be different, with the permittivity changing differently in response to variation of the bias voltage frequency and magnitude. The purpose of this experimental work was to study the dielectric properties of a liquid-crystalline compound with banana-like molecules in a broad temperature range of existence of the B_2 phase.

2. EXPERIMENT

The experiments were performed with a homolog representing a series of 4-chloro-1,3-phenylene-bis[4-(4-*n*-alkylphenyl)aminobenzoates] possessing a structure depicted in Fig. 1a. This compound forms an antiferroelectric B_2 phase in a temperature range from 75 to 127°C [14]. The transition from B_2 into an isotropic state is a first-order phase transition. The B_2 phase texture observed in a polarization microscope depends on the method of the cell surface preparation and on the temperature and field prehistory of a given sample. The

B_2 phase is characterized by a high spontaneous polarization on the order of 500 nC/cm^2 [14] (we obtained ~400 nC/cm^2 in [15]).

The LC cells were prepared by a conventional technique using glass plates with transparent electrodes. A planar orientation of the LC layer was provided by rubbing a polyimide film deposited onto the electrode. Two glass plates prepared in this way were assembled into a flat capacitor cell with an interelectrode gap determined by 10-μm-thick Teflon spacers. The overlapping area of the upper and lower electrodes was 4.5×4.5 mm^2.

The scheme of dielectric measurements is presented in Fig. 2. The probing sinusoidal signal with a frequency in the 100 Hz–10 kHz range from oscillator *1* and the slowly varying triangular voltage (for biased measurements) from ramp generator *2* operating at a repetition frequency of 0.01 Hz were fed to the input of summing amplifier *3*. The output signal comprising a sum of the ±95-V triangular bias and 0.25-V probing sinusoidal signals was applied to sample *4*. The measuring circuit represented a set of virtual devices provided by a PhysLab multipurpose program package [16]. In particular, a virtual lock-in detector *5* with recorder *6* was used to measure the amplitude and phase relationships of the harmonic components of a response current in a 3-kΩ load resistor *7*. The PhysLab virtual lock-in detector is capable of simultaneously measuring both real and imaginary components of the current passing through a sample. The possibility of separating these components is a basis of the method employed for determining the dielectric permittivity and losses of the LC sample studied. The sample temperature was measured using a platinum resistor *8* (temperature sensor) and a multimeter unit *9* from which the signal was transmitting via a serial computer port to the PhysLab recorder.

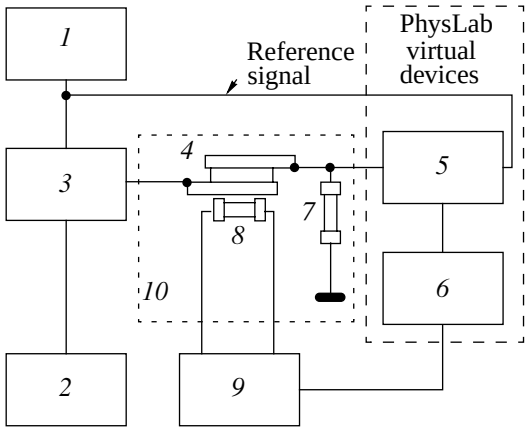

Fig. 2. Schematic diagram of the experimental setup with lock-in detector for studying the dielectric properties of LCs: (*1*) sinusoidal signal generator; (*2*) ramp generator; (*3*) summing amplifier; (*4*) LC cell; (*5*) lock-in detector; (*6*) recorder; (*7*) load resistor; (*8*) platinum temperature sensor; (*9*) multimeter; (*10*) temperature-controlled chamber.

3. THEORETICAL PRINCIPLES OF DIELECTRIC MEASUREMENTS

In the general case, the current density in a sample obeys the well-known relationship

$$j(t) = \sigma E(t) + \frac{\partial D(t)}{\partial t}, \quad (1)$$

where σ is the specific conductivity, $E(t)$ is the electric field, and $D(t)$ is the displacement. In order to determine a contribution from the spontaneous polarization to dielectric permittivity of a polar liquid crystal, it is convenient to write the displacement as

$$D(t) = \varepsilon_0 \varepsilon_1 E(t) + P(t), \quad (2)$$

where $\varepsilon_0 = 8.85 \times 10^{-12}$ F/m is the permittivity of vacuum, ε_1 is the LC permittivity without the spontaneous polarization contribution, and $P(t)$ is the contribution due to the spontaneous polarization of smectic layers aligned by the applied electric field. In Eq. (2), the terms ε_1 and $P(t)$ are macroscopic means over a manifold of smectic layers with different orientations of the spontaneous polarization vector. According to the model proposed in [11], the B_2 phase in the absence of the electric field is unpolarized ($P = 0$); as the applied field strength increases, the polarization grows and eventually reaches saturation ($P \approx P_S$) for field strengths significantly exceeding the polarization threshold level.

In order to study the voltage dependence of the dielectric properties of our LCs, a slowly varying bias field $E_b(t) = E_m F(t)$ of a triangular shape with large amplitude E_m was applied to a sample, which led to reorientation of the spontaneous polarization vectors of smectic layers in the field direction. The sample was simultaneously probed with a sinusoidal field $E_i(t) = E_{i0} \sin \omega t$ of small amplitude. Thus, the total field applied to the sample is the sum $E(t) = E_b(t) + E_i(t)$. Dependence of the polarization P on the applied electric field can be expressed as

$$\begin{aligned} P(E(t)) &\approx P(E_b(t)) + \left(\frac{dP}{dE}\right)_{E_b} E_i(t) \\ &= P(E_b(t)) + \varepsilon_0 \chi(E_b(t)) E_i(t) \end{aligned} \quad (3)$$

or, with an allowance for the frequency dispersion of the dielectric susceptibility χ, as

$$P(t) = P_{E_b} + \varepsilon_0(\chi' E_{i0} \sin \omega t - \chi'' E_{i0} \cos \omega t). \quad (4)$$

Here, the quantities χ' and χ" depend on the bias field $E_b(t)$ and represent the real and imaginary parts of the dielectric susceptibility χ. Substituting expressions (4) and (2) into Eq. (1), we obtain an expression for the current density through the sample. We will neglect dispersion of the permittivity ε_1, because the relaxation frequency of this value usually falls in the range of high

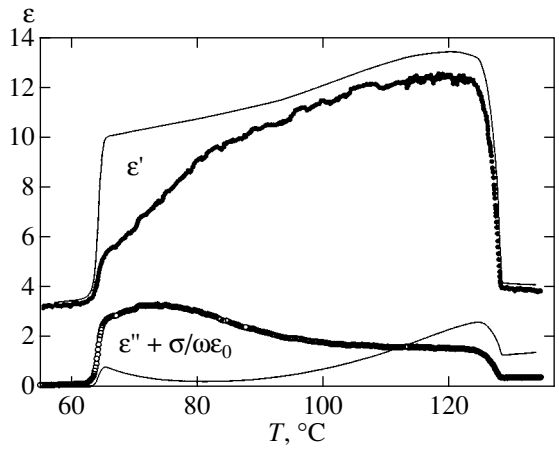

Fig. 3. The dielectric permittivity ε' and losses ε" + σ/ωε$_0$ as functions of the temperature for the isotropic and B_2 phases measured in a nonbiased sample using the probing signal frequencies f = 1 kHz (solid curves) and 10 kHz (filled and open circles).

frequencies (~1 MHz and above); in addition, we will ignore the change of ε_1 induced by the bias field, because these variations are small as compared to the change in χ related to the spontaneous polarization.

A voltage drop measured on the load resistor at a frequency ω can be expressed as follows:

$$U(t) = U_x(t) + U_y(t) = AR_L E_{i0}[(\sigma + \omega\varepsilon_0\chi'')\sin\omega t + \omega\varepsilon_0(\varepsilon_1 + \chi')\cos\omega t], \quad (5)$$

where A is the overlapping area of the upper and lower cell electrodes and R_L is the load resistance (Fig. 2). Using a probing sinusoidal signal with the base frequency ω and the scheme of lock-in detection tuned to this frequency, it is possible to measure the voltage components $U_y(t)$ and $U_x(t)$ proportional to the dielectric permittivity and losses, respectively. Possessing a relative phase shift of 90°, the two components, are readily separated by the phase-sensitive lock-in detector scheme.

The experimentally measured dielectric parameters are determined by the formulas

$$\varepsilon'' + \frac{\sigma}{\omega\varepsilon_0} \equiv \chi'' + \frac{\sigma}{\omega\varepsilon_0} = \frac{\overline{U_x}}{AR_L E_{i0}\omega\varepsilon_0},$$
$$\varepsilon' \equiv \chi' + \varepsilon_1 = \frac{\overline{U_y}}{AR_L E_{i0}\omega\varepsilon_0}, \quad (6)$$

where ε' and ε" are the real and imaginary components of the effective permittivity of an LC sample, and $\overline{U_x}$ and $\overline{U_y}$ are the effective (rms) voltages measured by the lock-in detector.

4. RESULTS AND DISCUSSION

Figure 3 shows the dielectric permittivity ε' and losses ε" + σ/ωε$_0$ of the isotropic and B_2 phases measured without bias (E_b = 0) as functions of the temperature in the sample cooling mode. The measurements were performed for the probing signal frequencies f = 1 and 10 kHz. The sharp increase in ε' observed for the B_2 phase is too large for a contribution from individual molecules related merely to a change in the molecular order upon the phase transition. It is obvious that only collective motions of molecules in the smectic layers possessing large spontaneous polarizations can lead to this large growth in the ε' value.

However, the model proposed in [11], which stipulates an antiferroelectric structure of racemic and chiral domains (and, hence, a high threshold for the polarization onset), also fails to explain the large increase in ε' observed for the B_2 phase in small fields. Therefore, the base concepts of this model have to be checked and refined.

As the temperature of the B_2 phase is lowered, the permittivity ε' monotonically decreases as well (as a result of decreasing relaxation frequency) and sharply drops upon crystallization (down to a value corresponding to the crystal). The contribution of electric conductivity to the dielectric losses (σ/ωε$_0$) decreases in inverse proportion to the probing field frequency ω and becomes negligibly small as compared to the imaginary part of the permittivity ε" at a sufficiently high frequency. This decrease can be seen on comparing the dielectric losses observed at 1 and 10 kHz in the isotropic phase.

In the Debye approximation, the complex permittivity in the relaxation region is described by the formula

$$\varepsilon^* = \varepsilon' - j\varepsilon'' = \varepsilon_\infty + \frac{\varepsilon_{\omega 0} - \varepsilon_\infty}{1 + j\omega\tau}, \quad (7)$$

where $\varepsilon_{\infty 0}$ is the static permittivity, ε_∞ is the high-frequency permittivity, and τ is the characteristic dielectric relaxation time. Using this formula, we can readily express the relaxation time as a function of the real and imaginary parts of the effective permittivity and the probing signal frequency:

$$\tau = \frac{\varepsilon''}{\omega(\varepsilon' - \varepsilon_\infty)}. \quad (8)$$

Figure 4 shows a plot of the dielectric relaxation time in the B_2 phase versus the inverse temperature, which was calculated by formula (8) using data on the temperature dependence of ε' and ε" measured at a probing signal frequency of 10 kHz (Fig. 3). The calculation was performed assuming that the dielectric losses at 10 kHz are determined predominantly by the imaginary part ε" of the complex permittivity. In the region of lower temperatures of existence of the B_2 phase (from 100°C down to the crystallization temperature of ~65°C), the τ versus $1/T$ curve is well described

by the Arrhenius equation $\tau = \tau_0 \exp(W/k_B T)$ with an activation energy of $W = 0.65$ eV (60 kJ/mol). A somewhat smaller value of the activation energy ($W = 0.55$ eV) was obtained for an analogous compound in [12]. The difference can be explained by the presence of a lateral chlorine atom in the central benzene ring of our compound, which can lead to a more pronounced retardation of the rotation of molecules about longitudinal axis.

A deviation of the experimental temperature dependence of the relaxation times from the Arrhenius law in the region of higher temperatures of existence of the B_2 phase probably indicates that some other mechanism of the dielectric relaxation becomes dominating in this region. Such a mechanism, involving rotation of the director on a cone around the normal to the smectic layer, is well known in chiral ferroelectric LCs [17]. This mechanism is characterized by a lower activation energy [12]—that is, by a less steep temperature dependence of the relaxation time—in agreement with the experimental data presented above. The temperature dependence of the repolarization time studied previously [15] by measuring a current generated in response to a meander signal was characterized by an activation energy of $W = 0.49$ eV. This value is smaller by a factor of almost one and a half than the activation energy for the mechanism of rotation about the longitudinal axis.

Figure 5 shows time variation of the dielectric permittivity ε' and losses $\varepsilon'' + \sigma/\omega\varepsilon_0$ over a single period of the triangular bias voltage. The periodic bias repetition frequency was 0.01 Hz, and the voltage amplitude was ±95 V. At a lower temperature in the region of existence of the B_2 phase (Fig. 5a), both curves display two narrow peaks (within each half-period) situated almost symmetrically relative to the point $U_b = 0$. This shape of response to the triangular bias is characteristic of repolarization currents in the antiferroelectric phase. At higher temperatures of the B_2 phase (Fig. 5b), we may also speak of two ε' peaks observed within each bias half-period. However, the two peaks are no longer symmetric relative to the point $U_b = 0$; the double peak corresponding to greater absolute value of the displacement dominates in both amplitude and area of the signal. Moreover, the ε' response to the bias exhibits a nonthreshold behavior: the ε' value increases with the bias field beginning from very small voltages.

A thresholdless increase in ε' with small bias voltages is also observed in the chiral smectic SmC* ferroelectric phase below a threshold voltage corresponding to the helicoid rotation onset. There is a narrow peak in ε' at $|U_b| \approx 40$ V observed with decreasing bias field, as well as a broad peak observed with increasing bias at approximately the same voltage. This behavior suggests that the B_2 phase features two polar subsystems, ferroelectric and antiferroelectric.

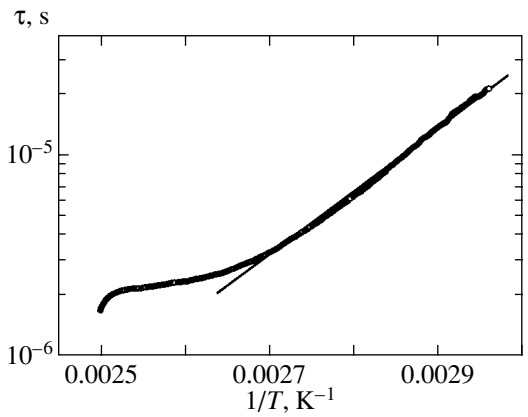

Fig. 4. A plot of the dielectric relaxation time τ phase versus the inverse temperature for the B_2 phase. Solid line shows the approximating Arrhenius plot $\tau = \tau_0 \exp(W/k_B T)$ with an activation energy of $W = 0.65$ eV.

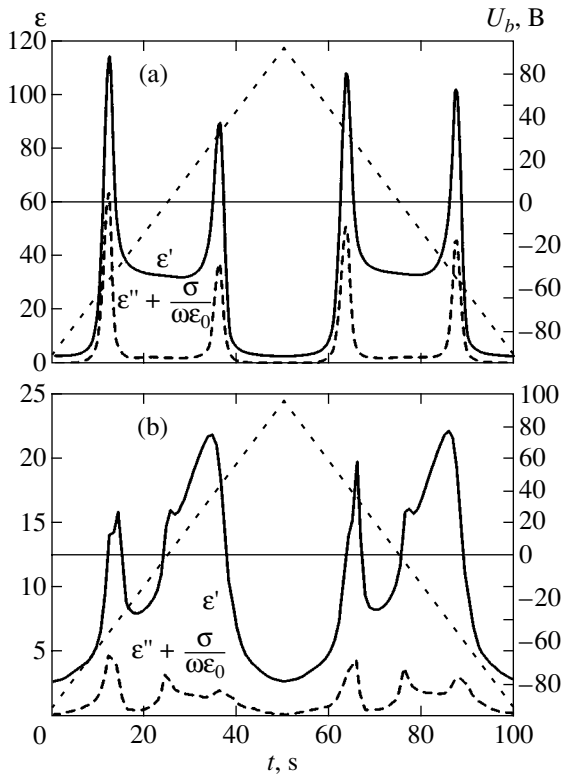

Fig. 5. Time variation of the dielectric permittivity ε' and losses $\varepsilon'' + \sigma/\omega\varepsilon_0$ measured over a single period of the triangular bias voltage U_b (dashed curve) at $T = 108$ (a) and 122°C (b).

It should be noted that investigations of the B_2 phase of banana-like LCs by method of repolarization currents gave ambiguous results. In some cases [12, 14], the response current showed evidence of a typical antiferroelectric behavior of the B_2 phase. However, Niori *et al.* [2, 18] observed the response characteristic of an antiferroelectric phase. An analysis of the features

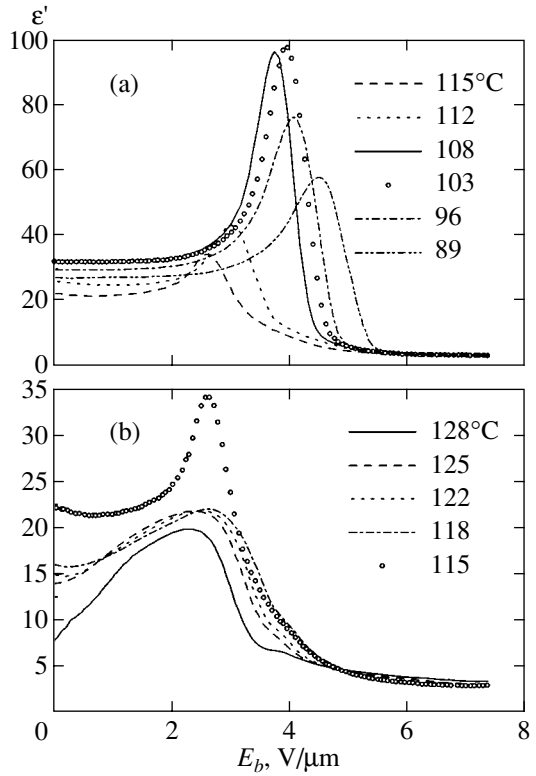

Fig. 6. The plots of permittivity ε' versus the bias field strength E_b measured at (a) lower and (b) higher temperatures in the region of existence of the B_2 phase.

observed in the dielectric spectra led to a conclusion that ferroelectric clusters are present in the B_2 phase [3]. According to our data [15], the behavior of the response current depends on the amplitude of the triangular bias voltage. When the amplitude is below the polarization switching threshold ($U_b < 40$ V), the response exhibits a ferroelectric character whereby a single current peak is observed in each bias half-period with increasing $|U_b|$. If the voltage amplitude exceeds the threshold, two current peaks appear within each bias half-period; being approximately symmetric relative to the point $U_b = 0$, these peaks are characteristic of the antiferroelectric behavior.

Figure 6 shows the plots of permittivity ε' versus the bias field strength E_b measured at various temperatures in the region of existence of the B_2 phase. At lower temperatures in this region (Fig. 6a), the permittivity weakly varies with the field strength below a threshold at which the field-induced transition from antiferroelectric to ferroelectric state takes place. At this point the permittivity first increases to a maximum and then drops to a minimum (characteristic of nonpolar liquid crystals). Analogous suppression of the dielectric permittivity by a large external field is also observed in the usual chiral ferroelectric LCs [17]. At higher temperatures of the B_2 phase, the permittivity ε' first increases with the bias field strength E_b, passes through a maximum, and decreases with increasing bias. The character of variation of ε' as a function of the bias field strength changes within the temperature interval of 115–118°C. The same interval contains a bending point observed on the temperature dependence of the spontaneous polarization P_S, which is accompanied by certain changes in the sample texture [15].

An analysis of the curves of plots of permittivity versus the bias field strength (Fig. 6) shows that the threshold field strength corresponding to the transition from antiferroelectric to ferroelectric state monotonically varies from 2.3 to 4.5 V/μm with increasing temperature; in the high-temperature region of existence of the B_2 phase, the threshold field strength varies rather insignificantly (from 2.3 to 2.6 V/μm).

The model proposed in [11] for description of the chiral domain structure in the antiferroelectric B_2 phase fails to explain the ferroelectric behavior of this phase manifested by large ε' values and their field dependence in the high-temperature region. However, a certain modification of this model might eliminate the discrepancies. The measurements of selective reflectance and circular dichroism [19] showed evidence of the presence of a chiral structure with large helix pitch. Such a structure may form provided that the tilt plane of molecules in the smectic layer would rotate on the passage to the adjacent layer by an angle of $\pm 180° + \alpha$, rather than by $\pm 180°$ as stipulated for the chiral domains in the original model [11]. According to the modified model, there is no complete compensation of spontaneous polarization in the adjacent smectic layers and the residual polarization $\delta P_S \approx \alpha P_S$ would exhibit precession with a period of $H \approx (360/\alpha)d$ along the normal to the smectic layers ($d \approx 50$ Å is the layer thickness). For $\alpha = 1°$, we can estimate the residual polarization at $\delta P_S = 0.017 \times 500$ nKl/cm^2 = 8.5 nKl/cm^2 and the helix pitch at $H = 1.8$ μm. Thus, we may speak of a chiral ferroelectric subsystem existing in the chiral domains of the antiferroelectric B_2 phase. This subsystem accounts for the manifestations of ferroelectric properties in the predominantly antiferroelectric B_2 phase.

5. CONCLUSION

We have studied the dielectric properties of an antiferroelectric B_2 phase representing a homolog ($n = 14$) from a series of 4-chloro-1,3-phenylene-bis[4-(4-*n*-alkylphenyl)aminobenzoates] with banana-like molecules. A complicated behavior of the dielectric response to triangular bias voltage observed in the high-temperature part of the region of existence of the antiferroelectric B_2 phase is explained by the coexistence of two polar subsystems, ferroelectric and antiferroelectric, in the domain structure. These subsystems are characterized by different shapes of the curves of permittivity versus bias field strength and by different threshold fields for the transition from antiferro- to ferroelectric state with a homogeneous spontaneous polar-

ization. The temperature dependence of the dielectric relaxation time in the B_2 phase was measured, and the corresponding activation energy was determined. A modification of the existing model of the antiferroelectric B_2 phase is suggested, which explains the features of the experimental data obtained.

ACKNOWLEDGMENTS

This study was supported by the Russian Foundation for Basic Research (project nos. 99-02-16484 and 01-02-16287), by *Deutsche Forschungsgemeinschaft*, and by *Deutsche Fond der Chemischen Industrie*.

REFERENCES

1. F. Tournilhac, L. M. Blinov, J. Simon, and S. V. Yablonsky, Nature **359**, 621 (1992).
2. T. Niori, T. Sekine, J. Watanabe, *et al.*, J. Mater. Chem. **6**, 1231 (1996).
3. H. Schmalfuss, W. Weissflog, A. Hauser, and H. Kresse, Proc. SPIE **4147**, 109 (2000).
4. E. Soto Bustamante, S. V. Yablonskii, B. I. Ostrovskii, *et al.*, Liq. Cryst. **21**, 829 (1996).
5. W. Weissflog, Ch. Lischka, T. Benne, *et al.*, Proc. SPIE **3319**, 14 (1998).
6. D. M. Walba, E. Körblova, R. Shao, *et al.*, Science **288**, 2181 (2000).
7. R. Meyer, L. Liebert, L. Strzelecki, and P. Keller, J. Phys. Lett. **36**, L69 (1975).
8. A. Fukuda, Y. Takanishi, T. Isozaki, *et al.*, J. Mater. Chem. **4**, 997 (1994).
9. L. M. Blinov, Liq. Cryst. **24**, 143 (1998).
10. I. Dozov, Europhys. Lett. **56**, 247 (2001).
11. D. R. Link, G. Natale, R. Shao, *et al.*, Science **278**, 1924 (1997).
12. G. Heppke, A. Jakli, S. Rauch, and H. Sawade, Phys. Rev. E **60**, 5575 (1999).
13. E. I. Kats and J. Lajzerowicz, Zh. Éksp. Teor. Fiz. **117**, 951 (2000) [JETP **90**, 826 (2000)].
14. W. Weissflog, Ch. Lischka, S. Diele, *et al.*, Mol. Cryst. Liq. Cryst. **328**, 101 (1999).
15. M. I. Barnik, L. M. Blinov, N. M. Shtykov, *et al.*, submitted to Liq. Cryst.
16. S. P. Palto, Doctoral Dissertation in Physics and Mathematics (Inst. Kristallografii Ross. Akad. Nauk, Moscow, 1998).
17. S. T. Lagerwall, *Ferroelectric and Antiferroelectric Liquid Crystals* (Wiley-VCH, Weinheim, 1999).
18. T. Sekine, Y. Takanishi, T. Niori, *et al.*, Jpn. J. Appl. Phys. **36**, L1201 (1997).
19. T. Sekine, T. Niori, M. Sone, *et al.*, Jpn. J. Appl. Phys. **36**, 6455 (1997).

Translated by P. Pozdeev

Journal of Experimental and Theoretical Physics, Vol. 94, No. 3, 2002, pp. 644–653.
Translated from Zhurnal Éksperimental'noĭ i Teoreticheskoĭ Fiziki, Vol. 121, No. 3, 2002, pp. 747–757.

SOLIDS
Electronic Properties

Optical Transitions on a Type II Semiconductor Interface in the Empirical Tight-Binding Theory

E. L. Ivchenko* and M. O. Nestoklon**

Ioffe Institute of Physics and Technology, Russian Academy of Sciences,
Politekhnicheskaya ul. 26, St. Petersburg, 194021 Russia

**e-mail: ivchenko@coherent.ioffe.rssi.ru*
***e-mail: nestoklon@coherent.ioffe.rssi.ru*

Received September 17, 2001

Abstract—A tight-binding theory is elaborated for multilayer semiconductor heterostructures of type II in which the states of electrons and holes are dimensionally quantized in adjacent layers and overlap in a narrow region near the interface. The major effort is focused on the calculation of linear photoluminescence polarization induced by the anisotropy of chemical bonds on the ideal interface under the radiation along the axis of growth. An expression for the matrix element of the optical transition on the type-II interface under arbitrary polarization of the emitted photon is obtained. The treatment is based on the sp^3 tight-binding model. The effect of the interface tight-binding parameters considered as free ones on the linear photoluminescence polarization is analyzed. The theory allows for the giant linear photoluminescence polarization discovered in the ZnSe/BeTe heterostructure; it also predicts that the polarization plane usually coincides with the plane containing the chemical bonds at the heterojunction. © *2002 MAIK "Nauka/Interperiodica".*

1. INTRODUCTION

The second-order tensor in crystals with cubic symmetry is isotropic. Therefore, optical properties of such crystals without effects of spatial dispersion and nonlinear susceptibility taken into account are also isotropic. In particular, the light absorption coefficient is independent of the propagation direction and polarization of the light wave, and photoluminescence is not polarized (if optical memory effects are neglected). The heterostructure grown on the basis of cubic composite materials possesses uniaxial anisotropy with respect to the growth axis; however, it is not clear whether lateral anisotropy, i.e., anisotropy in the interface plane, occurs. Suppose the composite materials CA and C'A' have the zinc-blende lattice (the T_d crystalline class), and the heterostructure CA/C'A' is grown in the [001] direction. The symbols C, C' and A, A' denote cations and anions, respectively. In a CA monocrystal, every atom, cation or anion, is in a tetrahedral surrounding of atoms of the other sort, which implies the tetrahedral symmetry of the crystal as a whole. For an atom on the ideal interface in a heterostructure, for example, atom A, two tetrahedral chemical bonds have the form C'–A and lie in one of the planes {110}, say, (110), and two other bonds A–C are in the orthogonal plane $(1\bar{1}0)$. Therefore, the interface CA/C'A' is described by the point group C_{2v}, which includes the axis of rotation $C_2 \parallel [001]$ and the reflection symmetry planes $(1\bar{1}0)$ and (110). These planes are not equivalent, since at C' ≠ C the two pairs of chemical bonds C'–A and A–C are not equivalent. It is clear that the answer to the question on the lateral anisotropy depends on how the physical properties of the heterostructure are affected by the behavior of the electron wave function in the interface region occupied by nonstandard atomic planes for which the adjacent atomic planes on the left and on the right are different in composition.

In structures of type I with a common cation (C = C') or anion (A = A'), interfaces that bound the heterolayer on the left and on the right, for example, the interfaces CA/C'A' and C'A'/CA for the heterolayer CA, are connected by the rotation-reflection element of the point symmetry S_4 with the transformation center at the middle of this layer. Since the transformation S_4 interchanges the planes $(1\bar{1}0)$ and (110), the lateral anisotropy in such structures that is induced by one interface is balanced out by the contribution of the other interface. However, for heteropairs without a common cation or anion (C ≠ C', A ≠ A'), the left and right interfaces can be asymmetric if for one of them the transition from the layer CA to C'A' is, for example, through the chemical bond C'–A in the sequence of atomic planes –C'–A'–C'~A–C–A–, and the transition CA/C'A' is through the bond C–A' in the sequence –C–A–C~A'–C'–A'– (the nonstandard chemical bond is designated by ~). The lateral optical anisotropy of structures with quantum wells of type I with a common atom became an subject of intensive theoretical and experimental study five years ago and continues to attract particular interest (see [1–5] and references therein). For cubic semiconductors A_3B_5 and A_2B_6, the main anisotropy mechanism is the mixing of heavy (*hh*) and light (*lh*) hole states on the interfaces (001) under the normal incidence. In earlier studies, the *hh*–*lh* mixing was invoked

to explain the fine structure of exciton levels in superlattices GaAs/AlAs [6]. In type-I structures, a typical estimate of the observed lateral anisotropy is 10% in relative units (for example, for the ratio of the difference of optical absorption coefficients with respect to the polarizations $[1\bar{1}0]$ and [110] to their sum).

An analysis of the polarization of edge photoluminescence of type-II heterostructures [7–14] showed that the optical anisotropy estimated on the basis of the degree of linear polarization is several dozen percent and can reach 70–80%. Recall that, in type-II heteropairs CA/C'A', the bottom of the conduction band is lower in one material, e.g., C'A', and the valence band top is higher in the other material, CA. For this reason, the electron wave function exhibits a dimensional quantization in the band C'A' and exponentially decays in the adjacent CA layers; the situation for the holes is converse. Since the matrix element of the interband radiative recombination is proportional to the overlapping of the electron and hole wave functions, we have that, for sufficiently large band discontinuities on the interface when the tunnel tails decay very quickly, only a small region adjacent to the interface contributes to the overlap integral. As a result, the value of the free carrier wave function considerably increases in the interface region, where the directions $[1\bar{1}0]$ and [110] are nonequivalent. This explains the giant linear photoluminescence polarization in multilayer samples ZnSe/BeTe [11]. This polarization is caused not by defects accumulated on the interface or, at least, not only by those defects; indeed, the polarization is stable with respect to the variation of temperature, external electric field, and an increase in the intensity of exciting light, which causes the photoluminescence intensity to increase by many orders of magnitude [12].

The main purpose of this paper is to develop a tight-binding theory suitable for the calculation of interband optical transitions on a type-II heterojunction, when the method of smooth envelopes (or the effective mass method) is inapplicable. Taking into account the experiments reported in [10–13], we use the simplest sp^3 model to find out whether the theory explains the giant linear photoluminescence polarization under such transitions. In the next section, we briefly present the calculation procedure for the energy spectrum and electron states in the tight-binding method. In Sections 3 and 4, we derive formulas for the reflection coefficient of electrons on the interface and find a relation between the reflection coefficient and the energy of electron or hole dimensional quantization. In Section 5, an expression for the interband matrix element of the optical transition in the framework of the sp^3 model is obtained. Sections 6 and 7 are devoted to the presentation of calculation results, discussion, and conclusions.

2. ELECTRON STATES IN THE sp^3 TIGHT-BINDING METHOD

We consider a periodic CA/C'A' heterostructure grown along the axis [001] consisting of alternating layers of binary compounds CA and C'A' with different cations and anions. The electron wave function in the tight-binding method is written in the form

$$\psi(\mathbf{r}) = \sum_{n,\alpha} C_n^{\alpha b}\phi_{n\alpha}(\mathbf{r}). \quad (1)$$

Here, $\phi_{n\alpha}(\mathbf{r})$ are the planar orbitals, n is the number of the atomic plane, and α is the orbital state index. For the states with a zero lateral wave vector, i.e., for the states with $k_x = k_y = 0$, the planar orbitals are related to the orthogonalized atomic orbitals Φ_α^b by the equation

$$\phi_{n\alpha} = \sum_{n_1, n_2} \Phi_\alpha^b(\mathbf{r} - \mathbf{a}_n - n_1\mathbf{o}_1 - n_2\mathbf{o}_2),$$

where n_1, n_2 are arbitrary integers, $\mathbf{o}_1 = (a_0/2)(1, 1, 0)$, $\mathbf{o}_2 = (a_0/2)(1, -1, 0)$, a_0 is the constant of the face-centered cubic lattice, and $\mathbf{a}_n$ is the position of an atom on the nth plane. The distance between neighboring cation and anion planes equals $a_0/4$. The orthogonal atomic orbitals Φ_α^b were suggested by Löwdin in [15] and are widely used for the calculation of electron states in the tight-binding method (see [16, 17] and references therein[1]). Below, we use the following enumeration of atomic planes. Even values of n run through anion planes, while the odd ones run through cation planes. For clarity, the coefficients in expansion (1) are supplied with an additional superscript $b = a$ for the anion ($n = 2l$, where l is an integer) and $b = c$ for the cation ($n = 2l + 1$). In the tight-binding method, the wave equation of motion of the electron with energy E is replaced by the system of linear equations for the coefficients $C_n^{\alpha b}$

$$(E_n^{\alpha b} - E)C_n^{\alpha b} + \frac{1}{2}\sum_{n' \neq n,\, \alpha'} V_{n,n'}^{\alpha b,\, \alpha' b'} C_{n'}^{\alpha' b'} = 0. \quad (2)$$

Here $E_n^{\alpha b}$ are the one-atom energies, and $V_{n,n'}^{\alpha b,\, \alpha' b'} = V_{n',n}^{\alpha' b',\, \alpha b}$ are the off-diagonal tight-binding parameters for the pair n, n'.

In the sp^3 tight-binding method, the atomic s and p orbitals are taken into account; hence, the pair of superscripts α, b runs through eight values sa, sc, $p_{x'}a$,

[1] Note that [16] contains an error in the equation connecting orthogonalized atomic orbitals (see [14] on page 374): the matrix element $S^{-1}(nb\mathbf{R}_i;\ mb'\mathbf{R}_j)$ must be replaced by $S^{-1/2}(mb'\mathbf{R}_j;\ nb\mathbf{R}_i)$.

$p_{x'}c$, $p_{y'}a$, $p_{y'}c$, p_za, and p_zc. For convenience, we choose the orbitals

$$p_{x'} = \frac{p_x - p_y}{\sqrt{2}}, \quad p_{y'} = \frac{p_x + p_y}{\sqrt{2}},$$

oriented along the axes $[1\bar{1}0]$ and [110] instead of the orbitals $p_x \parallel [100]$ and $p_y \parallel [010]$.

First, we consider system (2) for a homogeneous semiconductor crystal. At $k_x = k_y = 0$, this system splits into three independent subsystems—for s and p_z orbitals, for $p_{x'}$ orbitals, and for $p_{y'}$ orbitals. In the approximation of the closest neighbor interaction, which is used below, the first subsystem is reduced to the form

$$(E_{sc} - E)C_{2l-1}^{sc} + \frac{1}{2}(V_{ss}C_{2l-2}^{sa} + V_{ss}C_{2l}^{sa} - V_{sc,pa}C_{2l-2}^{p_za} + V_{sc,pa}C_{2l}^{p_za}) = 0, \tag{3a}$$

$$(E_{pc} - E)C_{2l-1}^{p_zc} + \frac{1}{2}(V_{xx}C_{2l-2}^{sa} + V_{xx}C_{2l}^{p_za} + V_{pc,sa}C_{2l-2}^{sa} - V_{pc,sa}C_{2l}^{sa}) = 0, \tag{3b}$$

$$(E_{sa} - E)C_{2l}^{sa} + \frac{1}{2}(V_{ss}C_{2l-1}^{sc} + V_{ss}C_{2l+1}^{sc} - V_{sa,pc}C_{2l-1}^{p_zc} + V_{sa,pc}C_{2l+1}^{p_zc}) = 0, \tag{3c}$$

$$(E_{pa} - E)C_{2l}^{p_za} + \frac{1}{2}(V_{xx}C_{2l-1}^{p_zc} + V_{xx}C_{2l+1}^{p_zc} + V_{pa,sc}C_{2l-1}^{sc} - V_{pa,sc}C_{2l+1}^{sc}) = 0, \tag{3d}$$

where the diagonal energies and parameters V_{ss}, V_{xx}, V_{xy}, $V_{sa,pc} = V_{pc,sa}$, and $V_{sc,pa} = V_{pa,sc}$ are determined according to [16]. The dependence of energy E on the electron wave vector $\mathbf{k} = (0, 0, k)$ for the orbital branches s–p_z is obtained by equating to zero the determinant

$$\begin{vmatrix} E_{sa} - E & V_{ss}\cos\phi & 0 & iV_{sa,pc}\sin\phi \\ V_{ss}\cos\phi & E_{sc} - E & iV_{sc,pa}\sin\phi & 0 \\ 0 & -iV_{sc,pa}\sin\phi & E_{pa} - E & V_{xx}\cos\phi \\ -iV_{sa,pc}\sin\phi & 0 & V_{xx}\cos\phi & E_{pc} - E \end{vmatrix} = 0, \tag{4}$$

where $\phi = ka_0/4$. Equation (4) is reduced to the form

$$A\cos^4\phi + B\cos^5\phi + C = 0, \tag{5}$$

$$A = (V_{ss}V_{xx} + V_{sa,pc}V_{sc,pa})^2, \quad B = D_1D_2 - A - C, \quad C = D_3D_4,$$

$$D_1 = (E_{sa} - E)(E_{sc} - E) - V_{ss}^2,$$

$$D_2 = (E_{pa} - E)(E_{pc} - E) - V_{xx}^2,$$

$$D_3 = (E_{sa} - E)(E_{pc} - E) - V_{sa,pc}^2,$$

$$D_4 = (E_{sc} - E)(E_{pa} - E) - V_{sc,pa}^2.$$

Now we find from (5)

$$\cos^2\phi = \frac{-B \pm \sqrt{B^2 - 4AC}}{2A}, \qquad \cos\frac{ka_0}{2} = f(E) \equiv \frac{-(A + B) \pm \sqrt{B^2 - 4AC}}{A}. \tag{6}$$

At the Γ point of the Brillouin band, $\phi = 0$, and Eq. (5) takes the form $D_1D_2 = 0$. The two roots of the equation $D_1 = 0$ determine the energy of Bloch symmetry states Γ_1, one of which, Γ_1^v, is deep in the valence band and the other, Γ_1^c, is in the conduction band. The roots of the other equation $D_2 = 0$ determine the top of the valence band Γ_{15}^v and the energy of the state Γ_{15}^c, which belongs to the conduction band.

For finite thickness layers, one must take into account solutions with all (including complex) values of k that satisfy Eq. (5) for the given energy value E (which is always real). In [18], such solutions are divided into four categories of complex band structure: (1) real k; (2) imaginary k; (3) $k = 2\pi/a_0 + ik''$, $k'' = \mathrm{Im}k \neq 0$; (4) $k = k' + ik''$, $k' = \mathrm{Re}k \neq 0, \pm 2\pi/a_0$, $k'' \neq 0$. It follows from (6) that if $B^2 - 4AC$ is positive, then the solutions belong to categories (1)–(3) when, respectively, (1) $|f| < 1$, (2) $f > 1$, and (3) $f < -1$. If $B^2 - 4AC < 0$, the solutions belong to category (4).

The subsystem for $p_{x'}$ orbitals has the form

$$U_+C_{2l-1}^{p_{x'}c} + (E_{pa} - E)C_{2l}^{p_{x'}a} + U_-C_{2l+1}^{p_{x'}c} = 0, \qquad U_-C_{2l-2}^{p_{x'}a} + (E_{pc} - E)C_{2l-1}^{p_{x'}c} + U_+C_{2l}^{p_{x'}a} = 0, \tag{7}$$

where $U_\pm = (V_{xx} \pm V_{xy})/2$. Equations for $p_{y'}$ orbitals are obtained from (7) by replacing $U_\pm$ by $U_\mp$. Notice that when the spin and spin-orbital interaction are neglected, the passage from the electron to the hole representation is done by replacing the sign of the energy E and of

all tight-binding parameters $V_{n,n'}^{\alpha b,\alpha' b'}$ and by complex conjugation of the coefficients $C_n^{\alpha b}$. In the case of a homogeneous semiconductor, dispersion of the orbital branches $p_{x'}$ and $p_{y'}$ can be written in the form

$$E(k) = \frac{E_{pc}+E_{pa}}{2} \pm R, \qquad R = \sqrt{D^2 + V(k)V(-k)}, \tag{8}$$

where

$$D = \frac{E_{pc}-E_{pa}}{2},$$

$$V(k) = U_+ \exp\left(\frac{ika_0}{4}\right) + U_- \exp\left(-\frac{ika_0}{4}\right),$$

$$U_\pm = \frac{V_{xx} \pm V_{xy}}{2}.$$

In this case, the solutions belong to the first three categories. Figure 1a illustrates the complex band structure calculated in the framework of the sp^3 tight-binding model for the parameters of ZnSe presented in [16]. Figure 1b illustrates the complex band structure of a model semiconductor with sp^3 parameters chosen so that the forbidden band width at the Γ point is 4.4 eV and the conduction bands Γ_1^c and Γ_{15}^c are close to each other according to the calculation presented in [19, 20]. Solid curves in Fig. 1 correspond to the s–p_z branches satisfying the dispersion Eq. (5); dashed curves correspond to solutions (8).

In heterostructures grown in the [001] direction, equations for the coefficients $C_n^{\alpha b}$ retain the form (3a), (7); however, the parameters $E_{\alpha b}$ and $V_{\alpha b,\alpha' b'}$ in the layers CA and C'A' are different from each other, and the values of those parameters for interface atomic planes can differ from the corresponding volume values.

3. THE ELECTRON REFLECTION COEFFICIENT ON AN ISOLATED INTERFACE

In this section, we calculate the reflection coefficient of an electron in the $p_{x'}$-orbital state that is incident on the interface from right to left

…–C'(–3)–A'(–2)–C'(–1)–A(0)–C(1)–A(2)–C(3)–….

The numbers of corresponding atomic planes are indicated in parentheses; the anion interface plane A is assigned the number $n = 0$, the axis x' lies in the plane of interface chemical bonds C'–A, and the axis $y' \perp x'$, z. It is assumed that the valence band top in the layer CA is higher than that in the layer C'A'. At $n \geq 0$, the solution is a sum of the incident and reflected waves

$$C_{2l}^{p_{x'}a} = C_{p_{x'}a}(-k)\exp\left(-ik\frac{a_0}{2}l\right) + \rho_{x'}C_{p_{x'}a}(k)\exp\left(ik\frac{a_0}{2}l\right),$$
$$C_{2l+1}^{p_{x'}c} = C_{p_{x'}c}(-k)\exp\left[-ik\frac{a_0}{4}(2l+1)\right] + \rho_{x'}C_{p_{x'}c}(k)\exp\left[ik\frac{a_0}{4}(2l+1)\right]. \tag{9}$$

Here, $\pm k$ are the real wave vectors of an electron with energy E ($k > 0$), and the coefficients $C_{p_{x'}c}(k)$ and $C_{p_{x'}a}(k)$ are related to the tight-binding parameters by the equations

$$C_{p_{x'}a}(k) = \sqrt{\frac{R+D}{2R}}, \quad \frac{C_{p_{x'}c}(k)}{C_{p_{x'}a}(k)} = -\frac{V(k)}{R+D}. \tag{10}$$

The solution at $n < 0$ is described by the imaginary wave vector $-i\kappa$ ($\kappa > 0$) and decays in absolute value when $n \longrightarrow -\infty$. The reflection coefficient ρ, which equals unity in absolute value, can be found from the equations

$$\tilde{U}_+ C_{-1}^{p_{x'}c} + (\tilde{E}_{pa} - E)C_0^{p_{x'}a} + U_- C_1^{p_{x'}c} = 0,$$
$$U'_- C_{-2}^{p_{x'}a} + (\tilde{E}_{pc} - E)C_{-1}^{p_{x'}c} + \tilde{U}_+ C_0^{p_{x'}a} = 0,$$

where the tilde symbol denotes the tight-binding parameters for the interface atoms, and the prime denotes the parameters for the atoms in the C'A' layer. Omitting intermediate manipulations, we present the final result:

$$\rho_{x'} = -\exp(i2\phi_{x'}), \tag{11}$$
$$\tan\phi_{x'} = \frac{U_+U_-\sin(ka_0/2)}{(\tilde{E}_{pa} - E - \Sigma_{x'})(R+D) - U_-^2 - U_+U_-\cos(ka_0/2)},$$
$$\Sigma_{x'} = \frac{\tilde{U}_+^2}{\tilde{E}_{pc} - E + \zeta_{x'}U'_-},$$
$$\zeta_{x'} = \exp\left(-\frac{\kappa a_0}{4}\right)\frac{C_{p_{x'}a}(-i\kappa)}{C_{p_{x'}c}(-i\kappa)} = -\exp\left(-\frac{\kappa a_0}{4}\right)\frac{R'+D'}{V'(-i\kappa)}.$$

Expressions for $\phi_{y'}$, $\Sigma_{y'}$, and $\zeta_{y'}$ are obtained by replacing U_+ and U_- by U_- and U_+.

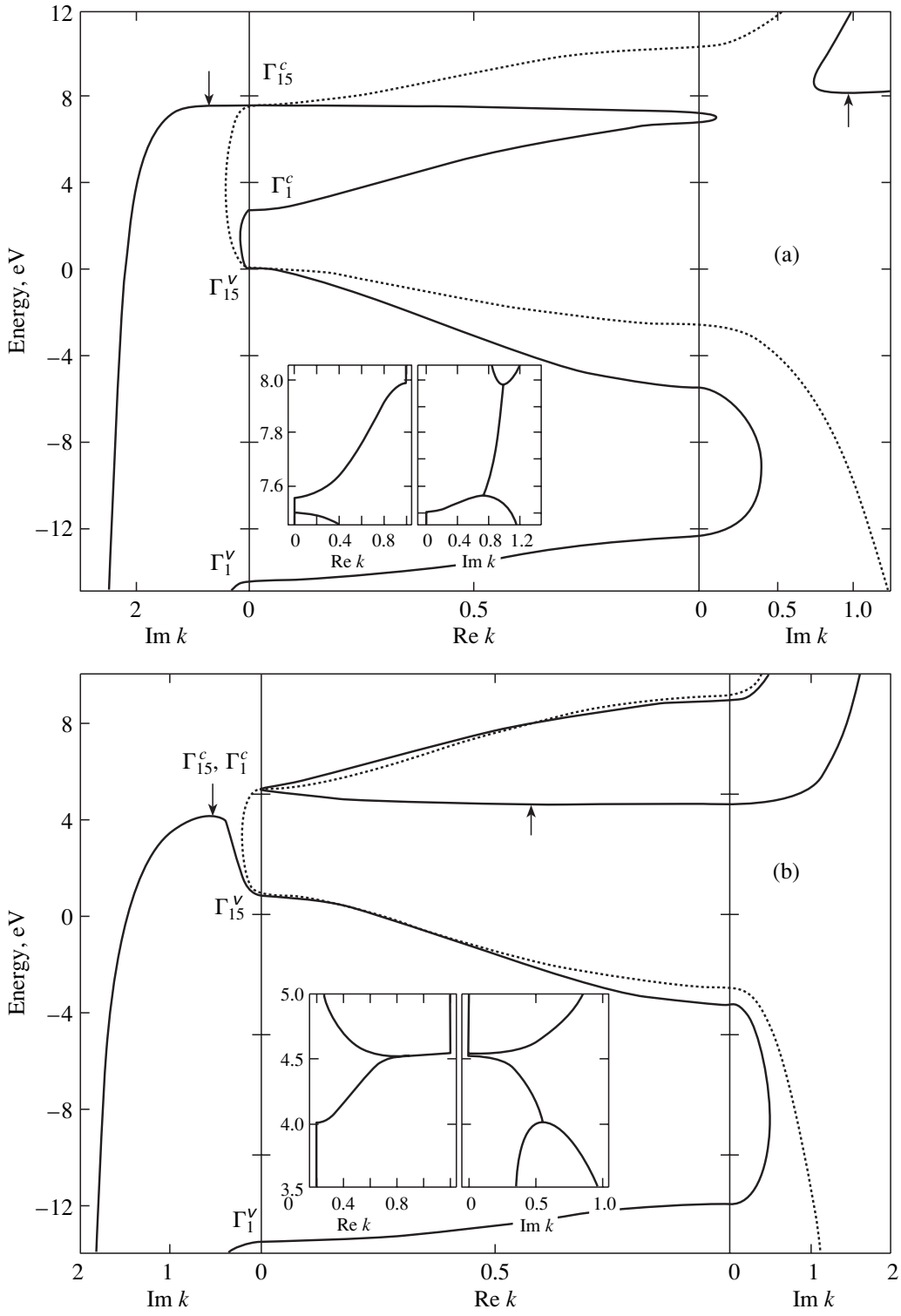

Fig. 1. Dispersion of an electron calculated for ZnSe (a) and BeTe (b) in the sp^3 tight-binding model. The left, middle, and right panels depict the dependence of energy on the wave vector k for solutions with purely imaginary, real, and complex (Re$k = 2\pi/a_0$) values of k, respectively. The inset shows the relationship of the energy with the real and imaginary parts of the wave vector for solutions of the fourth category. On the horizontal axis, the quantities are plotted in the units $2\pi/a_0$. In the calculation, the following values of the tight-binding parameters were used: the diagonal energy elements $E_{sa} = -11.8$ (a), –11.2 (b) eV; $E_{sc} = 0.02$ (a), 2.8 (b) eV; $E_{pa} = 1.5$ (a), 2.23 (b) eV; $E_{pc} = 6.0$ (a), 3.77 (b) eV; the off-diagonal tight-binding parameters are $V_{ss} = -6.2$ eV; $V_{xx} = 3$ (a), 2 (b) eV; $V_{sa,\,pc} = 3.5$ eV; $V_{pa,\,sc} = 6.3$ eV; and $V_{xy} = 5.0$ eV.

Substituting (11) into (9) and taking into account the equality of the coefficients $C_{p_{x'}a}(k) = C_{p_{x'}a}(-k)$, we find

$$C_{2l}^{p_{x'}a} = -2iC_{pa}(k)\exp(i\phi_{x'})\sin\left(k\frac{a_0}{2}l + \phi_{x'}\right),$$

$$C_{2l+1}^{p_{x'}c} = 2iC_{pa}(k)\exp(i\phi_{x'})$$

$$\times\left\{\frac{U_+}{R+D}\sin\left[k\frac{a_0}{2}(l+1) + \phi_{x'}\right]\right. \quad (12)$$

$$\left. + \frac{U_-}{R+D}\sin\left(k\frac{a_0}{2}l + \phi_{x'}\right)\right\}.$$

The subscript x' in $C_{p_{x'}a}$ is omitted since $C_{p_{x'}a} = C_{p_{y'}a}$.

4. RELATION BETWEEN THE REFLECTION COEFFICIENT AND THE ENERGY OF DIMENSIONAL QUANTIZATION OF A CHARGE CARRIER

Given the dependence of the reflection coefficient on energy E, we can write an equation for the energy of dimensional quantization of an electron (hole). Consider a structure with a layer CA of thickness a between thick layers C'A' with interfaces containing chemical bonds C'–A. Such a structure possesses the point symmetry D_{2d}, and the axes x' and y' coincide with intersection lines of the interface plane with the planes containing the interface chemical bonds on the left and right interfaces, respectively. The dimensionally quantized $p_{x'}$- and $p_{y'}$-orbital hole states are degenerate, and the equation for E can be written as

$$\rho_{x'}(E)\rho_{y'}(E) = \exp(-2ik(E)a). \quad (13)$$

Here, a is the distance between the anion interface planes. In order to make estimates, we can set $\rho_{x'}(E) = \rho_{y'}(E) = -1$, as is done for infinitely high barriers in the effective mass method. Then, e.g., for the ground state, Eq. (13) transforms to the equation

$$k(E) = \frac{\pi}{a}. \quad (14)$$

Similarly, we can calculate the reflection coefficient and write an equation for the energy of dimensional quantization of an electron in the conduction band of a structure consisting of a layer C'A' of thickness a' lying between thick layers CA. States in a homogeneous material can be found by solving four linear equations obtained from (3a)–(3d). However, the resulting expression for the reflection coefficient $\rho_{c.b.}$ is too cumbersome. For this reason, its values were found by the numerical solution of this system of equations. In the process, it was taken into account that in the framework of the sp^3 model the four wave vectors $\pm k$, $\pm i\kappa$ (k, κ are real) correspond to the value of E that is immediately above the conduction band bottom of the semiconductor, and the imaginary values of the wave vector $\pm i\kappa_1$, $\pm i\kappa_2$ correspond to the value of E that lies in the prohibited band. The quantity $\rho_{c.b.}$ is interpreted as the ratio of the reflected wave amplitude $-k$ to the amplitude of the incident wave k. If the layer thickness a' is sufficiently large so that $\exp(-\kappa a'/2) \ll 1$, then the energy of dimensional quantization can be calculated by formula (13) in which a must be replaced by a' and $\rho_{x'}\rho_{y'}$ by $\rho_{c.b.}^2$.

5. THE INTERBAND MATRIX ELEMENT OF THE OPTICAL TRANSITION ON TYPE-II INTERFACE

The matrix element of the optical transition for the polarization photon $\mathbf{e}$ is proportional to the matrix element of the inner product of the velocity operator $\hat{\mathbf{v}}$ with $\mathbf{e}$. To express the matrix elements of $\hat{\mathbf{v}}$ in terms of the coefficients $C_n^{\alpha b}$ of the resolution of $\psi(\mathbf{r})$ into the planar orbitals, we should first express $\hat{\mathbf{v}}$ in terms of the atomic orbitals $\Phi_\alpha^b(\mathbf{r} - \mathbf{a} - \boldsymbol{\tau}_b)$, where α is the orbital index and the vectors $\mathbf{a}$ and $\boldsymbol{\tau}_b$ specify the location of an elementary cell and the location of the atom of sort b within the cell. Atomic orbitals are completely determined by two parameters—α and the position of the atom $\mathbf{R} = \mathbf{a} + \boldsymbol{\tau}_b$. For convenience, we will sometimes use a redundant subscript b specifying the atom sort. The tight-binding Hamiltonian is determined by the matrix elements $H_{\alpha'\alpha}^{b'b}(\mathbf{R}', \mathbf{R})$.

In the tight-binding method, the expression for the matrix elements of the velocity operator can be found by using the formula

$$\hat{\mathbf{v}} = \frac{i}{\hbar}(H\mathbf{r} - \mathbf{r}H)$$

that relates the velocity and coordinate operators, taking the Hamiltonian H in the form $H_{\alpha'\alpha}^{b'b}(\mathbf{R}', \mathbf{R})$, and introducing the matrix elements of the coordinate operator $\mathbf{r}_{\alpha\alpha'}(\mathbf{R}, \mathbf{R}')$. As a rule, only intrasite matrix elements

$$\mathbf{r}_{\alpha'\alpha}(\mathbf{R}', \mathbf{R}) \equiv \langle \mathbf{R}', \alpha'|\mathbf{r}|\mathbf{R}, \alpha\rangle = (\mathbf{R}\delta_{\alpha'\alpha} + \mathbf{r}_{\alpha'\alpha})\delta_{\mathbf{R}', \mathbf{R}}, \quad (15)$$

are taken into account (see [21, 22] and references therein), where the contribution

$$\mathbf{r}_{\alpha'\alpha} = \langle \mathbf{R}, \alpha'|\mathbf{r} - \mathbf{R}|\mathbf{R}, \alpha\rangle$$

describes interorbital transitions within a single atomic site. Here we use the theory developed in [23] (see also [24–26]) in which it is assumed that $\mathbf{r}_{\alpha'\alpha} = 0$ and the optical transitions are uniquely determined by the tight-

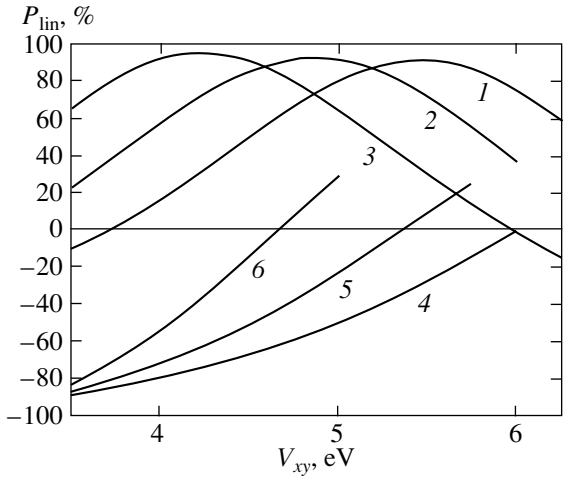

Fig. 2. The linear photoluminescence polarization in the ZnSe/BeTe heterostructure depending on the tight-binding parameter V_{xy} on the interface for the heterojunction with the interface coupling ZnTe (curves *1*, *2*, and *3*) or BeSe (curves *4*, *5*, and *6*). The tight-binding parameters for both materials are presented in the caption of Fig. 1. Curves *1*, *2*, and *3* are calculated, respectively, for the diagonal energy E_{pc} = 5, 6, 7 eV for the interface Zn and curves *4*, *5*, *6* for E_{pc} = 3, 4, 5 eV for the interface Be. For the other interface parameters, mean values, for example, E_{sa}(ZnTe) = [E_{sa}(ZnSe) + E_{sa}(BeTe)]/2, etc., were used.

binding parameters. Then, we obtain for the velocity operator the expression

$$\mathbf{v}^{b'b}_{\alpha'\alpha}(\mathbf{R}', \mathbf{R}) = \frac{i}{\hbar}(\mathbf{R} - \mathbf{R}')H^{b'b}_{\alpha'\alpha}(\mathbf{R}', \mathbf{R}).$$

It is seen that according to this theory the intra-atomic terms $\mathbf{v}^{bb}_{\alpha'\alpha}(\mathbf{R}, \mathbf{R})$ are equal to zero, and the interatomic terms are directed along the vector $\mathbf{R} - \mathbf{R}'$, i.e., along the chemical bond between the atoms $\mathbf{R}$ and $\mathbf{R}'$. In this case, the interatomic transitions between the planes $2l$, $2l - 1$ and $2l$, $2l + 1$ cause the emission of photons polarized in the direction of the axes $x' \parallel [1\bar{1}0]$ and $y' \parallel [110]$, respectively.

The optical matrix elements corresponding to the emitted photons polarized along the axes x' and y' are written as

$$M_j = i\frac{a_0}{4\hbar}\sum_l V^j_l, \qquad (16)$$

where

$$V^{x'}_l = V_{sa,\,pc}C^{sa*}_{2l}C^{p_{x'}c}_{2l-1} + V_{pa,\,sc}C^{sc*}_{2l-1}C^{p_{x'}a}_{2l} - V_{xy}(C^{p_za*}_{2l}C^{p_{x'}c}_{2l-1} - C^{p_zc*}_{2l-1}C^{p_{x'}a}_{2l}),$$

$$V^{y'}_l = V_{sa,\,pc}C^{sa*}_{2l}C^{p_{y'}c}_{2l+1} + V_{pa,\,sc}C^{sc*}_{2l+1}C^{p_{y'}a}_{2l} + V_{xy}(C^{p_za*}_{2l}C^{p_{y'}c}_{2l+1} - C^{p_zc*}_{2l+1}C^{p_{y'}a}_{2l}).$$

Here, M_j is the interband matrix element of the velocity operator $\hat{v}_j$ ($j = x', y'$); $V^{x'}_j$ is the contribution to $M_{x'}$ from the interatomic transitions between the anion plane $2l$ and the cation plane $2l - 1$; $V^{y'}_l$ is the similar contribution to $M_{y'}$ from transitions between the planes $2l$ and $2l + 1$; C^{sb}_n and $C^{p_zb}_n$ are the coefficients of the s and p_z orbitals in expansion (1) for the electron states in the lower conduction band Γ_1; $C^{p_jb}_n$ is the p_j-orbital coefficient for the p_j hole states in the valence zone; $V_{sa,\,pc}$, $V_{pa,\,sc}$, and V_{xy} are the off-diagonal elements of the s–p and p_x–p_y tight binding (see (3a) and (8)). For example, $V_{sa,\,pc}$ and $V_{pa,\,sc}$ are determined so that, for the atomic sites $\mathbf{R}'$ and $\mathbf{R}$ lying in the planes $n' = 2l$ and $n = 2l - 1$, we have

$$H^{ca}_{sp_z}(\mathbf{R}', \mathbf{R}) = \frac{V_{pa,\,sc}}{4}, \quad H^{ca}_{p_zs}(\mathbf{R}', \mathbf{R}) = -\frac{V_{sa,\,pc}}{4};$$

for $\mathbf{R}'$ and $\mathbf{R}$ lying in the planes $n' = 2l + 1$ and $n = 2l$, we have

$$H^{ca}_{sp_z}(\mathbf{R}', \mathbf{R}) = -\frac{V_{pa,\,sc}}{4}, \quad H^{ca}_{p_zs}(\mathbf{R}', \mathbf{R}) = \frac{V_{sa,\,pc}}{4}.$$

The factor 1/4 is obtained if we take into account that, for example,

$$H^{ca}_{sp_j} = \pm\sqrt{2}\frac{V_{pa,\,sc}}{4}, \quad H^{ca}_{p_js} = \pm\sqrt{2}\frac{V_{sa,\,pc}}{4}$$

and on each side of the atom belonging to the atomic plane (001) there are two nearest neighboring atoms of the other sort. Note that in [11] the terms in (16) proportional to V_{xy} are omitted. Below, we consider the radiative recombination of electrons and holes from the lower subbands of the dimensional quantization $e1$ and $h1$.

6. CALCULATION RESULTS AND DISCUSSION

The results of the calculation of linear luminescence polarization

$$P_{\text{lin}} = \frac{I_{1\bar{1}0} - I_{110}}{I_{1\bar{1}0} + I_{110}}$$

are presented in Fig. 2. Here $I_{1\bar{1}0}$ and I_{110} are the intensities of the components polarized along the corresponding axes. Note that the constants of lattices ZnSe and BeTe are close to each other; i.e., ZnSe/BeTe constitute a heteropair with consistent lattices; however, they are different from those of the volume semicon-

ductor ZnTe or BeSe. For this reason, we consider the tight-binding coefficients for interface atoms as independent parameters of the theory. Three dependences of P_{lin} on the interface coefficient V_{xy} depicted in the upper panel of Fig. 2 are calculated for the ZnTe interface at three different values of the diagonal energy E_{pc} = 5, 6, 7 eV for Zn atoms on the interface. The other parameters of the interface atoms were chosen by averaging the corresponding parameters of the volume materials constituting the heteropair. The curves $P_{\text{lin}}(V_{xy})$ in the lower panel are calculated for the BeSe interface at E_{pc} = 3, 4, 5 eV for the Be atom on the interface, while the other tight-binding parameters were averaged. Figure 2 suggests the main qualitative result of the present paper: in type-II heterostructures, the photoluminescence can be substantially polarized; the theory allows for large values of P_{lin} for ideal interfaces without considering anisotropic localized states caused by the nonideality of the interface. Figure 2 also suggests another important conclusion: as a rule, the luminescence polarization plane coincides with the plane of interface chemical bonds, which was predicted in [11] on the basis of a quantitative analysis. The coefficients $C_n^{\alpha\beta}$ in expansion (1), which appear in expression (16) for the matrix elements and were used in the calculation of the curves in Fig. 2, were calculated for periodic heterostructures with the ZnSe and BeTe layers 75 Å and 50 Å thick. In this case, the energy of dimensional quantization at the states $e1$ and $h1$ is 39 and 23 meV, respectively. The absolute values of the optical matrix elements are very sensitive to the layer thickness, whereas the polarization P_{lin} weakly depends on the electron and hole quantization energy in a wide range of thickness values. However, recall that we consider the electron and hole states only at $k_x = k_y = 0$.

The points in Fig. 3 show the contributions V_l^j made by the interatomic transitions $2l \longleftrightarrow 2l - 1$ (at $j = x'$) and $2l \longleftrightarrow 2l + 1$ (at $j = y'$) to the optical matrix element. As was predicted in [11], the maximum contribution to $M_{x'}$ is made by the pair of interface atomic planes Zn and Te, and the major contribution to the sum (16) is made by the terms with $l = 0, \pm 1$.

The dependence of the polarization degree P_{lin} on the discontinuity of valence bands V_h on the interface calculated for the interface ZnTe at V_{xy}(ZnTe) = 5 eV and $E_{n=-1}^{pc}$ = 5 eV is shown in Fig. 4. The change of the polarization sign and the fact that it attains the value –100% are explained as follows. As the discontinuity of bands decreases, the dependence of $V_l^{x'}$ on l becomes alternate, and (at a certain value of $V_h \approx 260$ meV) the sum of $V_l^{x'}$ over l in (16) goes to zero.

In the calculation (its results are presented in Figs. 2–4), we neglected intra-atomic (intrasite) transitions. At

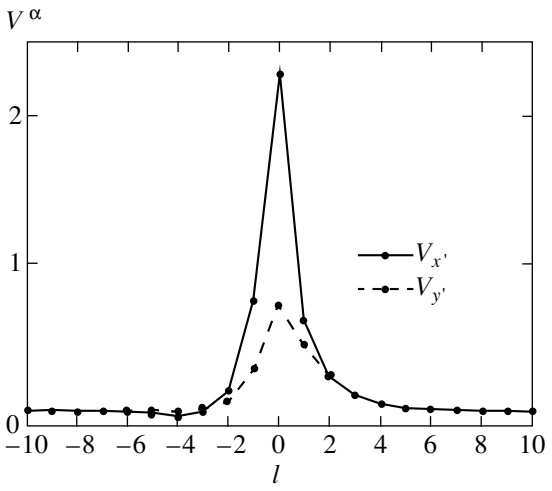

Fig. 3. The contribution V_l^{α} of various pairs of atomic planes $2l$, $2l - 1$ (the points connected by solid lines) and $2l$, $2l + 1$ (the points connected by dashed lines) to the interatomic matrix element of the optical transition M_{α} at the off-diagonal tight-binding matrix element V_{xy} = 5 eV for the Zn and Te interface atoms. The other parameters are the same as those used in the calculation of curve *1* in Fig. 2.

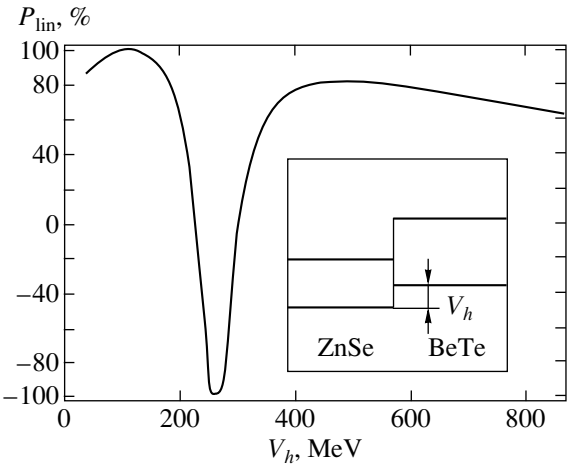

Fig. 4. Luminescence linear polarization as a function of the valence band discontinuity on the heterojunction. The calculation is done for the interface ZnTe at V_{xy}(ZnTe) = 5 eV; the other parameters are the same as those used in the calculation of curve *1* in Fig. 2.

the present time, no consensus on the relative contributions of intra- and interatomic transitions to interband optical matrix elements has been reached. In the studies [27–29], both transitions were taken into account; however, the values of the intra-atomic matrix elements of the momentum operator exceeded those of the cation–anion transitions. In the papers [30–32], the contribution of interatomic transitions was completely ignored. On the other hand, many researchers [23–26] com-

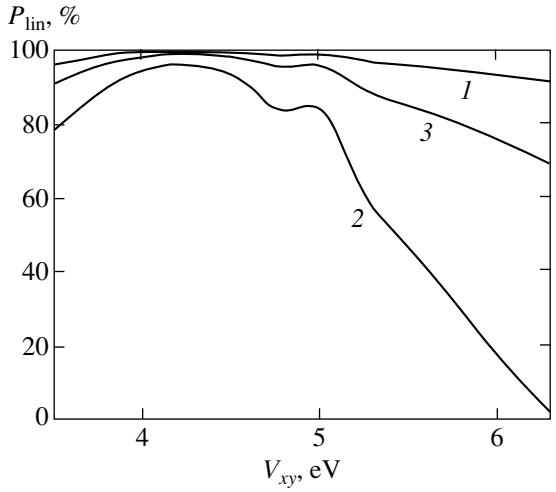

Fig. 5. Luminescence linear polarization as a function of the interface tight-binding parameter V_{xy} with only intra-atomic transitions taken into account: (*1*) $r^c_{sp} \neq 0$, $r^a_{sp} = 0$; (*2*) $r^a_{sp} = 0$, $r^a_{sp} \neq 0$; (*3*) $r^c_{sp} = r^a_{sp} \neq 0$. The calculation was carried out for the ZnTe interface at V_{xy}(ZnTe) = 5 eV with the other parameters identical to those used in the calculation of curve *1* in Fig. 2.

pletely neglected interatomic transitions. For comparison, it is of interest to calculate the dependence $P_{\text{lin}}(V_{xy})$ in the presence of only intra-atomic transitions. For this purpose, we set

$$\mathbf{r}_{\alpha'\alpha}(\mathbf{R}', \mathbf{R}) = \mathbf{r}^b_{\alpha'\alpha}\delta_{\mathbf{R}'\mathbf{R}}$$

and took into account the fact that the matrix elements $\mathbf{r}^b_{\alpha'\alpha}$ are nonzero for the pair of orbitals $\alpha' = s$, $\alpha = p_j$ or $\alpha' = p_j$, $\alpha = s$, so that

$$\mathbf{r}^b_{sp_j} = \mathbf{r}^b_{p_j s} = r^b_{sp}\mathbf{o}_j,$$

where $r^b_{sp} = z^b_{sp_z}$, and $\mathbf{o}_j$ is the unit vector corresponding to the axis j. The curves in Fig. 5 are calculated for three particular cases—when one of the parameters r^c_{sp} or r^a_{sp} is zero and when they are identical. The dependence $r^c_{sp}(r^a_{sp})$ on the cation (anion) sort was neglected. It is seen from Fig. 5 that the luminescence linear polarization can be very large under intra-atomic transitions as well.

7. CONCLUSIONS

In conclusion, we formulate the main results obtained in this study. A tight-binding theory was elaborated that makes it possible to calculate the anisotropy of indirect optical transitions in type-II AC/A'C' heterostructures grown from composite AC and A'C' materials with a zinc-blende lattice in the direction of the crystallographic axis [001]. The influence of the interface type (C'A or A'C) and the interface tight-binding parameters, such as the off-diagonal coefficient V_{xy}, the diagonal energy E_{pc}, and the band discontinuity on the heterojunction V_h, on the luminescence linear polarization is analyzed. In accordance with the experiment [10–13], the theory allows a giant luminescence linear polarization caused by the radiative recombination of electron–hole pairs on an ideal type-II interface. The calculation shows that the polarization usually follows the orientation of interface chemical bonds and changes its sign when the interface C'A (ZnTe) is changed for CA' (BeSe). The polarization degree is almost independent of the thickness d_{AC} and $d_{\text{A'C'}}$ of the layers AC and A'C' in a wide range of values. On the other hand, the oscillator strength for interband transitions strongly depends on d_{AC} and $d_{\text{A'C'}}$. The major contribution to the interband optical matrix element is determined by transitions between several cation and anion atomic planes adjacent to the interface; moreover, the maximum contribution is made by transitions between interface planes. Note that the sp^3 model is the simplest tight-binding model that makes it possible to describe microscopic electron wave functions both in the conduction band and in the valence band, which is necessary for the calculation of optical transition matrix elements. However, the above conclusions remain qualitatively valid for more complex tight-binding models, such as sp^3s^* [16] or sp^3s^*d [17]. In addition, our theory does not take into account the spin-orbital splitting of the valence band in composite materials. An analysis shows that the inclusion of the spin-orbital interaction for the optical transitions of type "conduction band–heavy holes subband" only leads to certain quantitative changes.

ACKNOWLEDGMENTS

The work was supported by INTAS, grant no. 99-00015, and by the Russian Foundation for Basic Research, project no. 00-02-16997.

REFERENCES

1. O. Krebs and P. Voisin, Phys. Rev. Lett. **77**, 1829 (1996).
2. O. Krebs, W. Seidel, J. P. André, *et al.*, Semicond. Sci. Technol. **12**, 938 (1997).
3. O. Krebs, D. Rondi, J. L. Gentner, *et al.*, Phys. Rev. Lett. **80**, 5770 (1998).
4. E. L. Ivchenko, A. A. Toropov, and P. Voisin, Fiz. Tverd. Tela (St. Petersburg) **40**, 1925 (1998) [Phys. Solid State **40**, 1748 (1998)].
5. A. A. Toropov, E. L. Ivchenko, O. Krebs, *et al.*, Phys. Rev. B **63**, 035 302 (2001).
6. E. L. Ivchenko, A. Yu. Kaminskiĭ, and I. L. Aleĭner, Zh. Éksp. Teor. Fiz. **104**, 3401 (1993) [JETP **77**, 609 (1993)].
7. D. Vignaud, X. Wallart, F. Mollot, and B. Sermage, J. Appl. Phys. **84**, 2138 (1998).

8. F. Fuchs, J. Schmitz, J. D. Ralston, *et al.*, Superlattices Microstruct. **16**, 35 (1994).
9. F. Fuchs, J. Schmitz, and N. Herres, in *Proceedings of the 23rd International Conference on Physics of Semiconductors*, Ed. by M. Scheffler and R. Zimmermann (World Scientific, Singapore, 1996), Vol. 3, p. 1803.
10. A. V. Platonov, V. P. Kochereshko, E. L. Ivchenko, *et al.*, Acta Phys. Pol. A **94**, 479 (1998).
11. A. V. Platonov, V. P. Kochereshko, E. L. Ivchenko, *et al.*, Phys. Rev. Lett. **83**, 3546 (1999).
12. D. R. Yakovlev, E. L. Ivchenko, V. P. Kochereshko, *et al.*, Phys. Rev. B **61**, 2421 (2000).
13. M. Schmidt, M. Grün, S. Petillon, *et al.*, Appl. Phys. Lett. **77**, 85 (2000).
14. O. Krebs and P. Voisin, Phys. Rev. B **61**, 7265 (2000).
15. P. O. Löwdin, J. Chem. Phys. **18**, 365 (1950).
16. P. Vogl, H. P. Hjalmarson, and J. D. Dow, J. Phys. Chem. Solids **44**, 365 (1983).
17. J. M. Jancu, R. Scholz, F. Beltram, and F. Bassani, Phys. Rev. B **57**, 6493 (1998).
18. Y.-C. Chang, Phys. Rev. B **25**, 605 (1982).
19. D. J. Stukel, Phys. Rev. B **2**, 1852 (1970).
20. M. Nagelstrasser, H. Dröge, H.-P. Steinrück, *et al.*, Phys. Rev. B **58**, 10 394 (1998).
21. M. Cruz, M. R. Beltran, C. Wang, *et al.*, Phys. Rev. B **59**, 15 381 (1999).
22. T. G. Pedersen, K. Pedersen, and T. B. Kriestensen, Phys. Rev. B **63**, 201101 (2001).
23. L. C. Lew Yan Voon and L. R. Ram-Mohan, Phys. Rev. B **47**, 15 500 (1993).
24. M. Graf and P. Vogl, Phys. Rev. B **51**, 4940 (1995).
25. P. V. Santos, P. Etchegoin, M. Cardona, *et al.*, Phys. Rev. B **50**, 8746 (1994).
26. T. Dumitrică, J. S. Graves, and R. E. Allen, Phys. Rev. B **58**, 15 340 (1998).
27. Y.-C. Chang and J. N. Schulman, Phys. Rev. B **31**, 2069 (1985).
28. Y.-C. Chang and D. E. Aspnes, Phys. Rev. B **41**, 12 002 (1990).
29. G. D. Sanders and Y.-C. Chang, Phys. Rev. B **45**, 9202 (1992).
30. Z. Xu, Solid State Commun. **76**, 1143 (1990)
31. L. M. Ramaniah and S. V. Nair, Phys. Rev. B **47**, 7132 (1993).
32. A. Selloni, P. Marsella, and R. Del Sole, Phys. Rev. B **33**, 8885 (1986).

Translated by A. Klimontovich

Journal of Experimental and Theoretical Physics, Vol. 94, No. 3, 2002, pp. 654–663.
Translated from Zhurnal Éksperimental'noĭ i Teoreticheskoĭ Fiziki, Vol. 121, No. 3, 2002, pp. 758–769.

SOLIDS
Electronic Properties

Superconductivity in the Exactly Solvable Model of Pseudogap State: The Absence of Self-Averaging

É. Z. Kuchinskiĭ* and M. V. Sadovskiĭ**

Institute of Electrophysics, Ural Division, Russian Academy of Sciences, ul. Komsomol'skaya 34, Yekaterinburg, 620016 Russia

**e-mail: kuchinsk@iep.uran.ru*

***e-mail: sadovski@iep.uran.ru*

Received October 4, 2001

Abstract—The features of the superconducting state are studied in the simple exactly solvable model of the pseudogap state induced by fluctuations of the short-range "dielectric" order in the model of the Fermi surface with "hot" spots. The analysis is carried out for arbitrary short-range correlation lengths ξ_{corr}. It is shown that the superconducting gap averaged over such fluctuations differs from zero in a wide temperature range above the temperature T_c of the uniform superconducting transition in the entire sample, which is a consequence of non-self-averaging of the superconducting order parameter over the random fluctuation field. In the temperature range $T > T_c$, superconductivity apparently exists in individual regions (drops). These effects become weaker with decreasing correlation length ξ_{corr}; in particular, the range of existence for drops becomes narrower and vanishes as $\xi_{corr} \longrightarrow 0$, but for finite values of ξ_{corr}, complete self-averaging does not take place. *© 2002 MAIK "Nauka/Interperiodica".*

1. INTRODUCTION

Among a large number of anomalies in the electronic properties observed in high-temperature superconductors (HTSC) based on copper oxides, the so-called pseudogap state [1, 2] existing in a broad region of their phase diagram has become an object of intense studies in recent years. There are two main trends in constructing the models of the pseudogap state of high-T_c superconductors. One of these trends is based on the popular model of formation of Cooper pairs above the superconducting transition temperature [3]. In the other trend, it is assumed that the pseudogap state is associated with fluctuations of the antiferromagnetic short-range order or with other similar fluctuations of the "dielectric" origin (e.g., fluctuations of charge density waves [2]).

In our opinion [2], the preferable scenario of the formation of the pseudogap state in HTSC is the pattern based on the existence (in the corresponding region of the phase diagram) of strong scattering of charge carriers from developed short-range fluctuations of the dielectric type (antiferromagnetic or charge density waves). This scattering leads to a considerable non-Fermi liquid rearrangement of the electron spectrum in certain regions of the momentum space in the vicinity of the Fermi surface around the so-called hot spots or near hot (flat) regions on this surface [2]. The preference of the dielectric and not superconducting scenario of the formation of a pseudogap [3] is confirmed by a series of experiments which are discussed, for example, in the review [2]. In the present work, we naturally adhere to the same point of view. It should be emphasized, however, that the origin of the pseudogap state in HTSC remains unclear and can be determined only as a result of further experimental investigations.

Most of the available theoretical publications are devoted to an analysis of the effect of the pseudogap on the properties of a system in the normal state, and only an insignificant number of such publications deal with the features of superconductivity in this state [4–6]. For example, superconductivity in a simple exactly solvable model of the pseudogap state, which is based on the model of the Fermi surface of a 2D system with hot spots [4], was considered by us in [5]. In this work, we used the exact solution for the pseudogap, which was obtained earlier [7] for the one-dimensional case, in the limit of very large correlation lengths of dielectric short-range fluctuations. It was proved that the superconducting gap averaged over short-range fluctuations generally differs from zero in the temperature range exceeding the mean-field superconducting transition temperature T_c corresponding, according to [5], to the emergence of a homogeneous superconducting state in the entire sample. It was hence concluded in [5] that, in the temperature range $T > T_c$, superconducting drops are formed in the system and exist down to the superconducting transition temperature T_{c0} in the absence of a dielectric pseudogap. This effect was attributed in [5] to the absence of self-averaging in the superconducting order parameter (gap) under the conditions when the correlation length of short-range fluctuations exceeds the coherence length (the size of Cooper pairs) in the theory of superconductivity.

The effects of finiteness of the correlation length of short-range fluctuations was taken into account in [6] under the assumption of self-averaging of the superconducting gap over such fluctuations. In this publication, the effect of the pseudogap on T_c was analyzed, the behavior of the gap in the region $T < T_c$ was considered, and the microscopic derivation of the Ginzburg–Landau expansion was carried out for $T \sim T_c$. We used the approach based on the almost exact solution of the general model of the pseudogap state with Gaussian short-range fluctuations, which was proposed in [8, 9] for the 1D case and generalized for the 2D problem in [10, 11]. In this approach, it is difficult to go beyond the scope of the assumption concerning the self-averaging of the superconducting gap. It should be noted that the presence or absence of such a self-averaging has been studied insufficiently. In most cases, self-averaging is just assumed from physical considerations with a reference to essentially different scales of lengths over which the superconducting order parameter (coherence length ξ_0) and the basic parameters of the electron subsystem (atomic spacing or the reciprocal Fermi momentum in the impurity problem [12–14] or the short-range correlation length ξ_{corr} in the pseudogap model under investigation [2, 5, 6]) change noticeably. In particular, in our model of pseudogap, we should expect complete self-averaging of the superconducting gap for $\xi_{corr} \ll \xi_0$ [2, 6]. We are not aware of publications in which the problem of self-averaging of the gap is investigated in an exactly solvable model of disorder.

The present work mainly aims precisely at such an investigation in the framework of a very simple (although, perhaps, not very realistic) 1D model of the pseudogap state induced by dielectric short-range fluctuations with a finite correlation length, which was proposed in a recent publication by Bartosch and Kopietz [15]. The exact solution proposed in this work and close essentially to the models considered earlier [7–9] makes it possible to carry out a sufficiently comprehensive analysis of the self-averaging problem under investigation in the 2D model of hot spots [4, 6, 11]. In addition, we will analyze the temperature dependences of the superconducting gap in a superconductor with a dielectric pseudogap.

2. SIMPLIFIED MODEL OF THE PSEUDOGAP STATE

Let us consider the exactly solvable model of the pseudogap state, proposed in [15], using a slightly different approach. We assume that an electron performs a one-dimensional motion in a periodic field of the form

$$V(x) = 2D\cos(Qx + \phi). \tag{1}$$

We choose $Q = 2p_F - k$, where p_F is the Fermi momentum and $k \ll p_F$ is a certain detuning from the preferred scattering vector $2p_F$.[1] We choose the electron spectrum in the following conventional form linearized near the Fermi level:

$$\begin{aligned} \xi_1 \equiv \xi_p &= v_F(|p| - p_F), \\ \xi_{p-2p_F} &= -\xi_p \ \text{(nesting)}, \\ \xi_2 \equiv \xi_{p-Q} &= -\xi_p - v_F k \equiv -\xi_p - \eta, \end{aligned} \tag{2}$$

where we have introduced the variable $\eta = v_F k$ (v_F is the Fermi velocity), which will be widely used in the subsequent analysis. Field (1) can be written in the form

$$\begin{aligned} V(x) &= D\exp(i2p_F x - ikx) \\ &+ D^*\exp(-i2p_F x + ikx), \end{aligned} \tag{3}$$

where the complex amplitude has been introduced as a result of the substitution $D \longrightarrow De^{i\phi}$.

Such a problem can be solved in an elementary way. In the two-wave approximation of the conventional band theory, the one-electron (normal) Green's function corresponding to the (diagonal) transition $p \longrightarrow p$ in the Matzubara representation has the form

$$\begin{aligned} g_{11}(i\varepsilon_n pp) &= \frac{1}{i\varepsilon_n - \xi_1} + \frac{1}{i\varepsilon_n - \xi_1} \\ &\times D^* \frac{1}{i\varepsilon_n - \xi_2} D \frac{1}{i\varepsilon_n - \xi_1} + \ldots \\ &= \frac{i_{\xi_n - \xi_2}}{(i\varepsilon_n - \xi_1)(i\varepsilon_n - \xi_2) - |D|^2} \\ &= \frac{i\varepsilon + \xi + \eta}{(i\varepsilon - \xi)(i\varepsilon + \xi + \eta) - |D|^2}, \end{aligned} \tag{4}$$

where we have introduced in the last equality the notation $\xi_p = \xi$ and $\varepsilon_n = \varepsilon$, which will be widely used below to simplify the form of the equations. We can also introduce the nondiagonal (anomalous) Green's function corresponding to the Umklapp process $p \longrightarrow p - Q$:

$$\begin{aligned} g_{12}(i\varepsilon_n pp - Q) &= \frac{1}{i\varepsilon_n - \xi_1} D^* \frac{1}{i\varepsilon_n - \xi_2} + \ldots \\ &= \frac{D^*}{(i\varepsilon_n - \xi_1)(i\varepsilon_n - \xi_2) - |D|^2} \\ &= \frac{D^*}{(i\varepsilon - \xi)(i\varepsilon + \xi + \eta) - |D|^2}. \end{aligned} \tag{5}$$

Let us now suppose that field (1) is random. Following [15], we consider a rather specific model of disorder, in which the detuning vector k is regarded as a ran-

[1] Such a choice of the vector for the antiferromagnetic superstructure or for a structure of the of charge density wave type implies incommensurate ordering and corresponding fluctuations.

dom quantity and its distribution function is written in the form of the Lorentzian[2]:

$$\mathcal{P}_k(k) = \frac{1}{\pi}\frac{\kappa}{k^2+\kappa^2}, \tag{6}$$

where $\kappa \equiv \xi_{\text{corr}}^{-1}$ and ξ_{corr} is the short-range correlation length. Phase ϕ in expression (1) is also regarded as a random quantity distributed uniformly on the interval from 0 to 2π:

$$\mathcal{P}_\phi(\phi) = \begin{cases} \dfrac{1}{2\pi} & \text{for } 0 \le \phi \le 2\pi, \\ 0, & \text{for remaining values.} \end{cases} \tag{7}$$

The field correlation function $V(x)$ at various points can be calculated elementary and is given by

$$\langle V(x)V(x')\rangle = 2D^2\cos[2p_F(x-x')] \times \exp[-\kappa|x-x'|], \tag{8}$$

where the angle brackets denote averaging over distributions (6) and (7). The random field with precisely this correlation function was considered in the well-known publication [16] as well as in [7–9], where it was assumed that the field is of the Gaussian type.[3] The random field $V(x)$ considered here is not Gaussian in the general case [15]. The Fourier transform (8) has the form of a typical Lorentzian defining the effective interaction of an electron with short-range fluctuations [2]:

$$V_{\text{eff}}(q) = 2D^2 \times\left\{\frac{\kappa}{(q-2p_F)^2+\kappa^2} + \frac{\kappa}{(q+2p_F)^2+\kappa^2}\right\}. \tag{9}$$

It is an interaction of this type that was considered in all publications on the "dielectric" pseudogap cited above.

Green's functions averaged over an ensemble of random fields of type (1) with distributions (6) and (7) are calculated by elementary integration. The mean value of the anomalous Green's function (5) is just equal to zero (after averaging over distribution (7)), which corresponds to the absence of a long-range dielectric order. The averaged Green's function (4) can easily be obtained by term-by-term integration of series (4) with respect to (6) and is given by

$$\begin{aligned} G(i\varepsilon_n p) &= \frac{1}{i\varepsilon_n - \xi_p} + \frac{1}{i\varepsilon_n - \xi_p} \\ &\times D^*\frac{1}{i\varepsilon_n + \xi_p + iv_F\kappa}D\frac{1}{i\varepsilon_n - \xi_p} \\ &+ \frac{1}{i\varepsilon_n - \xi_p}D^*\frac{1}{i\varepsilon_n + \xi_p + iv_F\kappa}D\frac{1}{i\varepsilon_n - \xi_p} \\ &\times D^*\frac{1}{i\varepsilon_n + \xi_p + iv_F\kappa}D\frac{1}{i\varepsilon_n - \xi_p} + \ldots \\ &= \frac{i\varepsilon_n + \xi_p + iv_F\kappa}{(i\varepsilon_n - \xi_p)(i\varepsilon_n + \xi_p + iv_F\kappa) - |D|^2}. \end{aligned} \tag{10}$$

This is the exact solution for the Green's function that was proposed in [15].

In the subsequent analysis, we can assume that not only the phase of field (1) fluctuates, but also its amplitude D, and the corresponding Green's function can be obtained by simple averaging of expression (10) with the corresponding distribution $\mathcal{P}_D(D)$. In particular, the amplitude distribution can be chosen in the form of the Rayleigh distribution [7, 8, 15]:

$$\mathcal{P}_D(D) = \frac{2D}{W^2}\exp\left(-\frac{D^2}{W^2}\right). \tag{11}$$

Averaging of correlators (8) and (9) in this case leads to the simple substitution $D \longrightarrow W$. The average electron Green's function now assumes the form

$$\begin{aligned} G(i\varepsilon_n p) &= \int_0^\infty dD\mathcal{P}_D(D) \\ &\times \frac{i\varepsilon_n + \xi_p + iv_F\kappa}{(i\varepsilon_n - \xi_p)(i\varepsilon_n + \xi_p + iv_F\kappa) - |D|^2} \\ &= \int_0^\infty d\zeta e^{-\zeta}\frac{i\varepsilon_n + \xi_p + iv_F\kappa}{(i\varepsilon_n - \xi_p)(i\varepsilon_n + \xi_p + iv_F\kappa) - \zeta W^2}, \end{aligned} \tag{12}$$

where W determines the energy width of the pseudogap. In the limit of large correlation lengths of fluctuations of field (1), i.e., for $\xi_{\text{corr}} \longrightarrow \infty$ ($\kappa \longrightarrow 0$), solution (12) coincides with that obtained in [7] for a Gaussian random field. For finite values of κ, it coincides with the solution proposed in [11] in the formal analysis of the accuracy of approximations used in [8, 9], where the general problem of an electron in a Gaussian random field with a paired correlator of type (8) was considered. In [11, 15], it was proved that the density of states corresponding to Green's function (12) possesses a characteristic blurred pseudogap in the vicinity of the Fermi level, the values of the density of states being quite close quantitatively [11, 15, 17] (virtually for all energy values in the incommensurate case) to the values obtained in [8] as well as to the results of

[2] In fact, we are speaking here of a specific model of phase fluctuations of field (1).

[3] For a Gaussian field, all higher order correlators of field $V(x)$ are factorized, according to Wick, through paired correlators (8).

exact numerical simulation of the problem with a Gaussian random field which was carried out in [18–20].[4]

If field (1) is created by fluctuations of a certain dielectric order parameter (e.g., antiferromagnetic order parameter or that of charge density waves), distribution (11) may correspond to its Gaussian fluctuations in the range of fairly high temperatures [10, 11]. As the temperature decreases below a certain characteristic value, the amplitude fluctuations become "frozen out" even before the emergence of the corresponding long-range order in the system (cf. [3, 21]) and we can simply set $D = W$, while the phase fluctuations are present down to very low temperatures. For this reason, we will use a solution of type (10), leading to a clearly manifested pseudogap for large correlation lengths ξ_{corr} [16], assuming the low-temperature mode of short-range fluctuations. Since we do not consider the microscopic aspects of dielectric fluctuations, all the parameters characterizing such fluctuations (like the correlation length $\xi_{corr} = \kappa^{-1}$ and amplitudes D and W, viz., the energy width of the pseudogap) are treated here as phenomenological parameters. The low- or high-temperature mode of short-range fluctuations can be realized in a similar way at temperatures differing, for example, from the superconducting transition temperature.

A generalization to the case of a 2D electron system typical of HTSC cuprates can be carried out on the basis of the model of hot spots on the Fermi surface which was considered in [4–6]. In this case, it is assumed that two independent systems of fluctuations of type[5] (1), which are oriented along the orthogonal axes x and y and which interact only with electrons from flat regions of the 2D Fermi surface, are orthogonal to these axes. We assume that the 2D potential in which an electron is moving is factorized in these directions: $V(x, y) = V(x)V(y)$ [4–6]. The size of flat (hot) regions is defined by parameter α, the angular size of a flat region viewed from the center of the Brillouin zone being equal to 2α [2, 4–6]. In particular, the value of $\alpha = \pi/4$ corresponds to a square Fermi surface (complete nesting), when the entire Fermi surface is hot. For $\alpha < \pi/4$, the Fermi surface contains cold regions on which the scattering from fluctuations of the dielectric order parameter is assumed to be absent and the electrons are treated as free. In this model, various characteristics defined by the integrals over the Fermi surface consist of additive contributions from hot and cold regions. The pseudogap rearrangement of the electron spectrum takes place only in the hot regions (and in their vicinity), while the Fermi liquid behavior is preserved in the cold regions [2].

This pattern is in qualitative agreement with the results of numerous ARPES experiments on underdoped HTSC cuprates [1, 2], which indicate that pseudogap anomalies appear in the vicinity of point $(0, \pi)$ in the Brillouin zone and vanish as we pass to its diagonal. The presence of flat regions on the Fermi surface for HTSC cuprates was also reliably observed in ARPES experiments made by several independent groups [2].

3. GOR'KOV EQUATIONS AND THEIR SOLUTION FOR THE PSEUDOGAP STATE

An analysis of superconductivity in a system with a pseudogap induced by short-range fluctuations of the dielectric type will be carried out under the simplest assumption concerning the existence of a pairing interaction of the BCS type, characterized by the attraction constant V, which, as usual, is assumed to have a nonzero value in a certain layer of width $2\omega_c$ in the vicinity of the Fermi level (ω_c is the characteristic frequency of quanta ensuring the attraction between electrons). The same approach was used by us in [4–6]. In the present work, we confine our analysis to the s-type pairing only. There are no principal difficulties for analyzing the d pairing typical of HTSC cuprates, but the presence of the angular dependence (anisotropy) of the superconducting gap in this case necessitates [4, 5] additional integration, which considerably increases the computing time. At the same time, it was proved in [4–6] that the effect of the pseudogap on superconductivity is virtually the same in the s and d cases, the only difference being in fact in the scales of the parameters leading to the corresponding changes in the main characteristics of the superconducting state (d pairing is less stable to the dielectrization of the electron spectrum than the s pairing).

Superconductivity in cold regions of the Fermi surface is described by the standard equations of the BCS theory. For this reason, we concentrate our attention on the derivation of the Gor'kov equations in the 1D model, which is equivalent to an analysis of hot regions in the 2D case [5, 6]. In fact, Green's functions (4), (5) for a 1D system in the periodic field (1) form the matrix

$$\begin{aligned} g_{11} &= \frac{i\varepsilon_n - \xi_2}{(i\varepsilon_n - \xi_1)(i\varepsilon_n - \xi_2) - |D|^2}, \\ g_{12} &= \frac{D^*}{(i\varepsilon_n - \xi_1)(i\varepsilon_n - \xi_2) - |D|^2}, \\ g_{21} &= \frac{D}{(i\varepsilon_n - \xi_1)(i\varepsilon_n - \xi_2) - |D|^2}, \\ g_{22} &= \frac{i\varepsilon_n - \xi_1}{(i\varepsilon_n - \xi_1)(i\varepsilon_n - \xi_2) - |D|^2}. \end{aligned} \tag{13}$$

[4] Using the method developed in [7], it is also possible to calculate exactly the two-particle Green's function and the corresponding frequency dependences of conductivity [15] in the model under investigation. Unfortunately, the specific form of the disorder being considered leads to a nonphysical behavior at zero frequency, which corresponds to an ideal conductor.

[5] It should be noted that this pattern is roughly similar to the concept of phase separation in HTSC cuprates (stripes) [22] if we treat the correlation length ξ_{corr} as a characteristic size (period) of stripe regions [2].

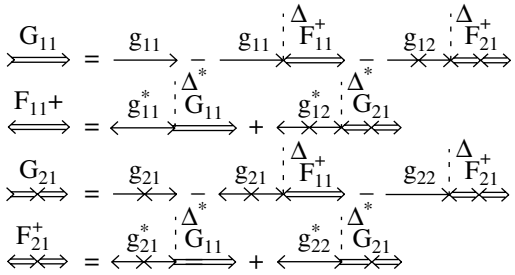

Fig. 1. Gor'kov equations in a 1D periodic field.

In the presence of Cooper pairing, the Gor'kov equations constructed on Green's functions of type (13) can be depicted by the graphs shown in Fig. 1. In analytic form, this system of equations can be written as

$$\begin{aligned} G_{11} &= g_{11} - g_{11}\Delta F_{11}^{+} - g_{12}\Delta F_{21}^{+}, \\ F_{11}^{+} &= g_{11}^{*}\Delta^{*} G_{11} + g_{12}^{*}\Delta^{*} G_{12}, \\ G_{21} &= g_{21} - g_{21}\Delta F_{11}^{+} - g_{22}\Delta F_{21}^{+}, \\ F_{21}^{+} &= g_{21}^{*}\Delta^{*} G_{11} + g_{22}^{*}\Delta^{*} G_{21}, \end{aligned} \tag{14}$$

where the superconducting gap is determined, as usual, from the relation

$$\begin{aligned} \Delta^{*} &= VT\sum_{n,\,p} F_{11}^{+}(\varepsilon_n p) \\ &= \lambda T\sum_{n}\int_{-\infty}^{\infty} d\xi_p F_{11}^{+}(\varepsilon_n \xi_p) \equiv \lambda T\sum_{n}\overline{F_{11}^{+}(\varepsilon_n)}. \end{aligned} \tag{15}$$

Here, $\lambda = N_0(0)V$ is the dimensionless constant of pairing interaction, and $N_0(0)$ is the density of states of free electrons at the Fermi level.

The solution of the system of equations (14) gives

$$\begin{aligned} G_{11} &= -\frac{1}{\mathrm{Det}}[(i\varepsilon + \xi_1)(\varepsilon^2 + \xi_2^2 + D^2 + \Delta) \\ &- D^2(\xi_1 + \xi_2)] = -\frac{1}{\mathrm{Det}}\{(i\varepsilon + \xi)[\varepsilon^2 + (\xi + \eta)^2 \\ &+ D^2 + \Delta^2] + D^2\eta\}, \\ F_{11}^{+} &= -\frac{1}{\mathrm{Det}}\Delta^{*}(\varepsilon^2 + \xi_2^2 + D^2 + \Delta^2) \\ &= -\frac{1}{\mathrm{Det}}\Delta^{*}[\varepsilon^2 + (\xi + \eta)^2 + D^2 + \Delta^2], \end{aligned} \tag{16}$$

where

$$\begin{aligned} \mathrm{Det} &= (\varepsilon^2 + \xi_1^2 + D^2 + \Delta^2)(\varepsilon^2 + \xi_2^2 + D^2 + \Delta^2) \\ &- (\xi_1 + \xi_2)^2 D^2 = (\varepsilon^2 + \xi^2 + D^2 + \Delta^2) \\ &\times (\varepsilon^2 + (\xi + \eta)^2 + D^2 + \Delta^2) - \eta^2 D^2, \end{aligned} \tag{17}$$

and D is the real amplitude of the fluctuation field (1). In accordance with relation (15), the Gor'kov Green's function F_{11}^{+} determines the energy gap of the superconductor. Taking into account the random nature of the field of dielectric fluctuations, Eq. (15) must be averaged over the fluctuations of phase $\eta = v_F k$ and amplitude D using distributions (6) and (11) (for the high-temperature fluctuation mode).

The cumbersome but direct calculations of the integral in Eq. (15) by the residue method give

$$\begin{aligned} \overline{F_{11}^{+}(\varepsilon)} &= \frac{\pi\Delta^{*}}{\sqrt{2}} \\ &\times \left\{\sqrt{\left(\tilde{\varepsilon}^2 + D^2 + \frac{\eta^2}{4}\right)^2 - \eta^2 D^2} + \tilde{\varepsilon}^2 + D^2 - \frac{\eta^2}{4}\right\}^{-1/2} \\ &\times \left\{1 + \frac{\tilde{\varepsilon}^2 + D^2 + \frac{\eta^2}{4}}{\sqrt{\left(\tilde{\varepsilon}^2 + D^2 + \frac{\eta^2}{4}\right)^2 - \eta^2 D^2}}\right\} \\ &\equiv \pi\Delta^{*}\mathscr{F}(\varepsilon, \Delta, \eta, D), \end{aligned} \tag{18}$$

where

$$\tilde{\varepsilon} = \sqrt{\varepsilon^2 + \Delta^2}. \tag{19}$$

Using now Eq. (15), we immediately obtain the following equation for the superconducting gap in the 2D model of hot regions [4–6]:

$$1 = 2\pi\lambda T\sum_{n=0}^{\left[\frac{\omega_c}{2\pi T}\right]}\left\{\tilde{\alpha}\mathscr{F}(\varepsilon, \Delta, \eta, D) + \frac{1 - \tilde{\alpha}}{\tilde{\varepsilon}}\right\}, \tag{20}$$

where $\tilde{\alpha} = (4/\pi)\alpha$ is the relative fraction of hot regions on the Fermi surface. The second term in Eq. (20) gives the standard BCS contribution from cold regions constituting the fraction $(1 - \tilde{\alpha})$ on the Fermi surface. Summation over n in Eq. (20) is carried out up to the maximum value determined by the integral part of the ratio $\omega_c/2\pi T$.

Using Eq. (20) and numerical calculations, we can find the gap width $\Delta(\eta, D)$ for fixed values of η and D (i.e., for the given value of the random field of fluctuations (1)) for any temperature. Then, by averaging over distributions (6) and (11), we can find the temperature dependences of the averaged gap. In particular, for the low-temperature mode of dielectric fluctuations, it is

sufficient to carry out averaging over phase η only; the superconducting gap in this case is given by

$$\langle\Delta\rangle = \frac{1}{\pi}\int_{-\infty}^{\infty} d\eta \frac{v_F\kappa}{\eta^2 + v_F^2\kappa^2}\Delta(\eta, D). \quad (21)$$

In the high-temperature approximation, averaging over amplitude D with distribution (11) must also be carried out:

$$\langle\Delta\rangle = \frac{2}{W^2}\int_0^{\infty} dD D\exp\left(-\frac{D^2}{W^2}\right)\frac{1}{\pi} \times \int_{-\infty}^{\infty} d\eta \frac{v_F\kappa}{\eta^2 + v_F^2\kappa^2}\Delta(\eta, D). \quad (22)$$

As a result, we obtain the temperature dependences of the averaged superconducting gap $\langle\Delta\rangle$ without resorting to any statistical assumptions like that concerning the self-averaging of the order parameter. Similarly, we can also calculate the temperature dependences of variance $\langle\Delta^2\rangle - \langle\Delta\rangle^2$, from which we can judge the extent of randomness of Δ, i.e., on the presence or absence of self-averaging. The results of corresponding calculations will be discussed in the next section.

It was noted in the Introduction that, in most publications on superconductivity in disordered systems, an analysis is carried out under the assumption of self-averaging of the superconducting gap Δ. In this case, Δ is in fact regarded as a nonrandom quantity independent of the random characteristics of the field in which the electrons forming Cooper pairs propagate. In our case, these are the amplitude D and the phase η of field (1); accordingly, the self-averaging over these parameters can be analyzed separately.

Let Δ be a parameter self-averaging over fluctuations of η. In this case, we can assume that Δ in Eq. (16) is independent of η. Accordingly, the anomalous Gor'kov function averaged over fluctuations of η has the form

$$\langle F_{11}^+\rangle = \frac{\Delta^*}{\pi}\int_{-\infty}^{\infty} d\eta \frac{v_F\kappa}{\eta^2 + v_F^2\kappa^2} \frac{\varepsilon^2 + (\xi + \eta)^2 + D^2 + \Delta^2}{(\varepsilon^2 + \xi^2 + D^2 + \Delta^2)(\varepsilon^2 + (\xi + \eta)^2 + D^2 + \Delta^2) - \eta^2 D^2}. \quad (23)$$

This integral can be evaluated directly; after cumbersome calculations, we obtain

$$\langle F_{11}^+\rangle = \Delta^* \times \frac{\tilde{\varepsilon}^2(1 + v_F\kappa/\tilde{\varepsilon})^2 + D^2(1 + v_F\kappa/\tilde{\varepsilon}) + \xi^2}{[(1 + v_F\kappa/\tilde{\varepsilon})\tilde{\varepsilon}^2 + \xi^2 + D^2]^2 + v_F^2\kappa^2\xi^2}. \quad (24)$$

Accordingly, we can also evaluate the integral of expression (24) appearing in the equation for the pseudogap:

$$\overline{\langle F_{11}^+\rangle} \equiv \int_{-\infty}^{\infty} d\xi \langle F_{11}^+\rangle = \frac{\pi\Delta^*(1 + v_F\kappa/2\tilde{\varepsilon})}{\sqrt{D^2 + \tilde{\varepsilon}^2(1 + v_F\kappa/2\tilde{\varepsilon})^2}}. \quad (25)$$

Thus, in spite of the cumbersome form of the anomalous Green's function (24), the inclusion of interaction with fluctuations in hot (flat) regions on the Fermi surface in the equation for the gap can be reduced to the standard renormalization,

$$\varepsilon \longrightarrow \varepsilon\left(1 + \frac{v_F\kappa}{2\tilde{\varepsilon}}\right) = \varepsilon\left(1 + \frac{v_F\kappa}{2\sqrt{\varepsilon^2 + \Delta^2}}\right),$$
$$\Delta \longrightarrow \Delta\left(1 + \frac{v_F\kappa}{2\tilde{\varepsilon}}\right) = \Delta\left(1 + \frac{v_F\kappa}{2\sqrt{\varepsilon^2 + \Delta^2}}\right), \quad (26)$$

similar to that emerging in the problem taking into account the effect of impurities on superconductivity [23] and already encountered in the context of the problem under investigation in [6]. The analogy with the impurity problem is almost complete since the quantity $v_F\kappa = v_F\xi_{\text{corr}}^{-1}$ is the characteristic reciprocal time of electron flight through a short-range region with a length on the order of ξ_{corr}. Naturally, the effect of the pseudogap is also associated with the emergence of the square of the dielectric gap D^2 in Eqs. (24) and (25).

Ultimately, the equation for the superconducting gap in the model of hot spots under the assumption of self-averaging over phase fluctuations assumes the form

$$1 = 2\pi\lambda T \times \sum_{n=0}^{\left[\frac{\omega_c}{2\pi T}\right]}\left\{\tilde{\alpha}\frac{1 + v_F\kappa/2\tilde{\varepsilon}}{\sqrt{D^2 + \tilde{\varepsilon}^2(1 + v_F\kappa/2\tilde{\varepsilon})^2}} + \frac{1 - \tilde{\alpha}}{\tilde{\varepsilon}}\right\}. \quad (27)$$

This equation can obviously be solved more easily than Eq. (20) with subsequent averaging (21). In the absence of fluctuations of the dielectric field amplitude D, which is the case in the low-temperature region of short-range fluctuations, it is precisely Eq. (27) that determines the mean-field (in terms of [5]) behavior of $\Delta(T)$ relative to fluctuations of the random field (1).

In the high-temperature region of short-range fluctuations with distribution (11) for D, under the assumption of self-averaging over the fluctuations of D also,

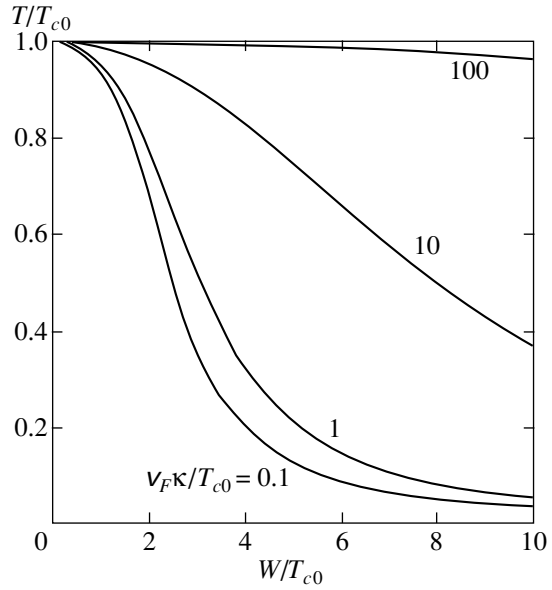

Fig. 2. Superconducting transition temperature in the low-temperature region of dielectric fluctuations as a function of the pseudogap width W for various values of the correlation length $v_F\kappa/T_{c0}$ of dielectric fluctuations.

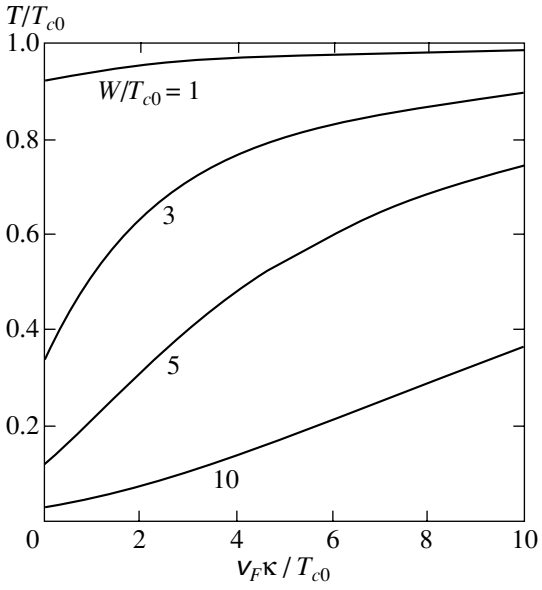

Fig. 3. Superconducting transition temperature in the low-temperature region of dielectric fluctuations as a function of the correlation length of these fluctuations for various values of the pseudogap width W/T_{c0}.

we obtain the following equation for the averaged superconducting gap:

$$1 = 2\pi\lambda T \sum_{n=0}^{\left[\frac{\omega_c}{2\pi T}\right]} \left\{ \frac{2\tilde{\alpha}}{W^2} \int_0^\infty dD D \exp\left(-\frac{D^2}{W^2}\right) \times \frac{1 + v_F\kappa/2\tilde{\varepsilon}}{\sqrt{D^2 + \tilde{\varepsilon}^2(1 + v_F\kappa/2\tilde{\varepsilon})^2}} + \frac{1-\tilde{\alpha}}{\tilde{\varepsilon}} \right\}. \quad (28)$$

This equation describes a situation similar to that considered in detail in our earlier publication [6], where we included the effect produced on superconductivity by Gaussian dielectric short-range fluctuations using the approach proposed in [8, 9]. In this case, fluctuations of field (1) are taken into account exactly, but it is assumed that Δ is self-averaging. It will be demonstrated below that all the results following from Eq. (28) are quite close to those obtained in [6]. As $\kappa \longrightarrow 0$ ($\xi_{corr} \longrightarrow \infty$), Eq. (28) is transformed into a similar mean-field equation derived in [5]. The superconducting transition temperature obtained from Eq. (27) or (28) can apparently be identified with the temperature at which an infinitely narrow gap (superconductivity) emerges uniformly in the entire sample [5].

In the next section, we will consider the results of numerical solution of Eqs. (27) and (28) in comparison with the results of exact analysis based on Eqs. (20)–(22).

4. BASIC RESULTS AND DISCUSSION

Let us now consider the results of a numerical analysis of the equations given in the previous section.[6]

Figures 2 and 3 show the superconducting transition temperature T_c in the low-temperature range of dielectric fluctuations (the temperature at which the mean-field gap defined by Eq. (27) vanishes) as a function of the pseudogap width W (which coincides in the present case with the dielectric gap amplitude D) and of the correlation length, respectively. The results are in qualitative agreement with the corresponding results for the high-temperature range of dielectric fluctuations (where T_c is defined by Eq. (28)) as well as with the results obtained by us earlier [6] in a somewhat different model of short-range dielectric fluctuations with a finite correlation length. Upon an increase in the pseudogap width W, the mean-field temperature T_c is suppressed. A decrease in the correlation length blurs the pseudogap [2, 8, 15] and, accordingly, diminishes the suppression of T_c.

Solid curves in Fig. 4 present the temperature dependences of the superconducting gap $\langle\Delta\rangle$ averaged over both amplitude D and phase η (the high-temperature region of short-range fluctuations, where $\langle\Delta\rangle$ is described by formula (22)) for various values of $v_F\kappa$. The dashed curves describe the corresponding mean-field temperature dependences of the superconducting gap, which were obtained under the assumption of self-averaging of the superconducting order parameter over

[6] In the numerical analysis, it was assumed that the fraction of flat regions on the Fermi surface is $\alpha = 2/3$.

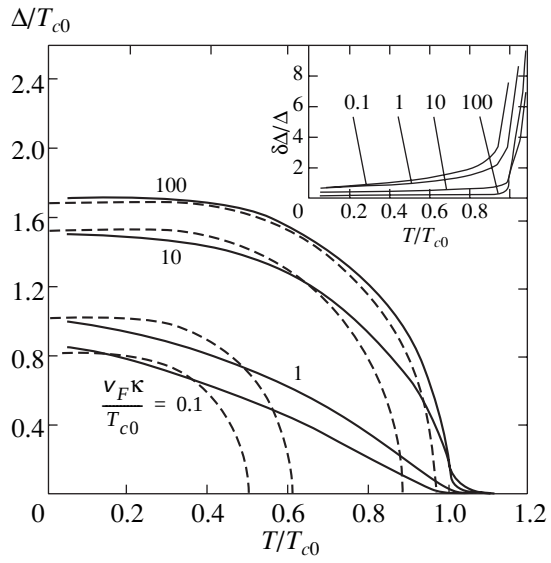

Fig. 4. Temperature dependence of the superconducting gap in the high-temperature region of dielectric fluctuations. Solid curves correspond to the superconducting gap $\langle\Delta\rangle$ averaged over amplitude D and phase η and described by expression (22). Dashed curves correspond to the mean-field superconducting gap defined by Eq. (28). The inset shows the temperature dependence of the relative root-mean-square fluctuation of the superconducting gap. The curves are plotted for $W/T_{c0} = 3$ and for various values of $v_F\kappa/T_{c0}$.

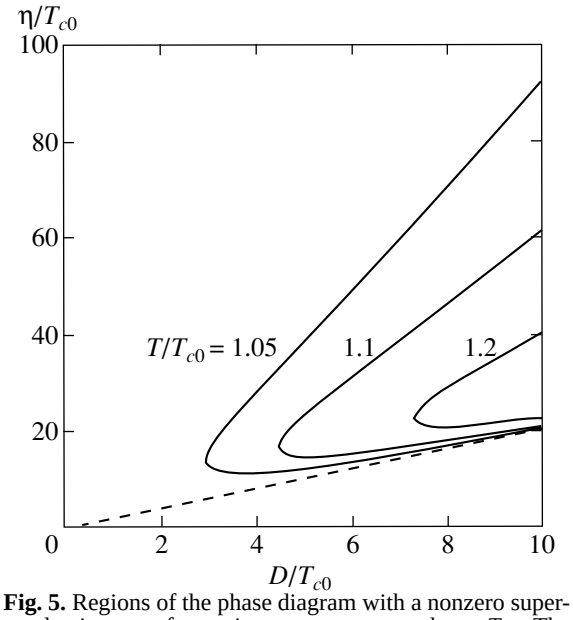

Fig. 5. Regions of the phase diagram with a nonzero superconducting gap for various temperatures above T_{c0}. The dashed line corresponds to $D = \eta/2$.

both the amplitude fluctuations and the phase fluctuations described by Eq. (28).

The superconducting gap averaged over fluctuations also differs from zero in a temperature range above the superconducting transition temperature T_c, which corresponds to vanishing of the mean-field superconducting gap (i.e., the gap which is homogeneous in the entire sample). Moreover, it can be seen that the superconducting gap averaged over fluctuations differs from zero in a narrow temperature region above the superconducting transition temperature T_{c0} in the absence of short-range fluctuations also. This is due to the fact that there exist fluctuations of phase η, for which the Fermi level falls to the region of the peaks of density of states, which are associated with the formation of the dielectric gap. Indeed, the density of states for a specific realization of phase η and of the dielectric gap amplitude D has the form

$$\frac{N(E)}{N_0(0)} = -\frac{1}{\pi N_0(0)}\mathrm{Im}\sum_{\mathbf{p}} g_{11}^R(Epp)$$

$$= \begin{cases} \dfrac{|E+\eta/2|}{\sqrt{(E+\eta/2)^2 - D^2}} & \text{for } |E+\eta/2| > D, \\ 0 \quad \text{for remaining values,} \end{cases} \tag{29}$$

where $g_{11}^R(Epp)$ is the retarded Green's function which can be obtained from Eq. (4) by the standard analytic continuation $i\varepsilon_n \longrightarrow E + i0$ and $N_0(0)$ is the density of states at the Fermi level in the absence of short-range fluctuations. Consequently, for $\eta/2 \approx D$, the Fermi level corresponds to the peaks of the density of states, which leads to an increase in the superconducting gap $\Delta(\eta, D)$. Moreover, an increase in the dielectric gap amplitude D broadens the peaks in the density of states (29); consequently, if the condition $\eta/2 \approx D$ remains in force, the superconducting gap $\Delta(\eta, D)$ increases with D. As a result, at any temperature above T_{c0} and for large amplitudes of the dielectric gap $D > D^*(T)$, the phase diagram plotted in the η vs. D coordinates always contains a narrow region in the vicinity of the straight line $\eta/2 = D$, in which the superconducting gap $\Delta(\eta, D)$ differs from zero (see Fig. 5). This leads to the emergence of an exponentially small tail on the temperature dependence of the superconducting gap $\langle\Delta\rangle$ averaged over fluctuations in the temperature range above T_{c0}.[7]

The inset to Fig. 4 shows the temperature dependence of the relative root-mean-square fluctuation $\delta\Delta/\Delta = \sqrt{\langle\Delta^2\rangle - \langle\Delta\rangle^2}/\langle\Delta\rangle$ of the superconducting gap for the high-temperature mode of dielectric fluctuations. In the case of large short-range correlation lengths ($\xi_0/\xi_{\mathrm{corr}} \ll 1$), the superconducting order parameter fluctuations are very strong in the entire temperature range, indicating the obvious non-self-averaging of

[7] In the model under investigation, this effect is obviously a consequence of the one-dimensional nature of the random field of fluctuations, leading to corresponding singularities in the density of states (29). For this reason, it may turn out to be not universal and inherent only in the given simplified model.

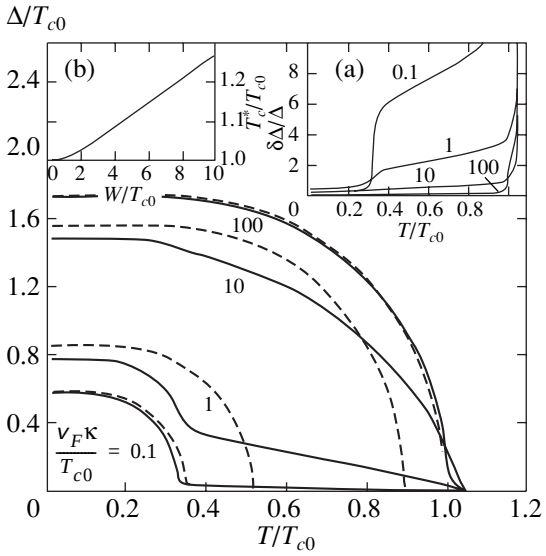

Fig. 6. Temperature dependence of the superconducting gap in the low-temperature region of dielectric fluctuations. Solid curves correspond to the superconducting gap $\langle\Delta\rangle$ averaged over phase η for a fixed amplitude $D = W$, described by expression (21). Dashed curves correspond to the mean-field superconducting gap defined by Eq. (27). Inset (a) shows the temperature dependence of the relative root-mean-square fluctuation of the superconducting gap. The curves are plotted for $W/T_{c0} = 3$ and for various values of $v_F\kappa/T_{c0}$. Inset (b) shows the dependence of the critical temperature T_c^* on the pseudogap width.

the superconducting order parameter. Surprisingly, the superconducting gap fluctuations are quite strong in the region of small correlation lengths also (at least in the temperature range $T > T_c$). In particular, the tail on the temperature dependence of $\langle\Delta\rangle$ for $T > T_c$ is noticeable even for $v_F\kappa/T_{c0} = 100$, when $\xi_0/\xi_{corr} \approx 30 \geq 1$.

Solid curves in Fig. 6 are the temperature dependences of the superconducting gap $\langle\Delta\rangle$ averaged over phase η (see Eq. (21)) in the low-temperature mode of dielectric fluctuations, when the amplitude fluctuations of the dielectric gap are frozen out and $D = W$. The dashed curves are the corresponding temperature dependences of the mean-field superconducting gap obtained under the assumption of self-averaging of the superconducting order parameter over the fluctuations of phase η, which are defined by Eq. (27). For large short-range correlation lengths, the averaged gap for $T < T_c$ is very close to the mean-field gap and has a relatively small tail in the range $T > T_c$. Such a behavior in the low-temperature mode of dielectric fluctuations is associated with the fact that, for $\xi_{corr} \longrightarrow \infty$, the randomness of such a model disappears altogether ($\eta = 0$, $D = W$). Accordingly, the root-mean-square fluctuation of the gap, which is shown in the inset to Fig. 6 for a large correlation length, is quite small for $T < T_c$, but increases sharply for $T > T_c$. As the correlation length decreases, the superconducting gap fluctuations $\delta\Delta$ for $T < T_c$ first increase just due to the increase in randomness (parameter $v_F\kappa$ determines the width of the distribution of phase η) and then decrease in the region $\xi_0/\xi_{corr} \gg 1$. In the tail region of the averaged superconducting gap ($T > T_c$), the superconducting gap fluctuations are very strong. Although they decrease with the short-range correlation length ξ_{corr}, they still remain significant even for small correlation lengths, i.e., in the region $\xi_0/\xi_{corr} \gg 1$.

As in the high-temperature mode of dielectric fluctuations, the tail on the temperature dependence of the average gap is observed for $T > T_{c0}$ also. This can be explained by the above-mentioned factors. However, the dielectric gap amplitude in the low-temperature mode is not random any longer, but is strictly fixed ($D = W$). For this reason, for $T_{c0} < T < T_c^*$, where T_c^* is determined by the condition $D^*(T_c^*) = W$, there exists a narrow region of phases near $\eta = 2W$ in which the superconducting gap $\Delta(\eta, W)$ differs from zero, but no such region is present for $T > T_c^*$ (see Fig. 5); T_c^* is the temperature to which the tail of the averaged gap extends, i.e., the critical temperature for the averaged gap $\langle\Delta\rangle$. It follows from the definition of T_c^* that it is obviously independent of the correlation length and depends only on W. Since the width of the peaks of the density of states (29) (and, hence, of $\Delta(\eta, D)$ also) increases with D as long as the condition $\eta/2 \approx D$ is satisfied, the value of T_c^* increases with W. The dependence of T_c^* on W is shown on the corresponding inset to Fig. 6.

5. CONCLUSIONS

In the present work, we have studied the features of the superconducting state in the framework of the extremely simplified model of the pseudogap in a 2D electron system, which has an exact solution. The main result is the obvious absence of complete self-averaging of the superconducting order parameter (energy gap) over the random field of dielectric fluctuations leading to the formation of the pseudogap state. This fact is quite astonishing from the viewpoint of the standard model of superconductivity in disordered systems [12–14]. The absence of self-averaging, which is manifested in the emergence of strong fluctuations of the gap, can be seen most clearly in the range of temperatures exceeding the mean-field superconducting transition temperature T_c that can be obtained from the standard equations written under the assumption of self-averaging of the order parameter. This temperature is identified by us with the temperature of the emergence of a homogeneous superconducting state in the entire sample, while the superconducting state in a real disordered system is inhomogeneous. The superconducting

state can exist in the range $T > T_c$ in the form of individual regions (drops) formed as a result of random fluctuations of the local density of electron states. In contrast to our previous publication [5], in which this pattern was considered in the limit of very large short-range correlation lengths $\xi_{corr} \longrightarrow \infty$, the application of the model [15] has made it possible to obtain the complete solution for arbitrary values of ξ_{corr}. This solution has demonstrated the absence of complete self-averaging of the superconducting gap even for $\xi_{corr} < \xi_0$, which contradicts the naive expectations following from the standard approach [2]. It was noted above that we are not aware of publications in which the self-averaging of Δ would be considered in the framework of exactly solvable models of disorder. In the present paper, such an analysis has been carried out. It is unclear, however, to what extent the obtained results will be preserved in more realistic models.

For further investigations associated with the given model, it would be interesting to analyze the behavior of the spectral density of the electron and tunnel densities of states as was done in our earlier work [5] in the limit $\xi_{corr} \longrightarrow \infty$. In particular, it would be interesting to investigate the problem of self-averaging of the density of states, which is assumed in the theory of disordered system almost in all cases.

As regards the comparison with the experimental data on high-temperature superconductors, it should be noted that the existence of microscopic superconducting regions coexisting with predominant regions of the semiconductor type with a typical pseudogap in the electron spectrum of $Bi_2Sr_2CaCu_2O_{8+\delta}$ films was clearly demonstrated in [24, 25] using the method of scanning electron microscopy for measuring the local density of states. These observations are in qualitative agreement with the main conclusions drawn on the basis of the model under investigation.

ACKNOWLEDGMENTS

The work was partly financed by the Russian Foundation for Basic Research (project no. 99-02-16285), CRDF (grant no. REC-005), and the Program of Fundamental Studies "Quantum Macrophysics" of the Presidium of the Russian Academy of Sciences, as well as in the framework of state contracts of the Ministry of Industry and Science nos. 108-11(00)-P under the program "Statistical Physics" and 107-1(00)-P (contract no. 7/01) under the HTSC program.

REFERENCES

1. T. Timusk and B. Statt, Rep. Prog. Phys. **62**, 61 (1999).
2. M. V. Sadovskiĭ, Usp. Fiz. Nauk **171**, 539 (2001).
3. V. M. Loktev, R. M. Quick, and S. G. Sharapov, submitted to Phys. Rep.; cond-mat/0012082.
4. A. I. Posazhennikova and M. V. Sadovskiĭ, Zh. Éksp. Teor. Fiz. **115**, 632 (1999) [JETP **88**, 347 (1999)].
5. É. Z. Kuchinskiĭ and M. V. Sadovskiĭ, Zh. Éksp. Teor. Fiz. **117**, 613 (2000) [JETP **90**, 535 (2000)]; Physica C (Amsterdam) **341–348**, 879 (2000).
6. É. Z. Kuchinskiĭ and M. V. Sadovskiĭ, Zh. Éksp. Teor. Fiz. **119**, 553 (2001) [JETP **92**, 480 (2001)].
7. M. V. Sadovskiĭ, Zh. Éksp. Teor. Fiz. **66**, 1720 (1974) [Sov. Phys. JETP **39**, 845 (1974)]; Fiz. Tverd. Tela (Leningrad) **16**, 2504 (1974) [Sov. Phys. Solid State **16**, 1632 (1974)].
8. M. V. Sadovskiĭ, Zh. Éksp. Teor. Fiz. **77**, 2070 (1979) [Sov. Phys. JETP **50**, 989 (1979)].
9. M. V. Sadovskiĭ and A. A. Timofeev, Sverkhprovodimost: Fiz., Khim., Tekh. **4**, 11 (1991); M. V. Sadovskii and A. A. Timofeev, J. Mosc. Phys. Soc. **1**, 391 (1991).
10. J. Schmalian, D. Pines, and B. Stojkovic, Phys. Rev. Lett. **80**, 3839 (1998); Phys. Rev. B **60**, 667 (1999).
11. É. Z. Kuchinskiĭ and M. V. Sadovskiĭ, Zh. Éksp. Teor. Fiz. **115**, 1765 (1999) [JETP **88**, 968 (1999)].
12. L. P. Gor'kov, Zh. Éksp. Teor. Fiz. **37**, 1407 (1959) [Sov. Phys. JETP **10**, 998 (1959)].
13. P. G. de Gennes, *Superconductivity of Metals and Alloys* (Benjamin, New York, 1966; Mir, Moscow, 1968).
14. M. V. Sadovskii, *Superconductivity and Localization* (World Scientific, Singapore, 2000); Phys. Rep. **282**, 225 (1997); Sverkhprovodimost: Fiz., Khim., Tekh. **8**, 337 (1995).
15. L. Bartosch and P. Kopietz, Eur. Phys. J. B **17**, 555 (2000).
16. P. A. Lee, T. M. Rice, and P. W. Anderson, Phys. Rev. Lett. **31**, 462 (1973).
17. M. V. Sadovskii, Physica C (Amsterdam) **341–348**, 811 (2000).
18. L. Bartosch and P. Kopietz, Phys. Rev. B **60**, 15488 (1999).
19. L. Bartosch, submitted to Ann. Phys. (Leipzig); cond-mat/0102160.
20. A. J. Millis and H. Monien, Phys. Rev. B **61**, 12496 (2000).
21. S. A. Brazovskiĭ and I. E. Dzyaloshinskiĭ, Zh. Éksp. Teor. Fiz. **71**, 2338 (1976) [Sov. Phys. JETP **44**, 1233 (1976)].
22. J. Tranquada, J. Phys. Chem. Solids **59**, 2150 (1998).
23. A. A. Abrikosov, L. P. Gor'kov, and I. E. Dzyaloshinskii, *Methods of Quantum Field Theory in Statistical Physics* (Fizmatgiz, Moscow, 1962; Prentice-Hall, Englewood Cliffs, 1963).
24. T. Cren, D. Roditchev, W. Sacks, *et al.*, Phys. Rev. Lett. **84**, 147 (2000).
25. T. Cren, D. Roditchev, W. Sacks, and J. Klein, submitted to Europhys. Lett.

Translated by N. Wadhwa

Journal of Experimental and Theoretical Physics, Vol. 94, No. 3, 2002, pp. 664–672.
Translated from Zhurnal Éksperimental'noĭ i Teoreticheskoĭ Fiziki, Vol. 121, No. 3, 2002, pp. 770–778.

SOLIDS
Electronic Properties

On the Theory of Magnetoresistance of Binary Composites in a Weak Magnetic Field: Numerical Experiment

B. Ya. Balagurov and V. A. Kashin

Emanuel' Institute of Biochemical Physics, Russian Academy of Sciences, Moscow, 119991 Russia

Received October 10, 2001

Abstract—A correction to the electric field strength linear in magnetic field **H** was found by computations for a two-dimensional disordered system. This correction was used to calculate and graphically tabulate two two-parameter functions present in the equation describing magnetoresistance in a wide range of parameter variations. This correction was also used to determine and tabulate the derivative of the function present in the equation for the effective Hall coefficient with respect to one of its arguments. The data obtained in this work combined with the earlier results of these authors allow the magnetoresistance of binary (composite) media to be completely described in the spirit of the similarity hypothesis. © *2002 MAIK "Nauka/Interperiodica".*

1. INTRODUCTION

The determination of the galvanomagnetic characteristics of three-dimensional nonuniform media (binary composites in particular) is a topical and fairly difficult problem even when magnetic field **H** is weak. The presence of additional (compared with the $\mathbf{H} = 0$ case) parameters complicates the problem and, for instance, leads to the possibility of varied critical behaviors of the effective Hall coefficient [1, 2]. Still more complex critical behavior should be expected for magnetoresistance, where the number of additional parameters is much larger. Nevertheless, certain progress has been made in developing the theory of galvanomagnetic properties of three-dimensional two-component media in a weak magnetic field.

The approximation linear in **H**, the Hall effect, was studied in several works (e.g., see [1–5]). Shklovskii [1] suggested an appropriate approximation formula to describe the effective Hall coefficient R_e in the vicinity of the metal–dielectric phase transition point. The results obtained in [1] give a qualitative description of R_e in the critical region; the question of a quantitative approach to the problem, however, remains open. Skal [2] obtained an exact (in the approximation linear in **H**) formal equation for R_e. This equation was not, however, given a proper theoretical analysis; it was only used for numerically studying the Hall coefficient. Lastly, in [3, 4], the equation for R_e in binary systems was brought to the level of a two-parameter function (see below) and written in an explicit form in terms of electric field strength in a medium at $\mathbf{H} = 0$. Note that the Hall coefficient was only considered in [3], and no technique for calculating approximations of high orders in **H** was suggested.

A scheme for consistently calculating the galvanomagnetic characteristics of binary composites in a weak magnetic field was suggested in [4]. In that work, perturbation theory (expansion in powers of **H**) was developed and, apart from the Hall coefficient, magnetoresistance was considered in much detail. The structure of the effective conductivity tensor part $\hat{\sigma}_e$ quadratic in **H**, that is, its dependence on the galvanomagnetic characteristics of separate components, was found [4]. The coefficients of these characteristics are determined by the properties of the medium at $\mathbf{H} = 0$ and are functions of two arguments, namely, concentration p and the ratio between component conductivities $h = \sigma_2/\sigma_1$. In the approximation quadratic in **H**, ten such functions that cannot be determined theoretically appear. One more similar function is present in the linear approximation.

Most of these functions are written in terms of electric field strength in the medium at $\mathbf{H} = 0$, which allows them to be determined within the framework of the standard conductivity problem. In addition, several relations between these functions established in [4] reduce the problem to calculating some of them. In the numerical experiment performed in [5], the functions mentioned above and present in the equations for the Hall coefficient and magnetoresistance were calculated alongside conductivity. Two functions (χ_x and χ_z) remained undetermined in [5]. Finding them requires calculating the correction to the electric field linear in **H**, which goes beyond the scope of the conductivity problem.

This work is concerned with determining the χ_x and χ_z values as functions of p and h in a wide range of variations of these arguments by numerical methods. For this purpose, we simulated the problem of the galvanomagnetic properties of binary composites using a pair of primitive cubic cells, main and auxiliary, to extend the two-dimensional dual problem to the three-dimensional case. The problem of electric field in a medium was solved iteratively [5, 6] in two stages. First, poten-

tials in all nodes of both lattices were found at $\mathbf{H} = 0$. At the second stage, corrections to these potentials linear in $\mathbf{H}$ were found. At both stages, we applied the Chebyshev method of polynomial acceleration of the main iterative process [6]. At the first stage, we used the same method for controlling the accuracy and correctness of calculations as in [5], which was based on analyzing the spread of total current values calculated for each sample cross section. At the second stage, the results were verified by comparing φ function values (the φ function is present in the equation for the effective Hall coefficient) determined by two different methods (see Section 5).

The general formulas found in [4] were used to calculate the χ_x and χ_z functions from the zeroth- and first-approximation potentials in the whole range of concentration p variations at three argument h values. The results are plotted below (Figs. 3, 4). The behavior of the χ_x and χ_z values in the vicinity of the metal–dielectric phase transition was fairly thoroughly analyzed, and the critical indices of these functions were estimated. It follows that the results obtained in [5] and this work can be used to quantitatively describe the magnetoresistance of binary composites whose properties are correctly reproduced by the lattice model. For the other disordered two-component systems, these results give a qualitative description of magnetoresistance "at the level of critical indices" (that is, in the spirit of the standard similarity hypothesis [7]).

The knowledge of correction $\mathbf{E}_1(\mathbf{r})$, linear in $\mathbf{H}$, to electric field allows a new approach to be used in studying the properties of function φ present in the equation for the effective Hall coefficient. The point is that $\mathbf{E}_1(\mathbf{r})$ can be used to determine the $\partial\varphi/\partial h$ derivative without cumbersome numerical differentiation. This allows critical indices and also one of the coefficients in the expansion of φ, which cannot be found from the data on function φ itself, to be determined by an essentially independent method. The results for φ from [5] and for the $\partial\varphi/\partial h$ derivative from this work therefore allow us to give a detailed description of the φ function in the whole interval of variations of each of its arguments including the critical region.

2. MAIN RELATIONS

The conductivity of an isotropic medium in magnetic field $\mathbf{H}$ is described by the tensor

$$\hat{\sigma} = \begin{pmatrix} \sigma_x & \sigma_a & 0 \\ -\sigma_a & \sigma_x & 0 \\ 0 & 0 & \sigma_z \end{pmatrix}, \quad (1)$$

where it is assumed that $\mathbf{H}$ is directed along the z axis. To simplify further formulas, we use the notation $\sigma_x = \sigma_{xx} = \sigma_{yy}$, $\sigma_z = \sigma_{zz}$, and $\sigma_a = \sigma_{xy} = -\sigma_{yx}$ for the transverse, longitudinal, and off-diagonal (Hall) conductivity tensor $\hat{\sigma}$ components, respectively. In a weak magnetic field ($\mathbf{H} \longrightarrow 0$), the σ_a value is linear, whereas corrections to σ_x and σ_z are quadratic in H,

$$\sigma_x = \sigma + \gamma_x, \quad \sigma_z = \sigma + \gamma_z; \quad \gamma_x \propto H^2, \quad \gamma_z \propto H^2. \quad (2)$$

Here, $\sigma = \sigma(\mathbf{r})$ is the medium conductivity at $\mathbf{H} = 0$. If $\mathbf{H} \longrightarrow 0$, the effective conductivity tensor σ_e components possess the same properties as $\hat{\sigma}$ in (1); namely, the expansion of σ_{ae} only contains odd powers of H, and the expansions of σ_{xe} and σ_{ze} only contain even H powers.

The effective conductivity σ_e of a two-component medium (binary composite) can, at $\mathbf{H} = 0$, be written in the form

$$\sigma_e = \sigma_1 f(p, h), \quad h = \frac{\sigma_2}{\sigma_1}, \quad (3)$$

where p is the concentration (the fraction of the occupied volume) of the first component and σ_i is the conductivity of the ith component. According to [4], in the approximation linear in $\mathbf{H}$, the Hall component can be written as

$$\sigma_{ae} = \sigma_{a2} + (\sigma_{a1} - \sigma_{a2})\varphi(p, h). \quad (4)$$

The φ function is determined by the properties of the medium at $\mathbf{H} = 0$ and can be expressed through the electric field as [4]

$$\varphi = \langle e_x^{(x)} e_y^{(y)} - e_y^{(x)} e_x^{(y)} \rangle^{(1)}, \quad (5)$$

$$e_\alpha^{(\nu)}(\mathbf{r}) = E_{0\alpha}^{(\nu)}(\mathbf{r})(\langle E_{0\nu}^{(\nu)} \rangle)^{-1}. \quad (6)$$

Here, $\langle \ldots \rangle^{(1)}$ is the integral over the volume of the first component divided by sample volume V_s, and $\mathbf{E}_0^{(\nu)}(\mathbf{r})$ is the electric field strength in the medium at $\mathbf{H} = 0$, where index ν denotes that the mean (over the whole V_s volume) $\langle \mathbf{E}_0^{(\nu)} \rangle$ vector is directed along the ν axis.

Let us write σ_{xe} and σ_{ze} in the form similar to (2),

$$\sigma_{xe} = \sigma_e + \gamma_{xe}, \quad \sigma_{ze} = \sigma_e + \gamma_{ze}; \quad \gamma_{xe} \propto H^2, \quad \gamma_{ze} \propto H^2, \quad (7)$$

where σ_e is the same as in (3). According to [4], γ_{xe} and γ_{ze} are expressed via the galvanomagnetic characteristics of separate components (γ_{xi}, γ_{zi}, and σ_{ai} where $i = 1, 2$) as follows:

$$\gamma_{xe} = \gamma_{x1}\psi_x^{(1)} + \gamma_{z1}\psi_x^{(2)} + \gamma_{x2}\psi_x^{(3)} + \gamma_{z2}\psi_x^{(4)} + \frac{(\sigma_{a1} - \sigma_{a2})^2}{\sigma_1}\chi_x, \quad (8)$$

$$\gamma_{ze} = \gamma_{x1}\psi_z^{(1)} + \gamma_{z1}\psi_z^{(2)} + \gamma_{x2}\psi_z^{(3)} + \gamma_{z2}\psi_z^{(4)} + \frac{(\sigma_{a1}-\sigma_{a2})^2}{\sigma_1}\chi_z. \quad (9)$$

Here, dimensionless coefficients $\psi_x^{(a)}$, $\psi_z^{(a)}$ ($a = 1, 2, 3, 4$) and χ_x, χ_z only depend on the properties of the medium at $\mathbf{H} = 0$ and are, like f and φ, functions of the p and h arguments. All $\psi_x^{(a)}$ functions are expressed through $\psi_z^{(a)}$ [4],

$$\psi_x^{(1)} = \frac{1}{2}\psi_z^{(1)} + \psi_z^{(2)}, \quad \psi_x^{(2)} = \frac{1}{2}\psi_z^{(1)},$$
$$\psi_x^{(3)} = \frac{1}{2}\psi_z^{(3)} + \psi_z^{(4)}, \quad \psi_x^{(4)} = \frac{1}{2}\psi_z^{(3)}. \quad (10)$$

The $\psi_z^{(a)}$ functions are in turn related to each other by two equations containing dimensionless conductivity f and its derivative [4],

$$\psi_z^{(1)} + \psi_z^{(2)} = f - h\frac{\partial f}{\partial h}, \quad \psi_z^{(3)} + \psi_z^{(4)} = \frac{\partial f}{\partial h}. \quad (11)$$

The $\psi_z^{(a)}$ functions can be written in terms of electric field strength in the medium at $\mathbf{H} = 0$ [4],

$$\psi_z^{(1)} = \langle \mathbf{e}_\perp^2 \rangle^{(1)}, \quad \psi_z^{(2)} = \langle \mathbf{e}_\parallel^2 \rangle^{(1)},$$
$$\psi_z^{(3)} = \langle \mathbf{e}_\perp^2 \rangle^{(2)}, \quad \psi_z^{(4)} = \langle \mathbf{e}_\parallel^2 \rangle^{(2)}, \quad (12)$$

where $\langle \ldots \rangle^{(i)}$ is the integral over the volume of the ith component divided by sample volume V_s. Here, $\mathbf{e}(\mathbf{r})$ is the same as in (6) (where, for instance, $\nu = x$), and $\mathbf{e}_\perp(\mathbf{r})$ and $\mathbf{e}_\parallel(\mathbf{r})$ are the transverse and longitudinal (with respect to $\langle \mathbf{E}_0 \rangle$) $\mathbf{e}(\mathbf{r})$ vector components. Note that discrete analogues of (5) and (12) were used in [5] to calculate and tabulate φ and $\psi_z^{(a)}$ ($a = 1, 2, 3, 4$) functions. In particular, the behavior of these functions in the vicinity of the metal–dielectric phase transition was studied, and the critical indices and the coefficients of the expansions of φ and $\psi_z^{(a)}$ in the critical region were estimated [5].

The determination of the χ_x and χ_z functions in (8) and (9) requires knowledge of correction $\mathbf{E}_1^{(\nu)}(\mathbf{r})$, linear in $\mathbf{H}$, to electric field strength, $\mathbf{E}^{(\nu)}(\mathbf{r}) = \mathbf{E}_0^{(\nu)}(\mathbf{r}) + \mathbf{E}_1^{(\nu)}(\mathbf{r}) + \ldots$. According to [4], this correction is proportional to $(\sigma_{a1} - \sigma_{a2})$. Therefore, setting

$$\mathbf{E}_1^{(\nu)}(\mathbf{r}) = \frac{\sigma_{a1}-\sigma_{a2}}{\sigma_1}\mathscr{E}^{(\nu)}(\mathbf{r}), \quad (13)$$

we obtain the following expressions for χ_x and χ_z at $\langle \mathscr{E}^{(\nu)} \rangle = 0$ [4]:

$$\chi_x = \frac{\langle E_{0x}^{(x)}\mathscr{E}_y^{(\nu)} - E_{0y}^{(x)}\mathscr{E}_x^{(\nu)} \rangle^{(1)}}{\langle E_{0x}^{(x)} \rangle \langle E_{0\nu}^{(\nu)} \rangle}, \quad \nu = x, y, \quad (14)$$

$$\chi_z = \frac{\langle E_{0x}^{(z)}\mathscr{E}_y^{(z)} - E_{0y}^{(z)}\mathscr{E}_x^{(z)} \rangle^{(1)}}{\langle E_{0z}^{(z)} \rangle^2}. \quad (15)$$

Note that, according to (13), the $\mathscr{E}^{(\nu)}(\mathbf{r})$ value does not contain magnetic field and is therefore, like $\mathbf{E}_0^{(\nu)}(\mathbf{r})$, of a "normal" order of magnitude. In calculating χ_x by (14), we may equally assume $\nu = x$ and $\nu = y$.

For the longitudinal magnetoresistance, we have

$$\frac{\Delta\rho_{ze}}{\rho_{ze}} = \frac{\rho_{ze}(\mathbf{H}) - \rho_{ze}(0)}{\rho_{ze}(0)},$$

where $\rho_z = 1/\sigma_z$ is the longitudinal specific resistance. In the approximation quadratic in $\mathbf{H}$, we have

$$\frac{\Delta\rho_{ze}}{\rho_{ze}} = -\frac{\gamma_{ze}}{\sigma_e} \quad (16)$$

with γ_{ze} from (9). Accordingly, for the transverse magnetoresistance, we have

$$\frac{\Delta\rho_{xe}}{\rho_{xe}} = \frac{\rho_{xe}(\mathbf{H}) - \rho_{xe}(0)}{\rho_{xe}(0)},$$

where $\rho_x = \sigma_x/(\sigma_x^2 + \sigma_a^2)$ is the transverse specific resistance. In the approximation quadratic in $\mathbf{H}$,

$$\frac{\Delta\rho_{xe}}{\rho_{xe}} = -\left(\frac{\gamma_{xe}}{\sigma_e} + \frac{\sigma_{ae}^2}{\sigma_e^2}\right) \quad (17)$$

with σ_{ae} from (4) and γ_{xe} from (8).

Note that the knowledge of the $\mathbf{E}_1^{(\nu)}(\mathbf{r})$ correction allows the φ function from (4) to be calculated by a formula different from (5). Using the method suggested in [4], it is easy to show that, at $\langle \mathscr{E}^{(\nu)} \rangle = 0$, we have

$$\varphi = \frac{f-h}{1-h} + (1-h)\frac{\langle \mathscr{E}_x^{(y)} \rangle^{(1)}}{\langle E_{0y}^{(y)} \rangle}. \quad (18)$$

Here, f is given by (3), and $\mathscr{E}^{(\nu)}(\mathbf{r})$, by (13). A comparison of the φ values calculated by (5) and (18) provides a means of controlling the correctness of $\mathbf{E}_1^{(\nu)}(\mathbf{r})$ correction calculations.

The method suggested in [4] can also be used to show that the derivative of $\varphi(p, h)$ with respect to h is expressed through $\mathbf{E}_1^{(\nu)}(\mathbf{r})$ [more exactly, through $\mathscr{E}^{(\nu)}(\mathbf{r})$]:

$$\frac{\partial\varphi}{\partial h} = -\frac{1}{h}\frac{\langle \mathbf{E}_0^{(x)}\mathscr{E}^{(y)} - \mathbf{E}_0^{(y)}\mathscr{E}^{(x)}\rangle^{(1)}}{\langle E_{0x}^{(x)}\rangle\langle E_{0y}^{(y)}\rangle}. \quad (19)$$

Equation (19) is valid at $\langle\mathscr{E}^{(x)}\rangle = \langle\mathscr{E}^{(y)}\rangle = 0$. Calculations of the $\partial\varphi/\partial h$ derivative by (19) allows us to obviate the necessity of laborious numerical differentiation and study the $\varphi(p, h)$ function in more detail, also in the critical region.

3. SIMULATION OF GALVANOMAGNETIC PHENOMENA

Studies of various properties of inhomogeneous media by numerical methods are as a rule performed for lattice models. For instance, the conductivity of binary systems was studied by simulating cubic lattices with randomly distributed bonds of two types (bonds with conductivities σ_1 and σ_2) [8] (also see [5]). Importantly, at a low concentration of one of the components, a separate "impurity" bond gives the same contribution to effective conductivity as a spherical inclusion in the continuous problem. This observation inspires hope that such a lattice model can correctly reproduce the principal features of the dependence of the conductivity of a binary composite on its arguments p and h in the whole range of their variations. It would be desirable to preserve the correspondence with the continuous model mentioned above also in lattice studies of the galvanomagnetic properties of binary media.

In this work, we suggest a technique for simulating galvanomagnetic phenomena with the use of a pair of lattices, main and auxiliary. The main lattice is primitive cubic, and its bonds are of the first type (conductivities σ_{x1}, σ_{z2}, and σ_{a1}) with probability p and of the second type (conductivities σ_{x2}, σ_{z2}, and σ_{a2}) with probability $(1 - p)$. The auxiliary lattice is also primitive cubic and is obtained from the main lattice by the transition to the lattice dual to it in the (x, y) plane and translation of vertical (parallel to the z axis) bonds (see Fig. 1). If bonds are distributed randomly, as is assumed in this work, the main and auxiliary lattices are interchangeable.

A discrete analogue of the direct current equation $\mathrm{div}\mathbf{j} = 0$ is the Kirchhoff law of the equality of the sum of currents coming to node $\mathbf{r}$ to the sum of currents flowing from $\mathbf{r}$. For a primitive cubic cell, the Kirchhoff law takes the form

$$\sum_{\Delta = \Delta_x, \Delta_y, \Delta_z} \{j_{\mathbf{r}, \mathbf{r}+\Delta} - j_{\mathbf{r}-\Delta, \mathbf{r}}\} = 0, \quad (20)$$

where the summation is over the nearest neighbors; that is, $\Delta_x = (1, 0, 0)$, $\Delta_y = (0, 1, 0)$, and $\Delta_z = (0, 0, 1)$. In (20), $j_{\mathbf{r}, \mathbf{r}+\Delta}$ is the current along the bond that connects nodes $\mathbf{r}$ and $\mathbf{r} + \Delta$.

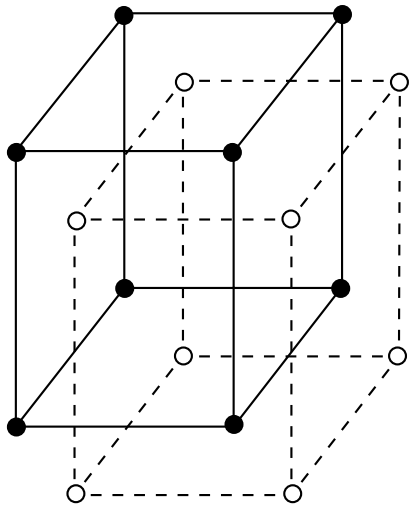

Fig. 1. Elements of the main (solid lines) and auxiliary (dashed lines) lattices.

Let each node $\mathbf{r}$ of the main lattice be assigned potential $V_\mathbf{r}$ and, accordingly, each

$$\rho = \mathbf{r} + \frac{\Delta_x}{2} - \frac{\Delta_y}{2}$$

node of the auxiliary lattice be assigned potential $\tilde{V}_\rho$. The equalities valid for the continuous model at $\mathbf{H} \neq 0$, namely,

$$j_x = \sigma_x E_x + \sigma_a E_y, \quad j_y = -\sigma_a E_x + \sigma_x E_y,$$
$$j_z = \sigma_z E_z,$$

where $\mathbf{E} = -\nabla V(\mathbf{r})$, then have the discrete analogues

$$\begin{aligned} j_{\mathbf{r}, \mathbf{r}+\Delta_x} &= \sigma^x_{\mathbf{r}, \mathbf{r}+\Delta_x}(V_\mathbf{r} - V_{\mathbf{r}+\Delta_x}) + \sigma^a_{\mathbf{r}, \mathbf{r}+\Delta_x}(\tilde{V}_\rho - \tilde{V}_{\rho+\Delta_y}), \\ j_{\mathbf{r}, \mathbf{r}+\Delta_y} &= -\sigma^a_{\mathbf{r}, \mathbf{r}+\Delta_y}(\tilde{V}_{\rho-\Delta_x+\Delta_y} - \tilde{V}_{\rho+\Delta_y}) \\ &\quad + \sigma^x_{\mathbf{r}, \mathbf{r}+\Delta_y}(V_\mathbf{r} - V_{\mathbf{r}+\Delta_y}), \\ j_{\mathbf{r}, \mathbf{r}+\Delta_z} &= \sigma^z_{\mathbf{r}, \mathbf{r}+\Delta_z}(V_\mathbf{r} - V_{\mathbf{r}+\Delta_z}). \end{aligned} \quad (21)$$

Here, $\sigma^{\gamma}_{\mathbf{r},\,\mathbf{r}+\Delta}$ ($\gamma = x, z, a$) is the conductivity of the bond between nodes $\mathbf{r}$ and $\mathbf{r}+\Delta$, and $j_{\mathbf{r},\,\mathbf{r}+\Delta_\alpha}$ ($\alpha = x, y, z$) are the currents flowing from node $\mathbf{r}$. Expressions for currents $j_{\mathbf{r}-\Delta_a,\,\mathbf{r}}$ coming to node $\mathbf{r}$ follow from (21), where the substitutions $\mathbf{r} \longrightarrow \mathbf{r} - \Delta_\alpha$ ($\alpha = x, y, z$) and $\rho \longrightarrow \rho - \Delta_\alpha$ ($\alpha = x, y$) should be made.

Substituting $j_{\mathbf{r},\,\mathbf{r}+\Delta_\alpha}$ from (21) and the corresponding expressions for $j_{\mathbf{r}-\Delta_a,\,\mathbf{r}}$, into (20) yields

$$\sum_{\Delta = \pm\Delta_x, \pm\Delta_y} = \sigma^{x}_{\mathbf{r},\,\mathbf{r}+\Delta}(V_{\mathbf{r}} - V_{\mathbf{r}+\Delta})$$

$$+ \sum_{\Delta = \pm\Delta_z} \sigma^{z}_{\mathbf{r},\,\mathbf{r}+\Delta}(V_{\mathbf{r}} - V_{\mathbf{r}+\Delta}) \qquad (22)$$

$$= -\sigma^{a}_{\mathbf{r},\,\mathbf{r}+\Delta_x}(\tilde{V}_{\boldsymbol{\rho}} - \tilde{V}_{\boldsymbol{\rho}+\Delta_y}) - \sigma^{a}_{\mathbf{r}-\Delta_x,\,\mathbf{r}}(\tilde{V}_{\boldsymbol{\rho}-\Delta_x} - \tilde{V}_{\boldsymbol{\rho}-\Delta_x+\Delta_y})$$

$$+ \sigma^{a}_{\mathbf{r},\,\mathbf{r}+\Delta_y}(\tilde{V}_{\boldsymbol{\rho}-\Delta_x+\Delta_y} - \tilde{V}_{\boldsymbol{\rho}+\Delta_y}) - \sigma^{a}_{\mathbf{r}-\Delta_y,\,\mathbf{r}}(\tilde{V}_{\boldsymbol{\rho}-\Delta_x} - \tilde{V}_{\boldsymbol{\rho}}).$$

Similarly, we find for the auxiliary lattice

$$\sum_{\Delta = \pm\Delta_x, \pm\Delta_y} \sigma^{x}_{\boldsymbol{\rho},\,\boldsymbol{\rho}+\Delta}(\tilde{V}_{\boldsymbol{\rho}} - \tilde{V}_{\boldsymbol{\rho}+\Delta})$$

$$+ \sum_{\Delta = \pm\Delta_z} \sigma^{z}_{\boldsymbol{\rho},\,\boldsymbol{\rho}+\Delta}(\tilde{V}_{\boldsymbol{\rho}} - \tilde{V}_{\boldsymbol{\rho}+\Delta}) \qquad (23)$$

$$= -\sigma^{a}_{\boldsymbol{\rho},\,\boldsymbol{\rho}+\Delta_x}(V_{\mathbf{r}+\Delta_x-\Delta_y} - V_{\mathbf{r}+\Delta_x}) + \sigma^{a}_{\boldsymbol{\rho}-\Delta_x,\,\boldsymbol{\rho}}(V_{\mathbf{r}-\Delta_y} - V_{\mathbf{r}})$$

$$- \sigma^{a}_{\boldsymbol{\rho},\,\boldsymbol{\rho}+\Delta_y}(V_{\mathbf{r}} - V_{\mathbf{r}+\Delta_x}) - \sigma^{a}_{\boldsymbol{\rho}-\Delta_y,\,\boldsymbol{\rho}}(V_{\mathbf{r}-\Delta_y} - V_{\mathbf{r}+\Delta_x-\Delta_y}).$$

In accordance with the procedure used to construct the auxiliary lattice, we can write

$$\sigma^{\gamma}_{\boldsymbol{\rho},\,\boldsymbol{\rho}+\Delta_x} = \sigma^{\gamma}_{\mathbf{r}+\Delta_x-\Delta_y,\,\mathbf{r}+\Delta_x},$$

$$\sigma^{\gamma}_{\boldsymbol{\rho},\,\boldsymbol{\rho}+\Delta_y} = \sigma^{\gamma}_{\mathbf{r},\,\mathbf{r}+\Delta_x},$$

$$\sigma^{\gamma}_{\boldsymbol{\rho}-\Delta_x,\,\boldsymbol{\rho}} = \sigma^{\gamma}_{\mathbf{r}-\Delta_y,\,\mathbf{r}},$$

$$\sigma^{\gamma}_{\boldsymbol{\rho}-\Delta_y,\,\boldsymbol{\rho}} = \sigma^{\gamma}_{\mathbf{r}-\Delta_y,\,\mathbf{r}+\Delta_x-\Delta_y}, \ldots$$

(where $\gamma = x, y, a$), and $\sigma^{z}_{\boldsymbol{\rho},\,\boldsymbol{\rho}\pm\Delta_z} = \sigma^{z}_{\mathbf{r},\,\mathbf{r}\pm\Delta_z}$.

Simultaneously solving (22) and (23) with the corresponding boundary conditions allows us to find the $V_{\mathbf{r}}$ and $\tilde{V}_{\boldsymbol{\rho}}$ potentials, which, in turn, makes it possible to calculate the galvanomagnetic characteristics of the lattice model under consideration. Note that (22) and (23) are valid at all $\mathbf{r}$ and $\boldsymbol{\rho}$ points, probably, except the boundary nodes (see Section 4).

If $\sigma^{a}_{\mathbf{r},\,\mathbf{r}+\Delta}$ and $\sigma^{a}_{\boldsymbol{\rho},\,\boldsymbol{\rho}+\Delta}$ do not depend on the coordinates, the right-hand sides of (22) and (23) equal zero, and the σ^{a} Hall component in the equation for the potentials vanishes. For this reason, the substitution

$$\begin{aligned} \sigma^{a}_{\mathbf{r},\,\mathbf{r}+\Delta} &\longrightarrow \sigma^{a}_{\mathbf{r},\,\mathbf{r}+\Delta} + \text{const}, \\ \sigma^{a}_{\boldsymbol{\rho},\,\boldsymbol{\rho}+\Delta} &\longrightarrow \sigma^{a}_{\boldsymbol{\rho},\,\boldsymbol{\rho}+\Delta} + \text{const} \end{aligned} \qquad (24)$$

does not change (22) and (23) and leaves the $V_{\mathbf{r}}$ and $\tilde{V}_{\boldsymbol{\rho}}$ potentials unchanged, although it transforms currents (21) (and the corresponding expressions for the $\tilde{j}_{\boldsymbol{\rho},\,\boldsymbol{\rho}+\Delta}$ currents) in an obvious way. An analogue of these substitutions in the continuous problem is the symmetry transformation [4] $\mathbf{E} = \mathbf{E}'$, $\mathbf{j} = \mathbf{j}' + \hat{C}\mathbf{E}'$, where $\hat{C}$ is a coordinate-independent antisymmetric tensor. This transformation does not change the direct current equation $\mathrm{curl}\mathbf{E} = 0$, $\mathrm{div}\mathbf{j} = 0$. The conductivity tensor is then transformed as $\hat{\sigma}(\mathbf{r}) \longrightarrow \hat{\sigma}'(\mathbf{r}) = \hat{\sigma}(\mathbf{r}) - \hat{C}$, which is equivalent to substitution (24). The existence of such a transformation, in particular, means that the correction to electric field strength linear in $\mathbf{H}$, $\mathbf{E}_1(\mathbf{r})$ is proportional to $\sigma_{a1} - \sigma_{a2}$.

This circumstance can be used as follows. Let us select the Hall component of the conductivity tensor of the second component σ_{a2} (or σ_{a1}) taken with the opposite sign as const in (24) and achieve the vanishing of all terms that refer to second-type (or first-type) bonds in the right-hand parts of Eqs. (22) and (23). This procedure can also be used to somewhat simplify calculations in numerically analyzing system (22), (23).

To conclude this section, note that the solution to the problem of the potential in the main (and, accordingly, auxiliary) lattice with one "defect" bond by (22) and (23) almost fully coincides with the solution to a similar continuous problem (e.g., see [9]). The only difference is the replacement of depolarization coefficients $n^{(\alpha)}$ [10] by their lattice analogues $N^{(\alpha)}$ (at $\sigma_x = \sigma_y \neq \sigma_z$),

$$N^{(z)} = \int_{-\pi}^{\pi}\int\int \frac{\sigma_z(1-\cos k_z)}{\sigma_x[(1-\cos k_x)+(1-\cos k_y)]+\sigma_z(1-\cos k_z)} \frac{d\mathbf{k}}{(2\pi)^3},$$

$$N^{(x)} = N^{(y)} = \frac{1}{2}(1 - N^{(z)}). \qquad (25)$$

The $N^{(\alpha)}$ values are close to the corresponding $n^{(\alpha)}$ coefficients at all $\sigma_x/\sigma_z \lesssim 1$. In particular, both $N^{(x)} = N^{(y)} = N^{(z)}$ and $n^{(x)} = n^{(y)} = n^{(z)}$ equal 1/3 at $\sigma_x = \sigma_y = \sigma_z$.

4. NUMERICAL EXPERIMENT ORGANIZATION

In this work, the numerical experiment was performed for a pair of primitive cubic cells, both of dimensions $N \times N \times N = 51 \times 51 \times 51$ nodes or, accordingly, $50 \times 50 \times 50$ bonds. In the general case of not weak magnetic fields **H**, systems (22) and (23) for $V_{\mathbf{r}}$ and $\tilde{V}_{\boldsymbol{\rho}}$ should be solved simultaneously. In a weak magnetic field, system (22), (23) can be solved using perturbation theory, by expanding in powers of **H**. The $V_{\mathbf{r}}$ and $\tilde{V}_{\boldsymbol{\rho}}$ potentials are then represented by the series

$$V_{\mathbf{r}} = V_{\mathbf{r}}^{(0)} + V_{\mathbf{r}}^{(1)} + \ldots, \quad \tilde{V}_{\boldsymbol{\rho}} = \tilde{V}_{\boldsymbol{\rho}}^{(0)} + \tilde{V}_{\boldsymbol{\rho}}^{(1)} + \ldots, \quad (26)$$

where $V_{\mathbf{r}}^{(n)}$ and $\tilde{V}_{\boldsymbol{\rho}}^{(n)}$ are the terms of the nth order in **H**.

In the approximation zeroth with respect to **H**, the $V_{\mathbf{r}}^{(0)}$ potentials are obtained from the system

$$\sum_{\boldsymbol{\Delta}} \sigma_{\mathbf{r},\,\mathbf{r}+\boldsymbol{\Delta}}(V_{\mathbf{r}}^{(0)} - V_{\mathbf{r}+\boldsymbol{\Delta}}^{(0)}) = 0, \quad (27)$$

where $\sigma_{\mathbf{r},\,\mathbf{r}+\boldsymbol{\Delta}}$ is the conductivity of the bond between nodes **r** and **r** + **Δ** at **H** = 0; the summation in (27) is over all the nearest neighbors. The $\sigma_{\mathbf{r},\,\mathbf{r}+\boldsymbol{\Delta}}$ value equals σ_1 with probability p ("pure" bonds) and σ_2 with probability $1 - p$ ("defect" bonds). Nodes of the two opposite external cell faces normal to the x axis are assigned constant potential values, 0 and 1, respectively. Periodic boundary conditions are set in the directions along axes y and z.

For performing calculations, system (27) is written as in [5], in the quasi-one-dimensional form

$$\hat{A}\mathbf{v}^{(0)} = \mathbf{b}^{(0)}. \quad (28)$$

Here, $\hat{A}$ is an $M \times M$ square matrix (so-called banded matrix), where $M = (N-1)^2(N-2)$. Vector $\mathbf{v}^{(0)}$ is a column of M elements representing the unknown potentials $V_{\mathbf{r}}^{(0)}$; vector $\mathbf{b}^{(0)}$ is a column of M elements of which only $(N-1)^2$ elements are nonzero. The right-hand side of (28) is nonzero because system (27) is inapplicable to nodes situated on the outside cell faces normal to the x axis.

The problem of finding zeroth-approximation potentials $\tilde{V}_{\boldsymbol{\rho}}^{(0)}$ satisfying the equations

$$\sum_{\boldsymbol{\Delta}} \sigma_{\boldsymbol{\rho},\,\boldsymbol{\rho}+\boldsymbol{\Delta}}(\tilde{V}_{\boldsymbol{\rho}}^{(0)} - \tilde{V}_{\boldsymbol{\rho}+\boldsymbol{\Delta}}^{(0)}) = 0 \quad (29)$$

in auxiliary lattice nodes is formulated similarly. The boundary potential values (0 and 1) are then assigned to nodes situated on the opposite outside auxiliary lattice faces normal to the y axis, and periodic boundary conditions are set in the x and z directions. For computational purposes, system (29) is also written in the quasi-one-dimensional form

$$\hat{\tilde{A}}\tilde{\mathbf{v}}^{(0)} = \tilde{\mathbf{b}}^{(0)}. \quad (30)$$

The $\hat{\tilde{A}}$ matrix and $\tilde{\mathbf{v}}^{(0)}$ and $\tilde{\mathbf{b}}^{(0)}$ vectors are constructed similarly to those present in (28).

Systems (28) and (30) were solved on a computer using an iterative technique. As in [5], the Chebyshev method for polynomial acceleration of the main iterative process [6] was used. The $V_{\mathbf{r}}^{(0)}$ and $\tilde{V}_{\boldsymbol{\rho}}^{(0)}$ potentials obtained in the computations were, in particular, used to determine the φ function by (5), which was one of the methods for checking correctness of calculations (see below). However, most importantly, these values were used as "seed" potentials in calculating corrections to $V_{\mathbf{r}}^{(0)}$ and $\tilde{V}_{\boldsymbol{\rho}}^{(0)}$ linear in **H**.

In the approximation linear in **H**, $V_{\mathbf{r}}^{(1)}$ are given by the system

$$\begin{aligned}
&\sum_{\boldsymbol{\Delta}} \sigma_{\mathbf{r},\,\mathbf{r}+\boldsymbol{\Delta}}(V_{\mathbf{r}}^{(1)} - V_{\mathbf{r}+\boldsymbol{\Delta}}^{(1)}) \\
&= -\sigma^a_{\mathbf{r},\,\mathbf{r}+\boldsymbol{\Delta}_x}(\tilde{V}_{\boldsymbol{\rho}}^{(0)} - \tilde{V}_{\boldsymbol{\rho}+\boldsymbol{\Delta}_y}^{(0)}) \\
&+ \sigma^a_{\mathbf{r}-\boldsymbol{\Delta}_x,\,\mathbf{r}}(\tilde{V}_{\boldsymbol{\rho}-\boldsymbol{\Delta}_x}^{(0)} - \tilde{V}_{\boldsymbol{\rho}-\boldsymbol{\Delta}_x+\boldsymbol{\Delta}_y}^{(0)}) \\
&+ \sigma^a_{\mathbf{r},\,\mathbf{r}+\boldsymbol{\Delta}_y}(\tilde{V}_{\boldsymbol{\rho}-\boldsymbol{\Delta}_x+\boldsymbol{\Delta}_y}^{(0)} - \tilde{V}_{\boldsymbol{\rho}+\boldsymbol{\Delta}_y}^{(0)}) \\
&- \sigma^a_{\mathbf{r}-\boldsymbol{\Delta}_y,\,\mathbf{r}}(\tilde{V}_{\boldsymbol{\rho}-\boldsymbol{\Delta}_x}^{(0)} - \tilde{V}_{\boldsymbol{\rho}}^{(0)}),
\end{aligned} \quad (31)$$

which follows from (22). Let us use the procedure described in Section 3 and make the substitution $\sigma^a_{\mathbf{r},\,\mathbf{r}+\boldsymbol{\Delta}} \longrightarrow \sigma^a_{\mathbf{r},\,\mathbf{r}+\boldsymbol{\Delta}} - \sigma_{a2}$. This yields (31), whose right-hand side only contains nonzero terms that refer to bonds of the first type, and these terms are proportional to $(\sigma_{a1} - \sigma_{a2})$. Let us make one more substitution

$$V_{\mathbf{r}}^{(1)} = \frac{\sigma_{a1} - \sigma_{a2}}{\sigma_1} U_{\mathbf{r}}. \quad (32)$$

The equation for $U_{\mathbf{r}}$ that follows from (31) can be written in the quasi-one-dimensional form

$$\hat{A}\mathbf{u} = \mathbf{b}^{(1)}, \quad (33)$$

which does not contain the $(\sigma_{a1} - \sigma_{a2})/\sigma_1$ small parameter. Here, $\hat{A}$ is the same matrix as in (28), **u** is the column of $U_{\mathbf{r}}$ values, and $\mathbf{b}^{(1)}$ is the column originating from the right-hand side of (31). Note that, like $V_{\mathbf{r}}^{(1)}$, the $U_{\mathbf{r}}$ values are zero on the outside lattice faces normal to x.

Equation (33) only differs from (28) in the form of the right-hand side. This equation was therefore solved

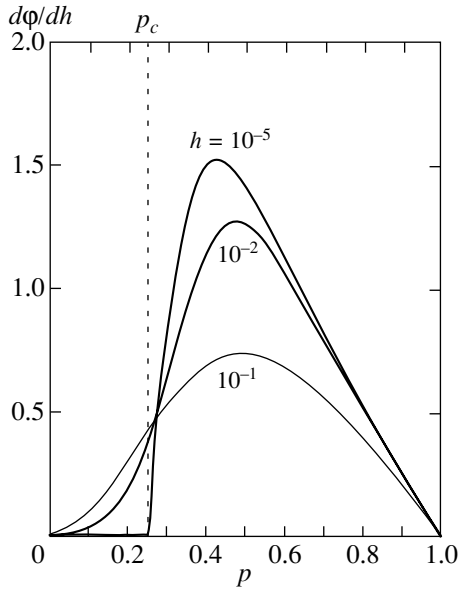

Fig. 2. Derivative $\partial\varphi/\partial h$ as a function of concentration p of the first component at three argument h values.

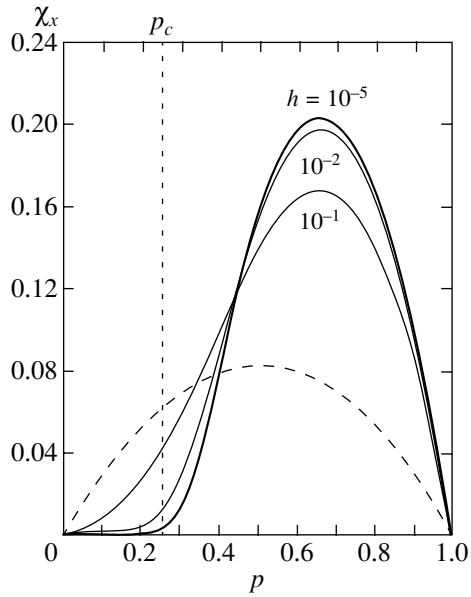

Fig. 3. Concentration dependence of $\chi_x(p, h)$ at three argument h values (solid lines) and dependence of χ_x on p at $h = 1$, $\chi_x(p, 1) = p(1 - p)/3$ (dashed line).

by exactly the same method as (28). A similar procedure was used to determine corrections $\tilde{V}_{\boldsymbol{\rho}}^{(1)}$ linear in $\mathbf{H}$ to the $\tilde{V}_{\boldsymbol{\rho}}^{(0)}$ potentials. The obtained $V_{\mathbf{r}}^{(1)}$ and $\tilde{V}_{\boldsymbol{\rho}}^{(1)}$ values were used to calculate the φ function, its derivative $\partial\varphi/\partial h$, and the χ_x function (see Section 5). The χ_z function was determined using a similar procedure to calculate $V_{\mathbf{r}}^{(0)}$ and $V_{\mathbf{r}}^{(1)}$ under the condition that the potential difference was applied in the z direction.

5. NUMERICAL EXPERIMENT RESULTS

When using (5), (14), (18), and (19) to calculate the corresponding effective galvanomagnetic characteristics of the lattices, we made the following substitutions:

$$\begin{aligned}
E_{0\alpha}^{(x)}(\mathbf{r}) &\longrightarrow V_{\mathbf{r}}^{(0)} - V_{\mathbf{r}+\boldsymbol{\Delta}_\alpha}^{(0)},\\
E_{0\alpha}^{(y)}(\mathbf{r}) &\longrightarrow \tilde{V}_{\boldsymbol{\rho}}^{(0)} - \tilde{V}_{\boldsymbol{\rho}+\boldsymbol{\Delta}_\alpha}^{(0)},\\
\mathscr{E}_\alpha^{(y)}(\mathbf{r}) &\longrightarrow U_{\mathbf{r}} - U_{\mathbf{r}+\boldsymbol{\Delta}_\alpha},\\
\mathscr{E}_\alpha^{(x)}(\mathbf{r}) &\longrightarrow \tilde{U}_{\boldsymbol{\rho}} - \tilde{U}_{\boldsymbol{\rho}+\boldsymbol{\Delta}_\alpha}
\end{aligned} \qquad (34)$$

($\alpha = x, y, z$) and performed the summation over nodes instead of the integration. In (34), $\tilde{U}_{\boldsymbol{\rho}}$ is related to $\tilde{V}_{\boldsymbol{\rho}}^{(1)}$ by (32). The χ_z function was determined by (15) using similar substitutions and the $V_{\mathbf{r}}^{(0)}$ and $V_{\mathbf{r}}^{(1)}$ potentials calculated on the condition that the potential difference was applied along z.

The determination of $\varphi(p, h)$ by (5) and (18) and a comparison of the results with those obtained in [5] showed that all three $\varphi(p, h)$ functions coincided in the whole range of argument p and h variations within the error of calculations. This coincidence was, in particular, evidence of the validity of $\mathbf{E}_1(\mathbf{r})$ correction determination.

According to [4, 5], the $\varphi(p, h)$ function in the vicinity of the metal–dielectric phase transition ($h \ll 1$, $|\tau| \ll 1$, and $\tau = (p - p_c)/p_c$, where p_c is the critical concentration) behaves as follows within the framework of the similarity hypothesis:

$$\tau > 0, \quad \Delta_0 \ll \tau \ll 1:$$

$$\varphi = \tau^l\left\{C_0 + C_1\frac{h}{\tau^{t/s}} + \ldots\right\},$$

$$|\tau| \ll \Delta_0: \varphi = h^u\left\{c_0 + c_1\frac{\tau}{h^{s/t}} + \ldots\right\}, \qquad (35)$$

$$\tau < 0, \quad \Delta_0 \ll |\tau| \ll 1:$$

$$\varphi = \frac{h^2}{(-\tau)^r}\left\{D_2 + D_3\frac{h}{(-\tau)^{t/s}} + \ldots\right\},$$

where $\Delta_0 = h^{s/t}$ is the size of the smearing region [7] and t and s are the critical effective conductivity indices. The l, u, and r indices are related by two equations [4], which allow u and r to be expressed through l,

$$u = \frac{s}{t}l, \quad r = 2\frac{t}{s} - l. \qquad (36)$$

The critical conductivity indices can be estimated as (e.g., see [5])

$$t \approx 2, \quad s \approx 0.7 \quad q \approx 0.8, \tag{37}$$

where q is the third conductivity index related to t and s as [7] $q + t = t/s$. Processing the numerical experiment data on φ ([5] and this work) yields

$$\begin{aligned} l &= 3.7 \pm 0.4, \quad u = 1.3 \pm 0.1, \quad r = 1.7 \pm 0.2, \\ C_0 &= 0.3 \pm 0.3, \quad c_0 = 1.4 \pm 0.7, \\ D_2 &= 1.5 \pm 0.8. \end{aligned} \tag{38}$$

The $\partial\varphi/\partial h$ derivative calculated by (19) is shown in Fig. 2. The critical behavior of the $\partial\varphi/\partial h$ value is determined by differentiating expansions (35). Processing the numerical experiment data on $\partial\varphi/\partial h$ by the corresponding equations gives

$$\begin{aligned} l - \frac{t}{s} &= 0.9 \pm 0.6, \quad u - 1 = 0.33 \pm 0.1, \\ r &= 1.8 \pm 0.3, \quad C_1 = 2.9 \pm 2.1, \\ uc_0 &= 1.8 \pm 0.8, \quad 2D_2 = 2.8 \pm 0.6. \end{aligned} \tag{39}$$

Considering fairly large errors in index and, especially, coefficient values, a comparison of (38) with (39) and (37) shows that the results obtained by two different methods satisfactorily agree with each other. Note that the C_1 coefficient can only be determined from the data on $\partial\varphi/\partial h$.

The $\chi_x(p, h)$ and $\chi_z(p, h)$ functions calculated by (14) and (15) are shown in Figs. 3 and 4. In the vicinity of the metal–dielectric phase transition, χ_x and χ_z should be expected to show a critical behavior of the form

$$\begin{aligned} &\tau > 0, \quad \Delta_0 \ll \tau \ll 1\text{: } \chi_x \approx X_0 \tau^{t_x}, \ \chi_z \approx Z_0 \tau^{t_z}, \\ &|\tau| \ll \Delta_0\text{: } \chi_x \approx x_0 h^{s_x}, \ \chi_z \approx z_0 h^{s_z}, \\ &\tau < 0, \quad \Delta_0 \ll |\tau| \ll 1\text{:} \\ &\chi_x \approx X_2 \frac{h^2}{(-\tau)^{q_x}}, \quad \chi_z \approx Z_2 \frac{h^2}{(-\tau)^{q_z}}. \end{aligned} \tag{40}$$

Here, only the main terms of the corresponding expansions are given. The critical indices in expansions (40) are related by equations similar to (36),

$$\begin{aligned} s_x &= \frac{s}{t} t_x, \quad q_x = 2\frac{t}{s} - t_x, \\ s_z &= \frac{s}{t} t_z, \quad q_z = 2\frac{t}{s} - t_z. \end{aligned} \tag{41}$$

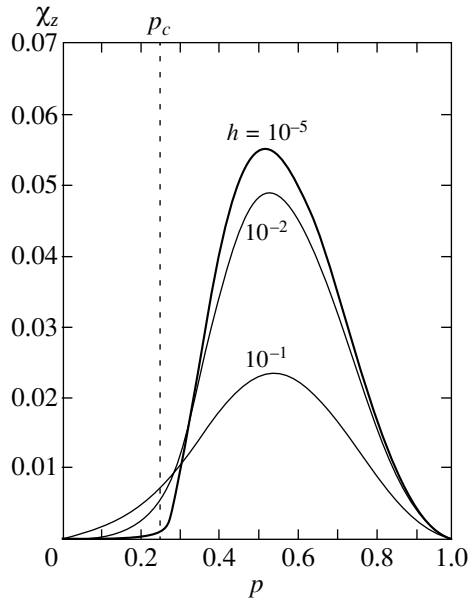

Fig. 4. Concentration dependence of $\chi_z(p, h)$ at three argument h values.

Processing the numerical experiment data on $\chi_x(p, h)$ and $\chi_z(p, h)$ in the critical region yields

$$\begin{aligned} t_x &= 1.9 \pm 0.1, \quad s_x = 0.74 \pm 0.03, \\ q_x &= 3.3 \pm 1.1, \quad X_0 = 0.26 \pm 0.05, \\ x_0 &= 0.26 \pm 0.04, \quad X_2 = 2.1 \pm 1.1, \end{aligned} \tag{42}$$

$$\begin{aligned} t_z &= 1.86 \pm 0.14, \quad s_z = 0.67 \pm 0.08, \\ q_z &= 3.4 \pm 1.2, \quad Z_0 = 0.3 \pm 0.1, \\ z_0 &= 0.3 \pm 0.2, \quad Z_2 = 1.8 \pm 1.1. \end{aligned} \tag{43}$$

The critical indices in (42) and (43) satisfy equations (41) within the error of their determination.

For randomly inhomogeneous two-component media, χ_x and χ_z satisfy the equalities [5]

$$\begin{aligned} \chi_x(p, h) &= \frac{1}{h}\chi_x\left(1 - p, \frac{1}{h}\right), \\ \chi_z(p, h) &= \frac{1}{h}\chi_z\left(1 - p, \frac{1}{h}\right). \end{aligned} \tag{44}$$

These equalities can be used to determine the $\chi_x(p, h)$ and $\chi_z(p, h)$ functions at $h > 1$ if their values at $h < 1$ are known in the whole range of concentration variations.

REFERENCES

1. B. I. Shklovskiĭ, Zh. Éksp. Teor. Fiz. **72**, 288 (1977) [Sov. Phys. JETP **45**, 152 (1977)].
2. A. S. Skal, Dokl. Akad. Nauk SSSR **260**, 602 (1981) [Sov. Phys. Dokl. **26**, 872 (1981)].

3. D. J. Bergman and D. Stroud, Phys. Rev. B **32**, 6097 (1985).
4. B. Ya. Balagurov, Zh. Éksp. Teor. Fiz. **93**, 1888 (1987) [Sov. Phys. JETP **66**, 1079 (1987)].
5. B. Ya. Balagurov and V. A. Kashin, Zh. Éksp. Teor. Fiz. **110**, 1001 (1996) [JETP **83**, 553 (1996)].
6. L. A. Hageman and D. M. Young, *Applied Iterative Methods* (Academic, New York, 1981; Mir, Moscow, 1986).
7. A. L. Efros and B. I. Shklovskii, Phys. Status Solidi B **76**, 475 (1976).
8. S. Kirkpatrick, Rev. Mod. Phys. **45**, 574 (1973).
9. B. Ya. Balagurov, Fiz. Tverd. Tela (Leningrad) **28**, 3012 (1986) [Sov. Phys. Solid State **28**, 1694 (1986)].
10. L. D. Landau and E. M. Lifshitz, *Course of Theoretical Physics*, Vol. 8: *Electrodynamics of Continuous Media* (Nauka, Moscow, 1992; Pergamon, New York, 1984).

Translated by V. Sipachev

Journal of Experimental and Theoretical Physics, Vol. 94, No. 3, 2002, pp. 673–676.
Translated from Zhurnal Éksperimental'noĭ i Teoreticheskoĭ Fiziki, Vol. 121, No. 3, 2002, pp. 779–783.

SOLIDS
Electronic Properties

Hall Effect in Three-Dimensional Layered Structures in Strong Magnetic Fields

S. E. Brener

Landau Institute for Theoretical Physics, Russian Academy of Sciences, Chernogolovka, Moscow oblast, 142432 Russia

e-mail: brener@itp.ac.ru

Received October 18, 2001

Abstract—A three-dimensional electron system with a corrugated-cylinder-type Fermi surface is considered. We show that the quantum Hall effect must be observed in such a system with a smooth random potential. Our results are in qualitative agreement with available experimental data. © *2002 MAIK "Nauka/Interperiodica".*

Strong magnetic fields open up possibilities for observing the quantum Hall effect (QHE) in three-dimensional (3D) layered structures. The possibility of observing the integer QHE in such structures was first pointed out by Azbel' [1]. The first experiments were carried out by Störmer *et al.* [2] on a GaAs/(AlGa)As superlattice; the three-dimensionality of the electron spectrum was checked experimentally. The QHE in a 3D layered system was also observed by Murzin *et al.* [3].

In this paper, we consider the integer QHE and peculiarities of the dependence of Hall conductivity σ_{xy} on the chemical potential in 3D systems with a smooth random potential in comparison with two-dimensional (2D) systems by using the semiclassical approach to localizing noninteracting electrons in a magnetic field. The following conditions are assumed to be satisfied:

$$l_H \ll L, \quad T \ll U_0.$$

Here, $l_H = (c\hbar/eH)^{1/2}$ is the magnetic length, L is the scale length of the random potential, T is the temperature, U_0 is the rms amplitude of the random potential $U(\mathbf{r})$, e is the electron charge, and c is the speed of light. In the 2D case where these conditions are satisfied, the electrons move along isolines of the random potential.

The dispersion law is taken in the form

$$\varepsilon = \frac{p_\perp^2}{2m_\perp} + t(p_z), \tag{1}$$

where $-t_0 \le t(p_z) \le t_0$. Here, p_z is the quasi-momentum along the magnetic field, and the band width t_0 is assumed to be small compared to the cyclotron energy $\hbar\omega_H$. To enable the localization of electrons, we also assume that $t_0 \ll U_0$.

In this case, the classical equations of electron motion are

$$\frac{dp_z}{dt} = -\frac{\partial U}{\partial z}, \quad \frac{dz}{\partial t} = \frac{dt(p_z)}{dp_z}, \tag{2}$$

$$\frac{d\mathbf{r}_\perp}{dt} = -\frac{\left[\frac{\partial U}{\partial \mathbf{r}_\perp} \times \mathbf{e}_z\right]c}{eH} + \frac{c[\mathbf{E} \times \mathbf{e}_z]}{H}. \tag{3}$$

Here, $\mathbf{e}_z$ is a unit vector along the magnetic field, and $\mathbf{E}$ is the electric field. By z and $\mathbf{r}_\perp$, we mean the coordinates of the leading center of the electron orbit. Note that these equations conserve the electron energy $\varepsilon = t(p_z) + U(\mathbf{r})$. Such equations were the subject of analysis in [4, 5]; in the former paper, the accuracy of these equations was estimated numerically. In [4], the motion along the z axis was assumed to be rapid compared to the motion perpendicular to the magnetic field. In this case, the motion has an adiabatic invariant,

$$\oint p_z dz = I(x, y),$$

where the integral is taken between turning points over z. Such an invariant must shape the projections of the electron trajectories onto the plane perpendicular to the magnetic field. However, as was pointed out in [5], this approach is too rough, because it disregards the possibility of an abrupt change of the turning points in z, which results in chaotization of the electron motion. Below, we assume the drift velocity perpendicular to the magnetic field to be of the order of the velocity along it, so the adiabatic approach becomes inapplicable.

In our problem, the percolation properties of the random potential play a significant role. In the 2D case, the unbounded electron trajectories carrying the current perpendicular to the electric field can take place only near the percolation threshold (for a potential whose statistical properties do not change with the substitution $U \longrightarrow -U$, the percolation threshold corresponds to $U = 0$) [6]. This leads to the QHE pattern [7] with cor-

rect values of the quantized Hall resistance. In this case, the transition between the plateaus occurs at a chemical potential close to $\hbar\omega_H(n+1/2)$ [i.e., near the $U(\mathbf{r}) = 0$ isolines], and the width of the transition region turns out to be small and determined either by quantum effects or by the applied electric field [8]. If we apply such reasoning to the 3D case, then, in contrast to the 2D case, the $U(\mathbf{r})$ = const level surfaces are definitely closed only when $U > U_c$ and $U < -U_c$ (we consider the symmetric case). Here, in contrast to the 2D case, the fraction of the volume occupied by open level surfaces is not zero but of the order of 1/2 [5]. If we are not interested in the detailed behavior of σ_{xy} at the boundary between the plateau and the transition region (see below for these details), then it will suffice to assume that all level surfaces are closed for $|U| > U_c$ and that there is one open level surface at each U for $|U| < U_c$; the set of such surfaces occupies a finite volume, which we call conductive for the reasons that will become clear below.

In contrast to the 2D case, the electrons do not move (to within the magnetic length) along level surfaces but get off them as $t(p_z)$ changes, so $\varepsilon - t_0 \le U \le \varepsilon + t_0$. [Here and below, ε is the sum of the potential energy of the electron and the kinetic energy of its motion along the magnetic field. We disregard the large $\hbar\omega_H(n+1/2)$, which does not change during the electron motion.] Under the condition $t_0 \ll U_0$, which is assumed to be satisfied, this is of little importance and the electron may be assumed to move along an level surface. Thus, the states with $\varepsilon > U_c + t_0$ and $\varepsilon < -U_c - t_0$ (or, ignoring t_0 compared to U_c, with $\varepsilon > U_c$ and $\varepsilon < -U_c$) are definitely localized. Since σ_{xy} does not change when the chemical potential varies in the region of localized states, these regions correspond to plateaus. When the chemical potential is between the plateaus, infinite current-carrying trajectories emerge. We take the ergodic hypothesis that the electron trajectory fills the entire energetically accessible space. This can be effected, for example, by short-range neutral impurities by which the electron can be elastically scattered.

In the absence of an external electric field, there is no average current because of statistical isotropy. In the semiclassical approximation, the average Hall current itself can be calculated from the formula

$$j_H = e\int_V \frac{d^3r}{V}\int_{-\pi\hbar/a}^{\pi\hbar/a}\frac{dp_z}{2\pi\hbar}\frac{d\mathbf{r}_\perp}{dt}n(p_z,\mathbf{r}), \tag{4}$$

where $d\mathbf{r}_\perp/dt$ is given by formula (3). Here, V is the volume of the 3D system; a is the lattice constant along the magnetic field; and $n(p_z, \mathbf{r})$ is the electron distribution function, which depends only on the electron energy $\varepsilon = U(\mathbf{r}) + t(p_z)$ (dissipation is ignored). At zero temperature,

$$\begin{aligned} n(p_z,\mathbf{r}) \equiv n(\varepsilon) &= 1/2\pi l_H^2 \ \text{ for } \ \varepsilon < \mu, \\ n(p_z,\mathbf{r}) \equiv n(\varepsilon) &= 0 \ \text{ otherwise} \end{aligned} \tag{5}$$

[μ is the chemical potential, which, as ε, is counted off from $\hbar\omega_H(n+1/2)$]. If the chemical potential is large and is in the gap of the density of states, so that the density is constant at any point in space, then, given that the first term on the right-hand side of Eq. (3) vanishes when averaged over space, it follows from formula (4) that

$$j_H = \frac{ce[\mathbf{E}\times\mathbf{e}_z]}{H}\frac{1}{2\pi l_H^2 a}.$$

This quantity gives a constant Hall conductivity on the plateau per filled Landau level:

$$\sigma_{xy} = \frac{e^2}{2\pi\hbar a}. \tag{6}$$

The Hall resistance changes with decreasing μ. At $\mu \approx U_c$, the chemical potential falls within the region of delocalized states, and some current-carrying states will be turned off with decreasing μ. Given (5), the expression for the average Hall current can be rewritten as

$$j_H = \int_{\varepsilon<\mu}\frac{d^3r}{V}\frac{dp_z}{2\pi\hbar}\frac{d\mathbf{r}_\perp}{dt}.$$

Let us pass from the integration over d^3r to the integration over dU with the substitution

$$\frac{d^3r}{V} \longrightarrow \mathcal{P}(U)dU,$$

where $\mathcal{P}(U)$ is the density of the random potential normalized to unity. We also take into account the fact that the average $d\mathbf{r}_\perp/dt$ is zero in the regions occupied by closed level surfaces and $c[\mathbf{E}\times\mathbf{e}_z]/H$ in the remaining regions, i.e., in the conductive volume. Since t_0 is small compared to U_0, we ignore the dependence of the integrand on p_z. Subtracting from the conductivity on the plateau (6) its part provided by the delocalized electron states with energies larger than the chemical potential, we finally obtain

$$\sigma_{xy}(\mu) = \frac{e^2}{2\pi\hbar a}\left(1-\gamma\int_\mu^{U_c}\mathcal{P}(U)dU\right). \tag{7}$$

Here, γ is a factor smaller than unity, which appears because not all level surfaces with $|U| < U_c$ belong to the conductive volume; γ depends weakly on the chemical potential unless it is close to the percolation thresholds. In what follows, we count off σ_{xy} from $ne^2/2\pi\hbar a$, where n is the number of Landau levels lying below the chemical potential. Similarly, increasing the chemical poten-

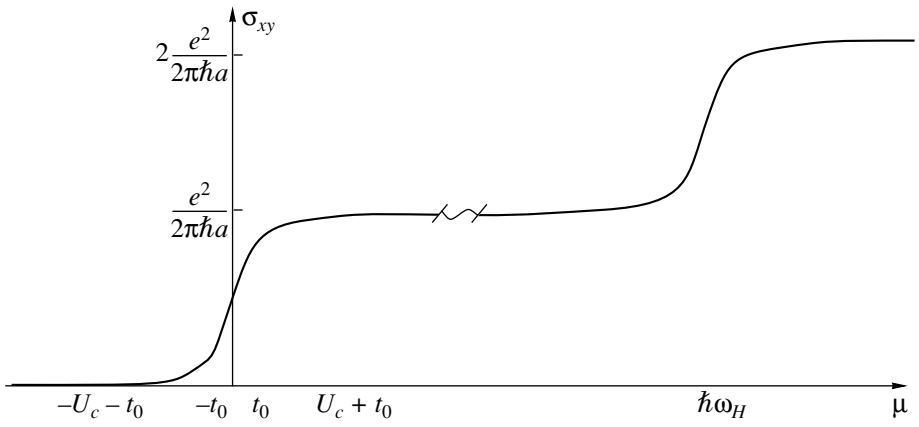

Hall conductivity versus chemical potential. The coordinate origin corresponds to $\mu = \hbar\omega_H(n + 1/2)$, $\sigma_{xy} = ne^2/2\pi\hbar a$.

tial from large negative values, we derive the following expression for the conductivity:

$$\sigma_{xy}(\mu) = \frac{e^2}{2\pi\hbar a}\gamma\int_{-U_c}^{\mu}\mathcal{P}(U)dU. \quad (8)$$

Expressions (7) and (8) are inapplicable in the immediate vicinity of the percolation thresholds, because we disregard t_0.

As was said above, γ is of the order of 1/2 virtually in the entire range $(-U_c; U_c)$. Therefore, using the well-known result of the percolation theory (see, e.g., [5, 6]),

$$\int_{-U_c}^{U_c}\mathcal{P}(U)dU \approx 0.7, \quad (9)$$

we can estimate $\sigma_{xy}(\mu = 0)$ from Eqs. (7) and (8). The first and second equations yield $(0.8–0.9)e^2/2\pi\hbar a$ and $(0.1–0.2)e^2/2\pi\hbar a$ respectively. The discrepancy stems from the fact that the electrons with energies in the range $(-t_0; t_0)$ have not only 3D conductivity channels but also 2D ones, similar to conventional channels in the 2D QHE [7, 8]. It thus follows that a sharper change in conductivity must be observed in a relatively narrow (no wider than $2t_0$) region in the vicinity of $\mu = 0$. The dependence $\sigma_{xy}(\mu)$ is schematically shown in the figure.

Let us consider the behavior of $\sigma_{xy}(\mu)$ in the vicinity of $\mu = -U_c - t_0$ (the vicinity of $U_c + t_0$ is considered in a similar way). Let $\mu = -U_c - t_0 + \delta$, where $\delta \lesssim t_0$. Now, we cannot ignore t_0 compared to U_0. The reasoning is the same as that used when deriving (7) from (4). We pass to the integration over dU over the region specified by the condition $\varepsilon < \mu$ but do not ignore the dependence of $n(\varepsilon)$ on p_z. It is also well known from the percolation theory [5] that the volume occupied by open level surfaces (the conductive volume) with $U \in (U_1; U_1 + dU)$ is zero for $|U_1| > U_c$ and proportional to $|(U_c - U_1)/U_c|^\beta dU$ near the percolation thresholds for $|U_1| < U_c$ with $\beta = 0.4$. Let us define the function $\mathcal{P}_\infty(U)$ in such a way that the conductive volume confined between U and $U + dU$ is $V\mathcal{P}_\infty(U)dU$. We obtain the domain of integration over U and p_z specified by the conditions

$$U + t(p_z) < \mu,$$
$$U > -U_c.$$

Thus, of importance are those values of p_z at which $t(p_z)$ are close to its minimum, where we may assume that

$$t(p_z) = -t_0 + \frac{p_z^2}{2m_\parallel},$$

and $1/m_\parallel$ is of the order of $t_0a^2/\hbar^2$. Passing to the variable $u = U + U_c$, we derive

$$j_H = \frac{ceE}{2\pi l_H^2 H}\int_{-\sqrt{2\delta m_\parallel}}^{\sqrt{2\delta m_\parallel}}\frac{dp_z}{2\pi\hbar}\int_0^{\delta - \frac{p_z^2}{2m_\parallel}}\mathcal{P}_\infty(u - U_c)du.$$

The function $P\mathcal{P}_\infty(U)$ in the domain under consideration is proportional to $[(U + U_c)/U_c]^\beta$. Hence, we find, to within a constant factor, that

$$\sigma_{xy} \sim \frac{e^2}{2\pi\hbar a}\frac{\delta^{\beta + 3/2}}{t_0^{1/2}U_0^{\beta + 1}} \approx \frac{e^2}{2\pi\hbar a}\frac{\delta^{1.9}}{t_0^{0.5}U_0^{1.4}}. \quad (10)$$

The difference between the Hall conductivity and its value on the plateau at $\mu = U_c + t_0 - \delta$ behaves in the same way.

The above estimate of the Hall conductivity is based on the neglect of quantum effects, with the most important of them being the possible electron localization along the magnetic field because of the quantum interference between the incident and scattered waves. As is well known from the theory of weak localization, a

magnetic field hinders the localization by destroying the phase coherence. This effect can be qualitatively estimated for a smooth random potential using the semiclassical approach. The displacement of the electron trajectory by δz from an level surface is of the order of $\delta z \sim Lt_0/U_0$, with the required time being

$$\tau \sim \delta z / \left(\frac{\partial t}{\partial p_z}\right) \sim \frac{L\hbar}{U_0 a}.$$

In this time, the electron displaces in the x, y plane by a distance

$$\delta r_\perp \sim \tau \frac{c}{eH}\frac{U_0}{L} \sim \frac{l_H^2}{a},$$

and the phase decoherence due to the magnetic field is

$$\delta\phi \sim \frac{e}{c\hbar} H \delta r_\perp^2 \sim \frac{l_H^2}{a^2}.$$

In the attainable magnetic fields at moderately large a, $\delta\phi$ is much larger than unity, implying that the interference corrections to the Hall conductivity are small. However, for $a \gtrsim l_H$, quantum effects will result in the motion being localized along the magnetic field and the above approach will be inapplicable. This may take place in superlattices with a large ($\gtrsim$30) number of atomic layers per each superlattice layer in strong ($\gtrsim$5 T) magnetic fields.

Experimentally, the dependence $\sigma_{xy}(H)$ rather than $\sigma_{xy}(\mu)$ is measured. It follows from (9), statistical symmetry of the potential, and the standard expression for the number of states per Landau level ($N = VeH/2\pi\hbar ca$) that the boundaries $H_{n\pm}$ of the nth plateau (if t_0 is ignored) are specified by the conditions

$$\frac{eH_{n\pm}}{2\pi\hbar a}(n \mp 0.15) = n_e.$$

Here, n_e is the bulk electron density. We see that the width of the first plateau is severalfold smaller than that in the 2D case and the widths of the next plateaus decrease in inverse proportion to n^2. Coupled with the fact that the condition $l_H \ll L$ is satisfied worse in weak magnetic fields, this explains why the authors of [2, 3] managed to observe only one or two plateaus.

The above reasoning shows that there are intrinsic factors in 3D layered structures responsible for the finite width of the transition region between the quantized Hall conductivities on the plateau, in contrast to the 2D case where the transition region can be made arbitrarily narrow by decreasing the temperature and the external electric field. This is consistent with the experimental data [2, 3] that give a smoother transition in the 3D case than in the 2D one.

ACKNOWLEDGMENTS

I wish to thank S.V. Iordansky for the statement of the problem and for fruitful discussions.

REFERENCES

1. M. Ya. Azbel', Solid State Commun. **54**, 127 (1985).
2. H. L. Störmer, J. P. Eisenstein, A. C. Gossard, *et al.*, Phys. Rev. Lett. **56**, 85 (1986).
3. S. S. Murzin, A. G. M. Jansen, and P. V. D. Linden, Phys. Rev. Lett. **80**, 2681 (1998).
4. M. Ya. Azbel' and O. Entin-Wohlman, Phys. Rev. B **32**, 562 (1985).
5. M. B. Isichenko, Rev. Mod. Phys. **64**, 961 (1992).
6. B. I. Shklovskii and A. L. Efros, *Electronic Properties of Doped Semiconductors* (Nauka, Moscow, 1979; Springer-Verlag, New York, 1984).
7. S. V. Iordansky, Solid State Commun. **43**, 1 (1982).
8. S. A. Trugman, Phys. Rev. B **27**, 7539 (1983).

Translated by V. Astakhov